SACEC

PROCEEDINGS

South African Chemical Engineering Congress 2021

20 - 22 September 2021
Virtual Congress

Editors:
LD van Dyk
CM Sheridan
KG Harding
JJ Scholtz

ISBN 978-1-991213-99-0

SAIChE
South African Institution of Chemical Engineers

Proceedings of the South African Chemical Engineering Congress 2021

20 – 22 September 2021

A virtual, international conference organised by the South African Institution of Chemical Engineers - an association for the advancement of Chemical Engineering in South Africa.

Editors: LD van Dyk, CM Sheridan, KG Harding and JJ Scholtz

Published by The South African Institution of Chemical Engineers

19 Lamone, Nature Street, North Riding, Johannesburg, 2170, Republic of South Africa

ISBN 978-1-991213-99-0 (Electronic)

All papers were peer-reviewed by two referees. The review process was a double-blind peer review process.

SCIENTIFIC COMMITTEE

M. Carsky
K. Harding
H. Mazema
L. van Dyk (Chair)
J. Case
D. Lokhat
J. Scholtz
D.S. van Vuuren
M. Chetty
T. Majozi
C.M. Sheridan (Chair)
E. Obwaka

LIST OF REVIEWERS

A. Adediran
B.F. Bakare
H. Brink
E. Chirwa
K. Harding
M. Lasich
T. Majozi
W. Mhike
K. Moothi
A.K. Naicker
F. Ntuli
J. Pocock
V. Russo
J. Scholtz
B. Srinivasan
K. Tumba
E. van Steen
D. Wright
S. Bada
M. Belaid
M. Carsky
M. Gadalla
Y. Isa
D. Lokhat
S. Marx
K. Moller
M. Moyo
K.S. Ng
E. Obwaka
J.H. Potgieter
Q. Reynolds
C.M. Sheridan
R. Srinivasan
L. van Dyk
D. Whitefield
S. Bandyopadhyay
D. Branken
M. Chetty
T. Goga
M. Krause
X. Liu
H. Mazema
K. Moodley
N. Muisa
J. Njalam'mano
B. Patel
R. Pott
S. Ramsuroop
J. Smith
N. Stacey
D.S. van Vuuren
M. Williams-Wynn

SAIChE

SACEC

SPONSORED BY:

SUGAR ILLOVO SOUTH AFRICA

AN ILLOVO SUGAR AFRICA COMPANY

MMrisk

80 YEARS pps SERVING PROFESSIONALS

EX NATURA UTILITAS

NWU®

UNIVERSITY OF THE WITWATERSRAND, JOHANNESBURG

UNIVERSITY OF JOHANNESBURG

DEPARTMENT OF CHEMICAL ENGINEERING TECHNOLOGY

UNIVERSITEIT VAN PRETORIA
UNIVERSITY OF PRETORIA
YUNIBESITHI YA PRETORIA

Faculty of Engineering, Built Environment and Information Technology

Fakulteit Ingenieurswese, Bou-omgewing en Inligtingtegnologie / Lefapha la Boetšenere, Tikologo ya Kago le Theknolotši ya Tshedimošo

SAIChE

SACEC

FOREWORD

The theme of the conference is titled “Entering the Anthropocene”. The Anthropocene is defined as a new geological period where human activity has a profound impact on the entire surface of the earth and is now the dominant geological force at play. This theme felt quite novel when we started planning for the congress four years ago, as a way of realigning our discipline for a future which is going to be very different to our past. Global events have, however, rapidly overtaken this sense of novelty. The COVID-19 pandemic interrupted and delayed our congress by 15 months, and it is now held in an entirely different format to what was initially envisaged.

Whilst the origins of SARS-COVID-2 are still somewhat uncertain, the possibility of a Coronavirus pandemic was envisaged before the pandemic. From a paper entitled “Bats, Coronaviruses, and Deforestation: Toward the Emergence of Novel Infectious Diseases?” by Afelt et. al., published in Frontiers in Microbiology in 2018: “The risk of emergence of a novel bat-CoV disease can therefore be envisioned.”; and “Even though the direct transmission of bat CoVs to humans has not been evidenced yet, the creation of conditions for more frequent encounters between bat CoVs, domestic animals and humans poses a significant threat for the future. Considering that the increasing impact of human activities on the ecosystems is unlikely to abate in SEA (Southeast Asia), it is necessary to increase CoV surveillance in wildlife, cattle, pets and humans to better understand the dynamics of interspecies transmission and improve risk assessment, early warning and intervention”. When I first read this paper, I felt utter astonishment. I wondered how the authors of the paper would have felt, given that we were unprepared for the scenario they described with such prescience. For me, the critical link is the connection between our activities and the impact to and response of the planetary system, with its highly complex interconnected feedback loops.

The consequence of our actions is profound. Remedying them, is an equally profound task. In 1921, an engineer named Thomas Midgely Jnr., working for General Motors discovered that adding TEL to petrol reduced engine knock. Midgley was awarded the ACS Nicholls medal in 1923 for this discovery and the result of this invention was the global introduction of TEL to fuel. Lead is a serious environmental contaminant with significant impact to human and environmental receptors. In the late 1920’s, the Frigidaire Corporation, a subsidiary of General Motors assembled a team of engineers and scientists to develop a new refrigerant due to the challenges with existing ones such as ammonia. This team included Thomas Midgely Jnr., and the resultant invention was a new, stable, non-toxic refrigerant called Freon – the original

CFC. For this work the Society for Chemistry awarded Midgely the Perkin medal in 1937. The consequence of this invention was the depletion of the ozone layer, which has had global consequences. Thomas Midgely Jnr., a chemical engineer has been described by Environmental historian J. R. McNeill, as that single organism that "had more impact on the atmosphere than any other single organism in Earth's history". It's worthy to note that both inventions were extremely useful towards solving very real problems.

To follow on from this, the Vienna Convention in 1985, followed by the Montreal Protocol in 1987, established the framework for international collaboration on removing substances which cause ozone layer depletion. Subsequently, the ozone hole is starting to recover. What makes this unique is that this was the first successfully implemented international protocol or treaty relating to protection of the environment in which, as a planet, we were able to collectively respond to a global risk.

Three weeks ago today, the UN announced that the era of leaded petrol was officially over, as Algeria, the final country adding lead to petrol ceased doing so. The UNEP spearheaded these efforts to eliminate TEL from fuel globally. Environmental levels of lead are declining globally, and it is through the efforts of engineers and scientists that we have been able to eliminate the use of both TEL and CFCs. I believe it is really important to highlight that we are able to enact positive change, not just negative.

It is humbling as an industry to acknowledge our role in contributing to the degradation of the earth planetary system. As a discipline, our role and mandate has always been to advance the quality of life for all through solving problems. These problems can be overcoming energy constraints, providing materials for our civilisation, providing transport solutions, providing food and water. The knock-on effects of providing these solutions, however, have sometimes been of greater magnitude than the problems being solved in the first instance. As a discipline, we are uniquely positioned to solve today's and tomorrow's problems by virtue of understanding the causality of these problems, and through what I believe is one of the chemical engineer's greatest attributes: a training which leads to the ability to recognise, understand and work within highly complex systems, as well as drilling down to understanding the very fine detail (as an example, chemical engineers design plants which require buses to drive across, whilst also being able to model the mass, heat and momentum transport across tiny particles within a single unit operation on such a plant).

In the same way that TEL and CFCs caused massive harm globally, chemical engineers can remedy and fix these local and global problems, through our professional problem-solving skills and by applying our discipline towards solving these problems. The future needs

chemical engineers.

In this conference, the largest category of submissions falls within the theme of ‘Environmental Process Engineering’. I think this reflects how we are changing as a discipline and an industry. It is with pride that we can call ourselves chemical engineers as we contribute towards solving the problems of our age: The Anthropocene.

Welcome to the South African Chemical Engineering Congress, 2021.

Craig Sheridan, FSAIChE.

SACEC 2021 Chair

20 September 2021

SAIChE

SACEC

LIST OF PAPERS PRESENTED

SAIChE

SACEC

SAIChE

SACEC

LIST OF POSTERS PRESENTATIONS

The following posters were presented at SACEC2021.

The removal of COD & anionic surfactants with chemical coagulation & electrochemical oxidation process for carwash wastewater: C. Steenberg and M. Aziz

Simulation studies on syngas and solid carbon production from waste tyre gasification using the fluidized bed, fixed bed, and rotary kiln reactors: L.I. Fajimi, A.T Akintola and B.O Oboirien

Magnetic induction and nanoparticles effects on anaerobic digestion of industrial wastewater for biogas production: E. Kweinor Tetteh and S. Rathilal

Treatment of petroleum refinery wastewater by application of combined electrocoagulation and electrooxidation and economical evaluation: S. Chakawa and M. Aziz

Energy recovery from solid waste via plasma gasification: S. Ncwane, I. Greeff and J. van der Walt

Simulation and modelling of syngas optimization using Aspen Plus: C.F. Nzeki T., M. Adonis and O. Oyekola

Improving the oxidation stability of Waste cooking oil based Biodiesel using natural antioxidants: E. Kongolo and O. Oyekola

Charaterization to determine sustainable technologies for edible and cosmetic oil waste treatment: P. Sigauke, E. Muzenda and T. Mamvura

Potential impact of the Covid-19 pandemic on plastic medical waste management in South Africa: A narrative review: Z.S. Mazhandu, E. Muzenda, M. Belaid and T. Nhubu

Valorisation of spent coffee grounds: N. Singh, M. Chetty and N. Deenadayalu

Heavy metal tolerance and Pb(II) mycoremediation potential of aspergillus piperis: M.M.M. de Wet and H. Brink

Microbial removal of Pb(II) using an upflow anaerobic sludge blanket (UASB) reactor: C. Hörstmann, J. Chimhundi, E. Chirwa and H. Brink

Fabrication and performance evaluation of tannin iron complex (TA-Fe III/ PES) UF membrane in treatment of oily wastewater: T. Makhani, O.O. Sadare, K. Moothi and M.O. Daramola

In pursuit of a low-cost carbon capture option in South Africa: N. Chiwaye, T. Majozi and M. O. Daramola

Thermogravimetric property and non-isothermal degradation kinetics of pine sawdust: U.M. Ikegwu, N.M. Okoro, M. Ozonoh and M.O. Daramola

Re-looking at distillation design in the new Anthropocene: N. Seedat, B. S. Kauchali and B. Patel

Pressure swing adsorption separation of acetylene and ethylene using cement hydrate: M. Lasich

Characterization of bio-oil generated from empty palm fruit bunch and the effect of particle sizes of the biomass on the composition and yield: E.S. Nelson, O. Sadare, A. Okewale, S. Iyuke and M.O. Daramola

Sugarcane bagasse ash derived nano silicon for application in inorganic-organic hybrid bulk hetero-junction solar cells: F Farirai, M. Airo, F. Otieno, M. Mupa and M.O. Daramola

Into the Insight of Advanced Analytical Techniques of Coal: Comparison of South African anthracite and bituminous coals using 13C SSNMR, FESEM-EDX, WAXRD, and UATR-FTIR: M. Mabuza, K. Premlall and M.O. Daramola

Modelling and simulation of leaching cobalt heterogenite ore in sulphuric acid: A.V. Chimedza

Virtual and remote labs: A SWOT analysis of the use of laboratory teaching software in higher education: T. Gore, L. Murugan, A. Singh, A. Philipp and A. Stark

A review of various feedstocks utilized in pyrolysis, gasification, and liquefaction processes: N. Nkosi, E. Muzenda, T. Nhubu and M. Belaid

Artificial Neural Network (ANN) for pressure-concentration-temperature- (P-C-T) curves of metal hydrides: Z.K. Simelane, A. Kolesnikov and M. Lototskyy

Fast pyrolysis of woody biomass in a dual fluidised bed – pilot scale commissioning

J. Reynders[1], M. Heydenrych[1]*, R. Merckel[1], Y-W. Wu[1]

[1] Department of Chemical Engineering, University of Pretoria, Pretoria 0001

*Corresponding author: mike.heydenrych@up.ac.za

ABSTRACT

There are several examples of commercial fast pyrolysis operations, but these processes tend to be complex particularly when scaled as well as thermally inefficient. A new fast pyrolysis process is described that has tight thermal integration, resulting in excellent thermal efficiency when converting biomass into liquid fuel and char. Silica sand serves as a heat transfer medium to transfer energy derived from the combustion of pyrolysis gases and char to the pyrolysis zone where solid biomass is converted to non-condensable gas, liquid fuel and char. This, combined with the heat recovery of combustion air, allows tight thermal integration of the processes in a single unit operation. In this paper, the performance of a pilot plant unit is discussed in terms of product mass and energy yield. The value of the char recovery is twofold: first, the char can be used to remediate the soil where the biomass was grown and return minerals to the soil, and second, it serves to sequestrate carbon, which makes the process carbon-negative overall.

Keywords: fast pyrolysis; dual fluidised bed; commissioning; performance analysis

1 INTRODUCTION

Fossil fuels have become synonymous with the chemical engineering industry. The implementation of cleverly engineered unit operations has created one of the biggest and longest-lasting industries in the world. Unfortunately, the world's resources are scarce and our impact on the earth is becoming more apparent to the point of becoming alarming. The engineering sectors are turning their attention towards more environmentally friendly operations and sustainable feedstocks to fuel the resource-consuming world that we live in.

First-generation biofuels such as biodiesel have made a remarkable impact on the world's view of sustainable resources, but biofuels generally depend on the resources currently used by the food industry. The infringement on agriculture is also a difficult issue as it affects the supply and demand for crops, which in turn may compromise food security. Thus, second-generation biofuels have arisen in order to alleviate the pressures on other industries with lignocellulosic biomass as the feedstock of choice. Agricultural, silvicultural, municipal and industrial wastes in the form of lignocellulosic biomass can find their place as a viable feed for second-generation biofuels.

One of the most frequently studied second-generation biofuel production techniques is pyrolysis. In this method, biomass is heated very rapidly to form pyrolysis products in the absence of oxygen. These

products consist of liquid, solid, and gaseous phases, namely bio-oil, biochar, and non-condensable gases (NCG) respectively. Research has been done in various pyrolysis projects at the University of Pretoria, focusing on novel scalable reactor designs and commissioning thereof. The project discussed here focuses on the construction and commissioning of the second-generation Combustion and Reduction Integrated Pyrolysis System (CRIPS 2) unit with additional analysis and determination of plant performance.

2 LITERATURE

2.1 Pyrolysis

Pyrolysis is simply the process of heating a feedstock, in this case lignocellulosic biomass, in the absence of oxygen. At temperatures ranging from 300 to 1000 °C, the biomass thermally decomposes and forms gaseous, liquid, and solid products through depolymerisation reactions (Dhyani & Bhaskar, 2018; Roy & Dias, 2017). There are three categories for biomass pyrolysis which are characterised by the heating rates at which the feedstock is processed. These categories have been dubbed fast/flash, intermediate, and slow pyrolysis. The heating rates alter the yields of solid, liquid, and gaseous products. Furthermore, the particle sizes used in the reactors must be taken into consideration as the heating rate of the solid feedstock is inversely proportional to the particle size. The parameters that define the process such as the heating rates and temperatures at which the reactions take place are shown in Table 1, and the product yields of the pyrolysis techniques are summarised in Table 2.

Table 1: Typical parameters and characteristics of pyrolysis processes (Roy & Dias, 2017)

Process Type	Temperature Range (°C)	Heating Rate (°C/min)	Residence Time
Slow Pyrolysis	300 – 550	0.1 – 0.8	5 min – 35 h
Intermediate Pyrolysis	300 – 450	3 – 5	10 min
Fast/Flash Pyrolysis	300 – 1000	10 – 1000	<2 s

Table 2: Typical product yields for pyrolysis processes (Roy & Dias, 2017)

Process Type	Biochar Yield (%)	Bio-oil Yield (%)	NCG Yield (%)
Slow Pyrolysis	25 – 35	20 – 50	20 – 50
Intermediate Pyrolysis	25 – 40	35 – 50	20 – 30
Fast/Flash Pyrolysis	10 – 25	60 – 75	10 – 30

2.2 Fast Pyrolysis

Fast and flash pyrolysis methods are geared toward maximum liquid yields, whereas the slower pyrolysis yields are focused more on the production of biochar which is not ideal for the liquid fuel industry. The biochar produced from fast pyrolysis is predominantly carbon due to the hydrocarbons

produced in the vapour phase (Singh & Chaudhary, 2017). Unlike the slower pyrolysis methods, fast pyrolysis requires very high heating rates, incredibly short residence times, and quick cooling to achieve high oil production rates. The residence time in the reactor must be minimised to reduce further cracking of the uncondensed pyrolysis oils. Furthermore, the hot vapour stream should be separated from the biochar to reduce cracking as the char has a high surface area which in turn catalyses such reactions. Finally, the vapours should be quenched to stop secondary reactions (Luque *et al*, 2016).

The reactor configurations for fast pyrolysis have been categorised as follows: screw/auger, ablative, rotating cone, bubbling fluidised bed, and circulating fluidised bed reactors (Bridgwater, 2013). The fluidised bed is the most well-understood reactor in fast pyrolysis research, and has also been proven to be the most successful reactor configuration (Agblevor, Besler & Wiselogel, 1996). Furthermore, the scale-up of fluidised bed reactors is the easiest compared to the other fast pyrolysis processes (Kan, Strezov & Evans, 2016). They come in two configurations: bubbling and circulating fluidised bed reactors. The general fluidised bed reactor uses a fluidised bed of sand and/or catalyst to transfer heat into the feedstock through conduction. The addition of catalysts in the bed will also assist in speeding up reactions – ideally the desired reactions.

2.3 Products of fast pyrolysis

Pyrolysis oil, colloquially termed bio-oil, is the condensate of the pyrolysis of biomass. It is a dark brown/red liquid reminiscent of crude oil. However, its composition is very similar to that of biomass feedstock. As noted in Table , the yield of pyrolysis oil reaches a maximum of 75 % for fast pyrolysis of woody biomass and its typical higher heating values are around 17MJ/kg. To put this into context, the typical higher heating value of crude oil is 42.1 MJ/kg (Culp, 1991). The relatively low heating values are largely attributed to the high water content (roughly 25 %) and the myriad of oxygenated compounds (Bridgwater, 2013). After reviewing the data collected by Dhyani & Bhaskar (2018), it was found that woody biomass produced bio-oil has the lowest variability in terms of energy content and composition and is thus a reliable benchmark for pyrolysis research.

3 EXPERIMENTAL PROCEDURE

3.1 Fast pyrolysis

The fast pyrolysis of woody biomass was performed using the novel CRIPS 2 dual-fluidised bed reactor as shown in Figure 1. The CRIPS 2 unit consists of two units namely the pyrolysis and combustion units with ancillary equipment such as the biomass feeding mechanism, bio-oil condenser and recirculation loop, and the flue extraction unit.

The novelty of the unit lies in the way in which it integrates heat by arranging the pyrolysis zone around the combustion zone in an annular fashion. The bed material is heated in the combustion unit with a combination of air, LPG, and residual biomass (in the form of biochar). The fluidisation of the

combustion bed material causes it to overflow through six angled holes in the refractory leading to the pyrolysis unit. The sand in the pyrolysis unit is fluidised using a gas distribution ring which also rotates the fluidised bed material with its angled nozzles. This setup ensures that the pyrolysis bed is well mixed and that the bed is constantly rotating clockwise around the unit towards a dead-zone. The dead-zone is an opening where the bed material falls into a controlled return screw feeder. From here, it is transported from the pyrolysis unit back to the combustion unit where it is reheated and decoked. The fluidisation gas in the pyrolysis unit is the recycled NCG formed from pyrolysis reactions and is recycled from the condensation loop. Biomass is fed perpendicular to the pyrolysis unit where it interacts with the hot fluidised bed material to form pyrolysis products, namely bio-oil, biochar, and NCG. These products leave the unit directly above the screw conveyor where they enter a cyclone which removes the biochar. The gaseous vapours then flow into a condensation loop where cold recycled bio-oil is mixed with the vapours to condense the new bio-oil. The remaining product is the NCG which is then recirculated to the pyrolysis distributor to fluidise the bed and again act as the carrier gas.

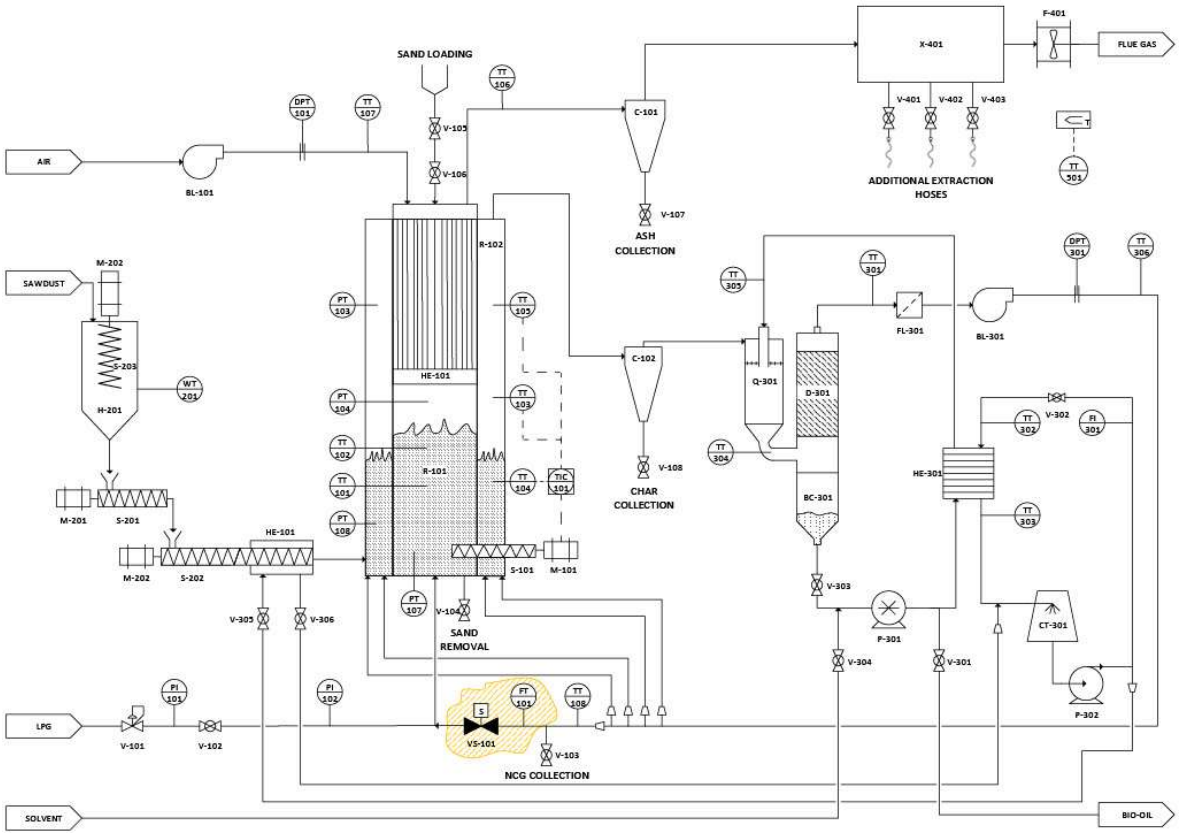

Figure 1: P&ID of the CRIPS 2 unit

The flue gas produced from the combustion of LPG, residual biomass, and air leaves the combustion unit and enters the air preheater (APH). The flue gas travels through the shell side of a modified shell and tube heat exchanger where its heat is exchanged with the incoming combustion air flowing through the tube side. Finally, the flue gas flows through a cyclone to separate any ash or sand fines before

leaving the vicinity via an extraction unit.

The commissioning of the CRIPS 2 unit took place over eight experimental runs. The first five runs aimed to keep the non-condensable gas recycle flow rate relatively high with varying biomass feed rates (Run-1 to 5). The last three runs (Run-6 to 8) reduced the NCG recycle flow rate to mitigate the overflow of the biochar cyclone while testing the effects of changing the biomass feed rate. All the experimental runs, however, operated at similar temperatures. The pyrolysis unit operated at 500 °C with the combustion unit operating between 700 to 900 °C depending on the energy demands for pyrolysis i.e., the energy required to heat the sand to maintain the pyrolysis unit at 500 °C.

3.2 Fast pyrolysis unit performance analysis

The performance of the CRIPS 2 unit is determined through mass and energy balances (see Figure 2).

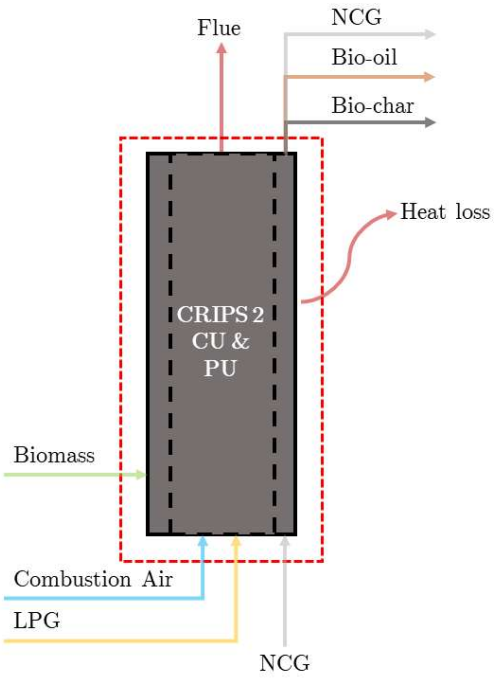

Figure 2: The control volume enclosing the CRIPS 2 unit illustrating the flow of mass and energy

The mass balance is determined by using various instruments such as differential pressure transmitters, load cells, and measuring the masses of the final product. The energy balances were determined from temperature data measured in the combustion and pyrolysis units with the aid of thermocouples and the outer reactor surface temperatures of the unit with the aid of an infrared thermometer. Experimental and literature values for the heat capacities and higher heating values in conjunction with the mass balance and temperatures allowed the system to be fully characterised. Temperature data in combination with thermal conduction (energy transferred between the refractory walls), convection, and radiation (energy transferred through the outer walls of the unit and ancillary equipment) was used to determine the thermal efficiency of the unit.

3.3 Starting materials

The feed material used during this project was *Eucalyptus grandis* in the form of very fine wood chips. The average diameter ranged from 448 to 489 µm and contained between 5.5 to 7.6 % moisture which falls in the range suitable for fast pyrolysis. The bed material used as the fluidisation medium consisted of silica sand with an average diameter of around 400 µm. LPG was used during the start-up process whereby the combustion and pyrolysis units are heated up to the correct temperatures for operation. Finally, ethylene glycol was employed as the initial solvent in the condensation of the bio-oils but was extensively diluted throughout the experimental runs.

3.4 Feedstock and product characterisation

Various methods were employed to characterise the biomass feedstock and the products from the commissioning of the CRIPS 2 unit. The results from the CRIPS 2 unit were compared to the literature values, the first-generation unit (CRIPS 1), and the data obtained from the spouted bed reactor (SBR) unit which was also developed by the Department of Bioprocessing (University of Pretoria). The SBR unit is a smaller laboratory-scale pyrolysis rig that allows for easier testing of various feedstocks and catalysts. Table 3 summarises the methods used for analysis and subsequent characterisation.

Table 3: Feedstock and products with their corresponding analytical methods

Analytical Method	Biomass	Bio-oil	Biochar	NCG	Ash
Particle size	X		X		
Moisture content	X	X	X		X
Ash content	X		X		X
ICP-OES	X		X		X
TGA	X		X		X
Bomb calorimetry	X	X	X		
BET	X		X		
GC				X	
Proximate Analysis		X			
Ultimate Analysis		X			

4 RESULTS AND DISCUSSION

4.1 Feed and product characteristics

4.1.1 Bio-oil

The CRIPS 2 unit produced pyrolysis oil in two phases that were not miscible with one another. The first phase was a watery liquid, deep red to brown in colour (depending on the amount of exposure to air) with a very strong pyrolysis odour. The second phase of the pyrolysis oil was a thick dark brown to black liquid reminiscent of honey which was completely opaque (Figure 3). The smell of this tar-like

substance was very similar to that of the first phase. The final experimental run consisted of reducing the NCG recycle flow rate and increasing the biomass throughput which produced the best results with an HHV of 7.2 MJ/kg (> 50 % moisture content) for the aqueous phase and up to 26 MJ/kg for the oil phase with an overall yield of approximately 30 %. Note that the incoming biomass had an HHV of approximately 18.96 MJ/kg on a dry basis.

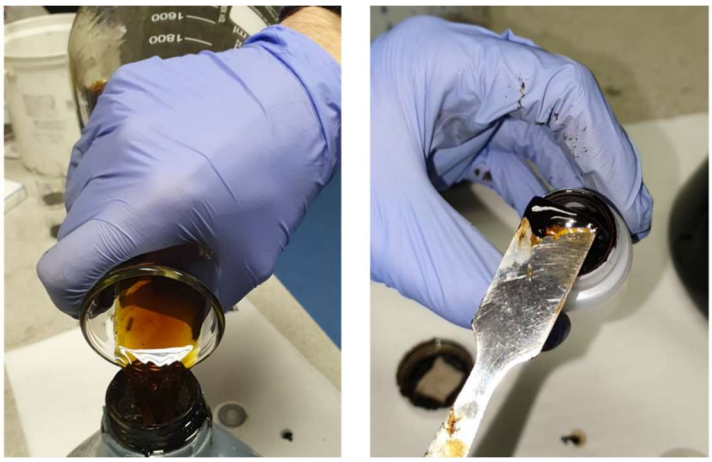

Figure 3: Left: Aqueous phase Right: Oil phase

4.1.2 Biochar

The biochar produced during the experimental runs showed promising results. The HHV of the biochar from the final run was approximately 22.5 MJ/kg which falls in the typical range for biochar energy content. This facilitates the possibility of using the solid product of pyrolysis as a means for renewable energy production, such as the case with charcoal. It was also observed that by altering the flow rates of biomass and NCG recirculation, one can gear the process to either produce more biochar or introduce the product into the combustion unit for additional heating, thus requiring less LPG.

4.1.3 Non-condensable gas

The NCG (non-condensable gases) formed via the pyrolysis and partial oxidation reactions were sampled after the NCG blower via a tap-off point. Analysis of the NCG found that the pyrolysis zone contained around 42 % more oxygen during low biomass throughput conditions compared to the high throughput conditions. These results correspond with the higher water content and subsequently decreased higher heating values in the bio-oils as mentioned in the bio-oil results. Therefore, this indicates that oxygen was indeed the cause of lower product quality. It is suspected that the combustion air distributor was too low in the fluidised bed relative to the NCG distributor for the pyrolysis bed. The difference in these heights means that the pressure drops are different over the beds and therefore will cause issues with air being transferred to the pyrolysis unit.

4.2 Pyrolysis unit performance

The novel reactor design allowed for consistent start-up conditions and reliable temperature control

(≈800 °C for the combustion unit and 500 °C for the pyrolysis unit). The rotating pyrolysis bed ensured that the temperatures in the pyrolysis zone were stable, and the temperature of the bed could be carefully controlled through the sand recycle mechanism. Images of the combustion zone during the start-up and pyrolysis conditions are shown in Figure 4Figure .

Figure 4: Left: Combustion of LPG below autoignition temperatures Centre: Combustion of LPG above autoignition temperatures Right: Combustion of the biochar during normal operation

The energy lost to the environment through the outer surface of the unit is significantly less than the previous iteration of the CRIPS unit with separated pyrolysis and combustion units. This new unit reduced the heat losses to the environment by 40 % through the integration of the combustion and pyrolysis units. Furthermore, the LPG requirements for running the unit was decreased by approximately 49 % using the air preheater.

5 CONCLUSIONS

The CRIPS 2 unit is a novel and efficient solution for the production and collection of fast pyrolysis products. The CRIPS 2 unit was successfully and safely commissioned and provided valuable results from eight experimental pyrolysis runs. *E. grandis* was pyrolyzed into bio-oil, biochar and non-condensable gases of which the majority of the biochar was consumed by the combustion zone to power the unit. The yield on bio-oil was found to be around 30 % with an HHV of up to 8.07 MJ/kg. It was then discovered that the low HHV and yields were caused by the increased oxygen content inside the pyrolysis unit which oxidises the products of pyrolysis to form water and carbon dioxide. However, the elemental analysis of the bio-oils confirms that similar ratios of carbon, hydrogen, oxygen, and nitrogen were present compared to typical bio-oils. Furthermore, the new design decreases heat losses to the environment by 40 % compared to the first iteration of the unit (CRIPS 1) thanks to the air-preheater and annular design. The modular design of the reactor also allows for easier upgrades and changes to the system (such as the opportunity for changing the combustion air distributors) and the heat integration aids in the scalability of the process with the temperature being tightly controlled. Finally, the rotating

fluidised bed inside the pyrolysis unit ensured consistent temperatures, controlled feed rates, tight thermal integration with the added benefit of the design only taking up a small footprint. The work carried out in this study will hopefully be continued and create further opportunities for pyrolysis and fluidised bed research as the foundations for a safe and reliable unit have been laid.

REFERENCES

Agblevor, F, Besler, S and Wiselogel, A (Apr. 1996) "Production of oxygenated fuels from biomass: impact of feedstock storage" *Fuel Science and Technology International*, *14*, (4): 589–612.

Bridgwater, AV (2013) *Fast pyrolysis of biomass for the production of liquids*, Woodhead Publishing: pp. 130–171.

Culp, AW (1991) *Principles of Energy Conversion, 2nd ed*. McGraw-Hill.

Dhyani, V and Bhaskar, T (2018) "A comprehensive review on the pyrolysis of lignocellulosic biomass" *Renewable Energy*, 129, 695–716.

Kan, T, Strezov, V and Evans, TJ (May 2016) "Lignocellulosic biomass pyrolysis: A review of product properties and effects of pyrolysis parameters" Renewable and Sustainable Energy Reviews, 57, 1126–1140.

Luque, R, Ki Lin, CS, Wilson, K and Clark, J (2016) *Handbook of Biofuels Production - Processes and Technologies (2nd Edition)*, Elsevier: pp. 393–394.

Rezaei, PS, Shafaghat, H and Daud, WMAW (Jan. 2014) "Production of green aromatics and olefins by catalytic cracking of oxygenate compounds derived from biomass pyrolysis: A review" *Applied Catalysis A: General*, 469, 490–511.

Roy, P and Dias, G (2017) "Prospects for pyrolysis technologies in the bioenergy sector: A review" *Renewable and Sustainable Energy Reviews*, 77, (May 2016): 59–69

Singh, LK and Chaudhary, G (2017) *Advances in Biofeedstocks and Biofuels, Volume 2 - Production Technologies for Biofuels*, John Wiley & Sons: p. 45.

Developing mathematical techniques for including hydraulic reactor models into biokinetic models with a focus on constructed wetlands

R. Stephenson[1], C.M. Sheridan[1]*, U. Kappelmeyer[2] and C. Harley[3]

[1] School of Chemical and Metallurgical Engineering, University of the Witwatersrand, Johannesburg, South Africa

[2] Department of Environmental Biotechnology, Hemholtz Centre for Environmental Research, Leipzig, Germany .

[3] School of Computer Science and Applied Mathematics, University of the Witwatersrand, Johannesburg, South Africa

*Corresponding author: craig.sheridan@wits.ac.za

ABSTRACT

Constructed wetlands are engineered systems aimed at utilizing the processes of natural wetlands for wastewater treatment. Biological, chemical and physical processes occur in constructed wetlands which aid the conversion of waste into non-harmful products (Kadlec and Wallace, 2009). To make more effective use of this treatment technology, it is important to understand the inner workings of constructed wetlands (Samsó and García, 2014). Numerical modelling aims to do just that. With a deeper understanding of the various processes, current design criteria can be improved and the efficiency of the treatment technology may be increased (Samsó and García, 2014). This paper gives the development of a new residence time distribution technique to describe the hydraulic behaviour of constructed wetlands and combine it with an existing and widely accepted biokinetic model, the Constructed Wetland Model No. 1.

Keywords: constructed wetlands, residence time distribution, constructed wetland model 1, mineralogy

TABLE OF NOMENCLATURE

Symbol	Unit	Description
A		Matrix of the production/degradation rates of each component in each process
C_{in}	mg/L	Inlet concentration
C_{out}	mg/L	Outlet concentration
C_0	mg/L	Initial concentration
$C(t)$	mg/L	Concentration as a function of t
$E(t)$	1/t	Residence time distribution as a function of t
$F(t)$	-	Cumulative distribution as a function of t
k		Reaction rate constant
m		Total number of components
n		Total number of time section
p		Total number of processes
t	Hour	Time
t_m	hour	Mean residence time
t_1	hour	Mean residence time of section1
t_2	Hour	Mean residence time of section 2
$T0$	Hour	Lower limit of time section 1
$T1$	Hour	Upper limit of time section 1, lower limit of time section 2
$T2$	hour	Upper limit of time section 2
τ	hour	Space time
V	L	Volume
$\dot{v}$	L/hour	Volumetric flowrate
γ_1	-	Weight factor of time section 1
γ_2	-	Weight factor of time section 2

1 INTRODUCTION

Many contaminants are present in wastewater which pose a risk to human health and the environment. Consequently, the treatment of wastewater is necessary and there are various treatment technologies available. A special focus on biological treatments, especially constructed wetlands, is discussed in this article. Biokinetic models have been developed for these processes which describe the transformation of various components including organic matter, nitrogen and, sulfur. One of the major benefits of these models is increased technology application for full-scale plant design, operation and, optimization. This also provides a common basis to make the outcomes of development and validation studies more comparable and compatible (Batstone *et al.*, 2002). The activated sludge model 1 (ASM1) is one of the original detailed kinetic models for a biological wastewater treatment process (Henze et al, 2000). Langergraber et al (2009) applied the concept of the ASM1 to constructed wetlands and used it as the basis to develop the Constructed Wetland Model 1 (CWM1). An adaption of this model is the focus of this paper.

2 LITERATURE

2.1 Processes in Constructed Wetlands

Organic material, nitrogen species and sulphur species are among the common contaminants found in wastewater. Various physical, chemical and biological processes occur in constructed wetlands which facilitate the treatment of wastewater. Processes include sedimentation, filtration, oxidation, nitrification, de-nitrification and, precipitation (Vymazal and Kröpfelová, 2008). The main biochemical processes modelled in Constructed Wetland No 1 are organics decomposition, nitrogen cycling and, sulfur transformation and so an understanding of these is most important. The role of dissolved oxygen is also considered. These processes are briefly discussed and current research in constructed wetlands modelling is also given.

Organic matter (OM) in wastewater typically takes two forms, particulate organic matter and dissolved organic matter. The breakdown of the two forms occurs via different processes. Organic matter present in wetlands has two sources, an external source and an internal source. The external source is from the influent wastewater, while the internal source is from the macrophytes in the system called root exudates (Headley and Tanner, 2012). The decomposition of dissolved OM can take place under aerobic, anoxic and anaerobic conditions(Saeed and Sun, 2012). Under aerobic conditions oxygen is the final electron acceptor. Oxygen can enter the system through three pathways: with the influent water, surface reaeration and through plant root release.

Inorganic nitrogen present in wastewater can take the form of ammonia, nitrite, nitrate, nitrous oxide and elemental nitrogen or dinitrous gas (Deblonde, Cossu-Leguille and Hartemann, 2011). Organic nitrogen pollutants include aromatics and amino acids (Rosal *et al.*, 2010). CWs were proposed as a

tool for the removal of nitrogen from agricultural wastewater in the 1990s, with surface flow constricted wetlands being the most commonly used type of wetland for this use (Mitsch, 1992; Vymazal *et al.*, 2020). Nitrogen transformation occurs through a variety of processes which include nitrification, denitrification and ammonification (Paul and Clark, 1996; Vymazal, 2007).

Sulfur is an important component in biochemical processes in constructed wetlands. There is high sulfur oxidation and reduction in constructed wetlands (Baldwin and Mitchell, 2012; Chen *et al.*, 2016). Sulfide is considered the main product of sulfur reduction and has the potential to reduce the treatment efficiencies of constructed wetlands as it inhibits ammonium/carbon removal and plant photosynthesis (Chen *et al.*, 2016). Two main pathways are considered for the removal of sulfide: precipitation with heavy metals and oxidation (Stein *et al.*, 2007; Wiessner *et al.*, 2010). Both chemical and microbial oxidation of sulfur take place in constructed wetlands (Wu *et al.*, 2013).

2.2 Modelling of constructed wetlands

Initial techniques for modelling constructed wetlands used a 'black box' approach with a qualitative understanding of what takes place in a constructed wetland but limited quantitative estimation of the role that the various processes play in the treatment of wastewater (Rizzo and Langergraber, 2016). Since physical, chemical and biological process all proceed simultaneously and influence one another, more advanced modelling techniques are required to fully understand the complexity of constructed wetlands (Langergraber, Giraldi, *et al.*, 2009). Recent effort has been put into developing process-based models which look into the treatment processes affecting effluent concentrations. Various numerical models exist which focus on one process occurring in constructed wetlands. The processes which have been modelled include water flow, particulate and solute transport, biokinetic processes, plant growth and clogging (Langergraber, 2016). Each of these models gives significant insight into the individual process which is being considered but limited research exists to consider the inter-relation of the processes or the modelling of their interactions.

Constructed Wetlands Model 1 (CWM1) is one of the most complex biokinetic models currently available and was developed by Langergraber et al. (2009). This biokinetic model is based on the IWA Activated Sludge Models (ASMs). CWM1 models the transformation and degradation processes of organic matter and nitrogen species through microbial processes to predict the effluent concentrations of components in a constructed wetland (Langergraber, Rousseau, *et al.*, 2009). However, this model is kinetic and does not account for the hydraulic processes occurring within the system or the reaction time. If the reaction time is quantified incorrectly, a kinetic model will not give accurate results, regardless of how detailed and comprehensive it may be. Given the non-ideal flow nature of these CWs, kinetic modelling techniques must be combined with accurate hydraulic modelling techniques in order for effective modelling of the system.

Currently there are two advanced process-based models which consider multiple processes of constructed wetlands. BIO_PORE is a reactive transport model which combines the biokinetic processes developed in CWM1 with oxygen and nutrient uptake by plants, hydraulic flow through heterogenous media based on Darcy's equation, as well as the attachment and detachment of solute particles (Samsó and García, 2013). HYDRUS Wetland Module is another mechanistic model which combines the biokinetic approach of CWM1 with variably saturated water flow (Richard's Equation), the transport of constituents, the influence of plants and water temperature. Both of these process-based models require special knowledge of numerical modelling and the understanding of advanced software. The aim of this paper is to develop a process-based numerical model which can be used with the understanding of the design of constructed wetlands but without requiring advanced numerical modelling skills.

Water movement is important in any water treatment plant and the same is true for a constructed wetland. The hydraulics of constructed wetlands are elaborate and non-ideal owing to the changing root structure and the complicated flow pathway of fluid through gravel or a soil matrix (Bonner et al., 2017). Macrophytes are a barrier to flow, and vary in size, shape and position. As a result, there is bypass and short circuiting around the plant mass, and dead zones are formed, which leads to a hold up of water in certain areas. There are also potential changes in flow paths due to plant development over time. Many investigations have found that there are 3 different hydraulic zones in constructed wetlands; the main flow path, a temporary storage zone, where components and water are exchanged with the main flow path, and thirdly a dead zone (Buchberger and Shaw, 1995; Zahraeifard and Deng, 2011). Short circuiting is also a possible hydraulic zone in wetlands. The extent of reaction for pollutants is determined by mixing, flow patterns of fluid elements and the time that each element resides in the wetland (Werner and Kadlec, 2000).

One of the ways to characterise the flow patterns of a reactive system is by finding its residence time distribution (RTD). The residence time distribution of a reactor gives the probability of a fluid element spending a specific amount of time in the reactor (Fogler, 2006). The RTD is obtained by running a flow tracer study on the system. A flow tracer study is a stimulus response experiment in which an inert flow tracer is injected either as an impulse or as a step change in concentration into the system inlet pipe and the tracer concentration is measured continuously at the system outlet. The data from these experiments are then used in RTD modelling methodologies to analyse the flow characteristics of the reactor. In typical RTD modelling.

The simplest RTD modelling technique used is the space time, which is given by Equation 1 (Fogler, 2006). This ratio assumes an ideal plug flow reactor (PFR). This is not the case for constructed wetlands. PFR and CSTR models, or combinations of these two have also been used to model constructed wetland

hydraulics (Kadlec, 1994; Buchberger and Shaw, 1995; Marsili-Libelli and Checchi, 2005). Kadlec and Wallace (2008) improved the typical PFR and CSTR model by using the tanks-in-series model which is characterised by a number of CSTRs in series and a gamma function. In 1994 Kadlec indicated that even a plug flow model with dispersion was inadequate to describe the flow patterns of constructed wetlands if any bypass or short circuiting took place. Many of the RTD models that currently exist are also site specific (Katsenovich *et al.*, 2009; Shih *et al.*, 2017)

$$\tau = \frac{V}{\dot{v}} \qquad \textbf{Equation 1}$$

An adaptation of flow modelling using standard impulse-response or step-change experiments and distribution mathematics can be combined with the CWM1 to potentially predict system exit concentrations and improve the understanding of how CWs work. The aim of this paper was to develop a model which does not assume a type of reactor and makes use of the raw data from a wetland and in doing so predicts output reaction concentrations combining the data with already established and accepted kinetics.

3 THE MODEL

Hydraulic residence time is an important factor to consider when designing and analysing chemical systems. Typically, when considering the effect of time on a system, a tracer experiment is done, and from it a mean residence time is obtained. This single value is then used to describe the average amount of time single fluid element or molecule has spent in the system, which is also considered the reaction of the fluid element or molecule. In theory this mean residence time accounts for the deviation from ideal flow behaviour. However, there is a great distribution of residence times that the individual molecules spend in the reactor. Some may short circuit through the system and have a reaction time much shorter than the mean residence time, while others may get caught in a dead zone and spend a much longer amount of time in the system. The reasons for these are as described above. These varying residence times affect the reaction time of these individual molecules and in the long run affect the composition of the outlet stream. As such the effect of time on such systems cannot be accurately described in with one single mean residence time. The model being developed and described can be used to more accurately account for the effect of time on a biological system, or any reactor system, by making use of multiple residence times and weight factors.

The concept of the model is that there are multiple flow paths in constructed wetlands, each of which have their own residence time. These flow paths ‘carry’ multiple tiny pockets of fluid which behave as micro-batch reactors. To account for transient and dead zones it can be assumed that a micro-batch reactor enters a transient zone at some point and then after some time re-enters one of the flow paths, but its residence time will be longer than that of the rest of the molecules in the flow path. There is limited interaction with the dead zones (Zahraeifard & Deng, 2011). There are therefore multiple batch

reactors moving along the wetland, although there is no requirement for this batch to flow through the reactor in an ideal manner. As the volume of these micro-batch reactors tends to 0, the batch system tends towards a molecular size.

The design equation of a simple batch reactor with a first order reaction taking place is the base equation which is to be expanded through the model development presented here. In an ideal reactor the space time could be used to indicate how much time the fluid elements spend inside a system. However, very few reactors behave ideally and so the non-ideal nature of systems must be accounted for.

3.1 Residence time distribution modelling technique

To gain an understanding of the hydraulic behaviour of a system tracer tests are conducted. There are two types of tracer test: Impulse response and step change. Each of these has benefits and draw backs. The resultant curve from an impulse response tracer test (which can be seen in Figure 1) is called the residence time distribution, or E(t), curve. E(t) is a quantitative description of how much time the fluid particles have spent in the reactor and is given by Equation 2 (Fogler, 2006). From here Equation 3 is used to calculate the single mean residence time of the system The mean residence time is then used in various methodologies or in simple reactor design equations to account for the non-ideal nature of a system, when the mean residence time is not equal to the space time. While the use of the mean residence time has been shown to be more accurate than using the space time, it is still not as accurate as one would hope for the reasons described above.

$$E(t) = \frac{C(t)}{\int_0^\infty C(t)dt} \qquad \textbf{Equation 2}$$

$$t_m = \frac{\int_0^\infty tE(t)dt}{\int_0^\infty E(t)dt} \qquad \textbf{Equation 3}$$

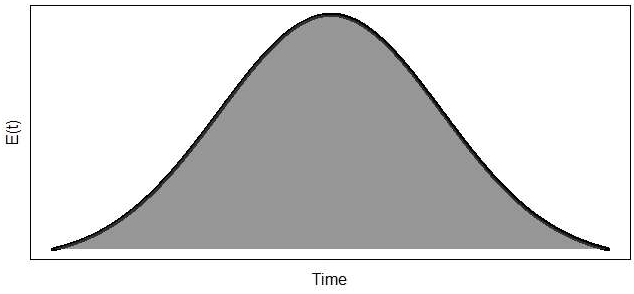

Figure 1: Typical E(t) response curve with area under the curve equal to 1

To describe and develop the concept it was assumed that the water flow in a CW can be described by two flow paths along the length of wetland, each with half the fluid volume of the system, so two micro-batch reactors had to be modelled. The area under the $E(t)$ curve is then divided into two portions as shown in Figure 2. There is an average amount of time that the fluid elements of each portion spend in

the reactor, this is defined as tj. The definition of t_m can then be extended to apply to Portion 1 and Portion 2 under the curve and is given by Equations 4 and Equation 5, respectively. The fraction of the area under the curve for each portion is defined as γ_j and can be conceptualised as a fraction of the total volume of the reactor. γ_1 and γ_2 are described by Equations 6 and 7, respectively and are defined as weighting factors. The sum of the weighting factors is equal to 1. The weighting factors make it possible to determine the contribution that each portion makes to the hydraulic flow behaviour of the system. For example, if the areas are each 50% of the total area, they would have a weight factor of 0.5 each and contribute equally to the hydraulic behaviour of the system. From this, it can be said that fraction γ_j, of the fluid passing through the reactor, spends an average time of t_j within the system. Each portion is assumed to behave as its own batch reactor moving along the length of the wetland. The solved batch reactor design equation is then adapted to include the two portions each with their own mean residence time and weight factor. A summation term is included to account for the two portions, and this is given by Equation 8.

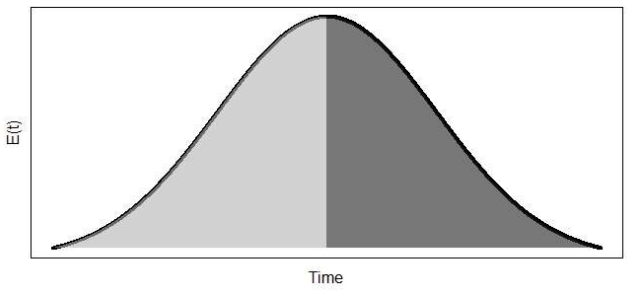

Figure 2: E(t) curve divided into 2 sections, each with an area of 0.5

$$t_1 = \frac{\int_{T0}^{T1} tE(t)dt}{\int_{T0}^{T1} E(t)dt} \qquad \textbf{Equation 4}$$

$$t_2 = \frac{\int_{T1}^{T2} tE(t)dt}{\int_{T1}^{T2} E(t)dt} \qquad \textbf{Equation 5}$$

$$\gamma_1 = \int_{T0}^{T1} E(t)dt \qquad \textbf{Equation 6}$$

$$\gamma_2 = \int_{T1}^{T2} E(t)dt \qquad \textbf{Equation 7}$$

$$C_{out} = \gamma_1 C_{in} e^{-kt_1} + \gamma_2 C_{in} e^{-kt_2} = \sum_{j=1}^{2} \gamma_j \, C_{in} e^{-kt_j} \qquad \textbf{Equation 8}$$

The concept described above can be expanded to include 10 sections as is visually represented in Figure 3. Each of the 10 sections represents a flow path carrying micro-batch rectors with a specific mean residence time and weight factor. The total outlet concentration of the system can then the be calculated as a sum of the effect of each section or flow path. in Equation 9. The general form of this is expressed in Equation 10 where there are 'n' flow paths examined within the system and therefore 'n'

sections under the curve.

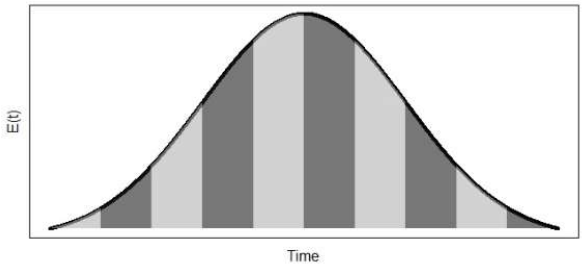

Figure 3: E(t) curve divided into 10 sections

$$C_{out} = \sum_{j=1}^{10} \gamma_j \, C_{in} e^{-kt_j} \qquad \textbf{Equation 9}$$

$$C_{out} = \sum_{j=1}^{n} \gamma_j \, C_{in} e^{-kt_j} \qquad \textbf{Equation 10}$$

3.2 Adaptation of CWM1 to the model

Currently, the CWM1, and the models it is based on, account only for the kinetic processes of the system. Both particulate and soluble components are considered in the model. All microorganisms are considered particulate matter and referred to as bacteria only (Langergraber, Rousseau, *et al.*, 2009). In the CWM1 reaction rates are given for 17 biological processes and the transformation of16 components is modelled. The components considered in the CWM1 are organic matter, nitrogen species, sulfur species and various bacterial groups. In the CWM1 reaction rates are given for the various biological processes which take place within a wetland. These include hydrolysis, growth and lysis of multiple bacterial metabolic groups. The reaction rates are given in a 17x1 matrix called the reaction rate matrix. The reaction rates given for growth of bacteria are based on Monod kinetics and as a result are not linear. Linear approximation techniques can be used to simplify these rates to first order to be used in the model. The first order rate constants are denoted k_i.

A second matrix, of dimension 17x16, is included in the model and links the reaction rates with the rates at which the various components that are produced and consumed according to each individual process. This is a stoichiometric coefficient matrix. In most cases the components are transformed in more than one reaction and these component rates become quite intricate, consisting of more than one term. Blank fields in the coefficient matrix indicate that the process does not influence the concentration of the specific species.

The second concept of the adapted model presented in this paper is to incorporate multiple reaction rates of multiple species into the batch reactor design equation. A matrix achieved by the dot product multiplication of the coefficient matrix and the reaction rate matrix produces a 16x17 matrix in which, at position $A_{i,l}$ the degradation of component ‘i' in process ‘l’ is described.

First order reaction rates are required for the model in its current format. Linearisation techniques can be applied to reduce the monod based kinetic to a first order rate. The first order rate constant is then denoted $k_{i,l}$. Matrix A is a matrix of first order rate constants. This matrix can be used in the batch reactor design equation with the inclusion of two summation terms; one for the components and one for the processes. This can be seen in Equation 11. There are a total of 'm' components and 'p' processes. The contribution of each process to the degradation or production of a specific component can be summed along the row of that component.

$$C_{out} = \sum_{i=1}^{m} C_{in,i} * e^{\sum_{l=1}^{p} A_{i,l} * t} \qquad \textbf{Equation 11}$$

The final step in the adapted model is to combine the concept of Equation 10 with the concept of Equation 11. This allows for combination of multiple time sections, with their respective weight factors, multiple processes and multiple species in one design equation. This can be seen in Equation 12.

$$C_{out} = \sum_{i=1}^{m} \sum_{j=1}^{n} \gamma_j C_{in,i} e^{\sum_{l=1}^{p} A_{i,l} t_j} \qquad \textbf{Equation 12}$$

4 CONCLUSIONS

The development of a hydraulic residence time distribution technique combined with an existing biokinetic model for constructed wetlands has been described here. Whilst the mathematics have been developed for application, the limitations of the model lie in the linearization of the biokinetic rates. By linearising these rate equations the errors are compounded and carried through. Development of the techniques towards eliminating these limitations is the subject of ongoing research and will form the basis of a future paper. In addition, future research will focus on testing the model at lab-scale for verification.

REFERENCES

Baldwin, D. S. and Mitchell, A. (2012) 'Impact of sulfate pollution on anaerobic biogeochemical cycles in a wetland sediment', *Water Research*. Elsevier Ltd, 46(4), pp. 965–974. doi: 10.1016/j.watres.2011.11.065.

Batstone, D. J. *et al.* (2002) 'The IWA Anaerobic Digestion Model No 1 (ADM1).', *Water Science and Technology*, 45(10), pp. 65–73. doi: 10.2166/wst.2008.678.

Buchberger, S. G. and Shaw, G. B. (1995) 'An approach toward rational design of constructed wetlands for wastewater treatment', *Ecological Engineering*, 4(4), pp. 249–275. doi: 10.1016/0925-8574(94)00053-8.

Chen, Y. *et al.* (2016) 'Sulfate removal and sulfur transformation in constructed wetlands: The roles of filling material and plant biomass', *Water Research*. Elsevier Ltd, 102, pp. 572–581. doi: 10.1016/j.watres.2016.07.001.

Deblonde, T., Cossu-Leguille, C. and Hartemann, P. (2011) 'Emerging pollutants in wastewater: A

review of the literature', *International Journal of Hygiene and Environmental Health*. Elsevier GmbH., 214(6), pp. 442–448. doi: 10.1016/j.ijheh.2011.08.002.

Fogler, H. S. (2006) *Elements of Reaction Engineering*. Fourth, *Pearson Education*. Fourth. Edited by N. R. Amundson. Westford.

Headley, T. R. and Tanner, C. C. (2012) 'Constructed wetlands with floating emergent macrophytes: An innovative stormwater treatment technology', *Critical Reviews in Environmental Science and Technology*, 42(21), pp. 2261–2310. doi: 10.1080/10643389.2011.574108.

Kadlec, R. H. (1994) 'Detention and mixing in free water wetlands', *Ecological Engineering*, 3(4), pp. 345–380. doi: 10.1016/0925-8574(94)00007-7.

Kadlec, R. and Wallace, S. (2009) *Treatment wetlands*. 2nd edn. Boca Raton: CRC Press. doi: 10.1002/1521-3773(20010316)40:6<9823::AID-ANIE9823>3.3.CO;2-C.

Katsenovich, Y. P. *et al.* (2009) 'Performance evaluation of constructed wetlands in a tropical region', *Ecological Engineering*, 35, pp. 1529–1537. doi: 10.1016/j.ecoleng.2009.07.003.

Langergraber, G., Rousseau, D. P. L., *et al.* (2009) 'CWM1: A general model to describe biokinetic processes in subsurface flow constructed wetlands', *Water Science and Technology*, 59(9), pp. 1687–1697. doi: 10.2166/wst.2009.131.

Langergraber, G., Giraldi, D., *et al.* (2009) 'Recent developments in numerical modelling of subsurface flow constructed wetlands', *Science of the Total Environment*. Elsevier B.V., 407(13), pp. 3931–3943. doi: 10.1016/j.scitotenv.2008.07.057.

Langergraber, G. (2016) 'Applying Process-Based Models for Subsurface Flow Treatment Wetlands: Recent Developments and Challenges', *Water*, 9(1), p. 5. doi: 10.3390/w9010005.

Marsili-Libelli, S. and Checchi, N. (2005) 'Identification of dynamic models for horizontal subsurface constructed wetlands', *Ecological Modelling*, 187, pp. 201–218. doi: 10.1016/j.ecolmodel.2005.01.043.

Mitsch, W. J. (1992) 'Landscape design and the role of created, restored, and natural riparian wetlands in controlling nonpoint source pollution', *Ecological Engineering*, 1(1–2), pp. 27–47. doi: 10.1016/0925-8574(92)90024-V.

Paul, E. . and Clark, F. . (1996) *Soil Microbiology and Biochemistry*. 2nd edn. San Diego: Academic Press.

Rizzo, A. and Langergraber, G. (2016) 'Novel insights on the response of horizontal flow constructed wetlands to sudden changes of influent organic load: A modeling study', *Ecological Engineering*. Elsevier B.V., 93, pp. 242–249. doi: 10.1016/j.ecoleng.2016.05.071.

Rosal, R. *et al.* (2010) 'Occurrence of emerging pollutants in urban wastewater and their removal through biological treatment followed by ozonation', *Water Research*, 44(2), pp. 578–588. doi: 10.1016/j.watres.2009.07.004.

Saeed, T. and Sun, G. (2012) 'A review on nitrogen and organics removal mechanisms in subsurface flow constructed wetlands: Dependency on environmental parameters, operating conditions and supporting media', *Journal of Environmental Management*. Elsevier Ltd, 112, pp. 429–448. doi: 10.1016/j.jenvman.2012.08.011.

Samsó, R. and García, J. (2013) 'BIO_PORE, a mathematical model to simulate biofilm growth and water quality improvement in porous media: Application and calibration for constructed wetlands', *Ecological Engineering*. Elsevier B.V., 54, pp. 116–127. doi: 10.1016/j.ecoleng.2013.01.021.

Samsó, R. and García, J. (2014) 'The cartridge theory: A description of the functioning of horizontal subsurface flow constructed wetlands for wastewater treatment, based on modelling results', *Science of the Total Environment*. Elsevier B.V., 473–474, pp. 651–658. doi: 10.1016/j.scitotenv.2013.12.070.

Shih, S. *et al.* (2017) 'Tracer Experiments and Hydraulic Performance Improvements in a Treatment Pond', *Water*, 9(2), p. 137. doi: 10.3390/w9020137.

Stein, O. R. *et al.* (2007) 'Seasonal influence on sulfate reduction and zinc sequestration in subsurface treatment wetlands', *Water Research*, 41(15), pp. 3440–3448. doi: 10.1016/j.watres.2007.04.023.

Vymazal, J. (2007) 'Removal of nutrients in various types of constructed wetlands', *Science of the Total Environment*, 380(1–3), pp. 48–65. doi: 10.1016/j.scitotenv.2006.09.014.

Vymazal, J. *et al.* (2020) 'Constructed wetlands with subsurface flow for nitrogen removal from tile drainage', *Ecological Engineering*. Elsevier, 155(May), p. 105943. doi: 10.1016/j.ecoleng.2020.105943.

Vymazal, J. and Kröpfelová, L. (2008) 'Removal of organics in constructed wetlands with horizontal sub-surface flow : A review of the field experience', *Science of the Total Environment*. Elsevier B.V., 407, pp. 3911–3922. doi: 10.1016/j.scitotenv.2008.08.032.

Werner, T. M. and Kadlec, R. H. (2000) 'Wetland residence time distribution modeling', *Ecological Engineering*, 15(1–2), pp. 77–90. doi: 10.1016/S0925-8574(99)00036-1.

Wiessner, A. *et al.* (2010) 'Dynamics of sulphur compounds in horizontal sub-surface flow laboratory-scale constructed wetlands treating artificial sewage', *Water Research*, 44(20), pp. 6175–6185. doi: 10.1016/j.watres.2010.07.044.

Wu, S. *et al.* (2013) 'Sulphur transformations in constructed wetlands for wastewater treatment: A review', *Ecological Engineering*. Elsevier B.V., 52, pp. 278–289. doi: 10.1016/j.ecoleng.2012.11.003.

Zahraeifard, V. and Deng, Z. (2011) 'Hydraulic residence time computation for constructed wetland design', *Ecological Engineering*. Elsevier B.V., 37(12), pp. 2087–2091. doi:

10.1016/j.ecoleng.2011.08.011.

Drilling Processes and Operations: A Major Contributor to the Anthropocene

M.O. Jimoh[1*], O.O. Sadare[2], A.O. Arinkoola[1,3], T.O. Salawudeen[1], W.O. Bello[2] and M.O. Daramola[2]

[1] Chemical Engineering Department, Faculty of Engineering and Technology, Ladoke Akintola University of Technology, Ogbomoso, Nigeria.

[2] Department of Chemical Engineering, Faculty of Engineering, Built Environment and Information Technology, University of Pretoria, Hatfield 0028, Pretoria, South Africa.

[3] Department of Petroleum Engineering, African University of Science and Technology, Abuja

*Corresponding: jimonseur2013@gmail.com; +2347065790838

ABSTRACT

Drilling operation during exploration of natural oil and gas has caused substantial impact on the planet, especially ocean acidification and habitat destruction. Water contamination and hydraulic fracture are major drilling activities with significant negative effects. The application of hydraulic fracturing in unconventional wells to increase the permeability of the porous media induces the slipping of formation bedrock which may ultimately result in several earthquakes. The CO_2 gas emitted through the gas flare drilling platform and other hydrocarbon gases are major greenhouse gases that contribute immensely to global warming. Limited options for produced water treatment and consequent eventual disposal of drilling wastes to water bodies have been reported to contribute immensely to marine environmental pollution. This pollution causes long-term and short-term danger to the environment. Despite all these challenges, the use of fossil fuels as a major source of energy has increased rapidly worldwide. Ultimately, without drilling, there is no fossil fuel. However, focus has been on the anthropogenic effects of fossil fuel burning without considering the processes leading to the extraction of the fossil fuel: the drilling operation. In this review, efforts were made to highlight various hazards associated with drilling processes with an emphasis on major impacts to the environment. This review is an attempt to provoke the thoughts of stakeholders in the sector.

Keywords: drilling operations; Anthropocene; hydraulic fracturing; drilling waste; greenhouse emissions

1 INTRODUCTION

Drilling is inevitable for crude oil and gas extraction. Oil and gas drilling are large sources of land, air and marine pollution, globally. These challenges have been made worse with the discovery of unconventional reservoirs and the advent of new technologies such as hydraulic fracturing. Hydraulic fracturing has paved the way for accessing hydrocarbons otherwise inaccessible with the conventional drilling process. Recently, exploration of natural gas across the globe has increased exponentially including fossil fuel and shale gas through drilling operations. The drilling process is one major activity of humans that has left a substantial mark on both the surface and the subsurface leaving long-term

effects on humans and the environment (Heed, 2009). Human drilling, especially for oil and gas extends to several kilometres. The future adverse effects of this are not always predictable. The socio-economic, environmental and climatic effects of drilling processes across the globe have contributed towards entering of the proposed geological time scale called the Anthropocene.

The Anthropocene is a proposed geological timescale in which various human activities severely impact the earth's geology and ecosystems (Achmon et al., 2018; Roka, 2020). It is a period where human actions globally disturb and agitate earth systems. Human activities become geological agents rather than vice versa. Burning of fossil fuels (coal, oil, and gas) has been reported to be the major driving force of the anthropogenic climate change due to emissions of various greenhouse gases (Ecobian et al., 2019; Tzompa-Sosa et al., 2017). The release of greenhouse gases, especially CO_2 from fossil fuel burning via various industrial activities, has led to a global rise in temperature, ocean acidification and severe weather changes across the globe (Levy, 2013; Tzompa-Sosa et al., 2017). However, access to and extraction of fossil fuel, especially natural oil and gas at the subsurface, requires drilling.

Accidental oil spills due to pipe leakages and equipment failure, emissions from heavy drilling equipment, treatments and disposal of drilling wastes (i.e., especially drilling fluids, emissions from trucks at drilling sites, geological slides due to injection of wastewater in ultra-deep wells) are major indicators that drilling operations adversely affects humans and environments (Williams et al. 2016; Bogacki and Macuda (2014). Presently, hundreds of thousands of active wells are located across the globe including Africa, Europe, and America. However, the devastating consequences of drilling operation on the earth's system have not received much attention in contrast to the combustion of fossil fuels. This article, therefore, highlights various drilling processes and activities. In particular, drilling effects on land, marine and atmospheric environments are discussed.

2 DRILLING OPERATIONS

2.1 Conventional drilling

Drilling is the process of creating a circular hole below the subsurface typically reaching 1000 ft of depth where natural oil and gas is trapped. So far, the only means of extracting oil from the subsurface is to drill a well. Conventional drilling is typically a vertical well drilling technique employed to retrieve natural oil and gas from the sub-surface. However, the increasing need to access oil trapped within less permeable formations necessitates the use of horizontal and directional drilling methods. These methods have enhanced the overall oil recovery which is otherwise not feasible using conventional (vertical) drilling. The drilling process has improved significantly with the advent of new technologies such as directional drilling, horizontal well drilling and the hydraulic fracturing (Lyons and Plisga, 2016). The advent of these technologies has led to the successful exploration and exploitation of unconventional

hydrocarbons such as coal-bed methane, shale oil and tight oil and gas (Verma and Sirvaiya 2016; Chen et al. 2014; Zou et al. 2015).

2.2 Directional drilling and Hydraulic fracturing

Accessing hydrocarbons from complicated formations such as shale, high temperature and high-pressure reservoirs, tight gas sandstone, and ultra-deep water requires the use of advanced technologies such as directional drilling and hydraulic fracturing. Directional drilling is the practice of drilling a non-vertical well-bore aimed at recovering oil and gas especially in an unconventional reservoir with extremely low permeability. The boring does not go vertically (in a straight line) but rather slanting at a known angle (Helmig, 2020). Directional drilling techniques have proved to dramatically enhance oil recovery in complicated reservoirs (Cremonese et al., 2019; Gao et al., 2009). Reservoir-well contact is also improved as several reservoirs can be accessed via a single bore, hereby reducing the detrimental effects at the surface (Chen et al., 2014).

Hydraulic fracturing (HF), also known as fracking is an important secondary drilling activity adopted for efficient production of oil trapped in low permeable formations such as shale. A high-pressure liquid mixture is injected into the well to create fractures on existing fissures which subsequently open up connected pore spaces and increase the amount of oil which can be extracted from reservoir. Despite these advantages, HF could be regarded as a dangerous process with effects that possibly linger for centuries. One important indicator of HF as a major contributor to the Anthropocene is the fact that it gives us continuous access to natural gas and crude oil which encourages further consumption of fossil fuels. With the increasing practice of HF, access to natural gas and crude oil becomes cheaper, hence resulting in further fossil fuel combustion. It is worthy to note that even natural gases that are considered cleaner fossil fuels create and generate emissions that could deplete the ozone layer and cause harm to the atmosphere (Adgate et al. 2014).

Contamination of the subsurface watersheds by the fracking fluid is another issue of major concern. Fracturing fluids basically consists of water, sand and potentially toxic chemicals (often undisclosed) that could penetrate the bed rock due to the fractures created, and subsequently contaminate public and other water supply. Additionally, several fractures created in the bed rock could allow crude oil and natural gas leaks to drinking water especially situations where well casings break down unexpectedly due to corrosion or excessive hydraulic pressure (Michelle et al., 2015).

Pressure build-up, due to the continuous deposit of fracking fluid in deep wells after several HF events, has been reported to be responsible for bed-rock slips leading to high magnitude earthquakes around drilling sites (Richard e al, 2015). Unfortunately, most drilling companies do not disclose the actual chemical compositions of the fracking fluid, making it more difficult to simulate projected long-term risks associated with improper disposal of fracking fluids. Water requirements for successful

operation of HF is also an emerging challenge especially in countries where water conservation practices are of paramount importance. Continuous engagement in HF, might result in extreme water crises in the near future. These issues among others are pointers that drilling contributes towards us entering the Anthropocene.

3 ONSHORE AND OFFSHORE DRILLING

Drilling operations could be on land, below the subsurface (onshore) or below the seabed (offshore). Both drilling techniques can be used for exploratory and production drilling (Traynor, and Sladen, 1997). However, offshore drilling is more expensive than onshore drilling because not only does it require a drilling rig but a complete platform which includes housing for staff, docking facilities and helicopter landing pad among others (Steinsvag et al., 2009). The massive structure of the platform requires substantial support to withstand the ocean waves, and hence is more expensive and requires longer setup times. About 70% of the natural oil and gas exploration comes from onshore drilling with the remaining 30% from offshore (Austin et al. 2004). Investing in more offshore drilling has created additional employment, increased oil production and boosted industrialization in all the concerned countries (Mason, 2009). However, both offshore and onshore drilling processes have their associated challenges, with offshore drilling posing larger risks to humans and environment (Mason, 2009).

Numerous cases of oil spills have been reported both at onshore and offshore drilling sites (White et al., 2014), with offshore drilling been the most impactful due to its location on sea and ocean beds. Oil spills are extremely harmful to marine life. They reduce the level of dissolved oxygen and prevent sunlight from penetrating the ocean surface thereby suffocating photosynthetic and other marine life in the vicinity (Gravitz et al, 2009). Aside the immediate effects on marine life and water pollution, the long-term detrimental effect on the ecosystem are difficult to assess.

High risks jobs offered by drilling operations, especially offshore drilling, cannot be underemphasized. Accidents on offshore drilling rigs are often fatal to humans (staff on platform) and the environment; especially the marine environment due to the distance between the rig and emergency rescue and remediation services. Investing in offshore drilling automatically increases onshore ecological and environmental damages. This is because onshore infrastructure is required to support, transport and process oil and natural gases extracted from the drill platform. The onshore infrastructure includes pipelines to transport natural gas and oil extracted to storage or processing facilities, waste treatment and disposal facilities, port terminals and processing refineries (Mason, 2009). All the onshore infrastructure supporting offshore drilling have their various associated harmful effects on environment, public health and ecosystem.

4 DRILLING WASTE DISPOSAL

Drilling process, either onshore or offshore, generate substantial quantities of toxic wastes including

drill cuttings, used drilling fluids, fracking fluids, and water with varying compositions (Bekhtar and Gagnan, 2012; Ahmadun et al., 2009). Drilling muds (fluids) are viscous fluids circulated through the drill pipe to maintain the well and transport drill cuttings to the surface among several other functions (Neff, 2002; Kelessidis et al. 2011; Arinkoola et al., 2018; Jimoh et al., 2021). The effluent from these operations is a mixture of formation water, oil, gas and injection water. It is a complex mixture whose composition is substantially affected by the geological properties of the formation and may consist of heavy metals, various complex organic and inorganic compounds that are of environmental concerns (Richard et al., 2015). Illegal dumping of these wastes leads to negative ecological and health consequences that can last for decades.

5 ENVIRONMENTAL AND HEALTH HAZARD

5.1 Effect on the atmosphere

Flaring of gas from onshore rigs and offshore drilling platforms are one of the major sources of air pollution during natural oil and gas extraction process. Fracking operations significantly affect the air by the release of methane during the initial period following hydraulic fracturing injection and transport of the fuel to customers (Howarth *et al.,* 2010). Trucks used to transport extracted oil emit carbon and other greenhouse gases. Methane emission contributes substantially to global warming. Emission of carcinogens such as CO_2 and benzene during conventional and hydraulic fracking were reported at various stages of drilling (Gao, 2010). Fracturing flow-back fluids are usually accompanied by substantial amount of methane and other greenhouse gases which are directly emitted into the surrounding atmosphere (EPA, 2010). Others include continuous emissions from gas venting and leaking equipment on drilling site, transportation and storage facilities, even after well completion (Lelieveld et al., 2005). The hypothesis is that, as the demand for energy for technological advancement increases, more drilling sites using the unconventional drilling techniques will continue to emerge, hence more methane and other greenhouse gases will be emitted.

5.2 Effect on human health

High levels of known carcinogens in air such as benzene have been attributed to natural gas drilling operations. (McKenzie et al., 2012). Common symptoms or complications among people living near fracking sites include fatigue, burning eyes, dermatologic irritation, headache, upper respiratory infections, gastrointestinal infections, musculoskeletal issues, neurological symptoms, alteration of immunological function, sensory impairment, liver abnormality, vascular, bone marrow, endocrine, and urologic problems (Colborn T, et al., 2011; Bamberger, M., 2012; 2011; Perry, S. L., 2013; Dey et al., 2015: Yermukhanova et al., 2017; and McKenzie al., 2017)

5.3 Effect on land and immediate community (Nigerian context)

5.3.1 Environmental Effect of Oil Drilling

Oil drilling has many harmful ecological and environmental effects. The process of drilling and extracting oil is complex and leaves many opportunities for errors or accidents as have been experienced in the Niger Delta. The Niger-delta region is the oil-bearing region in Nigeria. The economic and social challenges faced by people in communities living here are directly linked to mismanagement of environmental issues resulting from oil drilling. The discovery and drilling for crude oil in the Niger-delta has depleted the ecosystem via deforestation and obliteration of aquatic life. A region reported to have great potential to feed the West African sub-region with chances of exportation (Akpofure et al., 2004) is ecologically degraded and economically backward because of oil drilling.

The piping used to transport and extract oil is made of metals, which can corrode. This corrosion causes pipes to rupture and contaminates the land and waters which surround it. If the pipes do not rupture, contamination can still originate from large waste pits, often left unlined and open. Dust particles left from drilling may coat the surrounding areas, and flames from burning the natural gas found in oil fields cause air pollution.

Approximately, 1.5 million tonnes of crude oil have been spilled into the Niger Delta ecosystem over the past 5 decades. This volume is 50 times the estimated quantity of crude oil spilled in the popular Exxon Valdez spill in Alaska in 1989 (Niger Delta Resource Damage Assessment and Restoration Project, 2006).

5.3.2 Health Effect on Indigenous Communities

Oil spills into streams undoubtedly make their ways into the aquatic environment that harbours fish and other aquatic animals. As a result of toxic ingestion resulting from the consumption of contaminated fish and aquatic animals, many people suffer from severe skin rashes which require frequent medical attention to prevent swelling, and also from chronic headaches. Fainting spells, vomiting, chronic diarrhoea, headaches and unknown skin infections are common symptoms for those who consume contaminated aqua animals. Long term health effects include but not limited to miscarriages in women, lung disease, liver and kidney damage, nervous system disorder, brain damage, and many other chronic ailments (Kponee et al., 2015). Effluent from oil drilling may contain toxic heavy metals such arsenic, cadmium, mercury, lead, zinc and copper (Caenn et al., 2012). Consumption of these metals, even at very low concentration, is detrimental to human health and animal wellbeing. Heavy metals accumulate in the tissues of organism faster than it can be excreted.

Indigenous people of the Niger-delta in Nigeria have been fishing their ancestral lands and rivers for generations. However, due to hydrocarbon contamination, waterbodies became toxic, hence fish and aquatic animals have bio-accumulated metals. For example, a report from Kponee et al. (2015)

indicates that exposure to hydrocarbon-contaminated drinking water is statistically correlated to self-reported symptoms associated with petroleum-hydrocarbon exposure. The authors highlighted that symptoms such as headache, skin and eye irritation, anaemia, dizziness, bronchitis asthma are common for people living close to a hydrocarbon exploration site. Humans at the top of the food chain, consuming contaminated aquatic animals are continuously exposed to amplified health hazards. As long as indigenous people continue to rely on their lands and waterways for sustenance, the risk of feeding on hydrocarbon contaminated fishes and cultivation of toxic farmlands remains inevitable.

6 CONCLUSIONS

The drilling process is an important human activity whose impact on earth cannot be overlooked. Drilling processes can be considered as dangerous and extremely risky operations because of the fatal accidents and severe damage caused to the environment. To date, there are no sufficient measures to effectively mitigate the consequences of these disasters. The long-term detrimental effect of drilling because of increasing energy demand are not going to abated soon. Since the inception of industrialisation which is characterised by a continuous increase in the demand of energy, there has been increase in global average temperature by 1 °C. This has the potential to increase by 2.7 °C or more by the end of the century if no decisive actions are taken to mitigate these risks. However, the drilling process, being the only means of accessing energy from the subsurface, will likely increase in coming years due to the exponential increase in energy demand stemming from various technological advances. It can thus be concluded that drilling process and its accompanying activities are as dangerous as the fossil fuel burning itself. It is highly recommended that countries, such as South Africa, planning to engage in drilling activities for oil/gas exploration should critically consider environmentally benign technologies that will protect the natural environment as they embark on exploration activities rather than using known methods that cause environmental harm.

REFERENCES

Barnes, A.R., Finn, C.W.P and Algie, S.H. 1983. The prereduction and smelting of chromite concentrate of low chromium concentrate of low chromium-to-iron ratio. *The Journal of the South African Institute of Mining and Metallurgy*, March 1983: pp. 49-54

Achmon, Y., Achmon, M., Dowdy, F.R., Spiegel, O., Claypool, J.T., Toniato, J. and Simmons, C.W. 2018. Understanding the Anthropocene through the lens of landfill microbiomes. *Frontiers in Ecology and the Environment*, 16 (6): pp. 354–360.

Adgate, J.L., Goldstein, B.D., and McKenzie, L.M. 2014. Potential public health hazards, exposures and health effects from unconventional natural gas development. *Environmental Science & Technology* 48: pp 8307–8320.

Ahmadun, F.R., Pendashteh, A., Abdullah, L.C., Biak, D.R.A., Madaeni, S.S, Abidin, Z.Z. 2009. Review of technologies for oil and gas produced water treatment. Journal of *Hazardous*

Materials. 170: pp. 530–551.

Akpofure, E.A., Efere, M.L. and Ayawei, P. 2000. The adverse effects of crude oil spills in the Niger delta, Nigeria: Urhobo Historical Society.

Arinkoola A.O., Salawudeen T.O., Salam K.K., Jimoh M.O and Gafar A.O. 2018. Potential Evaluation and Optimization of natural biopolymer in water-based drilling mud. *Journal of Chemical and Petroleum Engineering,* 52(1): pp. 1-12.

Austin, D., Carriker, R., McGuire, T., Pratt, J., Priest, T. and Pulsipher, A.G., 2004. History of the Offshore Crude oil Natural Gas Industry in Southern Louisiana Interim Report Volume I: Papers on the Evolving Offshore Industry OCS Study MMS 2004-049. Contract 1435-01-02-CA-85169. Minerals Management Service, Gulf of Mexico OCS Region, United States Department of the Interior, New Orleans, Louisiana.

Bakhtyar, S. and Gagnon, M.M. 2012.Toxicityassessment of individual ingredients of synthetic-based drilling muds (SBMs). *Environmental. Monitoring and Assessment, 184*: pp. 5311–5325.

Bogacki, M. and Macuda, J. 2014. The influence of shale rock fracturing equipment operation on atmospheric air quality. *Archives of Mining Science*, 59: pp. 897−912.

Caenn R, Darley, H.C.H. and Gray, G.R. Chapter 12 - Drilling and Drilling Fluids Waste Management. In: Caenn R., Darley HCH,, Gray GR, editors. Composition and Properties of Drilling and Completion Fluids (Sixth Edition) Boston: Gulf Professional Publishing; 2011: pp. 617-654.

Chen P., Liu Y. and Ma T.S. 2014. Status and prospect of multi-well pad drilling technology in shale gas. *Petroleum and Drilling Technology,* 42(3): pp. 1–7

Cremonese, L, Weger, L.B., Gon, H. D., Batels., M. And Butler T. (2019). Emission scenarios of a potential shale gas industry in Germany and the United Kingdom. *Elementa Science of the Anthropocene*, 7: 18. DOI: https://doi.org/10.1525/elementa.359

Dey T, Gogoi K, Unni B, Bharadwaz M, Kalita M, Ozah D, Kalita M., Kalita J., Baruah P. K. And Bora T. 2015. Role of environmental pollutants in liver physiology: Special references to peoples living in the oil drilling sites of Assam. *PLoS ONE* 10(4): e0123370. doi:10.1371/journal.pone.0123370

EPA (2021) Greenhouse gas emissions reporting from the petroleum and natural gas industry. Background Technical Support Document. http://www.epa.gov/climatechange/emissions/downloads10/Subpart-W_TSD.pdf. Accessed 13 July, 2021

GAO (2010) Federal oil and gas leases: opportunities exist to capture vented and flared natural gas, which would increase royalty payments and reduce greenhouse gases. GAO-11–34 U.S. General Accountability Office Washington DC. http://www.gao.gov/new.items/d1134.pdf

Gao D, Tan C, and Tang H (2009). Limit analysis of extended reach drilling in South China Sea.

Petroleum Science. 6(2): pp. 166–171

Gravitz, M., Cosgove, S. & Kirby, M. 2009. Oceans Under the Gun: Livings Seas or Drilling Seas? Environment America Research and policy centre

Hecobian, A., Clements, A.L., Shonkwiler, K.B., Zhou, Y., MacDonald, L.P., Hilliard, N., Wells, B.L., Bibeau, B., Ham, J.M., Pierce, J.R., and Collett, J.L. 2019. Air toxics and other volatile organic compound emissions from unconventional oil and gas development. *Environ. Sci. Technol. Lett.,* 6: pp. 720−726.

Heede, R. 2014. Tracing anthropogenic carbon dioxide and methane emissions to fossil fuel and cement producers, 1854–2010**.** *Climatic Change*. 122 (1–2): pp. 229–241.

Helmig, D. 2020. Air quality impacts from oil and natural gas development in Colorado. *Elementa Science of the Anthropocene*, 8: 4. DOI: https://doi.org/10.1525/elementa.398

Howarth, R.W., Santoro, R. and Ingraffea A. 2011. Methane and the greenhouse-gas footprint of natural gas from shale formations. *Climate Change*, 106 (4): pp. 679-90.

Jimoh, M.O., Salawudeen, T.O, Arinkoola, A.O., and Daramola, M.O. 2020. Rheological study of a new water-based drilling fluid using Ubakala clay in the presence of natural polymers. *Chemical Engineering Communications,* https://doi.org/10.1080/00986445.2020.1774374.

Kelessidis, V.C., Poulakakis, E, and Chatzistamou, V. 2011. Use of Carbopol 980 and carboxymethyl cellulose polymers as rheology modifiers of sodium-bentonite water dispersions. *Applied Clay Science,* 54(1): pp. 63–69.

Kponee, K.Z., Chiger, A., Kakulu, I.I., Vorhees, D., Heiger-Bernays, W., 2015. Petroleum contaminated water and health symptoms: a cross-sectional pilot study in a rural Nigerian community. *Environmental Health,* 14, pp. 86.

Lelieveld, J., Lechtenbohmer, S., Assonov, S.S., Brenninkmeijer, C.A.M., Dinest, C., Fischedick, M., Hanke, T. 2005. Low methane leakage from gas pipelines. *Nature,* 434: pp. 841–842.

Levy, J. 2013. How big are the McMurdo Dry Valleys? Estimating ice-free area using Landsat image data. *Antarctic Science* 25(1): pp. 119–120.

Lyons, W.C. and Plisga, G.J. 2016. Standard handbook of petroleum and natural gas engineering, 3rd edition. Gulf Professional Publishing, Burlington

Mason, J.R., 2009. The Economic Contribution of Increased Offshore Oil Exploration and Production to Regional and National Economies. Hermann Moyse Jr., Louisiana Bankers Association Endowed Chair of Banking, Louisiana State University, E.J. Ourso College of Business for the American Energy Alliance, Washington, DC.

McKenzie, L.M., Witter, R.Z., Newman, L.S. and Adgate, J.L. 2012. Human health risk assessment of air emissions from development of unconventional natural gas resources. *Science of the Total Environment.* 424: pp. 79-87.

McKenzie, L.M., Allshouse, W.B., Byers, T.E., Bedrick, E.J., Serdar, B., Adgate, J.L., 2017. Childhood hematologic cancer and residential proximity to oil and gas development. *PLoS One.* 12, e0170423.

Mitchell, A.L., Tkacik, D.S., Roscioli, J.R., Herndon, S.C., Yacovitch, T.I., Martinez, D.M., Vaughn, T.L., Williams, L.L., Sullivan, M.R., Floerchinger, C., Omar, M., Subramanian, R., Zimmerle, D., Marchese, A.J. and Robinson, AL. 2015. Measurements of Methane Emissions from Natural Gas Gathering Facilities and Processing Plants: Measurement Results. *Env. Sci. & T.,* 49(5): pp. 3219–3227.

National Oil Spill Detection and Response Agency (NOSDRA). 2006. Oil spill recovery, clean-up, remediation and damage assessment regulations, 2011. Section 17: 6.

Neff, J.M. 2002. Bioaccumulation in marine organisms. Effects of contaminants from oil well produced water. Elsevier, Amsterdam, 452: pp. 336.

Perry, S.L. 2013. Using ethnography to monitor the community health implications of onshore unconventional oil and gas developments: examples from Pennsylvania's Marcellus Shale. *New Solutions,*23(1): pp.33-53.

Richard, J.D., Sam, A., Robert S.W., Robert B.J., Charlotte, A., Fred Worrall, Liam G.H., Jon, G.G., Mark, A.W. 2015. Oil and gas wells and their integrity: Implications for shale and unconventional resource exploitation. *Marine and Petroleum Geology*, 59: pp. 674-675

Roka, K. 2020. Anthropocene and Climate Change. In: Leal Filho W., Azul, A.M., Brandli L., Ozuyar, P.G. and Wall T. (eds) Climate Action. Encyclopaedia of the UN Sustainable Development Goals. Springer, Cham**.** https://doi.org/10.1007/978-3-319-95885-9_26

Steinsvag, K., Bratveit, M., Moen, B.Li.V., Austgulen, T., Hollund, B.E., Haaland, I.M., Naeeheim J., Svendsen, K. and Kromhout, H. 2008. Expert assessment of exposure to carcinogens in Norway's offshore petroleum industry. *Journal of Exposure Science and Environmental Epidemiology,* 18(2): pp. 175-182.

Traynor, J.J. and Sladen, C. 1997. Seepage in Vietnam – onshore and offshore examples. *Marine and Petroleum Geology*, 14: pp. 345-362.

Tzompa-Sosa, Z.A., Mahieu, E., Franco, B., Keller, C.A., Turner, A. J., Helmig, D., Fried, A., Richter, D., Weibring, P., Walega, J., Yacovitch, T.I., Herndon, S.C., Blake, D.R., Hase, F., Hannigan, J. W., Conway, S., Strong, K., Schneider, M., Fischer, E.V. 2017. Revisiting global fossil fuel and biofuel emissions of ethane. *J. Geophys. Res. Atmos*. 122: pp. 2493−2512.

Verma, A.K., Sirvaiya, A. 2016. Comparative analysis of intelligent models for prediction of Langmuir constants for CO_2 adsorption of Gondwana coals in India. *Geomech. Geophys. Geo. Energy. Geo. Res.,* 2(2): pp. 97–109

White, H.K., Lyons, S.L., Harrison, S.J., Findley, D.M., Liu, Y., and Kujawinski, E.B. 2014. Long-

Term Persistence of Dispersants following the Deepwater Horizon Oil Spill. *Environ. Sci. Technol. Lett.,* 1: pp. 295–299. doi: 10.1021/ez500168r

Williams, E.J., Tevlin, A.G., Murphy, J.G., Fischer, E.V., McKeen, S., Ryerson, T.B., Peischl, J., Holloway, J.S., Aikin, K., Langford, A.O., Senff, C.J., Alvarez, R.J., Hall, S.R., Ullmann, K., Lantz, K.O., and Brown, S.S. 2016. Influence of oil and gas missions on summertime ozone in the Colorado Northern Front Range. *J. Geophys. Res.,* 121: pp. 8712−8729.

Yermukhanova, L., Zhexenova, A., Izimbergenova, G., Turebaev, M., Bekbauova, A. and Zumabekov, E. 2017. Immunodeficiency states in persons residing in the oil-producing regions of Kazakhstan. *Research Journal of Medical Sciences* 11: pp. 16–18.

Zou, C., Zhai, G., Zhang, G., Wang, H., Zhang, G., Li, J., Wang, Z., Wen, Z., Ma, F., Liang, Y., Yang, Z., Li, X. and Liang, K. 2015. Formation, distribution, potential and prediction of global conventional and unconventional hydrocarbon resources. *Petroleum Exploration and Development,* 42(1): pp. 14–28.

Experimentation and modelling study on flue gas desulphurization using spray drying absorption.

L. Koech[1,2*], L. Lerotholi[1,2], R.C. Everson[1,3], B.B. Hattingh[1,3], H.L. Rutto[1,2], G. Grobler[4], H.W.J.P. Neomagus[1,3] and A. Moganelwa[1,5]

[1] Eskom Power Plant Engineering Institute (EPPEI) Specialisation Centre for Emissions Control.

[2] Department of Chemical Engineering, Vaal University of Technology, Vanderbijlpark Campus, Private Bag X021, Vanderbijlpark 1900, South Africa.

[3] Centre of Excellence for C-based Fuels & School of Chemical and Minerals Engineering, Faculty of Engineering, North-West University, Private Bag X6001, Potchefstroom 2520, South Africa.

[4] School of Mathematical and Statistical Sciences, North-West University, Private Bag X6001, Potchefstroom 2520, South Africa.

[5] Group Technology Engineering, Eskom Holdings SOC Ltd, 1 Maxwell Drive, Sunninghill 2191, South Africa

*Corresponding author: lawrencek@vut.ac.za

ABSTRACT

An investigation was undertaken to determine the performance of a laboratory-scale spray dryer (semi-dry process) involving flue gas desulphurization (FGD) to contribute to the understanding, modelling and design of an industrial process. The study consisted of a systematic experimentation programme using response surface methodology with a lab scale spray dryer to optimize the absorption of SO2. Parametric tests were conducted to analyze the influence of stoichiometric ratio (0.5-2.5), inlet gas phase temperature (120-200°C), slurry solid concentration (6-14%) and slurry pH (4-12) on SO2 absorption efficiency. The axial profiles of SO2 within the absorber space indicated two drying regimes i.e., constant rate and falling rate drying periods within the spray dryer. A predictive quadratic model correlating independent variables and the response was developed based on experimental findings. The model was found to provide a suitable fit with an R-squared coefficient of 0.93. The recommended optimal conditions for SO2 absorption were inlet gas phase temperature of 140°C, stoichiometric ratio of 2, slurry solid concentration of 8% and slurry pH of 10 which gave 90% SO2 removal efficiency.

Keywords: Spray drying absorption, semi-dry FGD, experimentation, sorbents, optimization.

1 INTRODUCTION

The removal of pollutant gases such as SO_2 and NO_x has gained a lot of interest for many years. They mostly emanate from the combustion of sulphur-containing coal in power plants resulting in emission of pollutant gases. This has resulted in the enactment of stringent laws and regulations governing industrial air pollution particularly SO_2 and subsequently necessitated the need to implement flue gas cleaning processes such as flue gas desulphurization (FGD) units in both new and existing power plants.

FGD technologies can be categorized as wet, dry, and semi-dry based on the state of the active

ingredient applied (Katolicky and Jicha, 2013). Spray drying absorption (SDA) is an attractive alternative to the wet FGD system due to smaller footprint requirement, ease of product handling, low capital cost, ease of retrofit to existing plants and less water consumption (Xie *et al*., 2017).

Despite its ability to remove SO_2 beyond legislative limits, the application of SDA in coal-fired power plants has been limited by high sorbent cost, low sorbent utilization and lower SO_2 removal efficiency compared to the wet FGD technology. It is therefore necessary to improve its desulphurization efficiency and sorbent utilization to make it more attractive in the industry. The reaction between hydrated lime ($Ca[OH]_2$) and SO_2 in the absorption chamber is an adsorption controlled reaction that mainly depends on a variety of factors such as sorbent surface properties, particle size, slurry solid concentration, humidity, approach to saturation temperature among others (Gassner *et al*., 2014)

In this study, a systematic approach using central composite design (CCD) was used to assess the influence of spray characteristics on the desulphurization efficiency using commercial hydrated lime as a sorbent. This was performed using a laboratory scale spray dryer by varying the spray characteristics such as stoichiometric ratio (0.5 - 2.5), inlet gas phase temperature (120 - 200°C), slurry solid concentration (6 - 14%) and slurry pH (4 - 12) which were chosen as independent variables. These limits were based on the results of trial experiments on the present work and considering SO_2 concentrations in industrial flue gas. RSM was then applied to assess the cross-influences of the variables on SO_2 removal efficiency. Optimization was carried out for the process variables with an aim of maximizing SO_2 removal efficiency.

2 EXPERIMENTAL

The absorption experiments were conducted in a laboratory scale Buchi B290 mini spray dryer. A schematic of the spray dryer is shown in Figure 1. The overall setup consisted of the following subsystems: sorbent slurry preparation, spray drying absorption chamber, flue gas analysis and other accessories.

Simulated flue gas was obtained by mixing 99% SO_2 with ambient air at controlled rate to achieve the required inlet SO_2 concentration. To achieve the desired inlet temperature, flue gas is heated using an electric heater located above the chamber before entering the spray chamber. The feed slurry comprised of commercial grade hydrated lime mixed with water using pre-determined ratios. Table 1 presents a summary of the chemical and physical properties of the hydrated lime used. The pH of the slurry was adjusted by adding 0.1M HCl into the feed slurry. The feed slurry was then injected into the spray dryer via a two-fluid nozzle located at the top of the spray chamber. The nozzle disperses the slurry into fine droplets which comes in contact with the heated flue gas in a co-current flow in the spray chamber. A final dry product is collected at the bottom of the chamber which is also captured by the cyclone separator. Throughout each experimental run, SO_2 concentration was monitored along the

spray chamber using Testo 340 combustion gas analyzer. This was done by continuously sampling the flue gas at 5 different points as depicted in Figure 1.

The hydrated lime sorbent was characterized using N_2 BET to determine their specific surface areas while the elemental analysis was carried out using XRF analysis. Scanning electron microscope (SEM) was used to obtain micrographs.

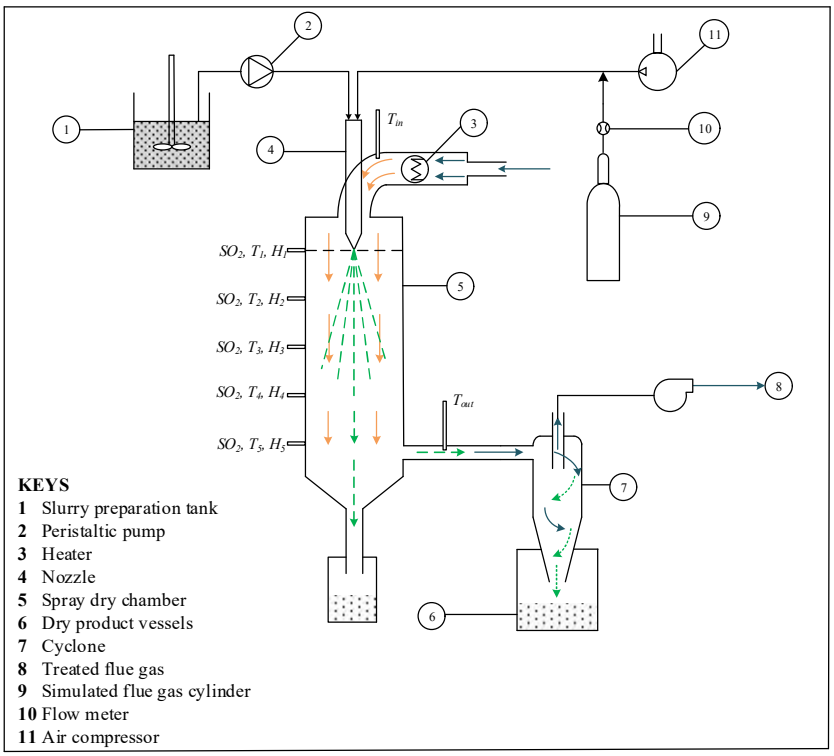

Figure 1: Lime spray drying experimental setup.

Table 1: Sorbent properties

Property	$Ca[OH]_2$
Composition (XRF)	89 wt% CaO
Mean particle size	< 75 µm
BET surface area (N_2)	4.24 m^2/g

2.1 Design of experiments and statistical analysis

In this study, response surface methodology (RSM) was used to optimize the experimental conditions for the absorption of SO2 from flue gas using a laboratory scale spray dryer. RSM is a mathematical and statistical technique useful for the modelling and analysis of problems in which a response of interest is influenced by several variables, with an objective to optimize this response (Myer and Montgomery, 2002). A full factorial design consisting of independent variables that were investigated is shown in Table 2. A central composite design component with quadratic model and $\propto = 2$ in the

Design Expert Software v13.0.1.0 was used to analyse the effects of process variables (inlet gas phase temperature, stoichiometric ratio, slurry solid content and slurry pH) on SO_2 absorption efficiency. Alpha (α) is the axial distance from the centre point and makes the design rotatable.

Table 2: Process parameters

Independent variable	**Code**	$\propto = -2$	$\propto = -1$	$\propto = 0$	$\propto = 1$	$\propto = 2$
Inlet gas temperature (°C)	x_1	120	140	160	180	200
Stoichiometric ratio (Ca:S)	x_2	0.5	1.0	1.5	2.0	2.5
Slurry solid concentration (wt%)	x_3	6	8	10	12	14
Slurry pH	x_4	4	6	8	10	12

The experimental data obtained were fitted into a second-order polynomial model and regression coefficients were obtained. The second-order polynomial model used in the response surface analysis was as follows:

$$Y = b_0 + \sum_{i=1}^{n} b_i x_i + \sum_{i=1}^{n} b_{ii} {x_i}^2 + \sum_{i=1}^{n-1} \sum_{j=i+1}^{n} b_{ij} x_i x_j \qquad \textbf{Equation 1}$$

Where Y is the predicted SO_2 absorption efficiency (ppm), b_0 is offset term, b_i are the linear coefficients, b_{ii} are the quadratic coefficients, b_{ij} are the interaction coefficients, and $x_{i,j=1,2\ldots,n}$ are the coded values for the independent variables investigated. The significance of the second-order model was evaluated by analysis of variance (ANOVA) and a lack of fit test which was then used to optimize spray dryer absorption efficiency for all the independent variables investigated. The model adequacy was evaluated based on the R-squared statistic (R^2).

3 RESULTS AND DISCUSSION

3.1 Sorbent characterization

Chemical analysis (XRF) of the commercial hydrated lime used a sorbent in this study indicated significant presence of Ca expressed as CaO (89.55 wt%) which is an active component in the chemisorption reaction. The was evident from XRD analysis which revealed strong presence of $Ca[OH]_2$ (portlandite) peaks appearing at 2θ = 20.9, 33, 39.5, 55, 59.5, 64 and 74° as shown in Figure 2. The diffraction patterns also revealed mild presence of quartz (SiO_2) appearing at 2θ = 24, 31, 42.5, 47, 49 and 53.5°. The presence of calcite peaks in the sample could have been due to contamination during preparation for XRD analysis. The surface morphology of the sorbent obtained from SEM analysis indicated a porous particle surface with rough texture as shown in Figure 3. This contributes to a high specific surface area as indicated in the BET N_2 surface area analysis of 4.24 m^2/g which is adequate surface area beneficial for desulphurization in spray drying.

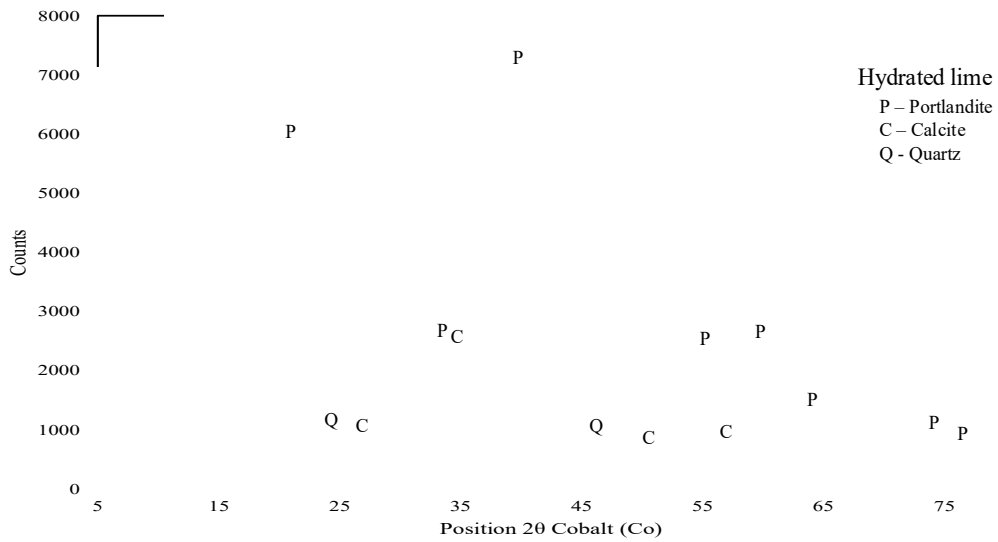

Figure 2: XRD diffraction pattern for hydrated lime sorbent

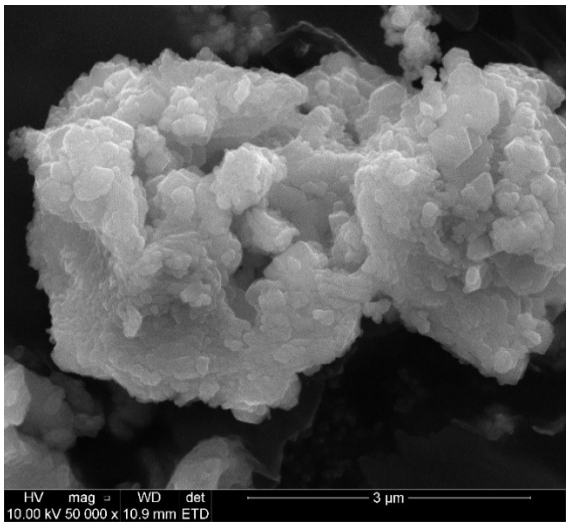

Figure 3: SEM image for hydrated lime sample

3.2 Model fitting

The percentage removal range of SO_2 for all the experiments conducted was between 48 and 93%. The correlation between the independent variables and the responses were developed using CCD based on the experimental findings. From CCD, the predictive quadratic model for SO_2 removal efficiency was obtained in terms of coded factors as shown below:

$$Y = 77 - 6.58x_1 + 8.58x_2 + 1.58x_3 + 3.42x_4 - x_1x_2 - 0.5x_1x_3 + 1.75x_1x_4 + 0.375x_2x_3 + 1.63x_2x_4 - 0.625x_3x_4 - 0.667{x_1}^2 - 3.04{x_2}^2 - 1.04{x_3}^2 - 0.792{x_4}^2 \quad \textbf{Equation 2}$$

$Y - SO_2\ removal\ efficiency\ (\%), x_1 - Temperature\ (℃), x_2 - Stoichiometric\ ratio$

$x_3 - Slurry\ solid\ concentration\ (\%), x_4 - Slurry\ pH$

The coded equation was useful in identifying the relative impact of the experimental variables by

comparing the model coefficients. Analysis of variance (ANOVA) was carried out to determine the significance test for the predictive model and the individual model terms. The results for lack of fit test and ANOVA are presented in Table 3. The model F-value of 28.33 and p-value of less than 0.0001 confirm that the selected model is a suitable fit. The p-values were also used to check the model terms, which indicate that the model term is significant if this value is less than 0.0500. In this case, all four model terms x_1, x_2, x_3 and x_4 have significant effect of SO_2 absorption efficiency. All interaction effects of the model terms except x_2x_4 are non-significant with p-values greater than 0.1000. The analysis also shows that the quadratic effects of all variables except ${x_2}^2$ were non-significant bearing p-values greater than 0.1000.

Table 3: Analysis of variance (ANOVA) for the quadratic model

Source	**Sum of squares**	**F-value**	**p-value**	
Model	3495.20	28.33	< 0.0001	Significant
x_1- Temperature	1040.17	118.05	< 0.0001	
x_2 - Stoichiometric ratio	1768.17	200.67	< 0.0001	
x_3 - Slurry solid concentration	60.17	6.83	0.0196	
x_4 - Slurry pH	280.17	31.80	< 0.0001	
x_1x_2	16.00	1.82	0.1978	
x_1x_3	4.00	0.4540	0.5107	
x_1x_4	9.00	1.02	0.3282	
x_2x_3	2.25	0.2554	0.6207	
x_2x_4	42.25	4.80	0.0448	
x_3x_4	6.25	0.7093	0.4129	
${x_1}^2$	12.19	1.38	0.2578	
${x_2}^2$	253.76	28.80	< 0.0001	
${x_3}^2$	29.76	3.38	0.0860	
${x_4}^2$	17.19	1.95	0.1828	
Residual	132.17			
Lack of Fit	132.17			
Cor Total	3627.37			

The precision of the predictive model was validated by assessing the linear relationship between experimental and predicted values. Figure 4 shows a regression graph for experimental and predicted values showing an acceptable fit of the data points along the line of unit slope. This gave an R-squared (R^2) value of 0.93 for the quadratic model which implies that the entire response variation can be attributed to the quadratic model.

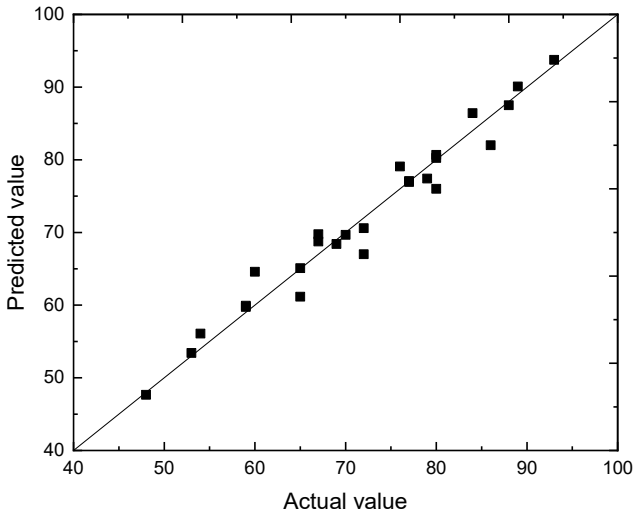

Figure 4: Regression graph of the predicted and experimental values

3.3 Influence of spray drying parameters on SO2 absorption.

SO_2 removal efficiency obtained under different experimental conditions ranged from 48 – 93%. The effects of all interactions of the independent variables on SO_2 absorption were represented using 3D surface plots generated by the variation of two independent parameters while keeping the other two constant at their respective central points. This gave six 3D surface response plots as shown in Figure 5 and Figure 6 which provide information of the effect of each independent variable and their interactive effects on the response (SO_2 removal efficiency).

The interactive effects of the temperature (x_1) and the stoichiometric molar ratio (x_2) on SO_2 removal efficiency under constant values of solid concentration (10%) and slurry pH (8) is shown in Figure 5(a). Stoichiometric ratio in lime spray drying is the ratio of the moles of the reactant in the feed slurry to the mols of SO_2 inlet into the scrubber. From Figure 5(a), an increase in the absorption efficiency was observed with increasing stoichiometric molar ratio. Improved SO_2 removal at high stoichiometric molar ratios is due to increased concentration of the reactant ($Ca[OH]_2$) which maintains the reaction front at the droplet surface and consequently reduces the liquid mass transfer resistance (Hill and Zank, 2000). On the other hand, increasing inlet gas phase temperature impacts negatively on SO_2 absorption efficiency as observed from the model plot. Higher inlet gas phase temperatures cause rapid evaporation and reduces the contact time necessary between the droplet and the flue gas. This eventually reduces the removal of SO_2 due to increased driving force for evaporation.

The combined effects of temperature (x_1) and slurry solid concentration (x_3) at constant values of stoichiometric ratio (1.5) and slurry pH (8) is shown in Figure 5(b). Slurry solid concentration was observed to have little impact on SO_2 absorption efficiency with a slight increase in the efficiency from 67-69% when solid concentration was varied from 8% to 12% which was attributed to the increase in the number of reactants (lime particles) available in the slurry for reaction with SO_2 (Scala *et al*., 2005).

Figure 6(b) illustrates the interactive effects of the slurry pH and the stoichiometric molar ratio on SO_2 absorption efficiency. This was conducted while keeping the inlet gas phase temperature and solid concentration constant at their respective central points. The model plot portrays a slight decrease in SO_2 absorption efficiency from 66% to 63% when the slurry pH was decreased from 10 to 6. The decreasing absorption at lower pH is due to increasing concentration of HCl that was used to adjust the slurry pH. Strong presence of HCl at lower pH increases the concentration of Cl^- ions present in the slurry, which will inhibit the dissolution of lime ($Ca[OH]_2$) particles i.e. diffusion of H^+ and Ca^{2+} ions withing the droplet (Zheng *et al*., 2002). We note that if the interaction term x_2x_4 is significant, it increases the risk of incorrectly identifying the effects of x_1, x_2, x_3 and x_4 on SO_2 absorption efficiency.

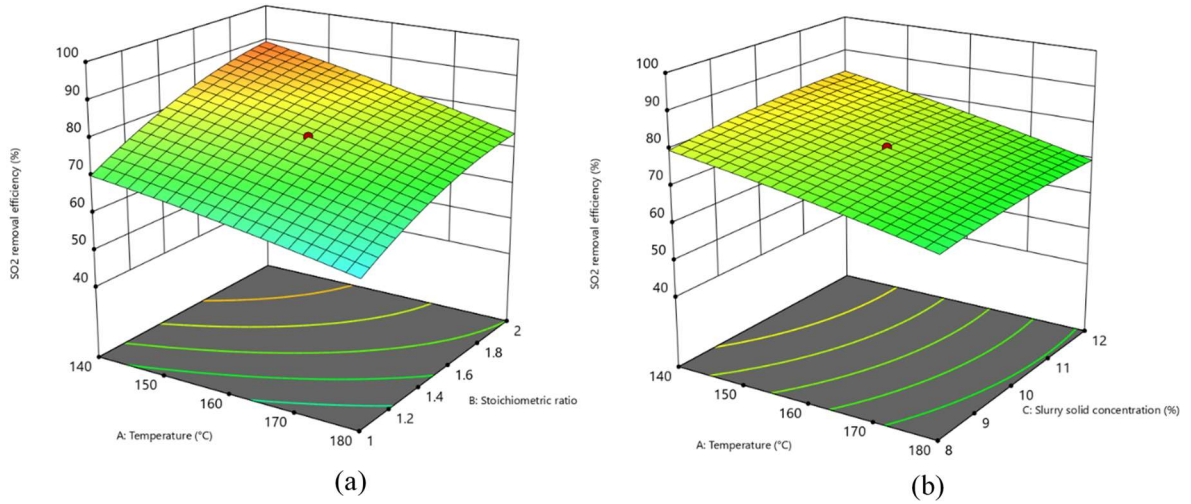

Figure 5: Interactive effects of inlet gas phase temperature with stoichiometric ratio (a), and inlet gas phase temperature with slurry solid concentration (b) on SO2 removal efficiency.

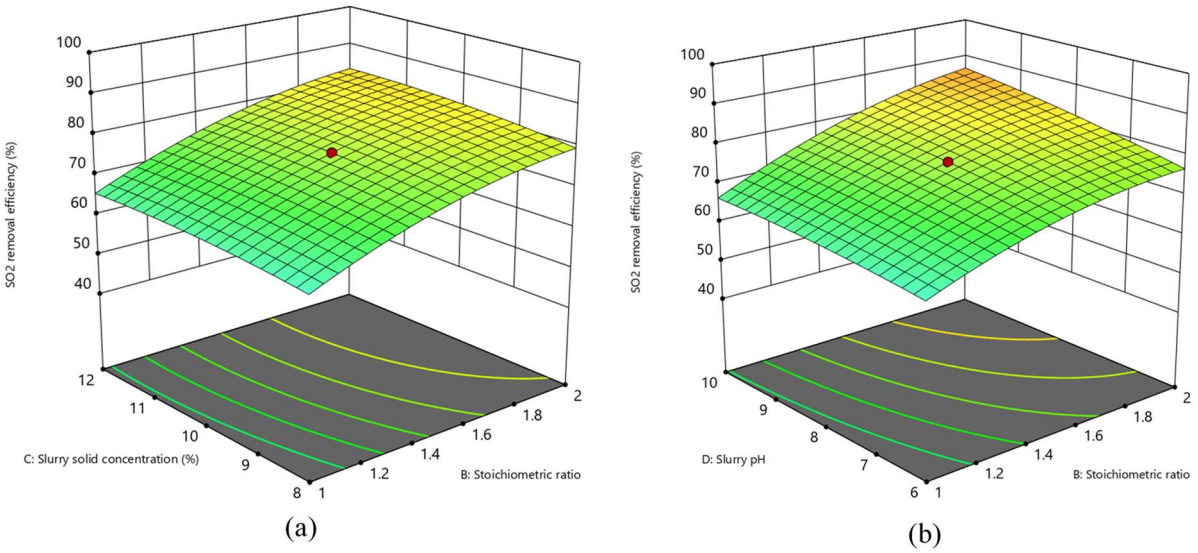

Figure 6: Interactive effects slurry solid concentration with stoichiometric ratio (a), and slurry pH with stoichiometric ratio (b) on SO2 removal efficiency.

3.4 Optimization of desulphurization variables

Spray drying absorption involves scrubbing of SO_2 from flue gas by contacting it with alkaline (lime) slurry. Efficient SO_2 removal requires operation of the spray dryer at most appropriate conditions of the variables. In the present study, independent variables were evaluated to get optimal conditions necessary to achieve maximum SO_2 absorption. Design expert v13.0.1.0 was used to generate the set of optimum conditions of independent variables with the predicted values of the response i.e., SO_2 removal efficiency using numerical optimization function called desirability. Desirability function is an objective function the most commonly used method for optimization of responses. It is based on the idea that the "quality" of a product or process that has multiple quality characteristics, with one of them outside of some "desired" limits, is completely unacceptable (Heckert *et al*., 2002). The method assigns a "score" between 0 (least) and 1 (most) to a response and chooses factor settings that maximize that score. If any of the responses falls outside their desirability range, the overall function becomes zero (Amjed *et al*., 2017). Optimization criteria chosen for all independent variables and responses is shown in Table 4:

Table 4: Criteria for numerical optimization of SO2 absorption

Variable/Response	Goal	Lower limit	Upper limit
x_1: Inlet gas temperature	minimize	140	180
x_2: Stoichiometric ratio	In range	1	2
x_3: Slurry solid concentration	minimize	8	12
x_4: Slurry pH	maximize	6	12
SO_2 removal efficiency	maximize	48	93

The optimum process conditions and response were generated from the software. The optimum conditions for independent variables based on the highest desirability value were found to be at inlet gas phase temperature of 140°C, stoichiometric molar ratio of 2, slurry solid concentration of 8% and slurry pH of 10. These set of optimum conditions produced SO_2 removal efficiency of 90% with a desirability of 0.98.

4 CONCLUSIONS

This study presents the findings of the influence of spray drying characteristics on SO_2 absorption efficiency. RSM was used to analyse and optimize the independent variables which include inlet gas phase temperature, stoichiometric molar ratio, slurry solid content and slurry pH. A predictive quadratic model correlating the variables and response was developed using CCD. The analysis of the model was found to best describe the relationship with an R-squared coefficient of 0.93 when compared to the experimental data. The model results indicated stoichiometric molar ratio as a variable with significant influence on the absorption of SO_2. Under the recommended optimal conditions of inlet gas phase

temperature of 140°C, stoichiometric ratio of 2, slurry solid concentration of 8% and slurry pH of 10, a removal efficiency of 90% for SO_2 can be achieved. This study contributes to the understanding of the interactive effects of the variables on the absorption of SO_2 and will help on efficient operation in spray drying FGD.

REFERENCES

Amjed, N. *et al.* (2017) 'Coal desulphurization and conditions optimization through response surface methodology, Khushab mines, Pakistan', *Energy Sources, Part A: Recovery, Utilization, and Environmental Effects*, 39(12), pp. 1235–1241.

Gassner, M. *et al.* (2014) 'A data-driven approach for analysing the operational behaviour and performance of an industrial flue gas desulphurisation process', in *Computer Aided Chemical Engineering*. Elsevier, pp. 661–666.

Heckert, N. A. *et al.* (2002) 'Handbook 151: NIST/SEMATECH e-Handbook of Statistical Methods'.

Hill, F. and Zank, J. (2000) 'Flue gas desulphurization by spray dry absorption', *Chemical Engineering and Processing: Process Intensification*, 39(1), pp. 45–52.

Katolicky, J. and Jicha, M. (2013) 'Influence of the Lime Slurry Droplet Spectrum on the Efficiency of Semi-Dry Flue Gas Desulfurization', *Chemical Engineering & Technology*, 36(1), pp. 156–166.

Myer, R. and Montgomery, D. C. (2002) 'Response Surface Methodology: process and product optimization using designed experiment', *John Wiley and Sons, New York*, (Journal), pp. 343–350.

Scala, F. *et al.* (2005) 'Spray-dry desulfurization of flue gas from heavy oil combustion', *Journal of the Air & Waste Management Association*, 55(1), pp. 20–29.

Scala, F., D'Ascenzo, M. and Lancia, A. (2004) 'Modeling flue gas desulfurization by spray-dry absorption', *Separation and Purification Technology*, 34(1), pp. 143–153.

Xie, D. *et al.* (2017) 'Semidry desulfurization process with in-situ supported sorbent preparation', *Energy & Fuels*, 31(4), pp. 4211–4218.

Zheng, Y. *et al.* (2002) 'Use of spray dry absorption product in wet flue gas desulphurisation plants: pilot-scale experiments', *Fuel*, 81(15), pp. 1899–1905.

An analysis of petroleum storage tank emissions and procedures to reduce the resulting environmental impact

T. Naidoo[1], P. Naidoo[1,2] and K. Moodley[1*]

[1] Thermodynamic Research Unit, School of Engineering, University of KwaZulu-Natal, Howard College Campus, King George V Avenue, Durban, 4041, South Africa

[2] Department of Process Engineering, Stellenbosch University, Banhoekweg, Stellenbosch, 7600, South Africa

[*]Corresponding author: moodleyk6@ukzn.ac.za

ABSTRACT

Climatic factors coupled with urbanization and its dependence on carbon-based fuel for a range of purposes, have highlighted a major concern regarding the rapid increase of hazardous gas emissions globally (Howari, 2015). The abatement of pollution, process impact on health and the environment, and safety protocols of emissions are important emerging issues. Oil and gas industries are significant contributors of volatile emissions. Large-scale accurate monitoring of emissions is difficult to quantify due to its complex nature. Therefore, knowledge from longstanding production process standards is necessary to ensure accurate emissions estimates. The estimation of emissions is also necessary for the implementation of emission control methods which actively work to limit emissions. Atmospheric storage tanks also represent a significant portion of industrial incidents, typically due to its fragility and inability to withstand slight overpressure. Inert gas padding is a safety system implemented in industry to prevent the chemical oxidation of the contents within the tank by controlling the pressure within the storage tanks (U.S. Environmental Protection Agency, 1992). This study reviews the current knowledgebase and handling practices for volatile organic compound emissions from petroleum storage tanks, examines suitable storage operating conditions, and aims to provide strategies for implementation to achieve safe control and handling of emissions by performing calculations based on API 2000 (Ciolek, 2006) and dynamic simulations on ASPEN Plus.

1 INTRODUCTION

The emission of hydrocarbon compounds such as Volatile Organic Compounds (VOCs) to the atmosphere poses a human health hazard and has a negative impact on the environment (Kihlman, et al., 2006). In South Africa, ozone levels in the troposphere are rising rapidly and the effects of climate change are being seen through water scarcity, resulting in issues with water restrictions, as well as crop losses which reduces food and water security (Sasol Limited, 2019).

In order to achieve and combat issues related to the United Nations Sustainable Development Goal 13: Climate Change, stringent regulation policies have been implemented to reduce ground level ozone by the monitoring and control of VOCs. This includes: The South African Carbon Tax Act 15 of 2019, which imposes carbon tax on emissions (Government Gazette: Republic of South Africa, 2019); The

National Atmospheric Emission Inventory System (NAEIS) is an integration between the management of Atmospheric Emission Licenses (AEL) and The National Environmental Management: Air Quality Act 39 of 2004, and imposes that process industries report their estimations of atmospheric emissions (Government Gazette, 2015). South Africa's commitment to a lower-carbon economy is further supported by the Paris Agreement (to which South Africa is a signatory), which aims to "reduce Greenhouse Gas (GHG) Emissions and limit the global average temperature increase to well below 2 degrees Celsius" (Nqwababa & Cornell, 2019).

Due to the reliance on fossil-fuel derived energy and the lack of available infrastructure, knowledge and commercialization of renewable energy sources, there are numerous challenges to integrating a low-carbon economy in South Africa (Nqwababa & Cornell, 2019). A leading anthropogenic source of VOC emissions include oil and gas industries in which refinery petroleum storage tanks are considered to be the single largest point source of VOC emissions (Howari, 2015). According to (Maxwell & Lawal, 2016), 31.5% of VOC emissions occur from gasoline or oil storage tanks and (IMPEL Network, 2000) suggested that tank areas contribute 42% of the total emission sources from an oil refinery

Many major industries have responded to the new South African legislation. Sasol, for example, has implemented an emission reduction roadmap based on a three-pillar emission-reduction framework which aims to reduce emissions by 10% in South African operations by 2030 (Sasol Limited, 2019). Currently, a common method used in petroleum industries for VOC emissions estimation was developed by The Environmental Protection Agency (EPA) (United States), which is based on the AP-42 model for air pollutant emission factors. Other methods including direct methods such as Leak Detection and Repair (LDAR) or DIAL (SAPREF, 2016), have been utilised to monitor VOC emissions in industry, however, in order for companies such as Sasol to accurately monitor and control their emission reduction targets, more reliable estimation methods using current plant data are required to predict VOC emissions over time. Technologies such as TANKS have been developed and commonly used in industry thus far, however, this process simulator is considered outdated and offers inaccurate estimates (Heath & Liu, 2016). Insight into new technologies which provide accurate estimates employing rigorous thermodynamic and transport calculations, are therefore required to properly control VOC emissions and monitor reduction methods.

To establish the effects of previous practices, and the consequences of future non-action, a comprehensive environmental impact assessment of VOC emissions from petroleum storage tanks is conducted in this work. This assessment highlighted the specific need for developing protocols and tools to assist in monitoring and control of VOC emissions from storage tanks, to reduce the impact on the environment, ensure process safety and abide with new legislature in South Africa.

ASPEN Plus ® is a versatile process simulation tool and is used commercially in many petroleum

industries for preliminary design and simulation. The software offers rigorous estimation of thermodynamic and transport properties, and also offers a rigorous tank design option. There is a scarcity of research in the literature regarding the estimation of VOC emissions using the ASPEN Plus ® platform, and the precision of the methods available in the software.

In this study a focus is placed on developing a method that improves the analysis and prediction of VOC emissions from petroleum storage tanks. Three case studies are considered that are aimed to understand the uncertainties and limitations involved using the proposed method, in comparison to other options. Manual calculations using the AP-42 method were also used to estimate breathing and working losses and a comparative study was done against empirical correlation estimates. Safe operating conditions were investigated by determining the effect of temperature and pressure of the storage tank; and an in-depth study on VOC emission reduction strategies was conducted for implementation in industry.

2 LITERATURE

2.1 Categories of tank emissions

There are six types of emissions which may occur from petroleum storage tanks, namely: 1) breathing losses, 2) standing losses, 3) filling losses, 4) emptying losses, 5) wetting losses and 6) boiling or evaporative losses (Taylor & Francis Group, 1971).

Breathing Losses

Breathing losses occur as a result of thermal expansion of vapours in the tank, barometric changes with pressure or from an increase in vaporization of the product, without altering the level of liquid in the tank, leading to an increase in vapours formed. Breathing losses also commonly occur when changes in pressure or volume thresholds are exceeded, thereby the losses are forced to escape into the atmosphere. It may occur in most tank types however, fixed roof tanks which lack proper insulation, have no insulation or designed for vacuum are more prone to experience higher breathing losses. However, fixed roof tanks with proper insulation and has good condition reflective paint, will have lower breathing losses. Pressure tanks designed to operate above two and a half psig has a very low probability of experiencing breathing losses. Floating roof tanks operate by reducing the vapour space within the tank thereby eliminating the possibility of breathing losses from occurring. Similarly, variable vapour space tanks reduce the breathing loss potential (Taylor & Francis Group, 1971).

Standing Losses

Standing losses are considered all losses other than breathing losses and losses resulting from a liquid level change. A significant amount of standing losses from floating roof tanks occur from poor maintenance or design. For example, when the seal and the shoe are improperly connected to the shell

of the tank, it provides a source of leakage. This may also provide a means for the release of vapour through the permeable membrane seal which is in the middle of the roof and shoe. Gaging hatches or pressure vacuum vents, various fittings from equipment as well as wind are other major factors which may contribute to the release of standing losses (Taylor & Francis Group, 1971).

Filling Losses

Filling losses occurs when the internal pressure of the tank is greater than the relief valve pressure and as a result, the expulsion of vapour occurs from a storage tank during the process of loading or filling the tank. Fixed roof tanks experience a high rate of losses by filling it has a lower pressure relief. Therefore, more filling losses are released into the atmosphere. Due to the increased capacity for the storage of vapours with variable vapour space tanks, variable vapour space tanks have a lower potential of emitting losses during the filling operation. Pressure tanks operate slightly differently, by condensing hydrocarbon vapours to reduce the loss of emissions during the loading process. However, floating roof tanks do not encounter filling losses and are subject to other sources of emissions (Taylor & Francis Group, 1971).

Emptying Losses

Emptying losses occur as a result of a decrease in partial pressure of hydrocarbon vapours when the vapour space of the tank expands faster than the rate of vaporization occurs, during emptying of the tank. During tank withdrawal, in order to sustain atmospheric pressure within the tank, a sufficient amount of air enters the tank to control this. Once equilibrium of the vapour molecules is reached, the capacity of the vapour space become overfilled with vapour which causes the vapour to be expelled into the air. This is known as the emptying losses. Fixed roof tanks are the most susceptible to emptying losses, whereas floating roof tanks are the least. Variable space tanks and pressure tanks may experience emptying losses only if the volume of the vapour exceeds the capacity of the vapour space (Taylor & Francis Group, 1971).

Wetting Losses

Wetting losses are minimal and occur as a result of lowering a floating roof during emptying of a tank which allows for the surface of the wetted tank walls to be exposed. The liquid on the tank walls are then vaporized and are termed wetting losses (Taylor & Francis Group, 1971).

Boiling Losses

When a liquid is boiled and vaporization occurs, boiling losses are emitted into the atmosphere. Boiling losses typically occur in fixed roof tanks compared to a pressure tank (Taylor & Francis Group, 1971).

2.2 Tank Parameters and types

The quantity of emissions emitted from storage tanks are largely reliant on the physical characteristics of the storage tank. The type of tanks, type of roof, shape of roof, storage tank shell colour and condition of the tank are all major factors that should be considered prior to the containment of liquids to ensure minimal emissions are being emitted into the atmosphere (ERA Environmental Management Solutions, 2019).

Several types of storage tanks exist and may be used to storage various chemical compounds. Common storage tanks used in industry include: external floating roof tanks, internal floating roof tanks, fixed roof tanks, pressure tanks, horizontal tanks and vapour variable space tanks (Ciolek, 2006). However, floating roof tanks are commonly used in industry to store volatile hydrocarbon liquids such as crude oil and light hydrocarbon products such as jet fuel, diesel and gasoline. These tanks are preferred due to its ability to keep the volatile vapours sealed below the roof during normal operating conditions, when it is more susceptible to escape (Simon, 2014).

The average emission factor method is the most commonly used method to determine storage tanks emissions and are based on emission factors as proposed by the Environmental Protection Agency (EPA). The emission estimates procedures for fixed roof, external floating roof, domed external floating roof and internal floating roof tanks are outlined below. These estimates are based on the AP-42 standards as approved by the US Environmental Agency (Ciolek, 2006).

2.3 Fixed Roof Tanks

The following equations can be applied to vertical cylindrical shelled tanks as well as fixed roof tanks in which the liquid contents have a known vapour pressure. The equations are limited to atmospheric storage tanks in which the tanks are vapour and liquid tight. The **total losses** from fixed roof tanks are a combination of the standing and working losses:

$$L_T = L_S + L_W \qquad \textbf{Equation 1}$$

Where:

L_T = Total losses [lb/year]

L_S = Standing storage losses [lb/year]

L_W = Working losses [lb/year]

Refer to Ciolek (Ciolek, 2006) for more details regarding the dimensionless factors used in the aforementioned equation.

2.4 Floating Roof Tanks

The total floating roof tank losses under normal operating conditions are a combination of rim seal, deck fitting, deck seam and withdrawal losses as per the following equation:

$$L_T = L_R + L_{WD} + L_F + L_D \qquad \textbf{Equation 2}$$

Where:

L_T = Total loss [lb/year]

L_R = Rim seal loss [lb/year]

L_{WD} = Withdrawal loss [lb/year]

L_F = Deck fitting loss [lb/year]

L_D = Deck seam loss – internal floating roof tanks only [lb/year]

(Ciolek, 2006) contains more information regarding the dimensionless factors in the aforementioned equations.

2.5 Empirical Correlations

Various types of correlations exist to estimate emissions from storage tanks. The Vasques-Beggs (VB), Environmental Consultants and Research (C/R), Equation of State calculation programmes, Gas Oil Ratio (GOR) and process simulators are some of the common types of estimation methods used (U.S. Environmental Protection Agency, 1992).

2.6 Vasques – Beggs

Empirical equations such as the Vasques-Beggs or Griswold and Ambler GOR Chart methods may be used to estimate hydrocarbon storage tank flashing emissions. The VBE equation is a simple equation that does not require a process simulation. Then equation requires eight input variables which include: separator pressure, temperature, specific gravity of the gas, API gravity, hydrocarbon volume, stock tank gas molecular weight, atmospheric pressure and the VOC fraction of the emissions from the tank. This method may be used to estimate emissions of dissolved gases in crude oils (U.S. Environmental Protection Agency, 1992). Some limitations of this method include overestimating or underestimating flashing losses and it does account for standing and working losses from storage tanks (Sills, 2019).

2.7 Environmental Consultants and Research (EC/R)

The EC/R equation is used to estimate flash emissions and occurs when there is a pressure drop across the stream flowing to the storage tank. The equation involves the estimation of the ratio of the liquid and vapour phase components which are based on the compositions of the flashed vapour and pressure of the tank. This, along with the throughput of the tank, mass fraction each liquid component and the liquid hydrocarbon density, are used to determine the tank flashing losses (kdheks.gov, 2006). Even though the simplicity of this equation makes it an attractive option, this method fails to calculate standing and working losses. It is also limited by its validity within the vapour pressure range of 1.6 atm and 5.1 atm (Sills, 2019).

2.8 Equation of State (EOS) Programmes

The E&P TANK simulation software can be used to determine working, breathing and flashing losses

from hydrocarbon storage tanks. It can be based on the Reid Vapour Pressure (RVP) method or AP-42 method. This programme utilizes an Equation of state (EOS) such as Peng-Robinson (PR) with the following inputs: Oil composition of the separator, temperature and pressure of the separator, sales RVP and API gravity and production rate and ambient pressure and temperature. However, this programme is outdated and does not account for the various types of tanks and fittings within the tank (Sills, 2019).

2.9 Gas Oil Ratio (GOR)

The GOR method is used to determine flashing losses from a pressurized liquid sample in a storage tank. A laboratory analysis of the sample is taken to obtain the concentrations of each component present in the flash emissions. This method is considered to represent the emissions most accurately and utilizes a simple equation that requires four inputs: The measured GOR, molecular weight of the stock tank, specification profile and the production of oil. However, this method fails to calculate standing and working losses and sampling of pressurized liquids may be difficult to acquire (Sills, 2019).

3 METHODICAL APPROACH

3.1 Outline of approach

A comparative study and environmental impact assessment (EIA) were conducted by using the following method:

- Flashing losses were predicted using Aspen Plus process simulator and various estimation equations;
- Working and breathing losses were predicted using the AP-42 method; and
- Various parameters were varied to determine its effect on the emissions – an EIA was conducted.

4 RESULTS AND DISCUSSION

This section discusses results for six major petroleum products: 1) crude oil, 2) ultra-low sulphur diesel (ULSD), 3) 95 unleaded petrol (ULP 95), 4) jet fuel (JET A1), 5) marine gas oil (MGO) and 6) cold tar, stored in its respective storage tank and applies various estimation procedures to determine flashing and working and breathing losses from the storage tanks. A comparative study is conducted to determine the effects of: the types of storage tanks, various estimation model equations and a simulation method of Aspen Plus.

4.1 Crude Oil Storage Tank

According to the study conducted by (Burr & Georgeson , 2013), flashing losses using the ProMax process simulator were estimated to be 110.8 tons/yr. A simulation conducted on Aspen Plus using similar conditions and compositions, as shown in Figure 1, yielded 110.6 tons/yr of flashing losses from the storage tank containing crude oil. A 0.18% uncertainty indicated that Aspen Plus offers a suitable predictive modelling method to estimate flashing losses from storage tanks.

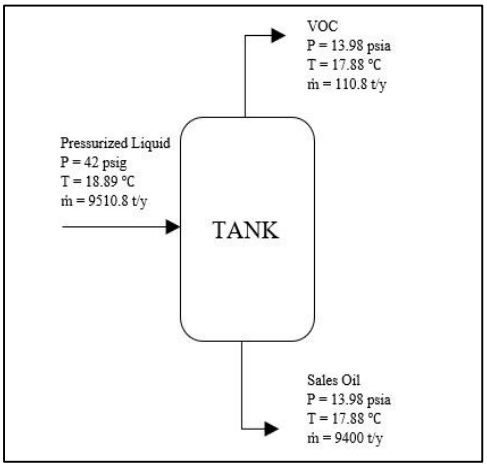

Figure 1: Crude oil storage tank with conditions

The total working and breathing losses are regarded as secondary fugitive emissions. It may be as a result of filling the tank in which the level of the liquid changes or through thermal expansion, relying on meteorological conditions, respectively. (Burr & Georgeson , 2013) estimated the working and breathing losses using the ProMax process simulator and was found to be 12.65 tons/yr. Aspen Plus fails to predict working and breathing losses therefore the AP-42 method as outlined in (Ciolek, 2006) by the US EPA, was used to estimate these losses. Using a fixed roof storage tank and assuming a cone shaped roof, 2.32 tons/yr of working and breathing losses were estimated with an uncertainty of 81.66% when comparing it to ProMax. Table below represents the comparison between the emission estimates.

Table 1: Comparisons of flash, working and breathing losses from ProMax and Aspen Plus

Flash Losses (tons/yr)			Total Working and breathing losses (tons/yr)		
ProMax[8]	Aspen Plus ®	Uncertainty (%)	ProMax[8]	Manual (AP-42)	Uncertainty (%)
110.8	110.6	0.18	12.65	2.32	81.66

According to the cited literature, internal floating roof tanks are considered to significantly reduce emissions through its floating head which reduces the vapour space of the storage tank. Working and breathing losses were calculated using the AP-42 method again, and a comparison was conducted on fixed roof and internal floating roof tanks in which crude oil was stored, Table 2 represents this. It can be noted that the fixed roof storage tank estimates 83.64% more emissions than the internal floating roof tank with emissions of 2.323 tons/yr and 0.380 tons/yr respectively, therefore, suggesting that the implementation of internal floating roof tanks in industry can significantly reduce the quantity of working and breathing losses emitted.

Table 2: Comparisons of working and breathing losses from a fixed roof and internal floating roof storage

tank containing crude oil

Fixed Roof Tank Emissions (tons/yr)	Internal Floating Roof Tank Emissions (tons/yr)	Uncertainty (%)
2.323	0.380	83.64

4.2 EPA Estimation Method on Petroleum Products

Total working and breathing losses for six petroleum products were, as shown in Table 3, were estimated using the AP-42 method and a comparison was conducted against fixed roof storage tanks and internal floating roof storage tanks. Ulta-low sulphur diesel, 95 unleaded petrol, jet fuel and marine gas oil were stored in a tank terminal in Durban, KwaZulu-Natal for (Golder Associates Africa (Pty) Ltd, 2019) and cold tar was stored at a facility in Secunda for (Caddick, 2019).

Table 3: Comparisons of working and breathing losses from a fixed roof and internal floating roof storage tank containing various petroleum products

Product	Emissions (Tons/yr)		Uncertainty (%)
	Fixed Roof Tank	Internal Floating Roof Tank	
Crude Oil	2,323	0,380	83.64
Ultra-low sulphur diesel	85,791	4,693	94.43
95 Unleaded petrol	1486,287	8,100	99.46
Jet Fuel (A1)	573,848	1,673	99.71
Marine gas oil	0,064	0,464	86.21
Cold tar	743,504	2,189	99.71

5 CONCLUSIONS

A literature review was conducted to review the current procedures and practices involved in estimating emissions and helped to determine the main factors involved in influencing emissions. Calculations were performed based on the commonly used AP-42 method which estimated that internal floating roof tanks yield lower emissions compared to fixed roof tanks. Aspen Plus was used to predict flashing losses from the storage tanks and compared to another process simulator, ProMax.

REFERENCES

Burr , B. L., & Georgeson , A. M. (2013). *Air Emissions Modeling Advances for Oil and Gas Production Facilities.* Oklahoma City: Bryan Research & Engineering, Inc.

Caddick, A. (2019). *Application for an Environmental Authorisation for the Clean Fuels 2 (CF 2) Proposed Tanks Expansion project at the Sasol Synfuels Operations in Secunda, Mpumalanga Province.* Pretoria: SRK Consulting .

Ciolek, M. (2006). *Emissioln Factor Documentation for AP-42, Section 7.1, Organic Liquid Storage Tanks.* NC: Research Triangle Park.

DEQ. (2006, August 28). *Air calculation of Flashing Losses/VOC Emissions from Hydrocarbon Storage Tanks.* Retrieved May 09, 2019, from DEQ (Department of Air Quality): http://www.deq.state.ok.us/aqdnew/resources/factsheets/CalculationLosses.pdf

Golder Associates Africa (Pty) Ltd. (2019). *Application for EA, AEL, nd GA for the proposed Lanele Oil Terminal 1 (Lot 1) Project at ambrose Park, in Bayhead, Durban: Air Quality Impact Assessment* . Midrand.

Government Gazette. (2015). Department of Environmental Affairs. Pretoria.

Government Gazette: Republic of South Africa. (2019). Carbon Tax Act, 2019. Cape Town.

Heath, C., & Liu, F. (2016). *Calculating tank emissions with TANKESP*. Retrieved October 16, 2019, from https://www.trinityconsultants.com/news/technology/calculating-tank-emissions-with-tankesp

Howari, F. M. (2015). Evaporation Losses and Dispersion of Volatile Organic Compounds from Tank Farms. *Environ Monit Assess, 10*, 187-273.

IMPEL Network. (2000). *Diffuse VOC Emissions.* Brussels: European Union Network for the Implementation and Enforcement of Environmental Law.

Kihlman, M., Mellqvist, J., SAmuelsson, J., Tang , L., & Chen, D. (2006). Monitoring of VOC emissions from refineries in Sweden using the SOF method. Sweden.

Maxwell, A., & Lawal, A. (2016). Petroleum Product Storage Tank, Design and Loss Control Management. *Society of Petroleum Engineers*.

Nqwababa, B., & Cornell, S. (2019). Sasol and Climate Change.

SAPREF. (2016). Sustainability Report 2016. Durban.

Sasol Limited. (2019). *Positioning for resilience in a lower-carbon future.*

Sills, L. (2019). Comparison of Emission Calculation Methodologies for the Oil and Gas Industry. Dallas: Oil and Gas Environmental Conference. Retrieved 05 10, 2019

U.S. Environmental Protection Agency. (1992). *Control Techniques for Volatile Organic Compound Emissions from Stationary Sources* . North Carolina: Emission Standards Division.

A narrative review of plastic waste pyrolysis: challenges and opportunities

Z.S. Mazhandu[1*], E. Muzenda[2,1], M. Belaid[1] and T. Nhubu[1]

[1] University of Johannesburg, Department of Chemical Engineering Technology, 55 Beit St, Doornfontein, Johannesburg, 2028, South Africa

[2] Botswana International University of Science and Technology, Department of Chemical, Materials and Metallurgical Engineering, P. Bag 16, Palapye, 00000, Botswana

*Corresponding author: zvanaka@gmail.com; +27 (0)11 472 0083

ABSTRACT

Plastic waste management (PWM) in South Africa entails mechanical recycling and landfilling. The objectives of this review study are to explore the possibility of using pyrolysis in PWM. The key findings are that most plastic types will result in high oil yield although PET and PVC may not be suitable candidates for pyrolysis due to the corrosive benzoic acid and HCl generated during their pyrolysis respectively and the calorific value (CV) of the produced oil which is also impacted negatively.

Keywords: plastic pyrolysis; pyrolysis conditions; pyrolysis reactors; pyrolysis of plastic waste; pyrolysis products

1 INTRODUCTION

Plastic waste management in South Africa entails mechanical recycling and landfilling. However, the percentage of plastic waste landfilled exceeds the quantity that is recycled. For example, the input recycling rate was 45.7% in 2019 (DeArmitt, 2019). In addition to the two afore-mentioned plastic waste management methods employed in South Africa, illegal dumping, burning and littering are also common (DeArmitt, 2019). Mazhandu et al. (Mazhandu *et al.*, 2020) also highlighted the constraints of mechanical recycling which include the deterioration of the plastic after repeated recycling cycles and contamination; consequently, this type of recycling lacks finality (Mazhandu *et al.*, 2020). It is imperative therefore to explore all the methods that are available to stamp out plastic waste leakage into the environment and one such method is pyrolysis which has been gaining attention globally as a potentially sustainable way to manage plastic wastes. Past studies that have been reviewed detailing life cycle assessments of mechanical recycling, landfilling, incineration and pyrolysis of mixed plastic wastes, have shown that landfilling and incineration overall have higher environmental impacts compared to mechanical recycling and pyrolysis. The objectives of this review study are:

- To determine the different types of pyrolysis processes and associated process conditions;
- To assess from past studies; the operating conditions and yields of various plastics;
- To identify the plastics best suited for pyrolysis;
- To determine the various types of pyrolysis reactors and assess advantages and disadvantages of

each system.

2 DATA SOURCES

Data was sourced from academic databases including Google Scholar, Scopus, Science Direct, Springer Link and Web of Science. Some of the key words and phrases used were plastic pyrolysis, conditions for pyrolysis, pyrolysis reactors, pyrolysis of polyethylene terephthalate (PET), pyrolysis of polyvinyl chloride (PVC) and pyrolysis of mixed plastic wastes, calorific value and proximate analysis.

3 PYROLYSIS PROCESS REVIEW

Pyrolysis refers to the thermal degradation of organics such as biomass or plastic in the absence of oxygen. Pyrolysis temperatures normally range from 300 to 1300 ^{0}C (Singh *et al.*, 2019) (Lord and Pfannkoch, 2012) (Zhang *et al.*, 2019). Pyrolysis products; namely oil, char and gas can be further processed into products of value (Basu, 2018). It can be catalytic or non-catalytic. In catalytic pyrolysis, the heat energy requirements are reduced although the disposal of the catalyst is also a challenge associated with this process (Miskolczi, Bartha and Angyal, 2009). Biomass pyrolysis has been studied at great lengths by researchers to gain an understanding of the reaction kinetics of pyrolysis. However, despite the popularity of biomass pyrolysis research, plastic waste appears to be more attractive, and this may tip the scales towards more research in plastic pyrolysis. According to Zhao et al. (Zhao *et al.*, 2020), unlike biomass, plastic contains a higher carbon and lower oxygen content which results in high liquid yield. Therefore, this makes plastic an ideal candidate for pyrolysis (Zhao *et al.*, 2020). Figures 1 to 4 show proximate analysis for the different plastic types. Data for the figures was sourced from Sharuddin et al. The proximate analysis of a fuel is defined as the measurement of ash, volatile matter, fixed carbon and moisture content expressed as a percentage (Suárez-Ruiz and Ward, 2008) (Nunes, Matias and Joao, 2017). According to Sharuddin et al. (Sharuddin *et al.*, 2016), the amount of volatile matter and ash content in a fuel determine how much oil and char are generated respectively. During pyrolysis, the higher the volatile matter, the higher the oil yield while a high ash content will result in less oil yield, and higher char and gas formation. The authors also argue that based on the proximate analyses of the various plastics reviewed, the results indicate that the pyrolysis of plastics will result in high oil yields since they contain a significant amount of volatile matter and low ash content.

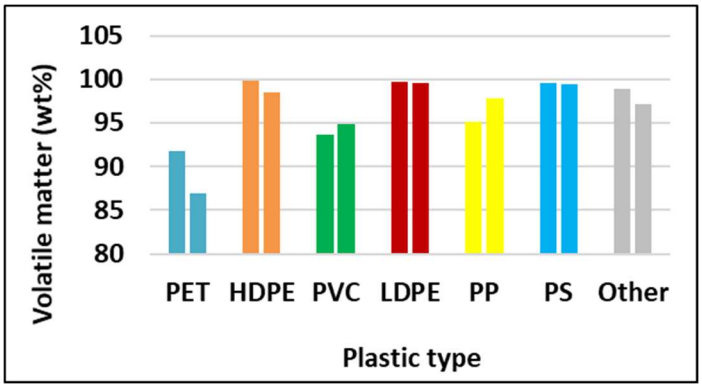

Figure 1: Volatile matter per plastic type, based on data from (Sharuddin et al., 2016)

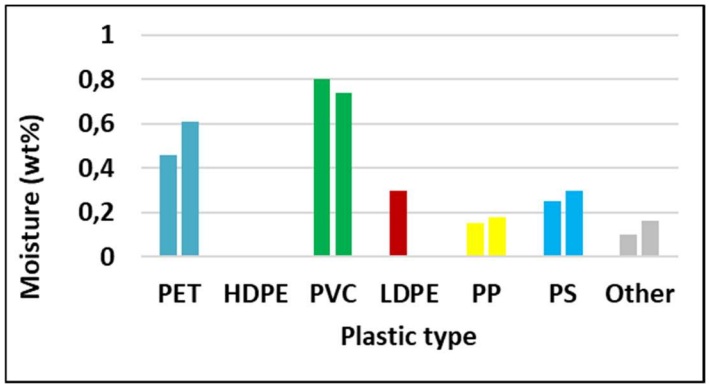

Figure 2: Moisture content per plastic type, based on data from (Sharuddin et al., 2016)

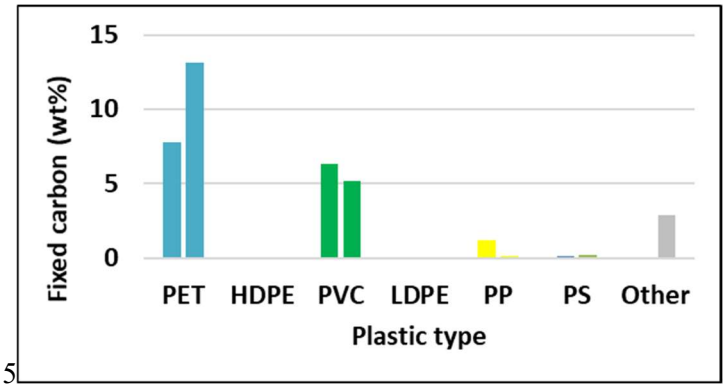

Figure 3: Fixed carbon per plastic type, based on data from (Sharuddin et al., 2016)

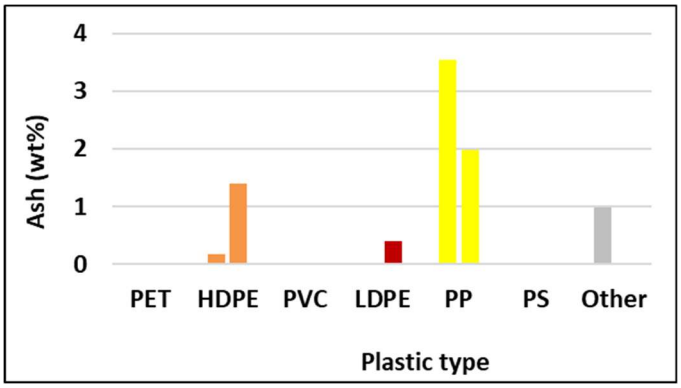

Figure 4: Ash content per plastic type, based on data from (Sharuddin et al., 2016)

Figure 1 shows that PET and PVC plastics had the least volatile matter among all the plastic variants studied. This in turn results in low liquid yield for these two variants. Miandad et al. (Miandad *et al.*, 2019) measured the calorific values of different oils produced using thermally activated and acid activated natural zeolites (TA-NZ and AA-NZ) from the different plastic types and mixtures as shown in Table 1 (Miandad *et al.*, 2019). The gross calorific values (GCVs) for all the plastic types and mixtures were higher (41.7 MJ/kg to 44.2 MJ/kg) than those for high quality coals; bituminous and anthracite which range between 33.5 MJ/kg and 34.6 MJ/kg for. Other solid and liquid fuels such as lignite, peat, petrol, kerosene, diesel, light fuel oil (LFO), heavy fuel oil (HFO) and residual fuel oil had the following GCVs: 21.65 MJ/kg, 15.9 MJ/kg, 47 MJ/kg, 46.3MJ/kg, 46 MJ/kg, 44.8 MJ/kg, 44 MJ/kg and 42.1 MJ/kg respectively (Carvill, 1993). This indicates that the CV for plastics, except for PET and PVC; is within the same range as that for petrol, kerosene, diesel (Miandad *et al.*, 2019), LFO and HFO, also alluding to the versatility of plastic. This is summarised in Table 2.

Table 1: Gross calorific value for various plastic types and mixtures (Miandad et al., 2019)

Feedstock	**TA-NZ (MJ/kg)**	**AA-NZ (MJ/kg)**
PS	41.7	42.1
PP	43.4	42.9
PE	42.9	43.5
PS/PP	42.5	42.9
PS/PE	42.6	43.7
PP/PE	44.1	43.7
PS/PE/PP	42.4	44.2
PS/PE/PP/PET	41.9	43.7

Table 2: Properties of plastic pyrolysis oil, diesel and gasoline *(Sharuddin et al., 2016)*

PHYSICAL PROPERTIES	Type of Plastics (Experimental typical value)						Commercial Standard Value (ASTM 1979)	
	PET	HDPE	PVC	LDPE	PP	PS	Gasoline	Diesel
Calorific value (MJ/kg)	28.2	40.5	21.1	39.5	40.8	43.0	42.5	43.0
API gravity @ 60^0F	n.a	27.48	38.98	47.75	33.03	n.a	55	38
Viscosity (mm^2/s)	n.a	5.08[a]	6.36[b]	5.56[c]	4.09[a]	1.4[d]	1.17	1.9-4.1
Density @ 15^0C (g/cm^3)	0.90	0.89	0.84	0.78	0.86	0.85	0.780	0.807
Ash (wt%)	n.a	0.00	n.a	0.02	0.00	0.006	-	0.01
Octane no. MON (min)	n.a	85.3	n.a	n.a	87.6	n.a	81-85	-
Octane no. RON (min)	n.a	95.3	n.a	n.a	97.8	90-98	91-95	-
Pour point (^{0}C)	n.a	-5	n.a	n.a	-9	-67	-	6
Flash point (^{0}C)	n.a	48	40	41	30	26.1	42	52
Aniline point (^{0}C)	n.a	45	n.a	n.a	40	n.a	71	77.5
Diesel index	n.a	31.05	n.a	n.a	34.35	n.a	-	40

*n.a., not available in literature; a viscosity at 40 ^{0}C; b viscosity at 30 ^{0}C; c viscosity at 25 ^{0}C; d viscosity at 50 ^{0}C

In plastic pyrolysis, the overall reaction would therefore be as represented in Figure 5.

Figure 5: Overall reaction for plastic pyrolysis, based on information from (Basu, 2018)

Factors which influence the characteristics of pyrolysis process products and yields are temperature, heating rate, residence time, pressure, composition of feed and type of reactor used (Singh *et al.*, 2019). According to Qureshi et al. (Qureshi, Oasmaa and Lindfords, 2019), lower process temperatures result in the formation of char and oil whilst at higher temperatures gas formation is promoted. In addition, higher heating rates result in bond cleavage while lower rates encourage production of char. On the other hand, pressure effects are only significant at low temperatures while at high temperatures pressure such effects are minimal. Long residence times favour the production of light hydrocarbons and non-

condensable gases (Qureshi, Oasmaa and Lindfords, 2019). Figures 6-8 summarise the expected outcomes after combining the afore-mentioned factors (Basu, 2018).

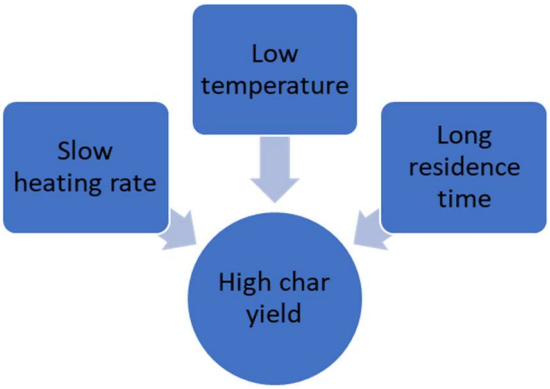

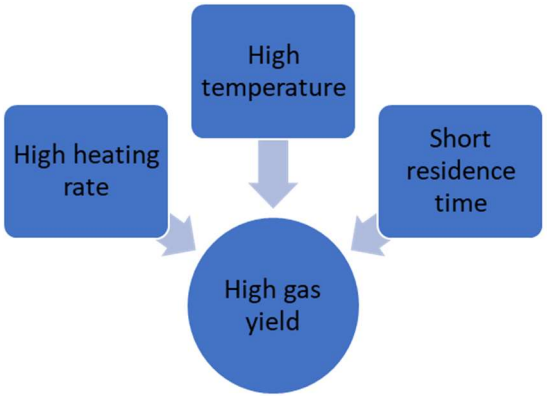

Figures 6 & 7: Conditions for High char yield and High gas yield respectively, based on information from (Basu, 2018)

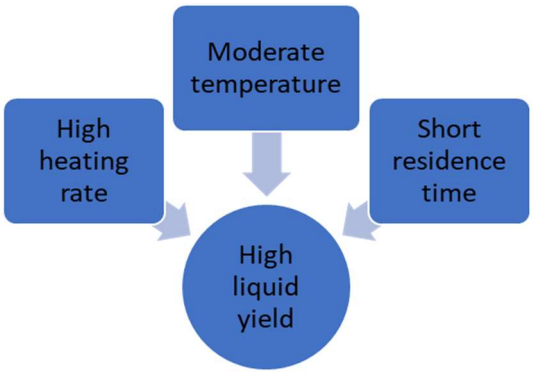

Figure 8: High liquid yield, based on information from (Basu, 2018)

Considering these conditions and the goal of the process, pyrolysis can either be described as slow (conventional), fast or flash depending on the operating conditions as indicated in Table 3 (Zhang *et al.*, 2019) (Matayeva *et al.*, 2019). In slow pyrolysis, the heating rate is less than 1^0C/s and favours char formation while in fast pyrolysis, liquid (oil) is formed from condensation and quenching of generated

vapours. In flash pyrolysis, residence times for vapours inside the reactor are shorter than those for slow and fast pyrolysis to prevent reduced oil yield through further cracking (Matayeva *et al.*, 2019).

Table 3: Types of pyrolysis processes, based on information from (Matayeva et al., 2019) and (Zhang et al., 2019)

Type of pyrolysis	Heating rate (^{0}C/s)	Temperature range (^{0}C)	Residence time (s)	Products	Common Reactor type
Slow pyrolysis	0.1 to 1	300-700	450-550	Char	Fixed bed, vacuum, drum, rotatory kilns, screw/auger
Fast	10-300	550-1250	0.5-10	Gas, oil, char	Ablative, various fluidised bed configurations, auger, rotating cones, entrained flow, vacuum
Flash	> 1000	800-1300	<0.5	Gas, oil, char (high yield of liquid phase) (Chisti, 2019)	Various fluidised bed configurations

As cited by Sharuddin et al. (Sharuddin *et al.*, 2016), (Jamradloedluk and Lertsatitthanakorn, 2014) analysed char produced from the pyrolysis of HDPE and found that it had a high calorific value of around 19 MJ/kg and minute sulphur quantities and consequently can be burnt with other wastes and coal as a fuel. However, the purity of char produced is also dependent on the feed composition. If the feed to the pyrolizer contains a significant quantity of inorganic compounds, the resulting char could be used as a road surfacing agent or building material (Jung *et al.*, 2010). Char can also be utilised in water treatment to remove contaminants through the process of adsorption (Miandad *et al.*, 2019) as well as use in activated carbon manufacture. From studies reviewed by Sharuddin et al. (Sharuddin *et al.*, 2016) although some of the studies indicated all the process parameters used, some did not indicate such information. Figure 9 shows the spread of operating temperatures used in the studies with the highest temperature at 740^{0}C in a study of PP pyrolysis conducted by Demirbas (Demirbas, 2004) and the lowest temperature used of 300^{0}C also in a study of PP pyrolysis by (Ahmad *et al.*, 2015). The optimum temperature range for pyrolysis is between 500-550 ^{0}C in the absence of a catalyst and 450 ^{0}C in the presence of a catalyst (Sharuddin *et al.*, 2018). Figure 10 shows the range of heating rates used in the various experiments conducted. The minimum and maximum heating rates were 3 ^{0}C/min and 25 ^{0}C/min in PP and HDPE pyrolysis respectively. Figure 11 shows the oil, gas and solid (char) yield from the different plastic types.

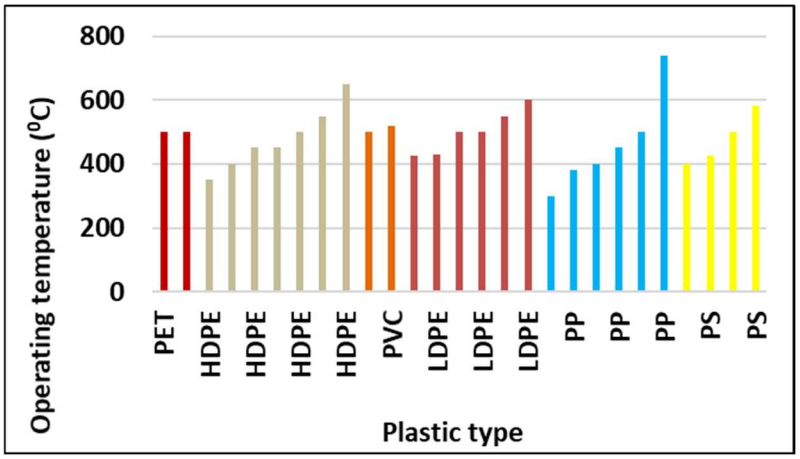

Figure 9: Operating Temperature Spread, based on data from (Sharuddin et al., 2016)

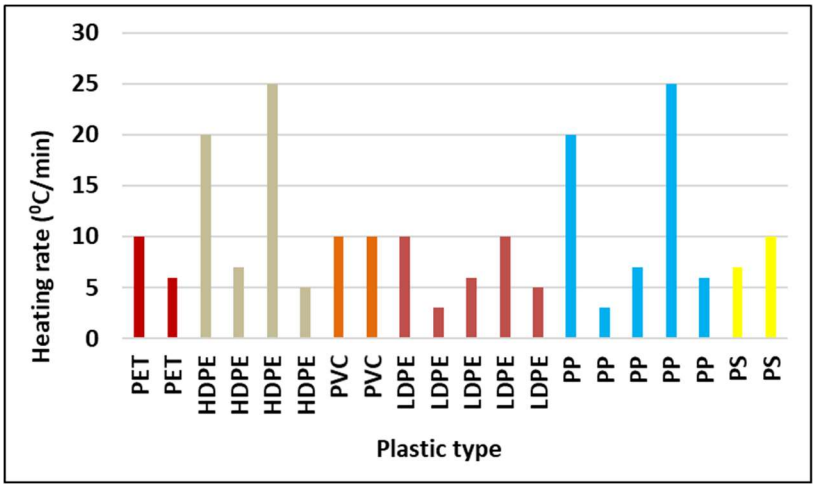

Figure 10: Heating Rate spread, based on data from (Sharuddin et al., 2016)

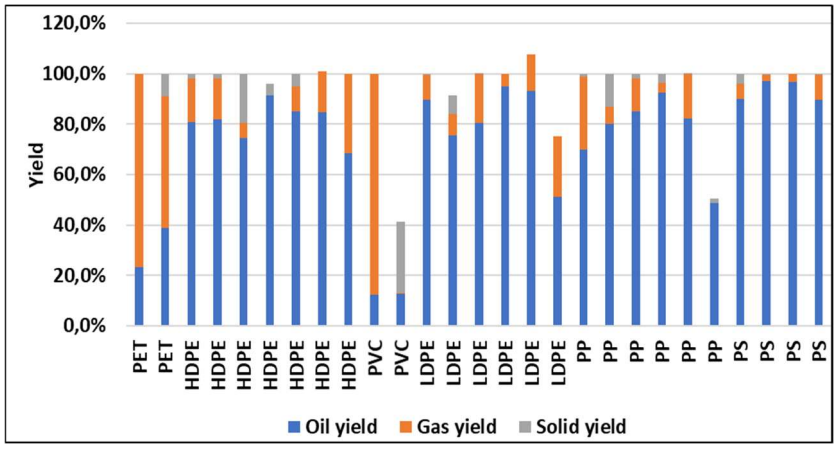

Figure 11: Spread of Yield (based on data from (Sharuddin et al., 2016)

PS had the highest average oil yield of 93%, followed by LDPE and HDPE with 81% each, PP with

76%, PET with 31% and PVC with 13%. PET and PVC pyrolysis resulted in the generation of the most non-condensable gases making them attractive if the goal is to generate gases for providing heat to the pyrolysis reactor (Sharuddin *et al.*, 2016). This showed a marked difference in the behaviour of plastics during pyrolysis. The low PET and PVC oil yield can be correlated to their low volatile matter content compared to other plastic variants as indicated in Figure 1, a view also supported by (Sharuddin *et al.*, 2016). PET pyrolysis also reportedly yielded oil laden with approximately 50% benzoic acid which is a corrosive chemical and can also cause blockages within pipes and equipment such as heat exchangers. Besides low yield in pyrolysis of PVC wastes, other drawbacks are the production of hydrochloric acid (HCl) as well as the contamination of the generated oil with chlorides which in turn not only reduces its value but also makes it corrosive. Miskolczi et al. (Miskolczi, Bartha and Angyal, 2009) found the highest concentration of HCl in the gas fraction, which would therefore require a calcium hydroxide solution containing scrubber downstream. The authors also assessed the effect of varying PVC concentration in mixed plastic wastes between 0% to 3% during thermal cracking and found that the yields of gasoline and light oil increased with increasing PVC content. The authors highlight the mechanism of breakage of main polymer chains through radicals in thermal cracking, with the chain breaking where there are electron density differences or weaknesses in the chain. The bond energy for the C-Cl bond in PVC pyrolysis is lower than the C-C and C-H bonds in HDPE, PP and PS. Consequently, due to the presence of chlorine in the PVC chain, that chain is broken first. During PVC thermal degradation, there is early onset of degradation of PVC at low temperatures ranging from 280-350 °C as highlighted by Alwaan (Alwaan, 2014), while McNeill et al. (McNeill, Memetea and Cole, 1995) give a range of 200-360^{0}C. The free radicals released during PVC dehydrochlorination encourage the breakdown of other polymers in the plastic waste mixture at low temperatures compared to PVC free wastes hence the high yield reported earlier . (Miskolczi, Bartha and Angyal, 2009).

3.1 Pyrolysis Reactors

According to Matayeva et al. (Matayeva *et al.*, 2019), most research in pyrolysis has been conducted on pyrolysis reactors. Various types of reactors that are used during pyrolysis can be grouped under fluidised or fixed bed as well as entrained bed. It is from these three groups that various pyrolyser designs are configured; some which are explained in greater detail in the ensuing sections. The main components making up a pyrolyser and their functions are highlighted in Table 4.

Table 4: Main components of a pyrolyser, based on information from (Matayeva et al., 2019)

Component	Function
Reactor	Where the chemical reactions occur
Cyclone	To separate generated char (solid) from the liquid and gaseous components
Condenser	To cool down the vapours followed by collection of generated liquid while non-condensable gases are recirculated in the system either to provide heat energy or for use as a fluidising medium.

3.1.1 Fluidised Bed Reactors (FBRs)

According to Dhyani and Bhaskar (Dhyani and Bhaskar, 2019), FBRs are employed in processes involving solid reactants. In this type of reactor, a fluidising medium in the form of a gas or liquid is passed through the bed of reactants at high velocity continuously, causing the solid particles to be suspended and behave in a fluid-like manner. In this reactor, the particles making up the bed serve as the heat transfer medium. These particles are circulated by the gas to the burners where they come into contact with oxygen or accompanying solid reaction products, heated and then recirculated to the reactor (Matayeva *et al.*, 2019). Among the various FBR configurations, the bubbling fluidised bed (BFB) reactor is well known and therefore it can be scaled up easily (Chemical Engineering World, 2019). Table 5 shows some of the advantages and disadvantages of fluidised bed reactors.

Table 5: Advantages and disadvantages of FBRs, based on information from (Sharuddin et al., 2016).

Advantages	Disadvantages
Good heat and mass transfer as well as mixing and high conversions	Its design and operation are riddled with complexities.
Residence times for gases are flexible	There is a possibility of the bed losing its fluidity
Can be operated continuously	Molten plastic sticks to the surfaces of particles in the bed
Thermal and catalytic cracking can be employed	Particle attrition can be problematic especially in circulating fluidised bed reactors
Maintenance costs are minimal	A pilot plant is a must have & grinding costs are high

Although Sharuddin et al. (Sharuddin *et al.*, 2016) highlight the complexity of operating FBRs as a disadvantage, Matayeva et al. (Matayeva *et al.*, 2019) attribute the popularity of FBRs to the good understanding of the engineering principles behind FBRs.

3.1.2 Fixed bed reactor (FBR)

A FBR operating in batch mode is considered as the oldest pyrolyser; with the heat of pyrolysis supplied externally or through an oven. Whilst the char remains in the reactor, the generated gas flows out as it expands in volume. An inert gas may also be introduced in the reactor to ensure that the formed gaseous product is removed effectively. Heating rate is slow and the product spends a significant

amount of time in the pyrolysis zone resulting in high char yield (Basu, 2018). Table 6 below shows the advantages and disadvantages of fixed bed reactors.

Table 6: Advantages and disadvantages of fixed bed reactors (Qureshi, Oasmaa and Lindfords, 2019)

Advantages	**Disadvantages**
Construction is not complex	Temperature control can be complicated
The reactor is not expensive to operate and maintain	Scaling up and batch operating may be riddled with complexities
Ability to incorporate two stages in the reactor	Channelling across the bed which affects even product distribution
It can be thermally or catalytically operated	There can be huge pressure drops associated with coke blockages

3.1.3 Rotating-Cone pyrolysis reactor (RCP)

In a RCP reactor, particles of biomass or plastic are introduced through the bottom of a cone rotating between 360 to 960 rev/min simultaneously with other solid particles which serve as heat carriers. Due to the action of centrifugal forces, the particles are swung to the heated walls and spiral upwards. For a biomass feed, heating rate is around 4700 ^{0}C/s due to good mixing in the pyrolyser. While the generated oil flows out through a tube, the char and sand overflow into an adjacent fluidised bed where the burning of char progresses through combustion. The heat generated is used to heat the rotating cone and other recycled solids as heat of pyrolysis. The RCP is characterised by a relatively short residence time for solids of approximately 0.5 seconds and an even shorter residence time for gases of approximately 0.3 seconds. The expected liquid yield is normally between 60 to 70%. Its advantages are that; no carrier gas is required as well as the excellent mixing in the pyrolyser. However, RCP configuration makes scaling up problematic (Basu, 2018).

3.1.4 Vacuum pyrolysis reactor (VPR)

A VPR, is made up of several circular plates which are heated and piled on top of each other. The feed to the reactor enters through the top and drops onto the ensuing plates by means of scrappers and is dried and pyrolyzed in the process. The heating rate in a VPR is quite slow and the vapour residence time inside the pyrolysis zone is short (Basu, 2018). The advantages and disadvantages of a VPR are shown in Table 7.

Table 7: Advantages and disadvantages of a VPR system, based on information from (Basu, 2018)

Advantages	**Disadvantages**
No carrier gas is required	The pyrolyser configuration is complex
-	Liquid yield is low ranging between 35% to 50% with a high char content.
-	There is a risk of fouling of the vacuum pump

3.1.5 Ablative Pyrolysis Reactor (APR)

In an APR, high pressures are developed between the feed particle and the reactor wall which is

heated. Consequently, there is continuous heat transfer from the wall to the biomass which in turn results in production of liquid. A major advantage of this type of pyrolysis system is the high liquid yield which is around 80% due to the rate of heat transfer that is high, as well as short residence time for the gases produced (Basu, 2018).

4 DISCUSSIONS AND CONCLUSIONS

Although there is a need for an increase in plastic recycling rates in South Africa; there remains plastic waste that is either contaminated, unrecyclable or cannot be recycled due to lack of recycling capacity. As other countries move to stem the practice of landfilling, this is an ideal time for South Africa to explore other plastic waste management practices such as pyrolysis. The introduction of pyrolysis of plastic wastes in South Africa has the potential to revolutionize the plastic industry in the country and Africa as a whole. Plastic waste-based fuels present an alternative to coal-based fuels. In addition, the char and gases produced can be used in various applications such as wastewater treatment and heat energy supply for the process respectively. However, although most plastics will result in high liquid yield, PET and PVC may not be suitable candidates for pyrolysis due to the benzoic acid and HCl generated respectively during their pyrolysis. Besides the corrosive nature of the compounds, the CV of the produced oil is also impacted negatively. Therefore, in any pyrolysis programmes that maybe initiated in SA, PVC and PET should be removed first and undergo mechanical recycling. If 55 000 tonnes of mixed plastic waste are pyrolised then this will potentially produce around 1928407.25 TJ of energy which in turn results in the avoided production of approximately 44 850 tonnes of diesel. The use of pyrolysis in waste management will result in a reduction in the amount of plastic waste that is landfilled which will not only be of benefit to the environment but will also result in job creation consequently improving the socio-economic and environmental profile of the country. However, PVC and PET streams should be removed from mixed plastic wastes destined for pyrolysis as these will lead to contamination of the oil.

REFERENCES

Ahmad, I. *et al.* (2015) 'Pyrolysis study of polypropylene and polyethylene into premium oil products', *International Journal of Green Energy*, 12(7), pp. 663–671. doi: 10.1080/15435075.2014.880146.

Alwaan, I. M. (2014) 'Kinetics of thermal degradation of recycled polyvinyl chloride resin', *International Journal of Chemical Engineering*. doi: 10.1155/2014/701092.

Basu, P. (2018) 'Pyrolysis', in *Biomass Gasification, Pyrolysis and Torrefaction: Practical Design and Theory*. Elsevier, pp. 155–187. doi: 10.1016/B978-0-12-812992-0.00005-4.

Carvill, J. (1993) *Mechanical Engineer's Data Handbook | ScienceDirect*.

Chemical Engineering World (2019) *BUBBLING FLUIDIZED BED REACTOR* . Available at: https://chemicalengineeringworld.com/bubbling-fluidized-bed-reactor/ (Accessed: 1 May

2021).

Chisti, Y. (2019) 'Introduction to algal fuels', in *Biofuels from Algae*. Elsevier, pp. 1–31. doi: 10.1016/b978-0-444-64192-2.00001-9.

DeArmitt, C. (2019) *South African Plastics Recycling Survey*.

Demirbas, A. (2004) 'Pyrolysis of municipal plastic wastes for recovery of gasoline-range hydrocarbons', *Journal of Analytical and Applied Pyrolysis*, 72(1), pp. 97–102. doi: 10.1016/j.jaap.2004.03.001.

Dhyani, V. and Bhaskar, T. (2019) 'Pyrolysis of biomass', in *Biomass, Biofuels, Biochemicals: Biofuels: Alternative Feedstocks and Conversion Processes for the Production of Liquid and Gaseous Biofuels*. Elsevier, pp. 217–244. doi: 10.1016/B978-0-12-816856-1.00009-9.

Jamradloedluk, J. and Lertsatitthanakorn, C. (2014) 'Characterization and utilization of char derived from fast pyrolysis of plastic wastes', in *Procedia Engineering*. Elsevier Ltd, pp. 1437–1442. doi: 10.1016/j.proeng.2014.03.139.

Jung, S. H. *et al.* (2010) 'Pyrolysis of a fraction of waste polypropylene and polyethylene for the recovery of BTX aromatics using a fluidized bed reactor', *Fuel Processing Technology*, 91(3), pp. 277–284. doi: 10.1016/j.fuproc.2009.10.009.

Lord, H. L. and Pfannkoch, E. A. (2012) 'Sample preparation automation for gc injection', in *Comprehensive Sampling and Sample Preparation*. Elsevier Inc., pp. 597–612. doi: 10.1016/B978-0-12-381373-2.00061-2.

Matayeva, A. *et al.* (2019) 'Development of Upgraded Bio-Oil Via Liquefaction and Pyrolysis', in *Studies in Surface Science and Catalysis*. Elsevier Inc., pp. 231–256. doi: 10.1016/B978-0-444-64127-4.00012-4.

Mazhandu, Z. S. *et al.* (2020) 'Integrated and consolidated review of plastic waste management and bio-based biodegradable plastics: challenges and opportunities', *Sustainability*, 12(20), p. 8360. doi: 10.3390/su12208360.

McNeill, I. C., Memetea, L. and Cole, W. J. (1995) 'A study of the products of PVC thermal degradation', *Polymer Degradation and Stability*, 49(1), pp. 181–191. doi: 10.1016/0141-3910(95)00064-S.

Miandad, R. *et al.* (2019) 'Catalytic Pyrolysis of Plastic Waste: Moving Toward Pyrolysis Based Biorefineries', *Frontiers in Energy Research*, 7(MAR), p. 27. doi: 10.3389/fenrg.2019.00027.

Miskolczi, N., Bartha, L. and Angyal, A. (2009) 'Pyrolysis of polyvinyl chloride (pvc)-containing mixed plastic wastes for recovery of hydrocarbons', *Energy and Fuels*, 23(5), pp. 2743–2749. doi: 10.1021/ef8011245.

Nunes, L., Matias, D. O. J. C. S. and Joao, C. P. D. S. (2017) *Torrefaction of Biomass for Energy Applications - 1st Edition*.

Qureshi, M. S., Oasmaa, A. and Lindfords, C. (2019) 'Thermolysis of plastic waste: Reactor comparison', in *Pyroliq 2019: Pyrolysis and liquefaction of biomass and wastes*. Cork.

Sharuddin, A. *et al.* (2016) 'A review on pyrolysis of plastic wastes', *Energy Conversion and Management*, 115, pp. 308–326. doi: 10.1016/j.enconman.2016.02.037.

Sharuddin, S. D. A. *et al.* (2018) 'Pyrolysis of plastic waste for liquid fuel production as prospective energy resource', *IOP Conference Series: Materials Science and Engineering*, 334(1). doi: 10.1088/1757-899X/334/1/012001.

Singh, R. K. *et al.* (2019) 'Impact of fast and slow pyrolysis on the degradation of mixed plastic waste: Product yield analysis and their characterization', *Journal of the Energy Institute*, 92(6), pp. 1647–1657. doi: 10.1016/j.joei.2019.01.009.

Suárez-Ruiz, I. and Ward, C. R. (2008) 'Basic Factors Controlling Coal Quality and Technological Behavior of Coal', in *Applied Coal Petrology*. Elsevier Ltd, pp. 19–59. doi: 10.1016/B978-0-08-045051-3.00002-6.

Zhang, Y. *et al.* (2019) 'Gasification technologies and their energy potentials', in *Sustainable Resource Recovery and Zero Waste Approaches*. Elsevier, pp. 193–206. doi: 10.1016/B978-0-444-64200-4.00014-1.

Zhao, D. *et al.* (2020) 'The Chemistry and Kinetics of Polyethylene Pyrolysis: A Process to Produce Fuels and Chemicals', *ChemSusChem*, 13(7), pp. 1764–1774. doi: 10.1002/cssc.201903434.

The Remediation of Carwash Wastewater with Chemical Coagulation and Adsorption Process

F. Roman and M. Aziz*

Environmental Engineering Research Group (EnvERG), Department of Chemical Engineering, Cape Peninsula University of Technology (CPUT), Bellville, Cape Town, South Africa (SA)

*Corresponding author: AzizM@cput.ac.za

ABSTRACT

This study aimed to apply a combined treatment process of chemical coagulation (CC) and adsorption to remove pollutants from carwash wastewater. The process efficiency was evaluated according to the removal of anionic surfactants (AS), turbidity, chemical oxygen demand (COD) and fats, oils, and grease (FOG). CC experiments were conducted using polyferric sulphate (PFS) at different concentrations. Results showed 120 mg/l PFS was the optimal concentration (Turbidity: 99%, FOG, 96%, COD: 79%, AS: 45%). The supernatant of the CC treatment process was applied to the adsorption process using a commercial powdered activated carbon (PAC). The PAC was characterised using Scanning Electron Microscopy (SEM) and Fourier Transform Infrared Spectroscopy (FTIR). Results showed the Freundlich isotherm fitted the data well with a monolayer adsorption capacity of 82.9 mg/g for AS and reached equilibrium within 60 minutes. Adsorption kinetic models investigated showed conformity of the pseudo-second order (PSO) model to the adsorption of AS. Thermodynamic adsorption parameters showed that the adsorption of AS onto PAC was endothermic and spontaneous. The adsorption mechanism was a combination of chemical and physical adsorption but dominated by chemical adsorption. The combined treatment process achieved an overall removal efficiency of COD: 98.5%, FOG: 100%, AS: 99% Turbidity: 99%, respectively.

Keywords: adsorption, chemical coagulation, polyferric sulphate, pseudo-second-order, thermodynamics

1 INTRODUCTION

Water shortages are one of the most critical issues globally as currently, less than 3% of the earth water supply is readily usable for human activities. Moreover, water demand has increased rapidly due to population growth and industrialisation (Sarmadi et al., 2020). Therefore, the development of industrial wastewater treatment technologies is essential for meeting global demand. Adopting these water strategies would alleviate the strain on the freshwater supply and prevent the degradation of ecosystems due to the entrance of different wastewaters. Industrial wastewaters include textiles, paper, dairy, carwashes, and the food industry as the most important sources of water pollution, even in low volumes. The carwash industry has attracted plenty of attention and requires high water volumes, generating large amounts of wastewater (Veit et al., 2020). Carwash wastewater is characterised by

having high surfactants, low levels of COD and FOG and low concentrations of metals which are harmful to the environment. CWW also contains phosphates, which cause excessive growth of plants in aquatic environments, biodegradable soaps, and detergents harmful to fish mucus membranes and gills, disrupting oxygen supply leaving fish susceptible to bacteria and parasites. Detergents can also kill fish in concentrations of 15ppm and fish eggs at 5ppm (Tony & Bedri, 2014). The benefit of carwash wastewater reuse includes environmental protection, economic proceeds and preservation of freshwater resources (Gönder et al., 2020). The standards for carwash wastewater reuse are unclear; however, Zaneti et al. (2013) reports washing water should ensure low turbidity, odourless, good chemical (corrosion and scaling) and microbiological quality (safety for operators and users). Integrated treatment processes are to be preferred to produce high-quality water for reuse.

Economic viability should also be considered when choosing a treatment method (Leiknes & Ødegaard, 2007). Many reclamation processes have been tried as remedial applications, such as membrane technology, adsorption, chemical coagulation (CC), oxidation processes and membrane bioreactor (MBR) (Moazzem et al., 2018); however, the performance has not been compared or ensured. CWW treatment systems generally comprise a primary and secondary treatment step. In the primary treatment systems, a significant portion of total solids and suspended organic material, including oil and grease, COD and BOD, are removed from CWW. Coagulation is highly effective in removing TSS and turbidity; however less effective for the removal of organic matter such as COD and BOD from greywater such as CWW (Foroughi et al., 2018). Therefore, it is preferred to be applied with other methods, especially adsorption or membrane processes. Adsorption is a common technique applied in wastewater treatment; however, it has not been widely applied in CWW treatment processes. The main reason for this could be the complex nature of CWW and cannot be treated by one unique process. However, in the limited studies, available adsorption has shown to be an efficient process for removing organic and inorganic pollutants such as surface-active substances, oil and grease, TDS and heavy metals (Enoh & Christopher, 2015). The main objective of this work is to provide an integrated CC-adsorption process for the treatment of carwash wastewater. The combined process was investigated in terms of COD, FOG and AS. The purpose of the investigation was to reduce these parameters in order to maximum allowed discharge standards or reuse purposes. Equilibrium adsorption, thermodynamic, and kinetic studies were used to evaluate the effective performance of AS ions removal on the adsorbent active sites surface.

2 EXPERIMENTAL PROCEDURE

2.1 Carwash wastewater characterisation

The wastewater used in this study was supplied from a carwash station in Cape Town, South Africa. The water obtained from the station was stored in a fridge at 4 ^{0}C before experiments. It has a COD of 1000 mg/l, FOG of 30 mg/l, AS of 35 mg/l, Turbidity of 100 NTU, and a TDS of 2300 mg/l. The pH

and conductivity values were measured as 7.5 and 3.5 ms/cm, respectively. The COD was measured using a Hanna Instruments multiparameter photometer (HI83399-02), the AS concentration was analysed using Hanna Instruments Anionic surfactant portable photometer (HI96769), the turbidity was measured using a Xylem Analytics turbidity meter (Turb 355 IR) and the TDS was measured using a Crison Instruments multimeter

2.2 Preparation of PFS and chemical coagulation treatment process

The polyferric sulphate (PFS) synthesis process was followed according to the well-known method proposed by Jiang & Graham (1998). PFS was applied to 1 L of carwash wastewater samples. The coagulant had a pH of 1.15, Fe (III) concentration of 40 g/l, the conductivity of 44.5 mS/cm, and an r (OH/Fe) molar ratio of 0.3. Chemical coagulation was performed using the jar test methodology. Samples were mixed at 300 rpm for 5 minutes, followed by 100 rpm for 25 minutes. The samples could settle for 1 hr, after which the supernatant was collected for analysis. The concentrations of PFS used were 40, 80 and 120 mg/l Fe(III) per 1 L of carwash wastewater. The parameters analysed were turbidity, COD, FOG and AS, where the best dosage was chosen.

2.3 Adsorbent characterisation

The activated carbon used in the research was obtained from a South African company, RotoCarb. The PAC was manufactured from macadamia nut shells through steam activation. The PAC had a mesh size of 0-100 microns. Size distribution was performed on the 1 kg sample, and 80% of particles had a size of <75 microns, 17.3% had a particle size between 75 and 55 microns, 1.78% had a size between 55 and 35 microns, and only 0.88% had a size of 35 microns and below. The activated carbon was characterised using Fourier Transform Infrared Spectroscopy (FTIR) to determine the functional groups and Scanning Electron Microscopy (SEM) for surface morphology.

2.4 The batch adsorption treatment process

Batch equilibrium adsorption studies were performed using supernatant collected from the chemical coagulation experiments. A volume of 25l was collected from the CC process using the best coagulant concentration. This volume was used for all sequential adsorption experiments. For the kinetic experiments of surfactant adsorption, the following experimental conditions were used: 500 ml of supernatant, 100, 200 and 300 mg/l PAC dosage, temperatures of 25, 37.5 and 50 0C, a pH 6 and a stirring speed of 200rpm. The pH of the samples was adjusted using 0.5M NaOH and H_2SO_4. Samples were collected at different contact times (10 min, 20 min, 30 min, 60 min, and 120 min), and the surfactants in solution at each time were determined. The samples collected were filtered through a 0.45 µm syringe filter. The final sample collected at equilibrium was analysed for COD, FOG, turbidity and AS. The AS concentration was analysed using Hanna Instruments Anionic surfactant portable photometer (HI96769). Table 1 represents the design matrix for the experiments.

Table 1: Adsorption experiments design matrix

Experiment No	pH	Dosage (mg/l)	Temperature (°C)
1	6	300	25
2	6	100	25
3	6	200	37,5
4	6	300	50
5	6	100	50
6	6	200	25
7	6	200	50
8	6	100	37,5
9	6	300	37,5

3 RESULTS AND DISCUSSION

3.1 Chemical coagulation treatment

Polyferric sulphate (PFS) was used in the chemical coagulation experiments to evaluate different PFS concentrations at initial wastewater pH of 7.5. The results of COD, FOG, AS, and turbidity removal efficiency are shown in Figure 1.

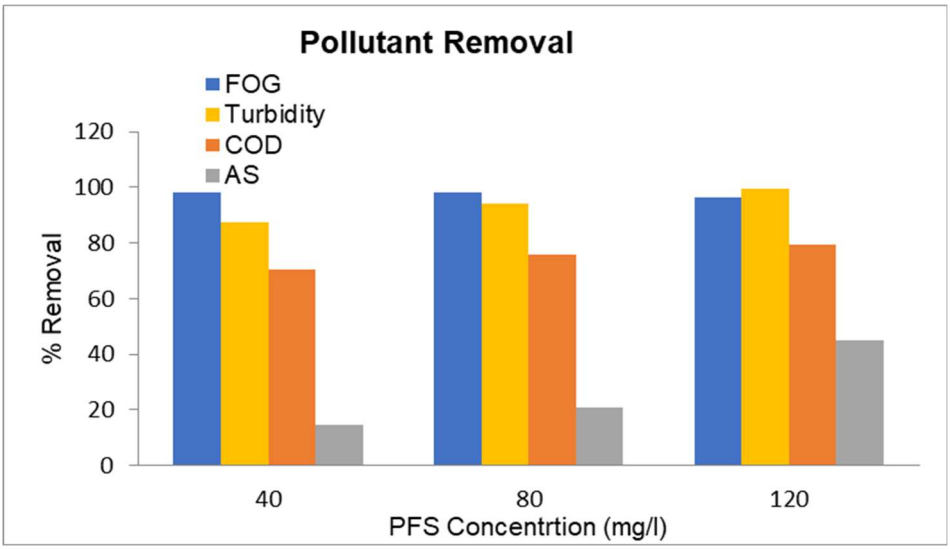

Figure 1: Effect of coagulant dosage on pollutant percentage removal

The addition of PFS to the CWW saw an initial drop in pH from 7.5 to as low as 6 due to the acidic nature of the coagulant. Figure 1 shows that at a concentration 40 and 80 mg/l, 99% of the oil (FOG) was removed, whereas at concentration 120 mg/l, 96%. Higher coagulant concentrations place positive charges on particle surfaces; therefore, re-dispersing solid particles can cause higher FOG concentrations at elevated coagulant dosages (Chatoui et al., 2017). The anionic surfactants (AS)

removal increases with an increase in the adsorbent dosage, although the removal percentage is much lower than COD and FOG. The 14% AS removal at 40 mg/l dosage increases significantly to 44% at 120 mg/l. The primary mechanism for the removal of AS via chemical coagulation is adsorptive micellar flocculation (AMF). AMF involves cationic species attraction to the surface of anionic micelles and the flocculation as their mutual electrostatic repulsion is neutralised. This process creates an aggregate that can be easily filtered (Talens-Alesson et al., 2006). The Fe^{3+} ions bind to the micelles causing the following simultaneous effects: it suppresses repulsive forces between micelles, causing them to flocculate and effectively removing micellar surfactant from solution in the form of an aggregate, and it binds organic compounds to the flocs. In addition to the coagulation process, the AMF mechanism removes AS and organic matter (Aboulhassan et al., 2006). The COD removal was between 70-79% and increased as PFS concentration increased. The difference between the lowest and highest dosage was less than 10%. The increase can be attributed to charge neutralisation which plays a major role in coagulation and flocculation processes. Positively charged ion species will destabilise negatively charged organic compounds through charge neutralisation, thus decreasing COD concentration. It can also be seen that residual turbidity decreased as the PFS dosage increased, showing the coagulant was not overdosed (Liang et al., 2009).

3.2 SEM and FTIR

SEM carbon provided, making it a good candidate for anionic surfactants' adsorption, was used to observe the surface of the adsorbent. The SEM analysis, shown in Figure 2, was conducted with a magnification of 5,000. Figure 2 shows the PAC's detailed surface characteristics, with many pores showing irregular granules (Dejang et al., 2015) and some debris occupying the pores' surface (Kuang et al., 2020). The SEM images also show the mesoporous structures that favour the adsorption of anionic pollutants.

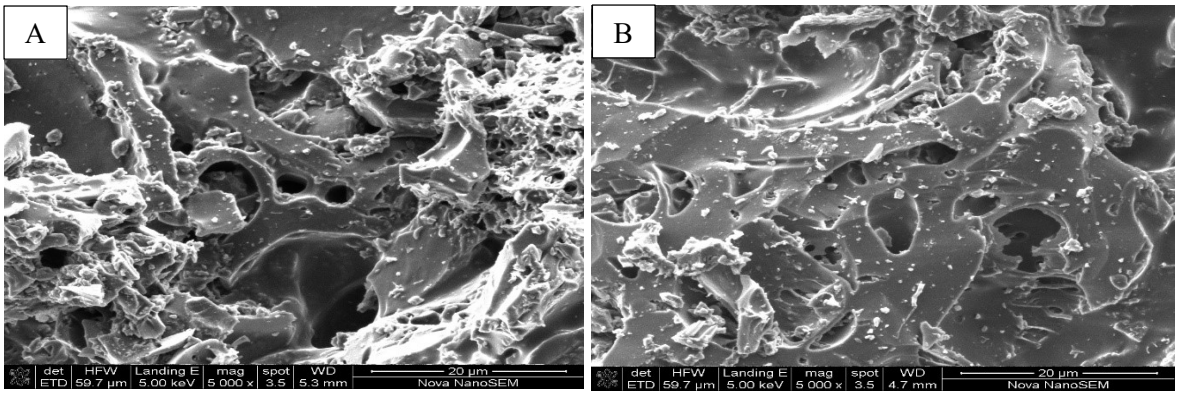

Figure 2: SEM analysis of PAC

Figure 3 shows an FTIR comparison between the new activated carbon and the CWW loaded activated carbon. The broadband around 3350-3500 cm^{-1} is standard in both spectra and attributed to O-H

stretching vibration. The loaded CWW wastewater exhibits a peak at 2900 cm^{-1} unique to itself and can be ascribed to a C-H stretching vibration and is observed only in the loaded activated carbon. The bands at 1650 cm^{-1} are present in both adsorbents and can be attributed to a C=O stretching vibration in carboxyl and alkene groups and aromatic rings. The bands at 1350 cm^{-1} can be assigned to C-C stretching; additionally, the bands at 1050 cm^{-1} can be attributed to C-O stretching in carboxyl acids, alcohols, phenols and esters (Martins et al., 2015). The band at 850 cm^{-1} found only in the loaded activated carbon represents the stretching oscillation of the C=C functional group, indicating that the carbon content increases in the activated carbon (Dao et al., 2020). The study performed by Gong et al. (2005) investigated the effect of chemical modification on anionic and cationic dye adsorption capacity of peanut hull found that carboxyl, amino, and hydroxyl groups had an impact on anionic dye removal. The study found that carboxyl groups bearing a negative charge slightly reduced the adsorption capacity of anionic dyes. When amino and hydroxyl groups were removed, anionic dyes' adsorption capacity was highly reduced, showing the importance of those groups in anionic dyes' adsorption. It shows that carboxyl and amine groups are essential for the adsorption of anionic species. These groups are found in the commercial activated carbon, making it a good option for anionic surfactants' adsorption.

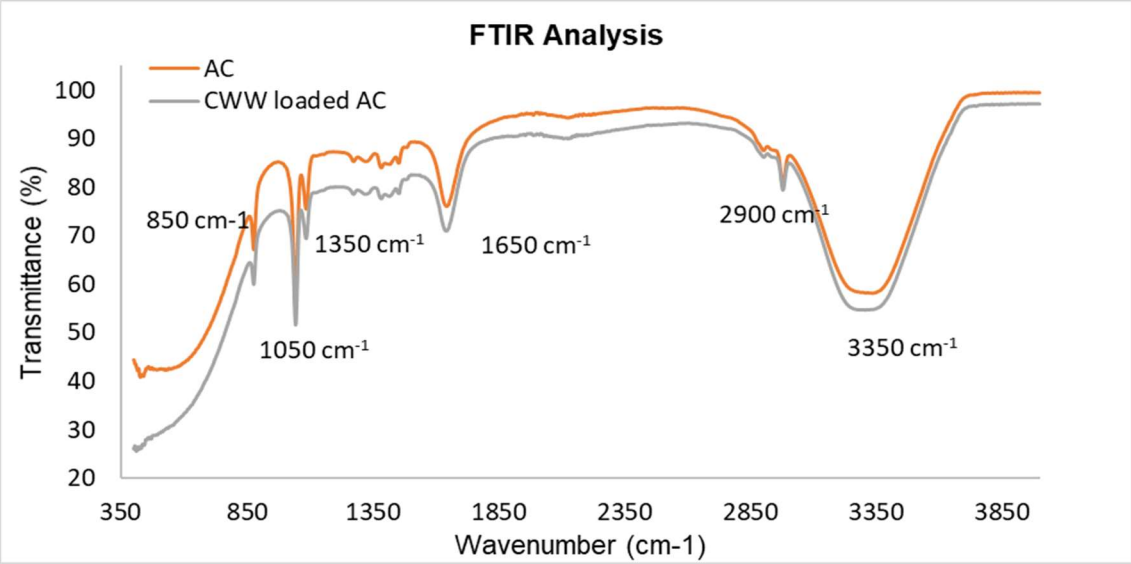

Figure 3: FTIR analysis of PAC

3.3 Nonlinear Isotherm Study

The findings from Figures 4 and Table 2 shows that the data follows the Freundlich adsorption isotherm. The Temkin isotherm follows the Freundlich isotherm closely, while the Langmuir and D-R isotherms did not fit very well. Table 2 presents the Freundlich and Temkin R^2 values of 0.99 across all temperatures. Still, the Langmuir and D-R isotherms R^2 values drop as the temperature increases showing a lack of fit at higher temperatures. Ayranci & Duman, (2007) investigated the removal of anionic surfactants from aqueous solutions using activated carbon and found that the data fitted the

Freundlich isotherm better than Langmuir. In a similar study performed by Gupta et al. (2003), a low-cost waste activated carbon was tested to remove sodium dodecyl sulphate (SDS) in aqueous solutions and found the data fitted best the Freundlich isotherm as well.

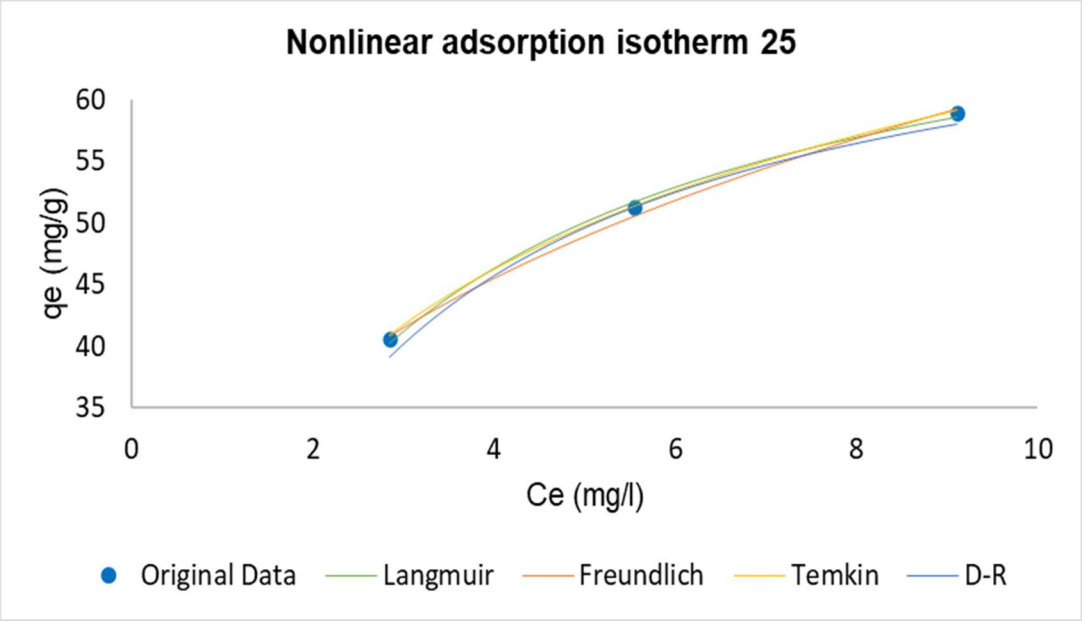

Figure 4: Nonlinear adsorption isotherm regression at 25^{0C}

Table 2: Nonlinear adsorption isotherm constants

Isotherms	Parameters	Temperature (^{0}C)		
		25	37,5	50
Langmuir	q_{max} (mg/g)	73,9	69,6	82,9
	K_L (L/mg)	0,41	2,38	4,225
	R_L	0,139	0,0272	0,0155
	R^2	0,997	0,94	0,85
Freundlich	K_F (mg/g) (L/mg)$^{1/n}$	29,4	48,7	58,26
	n	3,12	6,24	5,6
	R^2	0,99	0,99	0,99
Temkin	K_T (L/mg)	4,81	166,5	136,1
	b	158,3	263,5	208,7
	R^2	0,99	0,99	0,99
D-R	q (mg/g)	71,4	70,76	83,03
	K_{D-R} x 10^{-6} (mol^2/kj^2)	404	170	83
	E (KJ/mol)	35,16	54,23	77,61
	R^2	0,98	0,95	0,902

The same conclusion was reached in this study. The Freundlich exponent, 1/n, obtained in this study was 0.32, 0.16 and 0.17 for 25, 37.5 and 500 °C, respectively, indicating favourability as the values were between zero and one. The values of 1/n also indicate the degree of nonlinearity between solution concentration and the sorption process. If the value is below unity, the process is chemical, and if the value is above unity, the process is physical. The values of 1/n are below unity, thus showing the adsorption process is a chemical one (Jasper et al., 2020). Table 2 also shows large K_F values, which increase with temperature, showing the anionic surfactants are strongly adsorbed onto the activated carbon, and the adsorption process is favourable upon heating (Foo & Hameed, 2010).

3.4 Thermodynamic study

The Gibbs free energy measures the systems spontaneity and is significant for values less than zero (Papegowda & Syed, 2017). The thermodynamic adsorption parameters are summarised in Table 3. The negative values of ΔG^0 indicated the adsorption process happens spontaneously; the positive ΔH^0 values show the process is endothermic. An increase in temperature increased the uptake capacity of anionic surfactant ions. Positive ΔS_0 values showed an affinity of the adsorbent towards the adsorbate and that there was also greater randomness at the adsorbent-adsorbate interface (Obayomi et al., 2020).

Table 3: Adsorption thermodynamic properties

Concentration adsorbent (mg/l)	ΔH (kJ/mol)	ΔS (kJ/mol.K)	ΔG (kJ/mol)		
			298.15 K	310.65 K	323.15 K
100	20.456	0.084	-4.533	-5.581	-6.629
200	29.505	0.118	-5.744	-7.222	-8.700
300	74.549	0.272	-6.558	-9.958	-13.359

3.5 Nonlinear Kinetic Study

OrginLab 2021 software was used to perform a nonlinear regression analysis on the experimental data. It was fitted to pseudo-first order (PFO), pseudo-second-order (PSO) and intra-particle diffusion (IPD) and Elovich kinetics to determine the best-fit equation and compare the findings to linear regression (Figure 5). The results summarised in Table 4, followed the PSO kinetics making it the best model to describe the data. The PSO model was shown to have the highest R^2 values across all the runs.

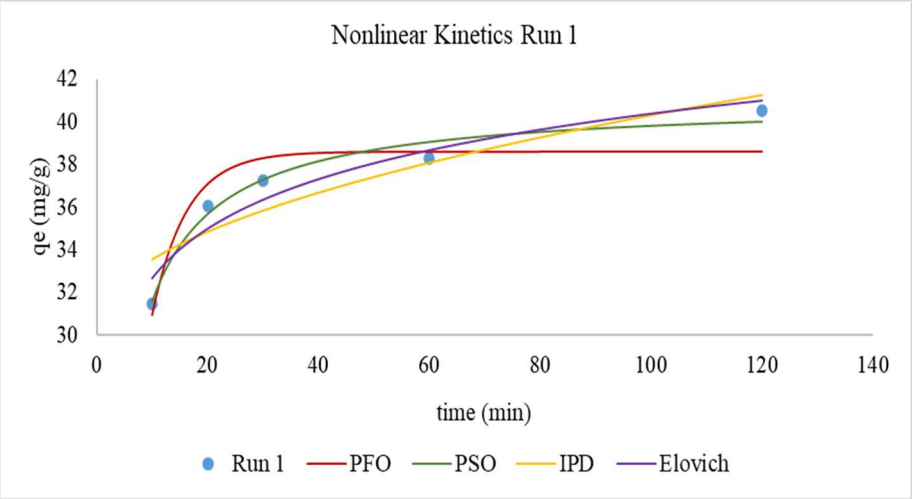

Figure 5: Nonlinear adsorption isotherm regression at 25^{0}C

The values of q_{exp} and qcal were well in agreement for the PSO kinetic model more than the PFO. The PSO model also exhibits significantly lower rate constants than the PFO, supporting the experimental and calculated qe values. The studies performed by Gupta et al. (2003) and Ayranci & Duman, (2007) both found the adsorption

Table 4: Nonlinearized adsorption kinetic constants

Equation	Parameter	1	2	3	4	5	6	7	8	9
PFO	$q_{e\ exp}$ (mg/g)	40,5	58,9	58,87	48,83	82,65	51,25	64,675	68,25	46,892
	$q_{e\ cal}$ (mg/g)	38,59	57,48	56,39	47,62	74,8	49,5	61,96	66,45	47,7
	k_f (min^{-1})	0,16	0,067	0,139	0,32	0,065	0,108	0,137	0,155	0,214
	R^2	0,86	0,91	0,8	0,49	0,8	0,93	0,906	0,859	0,86
PSO	$q_{e\ exp}$ (mg/g)	40,5	58,9	58,87	48,83	82,65	51,25	64,675	68,25	46,892
	$q_{e\ cal}$ (mg/g)	39,9	59,4	58,67	48,2	78,2	51,6	66,55	68,65	47,05
	ks (g/mg min)	0,00819	0,0016	0,0043	0,03319	0,00097	0,0034	0,00385	0,00516	0,01274
	R^2	0,97	0,95	0,967	0,84	0,91	0,98	0,99	0,96	0,99
IPD	K_{id}(mg/g.$min^{0.5}$)	0,98	3,4	1,36	0,21	4,08	1,98	1,91	1,51	0,67
	C (mg/g)	30,42	25,35	45,27	46,1	37,47	32,43	45,72	53,76	40,47
	R^2	0,81	0,78	0,83	0,77	0,90	0,77	0,79	0,71	0,72
Elovich	α (mg/g.min)	5873,19	19,039	1054,44	2,4E+16	63,32	163,09	1386,3	28833	1420000
	β (g/mg)	0,299	0,085	0,164	0,86	0,092	0,15	0,153	0,19	0,42
	R^2	0,91	0,87	0,95	0,97	0,87	0,9	0,91	0,85	0,87

Of anionic surfactants (AS) onto activated carbon to best follow the PSO reaction kinetics. The following PSO reaction kinetics further supports the adsorption of anionic surfactants onto activated carbon as chemisorption.

4 CONCLUSIONS

The integrated treatment process used in this study consisted of two steps, chemical coagulation and adsorption. The treatment processes were investigated to obtain the most favourable conditions for removing COD, FOG and AS in carwash wastewater. The process of chemical coagulation investigated the effect of coagulant dosage. The adsorption process investigated temperature, pH, and dosage effects on AS, COD, and FOG removal. The adsorption data were then fitted to adsorption isotherm and kinetic models to describe the process. The first step, chemical coagulation using a dosage of 120 mg/l, showed excellent removal efficiencies. At these conditions, the COD was reduced by 79.8%, the AS by 44.82%, the FOG by 96% and turbidity by 99.5%. The functional groups and morphological structures of the commercial activated carbon were determined using SEM and FTIR. It showed the activated carbon to have a porous structure and contain bonds promising for the adsorption of AS. The second step, adsorption using commercial PAC, showed excellent results at conditions of pH:6, dosage: 300mg/l and temperature of 50^0C. The results showed a COD removal of 94%, AS removal of 97% and FOG removal of 100%. Of the three operating parameters tested, it is noted that PAC dosage had the most significant effect increasing removal percentage by over 50% when moving from 100mg/l to 300mg/l. It can be assumed that adsorption of AS and COD onto PAC occurs best at low pH values and high temperatures. The process of adsorption of AS and COD onto PAC is endothermic, occurs spontaneously, and exhibits increased randomness as temperature increases. The adsorption is governed by pseudo-second-order reaction kinetics and follows the Freundlich and Temkin isotherms closely. The adsorption mechanism was revealed to be predominantly chemisorption with subordinate physical adsorption.

REFERENCES

Aboulhassan, M. A., Souabi, S., Yaacoubi, A., & Baudu, M. (2006). Removal of surfactant from industrial wastewaters by the coagulation-flocculation process. *International Journal of Environmental Science and Technology*, *3*(4), 327–332. https://doi.org/10.1007/BF03325941

Ayranci, E., & Duman, O. (2007). Removal of anionic surfactants from aqueous solutions by adsorption onto high area activated carbon cloth studied by in situ UV spectroscopy. *Journal of Hazardous Materials*, *148*(1–2), 75–82. https://doi.org/10.1016/j.jhazmat.2007.02.006

Chatoui, M., Lahsaini, S., Aguelmous, A., Souabi, S., Bahlaoui, M. A., & Jada, A. (2017). Removal of oil and grease from vegetable oil refinery wastewaters by coagulation-flocculation process. *Moroccan Journal of Chemistry Chatoui & J. Chem. Mor. J. Chem. Mor. J. Chem*, *5*(5), 4–683. http://revues.imist.ma/?journal=morjchem&page=login

Dao, M. T., Nguyen, T. T. T., Nguyen, X. Du, La, D. D., Nguyen, D. D., Chang, S. W., Chung, W. J., & Nguyen, V. K. (2020). Toxic metal adsorption from aqueous solution by activated biochars produced from Macadamia nutshell waste. *Sustainability (Switzerland)*, *12*(19). https://doi.org/10.3390/SU12197909

Dejang, N., Somprasit, O., & Chindaruksa, S. (2015). A Preparation of Activated Carbon from Macadamia Shell by Microwave Irradiation Activation. In *Energy Procedia* (Vol. 79). Elsevier B.V. https://doi.org/10.1016/j.egypro.2015.11.556

Enoh, B. S., & Christopher, W. (2015). Adsorption of metal ions from carwash wastewater by phosphoric acid modified clay: Kinetics and thermodynamic studies. *Adsorption*, *7*(4).

Foroughi, M., Chavoshi, S., Bagheri, M., Yetilmezsoy, K., & Samadi, M. T. (2018). Alum-based sludge (AbS) recycling for turbidity removal in drinking water treatment: an insight into statistical, technical, and health-related standpoints. *Journal of Material Cycles and Waste Management*, *20*(4), 1999–2017.

Gönder, Z. B., Balcıoğlu, G., Vergili, I., & Kaya, Y. (2020). An integrated electrocoagulation–nanofiltration process for carwash wastewater reuse. *Chemosphere*, *253*. https://doi.org/10.1016/j.chemosphere.2020.126713

Gong, R., Sun, Y., Chen, J., Liu, H., & Yang, C. (2005). Effect of chemical modification on dye adsorption capacity of peanut hull. *Dyes and Pigments*, *67*(3), 175–181. https://doi.org/10.1016/j.dyepig.2004.12.003

Gupta, S., Pal, A., Kumar Ghosh, P., & Bandyopadhyay, M. (2003). Performance of waste activated carbon as a low-cost adsorbent for the removal of anionic surfactant from aquatic environment. *Journal of Environmental Science and Health - Part A Toxic/Hazardous Substances and Environmental Engineering*, *38*(2), 381–397. https://doi.org/10.1081/ESE-120016902

Jasper, E. E., Ajibola, V. O., & Onwuka, J. C. (2020). Nonlinear regression analysis of the sorption of crystal violet and methylene blue from aqueous solutions onto an agro-waste derived activated carbon. *Applied Water Science*, *10*(6), 1–11. https://doi.org/10.1007/s13201-020-01218-y

Jiang, J. Q., & Graham, N. J. D. (1998). Preparation and characterisation of an optimal polyferric sulphate (PFS) as a coagulant for water treatment. *Journal of Chemical Technology and Biotechnology*, *73*(4), 351–358. https://doi.org/10.1002/(SICI)1097-4660(199812)73:4<351::AID-JCTB964>3.0.CO;2-S

Kuang, Y., Zhang, X., & Zhou, S. (2020). Adsorption of methylene blue in water onto activated carbon by surfactant modification. *Water (Switzerland)*, *12*(2), 1–19. https://doi.org/10.3390/w12020587

Leiknes, T., & Ødegaard, H. (2007). The development of a biofilm membrane bioreactor. *Desalination*, *202*(1–3), 135–143.

Liang, Z., Wang, Y., Zhou, Y., Liu, H., & Wu, Z. (2009). Hydrolysis and coagulation behavior of polyferric sulfate and ferric sulfate. *Water Science and Technology*, *59*(6), 1129–1135. https://doi.org/10.2166/wst.2009.096

Martins, A. C., Pezoti, O., Cazetta, A. L., Bedin, K. C., Yamazaki, D. A. S., Bandoch, G. F. G., Asefa, T., Visentainer, J. V., & Almeida, V. C. (2015). Removal of tetracycline by NaOH-activated carbon produced from macadamia nut shells: Kinetic and equilibrium studies. *Chemical Engineering Journal*, *260*, 291–299. https://doi.org/10.1016/j.cej.2014.09.017

Moazzem, S., Wills, J., Fan, L., Roddick, F., & Jegatheesan, V. (2018). Performance of ceramic ultrafiltration and reverse osmosis membranes in treating car wash wastewater for reuse. *Environmental Science and Pollution Research*, *25*(9), 8654–8668. https://doi.org/10.1007/s11356-017-1121-9

Obayomi, K. S., Bello, J. O., Yahya, M. D., Chukwunedum, E., & Adeoye, J. B. (2020). Statistical analyses on effective removal of cadmium and hexavalent chromium ions by multiwall carbon nanotubes (MWCNTs). *Heliyon*, *6*(6). https://doi.org/10.1016/j.heliyon.2020.e04174

Papegowda, P. K., & Syed, A. A. (2017). Isotherm, Kinetic and Thermodynamic Studies on the Removal of Methylene Blue Dye from Aqueous Solution Using Saw Palmetto Spent. *International Journal of Environmental Research*, *11*(1), 91–98. https://doi.org/10.1007/s41742-017-0010-x

Sarmadi, M., Foroughi, M., Najafi Saleh, H., Sanaei, D., Zarei, A. A., Ghahrchi, M., & Bazrafshan, E. (2020). Efficient technologies for carwash wastewater treatment: a systematic review. *Environmental Science and Pollution Research*, *27*(28), 34823–34839. https://doi.org/10.1007/s11356-020-09741-w

Talens-Alesson, F. I., Anthony, S., & Bryce, M. (2006). Removal of phenol by adsorptive micellar flocculation: Multi-stage separation and integration of wastes for pollution minimisation. *Colloids and Surfaces A: Physicochemical and Engineering Aspects*, *276*(1–3), 8–14. https://doi.org/10.1016/j.colsurfa.2005.10.003

Tony, M. A., & Bedri, Z. (2014). Experimental design of photo-Fenton reactions for the treatment of car wash wastewater effluents by response surface methodological analysis. *Advances in Environmental Chemistry*, *2014*.

Veit, M. T., Novais, Í. G. V., Juchen, P. T., Palácio, S. M., da Cunha Gonçalves, G., & Zanette, J. C. (2020). Automotive Wash Effluent Treatment Using Combined Process of Coagulation/Flocculation/Sedimentation–Adsorption. *Water, Air, and Soil Pollution*, *231*(10). https://doi.org/10.1007/s11270-020-04862-x

Zaneti, R. N., Etchepare, R., & Rubio, J. (2013). Car wash wastewater treatment and water reuse - A case study. *Water Science and Technology*, *67*(1), 82–88. https://doi.org/10.2166/wst.2012.492

Facile synthesis of photocatalysts for photocatalytic abatement of 2-chlorobiphenyl

D. Ashiegbu* and J.H. Potgieter*

School of Chemical and Metallurgical Engineering, University of the Witwatersrand, South Africa

*Corresponding authors: darlingtonashiegbu1985@yahoo.com; herman.potgieter@wits.ac.za

ABSTRACT

Due to the need to solve global energy crises and environmental problems, there is much interest in the development of efficient and effective semiconductor photocatalysts. ZnO nanoparticles and ZnO-BiOI 10% heterojunction were synthesized through facile synthesis methods. The structural and crystal phases, morphologies, elemental analysis, surface area measurements and optical properties were measured by XRD, SEM, energy dispersive spectroscopy, N2 adsorption-desorption isotherms via the BET method and UV-vis spectroscopy respectively. The photocatalytic activities of the as-synthesized photocatalysts were evaluated in the photocatalytic degradation of 2-CBP under solar simulation. Results obtained showed the superior photocatalytic activity of the ZnO-BiOI 10% composite. This is attributed to the optimum loading of BiOI into ZnO to form a p-n heterojunction which ensured effective charge separation, due to the formation of inner electric fields between two semiconductors.

Keywords: 2-CBP (2-chlorobiphenyl); solar simulation; heterojunction; semiconductor; facile synthesis methods

1 INTRODUCTION

The meteoric growth of the human population worldwide, coupled with accelerated industrial growth and energy demands, the emission of toxic pollutants (VOCs, POPs, heavy metals, toxic sludge, solvents) and industrial wastes into the air, water, and land has led to the contamination of our environment, climate change, and an increase in diseases (Xiao *et al*., 2015). Industrial effluent discharge is an ever-present issue challenging access to potable water globally. Humans and indeed all life forms all over the world are severely affected as a result of the consumption of impure water and presence of organic, inorganic, and microbial contaminants in water (Bora & Mewada, 2017). Consequently, remediation/clean-up of organic pollutants have become increasingly necessary. However, the process is expensive, costing nations and corporations a lot of money. In order to achieve a carbon free water, it has become imperative to develop and implement artificial methods for water and waste water treatment for the survival of the human race (Colmenares *et al*., 2015).

2 LITERATURE

The current practises in organic pollutant remediation (ozonation, reverse osmosis, filtration, adsorption, biological treatment, coagulation, incineration) have been reported to be inefficient and inadequate (García-Montaño *et al*., 2008). Incineration can result in the emission of toxic volatile gases,

while physical methods (adsorption, filtration, reverse osmosis, coagulation) have been reported to be expensive and may not totally eliminate organic pollutants, but may transform them to harmful intermediates (Vinita *et al*., 2010; Zelmanov & Semiat, 2008). A long treatment time is required in biological treatment processes, coupled with the presence of toxic and recalcitrant pollutants immune to the aforementioned, which may also cause unpleasant odour. Ozonation, although effective in some cases, has been reported to be unstable and also affected by temperature, pH and salts (García-Montaño *et al.,* 2008).

Polychlorinated biphenyls (PCBs) are synthetic compounds which have been detected in nearly every part of the global environment as pollutants, including water, sediments, air, fish and animals, and human adipose tissue, milk, and serum (Safe, 1992). There are about 209 congeners of PCBs with different structures and an empirical formula of $C_{12}H_{10-n}Cl_n$ (n=1-10) which differs depending on the number and positions of chlorine on the biphenyl skeleton (Khan et al., 2007). The commercial production of polychlorinated biphenyls is prohibited; however, they still pose major challenges due to the already released PCBs into the environment, in addition to the problem of inappropriate disposal of equipment containing PCBs. More than 1 million tons of PCBs are reported to have been produced globally (Furakawa & Fujihara, 2008; Safe, 1992), and over one-third have been dispersed in our environment (Zhang *et al*., 2016). Among the class of pollutants listed as persistent organic pollutants (POPs), polychlorinated biphenyls are among the 12 persistent organic pollutants (POP) compounds, together with the 209 PCB congeners (Li *et al*., 2008). PCBs have been reported to exhibit both thermal and chemical stability, which is beneficial for industrial uses (in capacitors and transformers, hydraulic fluids, rubber plasticizers, adhesives etc.), unfortunately, this also makes them a threat to our environment. They are persistent and show strong resistance to solar photodegradation and microbial biodegradation (Hong., 1998). Originally PCBs were abated by biodegradation, physical processes such as incineration, solvent extraction, adsorption, and chemical processes such as the use of nanoscale zero-valent iron via de-chlorination (Chu & Kwan, 2003; Jantunen *et al*., 2010; Kubátová *et al*., 2001; Wang *et al*., 2011; Weber *et al*., 2002; Wu *et al*., 2005). Incineration leads to the production of polychlorinated dibenzo-p-dioxins and polychlorinated dibenzo-furan (toxic by-products), bioremediation is unsuitable because of the highly oxidized and recalcitrant nature of PCBs to biological processes, adsorption requires large quantities of adsorbents and may cause waste disposal problems and regeneration of adsorbent. Some researchers have proposed the application of activated carbon (via sorption) and subsequent thermal treatment (for the solid residue), or super critical oxidation. However, these methods may not be cost effective (Khan *et al*., 2007; Kaštánek *et al*., 2004; Nollet *et al*., 2003). These days, photocatalysis has been proposed for the treatment of PCBs, however there are not a lot of studies in this regard.

Bismuth oxyhalides are considered as very promising because of their excellent photocatalytic

activity which is due to their satisfactory optical and electrical properties (Arumugam & Choi, 2020). Among the Bismuth ternary metal oxides, bismuth oxyiodide (BiOI), which has the narrowest band gap, and highest photocorrosion stability, is equipped with a strong absorption in the visible light region and also exhibits excellent best photocatalytic activity (Jiang *et al*., 2011; Liu *et al*., 2020). BiOI is classified as a p-type semiconductor with a band gap of 1.7-2.1 eV and belongs to the group V-VI-VII ternary semiconductors with layered crystal structures.

Despite the possession of a narrow band gap and visible light absorption range, BiOI is plagued with the problem of increased recombination of photogenerated carriers which affects its quantum efficiency. In light of this, adequate tailoring is mandatory to enhance the photo-activity of BiOI. The motivation for our own study is evidenced in the fact that ZnO, being an n-type semiconductor, will be ideal to form a heterojunction with BiOI which is a p-type semiconductor. We believe that coupling ZnO and BiOI into a heterojunction will improve the photocatalytic activity of our synthesized ZnO, because of the high-contact areas enabled by the fast charge transfer channel of BiOI and ZnO. To the best of our knowledge, there are no studies that have synthesized ZnO-BiOI through a facile hydrothermal process for the photocatalytic degradation of 2-chlorobiphenyl

3 EXPERIMENTAL PROCEDURE

3.1 Materials

All solvents and chemicals used in the experiments were of AR grade and therefore not subjected to any additional purification before use.

3.2 Preparation of pure ZnO and ZnO-BiOI 10% heterojunction

ZnO nanoparticles were synthesized via the sol-gel process. ZAD [$Zn(CH_3COO)_2{\cdot}_2H_2O$)] was used as precursor, ethanol as solvent and oxalic acid as surfactant. 11 grams of ZAD were dissolved in a beaker containing 300 ml of ethanol, which was subsequently poured into a 3-neck reactor set on a reflux apparatus and water bath. The solution was refluxed at 60ºC (±5) under vigorous stirring for 30 minutes. A clear solution was obtained. Oxalic acid was dissolved in a beaker containing 200 ml of ethanol and was subsequently added “drop wise” into the ZAD solution. On addition of oxalic acid, the formation of gels was observed as reflux was continued at 50ºC (±5) for 60 minutes. After refluxing, the xerogel was cooled to ambient temperature and oven dried overnight at 80ºC. After drying, the sample was collected and calcined at 500ºC in a furnace to obtain ZnO nanoparticles.

To synthesize ZnO-BiOI 10%, ZnO was suspended in 30 ml deionised water. A stoichiometric amount of bismuth nitrate pentahydrate [$Bi(NO_3)_3.5H_2O$] were added to ethanol (30 ml) under vigorous stirring. The latter was poured into the suspension and stirring was continued. A stoichiometric amount of potassium iodide (KI) was dissolved in deionized water and added dropwise into the mixed liquor under vigorous and continuous stirring. After an hour of stirring, the suspension changed to a yellow

colour. The mixed liquor was allowed to stir for 3 hours. The suspension was subsequently centrifuged at 4000 rpm for 15 minutes and dried in ambient air for 18 hours. The dried product was collected and ground in an agate mortar to obtain a series of ZnO-BiOI heterojunctions.

The surface morphologies and elemental analysis of the as-synthesized composites were determined using a Carl Zeiss Sigma FE-SEM equipped with an Oxford X-act EDS. Optical studies were conducted using a UV 1800 Shimadzu UV-Vis Spectrophotometer. X-ray diffraction measurements were determined with a Bruker D2 XRD instrument, while BET surface area measurements and isotherms were obtained using a Micrometrics TriStar 3000 instrument. The average particle sizes of the as-synthesized composites were calculated from diffraction peaks using the Debye-Scherrer relation, while band gap was calculated via Tauc plots established from UV-Vis spectra. A Hettich ROTOFIX Benchtop Centrifuge was used to separate some particles suspended in liquids during synthesis, while all pH values were determined using an OHAUS Starter 3100 pH meter. A GC-MS QP 2010 equipped with a Rxi-5ms column was used for all our photocatalytic degradation studies. The light source for this study was an AM 1.5G 100 mW/cm^2.

3.3 GC-MS process for 2-CBP measurements

The model pollutant (2-CBP) was analysed using a Shimadzu GC-MS QP 2010 equipped with a Rxi-5ms column of 30m length, an internal diameter of 0.25mm and a film thickness of 0.25µm. Helium was used as carrier gas and the injector temperature was set at 220°C. 1µl of sample was auto-injected into the column and the temperature program set at 140°C, held for 4 minutes and then ramped up to 240°C at a rate of 4°C/minute, and subsequently held for 10 minutes. The GC run was initiated after 3 minutes to isolate the solvent peak from the chromatogram because of the solvent cut off point. Our compound of interest was identified between 4 minutes to 10 minutes.

4 RESULTS AND DISCUSSION

4.1 SEM-EDS

The morphologies of the ZnO and ZnO-BiOI nanoparticles were investigated using FE-SEM. As shown in Fig. 1a, there is an observed high porosity with a sponge-like morphology and agglomeration due to the elevated temperature chemical reactions (500°C) for the ZnO nanoparticle. This resulted in a dense morphology due to total decomposition of the organometallic precursor. The SEM image of the ZnO-BiOI 10% heterojunction shows changes from the pure ZnO composite. There is observed penetration of BiOI in the ZnO which may have caused some agglomeration in addition to irregularly shaped aggregates and some plate-like morphology (as a result of BiOI). The EDS analysis as presented in Table 1 confirm the presence of the reference elements in addition to appropriate stoichiometry.

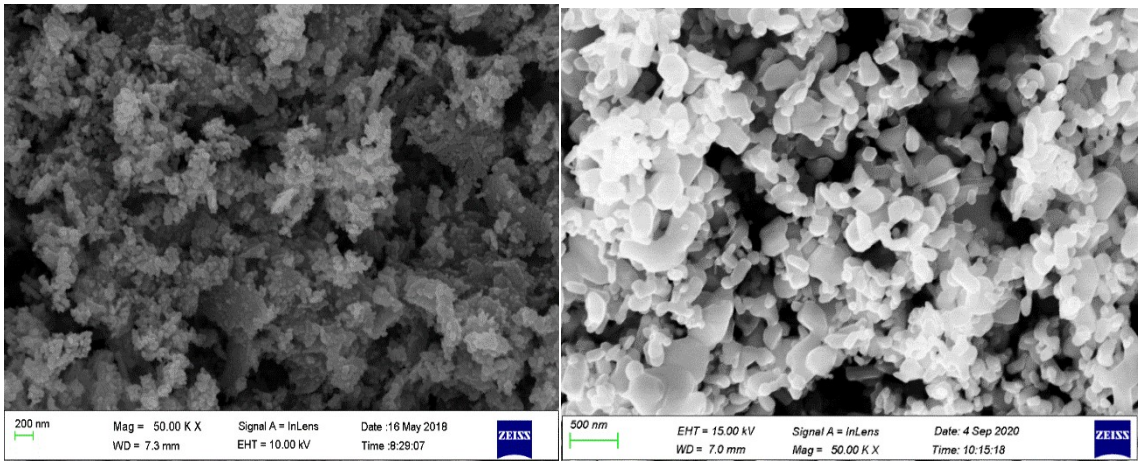

Figure 1: SEM images of (a) pure ZnO and (b) ZnO-BiOI composite

Table 1: EDS analysis of ZnO and ZnO-BiOI 10 %

ZnO			ZnO-BiOI 10 %		
Element	Weight %	Atomic %	Element	Weight %	Atomic %
O K	75.18	57.42	O K	18.38	51.17
Zn L	24.82	42.58	Zn K	65.38	44.55
			I L	6.00	2.10
			Bi M	10.24	2.18
Total	100.00	100		100.00	100.00

4.2 XRD pattern and average crystallite sizes

The XRD pattern of the as-prepared ZnO nanoparticles show sharp and intense peaks which were observed at 2θ with values of 31.7°, 34.4°, 36.1°, 47.3°, 56.3°, 62.6°, 66.3°, 67.9° and 69.1° which correspond to 100, 002, 101, 102, 110, 103, 200, 112 and 201 crystal planes of hexagonal ZnO. As displayed in Figure 2, the diffraction peaks of pure ZnO are intense and narrow showing high crystalline character. The ZnO-BiOI 10% heterojunction showed a peak at 29° (Figure 2) which corresponds to the 102 diffraction plane of BiOI. The XRD pattern of the as-prepared ZnO-BiOI 10% composite exhibits characteristic peaks of both pure BiOI and ZnO.

The average crystallite sizes of the as-synthesized composites were calculated from the most intense peaks of the XRD pattern from the FHWM using the Debye–Scherrer relationship shown in Equation 1:

$$D = k(\lambda/(\beta \cos \theta)) \qquad \textbf{Equation 1}$$

where λ = 1.54056 nm is the wavelength of X-ray diffraction used, θ is the Bragg diffraction angle of the XRD peak, β is the measured broadening diffraction line peak at an angle of 2θ at half its maximum

intensity (in radian). The average crystallite size of pure ZnO was determined to be 37.6 nm while that of ZnO-BiOI 10% composite was established to be 31 nm.

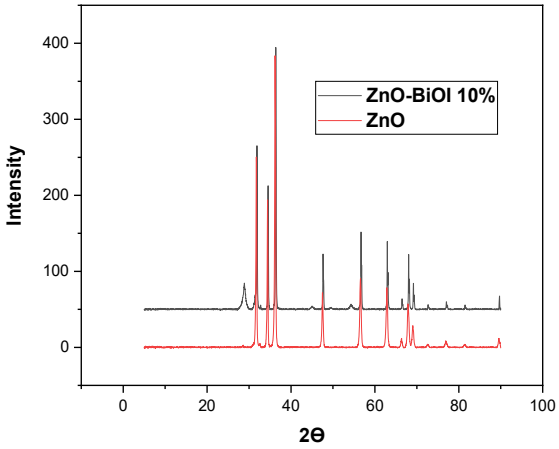

Figure 2: X-ray diffraction patterns of bare ZnO and ZnO-BiOI 10% composite

4.3 Textual properties of the as-prepared photocatalysts

The surface area of the ZnO was measured as 1.08 m^2/g, which is small compared to the ZnO-BiOI 10%. This smaller surface area is attributed to probable pore blockages. This means that the BET measurement probe gas will not properly adsorb inside the pores. The Barret-Joyner-Halender (BJH) pore size distribution plot is shown in Figure 3c with an average pore size width of 43.2 nm. The BET surface area measurement of the ZnO-BiOI 10% composite exhibited a measured surface area of 19.8 m^2/g with an average pore size diameter of 35 nm. The N_2 adsorption-desorption isotherm (Figure 3b) of the heterojunction is observed to exhibit a Type IV Isotherm with little H_{III} hysteresis. The BJH pore size distribution plot (Figure 3d) is classified as mostly mesoporous with some distribution macropores.

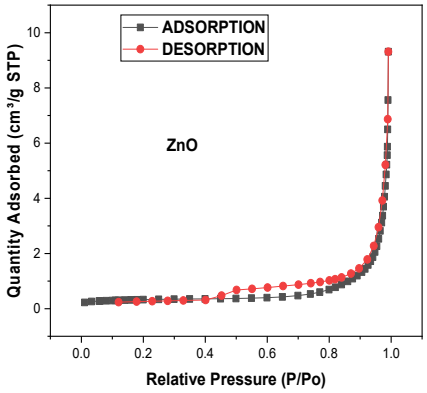

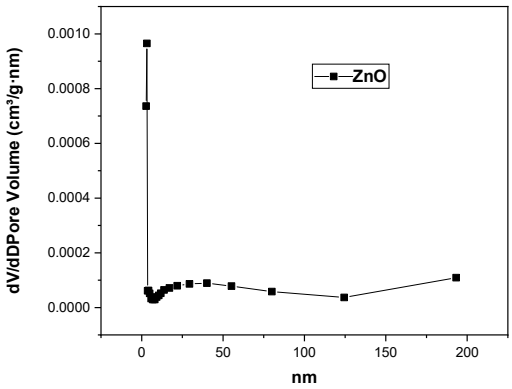

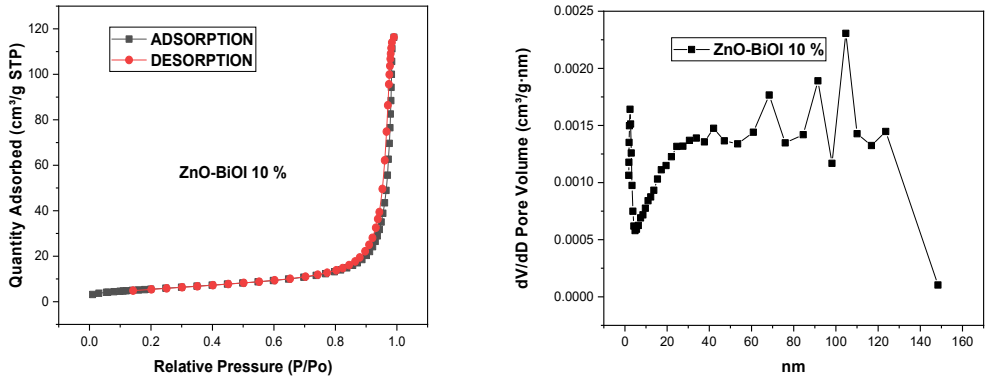

Figure 3: N_2 adsorption-desorption isotherms of (a)pure ZnO (b) ZnO-BiOI 10 % and BJH pore size distribution of (c) pure ZnO (d) ZnO-BiOI 10

4.4 Optical properties and bandgap measurements

A Shimadzu 1800 UV-vis spectrophotometer was used to determine the absorption properties of the composites. All spectra were recorded at ambient temperature at 200-900 nm range. The bandgaps of all the composites were calculated from Tauc's plot via the Kubelka–Munk equation (Equation 2) by extrapolating the linear portion of the plot of $(\alpha h\nu)^2$ vs the proton energy as shown in the equation below:

$$\alpha h\nu = A(h\nu - E_g)^n \qquad \textbf{Equation 2}$$

where α - absorption coefficient, A - constant, h - Plank's constant, ν - photon frequency, E_g - band gap (bg), and n = 1/2 or 2 for the transition being direct or indirect respectively. Extrapolating the linear portion in a plot of $(\alpha h\nu)^2$ against $h\nu$ gave us the bg values.

4.4.1 ZnO

The ZnO composite absorption spectrum showed maximum absorption at 373 nm (as shown in Figure 4a) in the UV region. This observation is in agreement with several other studies (Potti & Srivastava, 2012; He *et al.*, 2018; Thein *et al.*, 2017). Figure 4b shows the estimated band gap of the ZnO photocatalyst estimated via the Tauc's plot of the absorption spectrum. A band gap of 3.24 eV was estimated, showing the wide band gap nature of ZnO.

4.4.2 ZnO-BiOI 10%

Figure 4c shows the absorption spectra of the ZnO-BiOI 10% heterostructure. The absorbance of the composite was recorded at 378 nm. There was an observed slight red shift for ZnO-BiOI 10% due to the BiOI loading. A narrowing of the band gap was also observed for the heterojunction as shown in Figure 4d. With the introduction of BiOI at 10 % loading, the band gap narrowed down to 3.0 eV. This observation is attributed to visible light characteristic of BiOI.

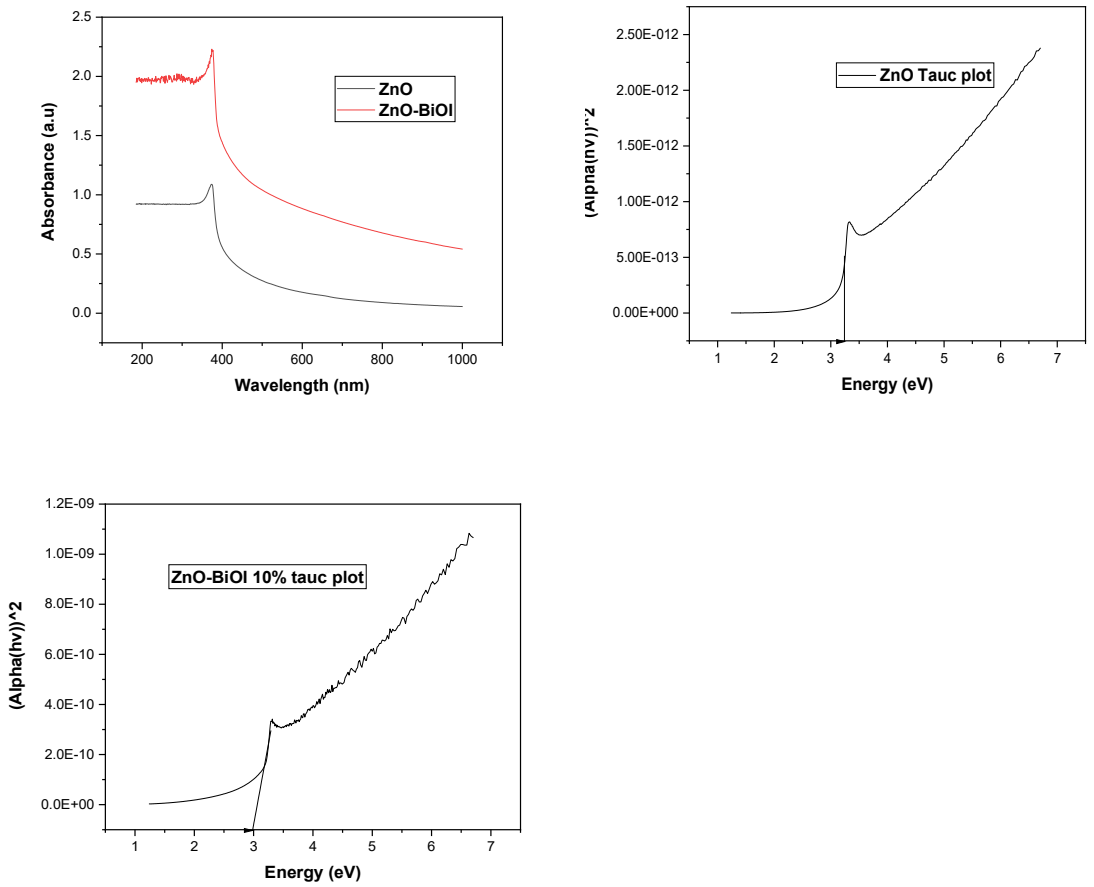

Figure 4: (a) ZnO and ZnO-BiOI 10% absorption spectra (b) ZnO Tauc plot showing band gap (c) ZnO-BiOI 10% Tauc plot showing band gap

4.5 Photocatalytic activity and mechanism

4.5.1 Photocatalytic performance

To assess the photo-activities of the composites, the degradation under simulated solar irradiation was undertaken. From Figure 5, it can be observed that the 2-CBP degradation efficiency was about 20 % when pure ZnO was applied. The reaction reached its peak at 150 minutes after which no further degradation was observed. On the other hand, ZnO-BiOI 10% achieved a degradation efficiency of nearly 60% at 150 minutes. Beyond 150 minutes, the photocatalytic activity levelled off and no further significant degradation was observed. The ZnO-BiOI 10% heterojunction photocatalyst showed more significant activity than the pure ZnO. The superior activity of the ZnO-BiOI 10% heterostructure is ascribed to increased light absorption and efficient charge separation in addition to the narrow bandgap and exposed reactive facets. Thus, the BiOI in the heterostructure acted as a photosensitizer. In addition, coupling ZnO and BiOI into a heterojunction enhanced the photocatalytic activity of the ZnO because of the high-contact areas enabled by the fast charge transfer channel of BiOI and ZnO. ZnO-BiOI 10%

heterostructure with a significantly larger surface area of 19.8 m^2/g and a significant pore volume was observed to exhibit the best photocatalytic activity. Thus, a larger surface area led to the subsequent formation of more hydroxyl radicals for more photocatalytic reaction centres. Several researchers made similar observations in their respective studies (Flores et al., 2014; Moafi et al., 2013; Mekasuwandumrong *et al.*, 2010; Ameen *et al.*, 2012).

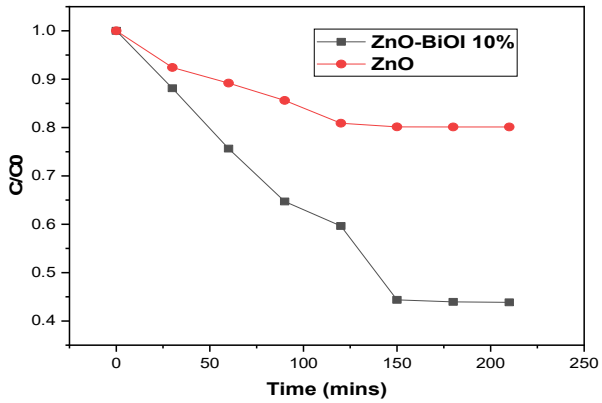

Figure 5: Comparison of the photo-activity of bare ZnO and ZnO-BiOI 10%

4.5.2 Proposed degradation mechanism

From the UV-Vis spectra of both ZnO and BiOI, the calculated band gaps were established as 3.24 eV and 1.23 eV respectively. A simplified band energy structure of ZnO and BiOI is shown in Figure 6a. ZnO being an n-type photocatalyst has its Fermi level close to its CB, while BiOI being a p-type photocatalyst has its Fermi level located close to its VB (Jiang et al., 2011). The introduction of BiOI into the ZnO lattice and subsequent p-n heterojunction construction leads to the realignment of the Fermi levels of the two materials. Photoexcited electrons transfer to the CB of ZnO, leaving the holes in the BiOI VB (Figure 6b). This takes place because the conduction band of BiOI is more negative than the conduction band of ZnO. In the same way, the valence band of ZnO is more positive than that of BiOI. This shows that separation efficiency of the ZnO-BiOI 10% composite is improved and in turn, the photocatalytic activity is also improved. From the experimental results, the photocatalytic mechanism is proposed as follows

$$BiOI \xrightarrow{h\nu(\lambda \geq 400nm)} BiOI\left(h_{VB}{}^{+} + e_{CB}^{-}\right) \qquad \textbf{Equation 3}$$

$$BiOI(e_{CB}^{-}) \xrightarrow{transfer} ZnO(e_{CB}^{-}) \qquad \textbf{Equation 4}$$

$$ZnO(e_{CB}^{-}) + O_2 \rightarrow ZnO + O_2^{\cdot -} \qquad \textbf{Equation 5}$$

$$O_2^{\cdot -} + H^{+} \rightarrow \dot{O}H \qquad \textbf{Equation 6}$$

$$O_2^{\cdot -} \text{ and } \dot{O}H + 2CBP \rightarrow Degradation(products) \qquad \textbf{Equation 7}$$

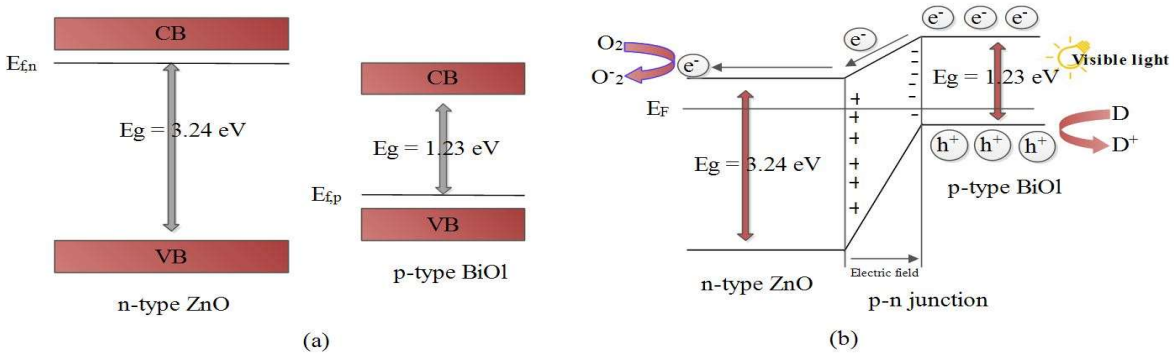

Figure 6: Proposed diagram of ZnO and BiOI band energy structure (a)before contact (b) after interfacial contact, p-n junction formation and improved charge separation process of the ZnO-BiOI 10% heterostructure under solar irradiation

5 CONCLUSIONS

ZnO-BiOI 10% heterojunction was prepared through a facile and direct method. The ZnO-BiOI 10% heterostructure with a reduced band gap of 3.0 eV, surface area of 19.8 m^2/g, pore volume of 0.180 cm^3/g and a pore size of 35 nm showed superior photocatalytic activity in the abatement of 2-CBP when compared with the bare ZnO nanoparticles. A possible photocatalytic degradation mechanism is proposed to explain the improvement in photocatalytic activity. The synthesized heterojunction photocatalyst shows potential for practical application in the remediation of water contaminated with calcitrant organic pollutants.

REFERENCES

Ameen, S., Seo, H., Akhtar, M. S., & Shik, H. 2012. Novel graphene / polyaniline nanocomposites and its photocatalytic activity toward the degradation of rose Bengal dye. *Chemical Engineering Journal*, *210*, pp. 220–228. https://doi.org/10.1016/j.cej.2012.08.035

Arumugam, M. and Choi, M. Y. 2020. Recent progress on bismuth oxyiodide (BiOI) photocatalyst for environmental remediation. *Journal of Industrial and Engineering Chemistry*, 81, pp. 237–268. doi: 10.1016/j.jiec.2019.09.013.

Bora, L. V. and Mewada, R. K. 2017. Visible/solar light active photocatalysts for organic effluent treatment: Fundamentals, mechanisms and parametric review. *Renewable and Sustainable Energy Reviews*, 76(April), pp. 1393–1421. doi: 10.1016/j.rser.2017.01.130.

Chu, W. and Kwan, C. Y. 2003. Remediation of contaminated soil by a solvent/surfactant system. *Chemosphere*, 53(1), pp. 9–15. doi: 10.1016/S0045-6535(03)00389-8.

Colmenares, J. C., Kuna, E., Jakubiak, S., Michalski, J., & Kurzydłowski, K. 2015. Polypropylene nonwoven filter with nanosized ZnO rods: Promising hybrid photocatalyst for water

purification. *Applied Catalysis B: Environmental*, 170–171, pp. 273–282. doi: 10.1016/j.apcatb.2015.01.031.

Flores, N.M., Pal, U., Galeazzia, R., & Sandoval, A. 2014. Effects of morphology, surface area, and defect content on the photocatalytic dye degradation performance of ZnO nanostructures. *Royal Society of Chemistry Advances*, *4*(77), pp. 41099–41110. https://doi.org/10.1039/C4RA04522J

Furakawa, K. and Fujihara, H. 2008. Microbial degradation of polychlorinated biphenyls: Biochemical and molecular features. *Journal of Bioscience and Engineering*, 105(5), pp. 433–449.

García-Montaño, J., Enech, X., García-Hortal, J. A., Torrades, F., & Peral, J. 2008. The testing of several biological and chemical coupled treatments for Cibacron Red FN-R azo dye removal. *Journal of Hazardous Materials*, 154, pp. 484–490. doi: 10.1016/j.jhazmat.2007.10.050.

Hong, C.S., Wang, Y. and Bush, B. 1998. Kinetics and products of the TiO2 photocatalytic degradation of 2-chlorobiphenyl in water. *Chemosphere*, 36(7), pp. 1653–1667.

Jantunen, A. P. K., Koelmans, A. A. and Jonker, M. T. O. 2010. Modeling polychlorinated biphenyl sorption isotherms for soot and coal. *Environmental Pollution*, 158(8), pp. 2672–2678. doi: 10.1016/j.envpol.2010.04.022.

Jiang, J., Zhang, X., Sun, P., & Zhang, L. 2011. ZnO / BiOI Heterostructures : Photoinduced Charge-Transfer Property and Enhanced Visible-Light Photocatalytic Activity. *The Journal of Physical Chemistry C*, 115, pp. 20555–20564. doi: 10.1021/jp205925z.

Kaštánek, P., Demnerová, K. and Ma, Y. 2004. Decontamination of wastewater contaminated by polychlorinated biphenyls (PCBs). *Water Science and Technology*, 50(2), pp. 131–138. doi: 10.2166/wst.2004.0107.

Khan, G. M., Kim, G. Y., Akinrelere, T. S., & Moon, S. H. 2007. Electroenzymatic mineralization of 2-chlorobiphenyl in synthetic wastewater. *Desalination*, 211(1–3), pp. 212–221. doi: 10.1016/j.desal.2006.03.595.

Kubátová, A., Erbanová, P., Eichlerová, I., Homolka, L., Nerud, F., & Šašek, V. 2001. PCB congener selective biodegradation by the white rot fungus Pleurotus ostreatus in contaminated soil. *Chemosphere*, 43(2), pp. 207–215. doi: 10.1016/S0045-6535(00)00154-5.

Li, G., Zhang, L. and Zhang, Z. 2008. Determination of polychlorinated biphenyls in water using dynamic hollow fiber liquid-phase microextraction and gas chromatography-mass spectrometry. *Journal of Chromatography A*, 1204(1), pp. 119–122. doi: 10.1016/j.chroma.2008.07.081.

Liu, H., Cai, J., Luo, M., Chen, C., & Hu, P. 2020. Novel mesoporous bismuth oxyiodide single-crystal nanosheets with enhanced catalytic activity. *RSC Advances*, 10(10), pp. 5913–5918. doi: 10.1039/c9ra10451h.

Mekasuwandumrong, O., Pawinrat, P., Praserthdam, P., & Panpranot, J. (2010). Effects of synthesis conditions and annealing post-treatment on the photocatalytic activities of ZnO nanoparticles in the degradation of methylene blue dye. *Chemical Engineering Journal*, *164*(1), 77–84. https://doi.org/10.1016/j.cej.2010.08.027

Moafi, H. F., Zanjanchi, M. A., & Shojaie, A. F. (2013). Tungsten-doped ZnO nanocomposite: Synthesis, characterization, and highly active photocatalyst toward dye photodegradation. *Materials Chemistry and Physics*, *139*(2–3), 856–864.

Nollet, H., Roels, M., Lutgen, P., Meeren, P. Van Der, & Verstraete, W. 2003. Removal of PCBs from wastewater using fly ash. *Chemosphere*, 53, pp. 655–665. doi: 10.1016/S0045-6535(03)00517-4.

Safe, S. 1992. Toxicology , Structure-Function Relation- ship , and Human and Environmental Health Impacts of Polychlorinated Biphenyls : Progress and Problems by Stephen Safe. *Environmental Health Perspectives*, 100, pp. 259–268.

Vinita, M., Praveena Juliya Dorathi, R. and Palanivelu, K. 2010. Degradation of 2,4,6-trichlorophenol by photo Fenton's like method using nano heterogeneous catalytic ferric ion. *Solar Energy*, 84(9), pp. 1613–1618. doi: 10.1016/j.solener.2010.06.008.

Wang, Y., Zhou, D., Wang, Y., Zhu, X., & Jin, S. 2011. Humic acid and metal ions accelerating the dechlorination of 4-chlorobiphenyl by nanoscale zero-valent iron. *Journal of Environmental Sciences*, 23(8), pp. 1286–1292. doi: 10.1016/S1001-0742(10)60543-8.

Weber, R., Takasuga, T., Nagai, K., Shiraishi, H., Sakurai, T., Matuda, T., & Hiraoka, M. 2002. Dechlorination and destruction of PCDD, PCDF and PCB on selected fly ash from municipal waste incineration. *Chemosphere*, 46(9–10), pp. 1255–1262. doi: 10.1016/S0045-6535(01)00268-5.

Wu, W., Xu, J., Zhao, H., Zhang, Q., & Liao, S. 2005. A practical approach to the degradation of polychlorinated biphenyls in transformer oil. *Chemosphere*, 60(7), pp. 944–950. doi: 10.1016/j.chemosphere.2004.11.079.

Xiao, J., Xie, Y. and Cao, H. 2015. Organic pollutants removal in wastewater by heterogeneous photocatalytic ozonation. *Chemosphere*, 121(November 2017), pp. 1–17. doi: 10.1016/j.chemosphere.2014.10.072.

Zelmanov, G. and Semiat, R. 2008. Phenol oxidation kinetics in water solution using iron(3)-oxide-based nano-catalysts. *Water Research*, 42(14), pp. 3848–3856. doi: 10.1016/j.watres.2008.05.009.

Zhang, W., Yu, T., Han, X., & Ying, W. 2016. Removal of 2-ClBP from soil–water system using activatedcarbon supported nanoscale zerovalent iron. *Journal of Environmental Sciences*, 47, pp. 143–152. doi: 10.1016/j.jes.2015.12.032.

Fluidization Behaviours of Nanoparticles

*K. Lubale, A.H. Mohammadi, E.M. Obwaka

[1] School of Chemical Engineering, University of KwaZulu Natal, Durban, South Africa

[2] Discipline of Chemical Engineering, University of KwaZulu Natal, Durban.

*Corresponding author: kankulubale@gmail.com

ABSTRACT

The experimental measurement of the pressures in a different region of the fluidized bed; in the plenum chamber, on the bed of the solid material, and above the bed of solid material was performed by using pressure transducers of model S-20, P#10471134 and the inverted manometers to investigate the behavior in the fluidization of samples of size 277 µm, 428 µm, 161 µm, and 338 µm. The applicability of the published correlation such as the Ergun equation was fitted to the experimental pressure drop measured using both measuring methods; the sphericities of the samples were measured using the fitted Ergun equation. The fluidization parameters such as minimum fluidization velocity, voidage, and height were measured from the experimental data and compared with the calculated minimum fluidization parameters obtained from the published correlation. The study on the behavior of the samples was to familiarize with the application of the published correlations in the investigation of the fluidization behavior of 13 nm aluminum oxide nanoparticle in size. Two methods were used during the experiment in the fluidization of nanoparticles materials; acoustic sound fluidization and Vibro-fluidization. During the enhanced fluidization by external forces of aluminum oxide nanoparticle, it was observed that pressure transducers of model S-20, P#10471134 were appropriated for pressure measurement; and the primary size of nanoparticles formed agglomerates, and their fluidization was of agglomerate particulate fluidization. The use of the Richardson and Zaki equation and stoke law in the experimental data was to estimate the size of the agglomerates formed during fluidization associated with mechanical vibration and acoustic sound.

Keywords: fluidization associate with external forces, nanoparticles, size of agglomerates.

1 INTRODUCTION

The handling of nanoparticles in the process industry is identifiable in many areas such as in cosmetics, painting, electronics, medicine; nanoparticles are used as catalysts due to their large surface area per volume of particles. Nanoparticles are those particles that exist on a nanometre scale. Their physical properties such as size and density can be determined in a fluidized bed system because nanoparticles can easily be transported, mixed when their hydrodynamics are well understood. Fluidization of nanoparticles become very attractive to daily life for many reasons when utilizing them in many sectors in the industry. In drug delivery, it has been found that nanotechnology is proven

beneficial in the treatment of cancer, AIDS, and many other diseases (Rizvi and Saleh, 2018). Processing nanoparticles in the fluidizing system is not as easy as it seems, much research has undergone fluidization of fine/ultrafine particles and has found difficulties fluidizing particles falling in Geldart category of group C (Wang *et al*., 2007). Geldart (1986) has classified the fluidization of particles according to different groups; and he has pointed out, that the fluidization of particles differs as their size changes. It has been reported that the fluidization of nanoparticles seems unrealistic in a conventional fluidization process due to the cohesive forces existing between particles. In most cases, they can be fluidized when an external force is applying to the fluidized system, and their fluidization is in the form of agglomerates and is called agglomerate fluidization. Before proceeding to the fluidization of nanoparticles it is very important to understand the theory governing the fine/ultrafine particles. The practice of the traditional fluidization technique has revelled the possibility of fluidizing particles of Geldart Groups A and B.

Fluidizing nanoparticles in a conventional fluidized bed is a complex matter that needs to be addressed by applying a modified methodology for the use of these nanoparticles in many sectors for applications. This complexity of fluidizing this group C material is due to the presence of the inter-particles forces existing between particles. To study the behavior of nanoparticles in the fluidization, it is of interest to be able to expose these materials under fluidization. The use of assisted method: fluidization assisted by acoustic sound and vibration to fluidized nanoparticles come into practice before obtaining any fluidization parameters of nanoparticles. Many researchers have undertaken methodologies to fluidize nanoparticles, however, the use of fluidization assisted by the vibration and acoustic sound for fluidization of 13 nm aluminum oxide nanoparticles have been used in the study of the fluidization.

2 LITERATURE

2.1 Classification of particles according to the Geldart group

Processing fluidization of solid particles without any knowledge makes the process difficult; it is important to know what class of solid particles belong, this will give a physical understanding of their behavior when applying fluidization. The work of Geldart (Wang *et al*., 2007) has proven the necessity of classifying particles when studying them in fluidization. He has classified solid particles according to their size and density difference.

Many researchers have taken their work on fluidizing particles of different sizes, and their results have demonstrated how different the fluidization behavior of solids particles are. Their results are just the confirmation of what was found by Geldart in working with particles of different sizes. He has categorized particles in four groups according to their fluidization behavior and these groups are comprising of Geldart group A, B, C and D.

2.2 Inter-particle forces existing between solid particles of Group C

The classification of Geldart group C particles is strongly dependent on inter-particles forces existing between particles, due to the existence of these forces, the solid particles of such characters are classified in group C from the Geldat's Chart. The fluidization of Group C particles become more difficult compared to Group A, B, and D. The inter-particle forces in solid particles of group A, B and D are insignificant compared to group C. As particles get smaller their inter-particle forces become more predominant. Geldart has defined those forces as the van der Waal force, electrostatics force, and capillary force between solid particles. When working on the solid particles, it is important to define those forces and their effect on particles when they are subjected to the process of fluidization. The solid particles of group C are classified as a powder or fine/ultrafine particles with a size range of less than 30μm. Nanoparticles are within this group. These forces dominate other forces when nanomaterials are fluidized in a conventional fluidized bed, because of this phenomenal existence of inter-particle forces between particles, the fluidization of nanoparticles become impractical because of the bed being lift up or occurrence of channelling or slagging when a gas fluid is injected to the fluidized bed. Some researchers (Zhu *et al.*, 2005) have attempted to fluidize nanoparticles in a conventional fluidized bed, they have found that fluidization could happen in form of agglomeration when a very large superficial velocity is applied that is more in magnitude to the minimum fluidization velocity of individual particles.

2.2.1 Van der Waals forces

At a molecular and atomic level, van der Waals force is the force that exists between two electronically charged particles, influencing the attraction situation occurring between particles. This interaction happens in two molecules, atom, surface, or intermolecular forces. In the case of a surface with an opposite charge when two particles are significantly close, there is an appearance of attraction. Literature has shown the van der Waal force is the most significant in all inter-particle forces and it dominates over the gravitational force (Raganati *et al.*, 2018)**.** Literature has proposed mathematical correlation to calculate this force, in this literature review, we are still defining, and more details like correlation will be provided in future work to have a clear understanding of the inter-particle forces between nanoparticles. Small size nanoparticles do have the presence of van der Waal forces in between two particles as defined above, these forces are responsible for the cohesiveness of these fine/ultrafine particles. And when nanoparticles are exposed to fluidization they tend to form agglomerates (Tamadondar *et al.*, 2016).

2.2.2 Electrostatic forces

Electrostatic forces in nanoparticles arise when two ultrafine particles slide, collide with each other when they are mixed. There is a transfer of electrons occurring into their surface layers when materials a brought into contact. This characteristic of nanoparticles being electrically charged under electrostatic

force is called contact electrification. It has been shown from the literature, a mathematical model of this form of force obeyed coulomb's theory. Many researchers have found that the electrostatic forces in nanoparticles are negligible compared to the van der Waal forces.

2.2.3 Capillary forces

Literature shows that in the presence of humidity capillary forces have an important contribution to the attraction between nanoparticles with a hydrophilic surface (Tamadondar *et al*., 2016). When the vapor pressure of the surrounding gas is close to the saturation pressure, capillary forces can be much larger than gravitational force and also van der Waals force as well. Generally, they increase with increasing humidity of the gas and decreasing material porosity. Many workers have considered nanoparticles of the nature of hydrophobic where the capillary forces are negligible compared to van der Waals forces.

2.3 Characteristics of Geldart Group C particles

Solid particles of Group C are those with a size below 30μm; literature has published work on the fluidization of Group C and demonstrated that materials of this Group do not fluidize easily in a conventional fluidized bed but they can be fluidized if the fluidization is associated with external forces, such as acoustic sound, mechanical vibration, magnetic, and electric fields, centrifugal fluidized bed, and the use of micro-jets as a secondary flow in the bed. Publishers have demonstrated, by associating forces to the fluidization of solid particles of Group C, the inter-forces in solid particles disrupt and cause spaces in between nanoparticles, and enhance the fluidization to occur. Due to the phenomenal behavior of nanoparticles, their fluidization is defined in the form of agglomerates.

2.3.1 Agglomerate fluidization

The study on the agglomerate fluidization of nanoparticles is recorded by many workers in the literature, and is defined by the fluidization of nanoparticles being grouped in particles called agglomerate fluidization. And it has been shown that there exist two forms of agglomerate; natural agglomerate when nanoparticles are packed for storage or transportation before fluidization; and the secondary agglomerate when nanoparticles are subjected to the fluidization processed. As demonstrated in the literature, the nanoparticles belonging to Group C are governed by the predominance of the inter-particles forces that make the fluidization of this type of solid particles difficult. These fine particles are characterized by the presence of channeling, slagging of the bed being lift as a plug when a gas velocity is injected into a fluidized bed (Zhu *et al.*, 2005). Due to the high magnitude of inter-particles forces of nanoparticles, it has been observed the fluidization may occur in form of agglomerate behaving like particles of group A, B, or C, and the superficial gas velocity required for the fluidization is highly compared to the normal minimum fluidization of individual nanoparticles in a conventional fluidized bed. It has been recorded that this fluidization of nanoparticles can be classified as agglomerate

particulate fluidization when smooth fluidization is observed and agglomerate bubbling fluidization when there is a presence of bubbles**.**

2.3.2 Agglomerate particulate fluidization

The cohesiveness of particles of Group C, especially nanoparticles is dominated by the inter-particles forces. Due to these forces, nanoparticles are in the form of agglomerate rather than single nanoparticle when they are transported or stored. Many works of the literature have proven the fluidization of nanoparticles to behave as smooth fluidization with high bed expansion when their characteristic of the fluidization is defined in the form of agglomerate. It has been mentioned in the literature, agglomerate particles can be considered as single particles and categorized as Group A, B, or C according to their agglomerate sizes. Their fluidization is depended on density differences and the size of agglomerate. It has found that particles having sizes less than 20 nm when fluidized is characterized as bubbleless or liquid-like fluidization and this type of fluidization is called agglomerate particulate fluidization. And this case, as stated above, when nanoparticles have been fluidized in the form of agglomerate particulate fluidization, there is an observation of smooth fluidization. Literature has shown that this type of fluidization obeys the Richardson- Zaki equation.

2.3.3 Agglomerate bubbling fluidization

The fluidization of nanoparticles as agglomerate bubbling fluidization is characterized by poor bed expansion, high minimum fluidization velocity, and occurrence of bubbles. The non-homogeneous of the agglomerate nanoparticles in the bed defined the size of the agglomerate being distributed within the bed. It has been found that the size of the agglomerate is high in magnitudes with a very large density difference.

2.4 Determination of the size of agglomerates

Solid particles that belong to group C are very important due to the increase in the surface-to-volume ratio, this property of solid particles of group C increases the heat and mass transfer in a fluidization process of particulate materials. It is evident, the prediction of the size of the agglomerate will characterize the fluidization of nanoparticles. As mentioned early, the agglomerate fluidization of nanoparticles is defined by the size of the agglomerate and their density different to classify them as agglomerate particulates fluidization or agglomerate bubbling fluidization. The fluidization parameters such, minimum fluidization velocity, bed expansion, the pressure drop across the fluidized bed column are correlated from the model and compared with the experimental value. We are emphasizing in agglomerate particulate fluidization as this has been experimentally shown and their size of agglomerates has been correlated using the Richardson-Zaki equation.

Morooka *et al*. (1988) worked on the energy balance model for agglomerate formation and disintegration and stated that the energy for the agglomerate formation is the same as the energy

required to break the agglomerate in two parts. They have assumed that the size of the agglomerate could be obtained by evaluating the energy generated by laminar shear plus the kinetic energy of agglomerate that is balanced with the energy required to break the agglomerate. (i.e., energy due to the inter-particle forces). It was noted from the literature that the value of n, which is the Richardson and Zaki exponent, an empirical parameter is a value of 5 as reported by many researchers in the small Reynold number regime, while n decrease as Reynold number increase.

$$m_p = \rho_p \times v_p \qquad \textbf{Equation 1}$$

Where m_p is defined as the mass of particles; and ρ_p as the density of particles

$$\varepsilon = \frac{v_B - v_p}{v_B} \qquad \textbf{Equation 2}$$

Where ε is defined as the voidage; v_B is the volume of the bed and v_p is the volume of the particles

$$AH_O\rho_P(1-\varepsilon_O) = AH_{mf}\rho_{bulk}(1-\varepsilon_{mf}) \qquad \textbf{Equation 3}$$

The equation 3 is the conservation of mass at initial state and at fluidization state

$$\varepsilon = 1 - \left[(1-\varepsilon_o) \times \frac{H_o}{H}\right] \qquad \textbf{Equation 4}$$

Where ε_o is defined as the initial voidage; and H_o is defined as the initial height

$$d_a = \sqrt{\frac{18\times\mu\times v_t}{(\rho-\rho_f)\times g}} \qquad \textbf{Equation 5}$$

Where d_a is defined as the average diameter.

3 EXPERIMENTAL PROCEDURE

3.1 Process description for the fluidization of nanoparticle using acoustic sound fluidized bed

A 0.12 m diameter fluidized bed was chosen to associate with the acoustic sound for the fluidization of nanoparticles. The fluidized bed was 0.49 m in height. A line from the set of rotameters was connected to the fluidized bed associated with acoustic sound where the airflow was controlled through the rotameter. A speaker was placed at top of the fluidized bed to produce waves from the sound coming from a 2 MHz function generator of model ALP-1614B, the working range of the frequency of the sound to the fluidized bed was from 0 to 200 Hz. The sound from the 2 MHz functional generators was sent to a speaker placed at top of the fluidized bed before the circulation of the flowing air through the fluidized bed. The processes for measuring devices were three pressure transducers of model S-20, they were connected at different measuring pressure tap on the fluidized bed. The first in the plenum, the second above the perforated plate, and the third few centimeters above the second. All pressures measuring devices were connected to controllers where pressure was recorded during fluidization. After, the air was allowed to flow through the fluidized bed column by controlling the flow from a

rotameter 1

3.2 Process description of fluidization of nanoparticles using vibro-fluidized bed

A vibro-fluidized bed is used to investigate the fluidization of nanoparticles enhanced by vibration, it was equipped with a control panel where the frequency of the vibration is controlled. Nanoparticles materials were poured into the vibro-fluidized bed; the fluidization of nanoparticles was occurring in a 0.5 meters in height and 0.16 meters in diameter, thereafter a frequency of 250 rpm was applied to the fluidized bed to initiate the vibration of the fluidized bed. One pressure transducer of model S-20 was connected to the measuring tap in the plenum chamber and another pressure transducer of the same model was connected on the measuring tap located on the bed of nanoparticles. All these pressures measurement devices were sending a signal to controllers located in the control room hut 2 where pressures were displayed. One was reading the pressure from the plenum chamber displayed from a digital display device and the other was reading the pressure from the bed of the nanoparticles displayed from a controller connected to a LapTop. Before the fluidization, a vibration was applied to the fluidized bed, thereafter, a fluidizing medium was allowed to flow through one of the rotameter. The reading from the rotameter was recorded including the bed expansion of nanoparticles and the pressures on the plenum chamber and the bed of the nanoparticles.

4 RESULTS AND DISCUSSION

4.1 The behaviour of nanoparticles in fluidization associated with eternal forces

The objectiveness of investigating the characteristics behaviour of aluminum oxide nanopowder, 13 nm primary particle (TEM), 99.8% trace metals basis in fluidization associated with external forces were of merger concern. In an appropriate turn, acoustic sound fluidization and vibro-fluidization of aluminum oxides were run in the main laboratory to observed the minimum fluidizations of the nanomaterials.

4.1.1 Acoustic sound fluidization of aluminum oxides nanoparticles

After the powder nanoparticles of aluminum oxides have been under fluidization enhanced with acoustic sound, it was observed the bed of nanomaterials expanded rapidly when the valve of the rotameter was open to permit the fluidizing medium to flow through the line. The initial height of the bed of nanoparticles was set at 15 cm and was reduced to 8 cm due to the formation of agglomerates of nanoparticles in the bed and loss of dust of nanoparticles at top of the fluidized bed. The recording of the measured variables such as bed expansion of nanoparticles, pressure in the plenum chamber of the fluidized bed, pressure on the bed of nanoparticles, and pressure above the bed of nanoparticles were reproduced after many runs. In the fifth run of acoustic sound fluidization, the bed of nanoparticles was at 8 cm. It was observed a small reading in the pressures in different parts of the fluidized bed when aluminum oxides nanoparticles were under fluidization. The rotameter reading was open and increased

with an increment of 1.

4.1.2 Determination of the size of agglomerates nanoparticles using scanning electron microscopy analysis (SEM)

After the acoustic sound fluidization of aluminum oxide nanoparticles, the forming agglomerate nanoparticles formed during fluidization were analyzed through the scanning electron microscopy analysis to visualize the structure of the agglomerate aluminum oxide nanoparticles and to determine the size distribution of the agglomerate formed. It was observed the agglomerate aluminum oxide nanoparticles were observed to be spherical. The maximum and minimum size of the agglomerate found were 21.59 µm and 9.783 µm respectively.

4.1.3 Determination of the size of the agglomerates nanoparticles using Stokes' Law

Aluminum oxide nanoparticles fluidized in a modified fluidized bed with acoustic sound, and the fluidization was of the form of agglomerate particulates fluidization. the agglomerate formed during the acoustic sound fluidization were distributed in the bed of the aluminum oxide nanoparticles, it was observed that the main cause of the fluidization of this nanoparticle in the acoustic sound fluidization was due to the formation of agglomerate, and the mean size of the agglomerate was estimated using the Stokes' Law. The mean diameter of the agglomerates was estimated at a value of 128 µm using Stokes' Law.

4.1.4 Determination of fluidization parameters

The pressure drop on the bed of aluminum oxide nanoparticles recorded after acoustic sound fluidization demonstrated a minimum fluidization velocity at a value of 0.03 m/s; the pressure drop remained unchanged when the pressure transducers recorded a pressure of 0.012 kPa. It was observed that the expansion of the bed of aluminum oxide nanoparticles started to occurred from the top of the bed to the bottom; the bed did not show any behaviour as the bed remained fixed while the superficial air velocity was injected to the acoustic sound fluidized bed. And the all bed of the aluminum oxide nanoparticles fluidized entirely at a height of 9.3 cm. The initial voidage of the aluminum oxide nanoparticles in the acoustic sound fluidized bed was calculated using the Richardson and Zaki equation. During the acoustic sound fluidization of this nanoparticle, it was observed the aluminum oxide nanoparticles demonstrated fluidization of the form of agglomerate particulate fluidization thus the Richardson and Zaki accommodated the calculation of parameters such as initial voidage, minimum fluidization voidage, voidage after minimum fluidization and the terminal velocity. The plot of the velocity and the height of the bed of aluminum oxide nanoparticle from a linearized Richardson and Zaki equation (Figure 1) shows a y-intercept representing the terminal velocity of 0.192 m/s, and an initial voidage was calculated from the plot to be 0.513.

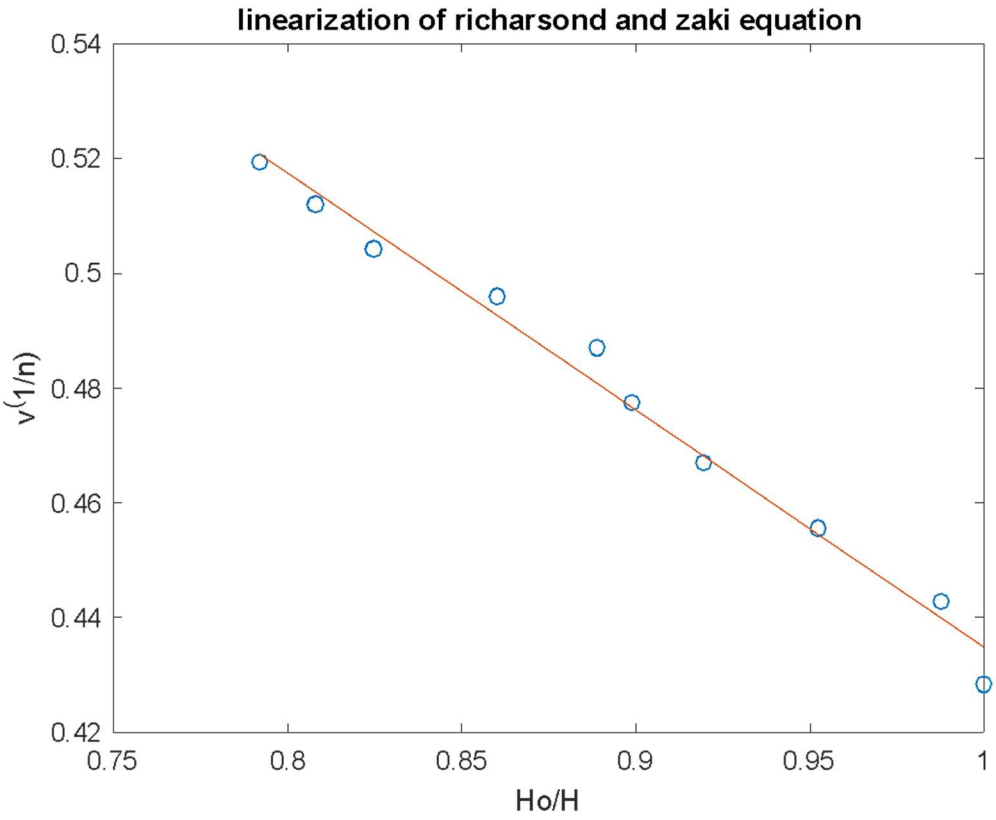

Figure 1: A linearized Richardson and Zaki equation from the acoustic sound fluidized bed of aluminum oxide nanoparticle with a y-intercept as the terminal velocity and the slope as the initial voidage at an index of 5

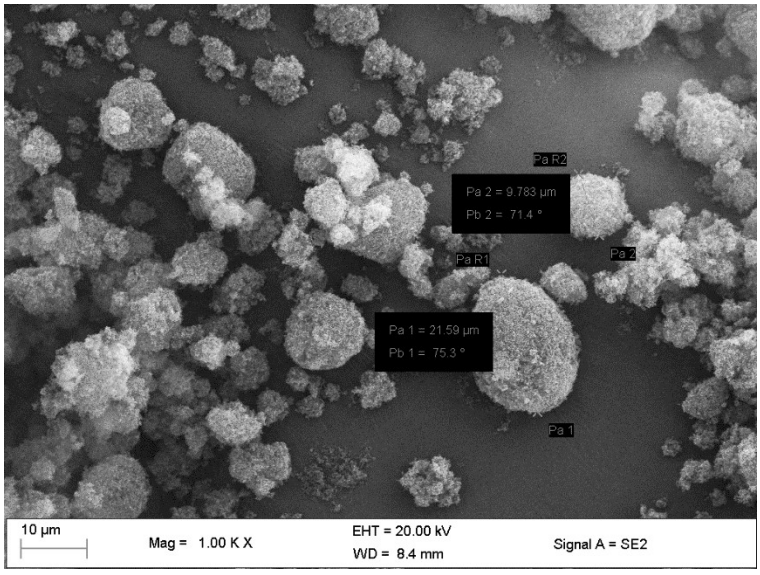

Figure 2: The SEM image of agglomerate formed during acoustic sound fluidization of aluminum oxide nanoparticles, picture taken at Microscopy and Microanalysis Unit at University of KwaZulu-Natal-Westville campus

4.2 Vibro-fluidization of aluminum oxides nanoparticles

The vibration from the two motors mounted on a vibrating plate where a fluidized bed was positioned, the applied vibrations were at a frequency of 2 and 4 Hz. The fluidized bed was simulated with vibration before the fluidizing medium was allowed to pass in the line. The expansion of the bed of nanoparticles was initiated by the flowing of the air. After the second run, the nanoparticles were forming agglomerate and fluidizing at the same time. It was observed that the expansion of the bed was so height and the behaviour of the aluminum oxide under vibro-fluidization demonstrated an agglomerate particulate fluidization. The increase of the pressure on the bed while the vibro-fluidization was occurring was recorded and a pressure profile was produced. Due to the primary size of the aluminum oxide nanoparticles, the complexity arises if the initial voidage could be determined using methodology performed in the conventional fluidization of samples collected in the main laboratory of the Discipline of Chemical Engineering. Because there was the formation of agglomerate during the vibro-fluidization of aluminum oxides nanoparticles and the loss dust of nanoparticles, it has necessitated the combination of the model voidage to the ratio of the initial height to the bed expansion with the mathematical representation of the superficial velocity for liquid fluidization.

4.2.1 Determination of the fluidization parameters

The initial voidage was calculated from a linearized Richardson and Zaki equation; the behavior of the aluminum oxide nanopowders under vibro-fluidization was of agglomerate particulates fluidization as its bed of nanoparticles expanded so higher at a frequency of 2Hz. In linearizing the Richardson and Zaki correlation, the graphical representation of the superficial velocity exponent to the fraction of the Richardson and Zaki index with the ratio of the initial height to the bed expansion produced a straight line where y-intercepted represented the terminal velocity and the initial voidage was calculated from the slop of the linearized graph.

The Richardson and Zaki index considered in the experiment was 5. From the slope of Figure 1, the initial voidage of aluminum oxide nanoparticles in a vibro-fluidized bed was calculated at a value of 0.5134. The superficial velocity was reaching 0.0105 m/s when the pressure on the bed of nanoparticles remained unchanged, it was observed that the pressure stayed unchanged when the pressure transducers recorded a pressure of value of 0.009 kPa. By using the minimum fluidization velocity, the bed expansion reached its minimum fluidization height when the bed of nanoparticles was at 11.7 cm. Graphically, the minimum fluidization voidage was interpreted by plotting the superficial velocity with the voidage as the bed expanded after minimum fluidization has reached. The minimum fluidization voidage was graphically read at a value of 0.56.

4.2.2 Determination of the size of agglomerates nanoparticles using scanning electron microscopy analysis (SEM)

The size of the agglomerate formed during the vibro-fluidization of aluminum oxide nanoparticles

was measured from the SEM analysis, during the analysis, the shape and structure of the agglomerates were visualized and measured (Figure 2). Noting that single nanoparticle created agglomerates which were able to break the complexity of the nanoparticle in fluidization. For common sense, the size of this agglomerate was important to study and investigate their size and structure as this allowed the fluidization of aluminum oxide nanoparticles to occur. The maximum and minimum size of agglomerate of aluminum oxide nanoparticles in vibro fluidization was found to be 25.57 µm and 11.39 µm respectively.

5 CONCLUSIONS

The fluidization enhanced my mechanical vibration and acoustic sound of 13 nm aluminum oxide nanoparticles demonstrated different behavior. The acoustic sound fluidization of 13 nm aluminum oxide with a frequency of 100 Hz in a 0.12 m of diameter was observed and the pressure profile on the bed of 13 nm aluminum oxide nanoparticles was obtained in 10 cm of a bed of nanoparticles. It was observed the formation of agglomerate during the acoustic sound of these nanoparticles distributed within the bed of an acoustic sound fluidized bed. In the vibro- fluidized bed, the 13 nm aluminum oxide demonstrated a lower minimum fluidization velocity measured during the experiment, and different vibration frequencies were applied to the vibro-fluidised bed of 13 nm of aluminum oxide; 2 Hz and 4 Hz. It was observed the bed of nanoparticle expanded much when 2 Hz was applied on the vibro-fluidised bed then 4 Hz and the minimum fluidization velocity at 4 Hz was found much lower compared to the minimum fluidization velocity at a lower frequency, thus the vibration influenced the fluidization behavior of 13 nm aluminum oxide nanoparticles.

REFERENCES

Ali, S. S., Al-Ghurabi, E. H., Ibrahim, A. A. & Asif, M. 2018. Effect of adding Geldart group A particles on the collapse of fluidized bed of hydrophilic nanoparticles. *Powder Technology,* 330**,** 50-57.

Arno, M. C., Inam, M., Weems, A. C., Li, Z., Binch, A. L., Platt, C. I., Richardson, S. M., Hoyland, J. A., Dove, A. P. & O'reilly, R. K. 2020. Exploiting the role of nanoparticle shape in enhancing hydrogel adhesive and mechanical properties. *Nature communications,* 11**,** 1-9.

Batista, C. A. S., Larson, R. G. & Kotov, N. A. 2015. Nonadditivity of nanoparticle interactions. *Science,* 350.

Blott, S. J. & Pye, K. 2006. Particle size distribution analysis of sand-sized particles by laser diffraction: an experimental investigation of instrument sensitivity and the effects of particle shape. *Sedimentology,* 53**,** 671-685.

Carrillo, J.-M. Y., Raphael, E. & Dobrynin, A. V. 2010. Adhesion of nanoparticles. *Langmuir,* 26**,** 12973-12979.

Dos Santos, A. P. & Levin, Y. 2019. Like-Charge Attraction between Metal Nanoparticles in a 1: 1 Electrolyte Solution. *Physical review letters,* 122**,** 248005.

Fabre, A., Salameh, S., Kreutzer, M. T. & Van Ommen, J. R. 2017. Modeling the size distribution in a fluidized bed of nanopowder. *Powder technology,* 312**,** 347-353.

Geldart, D. 1973. Types of gas fluidization. *Powder technology,* 7**,** 285-292.

Geldart, D. 1986. Gas fluidization technology.

Geldart, D. 2004. Expansion of gas fluidized beds. *Industrial & engineering chemistry research,* 43**,** 5802-5809.

Guo, D., Xie, G. & Luo, J. 2013. Mechanical properties of nanoparticles: basics and applications. *Journal of physics D: applied physics,* 47**,** 013001.

Hoo, C. M., Starostin, N., West, P. & Mecartney, M. L. 2008. A comparison of atomic force microscopy (AFM) and dynamic light scattering (DLS) methods to characterize nanoparticle size distributions. *Journal of Nanoparticle Research,* 10**,** 89-96.

Hotze, E. M., Phenrat, T. & Lowry, G. V. 2010. Nanoparticle aggregation: challenges to understanding transport and reactivity in the environment. *Journal of environmental quality,* 39**,** 1909-1924.

Kagan, C. R., Fernandez, L. E., Gogotsi, Y., Hammond, P. T., Hersam, M. C., Nel, A. E., Penner, R. M., Willson, C. G. & Weiss, P. S. 2016. Nano day: celebrating the next decade of nanoscience and nanotechnology. ACS Publications.

Khlebtsov, B. & Khlebtsov, N. 2011. On the measurement of gold nanoparticle sizes by the dynamic light scattering method. *Colloid Journal,* 73**,** 118-127.

Konert, M. & Vandenberghe, J. 1997. Comparison of laser grain size analysis with pipette and sieve analysis: a solution for the underestimation of the clay fraction. *Sedimentology,* 44**,** 523-535.

Li, J., Kong, J., He, S., Zhu, Q. & Li, H. 2018. Self-agglomeration mechanism of iron nanoparticles in a fluidized bed. *Chemical Engineering Science,* 177**,** 455-463.

López-López, M. T., Zubarev, A. Y. & Bossis, G. 2010. Repulsive force between two attractive dipoles, mediated by nanoparticles inside a ferrofluid. *Soft Matter,* 6**,** 4346-4349.

Matsuda, S., Hatano, H., Lin, H. & Tsutsumi, A. Fluidization Characteristics of Nanoparticles. Asian Pacific Confederation of Chemical Engineering congress program and abstracts Asian Pacific Confederation of Chemical Engineers congress program and abstracts, 2004. The Society of Chemical Engineers, Japan, 41-41.

Min, Y., Akbulut, M., Kristiansen, K., Golan, Y. & Israelachvili, J. 2010. The role of interparticle and external forces in nanoparticle assembly. *Nanoscience And Technology: A collection of reviews from Nature journals***,** 38-49.

Mishra, S., Keswani, C., Abhilash, P., Fraceto, L. F. & Singh, H. B. 2017. Integrated approach of agri-nanotechnology: challenges and future trends. *frontiers in Plant Science,* 8**,** 471.

Molteni, G., Bianchi, C. L., Marinoni, G., Santo, N. & Ponti, A. 2006. Cu/Cu-oxide nanoparticles as catalyst in the “click” azide–alkyne cycloaddition. *New Journal of Chemistry,* 30**,** 1137-1139.

Morooka, S., Kusakabe, K., Kobata, A. & Kato, Y. 1988. Fluidization state of ultrafine powders. *Journal of Chemical Engineering of Japan,* 21**,** 41-46.

Raganati, F., Chirone, R. & Ammendola, P. 2018. Gas–solid fluidization of cohesive powders. *Chemical Engineering Research and Design,* 133**,** 347-387.

Rizvi, S. A. & Saleh, A. M. 2018. Applications of nanoparticle systems in drug delivery technology. *Saudi pharmaceutical journal,* 26**,** 64-70.

Siegrist, M. 2010. Predicting the future: Review of public perception studies of nanotechnology. *Human and Ecological Risk Assessment,* 16**,** 837-846.

Sun, W. 2014. Interaction forces between a spherical nanoparticle and a flat surface. *Physical Chemistry Chemical Physics,* 16**,** 5846-5854.

Tamadondar, M. R., Zarghami, R., Boutou, K., Tahmasebpoor, M. & Mostoufi, N. 2016. Size of nanoparticle agglomerates in fluidization. *The Canadian Journal of Chemical Engineering,* 94**,** 476-484.

Taubner, H., Roth, B. & Tippkötter, R. 2009. Determination of soil texture: Comparison of the sedimentation method and the laser-diffraction analysis. *Journal of Plant Nutrition and Soil Science,* 172**,** 161-171.

Tohver, V., Chan, A., Sakurada, O. & Lewis, J. A. 2001. Nanoparticle engineering of complex fluid behavior. *Langmuir,* 17**,** 8414-8421.

Valverde, J. M. & Castellanos, A. 2006. Fluidization of nanoparticles: A modified Richardson-Zaki law. *AIChE journal,* 52**,** 838-842.

Wang, X. S., Rahman, F. & Rhodes, M. J. 2007. Nanoparticle fluidization and Geldart's classification. *Chemical Engineering Science,* 62**,** 3455-3461.

Zhu, C., Yu, Q., Dave, R. N. & Pfeffer, R. 2005. Gas fluidization characteristics of nanoparticle agglomerates. *AIChE Journal,* 51**,** 426-439.

Evaluation of two different reactor configurations for the simultaneous remediation AMD and pretreatment of lignocellulosic biomass

N.W. Burman[1,2*], K.G. Harding[1], C.S. Sheridan[3] and U. Kappelmeyer[4]

[1] School of Chemical and Metallurgical Engineering, University of the Witwatersrand, Johannesburg

[2] WEC Projects, Johannesburg

[3] School of Geography, Archaeology and Environmental Studies, University of the Witwatersrand, Johannesburg

[4] Department of Environmental Biotechnology Helmholtz Centre for Environmental research, Leipzig

*Corresponding author: nwburman@gmail.com

ABSTRACT

A process to simultaneously remediate acid main drainage (AMD) and pre-treat lignocellulosic biomass was investigated. In this lignocellulosic biomass is contacted with AMD, breaking down the carbohydrates in the biomass into sugars which can be utilized as a carbon source by sulfate-reducing bacteria (SRB) to perform dissimilatory sulfate reduction (DSR), which remediates the AMD. The breakdown in carbohydrates pretreats the biomass making it more susceptible to further enzymatic hydrolysis to produce glucose that can be fermented to produce bioethanol or other biochemicals. Two different reactor configurations have been experimentally evaluated: A, biomass first undergoes pretreatment at high temperature (90°C), producing a COD rich stream that is cooled and undergoes DSR in a separate reactor; B. biomass is pretreated and DSR occurs in the same reactor at ambient temperatures (30°C). The performance of these two reactor configurations was evaluated both in terms of the rate of sulfate reduction and the amount of glucose that was released after enzymatic hydrolysis. The amount of glucose released from enzymatic hydrolysis was found to be 22.0 g/L for A. and 26.1 g/L for B. The rate of sulfate reduction was found to be 0.019 g/L/day for A. and 0.073 g/L/day for B. This suggests that B. is better suited, although a further evaluation of operating and capital cost of both should be performed to determine which is more economically feasible.

Keywords: acid mine drainage (AMD); sulfate-reducing bacteria (SRB)

1 INTRODUCTION

The burning of fossil fuels has led to increasing atmospheric and oceanic temperatures, and the associated climate crisis (IPCC, 2014a). To overcome this, renewable alternatives to fossil fuel that are more environmentally sustainable need to be developed (IPCC, 2014b). Once sustainable alternative to petrol is the use of bioethanol produced from lignocellulosic biomass. Sources of lignocellulosic biomass include agriculture residue (corn stover, sugarcane bagasse) forestry waste (sawdust, wood chips), and energy crops (switchgrass, miscanthus, other long-stemmed grasses). In the production of lignocellulosic bioethanol, enzymatic hydrolysis of the cellulose present in the biomass is performed to

release glucose which can be fermented to produce bioethanol (Mosier *et al.*, 2005). Unfortunately, the presence of the ligno-hemicellulosic matrix surrounding the cellulose fibrils prevents cellulase enzymes from accessing the cellulose. To overcome this biomass first needs to be pre-treated, to break apart the lignocellulosic matrix before it can undergo efficient enzymatic hydrolysis. Although various pretreatments (chemical, physical, physico-chemical, and biological) have been found to be effective, the additional cost of pretreatment adds additional processing costs, making the process less economically feasible.

Biological pre-treatment, in which the ligno-hemicellulosic matrix is broken down by various enzymes secreted by micro-organisms, has been found to be more environmentally sustainable, the other forms of pretreatment due to the lower operating temperatures and chemical input (Sun and Cheng, 2002). Although various micro-organisms with hydrolytic activity have been identified, the slow rates of reactions require long residence times (Azman *et al.*, 2015). To overcome this there has recently been investigation into the combined chemical-biological pretreatment in which both chemicals and micro-organisms are used for the pretreatment of biomass (Sindhu, Binod and Pandey, 2016). Recently there has been investigation into the pretreatment of lignocellulosic biomass using the acidity present in acid mine drainage AMD (Magowo, Rumbold and Sheridan, 2015; Burman *et al.*, 2017; Burman, Harding, *et al.*, 2018; Burman, Sheridan, *et al.*, 2018; Burman, Harding and Sheridan, 2019; Greenway, 2019; Burman, Sheridan and Harding, 2020).

Acid mine drainage is highly acidic water (pH 2 – 4) with high concentrations of sulfate (<12 g/L) and metals (<5 g/L), that is formed through a series of geochemical reactions when sulfate-rich minerals are exposed to oxygen and water, often as a result of mining activity (both pit and shaft mining). This has a negative environmental effect when it enters natural water systems (Simate and Ndlovu, 2014) Widespread generation of AMD in both the Witwatersrand gold mining area and the Mpumalanga coalfields has caused environmental damage necessitating the need for remediation of water before it enters natural water systems. Current remediation consists of chemical neutralization which results in the precipitation of metals. Although effective, this is expensive and produces large volumes of toxic sludge. As the generation of AMD is ongoing, there is a need for more environmentally and economically sustainable remediation technologies.

Dissimilatory sulfate reduction (DSR) catalyzed by sulfate remediating bacteria (SRB) has been found to be effective at reducing the sulfate concentration and increasing the pH which results in the precipitation of metals (Sánchez-Andrea *et al.*, 2014). Various studies have demonstrated that lignocellulosic biomass can be used as a carbon source for sulfate-reducing bacteria (Magowo, Rumbold and Sheridan, 2015; Ramla and Sheridan, 2015). Although SRB may not utilize the lignocellulose directly as a substrate, a community of bacteria breaks down the lignocellulose, similar

to anaerobic digestion, into a product that can be utilized by the SRB for DSR. Studies found that various feedstocks including wood chips and sawdust (Chang, Shin and Kim, 2000; Neculita, Zagury and Bussière, 2008; Lefticariu *et al.*, 2015), rice husk (Chockalingam and Subramanian, 2006), grass cuttings (Greben *et al.*, 2009; Lefticariu *et al.*, 2015), sugarcane bagasse (Magowo, Rumbold and Sheridan, 2015), and indigenous South African grasses could be used to reduce the sulfate concentration and also increase the pH of AMD, in passive bioreactors (Magowo, Rumbold and Sheridan, 2015; Ramla and Sheridan, 2015).

Magowo et al (2015) also demonstrated that biomass that was used from the remediation of AMD in the presence of SRB, underwent pre-treatment in this process and hence produced a higher concentration and yield of glucose during enzymatic hydrolysis. This pre-treatment was attributed to the hydrolysis of the lignocellulosic matrix, catalyzed by the acidity present in the AMD. The effect of biological pre-treatment catalyzed by hydrolytic micro-organisms present was not considered.

The rate of sulfate reduction by SRB in AMD has been found to vary between 0.03 – 29 g/L/day. This large variance is thought to be due to variation in pH, substrate, reactor design, and source of inoculum (Sánchez-Andrea, Triana and Sanz, 2012). The large variation in rates of reaction reported in literature suggests that it is necessary to determine the rate of reaction for the specific conditions at which the system would operate.

Although previous studies by Ramla and Sheridan (2015) and Magowo et al (2015) demonstrated the suitability of remediating AMD using indigenous south African grass as a substrate, the rate of sulfate removal was not presented. In this study, the simultaneous pretreatment of long-stemmed South African Grass (using a combination of AMD and SRB) and remediation of AMD (using SRB) will be investigated. The rate of sulfate reduction and the quantity of glucose produced after enzymatic hydrolysis of pretreated by mass for two different reactor configurations will be compared.

2 EXPERIMENTAL PROCEDURE

Two different reactor configurations have been identified as feasible. In the separate pretreatment and AMD remediation reactor (SRP), biomass first undergoes pretreatment in AMD at high temperatures (90°C), to produce a high COD solution that will undergo remediation through DSR in a separate reactor at mesophilic temperatures (30°C). Pretreated biomass will undergo enzymatic hydrolysis in a separate reactor to produce fermentable sugars (Figure 1.A). In the combined remediation and pretreatment reactor configuration (CRP), biomass pretreatment and remediation of AMD through DSR occur in the same reactor at mesophilic temperatures (30°C). This is followed by the enzymatic hydrolysis of pretreated biomass in a separate reactor to produce fermentable sugars (Figure 1.B).

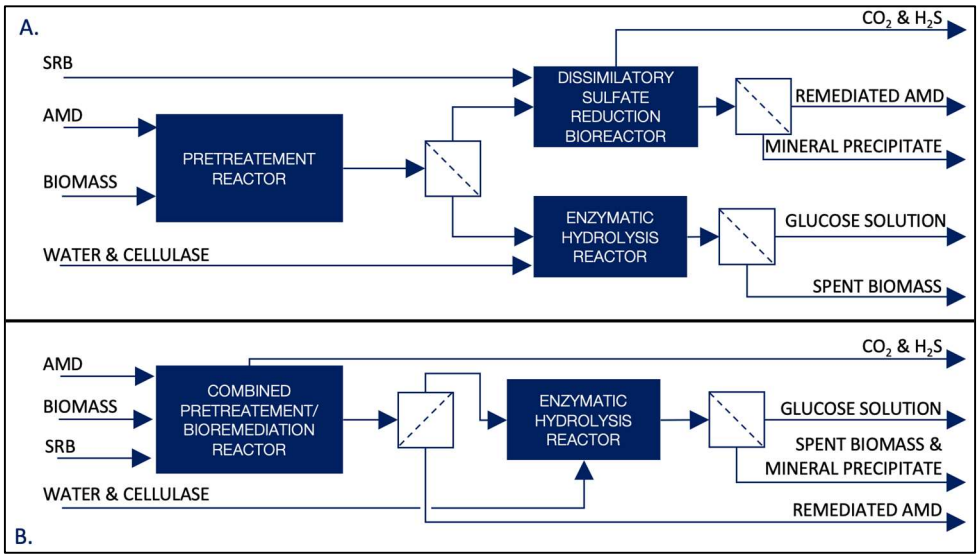

Figure 1: Different reactor configurations investigate. A. Separate remediation and pretreatment reactor configuration (SRP) B Combined remediation and pretreatment reactor configuration (CRP).

Different experimental setups were used to mimic the different reactor configurations as described below. As the experimental procedure used for the enzymatic hydrolysis was the same for both experiments this was only described once.

2.1 Materials

AMD was sourced from a coal mine in the eMalahleni district in South Africa. pH was determined using the Ohaus ST2100-F benchtop pH meter. Sulfate concentration was determined using a Merck Sulfate Test Kit #114548. Dissolved metal concentrations were determined by ICP-OES by UIS Analytical Services (www.uis-as.co.za) using method UIS-AC-T007.

An indigenous South African grass classified as *Eragrostis curvula* (Weeping Lovegrass or Oulandsgrass) was sourced from an agricultural supplier in Gauteng Province, South Africa. The structural composition of this grass was determined using the National Renewable Energy Laboratory (NREL) method (Sluiter et al., 2008b). This method first determines the extractives through soxhlet extraction then determines the monosaccharide composition by hydrolyzing the grass using a two-stage concentrated/dilute sulfuric acid, and then analyzing the hydrolysate for monosaccharides by high-performance liquid chromatography (HPLC). The only deviation from this method was the use of a single-stage soxhlet extraction using acetone as opposed to a two-stage ethanol/water extraction. The structural composition is presented in the results.

Celluclast 1.5 L cellulase enzyme (Novozyme), with an activity of 80 FPU/mL, was used for enzymatic hydrolysis at a dosage of 16.5 FPU/g substrate. This was mixed with 0.05 M sodium citrate buffer (pH 4.8).

2.2 Combined AMD remediation and pretreatment reactor configuration

Forty grams of *Eragrostis curvula* biomass were pretreated with 200 mL of AMD, bacterial community isolated from horse manure or a combination thereof in 250 mL Schott bottles. Pretreatment was carried out at 30°C and 130 RPM, for various times (5, 10, 15, 20, 25, and 32 days) after which the biomass was heated up to 95 °C for 2 hours to sterilize it before being washed, filtered and dried. The liquid filtrate was analyzed for the sulfate concentration. Liquid samples were taken at 0, 24, and 48 hours and analyzed for reducing sugar concentration. Pretreated biomass then underwent enzymatic hydrolysis.

2.3 Separate AMD remediation and pretreatment reactor configuration

Four hundred grams of biomass was pretreated with AMD in 2 L Schott bottles for 3 days at 90°C, to produce a COD rich AMD solution. Liquid samples were taken during pretreatment and evaluated for COD. After pretreatment biomass was separated from the COD rich solution, washed and dried before undergoing enzymatic hydrolysis. The COD rich AMD solution was used to determine the rate of sulfate reduction. The rate of sulfate reduction was determined by adding 200 mL of the COD rich AMD solution to 250 mL culture bottles that were inoculated with SRB. Culture bottles were incubated at 30°C and 130 RPM. Three different sources of SRB were evaluated, two were sampled from different locations on a coal mine in the Mpumalanga coalfields in South Africa (SRB-A, SRB-B), and the third was a pure culture of *Desulfovibrio desulfricans* (SRB-P) obtained from the culture collection of the Helmholtz Center for Environmental Research, Leipzig, Germany. To evaluate if the high concentration of sulfate and metals present in the water was toxic to the SRB and inhibiting the rate of sulfate reduction three different concentrations of AMD were evaluated (100%, 33%, and 10%), by diluting the COD rich AMD solution with deionized water. Liquid samples were taken at various times (6, 10, 27, 35, 44, and 55 days) and analyzed for sulfate concentration.

2.4 Enzymatic hydrolysis of pretreated biomass

Pretreated biomass was loaded into 250 mL Erlenmeyer flasks with 200 mL of 0.05M sodium citrate buffer (pH 4.8) loaded with 16.66 FPU/g Cellucalst 1.5L cellulase enzyme (Novozyme). Flasks were incubated at 45°C C and 100 RPM for 48 hours. After 48hrs, liquid samples were taken for analysis of reducing sugars.

2.5 Analytical methods

Reducing sugar concentration was analyzed using the DNS method (NREL, 1996) sulfate concentration was analyzed using the Merk sulfate Cell Test #114548 (www.sigmaaldrich.com), with Merk Spectroquant® NOVA 60. COD was determined using the Hatch Lange LCW 514 Test kit and DR LANGE CADAS 100 spectrophotometer. pH was measured using the WTW 526 benchtop pH meter equipped with a WTW pH Electrode SenTix 41.

3 RESULTS AND DISCUSSION

3.1 Biomass composition

The composition of the biomass is presented in Table 1 along with the standard deviation (SD). Results from previous studies are also presented for weeping love grass (Torget et al., 1990); switchgrass (Lee et al., 2007); elephant grass (Menegol et al., 2014) and dwarf Napier grass (Wongwatanapaiboon et al., 2012). Switchgrass, dwarf Napier grass, and elephant grass were chosen for comparison as they are grasses that have been found suitable feedstocks for bioethanol production.

Table 3: Experimentally determined structural composition of Weeping Lovegrass, compared to results presented in literature for Weeping Lovegrass and Switchgrass.

	This study		(Torget *et al.*, 1990)	(Lee *et al.*, 2007)		(Menegol *et al.*, 2014)		(Wongwatanapaiboon *et al.*, 2012)	
Biomass Type	Weeping Lovegrass		Weeping Lovegrass	Switchgrass		Elephant Grass		Dwarf Napier[3]	
Structural Composition	Mean %	SD %	Mean %[1]	Mean %	SD %	Mean %	SD %	Mean %	SD %
Hemicellulose	20.6	3.0	21.9%	28.5	3.5	20.51	0.023	34.19	1.24
Cellulose	35.3	3.0	36.7%	37.3	4.4	37.95	1.06	35.64	0.21
Acid Soluble Lignin	2.46	0.15	21.8%[2]	3.5	0.3	1.12	0.02	3.66	0.20
Acid Insoluble Lignin	26.1	5.19		16.2	0.5	19.65	0.78		
Ash	3.08	0.34	5.6%	5.9	1.0	8.53	0.23	0.13	0.12
Extractives	2.33	0.99	6.3%	3.1	0.7	8.84	0.83		
Other								26.38	1.38

[1]The standard deviation was not reported by this study.
[2]The lignin was not reported as acid-soluble and acid-insoluble lignin just as Klason lignin which was taken to be the total lignin content.
[3]The acid-insoluble lignin and extractives were not reported in this study, however, an "other" category was reported

As can be seen in Table 1, the composition of weeping love grass determined in this study is similar to that reported by Torget et al. (1990). The cellulose content was found to be similar for all different grasses presented (35.3–38.0%). The comparable cellulose content of weeping lovegrass to other grass species indicates that it would be a suitable feedstock for the production of bioethanol from the C6 sugar platform. There was, however, significant variation in the hemicellulose content in the grasses presented. The hemicellulose content was much higher in switchgrass (28.5%) and dwarf Napier grass (34.2%) than in weeping love grass (20.6–21.9%) and elephant grass (20.5%). The comparatively low hemicellulose content of weeping love grass indicates it would not be a good feedstock for the production of bioethanol through co-fermentation of both C5 and C6 sugars.

3.2 AMD composition

The AMD was found to be highly acidic (pH 2.4) with a high concentration of sulfate (12.5 g/L). There was also a high concentration of dissolved iron (4.29g/L) and low concentrations of dissolved magnesium (0.474 g/L) and aluminum (0.396 g/L). There were trace concentrations (< 0.1 g/L) of various other metal such as manganese, silicon, sodium, and zinc. Trace concentrations of other elements were found, however, elements with a concentration of < 10 mg/L were not listed.

The quality of the AMD used in this investigation was relatively strong, with previous studies reporting AMD pH of 2–3, and sulfate concentrations of 3,5 g/L (McCarthy, 2011). The low pH of AMD should enable effective pre-treatment of biomass.

3.3 Rate of sulfate reduction

The sulfate concentration over time is presented in Figure 2 for combined AMD remediation and biomass pretreatment, and in Figure 3 for separate AMD remediation and biomass pretreatment.

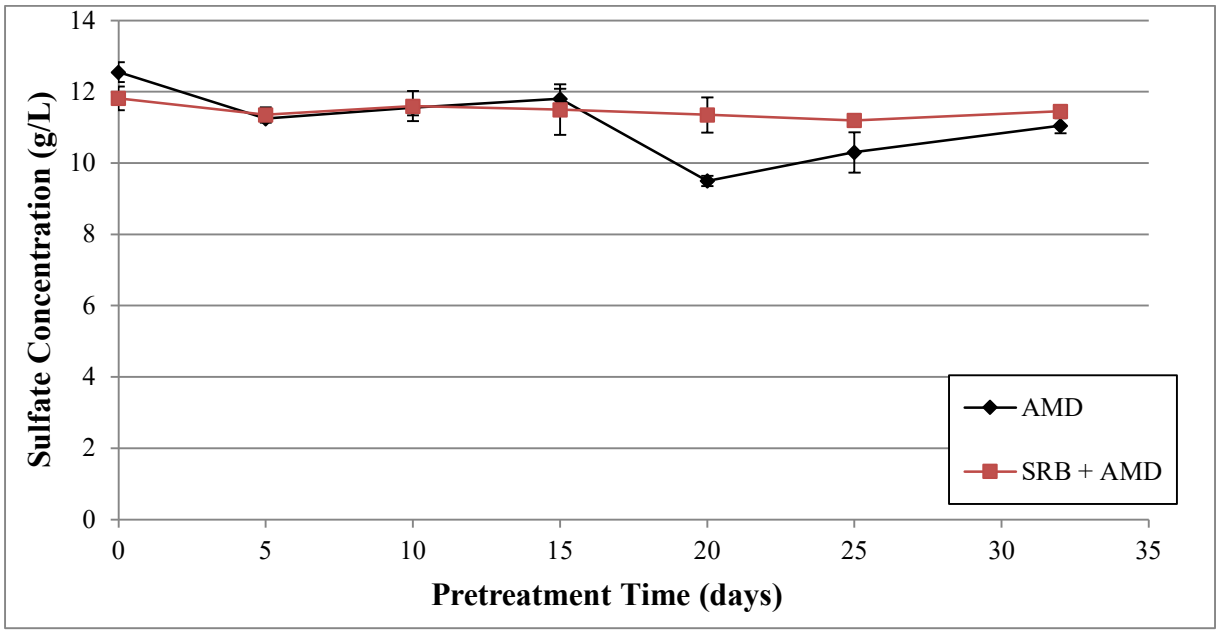

Figure 2: Sulfate concentration vs time in combined AMD remediation and biomass pretreatment at 30°C.

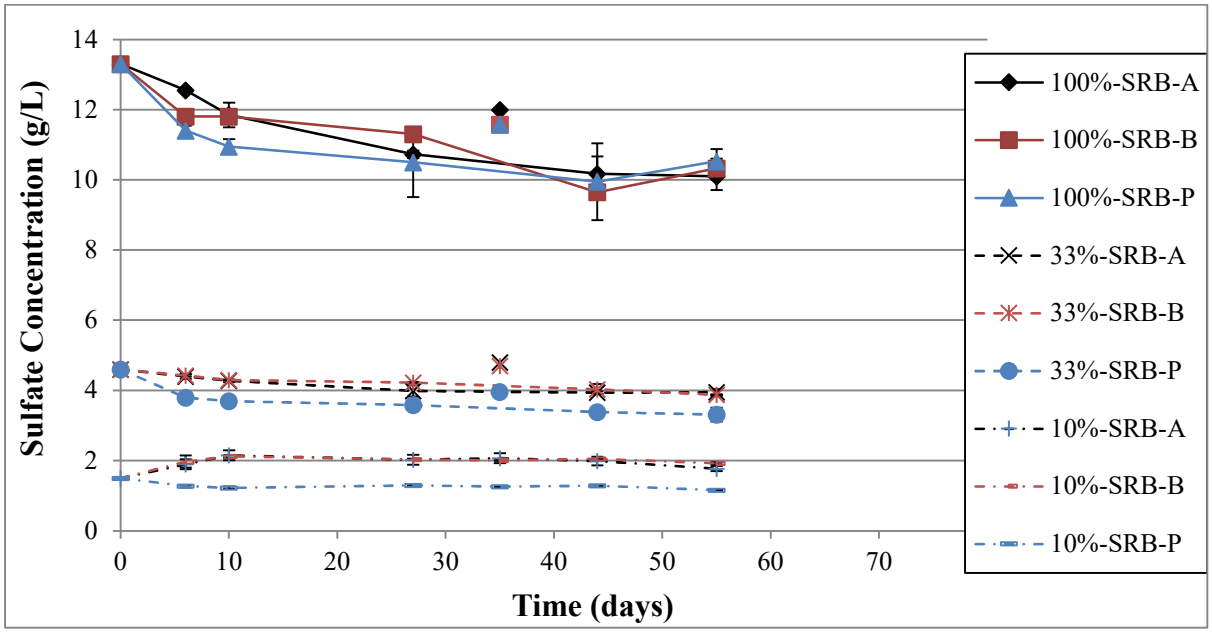

Figure 3: Sulfate concentration vs time in separate AMD remediation and biomass pretreatment at 30°C, at different AMD concentrations and using different sources of SRB. A & B are communities of SRB

As can be seen in Figure 2 the sulfate concentration did not significantly decrease with increased pretreatment time in CRP. The sulfate concentration of liquid from biomass pretreated with both SRB and AMD decreased from 12g/L to 11.5g/L after 32 days of pretreatment. The sulfate concentration of biomass pretreated with AMD alone decreased from 12.5 g/L to 11.4 g/L after 32 days of pretreatment

The rate of sulfate reduction was determined through fitting linear trend lines in Microsoft® Excel to the data of the concentration of sulfate over time. The rate of sulfate reduction in CRP was found to be 0.019 g/L/day.

As can be seen in Figure 3 for undiluted AMD the sulfate concentration decreased from 13.3 g/L to 10.5 g/L, 10.3 g/L and 10.1 g/L for SRB-A, SRB-B and SRB-P respectively. For 33% AMD the sulfate concentration decreased from 4.6 to 3.9 g/L, 3.9 g/L, 3.3 g/L for SRB-A, SRB-B and SRB-P respectively. For 10% AMD the sulfate decreased from 1.5 to 1.2 g/L for SRB-P. For SRB-A and SRB-B the sulfate initially increased to 2.1 due to a high concentration of sulfate in the inoculum and then decrease to 1.8 g/L and 1.9 g/L respectively. At day 35 the concentration of sulfate was found to increase slightly for all sources of SRB at 100% and 33% AMD concentrations. samples were thus assumed to be outliers, caused by experimental error.

The rate of sulfate reduction was determined through fitting linear trend lines in Microsoft® Excel to the data of the concentration of sulfate over time, excluding outliers. For 10% AMD dilution he rate of sulfate reduction was determined only after the maximum concentration was reached.

A summary of the rate of sulfate reductions determined in SRP is presented in Table 2.

Table 2: Rate of sulfate reduction determined in separate AMD remediation and biomass pretreatment

	Rate of sulfate reduction (g/L/day)		
Source of SRB	100% AMD	33.33% AMD	10% AMD
SRB-A	0.069	0.015	0.073
SRB-B	0.069	0.014	0.0037
SRB-P	0.071	0.028	0.0031

As can be seen in Table 2 the rate of sulfate reduction was fastest for 100% AMD, and this was faster than the rate of sulfate reduction in CRP (0.019 g/L/day). The different sources of SRB did not produce significantly different rate of reaction. Although the rate of sulfate reduction was faster in SRP than in CRP the rate of reduction is still very slow. The rate of sulfate reduction would need to increase significantly before this process could be economically feasible.

3.4 Enzymatic hydrolysis of pretreated biomass

The concentration of reducing sugar released after enzymatic hydrolysis of pretreated biomass vs pretreatment time is presented in Figure 4. As can be seen in Figure 4, in SRP, pretreatment with SRB was found to be the most effective form of pretreatment producing a reducing sugar concentration of +-22.5g/L after 5 days of pretreatment. The reducing sugar concentration did not increase with increasing pretreatment time. The concentration of reducing sugar produced from biomass pretreated with AMD increased slightly with increased pretreatment time. The concentration of reducing sugars produced from enzymatic hydrolysis of biomass pretreated with the combination of AMD and SRB was found to decrease with pretreatment times up to 15 days (10.0 g/L) after which it increased with increasing time to a maximum of 22.5 g/L reducing sugar after 32 days of pretreatment. Pretreatment of biomass with the combination of AMD and SRB was less effective than pretreatment with AMD or SRB individually up to 15 days of pretreatment. For longer pretreatment time (20-32 days) pretreatment with AMD and SRB was more effective than pretreatment with AMD alone, however slightly less effective than pretreatment with SRB alone. The initial decrease in the concentration of reducing sugars produced from biomass pretreated with AMD and SRB is not understood, and further experimental work would need to be conducted to determine the cause of this. At pretreatment times >15 days the concentration of reducing sugars produced from biomass pretreated with a combination of AMD and SRB increases rapidly until the end of the experiment (32 days). This suggests that the concentration of reducing sugars from biomass pretreated with a combination of SRB and AMD may be greater than that produced from biomass pretreated with SRB alone, at pretreatment times longer than 32 days. This would need to be verified experimentally. In separate AMD remediation and biomass pretreatment, enzymatic hydrolysis of pretreated biomass was found to produce a glucose concentration of 26.1 g/L.

This is higher than the glucose concentration achieved in SRP, indicating that SRP is better suited than CRP in terms of biomass pretreatment.

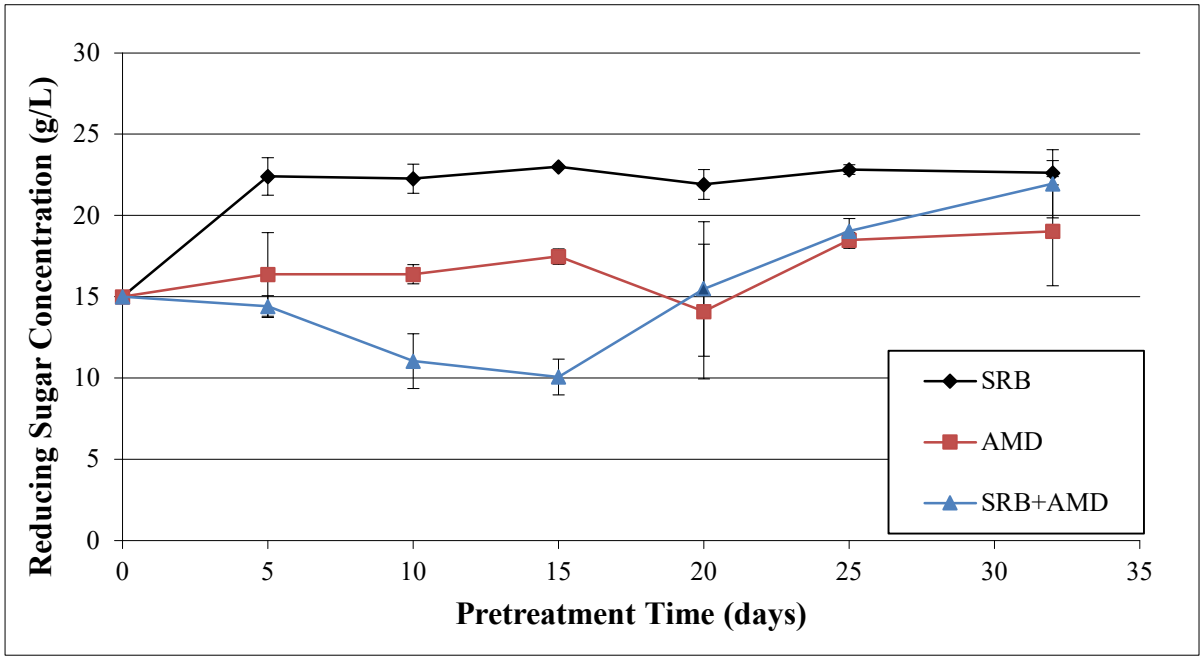

Figure 4: Reducing sugar concentration vs time after enzymatic hydrolysis of biomass pretreated with SRB, AMD, or SRB and AMD in combined AMD remediation and biomass pretreatment.

4 CONCLUSIONS

The rate of sulfate reduction was found to be higher in SRP (max 0.073 g/L/day) than in CRP 0.019 g/L/day). The concentration of glucose produced from biomass pretreated was found to be higher in SRP (26. g/L) than in CRP (max 22.0 g/L). SRP was thus found to better reactor configuration in terms of both the rate of sulfate reduction and final glucose concentration. Although SRP is better than CRP, in terms of both the rate of sulfa reduction and the final glucose concentration, the rate of sulfate was very low. For this process to be commercially viable the rate of sulfate reduction would need to increase substantially. It is recommended that further experimental work is conducted to optimize the rate of sulfate reduction, this should include investigating different sources of SRB, optimizing the reactor conditions (COD, ORP, temperature, mixing), and determining the toxicity of AMD to SRB.

REFERENCES

Azman, S. et al. (2015) 'Presence and role of anaerobic hydrolytic microbes in conversion of lignocellulosic biomass for biogas production', Critical Reviews in Environmental Science and Technology, 45(23), pp. 2523–2564. doi: 10.1080/10643389.2015.1053727.

Burman, N. W. et al. (2017) 'Flow Sheet and Sensitivity Analyses for the Bio-Remediation of Acid Mine Drainage Using Sulfate Reducing Bacteria and South African Grasses', in 2nd International Conference on Energy, Environment and Climate Change (ICEECC). Pointe Aux Piments, Mauritius.

Burman, N. W., Harding, K. G., et al. (2018) 'Evaluation of a combined lignocellulosic / waste water bio-refinery for the simultaneous production of valuable biochemical products and the

remediation of acid mine drainage', Biofuels, Bioproducts and Biorefining, 12(4), pp. 649–664. doi: 10.1002/bbb.1880.

Burman, N. W., Sheridan, C., et al. (2018) 'Modelling of low temperature dilute sulfuric acid pre-treatment of South African grass', Bioresource Technology Reports, 4, pp. 21–28. doi: 10.1016/j.biteb.2018.08.014.

Burman, N. W., Harding, K. G. and Sheridan, C. M. (2019) 'Lignocellulosic bioethanol production from grasses pre-treated with acid mine drainage: Modeling and comparison of SHF and SSF Author links open overlay panel', Bioresource Technology Reports, 7. doi: 10.1016/j.biteb.2019.100299.

Burman, N. W., Sheridan, C. M. and Harding, K. G. (2020) 'Feasibility assessment of the production of bioethanol from lignocellulosic biomass pretreated with acid mine drainage (AMD)', Renewable Energy. Elsevier Ltd, 157, pp. 1148–1155. doi: 10.1016/j.renene.2020.05.086.

Chang, I. S., Shin, P. K. and Kim, B. H. (2000) 'Biological treatment of acid mine drainage under sulphate-reducing conditions with solid waste materials as substrate', Water Research, 34(4), pp. 1269–1277. doi: 10.1016/s0043-1354(99)00268-7.

Chockalingam, E. and Subramanian, S. (2006) 'Studies on removal of metal ions and sulphate reduction using rice husk and Desulfotomaculum nigrificans with reference to remediation of acid mine drainage', Chemosphere, 62(5), pp. 699–708. doi: 10.1016/j.chemosphere.2005.05.013.

Greben, H. A. et al. (2009) 'Bioremediation of sulphate rich mine effluents using grass cuttings and rumen fluid microorganisms', Journal of Geochemical Exploration, 100(2–3), pp. 163–168. doi: 10.1016/j.gexplo.2008.01.004.

Greenway, N. (2019) The Bioremediation of Acid Mine Drainage Utilising Indigenous South African Grass as the Organic Carbon Source for Dissimilatory Sulfate Reduction. University of the Witwatersrand, Johannesburg.

IPCC (2014a) 'Climate Change 2014: Contribution of Working Groups I, II and III to the Fifth Assessment Report of the Intergovernmental Panel on Climate Change', in Core Writing Team, Pachauri, R. K., and Meyer, L. A. (eds). Geneva, Switzerland: IPCC, p. 151.

IPCC (2014b) 'Climate Change 2014: Mitigation of Climate Change. Contribution of Working Group III to the Fifth Assessment Report of the Intergovernmental Panel on Climate Change', in Eickemeier, P. et al. (eds). Cambridge, United Kingdom and New York, NY, USA: Cambridge University Press.

Lee, D. et al. (2007) Composition of Herbaceous Biomass Feedstocks. Brookings, SD. Available at: http://agbiopubs.sdstate.edu/articles/SGINC1-07.pdf.

Lefticariu, L. et al. (2015) 'Sulfate reducing bioreactor dependence on organic substrates for

remediation of coal-generated acid mine drainage: Field experiments', Applied Geochemistry. Elsevier Ltd, 63, pp. 70–82. doi: 10.1016/j.apgeochem.2015.08.002.

Magowo, E., Rumbold, K. and Sheridan, C. (2015) 'The Utilization of Cellulosic Biomass in treating AMD and the Subsequent Generation of Fermentable Sugars', in 10th International Conference on Acid Rock Drainage and IMWA Anual Conference, pp. 1–12.

Menegol, D. et al. (2014) 'Increased release of fermentable sugars from elephant grass by enzymatic hydrolysis in the presence of surfactants', Energy Conversion and Management. Elsevier Ltd, 88, pp. 1252–1256. doi: 10.1016/j.enconman.2014.02.071.

Mosier, N. et al. (2005) 'Features of promising technologies for pretreatment of lignocellulosic biomass', Bioresource Technology, 96(6), pp. 673–686. doi: 10.1016/j.biortech.2004.06.025.

Neculita, C. M., Zagury, G. J. and Bussière, B. (2008) 'Effectiveness of sulfate-reducing passive bioreactors for treating highly contaminated acid mine drainage: II. Metal removal mechanisms and potential mobility', Applied Geochemistry. Elsevier Ltd, 23(12), pp. 3545–3560. doi: 10.1016/j.apgeochem.2008.08.014.

NREL (1996) Measurement of Cellulase Activities Laboratory Analytical Procedure NREL/TP-510-42628, Laboratory Analytical Procedure.

Ramla, B. and Sheridan, C. (2015) 'The potential utilisation of indigenous South African grasses for acid mine drainage remediation', Water SA, 41(2), pp. 247–252. doi: 10.4314/wsa.v41i2.10.

Sánchez-Andrea, I. et al. (2014) 'Sulfate reduction at low pH to remediate acid mine drainage', Journal of Hazardous Materials. Elsevier B.V., 269(3), pp. 98–109. doi: 10.1016/j.jhazmat.2013.12.032.

Sánchez-Andrea, I., Triana, D. and Sanz, J. L. (2012) 'Bioremediation of acid mine drainage coupled with domestic wastewater treatment', Water Science and Technology, 66(11), pp. 2425–2431. doi: 10.2166/wst.2012.477.

Simate, G. S. and Ndlovu, S. (2014) 'Acid mine drainage: Challenges and opportunities', Journal of Environmental Chemical Engineering. Elsevier B.V., 2(3), pp. 1785–1803. doi: 10.1016/j.jece.2014.07.021.

Sindhu, R., Binod, P. and Pandey, A. (2016) 'Biological pretreatment of lignocellulosic biomass - An overview', Bioresource Technology. Elsevier Ltd, 199, pp. 76–82. doi: 10.1016/j.biortech.2015.08.030.

Sun, Y. and Cheng, J. (2002) 'Hydrolysis of lignocellulosic materials for ethanol production: A review', Bioresource Technology, 83(1), pp. 1–11. doi: 10.1016/S0960-8524(01)00212-7.

Torget, R. et al. (1990) 'Dilute Acid Pretreatment of Short Rotation Woody and Herbaceous Crops', Applied biochemistry and biotechnology, 24(25), pp. 115–126. doi: 10.1007/BF02920238.

Wongwatanapaiboon, J. et al. (2012) 'The Potential of Cellulosic Ethanol Production from Grasses in

Thailand', Journal of Biomedicine and Biotechnology. doi: 10.1155/2012/303748.

Seasonal characterisation of acid mine drainage in Mpumalanga coalfields region

J. Smith[1,2], C.M. Sheridan[2,3*], L.D. van Dyk[1,2] and K.G. Harding[1,2]

[1] School of Chemical Engineering, University of the Witwatersrand, Johannesburg, Private Bag 3, Wits, 2050, South Africa

[2] Centre in Water Research and Development, University of the Witwatersrand, Johannesburg, Private Bag 3, Wits, 2050, South Africa

[3] School of Geography, Archaeology and Environmental Studies, University of the Witwatersrand, Johannesburg, Private Bag 3, Wits, 2050, South Africa

*Corresponding author: Craig.Sheridan@wits.ac.za

ABSTRACT

In South Africa, sulfide is a large component of many of the natural ore bodies, in particular coal and gold ores. This results in large-scale problems such as acid mine drainage (AMD). AMD run-off or decant can corrode infrastructure and, if allowed to flow unchecked, will infiltrate ground and surface water bodies causing severe negative impacts on the surrounding environment. Sustainable, cost-effective treatment processes could mitigate such AMD problems. However, prior to designing treatment processes, the nature of the problem needs to be comprehensively quantified. In this study, the physical and chemical characteristics of AMD, emanating from two coal sites in Mpumalanga, are described and the ramifications of these properties, for the design of treatment processes, are discussed. The concentrations of total dissolved solids, total acidity, and dissolved iron varied by an order of magnitude between the sites. Reduced rainfall volumes were recorded during the winter months, and seasonal variability of AMD waters was shown in instances where reduced and increased concentrations coincided with increased and reduced rainfall volumes, respectively. Significant concentrations of aluminum, manganese and zinc could impact the effectiveness of active and passive treatment systems and should be considered in the design of a suitable treatment system.

Keywords: acid mine drainage (AMD), composition, correlation, regression

1 INTRODUCTION

Gold and coal mining activities in South Africa result in the formation of large quantities of acid mine drainage (AMD) (McCarthy, 2011). Given the immediacy of the decant issues, considerable attention has been given to AMD in the Western and Central Basins. A total of 126 coal mine operations have been identified in South Africa (DMR, 2017). Decant from coal mining sites in the Witbank–Middelburg area has historically flowed into the tributaries of the Olifants River causing significant increases in the salinity and sulfate levels of nearby dams, thus deleteriously affecting the quality of local water.

Mining operators are under a legal obligation to adhere to increasingly stringent environmental

compliance regulations, as stipulated in their water use licenses. Strictly regulated industrial water discharge limits imposed to prevent environmental damage, compounded with a growing demand for a limited water supply, necessitate consideration of treatment options to ensure sustained quality of receiving water bodies into the future and to facilitate the reuse of water. Development of sustainable, cost-effective AMD treatment processes would mitigate potential environmental damage that could result from decant of AMD water and facilitate the re-use of discharge water. The 2010 Inter-Ministerial Committee on AMD report recognized that ingress prevention and decant control would not limit the production of AMD and that treatment would still be required, and that the variability of water quality between the different basins would necessitate the use of different treatment technologies (Expert Team of the Inter-Ministerial Committee, 2010). Given the high density of coal fields in Mpumalanga, this research aims to facilitate the design of an appropriate treatment process for the AMD in this region. The aim of this work was to quantify seasonal physico-chemical parameters of AMD produced by a coal operation in Mpumalanga.

2 EXPERIMENTAL PROCEDURE

2.1 Sampling Procedure

Grab samples were taken from two AMD dams in the Mpumalanga coalfield region at monthly intervals during 2018 and in April 2019. Sample volumes of between 1 − 2.5 L were collected in glass or polypropylene containers. A 50 mL portion of filtered sample, and a 50 mL portion of unfiltered sample were preserved with acid to a pH of less than 2 using 1:1 ultrapure nitric acid, and the remaining sample was stored in a refrigerator at 4 °C. A total of 13 sampling events occurred for Site 1, while six took place for Site 2.

2.2 Analytical Methods

A range of physical and chemical parameters were analysed and the instrumentation and methodology used are as follows:

- pH: Ohause Starter 3100 combined pH and mV meter and a ST310 pH electrode.
- Redox Potential (Eh): Ohause Starter 3100 combined pH and mV meter and a STORP redox probe and a STREF 2 (saturated calomel) reference electrode. Eh values are reported relative to the standard hydrogen electrode (SHE) (Bednar et al., 2005).
- Electrical Conductivity (EC): Ohaus Starter 3100C conductivity meter and STCON3 electrode.
- Turbidity (NTU): HACH 2100N turbidimeter. Data are reported in Nephelometric Turbidity Units.
- Total dissolved solids (TDS): Gravimetric determination after filtration using a glass fibre (GF) filter, followed by drying of the filttrate to constant mass at 180 ºC (EPA Method 160.1).

- Total suspended solids (TSS): Gravimeteic determination after filteration through a GF filter and drying of the retained solids to constant mass at 103–105 ºC (EPA Method 160.2).
- Total acidity (TA): Potentiometric titration to pH 8.3 using 1.0 M NaOH.
- Major cations, sulfur and dissolved metals: Inductively coupled plasma–optical emission spectrometry (ICP–OES) and inductively coupled plasma-mass spectrometry (ICP–MS).
- Sulfate concentrations calculated from sulfur (S), assuming that all S was present as sulfate, and total ion (TI) concentrations were calculated by summing the individual cation and sulfate concentrations. Calcium and magnesium hardness were calculated by converting the elemental calcium and magnesium concentrations to the carbonate form.

3 RESULTS AND DISCUSSION

3.1 Physical and Chemical Parameters

The data for the physical parameters, as measured between 2018 and April 2019 for AMD Sites 1 and 2 in Mpumalanga are presented in Tables 1 and 2, respectively.

Table 1: Physical and chemical parameters as measured for Site 1 in Mpumalanga

Date	pH at 25 °C	Eh mV SHE at 25 °C	EC mS/m at 25 °C	NTU	TDS mg/L at 180 °C	TSS mg/L at 180 °C	TA mg/L $CaCO_3$ at pH 8.3	Total Ions mg/L
Site 1								
2018-02-01	2.94	642	3 460	19	19 640	63	10 500	18 575
2018-02-26	2.87	620	3 685	24	21 130	86	11 200	30 700
2018-03-26	2.57	682	2 335	3	12 015	29	5 760	9 720
2018-05-02	2.16	887	3 750	11	21 340	1	12 600	22 845
2018-05-31	2.87	632	3 725	241	23 180	321	10 700	20 895
2018-06-25	2.90	626	3 780	201	23 920	58	11 100	21 410
2018-08-02	2.49	689	3 940	123	23 950	55	11 700	18 900
2018-08-14	2.86	611	3 865	95	25 150	60	11 800	19 135
2018-09-04	2.99	621	3 985	413	19 575	100	11 900	19 515
2018-10-17	2.73	688	2 650	161	12 850	250	6 050	9 765
2018-11-22	2.84	628	3 790	29	23 830	21	11 100	17 250
2018-12-13	2.69	622	3 990	337	23 565	109	11 000	17 570
2019-04-04	2.64	640	3 705	241	26 635	110	11 100	17 200

These data were compared against the general discharge limits specified by the Department of Water Affairs and Forestry (DWAF, 2013). The general discharge limits indicated an acceptable pH range between pH 5.5-9.5, an EC of 70 mS/m above the intake to a maximum EC of 150 mS/m, and a

maximum TSS concentration of 25 mg/L. The remaining parameters are not controlled.

Table 2: Physical and Chemical parameters as measured for Site 2 in Mpumalanga

Date	pH at 25 °C	Eh mV SHE at 25 °C	EC mS/m at 25 °C	NTU	TDS mg/L at 180 °C	TSS mg/L at 180 °C	TA mg/L $CaCO_3$ at pH 8.3	Total Ions mg/L
Site 2								
2018-02-01	2.92	752	1090	20	5 820	62	1 480	6 028
2018-02-26	2.87	795	1465	408	9 175	199	2 160	7 346
2018-05-10	2.85	821	1055	205	6 680	80	1 260	6 035
2018-05-31	2.72	816	1720	99	9 900	52	3 440	8 462
2018-08-02	2.54	850	1935	248	10 700	170	3 673	7 646
2019-04-04	7.02	349	727	389	4 525	92	—	3 248

With the exception of the April 2019 sample from Site 2, pH values were acidic and reported pH values ranged between 2 – 3 which fell outside of the pH 5.5 DWAF lower general limit for discharge of wastewater into a water resource (DWAF, 2013). Although similar pH values were recorded for both sites, TA concentrations for Site 1 were an order of magnitude higher than those for Site 2. The acidity of water is defined as its capacity to neutralise a strong base to a predetermined pH and comprises the free protons and undissociated acids, i.e., strong, and weak acids as well as hydrolysable salts in a solution (Cook et al., 2000, Larson and Henley, 1955, Loftus, 2003). The higher TA concentrations for Site 1 would be indicative of the presence of increased concentrations of hydrolysable salts which was corroborated by the elevated EC measurements for Site 1 samples compared with those of Site 2. EC is a measure of the ability of water to conduct electric current and is dependent on the concentration of free ions in the water. All conductivities were significantly in excess of DWAF maximum general wastewater limit of 150 mS/m. The majority of TSS concentrations were in excess of the 25 mg/L DWAF general limit for discharge (DWAF, 2013). The pH and Eh values generally showed an inverse relationship and a lower average Eh of 661 mV was recorded for Site 1 compared with a more electropositive average of 801 mV for Site 2. The different Eh values could be as a result of differing concentrations of oxygen, pyrite, other metals and organic matter present in the rock (Johnson et al., 2012, Tutu et al., 2008). Gravimetrically determined TDS concentrations compared well against calculated TDS values, which were determined by multiplying the EC readings by 6.5, returning Pearson's correlations of 0.88 and 0.98 for Sites 1 and 2, respectively, at a 95 % confidence level (Rusydi, Wolkersdorfer and Hubert, 2015). This indicated a statistically significant relationship and analytical robustness between the TDS and EC data. The stronger correlation achieved between EC and TDS for Site 2 is probably due to the lower ion concentrations present in this AMD water. The

gravimetrically determined TDS, the sum of the total ions and the calculated TDS from EC data generally followed similar trends for the duration of the sampling period. For most sampling events, significantly larger variations were noted between the calculated TDS and total ion concentrations compared with the differences between the calculated TDS and the gravimetrically determined TDS for both sites. This could have been as a result of the complex chemistry of AMD waters and possible removal of contributory ions from solution by adsorption and precipitation resulting in under reporting of the contributary ion concentrations.

3.2 Major Cations and Anions

The cations calcium (Ca^{2+}), magnesium (Mg^{2+}), sodium (Na^{+}), potassium (K^{+}) and anion sulfur (S) data are presented in Table 3. Where specified, the Target Water Quality Range (TWQR) concentrations advised by the Department of Water Affairs (DWAF), and the South African National Drinking Water Standard (SANS 241:2015) regulatory limits are given (DWAF, 1996, SABS, 2015a).

The hardness of water is a measure of its capacity to react with soap. Water is classified as “very hard” if the total hardness exceeds 180 mg/L (Kamble, 2014, WHO, 2009); thus, as the Ca and Mg hardness contributions to total hardness are in excess of this concentration, the AMD waters from both sites are classified as very hard. Site 1 had a higher Mg hardness contribution (58 % average) than Ca hardness contribution to total hardness, while Site 2 showed a marginally higher Ca hardness contribution to total hardness (52 % average). The World Health Organisation Guidelines for drinking water indicate the probability of scum and calcium carbonate scale formation in waters with hardness values greater than 200 mg/L, while waters with a hardness values below 100 mg/L could cause corrosion of water pipes owing to decreased buffering capacity (WHO, 2017). Ca^{2+} and Mg^{+} concentrations were in excess of the target water quality range (TWQR) specified in the 1996 DWAF Water Quality Guidelines for Domestic use, while Na^{+} and K^{+} concentrations were below the specified TWQR (DWAF, 1996). The SANS: 241:2015 regulatory acute health limits for sulfate are given as 500 mg/L, which equates to 167 mg/L as S. Assuming all S is in the form of sulfate, the high concentrations reported would render that these waters are in excess of standard limits (SABS, 2015b).

Table 3: Site 1 and 2 data – major cations and anions

Date	Ca^{2+} mg/L	Ca Hardness mg/L as $CaCO_3$	Mg^{2+} mg/L	Mg Hardness mg/L as $CaCO_3$	Total Ca & Mg Hardness mg/L as $CaCO_3$	Na^{+} mg/L	K^{+} mg/L	S mg/L
Site 1								
2018-02-01	398	993	375	1 545	2 535	34	6.5	4345
2018-02-26	752	1 880	725	2 990	4 865	<1	18	6845
2018-03-26	310	775	201	827	1 600	20	4.0	2350
2018-05-02	462	1 155	428	1 760	2 915	36	10	5345
2018-05-31	440	1 100	410	1 690	2 790	39	10	4850
2018-06-25	439	1 095	405	1 670	2 765	44	11	4940
2018-08-02	446	1 115	396	1 630	2 745	58	3.2	4515
2018-08-14	433	1 080	349	1 440	2 520	58	13	4455
2018-09-04	437	1 090	365	1 505	2 595	58	14	4545
2018-10-17	324	809	209	860	1 670	35	3.3	2385
2018-11-22	409	1 020	338	1 395	2 415	71	12	4075
2018-12-13	418	1 045	348	1 435	2 475	76	15	4140
2019-04-04	429	1 070	314	1 290	2 365	56	12	4060
Site 2								
2018-02-01	655	1 635	375	1 545	3 180	34	5.6	1 525
2018-02-26	811	2 024	397	1 635	3 660	0.63	6.3	1 840
2018-05-10	633	1 581	333	1 370	2 950	39	13	1 545
2018-05-31	568	1 417	286	1 175	2 595	58	2.9	2 135
2018-08-02	447	1 117	315	1 295	2 415	58	3.9	1 980
2019-04-04	448	1 119	239	985	2 105	42	17	824
DWAF 1996 TWQR	32	—	30	—	—	100	50	—
SANS 241:2015	—	—	—	—	—	200	—	167

3.3 Metals

A total of 60 elements were analysed for the first sampling event to determine which were present in significant concentration. For the purposes of this paper, the discussion is limited to the dissolved metals results for the following elements: Fe, as a major metal contributor to AMD; arsenic (As), mercury (Hg), molybdenum (Mo), selenium (Se), and nickel (Ni) because of their noted presence in Witbank Coalfield 4 seam (Bergh, 2009); Mn, Zn, and cadmium (Cd), owing to the difficulty in removing these elements by adsorption; copper (Cu), tin (Sn), lead (Pb), and Al, because of the amphoteric nature of their hydroxides (Gazea et al., 1996, Fu and Wang, 2011). Data are presented in Table 4, together with the respective DWAF general discharge limits set for Sections 21 (f) and (h) and South African National

Standard (SANS) 241:2015 regulatory limits (DWAF, 2013, SABS, 2015b). Mo, As and Se data were not included as these elements were not detected and Hg was also omitted as all concentrations were below the 0.005 mg/L legislated limit.

Table 4: Dissolved Metals Concentrations

Date	Al mg/L	Cd mg/L	Cu mg/L	Fe mg/L	Mn mg/L	Ni mg/L	Pb mg/L	Sn mg/L	Zn mg/L
Site 1									
2018-02-01	365	0.02	0.07	4210	97	1.1	0.02	0.001	7.8
2018-02-26	518	—	—	7950	133	1.3	0.43	—	13
2018-03-26	222	—	—	1825	50	0.79	0.07	—	7.4
2018-05-02	354	0.02	0.34	5390	86	0.85	0.02	0.001	9.3
2018-05-31	371	0.02	0.26	4950	78	0.89	0.03	0.003	8.5
2018-06-25	373	0.01	0.09	5185	82	0.83	0.003	0.001	9.0
2018-08-02	442	—	0.08	3770	153	1.6	0.01	0.001	9.2
2018-08-14	300	—	0.02	4475	84	0.90	0.02	0.001	8.3
2018-09-04	259	—	0.02	4600	88	0.80	0.02	<0.0001	7.7
2018-10-17	191	—	0.06	1735	71	0.66	0.006	<0.0001	4.5
2018-11-22	206	—	0.02	3860	76	0.65	0.01	<0.0001	6.4
2018-12-13	193	—	0.02	3975	78	0.62	0.01	<0.0001	6.3
2019-04-04	213	—	0.04	3875	68	0.57	0.01	<0.0001	5.0
Site 2									
2018-02-01	157	0.010	0.10	160	44	1.3	0.02	0.005	3.1
2018-02-26	162	< 0.003	0.08	376	51	1.1	0.12	—	3.6
2018-05-10	126	0.007	0.13	199	35	1.2	0.005	0.004	2.5
2018-05-31	230	0.010	0.15	828	52	0.90	0.03	0.006	4.1
2018-08-02	144	0.004	0.09	646	58	0.92	0.006	0.001	3.3
2019-04-04	0.04	0.003	0.04	4.2	17	0.31	0.005	0.0002	0.44
DWAF 2013 general discharge limit	—	0.005	0.01	0.3	0.1	—	0.01	—	0.1
SANS 241:2015	<0.3	<0.003	—	<2	<0.1	<0.07	<0.01	—	<5

– = not determined

Where analysed, most Cd concentrations exceeded legislative limits and all except for two samples from Site 2 exceeded discharge limits; three of the six Pb concentrations for Site 2 were below limits, while all Site 1 concentrations, except for one sample, were at the 0.01 mg/L limit or higher. All Cu, Ni, Mn, and Site 1, Zn concentrations were in excess of legislated concentration limits, with Mn followed by Zn present in noticeably higher concentrations. Fe was significantly in excess of legislated

limits. No general discharge limits are available for Al and Ni, and these data were compared against the SANS 241:2015 regulatory limits, where they were found to be in excess of prescribed limits (SABS, 2015b). Al was present in significant concentrations. No guidelines were available for Sn, which, when detected, was present only in very low concentrations.

3.4 Significant Trends

Total acidity, EC, and dissolved Al, Fe and S concentrations showed similar trends over the time, while rainfall volumes showed an inverse trend.

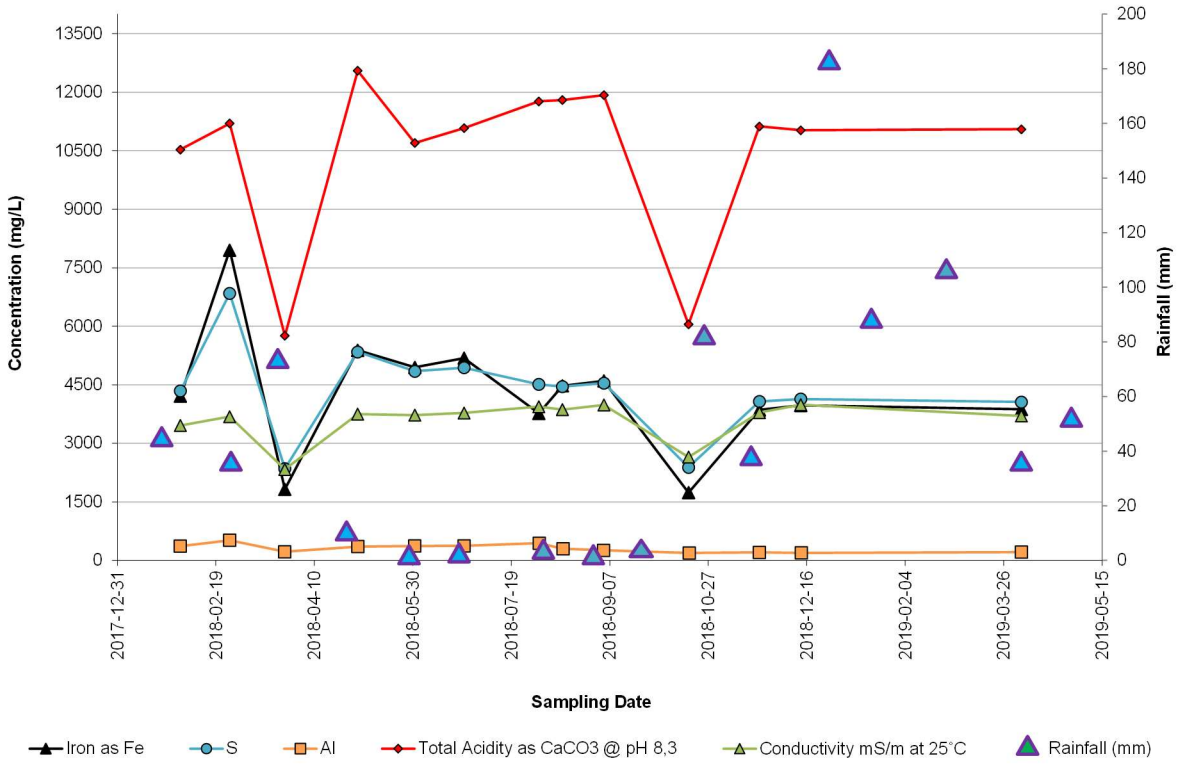

Figure 3: Variation in rainfall and total acidity, electrical conductivity, and dissolved aluminium (Al), iron (Fe), and sulfur (S) concentrations for Site 1 over the sampling period.

As shown in Figure 3, increased concentrations for the geochemical parameters measured at Site 1 were observed for the February sampling event which might have resulted from the reduced rainfall volumes from the previous month. The significant decrease in the concentrations observed for the March 2018 sampling event could be as a result of dilution effects caused by substantial rainfall that occurred immediately prior to this sampling event. Monthly rainfall data for the area, indicated a substantial increase in rainfall volume compared with the previous month (WorldWeatherOnline, 2019). Similarly, lower concentrations recorded for the October 2018 sampling event coincided with a significant increase in recorded rainfall volume. Lower rainfall was recorded for November 2018 and the concentrations increased to approach previously recorded levels. Site 1 showed no reduction in

geochemical parameter concentrations in December 2018 despite the significant rainfall recorded for that month, this is probably because the rainfall only occurred in the latter half of the month, after sampling had taken place. High rainfall was recorded for January and February 2019, but rainfall volumes decreased significantly in March, which might explain why the concentrations for Site 1 samples did not reflect any significant dilution effect from the concentrations recorded in December.

Site 2 sample concentrations showed an increase in February, which could be as a result of reduced rainfall levels from the previous sampling period. This was followed by a decrease in concentrations in April, probably as a result of the increased rainfall volumes over that period. Concentrations showed a significant increase at the end of May, which could be caused by net evaporation and dry climatic conditions during that time. Significantly reduced concentrations were recorded for the March 2019 sampling event and the sample was no longer acidic. The increased rainfall recorded from October 2018 to March 2019 could have provided sufficient dilution for natural remediation given the lower ion concentrations present in the Site 2 AMD, although remediation could also have been as a result of the effectiveness of ongoing remediation processes that were implemented at this site. These trends are shown in Figure 4.

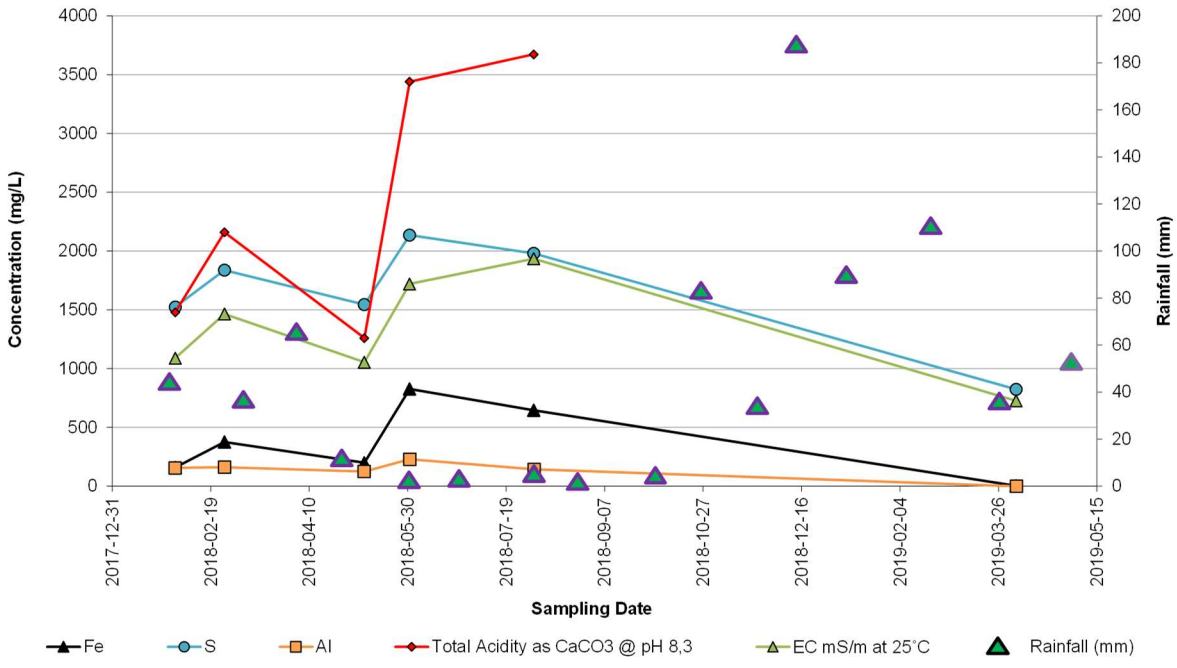

Figure 4: Variation in rainfall and total acidity, electrical conductivity, and dissolved aluminium (Al), iron (Fe), and sulfur (S) concentrations for Site 2 over the sampling period.

4 CONCLUSIONS

Characterisation of Mpumalanga coalfield AMD showed that there was significant variation in the physical and chemical parameters of these waters. Total acidity, dissolved Fe and TDS concentrations

varied by an order of magnitude between sites, and concentrations differed between sampling events. Reduced rainfall volumes were recorded in the winter months which coincided with increased concentrations, thus confirming the seasonal variability of AMD, which could, in turn, upset passive system dynamics. Pb, Cu, Mn, Zn, Al, S, Fe, Ni, and some Cd concentrations were in excess of legislative limits with Fe, and S present in very high, and Al, Mn, and Zn present in significant concentrations. Removal of Mn and Zn would not support passive treatment systems owing to their difficulty of removal by adsorption, whilst high concentrations of Al, given the amphoteric nature of aluminum hydroxides, would limit the effectiveness of active treatment systems. These factors should be accounted for when designing a suitable treatment system. More importantly, if a treatment process were required to switch between different AMD streams, cognizance must be taken of the extent of variability and should be built into the design. A strong correlation was observed between electrical conductivity and total dissolved solids, indicating analytical robustness between these parameters. Since total acidity, dissolved aluminum, iron, and sulfur showed similar trends over time, potential correlations that might exist between these parameters should be investigated.

REFERENCES

Bergh, J. 2009. Trace Element partitioning in the Witbank Coalfield 4 seam. *Paper: Fossil Fuel Foundation Indaba*, 11-12.

Cook, F. J., Hicks, W., Gardner, E. A., Carlin, G. D. & Froggatt, D. W. 2000. Export of Acidity in Drainage Water from Acid Sulphate Soils. *Marine Pollution Bulletin, 41(7-12)*, pp.319-326.

DMR. 2017. *Operating Mines in Mpumalanga* [Online]. Department of Mineral Resources of South Africa https://www.dmr.gov.za/mineral-policy-promotion/operating-mines/mpumalanga [Accessed 6 January 2020].

DWAF 1996. Department of Water Affairs and Forestry, 1996. South African Water Quality Guidelines (second edition). Volume 1: Domestic Use.

DWAF 2013. Department of Water Affairs and Forestry, Government Notice 665 in Government Gazette 36820, REVISION OF GENERAL AUTHORISATIONS IN TERMS OF SECTION 39 OF THE NATIONAL WATER ACT, 1998 (ACT NO. 36 OF 1998), DWAF general discharge limits set for Sections 21 (f) and (h)

Expert Team of the Inter-Ministerial Committee, D. 2010. Mine water management in the Witwatersrand Gold Fields with special emphasis on acid mine drainage. *Report to the Inter-Ministerial Committee on Acid Mine Drainage. Pretoria: Department of Water Affairs*.

Fu, F. & Wang, Q. 2011. Removal of heavy metal ions from wastewaters: a review. *Journal of environmental management,* 92, pp. 407-418.

Gazea, B., Adam, K. & Kontopoulos, A. 1996. A review of passive systems for the treatment of acid mine drainage. *Minerals engineering,* 9, pp.23-42.

Johnson, D. B., Kanao, T. & Hedrich, S. 2012. Redox transformations of iron at extremely low pH: fundamental and applied aspects. *Frontiers in microbiology, 3*, pp.96.

Kamble, R. 2014. Eccentric observation of total hardness in Lohara village, Chandrapur district, central India. *International Journal of Environment, 3*, pp.134-140.

Larson, T. E. & Henley, L. 1955. Determination of Low Alkalinity or Acidity in Water. *Analytical Chemistry, 27*, pp.851-852.

Loftus, T. 2003. *An Informational Resource for Operators of Lagoon Systems, Acidity and Alkalinity* [Online]. Maine Lagoon Systems http://www.lagoonsonline.com/laboratory-articles/acid.htm. [Accessed 6 December 2019].

McCarthy, T. S. 2011. The impact of acid mine drainage in South Africa. *South African Journal of Science, 107*, pp.01-07.

Rusydi, A. F. 2018. Correlation between conductivity and total dissolved solid in various type of water: A review. IOP Conf Ser: Earth Environ Sci 118:012019.

SABS 2015a. South African National Drinking Water Standard (SANS) 241-1: 2015 Second ed.

SABS 2015b. *South African National Drinking Water Standard (SANS) 241: 2015*

Tutu, H., McCarthy, T. & Cukrowska, E. 2008. The chemical characteristics of acid mine drainage with particular reference to sources, distribution and remediation: The Witwatersrand Basin, South Africa as a case study. *Applied Geochemistry, 23*, pp.3666-3684.

WHO 2009. *Calcium and magnesium in drinking-water: public health significance*, World Health Organization.

WHO 2017. Guidelines for drinking-water quality: fourth edition incorporating the first addendum. Geneva: World Health Organization; 2017. Licence: CC BY-NC-SA 3.0 IGO.

Wolkersdorfer, C. & Hubert, E. 2015. Establishing a Total Dissolved Solids: Electrical Conductivity Ratio for Mine Waters. *Agreeing on solutions for more sustainable mine water management*, pp.1-8.

WorldWeatherOnline. 2019. *Witbank Monthly Climate Averages, Mpumalanga, ZA* [Online]. World Weather Online. Available: https://www.worldweatheronline.com/witbank-weather-averages/mpumalanga/za.aspx [Accessed 21 August 2019].

Integrated development and optimisation of an organic acid-based hydrometallurgical process for treatment of spent lithium-ion batteries (LIBs)

S.A. Jeza, G. Akdogan* and C. Dorfling

Department of Process Engineering, Stellenbosch University, Private Bag X1, Matieland, 7602, South Africa

*Corresponding author: gakdogan@sun.ac.za

ABSTRACT

Lithium-ion batteries (LIBs) are the heart of the latest technology devices, but these batteries become harmful waste at the end of their life. This study aimed to develop an integrated and optimised acid organic acid-based hydrometallurgical process for the treatment of LIBs to recover metals after end-of-life. Citric acid was selected as the organic acid to leach LIBs; at the constant condition of 95 °C, 750 rpm stirring, S/L ratio of 20 g/L and 2 vol. % H_2O_2, the effect of lixiviant concentration (0.75 M, 1 M, 1.5 M, 2 M and 3 M) on metal equilibrium extraction was investigated. The concentration of 0.75M resulted in equilibrium metal extractions of 94.3% Li, 95.1% Co, 96.2% Mn and 95.7% Ni after 1 hour. Ni was the first metal to be recovered from a leachate solution using 0.07 M DMG at a pH of 6, followed by the solvent extraction of Mn using 10% D2EHPA at an O/A ratio of 3 and a pH of 5. Mn was stripped from the organic phase using 0.5 M H_2SO_4 at an O/A ratio of 1.33 followed by hydroxide precipitation. The aqueous phase from Mn solvent extraction mainly consisted of Co which was precipitated using NaOH at a pH of 13.5. Four products yielded include $Ni(OH)_2$ with more than 99.5% purity, followed by 89% $Mn(OH)_2$ product, 97% Li_2SO_4 product and lastly cobalt hydroxide based product with 68 % $Co(OH)_2$.

Keywords: leaching; metal recovery; recycling; spent lithium-ion batteries (LIBs)

1 INTRODUCTION

Lithium-ion batteries (LIBs) have significantly increased their application in mobile cell phones, cameras, computers, electrical vehicles (EVs), renewable energy storage and many other electrically powered devices (Chen, et al., 2015; Zheng, et al., 2018). Batteries that are discarded at their end of life can cause environmental pollution due to toxic chemicals present in discarded LIBs (Wang, et al., 2009). Currently, an estimated 10 billion LIB units are considered waste worldwide (Peng, et al., 2020). The characteristics that make LIBs be in demand or favourable, is the size, lightweight and superb electrochemical properties or high energy density over other rechargeable batteries such as nickel-cadmium, zinc-based, etc. (Fergus, 2010). The increasing rate of demand for the use of LIBs is also proportional to the increase of quantity discarded; the recycling of spent LIBs is compelling not only for saving the environment but also for the monetary incentive to recover valuable metals (Horeh, et al., 2016). At present, two main research areas namely pyrometallurgy and hydrometallurgy focus on

the recycling of spent LIBs (Chen, et al., 2015; Li, et al., 2015; Peng, et al., 2020; Mossali, et al., 2020; Wang, et al., 2017). This paper addresses this issue by an experimentally developed and optimised hydrometallurgical process flowsheet that utilises an organic acid for the recovery of the main metals of the LIBs.

2 LITERATURE

2.1 Structure of LIBs

Lithium-ion batteries consist of the anode, cathode, separator and electrolytes within the metal or plastic casing (Li, et al., 2013; Chagnes, et al., 2015). The anode is made from carbon (graphite) that is coated to the copper foil; the cathode which serves as the active material is a lithium oxide-based compound such as $LiCoO_2$, $LiMn_2O_4$, $LiFePO_4$, $LiNiO_2$, $Li(Ni_{0.33}Mn_{0.33}Co_{0.33})O_2$ or $Li(Ni_{0.8}Co_{0.15}Al_{0.05})O_2$ that is coated to the aluminium foil (Li, et al., 2013). The cathode material is bonded together with polyvinylidene (PVDF) as a mechanically and chemically stable material (Xu, et al., 2008). A separator is used to separate the anode and cathode from direct contact that can result in short-circuiting and is made from polymeric materials (polypropylene (PP) or polyethene (PE)), paper or paperboard (Vassura, et al., 2009; Zheng, et al., 2018). A separator should be able to allow lithium-ions to pass through from the cathode to an anode (Vassura, et al., 2009). The electrolytes consist of the solute (usually $LiClO_4$, $LiPF_6$, or $LiBF_4$) that is dissolved in a solvent that is generally the mixture of two or more organic solvents such as dimethylsulfoxide (DMSO), propylene carbonate (PC), and/ or diethyl carbonate (DEC) (Zheng, et al., 2018).

2.2 Potential Environmental Impact

There is a high rate of using LIBs across the globe and this results in an increase in their waste in landfill sites (Zeng, et al., 2014). The waste of LIBs in the landfills forms leachate of inorganic elements with poisonous metals during the biological and chemical decomposition process (Kjeldsen, et al., 2002). Water that enters landfills, especially during rainfalls, can transport this dangerous leachate to water sources for the society and pose environmental and health issues (Kjeldsen, et al., 2002; Li, et al., 2009). The World Health Organisation (WHO) and the United States Environmental Protection Agency (EPA) developed guidelines for threshold metal concentrations in drinking water to prevent the cause of carcinogenic diseases to humans (Winslow, et al., 2018). LIBs in landfill sites also cause fires due to overheating and short-circuiting of the LIBs (Wang, et al., 2012).

2.3 Organic Acid Leaching

The use of organic acids in the leaching of spent lithium batteries has emerged as a promising alternative to mineral acid-based hydrometallurgical processes in recent years. The organic acids that are mostly explored in different studies for leaching cathode materials of spent LIBs include citric acid, DL-malic acid, oxalic acid, acetic acid, tartaric acid, succinic acid, lactic acid, formic acid and aspartic

acid. The prominent factors that affect organic leaching include acid concentration, solid-to-liquid (S/L) ratio, temperature, reductant concentration, particle size and stirring speed. Few studies from the literature survey conducted and tabulated in Table 1 showed that:

i. The optimal leaching conditions for Li and Co using organic acid are achieved at acid concentrations between 0.1 and 2 M with 1 to 4% (v/v) H_2O_2, a temperature of 60-95°C and a leaching time as short as 20 minutes.

ii. Hydrogen peroxide is the most commonly used reductant in citric acid leaching processes.

Table 1: Organic acid leaching and metal extraction efficiencies

Material	OPTIMUM CONDITIONS					Reference
	Leachant + Reductant	**Temp (°C)**	**Time (min)**	**S/L (g/L)**	**Leaching Efficiency**	
Mixed Batteries	1.5M Citric Acid + 2 vol% H_2O_2	95	30	20	96% Li; 95% Co; 99% Ni	(Musariri, 2019)
	1M DL-malic Acid + 2 % H_2O_2	95	30	20	96% Li; 99% Co; 99% Ni	
$LiCoO_2$	0.1M Citric Acid + 0.02M Ascorbic Acid	80	360	2	~100% Li; ~80% Co	(Nayaka, et al., 2015)
Mixed batteries	2M Citric Acid + 1.25 vol% H_2O_2	60	120	30	~92% Li; ~81 Co	(Golmohammadzadeh, et al., 2017)
$LiCoO_2$	1.25M Ascorbic Acid	70	20	25	98.5% Li; 94.8% Co	(Li, et al., 2012)

2.4 Metal Recovery

Metals can be separated through a combination of solvent extraction, stripping and precipitation processes. The prevailing variables that require optimisation include the O/A ratio, organic phase concentration, stripping agent concentration, precipitation agent concentration, equilibrium pH, and molar ratio. Ni can be recovered from an organic solution using dimethylglyoxime ($C_4H_4N_2O_2$) as a precipitating agent (Chen & Zhou, 2014), while manganese can be recovered with D2EHPA through liquid-liquid extraction (solvent extraction) followed by stripping with H_2SO_4 (Chen & Zhou, 2014; Musariri, 2019). Cobalt can be covered using oxalate ion (Chen & Zhou, 2014; Chen, et al., 2015), and Li can be recovered using precipitation with phosphate or carbonate ion (Chen & Zhou, 2014; Chen, et al., 2015; Musariri, 2019). All the main metals can also be precipitated using sodium hydroxide (Musariri, 2019).

3 EXPERIMENTAL PROCEDURE

3.1 Cathode material characterization

The outer plastic battery casing was firstly removed by manually dismantling using a band saw, hammer, a side cutter and a flat screwdriver to recover individual cells. Individual cells were then discharged by soaking them in 1 wt.% NaCl solution for 48 hours to prevent short-circuiting and ignition during cutting and opening. After soaking and drying, each cell was cut using the electric band saw and opened to uncoil the anode, plastic separators and cathode. Copper foil with anode was recovered and separators were removed to recover the cathode material for the further leaching process. Cathode material was leached with 10 wt.% NaOH solution for 2 hours at room temperature, S/L ratio of 100 g/L and 300 rpm stirring. The dried cathode material was pulverised for characterisation by aqua regia digestion followed by ICP-OES analysis, scanning electron microscope (SEM) and X-Ray diffraction (XRD).

3.2 Organic acid leaching

Organic acid leaching using citric acid was performed in a 1 L leaching glass vessel with a Teflon lid and condenser. Citric acid was fully dissolved and the stirrer was stopped then cathode material was promptly added at an S/L ratio of 20 g/L and the stirrer was restarted and increased to a speed of 750 rpm. Directly after adding cathode material, 2 vol.% of H_2O_2 was added through the sampling port and samples were taken at fixed time intervals (5, 10, 20, 30, 40, 60, 80, 100 and 120 minutes) and filtered immediately using 0.22μm syringe filters.

3.3 Metal Purification

Ni was the first metal to be recovered from a leach solution using a DMG solution by investigating the effect of equilibrium pH. The pregnant leach solution was precipitated at room temperature and pressure, the molar ratio of Nickel to DMG (MRNC) of 0.5, 300 rpm stirring, 0.07M DMG concentration and 30 minutes reaction time. The recovered Ni-DMG solid was dissolved using 4 M HCl where DMG was recycled as a solid; Ni was then recovered from $NiCl_2$ solution as a solid $Ni(OH)_2$ using NaOH solution. The leach solution with reduced Ni concentration was subjected to a solvent extraction process to recover Mn using D2EHPA as an extractant in kerosene diluent by investigating the effect of equilibrium pH of (2, 3, 4 and 5) using 10% D2EHA concentration, an O/A ratio of 3, at room temperature and pressure, 300 rpm stirring and 10 minutes extraction time.

The loaded organic was stripped using 0.5M diluted sulfuric acid with 10 minutes reaction time, and Mn in loaded strip solution was precipitated using NaOH to recover Mn as $Mn(OH)_2$ solid with 30 minutes, the constant variables during stripping and precipitation were the room temperature and pressure, 300 rpm stirring. Li was recovered as a $LiSO_4$ solution after Mn precipitation from a stripping solution. Cobalt was recovered from leach solution as $Co(OH)_2$ solid after Ni precipitation and solvent

extraction of Mn by investing the effect of the molar ratio of phosphate to all metal in the solution (MRPM). The equipment used for both precipitation, solvent extraction and stripping were the glass beakers, stirrer plate, magnetic stirrer, pH meter from Thermo Scientific (model: ECPH603PLUSK), Whatman filters papers and a glass separatory funnel for two-phase separation. All experiments were repeated at least thrice at the optimized condition to assess repeatability.

4 RESULTS AND DISCUSSION

4.1 Cathode material characterization

ICP-OES result showed that the cathode material consists of 7.05% Li, 23.3% Co, 14.8% Mn, 19.3% Ni, 1.43% Al and 0.116% Fe. Figure 1 shows the SEM spectrum analysis with the dominant spike for Co. XRD analysis showed that the cathode active material consists of $LiMn_{0,375}Ni_{0,375}Co_{0,25}O_2$ and $LiNi_{0,05}Mn_{0,05}Co_{0,9}O_2$ with weight fraction of 76.7% and 20.8% respectively and 2.50% impurities.

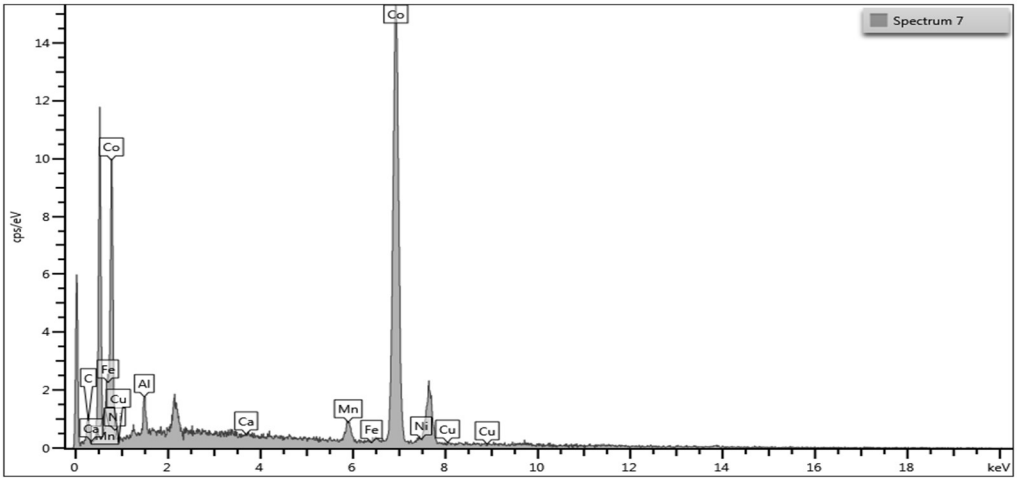

Figure 1: SEM-Spectrum for analysis

4.2 Citric acid leaching

Figure 2 shows the leaching results as the percentage of each metal extraction against time using different acid concentrations. 0.75M citric acid resulted in the maximum equilibrium extraction of 94.3% Li; 95.1% Co; 96.2% Mn and 95.7% Ni after 60 minutes. The extraction performance of all metals is comparable to the results reported by Musariri (2019) where all metals were more than 90% extracted. The amount of the cathode material leached to form metal citrate complexes is most likely to be solubility limited, and there is no solubility limit data available in the literature for the citric acid environment. Beyond an optimum acid concentration, the metal extraction is reduced since the system is much loaded with citrate molecules which prevent further formation of metal complexes, this phenomenon is solubility limit effect. When using an S/L ratio of 20 g/L and a stirring speed of 750 rpm, the optimal acid concentration and temperature were determined to be 0.75M and 95°C, respectively, with 2 vol. % H_2O_2 addition.

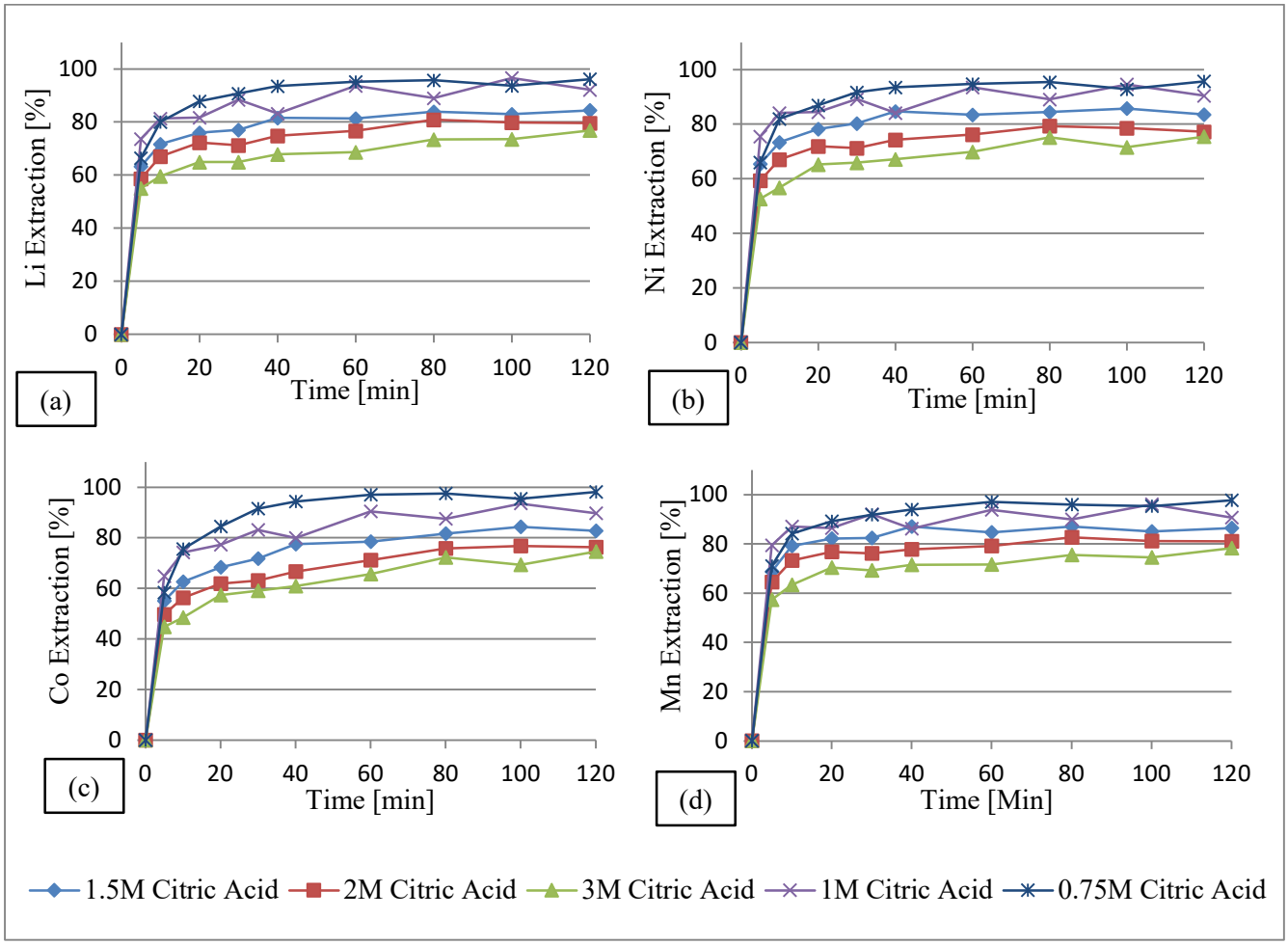

Figure 2: Effect of citric acid concentration on leaching Li, Co, Ni and Mn at 95°C, the solid-to-liquid ratio of 20 g/L, 750rpm stirring and 2 vol. % H_2O_2

4.3 Ni Recovery

The leachate from citric acid leaching mainly consists of four valuable components namely Li, Co, Mn and Ni, with concentrations of 1230.9 mg/L, 4746.0 mg/L, 2662.1 mg/L and 3448.5 mg/L, respectively. Ni is the first metal to be selectively precipitated using dimethylglyoxime ($C_4H_8N_2O_2$). The variables investigated to obtain optimum conditions for selective precipitation were the molar ratio of Ni^{2+} to $C_4H_8N_2O_2$ (MRNC) and equilibrium pH, and the results are shown in Figure 3. The condition of optimality is the trade-off between recovery and purity. Therefore, the optimum point for Ni recovery was selected at a pH 6 and 0.07 M DMG since it has a higher recovery than a pH of 7, and pH of seven has a higher operating cost since it requires a higher NaOH addition than a pH of 6. The recovered solid Ni-DMG (filter cake) was dissolved with a 4M HCl solution to recycle DMG and recover nickel as $Ni(Cl)_2$ solution. The remaining white solid (DMG) after the dissolution was dried and measured to obtain the percentage recovery of 98.0% DMG by mass, and the losses were most likely to be the results of sticking to the equipment. NaOH was then added to the $NiCl_2$ solution to precipitate nickel at a pH

of 11, the temperature of 55°C, stirrer speed of 300 rpm and 30 minutes reaction time; approximately 99% of Ni was recovered as $Ni(OH)_2$ solid with more than 99% purity. Ni-DMG purity in the plot legend refers to the purity of the Ni-DMG solid complex formed during precipitation with its optimum purity and optimum recovery of Ni through precipitation.

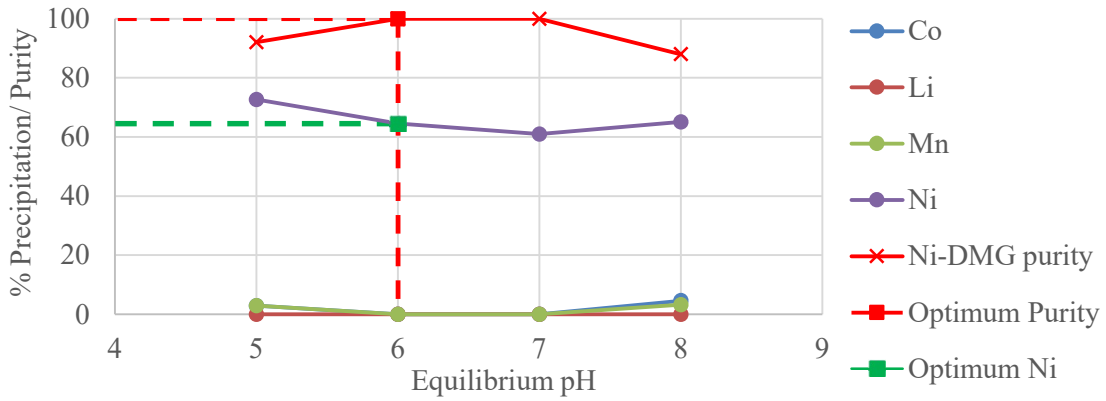

Figure 3: Ni precipitation with DMG as a function of pH at a constant concentration of 0.07M, room temperature of about 25°C, 300 rpm stirring, 30 minutes and MRNC of 0.5

4.4 Mn Recovery

Mn was recovered from the leach liquor after Ni-DMG precipitation. The reason for considering Mn recovery through solvent extraction is the fact that Co and Ni show a similar behaviour due to relatively the same effective nuclear charge which is stronger than Mn, although their stable oxidation state is 2+ from the loss of an electron in the 4S orbital as they are shielded by lower orbitals from the effective nuclear charge. Li also experiences a less significant nuclear charge than all other metals due to fewer protons in the nucleus. Three main factors that were investigated during Mn extraction are the O/A ratio, equilibrium pH and D2EHPA concentration by volume; the results are shown in Figure 41. The optimum point for solvent extraction was selected based on how much Mn was extracted as well as the Co and Ni co-extraction. Li co-extraction was not considered as a problem since it can be easily separated from a solution after Mn is precipitated in the pH range of 8-10 (Wang & Friedrich, 2015) Therefore, the point of a pH of 5, 10% D2EHPA concentration and O/A ratio of 3 was considered as the optimum point referred as “OP” in the plot legend with Mn extraction of about 94% extraction and about 5% co-extraction of Co and Ni, respectively.

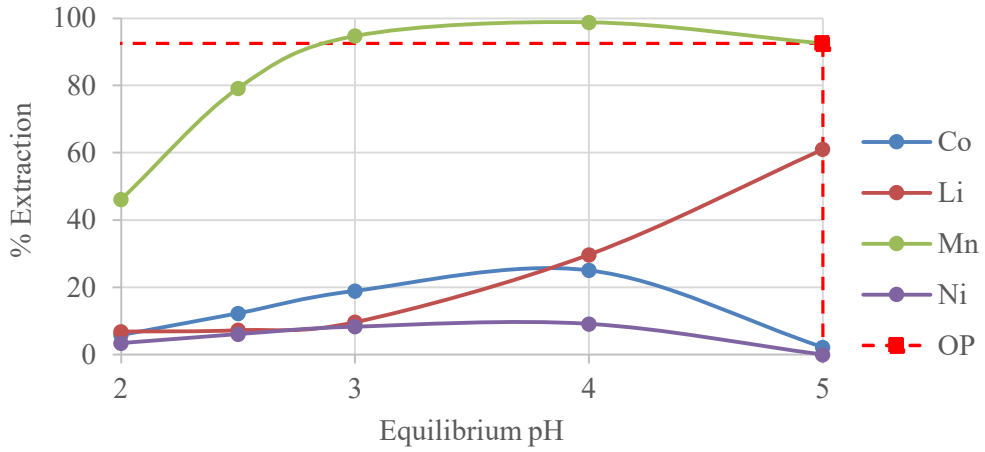

Figure 41: Plot of Mn extraction as a function pH at 25°C, 10% D2EHPA, 10 minutes, 300rpm stirring and O/A ratio of 3

The loaded organic from solved extraction was stripped with an aqueous solution (diluted sulphuric acid) to recycle the organic phase for re-extraction. Two parameters were investigated that includes the O/A ratio and concentration of the diluted sulphuric acid, and the result are shown in Figure 5.

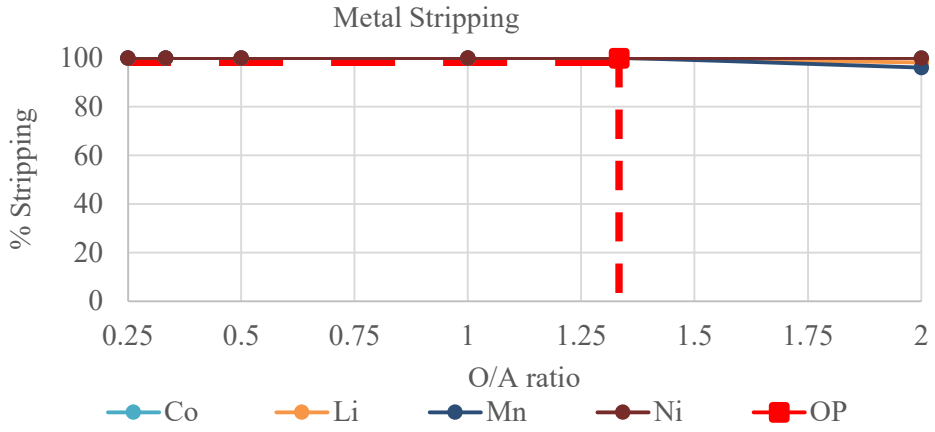

Figure 5: Mn stripping from organic phase of 10% D2EHPA for 10 minutes with 300rpm stirring at 25°C, using 0.50M diluted H_2SO_4 as a stripping agent

Therefore, an O/A ratio of 4/3 and 0.5 M concentration was considered as the optimum for the maximum extraction of all metals in the organic phase. It can be concluded that the amount of hydrogen cations must be sufficient to ensure maximum extraction, and this can be done by increasing the concentration of sulphuric acid or decrease the O/A ratio of the system. To produce a high purity Mn product, NaOH was used to precipitate Mn, but Co and Ni were expected to also come out as impurities. Therefore, an optimum pH was investigated. The pH of 12, room temperature, 30 minutes reaction time and 300 rpm stirring was considered at the optimum point with all Mn reporting in the product stream as $Mn(OH)_2$ solid with the least amount of Co and Ni co-precipitated, resulting in a product purity of 89.6% $Mn(OH)_2$. The remaining solution consists of a high purity Li metal as 97.2% purity Li_2SO_4,

which can be used in the pharmaceutical industry, energy sector and chemical industries that use $LiSO_4$ solution.

4.5 Co Recovery

The aqueous phase from Mn solvent extraction mainly consists of Co with Ni, Mn and Li as minor components in the system. The optimum molar ratio of phosphate to metals in the solution which is Co, Mn and Ni (MRPM) was investigated starting from zero. The reason for including zero is to find out the performance of hydroxide in precipitating metals as metal hydroxide. From an economic point of view, the use of phosphate increases both capital cost and operating cost. The addition of 0.5 M phosphate solution for precipitation of Co and other metals further dilutes the system, and more hydroxide is required to raise pH. Upon further diluting the system, the volume increases, resulting in a larger processing unit for precipitation than using only hydroxide.

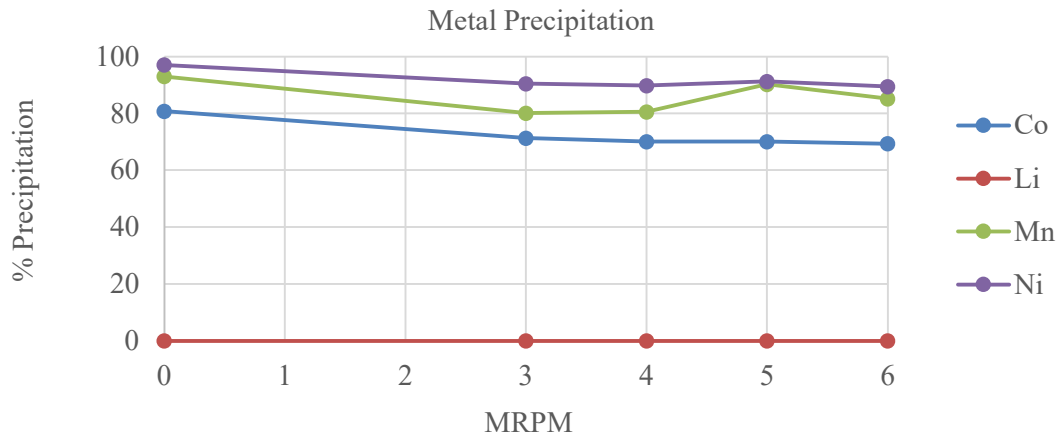

Figure 6: Co-precipitation as a function of MRPM in a citrate solution (after Mn solvent extraction) at 25°C, non-stirring, pH of 13.5 and 5-hours reaction time

It is concluded from Figure 6 that hydroxide precipitation at a pH of 13.5 is better than phosphate precipitation provided it is given sufficient time (5 hours) to precipitate. Thus, hydroxide precipitation of Co together with Ni and Mn was considered over phosphate precipitation, also as an economically viable option over phosphate precipitation which requires a larger processing unit and high operating cost, the product contains 68.2% $Co(OH)_2$, 23.6% $Ni(OH)_2$, 3.41% $Mn(OH)_2$, 4.76% $Al(OH)_3$, and 0.043% Li(OH).

5 CONCLUSIONS

This project aimed to develop an optimised and integrated organic acid-based hydrometallurgical process for the treatment of spent lithium-ion batteries (LIBs). The developed process involves three main sections for recycling (LIBs), namely: pre-treatment, organic acid leaching and metal purification. Based on leaching experimental results, the maximum extraction of 94.3 ± 0.457% Li, 95.1 ± 1.12%

Co, 96.2 ± 0.821%) Mn and 95.7 ± 0.614% Ni was achieved after 1-hour leaching using an S/L ratio of 20 g/L, 2 vol.% H_2O_2, 0.75 M citric acid and 750 rpm stirring. Ni was recovered as $Ni(OH)_2$ with the recovery of 99% in the precipitation unit for Ni with hydroxide and over 99.5% purity, and 98.0 ± 1.00% DMG was recovered after dissolving Ni from the Ni-DMG complex. The overall purity of $Mn(OH)_2$ (product 2) was 89.6%; the resulting strip solution was a product of high purity of about 97% (product 3) with one metal Li existing as $LiSO_4$. The overall recovery of Co at this stage was about 78.6% resulting in a mixed product (product 4) that is Co-based with 68.2% $Co(OH)_2$ purity.

REFERENCES

Chagnes, A., Barboux, P., Lorente, D., Christmann, P., Ekberg, C., & Petranikova, M. (2015). *Lithium Process Chemistry - Resources, Extraction, Batteries and Recycling* (1st ed.). (A. Chagnes, & J. Swiatowska, Eds.) Elsevier.

Chen, L., Chen, Y., Zhou, T., Liu, D., Hu, H., & Fan, S. (2015). Hydrometallurgical recovery of metal values from sulfuric acid leaching liquor of spent lithium-ion batteries. *Waste Management*, 349-356.

Chen, X., & Zhou, T. (2014). Hydrometallurgical process for the recovery of metal values from spent lithium-ion batteries in citric acid media. *Waste Management and Research, 32*(11), 1083–1093.

Fergus, J. W. (2010). Recent developments in cathode materials for lithium-ion batteries. *J. Power Sources, 195*(4), 939–954.

Golmohammadzadeh, R., Rashchi, F., & Vahidi, E. (2017). Recovery of lithium and cobalt from spent lithium-ion batteries using organic acids: Process optimization and kinetic aspects. *Waste Management. Elsevier Ltd, 64*, 244-254.

Horeh, N., Mousavi, S., & Shojaosadati, S. (2016). Bioleaching of valuable metals from. *J. Power Sources*, 257-256.

Kjeldsen, P., Barlaz, M. A., Rokker, A. P., Baun, A., Ledin, A., & Christensen, T. H. (2002). Present and Long-Term Composition of MSW Landfill Leachate: A Review. *Critical Reviews in Environmental Science and Technology, 32*(4), 297-336.

Li, L., Dunn, J. B., Zhang, X. X., Gaines, L., Chen, R. J., Wu, F., & Amine, K. (2013). Recovery of metals from spent lithium-ion batteries with organic acids as leaching reagents and environmental assessment. *Journal of Power Sources, 233*, 180-189.

Li, L., Fan, E., Guan, Y., Zhang, X., Xue, Q., Wei, Q., & Wu, F. (2017). Sustainable Recovery of Cathode Materials from Spent Lithium-Ion Batteries Using Lactic Acid Leaching System. *ACS Sustable Chemistry & Engineering, 5*, 5224-5233.

Li, L., Ge, J., Wu, F., Chen, S., & & Wu, B. (2009). Recovery of cobalt and lithium from spent lithium ion batteries using organic citric acid as leachant. *Journal of Hazardous Materials,*

176(1-3), 288–293.

Li, L., Lu, J., Ren, Y., Zhang, X. X., Chen, R. J., Wu, F., & Amine, K. (2012). Ascorbic-acid-assisted recovery of cobalt and lithium from spent Li-ion batteries. *Journal of Power Sources, 218*, 21-27.

Li, L., Qu, W., Zhang, X., Lu, J., Chen, R., Wu, F., & Amine, K. (2015). Succinic acid-based leaching system: A sustainable process for recovery of valuable metals from spent Li-ion batteries. *Journal of Power Sources, 282*, 244-251.

Li, L., Zhai, L., Zhang, X. X., Lu, J., Chen, J. R., Wu, F., & Amine, K. (2014). Recovery of valuable metals from spent lithium-ion batteries by ultrasonic-assisted leaching process. *Journal of Power Sources, 262*, 380-385.

Mossali, E., Picone, N., Gentilini, L., Rodrìguez, O., Perez, J. M., & Colledani, M. (2020). Lithium-ion batteries towards circular economy: A literature review of opportunities and issues of recycling treatments. *Journal of Environmental Management*(264).

Musariri, B. (2019). *Development of an environmentally friendly lithium-ion battery recycling process.* Masters Thesis, Stellenbosch University, Stellenbosch.

Nayaka, G., Manjanna, J., Pai, K., Vadavi, R., Keny, S., & Trpathi, V. (2015). Recovery of valuable metal ions from the spent lithium-ion battery using aqueous mixture of mild organic acids as alternative to mineral acids. *Hydrometallurgy, 151*, 73-77.

Peng, C., Lahtinen, K., Medina, E., Kauranen, P., Karppinen, M., Kallio, T., . . . Lundstrom, M. (2020). Role of impurity copper in Li-ion battery recycling to LiCoO2 cathode materials. *Journal of Power Sources, 450*.

Vassura, I., Morselli, L., Bernardi, E., & Passarini, F. (2009). Chemical characterisation of spent rechargable batteries. *Waste Manage, 29*, 2332-2335.

Wang, H., & Friedrich, B. (2015). Development of a Highly Efficient Hydrometallurgical Recycling Process for Automotive Li – Ion Batteries. *Journal of Sustainable Metallurgy*, 168-178.

Wang, M.-M., Zhang, C.-C., & Zhang, F.-S. (2017). Recycling of spent lithium-ion battery with polyvinyl chloride by mechanochemical process. *Waste Management, 67*, 232-239.

Wang, Q., Ping, P., Zhao, X., Chu, X., & Sun. (2012). Thermal runaway caused fire and explosion of lithium ion battery. *Journal of Power Sources, 2085*, 210-224.

Wang, R. C., Lin, Y. C., & Wu, S. H. (2009). A novel recovery process of metal values from the cathode active materials of the lithium-ion secondary batteries. *Hydrometallurgy. Elsevier B.V., 99*(3-4), 194-201.

Wang, S., & Yu, J. (2020). Evaluating the electric vehicle popularization trend in China after 2020 and its challenges in the recycling industry. *Waste Management & Research* , 1-10.

Winslow, K. M., Laux, S. J., & Townsend, T. G. (2018). A review on the growing concern and

potential management strategies of waste lithium-ion batteries. Resources, Conservation & Recycling, 129, 263-277.

Xu, J., Thomas, H., Francis, R., Lum, K., Wang, J., & Liang, B. (2008). A review of processes and technologies for the recycling of lithium-ion secondary batteries. Journal of Power Sources.

Zeng, X., Li, J., & Narendra, S. (2014). Recycling of Spent Lithium-Ion Battery: A Critical Review. Critical Reviews in Environmental Science and Technology, 44(10), 1129-1165.

Potential of Deep Eutectic Solvents for the Generation of Reactive Oxygen Species

D.O. Adeoye[1,3*], Z.S. Gano[2], S.M. Shuwa[1], A.Y. Atta[1], S. I. Iwarere[1], B. Y. Jubril[1] and M. Daramola[4]

[1] Department of Chemical Engineering, Ahmadu Bello University, Zaria, Nigeria.

[2] National Research Institute for Chemical Technology, Zaria, Nigeria.

[3] Nigerian Institute of Leather and Science Technology, Zaria, Nigeria.

[4] Department of Chemical Engineering, University of Pretoria, South Africa.

*Corresponding Author: yawehst2006@gmail.com

ABSTRACT

Many organic processes are initiated, and proceed by reactive oxygen species. The technology for the generation of these species in industrial processes over the years has been through metal-catalyzed oxidative reactions that are exposed to non-ionizing radiation. The major drawback has been the non-environmentally friendly nature and toxicity of some of these radiation sources as well as the complete removal of the metal-containing sludge generated from using conventional catalysts. Deep Eutectic Solvents (DESs) have found a wide range of industrial applications due to their tune-able characteristics. These characteristics have made for their excellent applications in the production of pharmaceutics, the removal of heavy metals from wastewater; as electrolytes in electro-deposition processes, in biodiesel synthesis, and in the dehydration of natural gas to mention but a few. The application of DESs in the synthesis of organic compounds as solvents and/or catalysts is still at its infancy. Some works have shown the ability of certain DESs to generate oxygen atoms during oxygen transfer reactions. This prompted the investigation into its ability to generate other reactive species. This paper provided current information on the potential of DESs for the production of peroxyacids that can eventually facilitate the generation of hydroxyl radicals (•OH). This will further broaden the application of DESs in organic synthesis and degradation processes, as well as in wastewater treatment.

Keywords: Deep Eutectic Solvent; H_2O_2; Reactive Oxygen Specie; OH radical; Organic Pollutant

1 INTRODUCTION

Reactive oxygen species are radicals and/or molecular species with known physicochemical properties. They are required in major organic synthesis for reactions to occur. They react with organic species to create intermediates that facilitate organic synthesis but are short-lived. Organic synthesis, over the years, has been carried out by the use of metal-catalyzed oxidative processes in solvents (1–3). The increase in demand for solvents (inorganic and organic) in industrial processes has been estimated to be USD 47.37 billion in 2018 and is predicted to attain USD 64.32 billion by 2026 (4). Due to the projected increase in the volume of solvents needed in industries, the need for greener solvents as renewable substitutes is still trending research because conventional organic solvents are known to be

flammable, toxic, volatile, and require energy-consuming processes to be reused (5).

Recently, the research spotlight has been beamed towards the utilization of Ionic Liquids (ILs) that act as both solvents and catalysts aimed at improving both the yield and selectivity of the product (6–10). Ionic Liquids (ILs) have been deeply researched into as green solvents but their drawbacks include broad choices of cations and anions which results in numerous types having varying negative impacts on the environment (phytotoxicity and toxicity to aquatic ecosystems); as well as their complex, time-consuming and expensive preparation methods (11–13). This has prompted further research into other types of green solvents with DESs emanating as the suitably auspicious substitute (14). With the unending need for greener solvents, the growth of the solvent market is geared towards the use of biodegradable and ecosystem-friendly solvents. This is been strictly monitored by the Environmental Protection Agency (EPA) regulations. Abbot et al in their work named Deep Eutectic Solvents as a new generation of green solvents which is widely accepted as an ideal substitute to ILs and organic solvents.

Deep Eutectic Solvents (DESs) are prepared mostly by the combination of a Hydrogen Bond Donor (HBD) with a Hydrogen Bond Acceptor (HBA). This results in a eutectic liquid with a low melting point when compared with the melting points of the individual constituents. DESs have been embraced prominently as an extremely good replacement for ILs because they are readily available, stable thermally, biologically degradable, non-poisonous, and inexpensive (15–19). Therefore, DESs have demonstrated their promising importance due to their high-ranking chemical qualities which makes them have extensive engineering applications. These applications include: as catalysts in organic processes and reactions; gas entrapment and segregation; storage of proteins; chemistry of polymers; development of smart nanomaterials; drug dissolution; and biopolymer solubilization among others (17,19,20).

2 LITERATURE REVIEW/STATE OF THE ART OF DESs

DESs production process in which quaternary ammonium salts are HBA entails the use of an easy one-pot method that involves the blending of the HBA alongside different organic compounds and inorganic salts as HBD. Through diverse researches, a large variety of hydrogen bond acceptors such as Choline chloride, Betain and quaternary salts of ammonium/phosphonium, and hydrogen bond donors which includes Amide, Carboxylic acids, Esters and Polyols, have been explored which has facilitated the ease of tuning eutectic compositions and eutectic temperature (17,21) Therefore, DESs have demonstrated their promising importance due to their high ranking chemical qualities which makes them have extensive engineering applications. These applications include: as catalysts in organic processes and reactions; gas entrapment and segregation; storage of proteins; chemistry of polymers; development of smart nanomaterials; drug dissolution; and biopolymer solubilization among others (17,19,21).

They present the under-listed excellent characteristics among others (22–24):

a. Low-priced due to low cost and readily available precursors or starting materials.
b. Simple synthesis method without the need for purification and waste disposal.
c. Safe to be used because most of the formulations are non-toxic.
d. Biodegradable
e. Environmentally friendly that's why they are called “green solvents”.
f. Good biocompatibility since quaternary ammonium salts such as choline chloride was used as an additive in chicken feed.
g. Very low volatile organic compound (VOC) compared to ordinary solvent.
h. Sustainable.
i. Non-flammable and non-reactive to water.

The classification of deep eutectic solvents is typically into four categories. In Table 1, different types of deep eutectic solvents depicting the HBA and HBD combinations have been captured. The type C DES has been the principal focal point in most researches. The cationic portion (Cat^+) in DES is normally Quaternary Ammonium (QA) salts, Quaternary Phosphonium (QP) salts, and in some cases Sulphonium salt (19). The anionic portion (X^-) usually interacts with protons emanating from the donating RZ group (where R = alkyl group and Z = $CONH_2$, COOH, or OH) through hydrogen bonding. The commonly used QA salt for DES manufacturing is choline chloride. This is because it is cheap, readily available, biocompatible, and has low toxicity.

Table 1: Classes of Deep Eutectic Solvents (Adapted from (19))

Type	General Formula	Terms	Combination
A	$Cat^+X^- zMCl_x$	M= Zn, Sn, Al, Ga, In	Metal salt + Organic salt
B	$Cat^+X^- zMCl_x{\cdot}YH_2O$	M=Cr, Co, Cu, Ni, Fe	Metal salt hydrate + organic salt
C	$Cat^+X^- zRZ$	Z= $CONH_2$, COOH, OH	Organic salt + HDB
D	$MCl_x+RZ=MCl^+_{x-1}{\cdot}RZ+MCl^-_{x-1}$	M= Al, Zn and Z= $CONH_2$, OH	Metal salt hydrate + HBD

Type A DES is made up of QA salt and metal halide, while type B is made up of QA salt and metal halide hydrate. Type C DES contains an organic salt and hydrogen bond donor, and type D contains metal chloride and HBD. This work is focused on type C DES because it is the most suitable and applicable for our targeted process. The type C DES which is made up of an organic salt as the hydrogen bond donor can also be further classified into four. These are:

i. *Low Transition Temperature Mixtures (LTTMs)* – these are majorly produced by combining natural high-melting-point precursors that are transformed into a liquid through hydrogen bonding, and they have remarkable applications in organic synthesis (25–27) biofuel processing (28,29), and catalysis (30,31).
ii. *Natural Deep Eutectic Solvents (NADESs)* - are manufactured through the process of combining organic salts with naturally occurring organic compounds such as citric acid, fructose, glucose,

proline, and supplementary substances to form highly viscous liquids at well-defined molar proportions (32). Their manufacturing, categorization, qualitative and quantitative description, and use include usage in extraction and biomass pretreatment (17,18,33–37). Their use has also extended to pharmaceuticals, cosmetics, food, and agriculture (38). Furthermore, they are used as solvents for organic and inorganic compounds and as an environment for enzymatic reactions (38).

iii. *Carboxylic Acid-Based Deep Eutectic Solvents (CADESs)* – here hydrogen bond donor includes different carboxylic acids (20,39,40).

iv. *Therapeutic Deep Eutectic Solvents (THEDESs)* – these represent a subgroup of NADES with a pharmaceutically active ingredient as a major constituent (41,42)

DESs can also be classified based on their affinity for water which makes them either hydrophobic or hydrophilic. Hydrophobic DES (HDES**)** are water-insoluble deep eutectic solvents. The concept of HDES was introduced by Van Osch *et al* (2015). Their work included mixing different QA salts alongside capric acid. The hydrophobic solvent produced was then used for the extraction of volatile organic compounds that are insoluble in water. The outcome of this was a process with high extraction yield and efficiency (43). Since then, active research has been on-going to explore how HDES is manufactured and its use in different fields. Hydrophilic DESs are water-soluble DESs. The majority of the synthesized and reviewed DESs are hydrophilic and LTTMs and NADES fall into this category.

3 DES FOR OXIDATION REACTIONS

DESs have been used in different types of oxidation reactions. It is interesting to know that DESs have been used to activate oxidants such as H_2O_2, N-bromosuccinimide (NBS), Oxygen (O_2) atom, and peroxy monosulphate (PMS) among others.

Table 2:Oxidation Reactions using Deep Eutectic Solvents

DES	Oxidant	Reaction	Result	Reference
ChCl/Urea	N-bromosuccinimide (NBS)	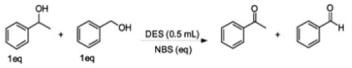	Yield =100 % 5 min @ 60 ºC 40 min @ room temperature	(53)
ChCl/*p*-TsOH TBAC/*p*-TsOH	H_2O_2	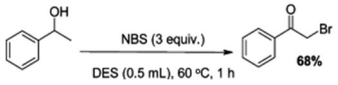	Yield = 90.7 % Feed ratio=2.5 wt.% DES molar ratio = 1:1 80 ºC , 1 hour	(54)
ChCl and 1,1,1,3,3,3-Hexafluoro-2-Propanol (HFIP)	H_2O_2	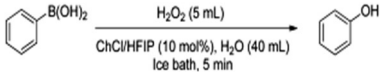	Yield = 95 % phenol Room temperature 10 mol% DES 5 ml H_2O_2, 5 minutes	(58)
ChCl/Oxalic acid	H_2O_2	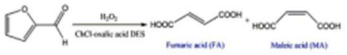	50-60 ºC Yield = 95.7 %	(44)
ChCl/Urea	H_2O_2	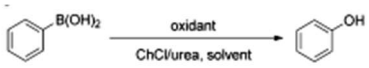	Room temperature 10 mol% DES 5 ml H_2O_2, 92 % phenol yield, 5 minutes	(28)
N,N-dimethyl-(4-(2,2,6,6-tetramethyl-1-oxyl-4-piperidoxyl)butyl)dodecyl ammonium salt ([Quaternium-TEMPO]$^+$Br$^-$)/urea	O_2	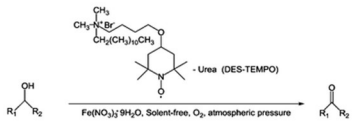	$Fe(NO_3)_3{\cdot}9H_2O$ (co-catalyst), 60 ºC, 90 min, 100 % yield 99 % selectivity	(16)
$CoCl_2$-ChCl/2PEG	Peroxymonosulphate (PMS)	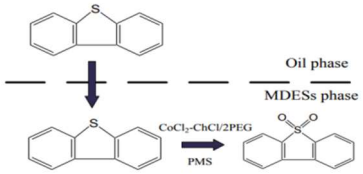	20 °C, 60 min. 100 % sulfur removal	(59)
p-TsOH/PEG	O_2	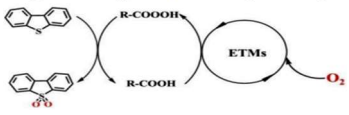	30 min, 70 ºC, 100 % removal of Dibenzotheophene (DBT)	(45)

DES had been demonstrated to activate hydrogen peroxide effectively by the formation of multiple hydrogen bonds. Wang et al (2013) designed a procedure for a sustainable oxidative hydroxylation of Phenyl boronic acid while H_2O_2 served as oxidant and ChCl/Urea with water as solvents. The urea portion of the DES polarized the oxidant through H-bonding resulting in an electrophilic activation of H_2O_2 as depicted in Scheme 1. The activated peroxide as seen in Scheme 2 thereafter attacks the boronic acid. Subsequent migration coupled with the hydrolysis of phenyl gave the final product at room

temperature operating conditions. The optimization of the reaction was achieved with 10mol% ChCl/Urea, 5 mol % H2O2, and 2ml water.

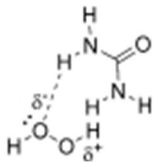

Scheme 1: Electrophilic Activation of H_2O_2 by Urea (28)

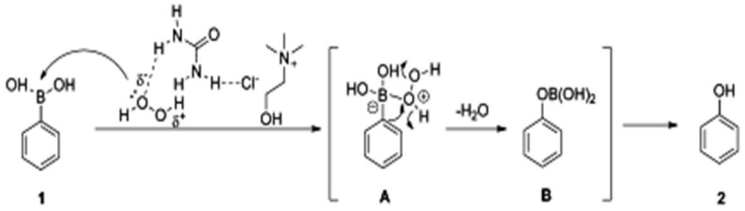

Scheme 2: Synthesis of Phenol from Phenyl boronic acid by the activated H_2O_2 (58)

Also, Berkessel and Adrio carried out a meticulous investigation of the epoxidation of olefins while using hydrogen peroxide alongside 1,1,1,3,3,3- hexafluoro-2-propanol (HFIP). A detailed mechanism of the reaction was reported and multiple hydrogen bonds were identified has been responsible for the reaction (60).

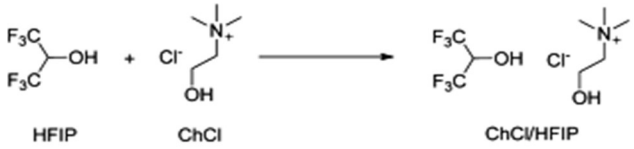

Scheme 3: Choline Chloride/ 1,1,1,3,3,3- hexafluoro-2-propanol (HFIP) DES (46)

HFIP has been reported to display large hydrogen bond donor ability, great ionizing power, ability to solvate water, as well as low nucleophilicity. Its high hydrogen bond donor ability makes it suitable for the formation of type C deep eutectic solvent when in combination with an organic salt such as choline chloride (Scheme 3). It has been researched to have a great effect on organic transformations (61,62), and interestingly it can activate hydrogen peroxide for oxidation reactions (63,64). The activation of H_2O_2 by HFIP proceeds in two stages, viz:

a. acting as a strong hydrogen bond donor
b. juxtaposing of positive and negative partial charges within the transition states (60).

The hydrogen bonding ability of the O-H hydrogen atom coupled with fluorine's strong electron-withdrawing properties leads to the generation of electrophilically activated hydrogen peroxide intermediates as seen in Scheme 4 (65).

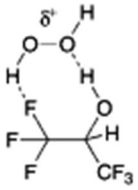

Scheme 4: Electrophilic Activation of H_2O_2 by HFIP (65)

Wang *et al* (2014) produced an outstanding yield of phenols at room temperature, within 5 to 10 minutes through an eco-friendly practical oxidative hydroxylation of aryl/heteroaryl boronic acids. DES composed of ChCl and 1,1,1,3,3,3-hexafluoro-2-propanol (HFIP) acted as the catalyst while the oxidant was hydrogen peroxide. Recovery of the DES was by simple filtration coupled with evaporation, and there was no distinctive loss of its activity after been used five times. Their newly developed protocol was more environmentally friendly, the substrates had broad compatibility, there was no need for the use of metal and additives, as well as gram-scale production (58).

In the work done by Wang and co-workers as captured in Scheme 5, the activated hydrogen peroxide was shown to attack the boronic acid to produce an intermediate. The migration of the phenyl group from boron atom to an oxygen atom of H_2O_2 resulted in a boronate ester (B). This thereafter hydrolyses to give phenol as the final product (58).

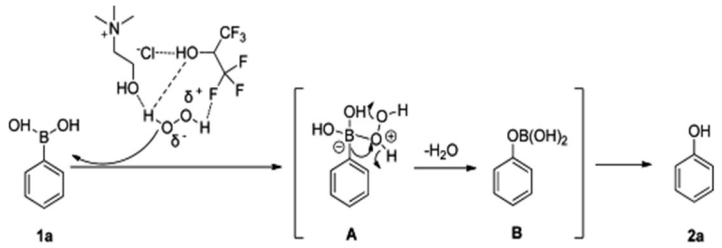

Scheme 5: Synthesis of Phenol from Phenyl boronic acid by the HFIP activated H_2O_2 (58)

In general, the schemes 1,2,3,4,5 above involve:

a. the activation of H_2O_2 by a component of DES through multiple hydrogen bonds which leads to the polarization of the O-O bond in H_2O_2
b. less negatively charged polarized oxygen atom of H_2O_2 experience a nucleophile attack
c. the organic reaction of activated H_2O_2 with the substrate by oxygen transfer

It is important to note that not all organic reactions can occur through oxygen transfer alone. Others can only proceed in the presence of other Reactive Oxygen Species (ROS) such as hydroperoxyl radical ($\bullet\ OOH$), superoxide ($\bullet O_2^-$), and hydroxyl radical ($\bullet\ OH$) amongst others. This, therefore, necessitates the investigation of the possibility of generating other types of ROS from DES with OH radical being of particular interest.

4 DES FOR THE GENERATION OF HYDROXYL RADICAL (•OH)

The production of OH radicals from DES can be achieved by two major steps. These are:

1. Formation of peroxy acids
2. Homolysis of the peroxy acids

4.1 DES for the formation of peroxy acids/peracids

Peroxy acids are peroxides produced by reacting carboxylic acids with hydrogen peroxide in the company of a strong acid. They are strong oxidants and are more reactive than hydrogen peroxide. The oxidation capability of peroxides is connected to the substituent's electronegativity. Electrophilic peroxides are known to be stronger oxygen-atom transfer agents because their tendency to donate oxygen-atom corresponds with the acidity of the O-H bond.

Dai *et al* (2014) as part of their program for renewable catalysis and synthesis established the fact that certain DESs could systematically activate hydrogen peroxide. The competency of the oxidation was explained by a synergy between ChCl/*p*-TSA and H_2O_2. A strong hydrogen bond was formed between the DES and H_2O_2, thereby increasing the electrophilicity of one of the peroxy oxygen atoms of H_2O_2 (66).

According to Wang *et al* (2013), the proposed mechanism for activating hydrogen peroxide productively by DES is initiated by polarizing the peroxide bond by hydrogen bonding. The activated peroxide in turn invades targeted compounds which results in the final product. The carboxylic acids in DESs are usually oxidized into peracids when reacted with hydrogen peroxide. Targeted reactants are in turn oxidized by the peracids formed by the DESs and the peroxy acids undergo simultaneous reduction. The reduced peracid can thereafter be further oxidized by hydrogen peroxide, leading to the beginning of another catalytic cycle (28).

The contemporary standard protocol for oxidative desulphurization in which organic acids are used as catalysts is connected to the generation of peroxy acids (peracids) (67). Desulphurization by oxidation in the oxalate-based DESs together with H_2O_2 involves the generation of intermediates which are radicals of peracids. Percaids are powerful oxidizing agents that are produced by the interaction of H_2O_2 with carboxylic acids.

Since the electronegativity of the substituent of peracids is higher than that of hydrogen, they tend to be more aggressive oxidizing agents. Asides the fact that they are strong oxidizing agents; they are also an excellent source for the generation of OH radical because the peroxy-oxygen atom bond can easily be dissociated which makes it easy to disintegrate by homolytic fission.

4.2 Homolysis of peroxy acids for the generation of OH radical

The homolysis of peracids at the O-O bond has been proven to generate radicals (including •OH) that are capable of interacting with the organic contaminants to degrade them (68). Heywood *et al* (1961)

proposed the mechanism for the homolytic fission of peracetic acid and the mechanism proposed is as follows:

$$CH_3COOH + H_2O_2 \rightarrow CH_3COOOH + H_2O \quad \textbf{Equation 1}$$

$$CH_3COOOH \overset{homolysis}{\rightleftarrows} CH_3COO\bullet + \bullet OH \quad \textbf{Equation 2}$$

The formed hydroxyl radical can invade not only the organic pollutant but also the peracetic acid molecule itself.

$$CH_3COOOH + \bullet OH \rightarrow CH_3CO\bullet + O_2 + H_2O \quad \textbf{Equation 3}$$

$$CH_3COOOH + \bullet OH \rightarrow CH_3COOO\bullet + H_2O \quad \textbf{Equation 4}$$

The very unstable primary acyloxy radical separates into a methyl radical as well as carbon dioxide by monomolecular decarboxylation (69).

$$CH_3COO\bullet \rightarrow \bullet CH_3 + CO_2 \quad \textbf{Equation 5}$$

$$2CH_3COO\bullet \rightarrow 2\bullet CH_3 + 2CO + O_2 \quad \textbf{Equation 6}$$

However, reactions having a resonance stabilized carbon-centered radicals are reversible and the reversible reaction is succeeded by interacting the methyl radicals with oxygen to generate weak peroxy radicals (70).

$$\bullet CH_3 + O_2 \rightarrow \bullet CH_3OO \quad \textbf{Equation 7}$$

This reaction in equation 7 is known to be quick in oxygen-rich environments, thereby limiting the number of methyl radicals in the reacting media (71). The primarily formed hydroxyl radical reacts side-by-side with $CH_3C(=O)O\bullet$ to produce fresh peracid molecule, thereby re-initiating the oxidation cycle (72).

$$\bullet OH + CH_3COO\bullet \rightarrow CH_3COOOH \quad \textbf{Equation 8}$$

It is imperative to note that all generated radicals can react with the target organic compound, thereby adding to its degradation and oxidation.

5 CONCLUSIONS

Despite the remarkable achievements in the use of metal-catalyzed and metal-free oxidation processes, there is still a need to enhance the environmentally friendliness and cost-effectiveness of these materials in the processes. The use of ionic liquids for the generation of reactive species also have drawbacks such as the selection of non-hazardous ILs, biodegradability, and non-toxicity of used ILs, and synthesis from non-expensive and readily available raw materials.

DESs are proposed as potential substitute because of their low toxicity and environmental friendliness. Over the years, deep eutectic solvents have been used as both solvents and catalysts in

many processes. Their use in these processes has exposed them to various operating conditions, and different oxidants. Worthy of note is their ability to catalyze and activate hydrogen peroxide, a powerful oxidizing agent for the generation of reactive oxygen species which makes them important catalysts in oxidation reactions. Different research works have proven the ability of some deep eutectic solvents to generate oxygen atoms during oxygen transfer reactions. In short, this overview presented in this article has underpinned the potentials of DESs for the generation of hydroxyl radicals (•OH). The study also suggested sustainable protocols for generating OH radicals from DESs.

REFERENCES

1. Lipshutz BH, Gallou F, Handa S. Evolution of solvents in organic chemistry. ACS Sustain Chem Eng. 2016;4(11):5838–49.
2. Díaz-Álvarez AE, Francos J, Lastra-Barreira B, Crochet P, Cadierno V. Glycerol and derived solvents: New sustainable reaction media for organic synthesis. Chem Commun. 2011;47(22):6208–27.
3. Z. Andrade C, Alves L. Environmentally Benign Solvents in Organic Synthesis: Current Topics. Curr Org Chem. 2005;9(2):195–218.
4. Reports And Data. Solvents Market to Reach USD 17.99 Billion by 2026 | Reports and Data (June 06, 2019). Retrieved from https://www.globenewswire.com/news release/2019/06/06/1865517/0/en/Solvents-Market-To-Reach-USD-17-99-Billion-By-2026- Reports-And-Data.html. Globenewswire. Accessed June 2020.
5. Clarke CJ, Tu WC, Levers O, Bröhl A, Hallett JP. Green, and Sustainable Solvents in Chemical Processes. Chem Rev. 2018;118(2):747–800.
6. Kumar M, Trivedi N, Reddy CRK, Jha B. Toxic effects of imidazolium ionic liquids on the green seaweed Ulva Lactuca: Oxidative stress and DNA damage. Chem Res Toxicol. 2011;24(11):1882–90.
7. Dharaskar Swapnil A. Ionic Liquids (A Review): The Green Solvents for Petroleum and Hydrocarbon Industries. Res J Chem Sci. 2012;2(8):80–5.
8. Rong M, Liu C, Han J, Wang H. Catalytic oxidation of alcohols by a double functional ionic liquid [bmim]BF4. Catal Commun. 2009;10(4):362–4. http://dx.doi.org/10.1016/j.catcom.2008.09.009
9. Karthikeyan P, Arunrao AS, Narayan MP, Kumar SS, Kumar SS, Bhagat PR. Selective oxidation of alcohol to carbonyl compound catalyzed by L-aspartic acid coupled imidazolium-based ionic liquid. J Mol Liq. 2012;173:180–3. http://dx.doi.org/10.1016/j.molliq.2012.06.018
10. Parvulescu VI, Hardacre C. Catalysis in ionic liquids. Chem Rev. 2007;107(6):2615–65.
11. Amde M, Liu JF, Pang L. Environmental Application, Fate, Effects, and Concerns of Ionic

Liquids: A Review. Environ Sci Technol. 2015;49(21):12611–27.

12. Dai C, Zhang J, Huang C, Lei Z. Ionic Liquids in Selective Oxidation: Catalysts and Solvents. Chem Rev. 2017;117(10):6929–83.
13. Zhang Y, Bakshi BR, Demessie ES. Life cycle assessment of an ionic liquid versus molecular solvents and their applications. Environ Sci Technol. 2008;42(5):1724–30.
14. Guajardo N, Carlesi C, Schrebler R, Morales J. Applications of Liquid/Liquid Biphasic Oxidations by Hydrogen Peroxide with Ionic Liquids or Deep Eutectic Solvents. Chempluschem. 2017;82(2):165–76.
15. Abbott AP, Capper G, Davies DL, Rasheed RK, Tambyrajah V. Novel solvent properties of choline chloride/urea mixtures. Chem Commun. 2003;(1):70–1.
16. Zhang Y, Lü F, Cao X, Zhao J. Deep eutectic solvent supported TEMPO for the oxidation of alcohols. RSC Adv. 2014;4(76):40161–9. http://dx.doi.org/10.1039/C4RA05598E
17. Dai Y, van Spronsen J, Witkamp GJ, Verpoorte R, Choi YH. Natural deep eutectic solvents as new potential media for green technology. Anal Chim Acta. 2013;766:61–8. http://dx.doi.org/10.1016/j.aca.2012.12.019
18. Paiva A, Craveiro R, Aroso I, Martins M, Reis RL, Duarte ARC. Natural deep eutectic solvents - Solvents for the 21st century. ACS Sustain Chem Eng. 2014;2(5):1063–71.
19. Smith EL, Abbott AP, Ryder KS. Deep Eutectic Solvents (DESs) and Their Applications. Chem Rev. 2014;114:11060–82.
20. Ge X, Gu C, Wang X, Tu J. Deep eutectic solvents (DESs)-derived advanced functional materials for energy and environmental applications: Challenges, opportunities, and future vision. J Mater Chem A. 2017;5(18):8209–29. http://dx.doi.org/10.1039/C7TA01659J
21. Florindo C, Oliveira FS, Rebelo LPN, Fernandes AM, Marrucho IM. Insights into the synthesis and properties of deep eutectic solvents based on cholinium chloride and carboxylic acids. ACS Sustain Chem Eng. 2014
22. Zhang Q, De Oliveira Vigier K, Royer S, Jérôme F. Deep eutectic solvents: Syntheses, properties, and applications. Chem Soc Rev. 2012;41(21):7108–46.
23. Hayyan M, Hashim MA, Hayyan A, Al-Saadi MA, AlNashef IM, Mirghani MES, et al. Are deep eutectic solvents benign or toxic? Chemosphere. 2013;90(7):2193–5. http://dx.doi.org/10.1016/j.chemosphere.2012.11.004
24. Abbott AP, Alaysuy O, Antunes APM, Douglas AC, Guthrie-Strachan J, Wise WR. Processing of leather using deep eutectic solvents. ACS Sustain Chem Eng. 2015;3(6):1241–7.
25. Avalos M, Babiano R, Cintas P, Jiménez JL, Palacios JC. Greener media in chemical synthesis and processing. Angew Chemie - Int Ed. 2006;45(24):3904–8.
26. Patil UB, Shendage SS, Nagarkar JM. One-pot synthesis of nitriles from aldehydes catalyzed by a

deep eutectic solvent. Synth. 2013;45(23):3295–9.

27. Wang L, Dai DY, Chen Q, He MY. Rapid, sustainable, and gram-scale synthesis of phenols catalyzed by a biodegradable deep eutectic mixture in water. Asian J Org Chem. 2013;2(12):1040–3.
28. Hayyan M, Mjalli FS, Hashim MA, AlNashef IM. A novel technique for separating glycerine from palm oil-based biodiesel using ionic liquids. Fuel Process Technol. 2010;91(1):116–20. http://dx.doi.org/10.1016/j.fuproc.2009.09.002
29. Shahbaz K, Mjalli FS, Hashim MA, AlNashef IM. Using deep eutectic solvents based on methyl triphenylphosphonium bromide for the removal of glycerol from palm-oil-based biodiesel. Energy and Fuels. 2011;25(6):2671–8.
30. Francisco M, Van Den Bruinhorst A, Kroon MC. New natural and renewable low transition temperature mixtures (LTTMs): Screening as solvents for lignocellulosic biomass processing. Green Chem. 2012;14(8):2153–7.
31. Ruß C, Burkhard K. Low melting mixtures in organic synthesis – an alternative to ionic liquids? Green Chem. 2012;14(11):2969–82. http://xlink.rsc.org/?DOI=C5TC02043C
32. Choi YH, van Spronsen J, Dai Y, Verberne M, Hollmann F, Arends IWCE, et al. Are natural deep eutectic solvents the missing link in understanding cellular metabolism and physiology? Plant Physiol. 2011;156(4):1701–5.
33. Radosevic K, Curko N, Svrcek VG, Bubalo MC, Tomasevic M, Ganic KK, et al. Natural deep eutectic solvents as beneficial extractants for enhancement of plant extracts bioactivity. LWT-Food Sci Technol. 2016;(73):45–51.
34. Lynam, J.G., Kumar, N. and Wong, M.J. (2017). Deep eutectic solvents' ability to solubilize lignin, cellulose, and hemicellulose; thermal stability; and density. *Bioresource technology*, 238:684-689.
35. Fernández M de Los Á, Boiteux J, Espino M, Gomez FJV, Silva MF. Natural deep eutectic solvents-mediated extractions: The way forward for sustainable analytical developments. Anal Chim Acta. 2018;1038:1–10. https://doi.org/10.1016/j.aca.2018.07.059
36. Liu Y, Friesen JB, McAlpine JB, Lankin DC, Chen SN, Pauli GF. Natural Deep Eutectic Solvents: Properties, Applications, and Perspectives. J Nat Prod. 2018;81(3):679–90.
37. Satlewal A, Agrawal R, Bhagia S, Sangoro J, Ragauskas AJ. Natural deep eutectic solvents for lignocellulosic biomass pretreatment: Recent developments, challenges, and novel opportunities. Biotechnol Adv. 2018;36(8):2032–50. https://doi.org/10.1016/j.biotechadv.2018.08.009
38. Vanda H, Dai Y, Wilson EG, Verpoorte R, Choi YH. Green solvents from ionic liquids and deep eutectic solvents to natural deep eutectic solvents. Comptes Rendus Chim. 2018;21(6):628–38.

https://doi.org/10.1016/j.crci.2018.04.002

39. Abbott AP, Boothby D, Capper G, Davies DL, Rasheed R. Deep Eutectic Solvents Formed Between Choline Chloride and Carboxylic Acids. J Am Chem Soc. 2004;
40. Li JJ, Xiao H, Tang XD, Zhou M. Green Carboxylic Acid-Based Deep Eutectic Solvents as Solvents for Extractive Desulfurization. Energy and Fuels. 2016;30(7):5411–8.
41. Aroso IM, Craveiro R, Rocha Â, Dionísio M, Barreiros S, Reis RL, et al. Design of controlled release systems for THEDES - Therapeutic deep eutectic solvents, using supercritical fluid technology. Int J Pharm. 2015;492(1–2):73–9. http://dx.doi.org/10.1016/j.ijpharm.2015.06.038
42. Aroso IM, Silva JC, Mano F, Ferreira ASD, Dionísio M, Sá-Nogueira I, et al. Dissolution Enhancement of active pharmaceutical ingredients by therapeutic deep eutectic systems. Eur J Pharm Biopharm. 2016;98(November):57–66. http://dx.doi.org/10.1016/j.ejpb.2015.11.002
43. Van Osch DJGP, Zubeir LF, Van Den Bruinhorst A, Rocha MAA, Kroon MC. Hydrophobic deep eutectic solvents as water-immiscible extractants. Green Chem. 2015;17(9):4518–21.
44. Ni Y, Bi Z, Su H, Yan L. Deep eutectic solvent (DES) as both solvent and catalyst for oxidation of furfural to maleic acid and fumaric acid. Green Chem. 2019;21(5):1075–9.
45. Sun L, Su T, Xu J, Hao D, Liao W, Zhao Y, et al. Aerobic oxidative desulfurization coupling of Co polyanion catalysts and: P -TsOH-based deep eutectic solvents through a biomimetic approach. Green Chem. 2019;21(10):2629–34.
46. Wang L, Zhu KQ, Chen Q, He MY. Facile and environmentally friendly halogenation of BODIPYs in a deep eutectic solvent. Dye Pigment. 2015;112:274–9. http://dx.doi.org/10.1016/j.dyepig.2014.07.024
47. Cicco L, Ríos-Lombardía N, Rodríguez-Álvarez MJ, Morís F, Perna FM, Capriati V, et al. Green Chemistry. Green Chem. 2018;
48. Piemontese L, Sergio R, Rinaldo F, Brunetti L, Perna FM, Santos MA, et al. Deep Eutectic Solvents as Effective Reaction Media for the Synthesis of 2 - Hydroxyphenylbenzimidazole - based Scaffolds en Route to Donepezil - Like Compounds. Molecules. 2020;25(574):2–15.
49. Morales RC, Tambyrajah V, Jenkins PR, Davies DL, Abbott AP. The regiospecific Fischer indole reaction in choline chloride·2ZnCl2 with product isolation by direct sublimation from the ionic liquid. Chem Commun. 2004;
50. Singh BS, Lobo HR, Shankarling GS. Choline chloride-based eutectic solvents: Magical catalytic system for carbon-carbon bond formation in the rapid synthesis of β-hydroxy functionalized derivatives. Catal Commun. 2012;24:70–4. http://dx.doi.org/10.1016/j.catcom.2012.03.021
51. De Santi V, Cardellini F, Brinchi L, Germani R. Novel Brønsted acidic deep eutectic solvent as reaction media for esterification of a carboxylic acid with alcohols. Tetrahedron Lett. 2012;53(38):5151–5. http://dx.doi.org/10.1016/j.tetlet.2012.07.063

52. Azizi N, Batebi E. Highly efficient deep eutectic solvent catalyzed ring-opening of epoxides. Catal Sci Technol. 2012;2(12):2445–8.
53. Azizi N, Khajeh M, Alipour M. Rapid and selective oxidation of alcohols in a deep eutectic solvent. Ind Eng Chem Res. 2014;53(40):15561–5.
54. Yin J, Wang J, Li Z, Li D, Yang G, Cui Y, et al. Deep desulfurization of fuels based on an oxidation/extraction process with acidic deep eutectic solvents. Green Chem. 2015;17(9):4552–9.
55. Assanosi A, Farah MM, Wood J, Al-Duri B. Fructose dehydration to 5HMF in a green self-catalyzed des composed of N, N-diethylethanolammonium chloride, and p-toluenesulfonic acid monohydrate (p-TSA). In: Comptes Rendus Chimie. 2016.
56. Gawade AB, Yadav GD. Biomass and Bioenergy Microwave-assisted synthesis of 5-ethoxy methyl furfural in one pot from D - fructose by using deep eutectic solvent as catalyst under mild condition. Biomass and Bioenergy. 2018;117 (July 2016):38–43. https://doi.org/10.1016/j.biombioe.2018.07.008
57. Rushell E, Tailor YK, Khandelwal S, Verma K, Agarwal M, Kumar M. Deep eutectic solvent promoted synthesis of structurally diverse hybrid molecules with privileged heterocyclic substructures. New J Chem. 2019;43(31):12462–7.
58. Wang L, Dai DY, Chen Q, He MY. Rapid and green synthesis of phenols catalyzed by a deep eutectic mixture based on fluorinated alcohol in water. J Fluor Chem. 2014;158:44–7. http://dx.doi.org/10.1016/j.jfluchem.2013.12.006
59. Xu H, Zhang D, Wu F, Wei X, Zhang J. Deep desulfurization of fuels with cobalt chloride-choline chloride/polyethylene glycol metal deep eutectic solvents. Fuel. 2018;225(March):104–10. https://doi.org/10.1016/j.fuel.2018.03.159
60. Berkessel A, Adrio JA. Dramatic acceleration of olefin epoxidation in fluorinated alcohols: Activation of hydrogen peroxide by multiple H-bond networks. J Am Chem Soc. 2006;128(41):13412–20.
61. Khaksar S, Talesh SM. A simple, efficient, and green procedure for the synthesis of bis-indolyl methanes in 1,1,1,3,3,3-hexafluoro-2-propanol. J Fluor Chem. 2012;135:87–90.
62. Khaksar S, Talesh SM. Transition metal-free oxidation of activated alcohols to aldehydes and ketones in 1,1,1,3,3,3-hexafluoro-2-propanol. J Fluor Chem. 2012;140:95–8.
63. Berkessel A, Andreae MRM, Hans S, Johann L. Baeyer±Villiger Oxidations with Hydrogen Peroxide in Fluorinated Alcohols: Lactone Formation by a Nonclassical Mechanism. Angew Chemie Int Ed. 2002;41(23):4481–4.
64. Legros J, Crousse B, Bonnet-Delpon D, Bégué JP. Urea-hydrogen peroxide/hexafluoro-2-propanol: An efficient system for a catalytic epoxidation reaction without a metal. European J

Org Chem. 2002;(19):3290–3.

65. Neimann K, Neumann R. Electrophilic activation of hydrogen peroxide: Selective oxidation reactions in perfluorinated alcohol solvents. Org Lett. 2000;2(18):2861–3.
66. Dai DY, Wang L, Chen Q, He MY. Selective oxidation of sulfides to sulfoxides catalyzed by deep eutectic solvent with H_2O_2. J Chem Res. 2014;38(3):183–5.
67. Fierro JLG. Oxidative processes of the desulfurization of liquid fuels. 2010;(January):879–90.
68. Rokhina E V., Makarova K, Golovina EA, Van As H, Virkutyte J. Free radical reaction pathway, thermochemistry of peracetic acid homolysis, and its application for phenol degradation: Spectroscopic study and quantum chemistry calculations. Environ Sci Technol. 2010;44(17):6815–21.
69. Heywood, D., Phillips, B., & Stansbury HA. Free radical hydroxylations with peracetic acid. J Org Chem. 1961;26(1):281.
70. El-Agamey A, McGarvey DJ. Evidence for a lack of reactivity of carotenoid addition radicals towards oxygen: A laser flash photolysis study of the reactions of carotenoids with acyl peroxyl radicals in polar and non-polar solvents. J Am Chem Soc. 2003;
71. Shi HC, Li Y. Formation of nitroxide radicals from secondary amines and peracids: A peroxyl radical oxidation pathway derived from electron spin resonance detection and density functional theory calculation. J Mol Catal A Chem. 2007;271(1–2):32–41.
72. Baciocchi, R., Ciotti, C., Cleriti, G., & Chiavola A. Peroxy-acids as an innovative oxidant for the remediation of contaminated sediments. In: Paper presented at the FZK/TNO Conference on contaminated soils. 2008.

The Use of Basic Oxygen Furnace Slag as a Substitute for Lime in Acid Mine Drainage Treatment

T.S. Naidu[1*], L.D. van Dyk[1] and C.M. Sheridan[2]

[1]School of Chemical Engineering, University of the Witwatersrand, Johannesburg, South Africa

[2]School of Geology, University of the Witwatersrand, Johannesburg, South Africa.

[*]Corresponding author: tsnaidu@live.co.za

ABSTRACT

Acid mine drainage (AMD) and basic oxygen furnace slag (BOFS) are both waste products produced in massive quantities throughout the world in the mining and steel industries. These products require extensive treatment before release back into the environment or before reuse in other industries can occur. A method to treat AMD using BOFS was thus conceptualized with the aim of treating AMD and BOFS for further reuse. An investigation into the replacement of lime (a traditional reagent) with BOFS in AMD treatment was conducted in this regard, to determine if BOFS was effective in raising the pH of AMD and subsequently lowering the metal and sulfate content via precipitation reactions. A number of titration experiments were undertaken to determine the extent of treatment and it was found that BOFS is effective in the treatment of AMD. Literature was consulted to determine the most likely mechanism for removal. It was found that treatment occurred via hydration and dissociation of BOFS (resulting in leaching and partial dissolution of the BOFS) which subsequently led to the precipitation of metal hydroxides, oxides, sulfates, sulfides and silicates in a sludge.

Keywords: acid mine drainage; basic oxygen furnace slag; alkaline materials

1 INTRODUCTION

Acid mine drainage (AMD) is a major environmental problem in many countries, resulting from oxidation of sulfide minerals which are exposed to the atmosphere by mining and excavation activities. AMD can be (and is commonly) treated by adding a source of alkalinity (traditionally hydrated lime or limestone), which causes the pH to increase and subsequently precipitates a sludge (typically composed of gypsum, iron and aluminium hydroxides and other metals that could be contained within the AMD) (Sephton & Webb 2019). The collective cost of treatment of AMD polluted waters is very high, and alternative, cheaper methods are continuously being explored.

Other large global industries are also producing waste on large scale and are continuously looking for reuse avenues of these products. Approximately two billion tonnes of alkaline wastes and residues are produced each year in many industries (steel production, aluminium refining and coal power plants), with an estimated total production of 90 billion tons (Gomes et al. 2016) being produced since 1750 (Spear 2019). These wastes materials are commonly disposed of or stored in waste piles or landfill sites and can become an environmental hazard if allowed to generate dust, or if rainwater infiltrates the waste,

causing leaching of alkalinity and seepage into natural water bodies or soil. Reuse avenues for these wastes are also continuously being researched.

In this regard, these products could potentially be utilized to treat AMD as a replacement for lime. Both the cost of treatment of AMD and the alkaline waste residue could be lowered, and the reuse of waste products could contribute to the establishment of a circular economy. This research focusses on the use of one alkaline waste product, Basic Oxygen Furnace Slag (BOFS) and compares the cost and extent of AMD treatment achieved via BOFS addition with that of traditional lime treatment.

2 LITERATURE

2.1 Alkaline materials to treat AMD

AMD is characterized by (i) low pH levels, (ii) high metal(loid)s and (iii) high sulfur concentrations (Blodau 2006). Treatment methods are thus aimed at addressing these detrimental characteristics, and the addition of an alkaline material combats (to varying degrees) all three of these issues. A variety of techniques and materials have been tested and/or employed to treat and to control AMD after it is produced and at its source. These include limestone, magnesia, sodium hydroxide (Trexler et al. 1975), fly ash, cement kiln dust, green liquor dregs (Faz, Rivera & Acosta 2020) and bauxite refinery residues (Kaur, Couperthwaite & Millar 2018). Recently, the use of waste metallurgical slags - in particular BOFS - have also been reported to show potential in the treatment of AMD (Naidu, Chauhan, Xiong, Sheridan, & van Dyk, 2020; Naidu, van Dyk, Sheridan, & Grubb, 2020; Name & Sheridan, 2014). The addition of alkaline materials encourages the rise in pH and the precipitation of iron oxyhydroxides and heavy metals that can then be removed through co-precipitation (Glover 1983). The mechanism of treatment using alkaline materials is as follows:

(i) hydration of metal oxide components to form hydroxides as shown in Equation 1 below.

$$MO + H_2O \leftrightarrow M(OH)_2 \qquad \textbf{Equation 1}$$

(ii) dissociation of hydroxide components in the AMD solution which increases the pH as shown in Equation 2.

$$M(OH)_2 \leftrightarrow M^{2+} + 2OH^- \qquad \textbf{Equation 2}$$

(iii) formation of solid metal hydroxides, sulfates and sulfides (these are presented in the findings and results).

Although the addition of alkaline materials (be it pure lime or a waste product containing other components or contaminants) results in very similar chemical reactions and treatment scheme, the availability of certain alkaline constituents in the waste, and thus the rate of treatment as well as the presence of other elements in the waste, results in a slightly different treatment mechanism. The extent and mechanism of BOFS treatment is therefore assessed in this study with specific focus on the

precipitation reactions that occur, the extent of pH rise and the extent of metal removal via precipitation. The Acid neutralizing capacity (ANC) of BOFS is also determined. Where possible, comparisons between lime and BOFS are evaluated.

3 EXPERIMENTAL PROCEDURE

3.1 Acid neutralizing capacity (ANC) of BOFS

BOFS particles (varying masses and particle sizes) were put into contact with AMD (varying volumes) sourced from a coal mine tailings storage facility (TSF) in Emalahleni, South Africa, in a plug flow reactor and a continuously agitated reactor. The pH change was assessed (pH was measured using a DF Robot combined pH and ORP meter). The alkalinity of the system was also measured using titration methods. The total alkalinity calculated was calculated using Equation 3.

$$Total\ alkalinity\ (as\ \frac{mg}{L}\ of\ CaCO_3) = \frac{B \times N \times 50 \times 1000}{ml\ sample} \qquad \textbf{Equation 3}$$

Where B is the total volume (ml) of standard acid used in titration to pH 4.5, N is the normality of the acid (m.eq/mL), 50 is the mg equivalent of $CaCO_3$ (mg/m.eq)and 1000 is used to convert from ml to L.

Oxide content on the surface of the slag was evaluated using XRD as well as Scanning electron microscopy (SEM) and Energy Dispersive X-Ray Analysis (EDA). Lime, quicklime and hydrated lime (obtained in powdered form from a local chemical distributor in Johannesburg, South Africa) where used in a similar way in this experiment to determine the difference in mass required to treat the AMD to the same pH level. This was used to perform a cost analysis of the raw materials and allow for comparison of the different alkaline materials.

3.2 Identification of metal species removal/precipitation mechanism

- Liquid samples were taken periodically from the reactors to assess for aluminium, calcium, iron, magnesium, manganese and sulfate concentration using an Agilent 2000 series atomic spectrometer (AAS) for the metal species. Turbidimetric spectrophotometric tests (using a Merck Spectroquant Pharo 300) (American Public Health Association, 1975; Center for Bioprocess Engineering Research, 2016)) for the sulfate species. Samples were filtered to remove solids using 0,45 µm filters, diluted on a 1:3 ratio with deionized water and acidified with 0.6 ml of nitric acid prior to analysis. This was done to measure the difference in concentration in dissolved and precipitated metals in the samples. Dilution was necessary to ensure the concentrations within the samples were within range of the AAS instrument. Standard concentration solutions were used for each test to calibrate the AAS instrument. Metal species and sulfate concentrations were measured to assess what type of precipitation reactions were occurring.
- The “spent” BOFS was assessed before and after the neutralizing reaction using X-Ray Diffraction (XRD) and Rietveld quantification analyses. XRD sample preparation included grinding 3 g of

sample and spiking it with fluorite on a 90:10 weight basis. A Siemens D500 computer automated diffractometer was used to perform XRD. XRD was performed to investigate how the chemical makeup of the BOFS had changed and what had become available in the AMD solution to act as counterions to facilitate precipitation.

- Sludge formed in the reactor was collected, acidified and assessed using the same AAS procedure. This was done to determine what types of precipitates had formed and to determine if the elemental species balanced across all evaluations.

4 RESULTS AND DISCUSSION

Two types of AMD were used, each with varying concentrations of sulfates and the metals of interest. The initial pH of both AMD sources was the same. The composition of both AMD sources is presented in Table 1.

Table 1: Concentrations of components of interest in two different types of AMD sourced from two different AMD dams in Emalahleni, South Africa

AMD Type	pH	Aluminium (mg/L)	Calcium (mg/L)	Iron (mg/L)	Magnesium (mg/L)	Manganese (mg/L)	Sulfate (mg/L)
Type A	2.44	434.89	110.83	3039.60	105.67	88.29	12955.62
Type B	2.47	497.25	175.38	3506.88	94.04	197.68	5199.92

An XRF and XRD analysis was performed on the BOFS and the major oxides found are shown in Table 2. In addition to this, small amounts of other elements were also found in the BOFS which were not present in oxide form.

Table 2: Major oxides in BOFS used for AMD treatment

Oxide	wt.%
CaO	41.6
Fe_2O_3	20.5
SiO_2	14.4
MgO	7.2
Al_2O_3	2.8
SO_3	0.4
Loss on ignition (LOI)	5

4.1 ANC of BOFS

An important thing to note in the comparison between lime (quicklime or hydrated lime) and BOFS is the availability of free lime in the sample (components that are available to hydrate and raise the pH of the media). Lime and free lime generally refer to the CaO component of the sample, however BOFS contains multiple other units in oxide and silicate form that dissolve in liquid media and contribute to the neutralization or pH rise of the media. Table 3 shows the availability of oxides (that can readily hydrate in liquid media) in lime and BOFS. It should be noted that although the free lime content in BOFS is 13 %, this only refers to the components found on the surface of the solid particle. As dissolution occurs (largely following Lagergren kinetics (Tamlyn S. Naidu et al. 2020)), more oxide components become available. The size of the BOFS particle used will also affect the amount of free oxide content – smaller particles have a larger availability of neutralizing/alkaline components than larger particles.

Table 3: Free oxide content in quicklime, hydrated lime (Tolonen et al. 2014) and BOFS with particle aperture between 2000-3350 microns (determined via SEM and EDA) where Wollastonite found on the surface of the particle was not considered a free oxide (due to its insolubility in water).

Alkaline material	Oxide content (Total %)	Free oxide content (%)
Quicklime	94	91
Hydrated lime	73	71
BOFS	87	13

Although the free oxide content of BOFS is significantly less than that of normal quicklime or hydrated lime, the BOFS still exhibited success in neutralizing AMD. 80g of slag was able to raise the pH of a sample of Type A AMD with an initial pH of 2.44 to (i) a pH of 7 in 540 minutes and (ii) a pH of 10 in 1365 minutes. This is shown in Figure 1.

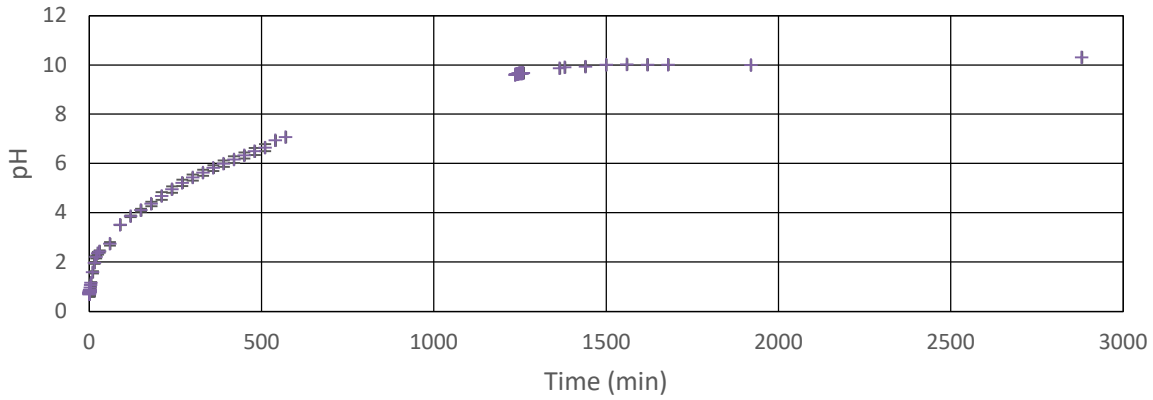

Figure 1: pH change over time in 800 ml of Type A AMD in a constantly agitated reactor when 80 g of slag with particle aperture between 2000-3350 microns has been added.

The pH rise was directly related to (i) the volume of AMD, (ii) the composition of AMD, (iii) the amount of BOFS, (iv) the particle size of the BOFS and the (v) allowed reaction time. For example, 15 g of slag fines (aperture of 1000 microns or less) was able to increase the pH of 1500 ml of Type B AMD (significantly lower initial sulfate and iron concentration) to a pH of 7 in 55 minutes, and similarly 67 g of fine BOFS was able to raise 200 ml of this Type B AMD to a pH of 7 in 5 minutes. The alkalinity addition corresponding to the last data point collected in the experiment shown in Figure 1, was 2897 units of alkalinity as $CaCO_3$ in mg/L.

4.2 Identification of metal species removal/precipitation mechanism

4.2.1 Aluminium

The initial concentration of aluminium in the AMD (Type A) was 434 mg/L. Aluminium in acidic media most commonly forms an aqueous cation, with an oxidation number of +3 (Harding, Johnson & Janes 2002). Addition of an alkaline material (which will hydrate and dissociate to form hydroxide units) to the solution, will first precipitate an insoluble aluminium hydroxide (by Equation 4):

$$Al^{3+}(aq) + 3OH^{-}(aq) = Al(OH)_3(s) \qquad \textbf{Equation 4}$$

This was considered the main mechanism of aluminium removal in the system. It is important to note that both aluminium oxide and hydroxide species are amphoteric in nature. In acidic solutions, they will dissolve and assist with neutralizing the acid (by Equation 5):

$$Al(OH)_3(s) + 3H^{+}(aq) = Al^{3+}(aq) + 3H_2O(l) \qquad \textbf{Equation 5}$$

Excess hydroxide units in the solution could also cause the aluminium hydroxide to form a tetrahydroxyaluminium ion via Equation 6:

$$Al(OH)_3(s) + OH^{-}(aq) = [Al(OH)_4]^{-}(aq) \qquad \textbf{Equation 6}$$

Aluminium sulfate or sulfide could also potentially form as there is an excess of sulfate ions in the AMD. However, aluminium sulfate has a very high K_{sp} (69.2) which means it will not precipitate. Similarly, aluminium sulfide, also with a very high K_{sp} is rapidly hydrolysed in an aqueous solution to form aluminium hydroxide and hydrogen sulfide gas – thus it is unlikely that removal of aluminium occurred in this manner. Aluminium was removed from the solution almost completely (to a concentration of 10.7 mg/L) at a pH of 3.8 and redissolution did not occur even at a pH level of 9.

4.2.2 Calcium and Magnesium

Calcium and magnesium were present in the AMD at a concentration of 110 mg/L and 115 mg/L respectively. Calcium (as well as magnesium) was also added to the solution through the dissolution (hydration and dissociation) of the BOFS. Calcium and magnesium in aqueous solutions are found in

the form of a positive cation with an oxidation number of 2+. Both calcium oxide and calcium hydroxide have an intermediate solubility in water and calcium will not precipitate out of solution as either of these species. Calcium sulfate has a higher K_{sp} than calcium hydroxide (experimentally exhibiting a solubility of 0.274% w/w compared to calcium hydroxide which exhibited a solubility of 0.12% w/w in water at 20 ° C (Royal Society of Chemistry 2020)), however due to the saturation of the solution with sulfates (initial Type A AMD concentration of 12955 mg/L) and the reaction of the hydroxyl group with multiple other elements – the bulk of the calcium removal is achieved via gypsum precipitation. Despite the precipitation of calcium sulfate, the calcium concentration increased in the system with increasing pH. When the BOFS comes into contact with liquid, hydration will take place and calcium hydroxide will form. If this hydrated BOFS is then exposed to air, carbon dioxide will react with this to form calcium carbonate (by Equation 7) which has a low solubility in water:

$$Ca(OH)_2\ (aq) + CO_2\ (g) = CaCO_3\ (s) + H_2O\ (l) \qquad \textbf{Equation 7}$$

The pH raising capacity of BOFS in neutral solutions will thus be lowered if this occurs, however further reaction with an acidic media can result in the formation of carbon dioxide and water (Equation 8):

$$CaCO_3\ (s) + 2H^+\ (aq) = Ca^{2+}\ (aq) + CO_2\ (g) + H_2O\ (l) \qquad \textbf{Equation 8}$$

It is thus recommended to keep the BOFS dry before use as a reagent, and once it is in use keep the particles submerged. Magnesium is most likely removed from the solution in the form of magnesium sulfate (which has a solubility of 33.7% w/w in water) and magnesium hydroxide (which is soluble in acidic solutions but less so in basic solutions (Royal Society of Chemistry 2020)). Magnesium decreased in solution at a pH of 9 (to a concentration of 61.7 mg/L).

4.2.3 Iron

Under acidic conditions, the most stable oxidation state of iron is 2+. If the AMD is aerated then the redox potential of the water is such that it allows for oxidation of the ferrous iron (2+) contained in the solution to ferric iron (3+) which can then precipitate as iron hydroxide, $Fe(OH)_3$ via reactions described by equations 9 and 10 (Silver 2012).

$$4Fe^{2+}\ (aq) + 3O_2\ (g) + 2H^+(aq) = 2Fe^{3+}\ (aq) + H_2O\ (l) \qquad \textbf{Equation 9}$$

$$Fe^{3+}\ (aq) + 3OH^-\ (aq) = 2Fe(OH)_3\ (s) \qquad \textbf{Equation 10}$$

Fe^{3+} has a low solubility at certain pH levels and generally precipitates out of solution. In the case that the system is anaerobic and if excess CO_3^{2-} is available in the solution (as may be the case if BOFS is hydrated and then exposed to air) the $Fe(HCO_3)_2$ salt is formed. Upon exposure to air this leads to the formation of FeCO3 and then to iron (III) oxide. During experiments, iron was almost completely removed at a pH of 7 (from an initial concentration of 3039 mg/L to 0.289 mg/L).

4.2.4 Manganese

Under acidic conditions, the most stable oxidation state of manganese is 2+. In this reduced (Mn^{2+}) state, manganese is moderately soluble in the form of $MnSO_4$ and thus very little Mn removal is attributed to $MnSO_4$ formation and precipitation. At pH levels of 8 and above, manganese can precipitate as $MnCO_3$ and $Mn(OH)_2$. In aerated systems (under oxidizing conditions), Mn in the 3+ and 4+ can also form MnO_2, Mn_2O_3 and Mn_3O_4 even at lower pH levels – compounds which are all insoluble in water. It should be noted that is iron (II) is present in solution manganese will not precipitate at neutral conditions. Manganese in the system decreased from 88 mg/L to 52 mg/L at a pH level between 6 and 9. It should be noted that initially manganese increased in the system – this could be attributed to dissolution of manganese containing compounds in the BOFS (XRF analysis shows Mn makes up 3% by weight of BOFS).

4.2.5 Sulfate

Sulfate in the system is likely to form any of the compounds found in Table 4. The most likely way that sulfate is removed is via the precipitation of calcium sulfate. Calcium becomes abundantly available in the solution through the dissolution of the BOFS and can then bind with the sulfate ion to form a nearly insoluble product. The solubility of each possible sulfate compound is shown below – it is likely that a small percentage of sulfate is also removed via formation of small amounts of other compounds. Sulfate decreased to 269 mg/L at a pH of 11.4.

Table 4: Solubility of sulfate compounds % weight/weight in water at 25° C

Magnesium Sulfate	33.7
Manganese (II) Sulfate	62.9
Iron (II) Sulfate	26.3
Calcium Sulfate	0.274
Iron (III) Sulfate	Slightly soluble
Aluminium Sulfate	36.4

4.2.6 Sediment/precipitate formed

An SEM and EDA analysis was performed on the precipitate which had formed on the surface of the BOFS particle. This precipitate is shown in Figure 2.

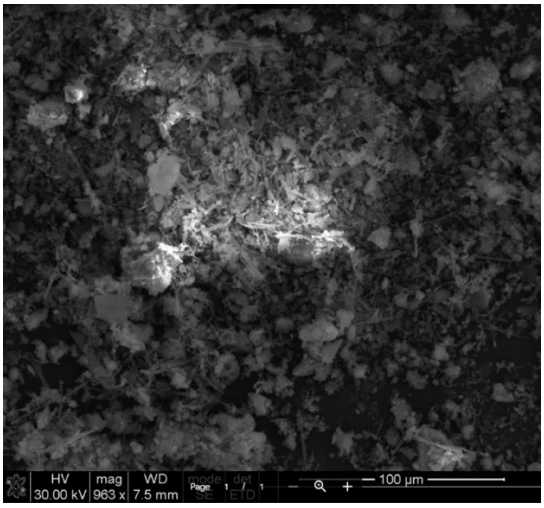

Figure 2: SEM of precipitate formed after reaction of BOFS and AMD for a period of 32 hours.

The results from the SEM and AAS run on the acidified precipitate, showed that aluminium, calcium, iron, magnesium, manganese and silicate had all precipitated. The SEM and EDA were able to identify oxides and silicates but not sulfates or hydroxides, however it is likely (given the chemistry of the AMD solution and the difference in initial concentration and pH and final concentration and pH) that most precipitates formed were sulfates and hydroxides.

4.2.7 Cost Analysis

Slag management companies sell BOF slag at a cost of R100/ton inclusive of value added tax (VAT) (Vermuelen 2019). This cost is applicable to any particle size as the management company mills the slag to the desired size. Protea Chemicals provides hydrated powdered lime at an estimated cost of R3500/ton (Naidoo 2021) and dolomitic lime is sold at prices between R302.45 and R408.25 (Swartz 2021). The pH of the system (for typical neutralization applications) should be at 7, however if different levels of precipitation for different metal species is desired to be achieved, then higher pH values could be established. The amount of lime in comparison to the amount of BOF slag required to increase the pH of 1L of Type B AMD to a pH of 7 at a reaction time of between 30 and 55 minutes, in terms of the associated cost, is shown below in Table 5 (Department of Mineral Resources 2010; Maree et al. 2013; United States Geological Survey Mineral Resources Program 2014; Othman, Sulaiman & Sulaiman 2017; U.S. Geological Survey 2020).

Table 5: Cost of raw material when treating 1 L of AMD to a pH of 7 in 30 - 55 minutes.

pH	Dolomitic Lime (R/L)	Quicklime (R/L)	Hydrated lime (R/L)	BOF slag (R/L)
7	0.008	0.0073	0.025	0.001

According to this data, BOF slag is the cheapest lime source for AMD treatment of those considered.

5 CONCLUSIONS

BOFS proved to be effective in the treatment of AMD with respect to pH, metal and sulfate concentrations – successfully raising the pH (to a range of pH levels depending on mass to volume ratios) and precipitating metal and sulfate compounds. Further investigation into the use of the sludge in a recycle stream (high density sludge processes) would need to be conducted to determine whether BOFS will also be effective in these systems. Investigation into the reuse of the sludge and the spent BOFS will also have to be done extensively in order to determine if these byproducts are similar to that of lime AMD treatment plants.

REFERENCES

Blodau, C., 2006, "A review of acidity generation and consumption in acidic coal mine lakes and their watersheds," *Science of the Total Environment*, 369(1–3), 307–332.

Department of Mineral Resources, 2010, *Lime Industry in South Africa, 2010*, South Africa.

Faz, A., Rivera, J. & Acosta, J.A., 2020, "Environmentally sustainable acid mine drainage remediation : Use of natural alkaline material," *Journal of Water Process Engineering*, 33(July 2019), 101064.

Glover, H.G., 1983, "Mine water pollution - an overview of problems and control strategies in the United Kingdom," *Water Science and Technology*, 15, 59–70.

Gomes, H.I., Mayes, W.M., Rogerson, M., Stewart, D.I. & Burke, I.T., 2016, "Alkaline residues and the environment : a review of impacts , management practices and opportunities," *Journal of Cleaner Production*, 112, 3571–3582.

Harding, C., Johnson, D.A. & Janes, R., 2002, *Elements of the P Block*, llustrated, Royal Society of Chemistry.

Kaur, G., Couperthwaite, S.J. & Millar, G.J., 2018, "Performance of bauxite refinery residues for treating acid mine drainage," *Journal of Water Process Engineering*, 26(May), 28–37.

Maree, J., Mujuru, M., Bologo, V., Daniels, N. & Mpholoane, D., 2013, "Neutralisation treatment of AMD at affordable cost," *Water SA*, 39(2).

Naidoo, K., 2021, *Indicative cost of pure hydrated powdered lime interview*.

Naidu, Tamlyn S., Chauhan, D., Xiong, F., Sheridan, C.M. & Dyk, L.D. van, 2020, *An Assessment of Basic Oxygen Furnace Slag Dissolution for Application in AMD Dam Remediation using Waste Products from the Steel Manufacturing and Sugar Industries*, in J. Baker, E. Matinde, L. Ochieng, G. Pretorius & J. Wates (eds.), *SAIMM Mine Tailings Conference*, 51–62, South African Institute of Mining and Metallurgy, Johannesburg, South Africa.

Naidu, Tamlyn S, Dyk, L.D. Van, Sheridan, C.M. & Grubb, D.G., 2020, "Sugar and Steel By-Product Utilization in Acid Mine Drainage Remediation," *Journal of Hazardous, toxic*

and radioactive waste, 24(1), 1–10.

Name, T. & Sheridan, C., 2014, "Remediation of acid mine drainage using metallurgical slags," *Minerals Engineering*, 64, 15–22.

Othman, A., Sulaiman, A. & Sulaiman, S.K., 2017, "The use of quicklime in acid mine drainage treatment," *Chemical Engineering Transactions*, 56, 1585–1590.

Royal Society of Chemistry, 2020, *ChemSpider*.

Sephton, M.G. & Webb, J.A., 2019, "Applied Geochemistry Applications of Portland cement blended with fl y ash and acid mine drainage treatment sludge to control acid mine drainage generation from waste rocks," *Applied Geochemistry*, 103(January), 1–14.

Silver, J., 2012, *Chemistry of Iron*, Illustrate, Springer Science & Business Media.

Spear, B.J., 2019, "Iron and steel patents : The sinews of the GB Industrial Revolution," *World Patent Information*, 58(August), 101901.

Swartz, P., 2021, *AgLime Price List*.

Tolonen, E., Sarpola, A., Hu, T., Rämö, J. & Lassi, U., 2014, "Acid mine drainage treatment using by-products from quicklime manufacturing as neutralization chemicals," *Chemosphere*, 117, 419–424.

Trexler, B.D.Jr., Ralston, D.R., Reece, D.R. & Williams, R.E., 1975, "Sources and causes of acid mine drainage," *Mines Geol.*, 165, 1–129.

United States Geological Survey Mineral Resources Program, 2014, *Lime Prices in The United States by Type*, *Index Mundi*.

U.S. Geological Survey, 2020, "Lime," *Mineral Commodity Summaries*, 1(703).

Vermuelen, I., 2019, *Consultation/Quote from Phoenix Slag*

Design, construction and testing of a laboratory-scale membrane distillation bioreactor (MDBR) for water purification

K. Patel[1*] and C. Sheridan[2]

[1]School of Chemical and Metallurgical Engineering, University of the Witwatersrand, Johannesburg, South Africa

[2]Department of Geography, Archaeology and Environmental Studies, University of the Witwatersrand, Johannesburg.

[*]Corresponding author: patel.kavisha24@gmail.com

ABSTRACT

The pulp and paper industry produces a significant amount of wastewater that contains a variety of organic and inorganic contaminants, making it nearly impossible to discharge directly into a water source. As a result of the condition of the untreated mill effluent and strict environmental regulations, significant pressure has been placed to develop suitable technologies capable of treating and reusing this wastewater. This study evaluates the potential of the membrane distillation bioreactor (MDBR) for the treatment and reuse of pulp and paper mill effluent. The MDBR is a wastewater treatment technology combining the conventional membrane bioreactor (MBR) with membrane distillation (MD). This technology is best suited to applications which require a high quality water product and a long residence time for the effective removal of problematic organics. The system alone is potentially able to accomplish wastewater treatment and reuse in one step that is without the need for any post-treatment processes. Such key features make the MDBR an attractive treatment option. The study is still on-going. The MDBR developed in this study has the potential to improve water quality, reduce sludge production and greatly minimize the discharge of wastewater into rivers and streams.

Keywords: membrane distillation bioreactor; pulp and paper mill effluent; wastewater reclamation

1 INTRODUCTION

South Africa has been facing a growing scarcity of water due to increasing domestic and industrial demands in conjunction with increased pollution of freshwater resources (Meng, Hsu, Ye, & Chen, 2015). The reuse of treated industrial and domestic wastewater is a potential way forward to address the water problems faced.

Separation technology such as the membrane bioreactor (MBR) are used at wastewater treatment plants to treat wastewater such that it can meet reuse standards. However, the MBR is not always able to retain slowly biodegradable organic substances resulting in an elevated amount of organics in the treated MBR effluent. It is therefore not possible to use this water directly for reuse applications and hence post-treatment processes are still required (Sert et al., 2017).

Currently, research is being conducted on the integration of the MBR system with the high retention

process known as membrane distillation (MD). The resulting combined process, the membrane distillation bioreactor (MDBR), is a membrane separation process that is driven by the temperature difference induced across a hydrophobic membrane, allowing only volatile components such as water vapour to pass through. This advanced system has the potential to produce high quality water whilst effectively retaining non-volatile organics and salts which are biodegraded by thermophilic organisms (Khaing, Li, Li, Wai, & Wong, 2010). The MDBR is therefore potentially able to provide significant advantages over conventional membrane separation processes and can be used for the purpose of improving water quality in South Africa.

Although a limited number of studies on this system exist, the study described in this paper will experimentally determine the potential of the MDBR system to treat and reuse pulp and paper mill effluent. The laboratory scale MDBR will be evaluated in terms of water quality and its potential to meet reuse requirements, flux performance, the rejection of non-volatiles, and the membrane fouling phenomenon.

2 LITERATURE

2.1 The membrane bioreactor (MBR) for wastewater treatment and reuse

The MBR has been identified as a promising technology that can help municipalities and industries to manage their water resources effectively. The MBR system has been successfully implemented at several full-scale municipal and industrial wastewater treatment plants in South Africa (Kadam & Chuan, 2016). This technology, which is a combination of a biological treatment process (based on the activated sludge process) and membrane filtration, also has the potential to treat wastewater so that it can meet reuse standards (Kadam & Chuan, 2016). Ultrafiltration (UF) and microfiltration (MF) membranes are commonly employed in MBR systems to separate the solid content in the mixed liquor from the treated water. These pressure-driven filtration membranes are used to retain larger molecules; the MF membrane is used for the separation of suspended solids with a particle size range of 0.08–10µm while the UF membrane separates macromolecular solids with a particle size range of 0.01–0.1µm (Kadam & Chuan, 2016; Sert et al., 2017).

The effective solid-liquid separation that is accomplished by the MBR provides a series of advantages which include a smaller footprint when compared with conventional wastewater treatment systems, reduced sludge production and a more stable and better quality effluent (Fraga, García, Hooijmans, Míguez, & Brdjanovic, 2017; Huang, Xiao, & Shen, 2010). However, the treated MBR effluent may still contain dissolved salts and slowly biodegradable organic substances. It is therefore not necessarily possible to use this water directly for reuse applications such as irrigation and process water (Sert et al., 2017). Hence post-treatment processes, such as nanofiltration (NF) and reverse osmosis (RO), are still required for the removal of molecular solids, dissolved salts and organics (Kadam & Chuan, 2016).

Apart from this, the MBR is also associated with high capital and operational costs and has a high tendency for membrane fouling (Fraga et al., 2017).

2.2 Membrane distillation (MD) as a wastewater treatment option

MD is a membrane separation process that uses the vapour pressure difference, that is created by the trans-membrane temperature difference, across the membrane as the driving force for solid-liquid separation (Wu et al., 2017). The MD process is operated at low temperatures (within the range of 25°C to 80°C) and at atmospheric pressure (Carnevale, Gnisci, Hilal, & Criscuoli, 2016; Phattaranawik, Fane, Pasquier, & Bing, 2008). The operational principle of this process is based on separation by means of phase equilibria. This occurs as follows:

(1) During the MD process, the microporous hydrophobic membrane comes into contact with the heated feed on one side.

(2) The hydrophobic nature of the membrane creates a vapour-liquid interface at the membrane pore entrance and thus, only volatile components (such as water vapour) are transported across the membrane.

(3) The vapour is then condensed on the opposite side of the membrane by the permeate or the cooling stream (Curcio & Drioli, 2005; Shuwen Goh, Zhang, Liu, & Fane, 2013).

In this manner, the system can retain recalcitrant compounds, non-volatile solutes and low-molecular weight organics and is therefore able to produce treated water of high quality (Shuwen Goh, Zhang, Liu, et al., 2013).

The use of MD as a separation process has many benefits, some of which include 100% (theoretical) rejection of non-volatile compounds and dissolved salts, and moderate operating conditions that is lower operating temperatures and pressures than those used in the conventional pressure-driven membrane separation processes. These conditions also place less requirements on the mechanical properties of the membrane being used. In addition, the process is able to utilize alternative energy sources such as solar power or waste heat, and is easy to combine with other treatment processes such as UF and RO (Alkhudhiri, Darwish, & Hilal, 2012). Based on these distinct advantages, the MD process has been applied for seawater desalination, wastewater treatment and solute recovery (Wu et al., 2017).

The first MD patent was granted in 1963 (Wang & Chung, 2015). However, slow progress related to the development of the MD process was observed. This was mainly due to the unavailability of appropriate membranes for the application, insufficient knowledge regarding module design, the membrane wetting phenomenon, low flux performance and the high energy consumption of the process (Drioli, Ali, & Macedonio, 2015; Wang & Chung, 2015). Since then, MD has become more attractive due to the growing research activities in this field. It has been applied at a laboratory scale for the

treatment of industrial wastewaters which include petrochemical wastewater, olive mill wastewater (Li, Wu, Sun, Cheng, & Liu, 2016), radioactive wastewater (Liu & Wang, 2013), as well as textile dying wastewater (Carnevale et al., 2016). In these studies, MD has achieved good permeate water quality and has also demonstrated less fouling on the membrane (Li et al., 2016). The MD process has also been used in the food industry for milk and juice concentration and in pharmaceutical and biomedical industries processing (Kim, Lee, & Cho, 2016). MD is yet to be commercialized because of its high energy consumption, although a few pilot plants are in operation (Tijing et al., 2015).

Since MD is able to operate at higher concentrations, has a high retentive ability and is merely used to concentrate waste and not treat it, it should be integrated with other separation technologies in order to maximize its overall performance (Shuwen Goh, Zhang, Liu, et al., 2013; Wang & Chung, 2015)

2.3 The membrane distillation bioreactor (MDBR) for wastewater reclamation

The MDBR is a hybrid system that combines the MD process with the MBR's thermophilic bioprocess. This separation technology is based on the same operational principle of MD however, there are two distinct differences related to its operation: (1) The MD membrane module is submerged in the bioreactor and (2) Air is supplied to the system in order to provide oxygen to the thermophilic bacteria and to decrease the effects of membrane fouling (Phattaranawik et al., 2008). The MDBR process is operated at atmospheric pressure and within a temperature range of 45°C-80°C. The temperature of the system will however, be determined by the activity of the thermophiles (S. Goh, Zhang, Liu, & Fane, 2015). Operation of the MDBR at these thermophilic conditions enhances the biodegradation of organics and results in a low sludge yield (Wijekoon et al., 2014).

The MDBR is able to provide additional benefits when compared to its individual separation counterparts namely the MBR and the MD process. The inclusion of biomass in this process aids with the biological removal of dissolved salts, non-volatile solutes and low-molecular weight organics, which the MBR and the MD process are not able to perform in their own capacity (Shuwen Goh, Zhang, Zhang, et al., 2013). Table 1 summarizes the key differences between the MDBR and the MF/UF-MBR.

Table 1: Key differences between the MDBR and the MF/UF-MBR (Phattaranawik et al., 2008)

Characteristic	MF/UF-MBR	MDBR
Driving force	Pressure (suction preferred)	Thermal (temperature difference), at atmospheric pressure
Membrane	UF or MF, hydrophilic preferred	Porous, hydrophobic MF such as polytetrafluoroethylene (PTFE) and polyvinylidene fluoride (PVDF) (preferred)
Phase in membrane pores	Liquid	Vapour, gas
Retention of target compounds and microorganisms by membranes	Incomplete: for MF less than 50% for small organic compounds, spores and small virus	100% for salts, non-volatile organic compounds, and microorganisms
Permeate quality	Dependent on biological activity; total organic carbon (TOC) of 3-10 ppm	Independent of biological activity, comparable to distillation product; TOC < 0.8 ppm
Inorganics	Salts not retained	Salts retained and discharged with waste sludge
Start-up time	Slow	Potentially faster
Organic retention time (ORT) and hydraulic retention time (HRT)	ORT ~ HRT	ORT~∞*, independent of HRT, *until organics become carbon dioxide (CO_2) or volatile
Flux	10-30 L/m^2h (typically)	2-15 L/m^2h (~RO fluxes) at 55°C
Membrane integrity monitoring	Particle counting techniques, laser-turbidity monitoring, intermittent pressure decay tests	Conductivity monitoring on a continuous basis

The MDBR is also potentially able to achieve wastewater reclamation in one stage as compared to a conventional system consisting of a MBR with RO as a post-treatment step (Phattaranawik et al., 2008). Table 2 shows a qualitative comparison of costs associated with the MDBR and the dual MBR with RO process. The comparison indicates that the MDBR is a more cost-effective process. This is because the MDBR is a single process and the treated water is of a high quality, therefore not requiring any further treatment downstream.

Table 2: Qualitative comparison of costs associated with the MDBR systems and the dual MBR and RO systems (Phattaranawik et al., 2008)

Items	**Hybrid UF-MBR + RO**	**Novel MDBR**
I. Capital Costs		
Footprint	Larger than MDBR – expected because there are two processes: MBR and RO	Lower, but larger than conventional MBR (lower flux)
Membranes and modules	Higher cost because there are two processes: MBR and RO. Pressure vessels for RO	Single process at atmospheric pressure, but more than MBR due to materials and lower flux
Piping systems and valves and pumps	Higher cost, due to high pressure piping and pumps for RO	Low; operated at atmospheric pressure
Membrane integrity monitoring system	Higher cost; sophisticated instruments required	Lower cost; continuous monitoring by flow and conductivity
Heat exchangers	Not required	Requires good heat exchange and cooling systems
II. Energy and operating costs		
Energy sources for process operations	Electricity only	Low grade waste heat, solar energy Electrical power is low
Labour cost	Potentially higher due to two processes	Potentially lower
Sludge disposal	Potentially higher	Potentially lower
III. Maintenance costs		
Various	Potentially higher, due to higher pressures, more equipment, etc.	Potentially lower

The MDBR has only been applied at a laboratory scale for the treatment of synthetic wastewater and petrochemical wastewater (Shuwen Goh, Zhang, Zhang, et al., 2013). Phattaranawik et al., (2008) conducted one of the first MDBR studies using synthetic wastewater and achieved a high quality permeate with a low total organic carbon (TOC) content. Khaing et al., (2010) demonstrated the feasibility of using the MDBR for petrochemical wastewater reclamation as the salt rejection rate was found to be 99.75%. Goh et al., (2013) achieved a TOC and total nitrogen (TN) removal efficiency of 88% and 68% respectively when using synthetic wastewater as the feed source. These results show the potential of the MDBR for water reuse applications.

3 EXPERIMENTAL PROCEDURE

3.1 Experimental set-up

A laboratory scale MDBR (with a reactor volume of 3.6 L) constructed from heat-resistant glass is used in this study. Figure 1 depicts a schematic process flow diagram. The MDBR is maintained at a set temperature of 45ºC using a hot plate. A double-faced flat sheet membrane module is submerged in the MDBR, allowing for effective vapour-liquid transfer. Specifications of the membrane obtained from National Separations is provided in Table 3. The permeate stream is circulated from the membrane module to a permeate tank and then to a condenser using a peristaltic pump. Product water is collected from the overflow tank.

3.2 Acclimatization of microorganisms

Mesophilic microorganisms and phenol-rich wastewater were obtained from a pulp and paper mill. The batch study was conducted for two cases namely Batch A and Batch B in 1 L glass cylinders. Acclimatization occurred at a target temperature of 45ºC using hot plates. Nutrients such as Potassium Nitrate (KNO_3) and Potassium Dihydrogen Phosphate (KH_2PO_4) were added in order to maintain the chemical oxygen demand: nitrogen: phosphate (COD:N:P) ratio as 100:5:1 (Sundararaman, 2016) and to sustain the growth of the microorganisms. An aquarium air pump was used for aeration.

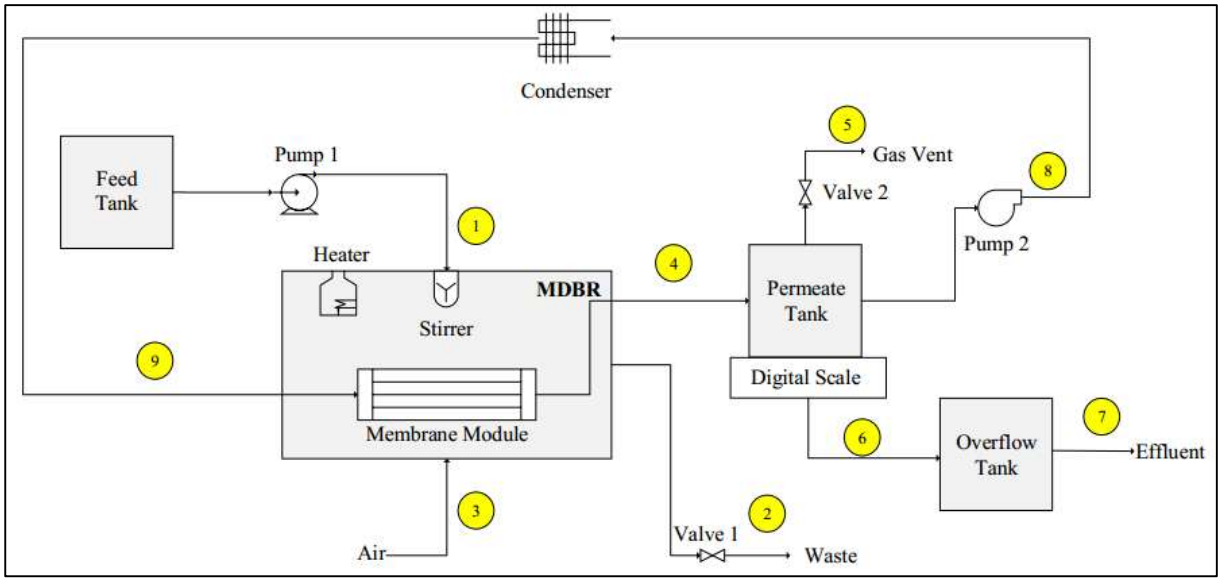

Figure 1: Schematic process flow diagram of the MDBR system

Table 3: Specifications of the membrane

Item	Specification
Membrane type	Flat sheet
Membrane material	Polytetrafluoroethylene (PTFE)
Membrane pore size	0.2µm
Membrane diameter	100mm
Membrane thickness	65µm

4 RESULTS AND DISCUSSION

4.1 Total suspended solids (TSS) test

A TSS test was conducted in order to determine if microorganism acclimatization had occurred. As shown in Figure 2, it is found that the microorganisms in the system required approximately 24 days to acclimatize to the phenol-rich wastewater and the target temperature of 45ºC. It is evident from the graph that Batch A contains a more stable species because from day 1, the biomass increased gradually and stabilised until day 29. Batch B is observed to have experienced fluctuations throughout the acclimatization process and this could be attributed to non-ideal conditions and the variation of microorganisms in the wastewater.

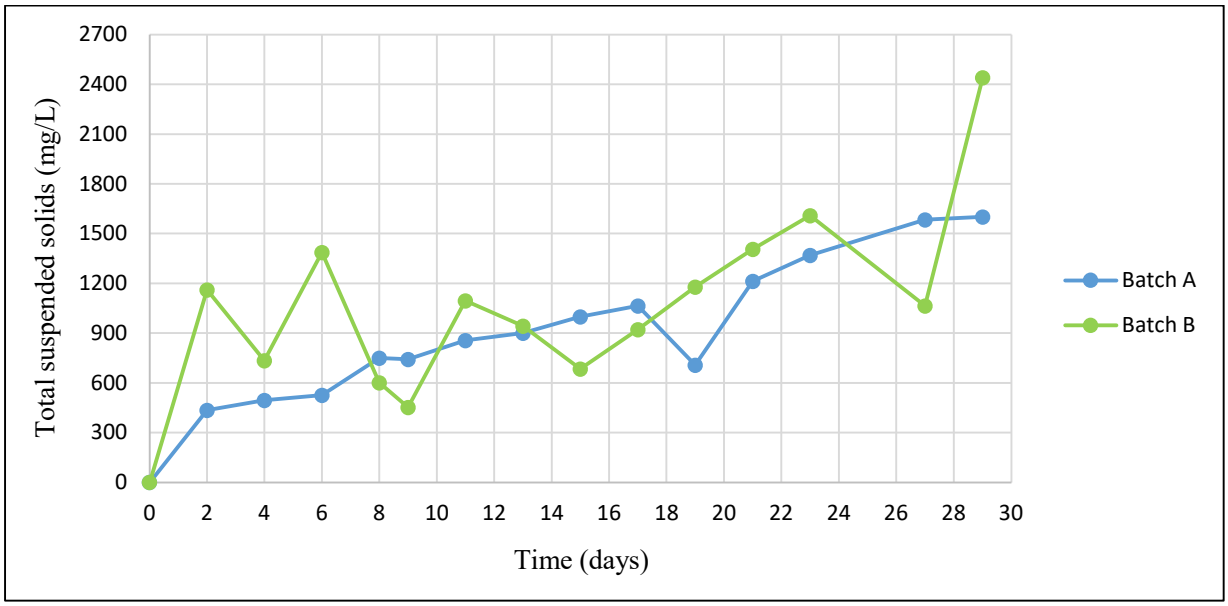

Figure 2: TSS as an indicator of microorganism growth

4.2 System operation

The advent of COVID-19 together with load-shedding has had a significant negative effect on the experimental programme. The MDBR has been shown to be operational, however, the intermittent

ongoing interruptions to the experimental programme (every time a Covid case was recorded in the building, the laboratory was shut down) have prevented the acquisition of meaningful data with which modelling and design optimisation be conducted. Notwithstanding this, it is believed that the demonstration of the MDBR as a functional wastewater treatment unit is useful and as experimental data becomes available, it will be reported upon.

5 CONCLUSIONS

At present there is no evidence highlighting any work done on the MDBR in South Africa. Considering the current water situation in South Africa, it would be beneficial to assess the treatment and water reuse potential of this water treatment system and determine whether such a process would be viable for industry. This study therefore builds on existing water research within the South African context.

REFERENCES

Alkhudhiri, A., Darwish, N., & Hilal, N. (2012). Membrane distillation: A comprehensive review. *Desalination, 287*, 2-18. doi:10.1016/j.desal.2011.08.027

Carnevale, M. C., Gnisci, E., Hilal, J., & Criscuoli, A. (2016). Direct Contact and Vacuum Membrane Distillation application for the olive mill wastewater treatment. *Separation and Purification Technology, 169*, 121-127.

Curcio, E., & Drioli, E. (2005). Membrane Distillation and Related Operations—A Review. *Separation & Purification Reviews, 34*(1), 35-86.

Drioli, E., Ali, A., & Macedonio, F. (2015). Membrane distillation: Recent developments and perspectives. *Desalination, 356*, 56-84.

Fraga, F. A., García, H. A., Hooijmans, C. M., Míguez, D., & Brdjanovic, D. (2017). Evaluation of a membrane bioreactor on dairy wastewater treatment and reuse in Uruguay. *International Biodeterioration & Biodegradation, 119*, 552-564.

Goh, S., Zhang, J., Liu, Y., & Fane, A. G. (2013). Fouling and wetting in membrane distillation (MD) and MD-bioreactor (MDBR) for wastewater reclamation. *Desalination, 323*, 39-47.

Goh, S., Zhang, J., Liu, Y., & Fane, A. G. (2015). Membrane Distillation Bioreactor (MDBR) - A lower Green-House-Gas (GHG) option for industrial wastewater reclamation. *Chemosphere, 140*, 129-142.

Goh, S., Zhang, Q., Zhang, J., McDougald, D., Krantz, W. B., Liu, Y., & Fane, A. G. (2013). Impact of a biofouling layer on the vapor pressure driving force and performance of a membrane distillation process. *Journal of Membrane Science, 438*, 140-152.

Huang, X., Xiao, K., & Shen, Y. (2010). Recent advances in membrane bioreactor technology for wastewater treatment in China. *Frontiers of Environmental Science & Engineering in China, 4*(3), 245-271.

Kadam, P. D., & Chuan, H. H. (2016). Erratum to: Rectocutaneous fistula with transmigration of the suture: a rare delayed complication of vault fixation with the sacrospinous ligament. *Int Urogynecol J, 27*(3), 505.

Khaing, T.-H., Li, J., Li, Y., Wai, N., & Wong, F.-s. (2010). Feasibility study on petrochemical wastewater treatment and reuse using a novel submerged membrane distillation bioreactor. *Separation and Purification Technology, 74*(1), 138-143.

Kim, S., Lee, D. W., & Cho, J. (2016). Application of direct contact membrane distillation process to treat anaerobic digestate. *Journal of Membrane Science, 511*, 20-28.

Li, J., Wu, J., Sun, H., Cheng, F., & Liu, Y. (2016). Advanced treatment of biologically treated coking wastewater by membrane distillation coupled with pre-coagulation. *Desalination, 380*, 43-51.

Liu, H., & Wang, J. (2013). Treatment of radioactive wastewater using direct contact membrane distillation. *J Hazard Mater, 261*, 307-315.

Meng, S., Hsu, Y.-C., Ye, Y., & Chen, V. (2015). Submerged membrane distillation for inland desalination applications. *Desalination, 361*, 72-80. doi:10.1016/j.desal.2015.01.038

Phattaranawik, J., Fane, A. G., Pasquier, A. C. S., & Bing, W. (2008). A novel membrane bioreactor based on membrane distillation. *Desalination, 223*(1-3), 386-395.

Sert, G., Bunani, S., Yörükoğlu, E., Kabay, N., Egemen, Ö., Arda, M., & Yüksel, M. (2017). Performances of some NF and RO membranes for desalination of MBR treated wastewater. *Journal of Water Process Engineering, 16*, 193-198.

Sundararaman, S., and Sathiyapriya, A., (2016). Acclimatization of an Industrial Pharmaceutical Wastewater in an Aerobic Batch Mode of Operation. *International Journal of Environmental Research and Development, Voume 6*, pp. 1-10.

Tijing, L. D., Woo, Y. C., Choi, J.-S., Lee, S., Kim, S.-H., & Shon, H. K. (2015). Fouling and its control in membrane distillation—A review. *Journal of Membrane Science, 475*, 215-244.

Wang, P., & Chung, T.-S. (2015). Recent advances in membrane distillation processes: Membrane development, configuration design and application exploring. *Journal of Membrane Science, 474*, 39-56.

Wijekoon, K. C., Hai, F. I., Kang, J., Price, W. E., Guo, W., Ngo, H. H., Nghiem, L. D. (2014). A novel membrane distillation-thermophilic bioreactor system: biological stability and trace organic compound removal. *Bioresour Technol, 159*, 334-341.

Wu, Y., Kang, Y., Zhang, L., Qu, D., Cheng, X., & Feng, L. (2017). Performance and fouling mechanism of direct contact membrane distillation (DCMD) treating fermentation wastewater with high organic concentrations. *Journal of Environmental Sciences*.

Removal of zinc and copper ions from industrial wastewater using bio-waste: a case study on water hyacinth

N. El-Tahhan[1], T. Majozi[1*] and M. Gadalla[2]

[1] NRF-DST Sustainable Process Engineering, School of Chemical and Metallurgical Engineering, University of the Witwatersrand, Private Bag 3, WITS 2050, Johannesburg, South Africa

[2] Department of Chemical Engineering, Port Said University, 42523 Port Said, Egypt

*Corresponding author: Thokozani.Majozi@wits.ac.za

ABSTRACT

The investigation presents the result of study on adsorption of zinc and copper from aqueous solutions by dried water hyacinth as a low-cost sorbent. The influence of pH, contact time, adsorbent dosage and initial concentration was studied using batch adsorption experiments. Experimental results indicate that the best contact times for the removal of Zn (II) and Cu (II) using dried water hyacinth were 10 and 60 minutes, respectively. Furthermore, the best pH and dosage of adsorbent were respectively found to be 4 and 3 g for Zn (II), while 6.5 and 1 g were respectively attained for Cu (II). The maximum removal of Zn (II) was 71 % at low initial metal ion concentration of 10 ppm which is equivalent to 0.32 mg/g adsorption capacity and 86% for Cu (II) at 20 ppm which is equivalent to 0.855 mg/g. Langmuir and Freundlich isotherm models were employed in carrying out the equilibrium studies. The experimental data were found to proceed with the Freundlich model for both zinc and copper as evidenced from the higher coefficients of determination (R2) values. The experimental data was also subjected to pseudo-first-order and the pseudo-second-order kinetic models.

Keywords: Biosorption, Water hyacinth (E. crassipes), Heavy metal ions, Isotherms, Kinetics.

1 INTRODUCTION

Solving the heavy metals contamination of water has been a major preoccupation of researchers for many years due to the adverse effects their toxicities have on the aquatic life, human beings and environment. This is because they do not biodegrade unlike organic pollutants, making their presence in industrial effluents and drinking water a public health concern (Anzeze et al., 2014). Heavy metals are usually present in most industrial wastewater streams that emanate from industrial processes such as metal plating, battery manufacturing paints, pigments, ceramic and glass industries. Whenever toxic heavy metals are exposed to the natural eco-system, their accumulation in human bodies usually occurs through either the direct intake or food chains (Prabha and Udayashankara, 2014). Copper and zinc are examples of these heavy metals, several industries like mining, painting, dyeing, battery manufacture and other industries discharge effluent containing Cu (II) to water ways. Short periods of exposure can cause gastrointestinal disturbance, including nausea and vomiting. Use of water containing copper that exceeds the permissible level over many years could cause liver or kidney damage. (Ye et al., 2012).

Zinc (Zn) is an essential requirement for a healthy body, excess zinc can be harmful, and cause zinc toxicity. Zinc (II) is a well-known toxic metal ion and can threaten human life by bio-accumulating in the food chain. Zn can cause nonfatal fume fever, pneumonitis, and is a potential hazard as an environmental pollutant (Zhang et al., 2017; Zwain et al., 2014).

Adsorption technique is a highly effective method because it is a simple and cost effective method for recovering and eliminating heavy metal ions from dilute solutions (Dehghani et al., 2016).

Water hyacinth (*Eichhornia crassipes*) is a promising bio-sorbent. This vascular fast growing floating plant is commonly found in tropical and subtropical regions of the world with a well-developed fibrous root system and large biomass. It is the global most terrible marine weed. It causes similar problems to those posed by water lettuce, such as clogging canals, rivers and lakes; displacing native plants and animals; and interfering with the irrigation of many crops, navigation, fishing and the activity of electric power stations. Water hyacinth was recognized by the International Union for Conservation of Nature (IUCN) as one of the 100 maximum harsh destructive species and documented as one of the top 10 worst weeds in the world (Holm et al., 1977).

Consequently, we select water hyacinth as a low-cost adsorbent to study the removal efficiency of copper and zinc. The aim of this study is to observe the removal efficiency of water hyacinth stem and shoot without any treatment and with particle size 2-3 mm. The adsorption capacity was conducted in relation to various parameters such as pH, contact time, amount of adsorbent and initial metal ion concentration.

2 LITERATURE

In the recent past, some researchers have emphasized using aqua vascular weed for removal of heavy metals like water hyacinth. In (2021) Hemalatha, Narayanan and Sanchitha investigated the potential of powdered parts of (leaves, petiole, root) water hyacinth through influential parameters such as biosorbent dosage, initial concentration of heavy metals, initial pH and contact time. Batch adsorption studies were conducted followed by column studies. Results showed that the dried biomass of *Eichhornia crassipes* proved to be a good adsorbent with less cost, maintenance and operating conditions. Biomass prepared from petiole showed high chromium removal, whereas the root sample showed better zinc removal. In (2019) Chivhanga et al. used magnetic biochar (Fe_2O_3-EC) derived from water hyacinth in the removal of Cu^{+2} and Zn^{+2} from aqueous solution using batch adsorption process. Batch adsorption studies on the effects of temperature, biosorbent dosage, contact time, and initial metal ion concentration were carried out. Fe_2O_3-EC exhibited optimum contact time, biosorbent dosage, and pH values of 65 min, 1.2 g, and 6, respectively. The results have demonstrated that the use of Fe_2O_3-EC in metal ion removal could provide an alternative way to manage and utilize this highly problematic invasive species. Neris et al. (2019) used modified water hyacinth as adsorbent to remove Pb^{2+}, Ni^{2+} and

Zn^{2+} ions from aqueous single and tri-element systems. They found that the maximum single-element adsorption capacities of water hyacinth for Ni^{2+}, Zn^{2+} and Pb^{2+} ions were 28.6 ± 3.9, 18.9 ± 1.6 and 76.8 ± 4.7 mg g^{-1} at 25.0°C, respectively. The selectivity order of water hyacinth fiber in single and tri-element systems is $Pb^{2+} >> Zn^{2+} \geq Ni^{2+}$. Sarkar, Rahman and Bhoumik (2017) used water hyacinth shoot powder to remove chromium and copper from tannery effluent using filtration process. Their finding indicates that Cr and Cu removing capacity of water hyacinth were satisfactory and water hyacinth is a potential adsorbent which can be used as alternative in the sustainable Cr and Cu removal technology for wastewater purification system. and Hassoon and Najem (2017) have as well utilized water hyacinth powdered leaves to remove cadmium, copper, lead and chromium from aqueous solution with higher removal efficiencies observed.

3 EXPERIMENTAL PROCEDURE

3.1 Biomass preparation

Water hyacinth (Eichhornia crassipes) plants were collected from small canal in El Sharkaya, Egypt. The collected plant was washed many times with tap water to remove adhering dirt, and later washed using distilled water until it was certain that there was no foreign material on the sample plants and the washed-off water appeared clean. The washed plants were then cut into roots, shoots and stems. It must be noted that only the stems and shoots are used in this research. These stems and shoots were then sun dried on marble sheet at an average temperature of 30℃ for 10 days. The dried brown plant biomass was grinded to 2-3 mm. The dried water hyacinth particles were stored in pre-cleaned glass jar. This prepared water hyacinth was used for the experiments.

3.2 Preparation of Stock Solution

Zinc sulfate ($ZnSO_4 .7H_2O$) of Mwt 287.54 and copper sulfate ($CuSO_4 .5H_2O$) of Mwt 249.5 were used to prepare the stock solution of metal ions in aqueous form. The stock solution was prepared by dissolving the exact quantity of metal salt in 1000 ml distilled water to obtain the required concentration in ppm (mg/l).

3.3 Batch Bio-Sorption Experiments

Batch biosorption experiments were carried out at room temperature (33±2 ºC), given mass of adsorbent with 50 ml of metal ions solution of desired concentration in 100 ml glass containers. After the adsorbate had had the desired contact time of interaction with the dried hyacinth, the samples were filtered using Whatman filter paper no. 42. All the residual concentrations of Cu and Zn after the adsorption process were analyzed using the DR 2010 Spectrophotometer. The amount of biosorption (q) was calculated by using the Equation (1) below.

$$q = [C_0 - C_e] \frac{v}{m} \qquad \textbf{Equation 1}$$

The biosorption efficiency of the metal ion was calculated from Equation (2):

$$\%\ removal = \frac{[Co - Ce]}{Co} \times 100 \qquad \textbf{Equation 2}$$

Where Co= is the initial concentration (mg/l), C_e = is the final concentration (mg/l), υ = is the volume of the solution (L), m = is the amount of bio-sorbent used in (g).

3.4 Adsorption Isotherm

Adsorption isotherm is an empirical relationship used to predict how much solute can be adsorbed by adsorbent. In this study the linearized forms of Freundlich and Langmuir were compared. Freundlich sorption isotherm can be represented by Equation 3:

$$Ln\ q_e = ln\ K_f + \left(\frac{1}{n}\right) lnC_e \qquad \textbf{Equation 3}$$

Where K_f = Freundlich characteristic constant (mg/g), obtained from the intercept of ln (q_e) versus ln C_e linear plot, $1/n$ = heterogeneity factor of sorption, obtained from slope of ln qe versus ln C_e linear plot, q_e = amount of metal adsorbed onto the adsorbent mg/g and is calculated from the following equation:

$$q_e = (C_e - C_o)\frac{v}{m} \qquad \textbf{Equation 4}$$

Freundlich isotherm was used for the concentration range from 20 ppm to 400 ppm, volume of solution used (V) is 50 ml and mass of adsorbent (m) is 1 g for both metal ions.

The Langmuir equation can be linearized as shown in Equation (5):

$$\frac{1}{q_e} = \frac{1}{q_m} + \frac{1}{q\ K_l\ c_e} \qquad \textbf{Equation 5}$$

Where C_e = Concentration of anions [mg/L], q_e = Adsorption equilibrium, [mg/g], q_m= The theoretical maximum adsorption capacity [mg/g]

K_l= Langmuir equilibrium constant related to the theoretical maximum adsorption capacity.

3.5 Kinetic Study

Two types of kinetics are generally used and compared, namely the pseudo-first order and pseudo-second order rate laws.

Pseudo-first order rate law, K_1

The equation for pseudo-first order kinetics was introduced initially by Lagergren. In the literature, it is generally used in the form proposed by Ho and McKay.

$$ln\ (q_e - q_t) = ln\ q_e - K_1 t \qquad \textbf{Equation 6}$$

Where q_t is the amount of adsorbed solute at different times, $q_e$is value at equilibrium, K_1 is the

pseudo-first order rate constant, t is time.

Pseudo-second order rate law, K_2

The formula for pseudo-second order kinetics is generally employed in the form proposed by Ho and McKay as follows:

$$\frac{t}{q_t} = \frac{t}{q_e} + \frac{1}{K_2\, q_{e2}} \qquad \textbf{Equation 7}$$

Where K_2 = The pseudo-second order kinetic rate constant

4 RESULTS AND DISCUSSION

4.1 Effect of contact time

Contact time has a great effect on the removal of both zinc and copper ions. Effect of contact time on adsorption of Zn (II) and Cu (II) ions was investigated keeping the biomass in contact with the metal ion solution for different time periods between 0 to 90 minutes for Zn (II) and 0 to 75 minutes for Cu (II). Initially ion uptake was rapid for both zinc and copper because there are sufficient and readily available sites for biosorption to occur. Subsequently, biosorption increased in the second phase but with a much slower rate until an equilibrium was reached. For Cu (II), increasing the contact time also increased the adsorption percentage until there was no change observed after 60 minutes. This indicates that the equilibrium concentration was obtained in one hour as there was no significant change in equilibrium after that time. The maximum removal was noted at 60 minutes, and the percentage of removal of copper by water hyacinth observed was 85.5%. This indicates that the adsorption capacity of the dried water hyacinth was very efficient. In the case of Zn (II), increasing the contact time from 0 to 10 minutes led to a rapid uptake of the heavy metal until the percentage removal reached 33.9%. Beyond this point, it was observed that the adsorbed solute tends to desorb back into solution as depicted in Figures 1 and 2. These results agree with previous studies (Obi, 2015; Rani et al., 2017).

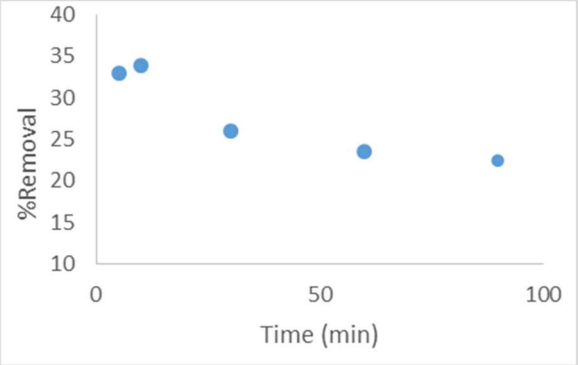

Figure 1: Effect of contact time on Zn(II) sample of concentration 20 ppm

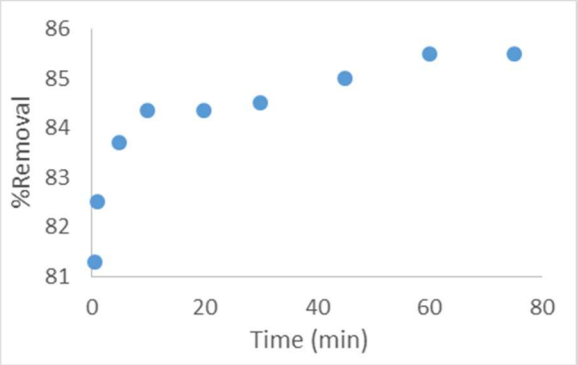

Figure 2 Effect of contact time on Cu(II) sample of concentration 20 ppm

4.2 Effect of Adsorbent Dosage

The availability and accessibility of the adsorption sites is controlled by adsorbent dosage. The effect of adsorbent at various doses (0.2, 0.5, 1, 1.5, 2.5 and 3 gm)/50 ml of zinc ions solution and (0.25, 0.5, 0.75,1 and 1.5 gm)/50 ml of copper ions solution, reveals that the percentage of removal of both zinc and copper increased with increasing weight of adsorbent. The rate of adsorption depends on the driving forces per unit area and in this case, since the initial concentration is constant, increasing the adsorbent dosage led to an increase in the surface area available and thus increased uptake of the heavy metal. This explanation agrees with previous studies on many other adsorbents (Ahmed et al., 2016; Al Saadi et al., 2016; Jami et al., 2016). The effect of varying doses of water hyacinth is graphically presented in Figures 3 and 4.

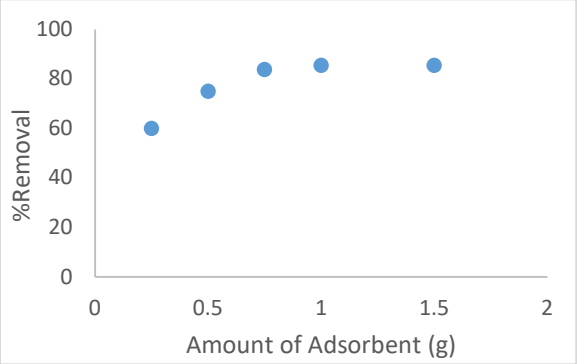

Figure 3: Removal efficiency of Cu(II)ions versus amount of adsorbent (initial conc. 20 ppm, pH 6.5, contact time 60 min. and temp 25±2)

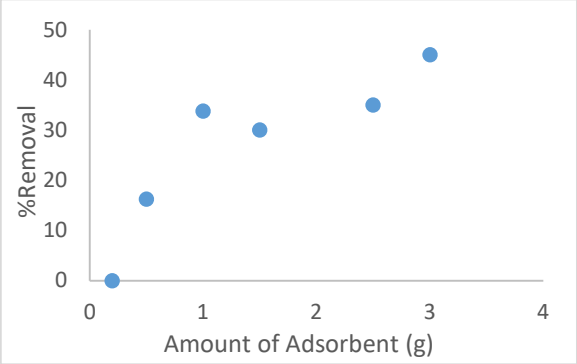

Figure 4: Removal efficiency of Zn(II) ions versus amount of adsorbent (initial conc. 20 ppm, pH 6.5, contact time 10 min. and temp. 25±2)

4.3 Effect of pH

Different sets of experiments were conducted by adjusting the pH from 2-10 to study the effect of pH on adsorption of zinc and copper at a concentration of 20 ppm and 1 g adsorbent for 60 min. Based on the obtained results, the removal efficiency increased and then slightly decreased. According to the conducted studies, the lower the pH, the more H^+ ions competing with the metal ions for adsorption sites, thus reducing their adsorption. On the other hand, the higher the pH, the less the H+ ions competing with metal ions for adsorption sites , thus increasing their adsorption which explains the results presented in Figures 5 and 6.

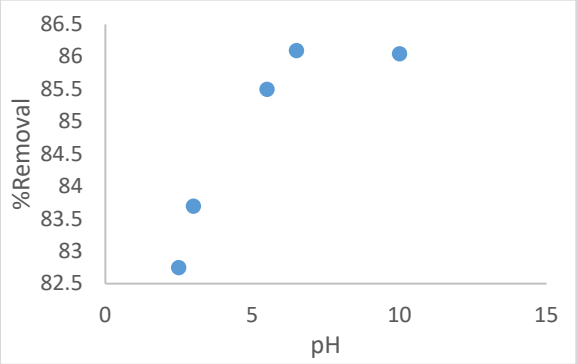

Figure 5: Removal efficiency of Cu (II) ions by adsorbent versus pH (initial concentration 20 ppm, contact time 60 min., amount of adsorbent 1 g and temp 25±2)

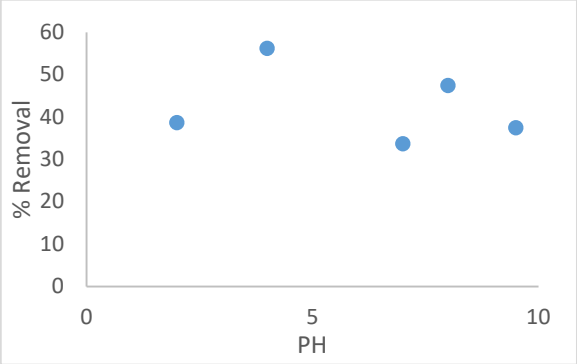

Figure 6: Removal efficiency of Zn (II) ions by adsorbent versus pH (initial concentration 20 ppm, contact time 60 min., amount of adsorbent 1 g and temp 25±2)

This result is in agreement with previous studies on many other adsorbents (Al-Hashimi and Al-Safar, 2013; Amosa, 2016; Jeyaseelan and Gupta, 2016) for the removal of copper and some other ions. The percentage of removal is maximum at pH 6.5 with a removal efficiency of 86.1%, thus pH 6.5 was selected. At a pH higher than 6.5 the amount adsorbed was found to be constant as all the adsorbent pores become saturated. For zinc, the percentage of removal is maximum at pH 4 with removal efficiency 56.25%.

4.4 Effect of Initial Metal Ion Concentration

Varying concentrations of 10–400 mg/l of Zn (II) and Cu (II) were experimented with the adsorbent dosage fixed at, the effect is as given in Figures 7 and 8.

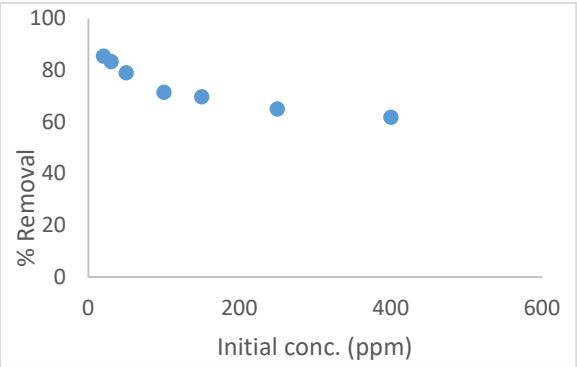

Figure 7: Removal efficiency of Cu(II) ions versus initial Concentration (pH=6.5, contact time 60 min. amount of adsorbent 1 g)

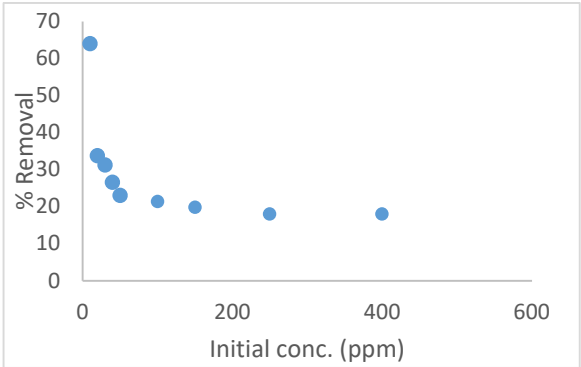

Figure 8: Removal efficiency of Zn(II) ions versus initial concentration (pH=6.5, contact time 10 min. amount of adsorbent 1 g)

It was observed that the percentage of removal is high at low concentrations and as the concentration increases the percentage of removal decreases. At lower concentrations all the metal ions interact with

the binding sites, thereby giving the maximum adsorption. On the other hand, at higher concentrations, metal ions will look for free binding sites, but due to lack of binding sites, the adsorption decreases at high concentrations (Aly et al., 2014).The difference in the uptake of copper and zinc may be due to the fact that interaction of the copper ions and zinc ions with the surface of the adsorbent is different. Also is may be due to the size of the ions, this could be verified using FTIR.

4.5 Adsorption Isotherm and Models

The isotherm constants and corresponding coefficients of determination for the adsorption of Zn (II) and Cu (II) are presented in Table 1. The Freundlich isotherm model fitted best with experimental data of the adsorption studies as it poses higher R^2 values for both zinc and copper.

Table 1: Isotherm constants for the adsorption of Zn (II) and Cu (II) ions on dried water hyacinth:

Metal Ions	Freundlich Constants			Langmuir Constants		
	K_f (mg/g)	n	R^2	K_L (L/g)	q_m (mg/g)	R^2
Zn (II)	21.366	1.370	0.9879	0.0124	11.876	0.8205
Cu (II)	2.423	1.499	0.9981	0.0118	17.699	0.8484

4.6 Kinetic Study

The plots and intercepts of curves were used to determine the first order constant K_{pf}, capacity q_e and the corresponding coefficients of determination (R^2_1) values.

The pseudo-second-order kinetic model suggests that the values of K_{ps} and corresponding coefficients of determination (R^2_2) values were determined from the slope. The coefficient of determination for the second-order kinetics model ($R^2_{2)}$ are greater, almost unity and the results are presented in Table 2. A similar phenomenon was observed in heavy metal ions onto different adsorbents (Farooq et al., 2010; Jeyaseelan and Gupta, 2016), hence, pseudo second-order model can be considered.

Table 2: Adsorption kinetic parameters of Zn (II) and Cu (II) ions on dried water hyacinth:

Metal Ions	Pseudo Second Order Kinetic Model		
	K_{sp}(g/mg)	q_e(g/mg.min)	R^2_2
Zn (II)	1.763	0.222	0.9982
Cu (II)	9.34	0.854	1

5 CONCLUSIONS

This study demonstrates that *E. crassipes* is a promising adsorbent for the removal of Zn (II) and Cu (II) ions from aqueous solutions. Water hyacinth biomass revealed that the biosorption process was dependent on the pH of the aqueous solution, contact time and concentration of Zn (II) and Cu (II) ions in the solution. The equilibrium data fitted well with Freundlich isotherm model with coefficient of determination (R^2) values of 0.9981 and 0.9879 for copper and zinc, respectively. The kinetic study revealed that the adsorption data obeyed the pseudo second-order model better than the pseudo first-order model given the higher R^2. It can therefore be concluded that *E. crasippes* is an effective alternative biomass suitable for use as adsorbent for the removal of Zn (II) and Cu (II) ions from industrial wastewater due to the high adsorption capacity characterized by this study. Besides, it is naturally and abundantly available at a low cost, and it can be used in the removal of heavy metal pollutants in water and wastewater hence conserving the environment.

REFERENCES

Ahmed, Y.M., Al-Mamun, A., Jameel, A.T., AlKhatib, M.F.R., Amosa, M.K., AlSaadi, M.A. 2016. Synthesis and Characterization of Carbon Nanofibers Grown on Powdered Activated Carbon. *Journal of Nanotechnology*, 2016, 10.

Al-Hashimi, M.A.I., Al-Safar, M.M. 2013. Removal of Cadmium from Polluted Aqueous Solutions Using Agricultural Wastes. *Journal of Environmental Studies*, 10, 31-38.

Al Saadi, M.A., Al Mamun, A., Alam, M.Z., Amosa, M.K., Atieh, M.A. 2016. Removal of Cadmium from Water by CNT-PAC Composite: Effect of Functionalization. *Nano*, 11(1), 7.

Aly, Z., Graulet, A., Scales, N., Hanley, T. 2014. Removal of aluminium from aqueous solutions using PAN-based adsorbents: characterisation, kinetics, equilibrium and thermodynamic studies. *Environmental Science and Pollution Research*, 21(5), 3972-3986.

Anzeze, D.A., Onyari, J.M., Shiundu, P.M., Gichuki, J.W. 2014. Adsorption of Pb (II) Ions from Aqueous Solutions by Water Hyacinth (Eichhornia Crassipes): Equilibrium and Kinetic Studies. *International Journal of Environmental Pollution and Remediation (IJEPR)*, 2, 89-95.

Dehghani, M.H., Sanaei, D., Ali, I., Bhatnagar, A. 2016. Removal of chromium(VI) from aqueous solution using treated waste newspaper as a low-cost adsorbent: Kinetic modeling and isotherm studies. *Journal of Molecular Liquids*, 215, 671-679.

Farooq, U., Kozinski, J.A., Khan, M.A., Athar, M. 2010. Biosorption of heavy metal ions using wheat based biosorbents–A review of the recent literature. *Bioresource technology*, 101(14), 5043-5053.

Hassoon, H.A., Najem, A.M. 2017. Removal of Some Traces Heavy Metals from Aqueous Solutions by Water Hyacinth Leaves Powder. *Iraqi Journal of Science*, 58(2A), 611-618.

Hemalatha D., Narayanan R., Sanchitha S.(2021). Removal of Zinc and Chromium from industrial

wastewater using waterhyacinth (E. crassipes) petiole, leaves and root powder: Equilibrium study. Materials Today: Proceedings 43 (2021) 1834-1838.

Holm, L.G., Plucknett, D., Pancho, J.V., Herberger, J.P. 1977. The world's worst weeds. Distribution and biology. East-West Center Book, Univ. *Honolulu,: Press Hawaii*.

Jami, M.S., Rosli, N.-S., Amosa, M.K. 2016. Optimization of Manganese Reduction in Biotreated POME onto 3A Molecular Sieve and Clinoptilolite Zeolites. *Water Environment Research*, 88(6), 566-576.

Jeyaseelan, C., Gupta, A. 2016. Green Tea Leaves as a Natural Adsorbent for the Removal of Cr (VI) From Aqueous Solutions. *Air, Soil and Water Research*, 9, ASWR. S35227.

Neris, J. B. ; Luzardo, F. H. M. ; Santos, P. F. ; Almeida, O. N. de ; Velasco, F. G.(2019). Evaluation of single and tri-element adsorption of Pb^{2+}, Ni^{2+} and Zn^{2+} ions in aqueous solution on modified water hyacinth (*Eichhornia crassipes*) fibers. *Journal of Environmental Chemical Engineering* 7(2019) No.1.

Nyamunda B. , Chivhanga T. Guyo U. , Chigondo F. 2019. Removal of Zn (II) and Cu (II) Ions from Industrial Wastewaters Using Magnetic Biochar Derived from Water Hyacinth. *Journal of Engineering* (2019) 1-11.

Obi, C. 2015. Sorption characteristics of water hyacinth leaf biomass on the removal of Cu (ii) ion from aqueous solution. *International Journal of Innovative Agriculture and Biology Research*, 3(3), 36.

Prabha, R.T., Udayashankara, T.H. 2014. Adsorption of copper metal ions from aqueous solution using rice husk and groundnut shell. *International Journal of Science and Research (IJSR)*, 3(8), 705-709.

Sarkar M., Rahman A. and Bhoumik N. 2017. Remediation of chromium and copper on water hyacinth (*E. crassipes*) shoot powder. *Water Resources and Industry* 17 (2017) 1–62.

Ye, H., Zhang, L., Zhang, B., Wu, G., Du, D. 2012. Adsorptive removal of Cu(II) from aqueous solution using modified rice husk. *International Journal of Engineering Research and Applications (IJERA)*, 2(2), 855-863.

Zhang, X., Hao, Y., Wang, X., Chen, Z. 2017. Rapid Removal of Zinc(II) from Aqueous Solutions Using a Mesoporous Activated Carbon Prepared from Agricultural Waste. *Materials*, 10(9), 1002.

Zwain, H.M., Vakili, M., Dahlan, I. 2014. Waste Material Adsorbents for Zinc Removal from Wastewater: A Comprehensive Review. *International Journal of Chemical Engineering*, 2014, 13.

Catalytic Pyrolysis of Municipal Solid Waste: Effect of South African synthesized zeolite on PE plastic waste

O.A. Olagunju* and S.L. Kiambi

Chemical Engineering Department Durban University of Technology, P.O. Box 1334, Durban 4000, South Africa.

*Corresponding Author: gilbert4life2004@yahoo.com

ABSTRACT

Zeolite Socony Mobil–5 (ZSM-5) was produced by metakaolinizing a South African kaolin deposit in Grahamstown and mixing it with sodium hydroxide (NaOH), tetrapropylammoniumbromide (TPABr), sodium silicate pentahydrate ($Na_2SiO_3.5H_2O$) solution, and deionized water to produce mole fractions of $20SiO_2$:$0.05Al_2O_3$:$1.5Na_2O$:2TPABr:$200H_2O$. Scanning electron microscopy (SEM), x-ray diffraction (XRD), and Brunauer–Emmett–Teller (BET) surface area were used to analyze the produced zeolite. The findings revealed that the generated sample was ZSM-5. The synthesized zeolite consists of 179,9 m2/g, 49,262A, and 0,05 cm3/g of specific surface area, pore size, and pore volume respectively. The influence of the produced ZSM-5 on plastic waste was studied at the temperature range from 300 °C to 500 °C. Polythene bags were employed as feedstock for the experiment. The liquid fuel produced from the catalytic pyrolysis was evaluated using a gas chromatograph-mass spectrometer (GC–MS). A significant range of hydrocarbons were obtained as a result of the effective conversion of plastic waste to liquid fuels demonstrated by the results obtained in this study. Kaolin zeolite of South African origin, synthesized into zeolite, has shown excellent promise as a natural zeolite catalytic material for plastic waste pyrolysis.

Keywords: South African Kaolin, ZSM-5, municipal plastic waste, catalytic pyrolysis process, hydrocarbons

1 INTRODUCTION

Plastic has played an important role in everyday life, despite the fact that its continued use has resulted in a massive accumulation of plastic waste cluttering the environment for more than two decades. Plastics are in high demand due to their versatility in industrial and clinical applications (Ajibola et al., 2018). The flexible characteristics of Polyethylene (PE), Polythene Terephthalate (PET), and Polystyrene (PS) plastics makes them a vital resource for technological improvements (Olagunju and Kiambi 2021).

Plastic wastes (PE, PET, and PS) make up the majority of municipal solid wastes (MSW) in developing countries (Shah 2010). Because of the constant generation of MSW and the ineffective treatment methods used in these countries, managing MSW has become an uphill challenge. This has resulted in not just environmental issues, but also human beings and marine life have been

endangered (UNEP, 2009). Furthermore, many African countries have not implemented modern established technologies for MSW treatment, preferring instead to use the traditional method of landfilling, which has proven to be ineffective (Ajibola et al. 2018).

There are four major methods of reprocessing plastic waste streams: These are primary recovery, which entails converting waste materials into products with similar properties to the initial plastic waste; secondary recovery, which entails converting waste materials into a new product that is distinct from the initial waste material; and third recovery, which entails converting plastic waste material into a new product that is distinct from the original material. The third recovery approach involves using these wastes as raw materials to make valuable chemical and hydrocarbon products, and the fourth recovery method involves combustion of long chain polymetric material to generate energy. Pyrolysis is one of the processes for converting long-chain organic compounds (plastic waste) into environmental friendly fuels (Olagunju and Kiambi 2021).

Pyrolysis is a method of converting long-chain hydrocarbons compounds into monomers by thermal disintegration at temperatures ranging above 400 degrees Celsius (Rehan et al., 2017). Investigators have previously used varieties of catalytic materials to improve the efficiency of plastic waste pyrolysis, including ZSM-5, FCC, and MCM-41, among others. Catalyst accelerates the pace of reaction, reduces reaction time, and minimizes contaminants in the produced oil (Ratnasari et al., 2017; Serrano et al., 2012).

The utilization of a catalyst in the pyrolysis of plastic waste to hydrocarbons has been described by several researchers. From catalytic pyrolysis of PE employing HZSM-5, Uemichi (1998) observed a significant liquid oil production. Using enhanced MCM-41 and HZSM-5 catalysts, Gaca et al. (2008) achieved significant liquid conversion, mostly aromatic hydrocarbons, during the pyrolysis of plastic wastes. Lin et al. (2004) employed blended mesoporous SiO2-Al_2O_3 with HZSM-5 as a catalyst which resulted in significant oil product. The use of available commercial catalysts in the pyrolysis of PW has the benefit of improving the oil quality. The exorbitant cost, unfortunately, raises the process's cumulative cost of production, making this methodology less appealing.

Zeolites are ion-exchanging crystals with micro-pore diameters that are thermally stable across a wide temperature range. Its use in the breakdown of long-chain hydrocarbons is well-known, particularly in the petrochemical industry. Zeolite Y, for example, is a strong faujasite absorbent with a high silica-alumina ratio ranging from 1.5 to 3.8. (Sakaki et al., 2013; Auerbach et al., 2003).

There are two types of catalysts: natural and synthetic. The application of clay as a feedstock for catalyst production has brought a lot of positive results (Liu et al., 2003; Chandrasekhar and Pramada 1998). Over the years, ZSM-5 catalysts have been synthesized and characterized using expensive chemicals over. Finding a less expensive alternative will save costs and ensure the catalyst's long-term

viability. Researchers such as: Panpa and Jinawath, (2009) utilized rice husk ash, Chareonpanich et al., (2004) used fly ash, Feng et al., (2009a) used kaolinite, Jiang et al., (2014) used palygorskite, and Salou et al., (2001) used kanemite as alternative cheap source in separate investigations. However, because there are some chemicals in their mineralogical composition that may impact the derived catalyst, they are ineffective as raw materials for zeolite synthesis.

Jiang et al. (2014) used rich silica-containing palygorskite as raw material, and Panpa and Jinawath (2009) used rice husk as starting materials to make ZSM-5, but adding aluminum to balance the Si/Al ratio was unfavorable, preventing the production of ZSM-5. Fly ash was discovered to be a viable source of ZSM-5 (Chareonpanich et al., 2004). Unfortunately, high temperatures of above 200 °C are required for the synthesis of pure ZSM-5, and yields are often low. The low product yield and high energy requirements caused by the high temperatures necessitate process modification. Kaolin has been successfully transformed to a variety of zeolites using it as a starting material (Belviso et al., 2013; Chandrasekhar and Pramada, 2008; Kovo and Holmes, 2010).

Kaolin-based zeolite is regarded as a low-cost and inexhaustible catalytic material (Lijalem Ayele Regassa, 2016). The majority of research conducted has been on commercialized kaolins, which are primarily employed in zeolite A production. The current project will aim to create ZSM-5 zeolite using kaolin mined from Grahamstown, South Africa. The synthesis of ZSM-5 from kaolin in this geological location, as well as its use as a catalyst in the pyrolysis of PW, do not appear to have been documented. Polyethylene was chosen as the feedstock because it is one of the most frequent plastics found in high concentrations in the plastic waste stream of municipal solid waste material.

The primary objective of this investigation was to transform waste plastics into oil products that might be used as liquid fuels or chemical feedstock. The effects of operating factors such as time and temperature on the constituents of the oil produced from the catalytic pyrolysis of the PW process will also be addressed.

2 EXPERIMENTAL

2.1 Materials and Methods

Polyethylene was used as the raw material in this investigation. This material was sourced from the Durban University of Technology's cafeteria garbage bins in Durban, South Africa. The material was sorted, rinsed, and then shredded into tiny pieces prior to the commencement of this experiment. Kaolin from G&W mineral resources in the Eastern Cape region of South Africa, which has a Silica - Alumina ratio of 2.91 served as Si/Al source. It was calcined at 600 °C for 2 hours (66.58 percent SiO_2 and 22.81 percent Al_2O_3 respectively). Sodium silicate composition solution with 26.5 percent SiO_2 and 10.6 percent Al_2O_3 and TPABr were all purchased from Sigma Aldrich. However, Nitric acid 55 percent, was procured from Ace enterprises chemical association. These chemicals were used exactly

as they were, with no further treatment.

2.2 Synthesis of Kaolin-based ZSM-5 Zeolite

The needed amount of G&W metakaolin and sodium hydroxide were dissolved in deionized (DI) water, and TPABr was combined independently with the required quantity of DI water in the synthesis of kaolin-based ZSM-5. The sodium silicate solution and the NaOH/Kaolin solution were added to the TPABr solution at the same time while stirring. The pH was controlled using nitric acid until the solution combination was homogeneous. The formed gel was transferred to a stainless steel Teflon-lined autoclave cup and hydrothermally treated for two days at 180 degrees Celsius. The final product was washed in DI until it had a pH of less than 8. The sample was dried overnight at 80 degrees Celsius and then calcined for 5 hours at 550 degrees Celsius. The produced dried powder was therefore characterized and analyzed.

2.3 Characterization

Bruker AXS, D8 Advance fitted with Tube (Cu-Ka radiation (lKa1=1.5406 Å) and Detectors Lynx Eye (Position sensitive detector) at V_20 variable slit, 40 kilovolts, and 40mA recorded X-ray diffraction (XRD) patterns and average crystallite size. A 0.5° to 130° 2incremental width was used, with a constant increment of 0.034° and a scan rate of 0.5 sec per step. OriginPro 2018 software was used to analyze the diffraction data and estimate the amount of each phase in the sample. Scanning electron microscopy FEI Nova NanoSEM 230 with an energy dispersive laser fitted with a strong absorption lenses were used to analyze the structure. The Oxford X-Max EDS detector was used using INCA software. The BET machine was used to measure and analyze surface area, pore size, and pore volume.

2.4 Experimental procedures

The prepared material was loaded into the reactor, and the reaction's operational parameters were set. The stainless steel reactor setup, which has a cylindrical shape and was appropriately lagged, is shown in Figure 1. To purge the system, N_2 gas was applied, and the unit was heated using an electric furnace with a temperature controller to adjust the temperature. The reactor is linked to a condenser and a container for collecting the pyrolytic hydrocarbon produced.

With this research study, the appropriate waste-to-catalyst ratio (100g/10g) were loaded into the reactor. The system was purged of air for 10 minutes using N_2 gas delivered at a flowrate of 20 ml / minute. At the start of each run, the furnace was turned on so that the process working temperature can be established. The PE feedstock gradually decomposes as the temperature rises in the reactor during the catalyzed pyrolysis process. The vapor flows through the catalyst bed for further reaction before exiting the chamber and being condensed in the condenser before being received as liquids in the container. The generated liquid oil was analyzed using gas chromatography–mass spectrometry (GC–MS). The formula used in determining the produced liquid oil, gas, and char (Patil et al., 2017) is as

follows.

Char (weight percent) = (Amount of Char produced / Amount of feedstock) * 100% **Equation 1**

Liquid oil (weight percent) = (liquid yield / Amount of feedstock) * 100% **Equation 2**

Gas (weight percent) = 100 - (Char (weight percent) + Liquid oil (weight percent)) **Equation 3**

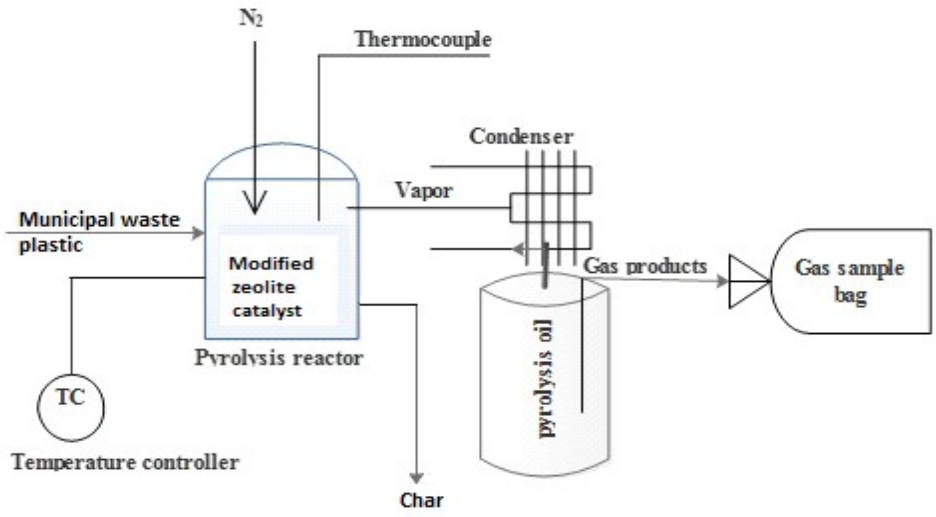

Figure 1: Diagram of the pyrolysis experiment setup.

3 RESULTS AND DISCUSSION

3.1 X-ray diffraction (XRD) studies

Figure 2 shows the XRD pattern of ZSM-5 utilizing metakaolin that was calcined at 650°C for 2 hours. The distinctive peaks of ZSM-5 are in the range of 7.9 to 23.1° 2θ, indicating nucleation with a significant amount of quartz as an impurity at 20.9 and 26.6° 2θ, confirming the creation of the crystalline ZSM-5 phase (Mohiuddin et al., 2016; Salou et al., 2001). Using OriginPro 2018 edition, the percentage (%) crystallinity and average crystal (grain) size were determined to be 87 percent crystallinity and 28 nm, respectively. The pyrolysis process relies on these two variables. The BET surface area analyser was used to calculate the specific surface area, pore size, and pore volume of 179.9 m^2/g, 49.262A, and 0.05 cm^3/g, respectively. The specific surface area of the catalyst is increased by increasing the crystal size, and the zeolite's outer surface area is increased by increasing the intense surface porosity (Wibowo et al., 2017). The combined effect of the two parameters has an effect on the effective surface area. This demonstrates that the kaolin-based ZSM-5, which has a large surface area, has the potential to provide significant reaction rates and efficiency.

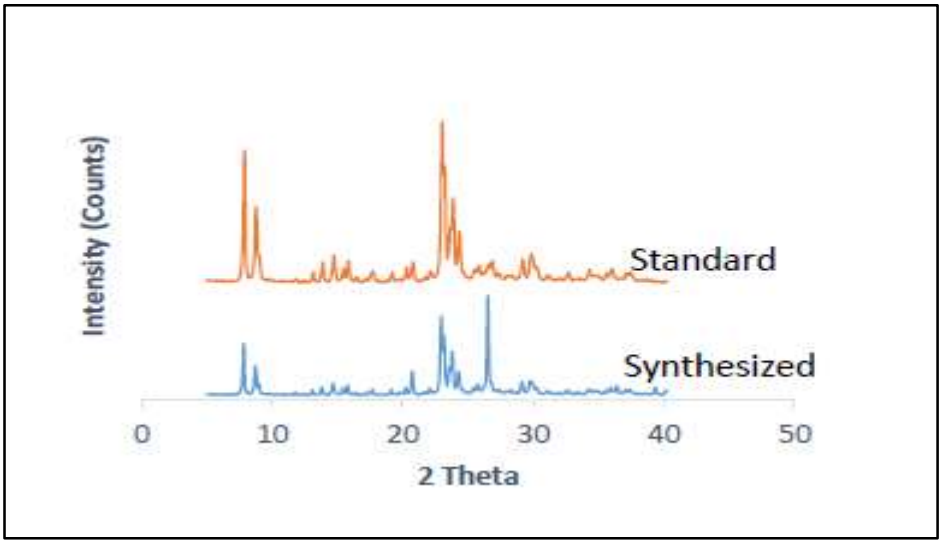

Figure 2: Kaolin-based ZSM-5 zeolite XRD patterns

3.2 Scanning electron microscopy (SEM) studies

SEM is a method for interpreting the form and size distribution of zeolite crystals. ZSM-5 crystals' configuration, formation, and structure are often tightly controlled and dependent on synthesis parameters including crystallization temperature, duration, and age. Mohiuddin (2016) investigated the synthesis of ZSM-5 utilizing impure kaolin under a variety of conditions, resulting in a variety of morphologies. Therefore, in this current work, the morphology of kaolin-based ZSM-5 nanocrystals produced at 180 °C, 48hr, and 48hr crystallization temperature, time, and aging, respectively, is shown in Fig. 3. The kaolin-based ZSM-5 has an orthogonal shape and is well crystalline, with an average crystal size of 28 nm, indicating the presence of an intergrown crystal with some amorphous material. The aggregation of their high surface Gibbs free energy results in orthogonal nanocrystals (Wu et al., 2013).

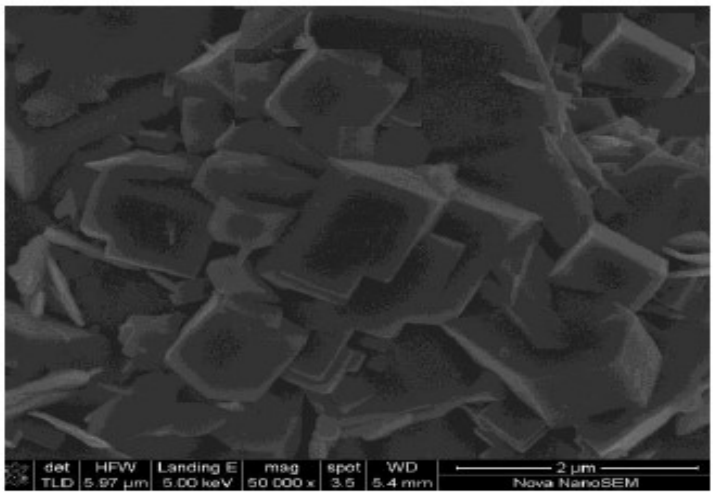

Figure 3: SEM imagery of kaolin-based ZSM-5 zeolite produced

3.3 Effect of temperature on the feedstock

The reaction was operated between temperature 300 and 500 degrees Celsius. At each temperature, the degradation response was carried out for 90 minutes. During the process, the influence of temperature on the products yield from catalytic degradation of PE waste was considered. the decomposition begins at 300 ºC and rises considerably from 350 ºC to 400 ºC. The degradation reaction was done in batches and it took 90 minutes to complete each run. The gas yield rises with increasing temperature from 350 Celsius to 400 Celsius and then nearly stays constant till 450 degrees Celsius. Oil production begins at 350 degrees Celsius and rises to 450 degrees Celsius. At 400 Celsius, total conversion was 89 percent. The quantity of products dispersion for oil, gas, and char is shown in Figures 4.

Aguado et al. (2017) discovered a similar result utilizing TGA during the breakdown of waste HDPE in the presence of an acid catalyst (ZSM-5). At 400 ºC, the product of interest (oil) yielded 89 percent, which is close to the 89.10 percent oil yield recorded at 450 ºC. As a result, increase in temperature above 400 ºC have no significant influence on product yield and therefore, it can be concluded that the maximum oil yield is at 400 °C.

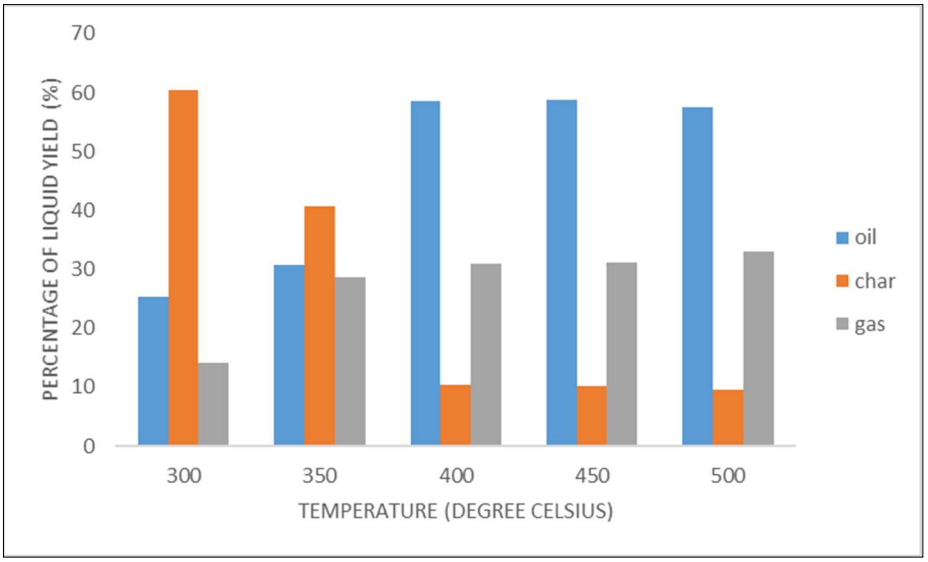

Figure 4: Influence of operating parameter; the temperature on produced liquid, char, and gas.

3.4 Effect of time on the produced oil

At the optimal temperature of 400 ºC, the influence of process parameter time was studied. The reaction time was measured with an increase of 30 minute, commencing at 30 minutes and ending at 150 minutes. Figures 5 depicts the findings of the observations. The oil yield was 49.60 % after 30 minutes of reaction time, and it rapidly climbed to 58.20 % after 90 minutes of reaction time. There is no significant difference beyond the 90-minute reaction time. At an optimum temperature of 400 ºC, a response time of 90 minutes is regarded optimum for the catalytic degradation of PE.

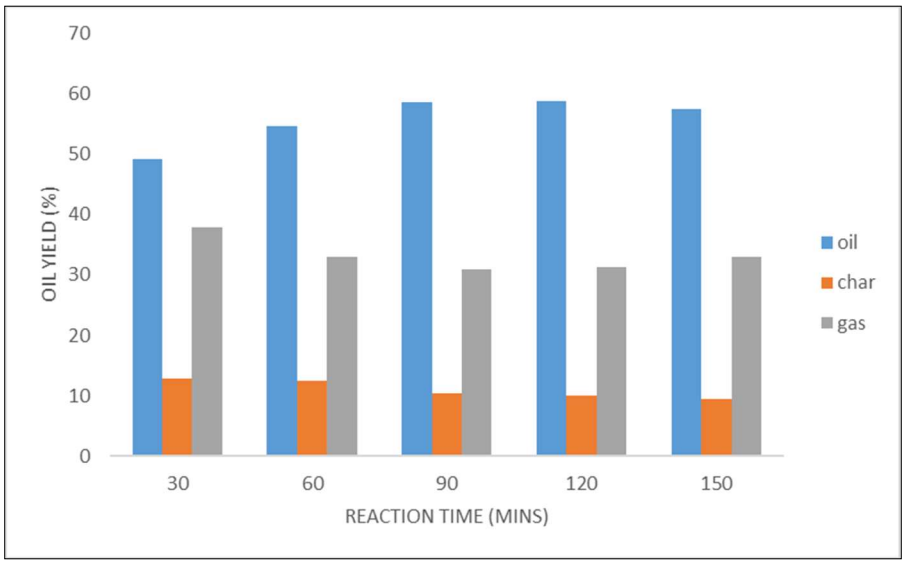

Figure 5: Influence of operating parameter; the reaction time on produced liquid, char, and gas.

3.5 Characterization of the produced liquid oil

The physical properties of the liquid fuel produced under the optimal reaction parameters were investigated. The findings of the hydrocarbon fraction studies were compared to the ASTM standards of fossil fuel products. For the catalytic fuel and its fractions, physical characteristics such as Refractive Index, Density, Specific Gravity, API Gravity, Viscosity, Kinematic Viscosity, Flash Point, Pour Point, ASTM BP range, and Calorific value were evaluated.

Table 1: Physical properties of the catalytic fuel produced

Physical properties	Oil fraction produced	ASTM standards		
		Diesel	Gasoline	Kerosene
Refractive index	1.430	1.484	1.434	1.440
Density (g/ml)	0.73	0.83–0.85	0.72–0.74	0.78–0.82
Specific gravity	0.733	0.83–0.85	0.72–0.74	0.78–0.82
API gravity Viscosity	61.46	34.97	65.03–62.34	49.91–41.06
Kinematic viscosity (mm^2/s)	1.14	2.4–5.3	1.076–1.140	1.54–2.20
Flash point	35.8	55–60	37.8–38	50–55
Pour point	-	-	-	-
Cal. value (MJ/kg)	45.8	43.7	46.9	45.5

Almost all of the determined fraction values were virtually equal to the petroleum products according to the results. Table 1 shows a comparison of the physical properties of the catalytic fuel produced.

4 CONCLUSIONS

Kaolin-base ZSM-5 was produced and used as a catalyst with specific surface area, pore size, and pore volume of 179.9 m^2/g, 49.262Å, and 0.05 cm^3/g, respectively, using localized kaolin from SA. The source material used for this pyrolysis experiment was polyethylene (PE) plastic wastes. The results of this research reveal that this source material may be used to produce a variety of valuable chemicals products and hydrocarbons. A range of hydrocarbons (C_4-C_{12}) of 58.60% was produced with a total conversion rate of 89.10% at the optimal temperature of 400 ºC and reaction time of 90 mins respectively.

ACKNOWLEDGEMENTS

The authors would like to express their gratitude to the National Research Fund (NRF) of South Africa and the Durban University of Technology for their financial support.

REFERENCES

Aguado J, Serrano D.P, San Miguel G., Escola J.M, Rodrıguez J.M. 2017. Catalytic activity of zeolitic and mesostructured catalysts in the cracking of pure and waste polyolefins. J Anal Appl Pyrol;78:153–61.

Ajibola, A.A., Omoleye, J.A. and Efeovbokhan, V.E. 2018. Catalytic cracking of polyethylene plastic waste using synthesized zeolite Y from Nigerian kaolin deposit. Appl Petrochem Res 8, 211–217. https://doi.org/10.1007/s13203-018-0216-7

Al-Salem, S.M, Antelava, A, Constantinou, A, Manos, G and Dutta, A. 2017. A review on thermal and catalytic pyrolysis of plastic solid waste. J Environ Manage 197(1408):177–198.

Al-Salem, S.M. 2009. Establishing an integrated databank for plastic manufacturers and converters in Kuwait. J Waste Manag 29:479–484.

Artetxe, M., Lopez, G., Amutio, M., Barbarias, I., Arregi, A., Aguado, R., Bilbao, J., Olazar, M. 2015. Styrene recovery from polystyrene by flash pyrolysis in a conical spouted bed reactor. Waste Manage. 45, 126–133.

Auerbach, S.M, Carrado KA, Dutta, P.K. 2003. Zeolite science and technology, New York, Basel, pp. 11–30.

Belviso, C., Cavalcante, F., Lettino, A., Fiore, S., 2013. A and X-type zeolites synthesized from kaolinite at low temperature. Appl. Clay Sci. 80-81, 162–168.

Chandrasekhar S. and Pramada P.N. 1998. Investigation on the synthesis of zeolite NaX from Kerala kaolin. J Porous Mater 6:283–284.

Chandrasekhar, S., Pramada, P.N., 2008. Microwave-assisted synthesis of zeolite A from metakaolin.

Micropor. Mesopor. Mater. 108, 152–161.

Chareonpanich, M., Namto, T., Kongkachuichay, P., Limtrakul, J., 2004. Synthesis of ZSM-5 zeolite from lignite fly ash and rice husk ash. Fuel Process. Technol. 85, 1623–1634.

Chen, D., Yin, L., Wang, H., He, P. 2014. Pyrolysis technologies for municipal solid waste: a review. Waste Manage. 34, 2466–2486.

de Marco, I., Caballero, B.M., López, A., Laresgoiti, M.F., Torres, A., Chomón, M.J. 2009. Pyrolysis of the rejects of a waste packaging separation and classification plant. J. Anal. Appl. Pyrol. 85 (1–2), 384–391.

Demirbas, A. 2004. Pyrolysis of municipal plastic wastes for recovery of gasoline range hydrocarbons. J. Anal. Appl. Pyrol. 72, 97–102.

Feng, H., Li, C., Shan, H., 2009a. Effect of calcination temperature of kaolin microspheres on the in situ synthesis of ZSM-5. Catal. Lett. 129, 71–78.

Frediani, P., Undri, A., Rosi, L., Frediani, M. 2014. Waste/Contaminated Polystyrene Recycling through Reverse Polymerization. Lynwood ed., Nova Publisher. ISBN: 978-1-63321-371-5.

Gaca, P., Drzewiecka, M., Kaleta, W., Kozubek, H., and Nowinska, K. 2008. Catalytic degradation of polyethylene over mesoporous molecular sieve MCM-41 modified with heteropoly compounds. Polish J. Environ. Stud. 17, 25–35.

Hernández, M.R., Gómez, A., García, A.N., Agulló, J., Marcilla, A. 2007. Effect of the temperature in the nature and extension of the primary and secondary reactions in the thermal and HZSM-5 catalytic pyrolysis of HDPE. Appl. Catal. A 317, 183–194.

Jiang, J., Duanmu, C., Yang, Y., Gu, X., Chen, J., 2014. Synthesis and characterization of high siliceous ZSM-5 zeolite from acid-treated palygorskite. Powder Technol. 251, 9–14.

Jung, S.H., Kim, S.J., Kim, J.S. 2013. The influence of reaction parameters on characteristics of pyrolysis oils from waste high impact polystyrene and acrylonitrile–butadiene–styrene using a fluidized bed reactor. Fuel Process. Technol. 116, 123–129.

Kovo, A.S., Holmes, S.M., 2010. Effect of aging on kaolin-based zeolite Y from Ahoko Nigeria using a novel metakaolinization technique. J. Disper Sci Technol. 31, 442–448.

Lee, S., Yoshida, K., Yoshikawa, K. 2015. Application of waste plastic pyrolysis oil in a direct injection diesel engine: for a small scale non-grid electrification. Energy Environ. Res. 5 (1). 1927-0569.

Li, A.M., Li, X.D., Li, S.Q., Ren, Y., Chi, Y., Yan, J.H., Cen, K.F. 1999. Pyrolysis of solid waste in a rotary kiln: influence of final pyrolysis temperature on the pyrolysis products. J. Anal. Appl. Pyrol. 50, 149–162.

Lijalem Ayele Regassa 2016. Synthesis and Characterization of Zeolite A Studies of its application as detergent builder and in tannery wastewater treatment Lijalem Ayele Regassa A Thesis

Submitted to Department of Chemistry Presented in Fulfilment of the R.

Lin, Y. H., Yang, M. H., Yeh, T. F., and Ger, M. D. (2004). Catalytic degradation of high density polyethylene over mesoporous and microporous catalysts in a fluidized-bed reactor. Polym. Degrad. Stab. 86, 121–128. DOI: 10.1016/j.polymdegradstab.2004.02.015.

Liu X, Yan Z, Wang, H. and Luo, Y. 2003. In-situ synthesis of NaY zeolite with coal-based kaolin. J Nat Gas Chem 12:63–70.

Lopez, A., Marco, D.I., Caballero, B.M., Laresgoiti, M.F., Adrados, A. 2011. Influence of time and temperature on pyrolysis of plastic wastes in a semi-batch reactor. Chem. Eng. J. 173, 62-67.

Miandad, R., Barakat, M., Rehan, M., Ismail, I.M.I., Nizami, A.S. 2016b. The energy and value-added products from pyrolysis of waste plastics. In Book, 'Recycling of Solid Waste for Biofuels and Bio-chemicals' under Series Title: Environmental Footprints and Eco-design of Products and Processes. Springer Science+Business Media, Singapore. http://dx.doi.org/10.1007/978-981-10-0150-5_12.

Miandad, R., Barakat, M.A., Aburiazaiza, A.S., Rehan, M., Nizami, A.S. 2016a. Catalytic pyrolysis of plastic waste: a review. Process Saf. Environ. Prot. 102, 822–838. http://dx.doi.org/10.1016/j.psep.2016.06.022.

Miandad, R., Barakat, M.A., Rehan, M., Aburiazaiza, A.S., Ismail, I.M.I. and Nizami, A.S. 2017 Plastic waste to liquid oil through catalytic pyrolysis using natural and synthetic zeolite catalysts, Waste Management, Volume 69, 2017, pp 66-78, ISSN 0956-053X, https://doi.org/10.1016/j.wasman.2017.08.032.

Mo, Y., Zhao, L., Wang, Z., Chen, C.L., Tan, G.Y.A., Wang, J.Y. 2014. Enhanced styrene recovery from waste polystyrene pyrolysis using response surface methodology coupled with Box-Behnken design. Waste Manage. 34, 763–769.

Mohiuddin, E., Isa, Y. M., Mdleleni, M. M., Sincadu, N., Key, D., and Tshabalala, T. 2016. Synthesis of ZSM-5 from impure and beneficiated Grahamstown kaolin: Effect of kaolinite content, crystallization temperatures and time, Applied Clay Science, 119(November), pp. 213-221. DOI: 10.1016/j.clay.2015.10.008.

Olagunju, O.A., and Kiambi, S.L. 2021. Application of synthesized selected South African kaolin deposit on catalytic pyrolysis of municipal plastic waste. Virtual International Conference on Green Technologies for Sustainable Development, Dharmsinh Desai University, India, 09 – 11 March 2021.

Onwudili, J.A., Insura, N., Williams, P.T. 2009. Composition of products from the pyrolysis of polyethylene and polystyrene in a closed batch reactor: effects of temperature and residence time. J. Anal. Appl. Pyrol. 86, 293–303.

Panpa, W., Jinawath, S., 2009. Synthesis of ZSM-5 zeolite and silicalite from rice husk ash. Appl.

Catal. Environ. 90, 389–394.

Patil L, Varma K, Gajendra S, Mondal P. 2017. Thermocatalytic degradation of high density polyethylene into liquid product. J Polym Environ 1–10.

Ratnasari, D. K., Nahil, M. A., and Williams, P. T. 2017. Catalytic pyrolysis of waste plastics using staged catalysis for production of gasoline range hydrocarbon oils. J. Anal. Appl. Pyrolysis 124, 631–637. DOI: 10.1016/j.jaap.2016.12.027.

Rehan, M., Miandad, R., Barakat, M. A., Ismail, I. M. I., Almeelbi, T., Gardy, J. 2017. Effect of zeolite catalysts on pyrolysis liquid oil. Int. Biodeterior.Biodegrad. 119, 162–175. DOI: 10.1016/j.ibiod.2016.11.015.

Rehan, M., Miandad, R., Barakat, M., Ismail, I., Almeelbi, T., Hassanpour, A., Khan, M. Z., Demirbaş, A., Nizami, Abdul-Sattar. 2017. Effect of zeolite catalysts on pyrolysis liquid oil. International Biodeterioration & Biodegradation. 119. 162–175. 10.1016/j.ibiod.2016.11.015.

Ringer, M., Putsche, V., Scahill, J. 2006. Large-scale pyrolysis oil production: a technology assessment and economic analysis. A technical report by National Renewable Energy Laboratory (NREL), US. NREL/TP-510-37779. Available from: <http://www.nrel.gov/docs/fy07osti/37779.pdf>.

Sakaki AS, Roozbehani B, Shishesaz M, Nasrin A. 2013. Catalytic degradation of the mixed polyethylene and polypropylene into middle distillate products. Clean Technol Environ Policy 16:901–910.

Salou, M., Kooli, F., Kiyozumi, Y., Mikamizu, F., 2001. Effect of aluminum source and content on the synthesis of zeolite ZSM-5 from kanemite via solid-state transformation. J. Mater. Chem. 11, 1476–1481.

Seo, Y.H., Lee, K.H., Shin, D.H. 2003. Investigation of catalytic degradation of high-density polyethylene by hydrocarbon group type analysis. J Anal Appl Pyrolysis 70:383–398.

Serrano, D. P., Aguado, J., and Escola, J. M. 2012. Developing advanced catalysts for the conversion of polyolefinic waste plastics into fuels and chemicals. ACS Catal. 2, 1924–1941. DOI: 10.1021/cs3003403.

Shah, S.H. 2010. Low temperature conversion of plastic waste into light hydrocarbons. J Hazard Mater 179(1–3):15–20.

Uemichi, Y., Hattori, M., Itoh, T., Nakamura, J., and Sugioka, M. 1998. Deactivation behaviors of Zeolite and Silica– Alumina catalysts in the degradation of polyethylene. Ind. Eng. Chem. Res. 37, 867–872. DOI: 10.1021/ie970605c.

Undri, A., Frediani, M., Rosi, L., Frediani, P. 2014a. Reverse polymerization of waste polystyrene through microwave-assisted pyrolysis. J. Anal. Appl. Pyrol. 105, 35– 42.

Undri, A., Meini, S., Rosi, L., Frediani, M., Frediani, P. 2013. Microwave pyrolysis of polymeric

materials: waste tires treatment and characterization of the value added products. J. Anal. Appl. Pyrol. 103, 149–158.

UNEP 2009. Converting waste plastics into a resource. Osaka, pp. 1–15.

Wibowo, E., Sutisna, Rokhmat, M., Murniati, R., Khairurrijal and Abdullah, M. 2017 Utilization of Natural Zeolite as Sorbent Material for Seawater Desalination, Procedia Engineering. The Author(s), 170, pp. 8-13. DOI: 10.1016/j.proeng.2017.03.002.

Wu, G., Wu, W., Wang, X., Zan, W., Wang, W. and Li, C. 2013. Nanosized ZSM-5 zeolites: Seed-induced synthesis and the relation between the physicochemical properties and the catalytic performance in the alkylation of naphthalene, Microporous and Mesoporous Materials. Elsevier Inc., 180, pp. 187-195. DOI: 10.1016/j.micromeso.2012.11.011.

What Material Flow Analysis (MFA) and Life Cycle Assessment (LCA) reveal about plastic polymer production and recycling in South Africa

T. Goga[1*], K.G.. Harding[2] and H. von Blottnitz[1]

[1] Environmental and Process Systems Engineering Research Group, Department of Chemical Engineering, University of Cape Town (UCT), Rondebosch, 7701, South Africa

[2] Industrial and Mining Water Research Unit (IMWaRU), School of Chemical and Metallurgical Engineering, University of the Witwatersrand (WITS), Johannesburg, 2050, South Africa.

*Corresponding author. GGXTAA001@myuct.ac.za

ABSTRACT

Global production and consumption of plastics has increased significantly in recent years. The environmental impacts associated with this trend have received growing attention internationally with single-use plastic packaging responsible for most plastic pollution. Locally, the South African Plastic Pact aims to transform the current linear sector model into a circular system by setting targets for increased recycling rates and recycled content. The aim of this research is to document and quantify the impacts of implementing such circular interventions across the plastic life cycle. Industrial ecology tools, Material Flow Analysis (MFA) and Life Cycle Assessment (LCA), are used to generate mass-based indicators as well as indicators of potential damage such as the global warming potential. An initial carbon footprint analysis revealed that the South African plastic industry generated 17.9 Mt CO2eq. emissions in 2018, with 52% of these due to the local coal-based polymer production process. The end-of-life stage lacks proper waste collection for a third of the population, but contributed only 2% to the total greenhouse gas emissions, with recycling having a minimal environmental impact. Further analysis will reveal the impact of increasing mechanical recycling rates on the material flows of local polymer production and imports as well as the extent to which other environmental impacts can be reduced.

Keywords: Plastics, Material Flow Analysis, Life Cycle Assessment, Recycling, South Africa

1 INTRODUCTION

Plastics play a crucial role in modern day existence due to their unique properties of chemical resistance, durability and low cost. As a result, plastic production globally has increased rapidly by 4% between 2010 and 2015 (Geyer, Jambeck and Law, 2017). However, historical and current levels of consumption and disposal have led to several environmental concerns. Approximately 4-8 % of the world's oil and gas production is used as fossil fuel feedstock for plastics production contributing to global greenhouse gas emissions (World Economic Forum, 2016). Additionally, poor waste management of short-lived plastics, which are typically discarded or disposed of in landfills within a year of manufacture, has contributed to plastic pollution in the natural environment.

There have been various solutions proposed to tackle the issues associated with the plastics life cycle. The circular economy (CE) concept is described as "an industrial economy that is restorative or regenerative by intention and design" which aims to replace the 'end-of-life' concept with restoration for the elimination of waste" (Ellen MacArthur Foundation, 2013). Aligned to the principles of CE is the 'New Plastics Economy' which aims to deliver improved environmental and economic systems by dissociating from fossil-based input materials, reducing plastic leakage into the ecosphere, and creating an effective after-use plastics economy (Ellen MacArthur Foundation, 2017). In line with this vision, The South African Plastic Pact has undertaken to transform the country's packaging sector by 2025, setting targets centred around the concepts of materials reuse, recycle, and recovery (The SA Plastic Pact, 2021).

2 LITERATURE

2.1 The plastics industry in South Africa

The South African plastics industry is responsible for the conversion of over 1.8 million tons of both locally produced and imported polymer as well as recyclate (Department of Trade and Industry, 2020). In terms of end-of-life management, there is a large disparity in the provision of formal waste management services with just under 32% of South African households lacking access to basic refuse removal services (Rodseth, Notten and von Blottnitz, 2020). Although recent plastic recycling surveys report high recycling rates of over 40%, only a small fraction of recyclate is a suitable substitute for virgin polymer (Plastics SA, 2019). Furthermore, a fragmented waste management system leads to the disposal of a large proportion of post-consumer material in illegal dumps and unlicensed landfill sites which increases the potential of plastic leakage into the environment.

As the 32nd highest producer of plastics globally, the South African plastics industry forms one of the key segments of the local chemicals manufacturing sector. The production of monomers, namely ethylene and propylene, are by-products of the coal-to-liquids (CTL) process employed by Sasol (Sasol, 2019).. This process is recognised as a major emitter of carbon dioxide and plans are being developed to address this concern, as this industrial inheritance is increasingly understood to be incompatible with global goals to reduce greenhouse gas emissions to net-zero by mid-century.

2.2 Industrial ecology tools

As waste management strategies evolve from disposal to recovery and reuse, indicators/tools are required to measure and monitor progress. Material Flow Analysis (MFA), a tool used in resource and waste management, is defined as a systematic assessment of the flows and stocks of material within a system defined in space and time (Brunner and Rechberger, 2004). As a material accounting tool, it is used to compare inputs, accumulation and outputs of a process on various levels. On the other hand, Life Cycle Assessment (LCA) is an analytical assessment tool used to determine the potential

environmental impact of a product or process through its life cycle (International Organisation for Standardisation, 2006). The guidelines dictate that the assessment consists of four phases namely goal and scope definition, inventory analysis, impact assessment and interpretation. Both methods of assessment can be combined as MFA can be considered a technique to obtain data required for the life cycle inventory, particularly in systems analysis.

There have been numerous MFAs conducted for plastics on a local and national scale for countries in Asia and Europe. In Austria, consumption increased by 15% within a ten-year period while the growth in India was projected at increasing by a factor of six between 2000 and 2030 (Mutha, Patel and Premnath, 2006; Bogucka, Kosińska and Brunner, 2008). Recently, Babayemi et al. (2019) presented the first continental analysis of mass importation and consumption of polymers and plastics products in Africa, with the assessment highlighting a strong link between GDP and plastic consumption. In the case of South Africa, plastic MFAs have been commissioned by the Department of Environmental Affairs to determine issues plaguing the plastics sector as well as provide guidance regarding policies to support sound end-of-life management (Department of Environmental Affairs, 2017). Another joint research project has also been published where a local inventory of plastic flows was used to identify plastic pollution and leakage hotspots (IUCN-EA-QUANTIS, 2020). In both cases, the scope of the investigation differs which results in a variation in the estimated quantities of waste generated and disposed.

To minimise environmental impacts caused by plastic waste, Life Cycle Assessments have been conducted for national waste management systems. Results for Spanish and Austrian case studies indicated that mechanical recycling was the most favourable waste management option (Sevigné-Itoiz *et al.*, 2015; Van Eygen, Laner and Fellner, 2018). On a global scale, Zheng and Suh (2019) evaluated projected life-cycle GHG emissions for conventional and bio-based plastics. It was found that a combination of strategies (introducing renewable energy, increasing recycling, and curbing demand) could reduce future emissions. In Africa, LCA-based research is limited with few studies focusing on the quantification of plastic related impacts. In their ranking of waste management processes for municipalities in Africa, Friedrich and Trois (2011) found the greatest GHG savings achieved through recycling while the highest emissions were recorded for waste disposed of in landfills. Studies have also been conducted for carrier bags by Sevitz, Brent and Fourie (2003) with updated research conducted by the Council for Scientific and Industrial Research (CSIR) incorporating additional impacts such as persistence, employment and affordability (Russo, Stafford and Nahman, 2020). Significant findings show that reusable fossil fuel-based plastic bags have low environmental impacts in all categories other than persistence of plastics in the environment.

The aim of this study is to firstly establish a baseline model to describe the status quo of the South

African plastics sector in terms of material flows and their subsequent environmental impacts, and thereafter to explore the impacts of implementing a mitigation strategy, namely an increased mechanical recycling rate to satisfy the aims of the SA Plastic Pact.

3 METHODS

3.1 Material flow analysis (MFA)

A mass balance was compiled incorporating major process activities such as conversion, use, disposal, recycling and trading for 2018.

Figure 1 portrays the model showing relevant input and output flows.

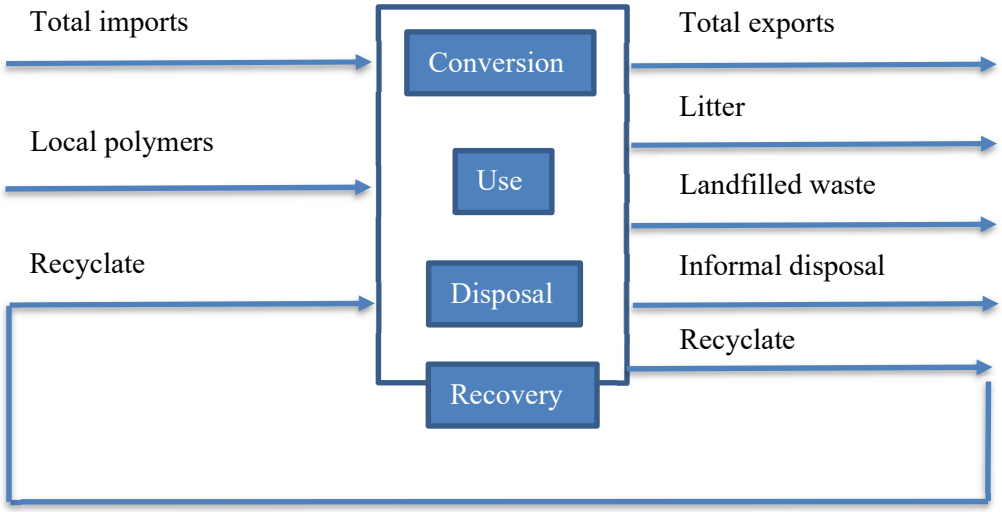

Figure 1: Inputs and output flows of the MFA

Imported polymers, products and packaging as well as exported goods were included with data sourced from the South African Revenue Services (SARS) under tariff code 39. Imported recyclate was also considered under total imports. In terms of recovery, figures for recyclate were obtained from the annual South African plastics recycling survey with 2.2% of plastics recovered from the waste stream exported to be recycled internationally (Plastics SA, 2019). Informal disposal of waste represents the portion of plastic waste that remains uncollected and untreated via formal management processes and is typically discarded in open dumps. Unlike other regions, South Africa does not implement waste incineration on a commercial scale. Landfill disposal is the standard employed, but not always to regulated standards. As a result, an estimated half of the formally disposed waste ends up in what is termed ‘deficient landfills’.

3.2 Life cycle assessment (LCA)

Disaggregation of the total plastic flows obtained in the MFA was necessary to obtain individual polymer flows. The polymers considered include the six major polymers consumed in South Africa viz. Low-density Polyethylene, High-density Polyethylene, Polypropylene, Polyethylene Terephthalate,

Polyvinyl Chloride, and Polystyrene (LD-PE, HD-PE, PP, PET, PVC, and PS) as well as an additional category to represent other plastics. SimaPro was utilised as the modelling software with most datasets sourced from the ecoinvent database. To accurately portray local polymer production, the South African dataset representing the Fischer-Tropsch synthesis process was incorporated into the model. Similarly, the end-of-life management scenario depicted in the MFA was modelled by constructing a disposal scenario to reflect accurate proportions of waste flows. Where local data was unavailable, international datasets were modified with the inclusion of the local electricity mix. The impact analysis was undertaken based on the single indicator of global warming potential with the impact assessment method selected as IPCC 2013.

3.3 Model of future flows

Flows depicted in the baseline model were projected to estimate future material flows. Based on an annual growth rate of 2% and 4% respectively, plastic flows were calculated for the year 2025. Thereafter, a mitigation strategy was modelled, and the changes analysed. In particular, the rate of mechanical recycling was increased to satisfy two of the objectives set by the SA Plastic Pact. This revolved around achieving a higher recycled content at 30% and an increased recycling rate of 70%. To construct the future model, it was assumed that the production of local polymer would be constrained and would reach a maximum threshold. This would entail that the balance of feedstock supply would be satisfied by importing polymers. Although the increased recycling rate will ensure higher collection of material for recycling, there would still be a significant quantity of waste that needs to be disposed. Due to the ongoing initiatives by Producer Responsibility Organisations (PROs), it is anticipated that waste generated from non-serviced households would decrease. A small fraction of waste would be still transported to sanitary landfill sites with the remainder discarded under deficient landfill conditions.

4 RESULTS AND DISCUSSION

4.1 Baseline Model

4.1.1 MFA for 2018

The results for the MFA on an annual basis are displayed in Figure 2. The Sankey diagram depicts major inputs, outputs and activities for 2018 with quantities expressed in kilotons. Circularity is shown in the diagram in the form of the recycling loop with accumulation built into the model to account for build-up of stock within the system.

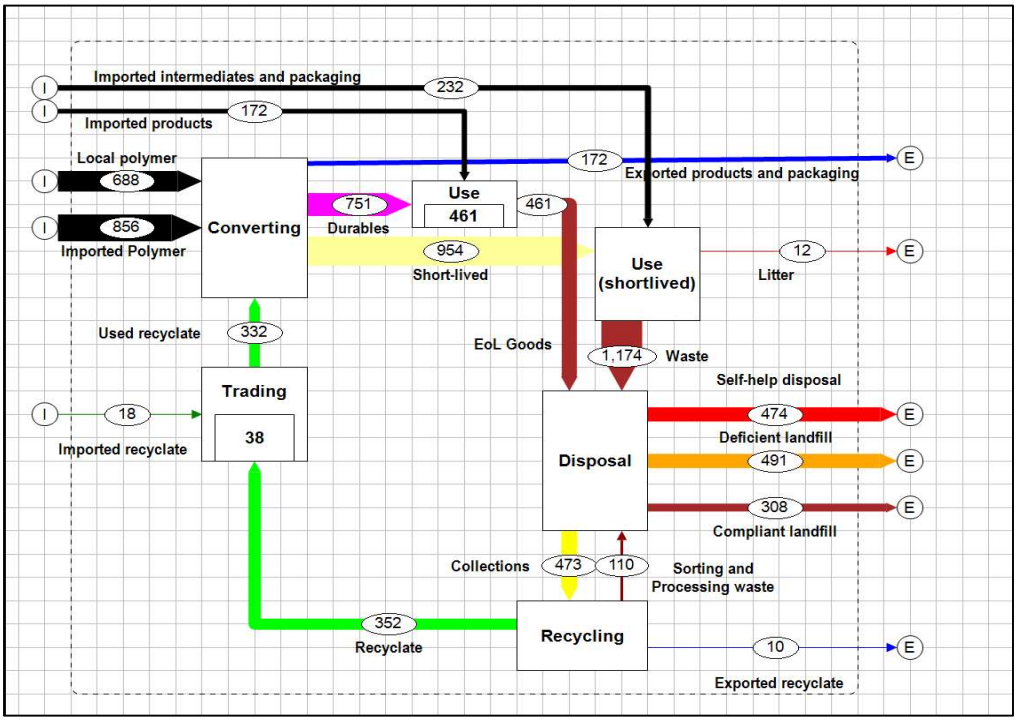

Figure 2: Sankey diagram depicting results of MFA of plastics in South Africa for 2018

The quantity of polymer produced locally, which was calculated via a mass balance, was 20% less than the quantity of imported polymers. After the conversion process, domestic consumption was sub-divided into short-lived products and durables, with 40% of plastics locally produced embedded in long-lived applications (Plastics SA, 2019). Post-use, the amount collected for recycling excluded the non-plastic 'obsolete' material that typically forms part of the collected material. Results indicate that most of the waste is discarded via self-help disposal, a practice common amongst rural households and urban informal settlements, as well as compliant and deficient landfills. Contrary to popular belief, the amount of direct litter generated is a relatively small amount. To evaluate the performance of the recovery and recycling loops, several mass-based indicators were calculated with the results presented in Table 1. The input recycling rate, which is a commonly cited indicator, is 9.2% higher compared to the recycling rate of 31.1% in Europe (Plastics SA, 2018). The recycled content, which is an alternative circularity indicator and is calculated as the fraction of used recyclate used in the production process, is 17.7%.

Table 1: Mass-based Indicators based on MFA for 2018

Indicator	**Value (%)**	**Definitions**
Collection rate	28.9	Collections/ Total waste
Input recycling rate	40.3	Collections/ Short-lived waste
Output recycling rate	30.9	Recyclate (local & exported)/ Short-lived waste
Recycled content	17.7	Used recyclate/ Total production

4.1.2 LCA for 2018

The provisional results for a life cycle-based carbon footprint are presented in Figure 3. The inner ring represents the total GHG emissions to produce plastic products consumed in South Africa, exported products, and imported products as well as end-of-life management of local plastic goods post-consumer use. The outer ring expands on the production process by showing the distribution of impacts between polymer production, conversion and end-of-life impacts. The latter are partitioned to illustrate individual impacts for littering, recycling and disposal.

The assessment revealed that the South African plastics industry was responsible for emitting 17.9 Mt_{eq} CO_2 over its life cycle. This is equivalent to 3.8% of the total emissions for South Africa in 2018 and is greater than the annual emission load for several entire country emissions, e.g. Kenya or Slovenia (Global carbon project, 2021). From the graph, it is evident that the production process (comprising both polymer production and conversion) is responsible for most of the burdens compared to the end-of-life management process. This is mainly due to the local production of monomers (propylene and ethylene) from coal with impacts also arising due to the local energy mix which is dominated by coal-fired power. The local conversion process is also significant, contributing to 17% of the total impacts with emissions attributed to electricity produced by the country's energy grid. In terms of treatment post-use, the disposal process accounts for a significant quantity of impacts which is ascribed to the burning of plastic waste that generally occurs at some homes or in dump sites.

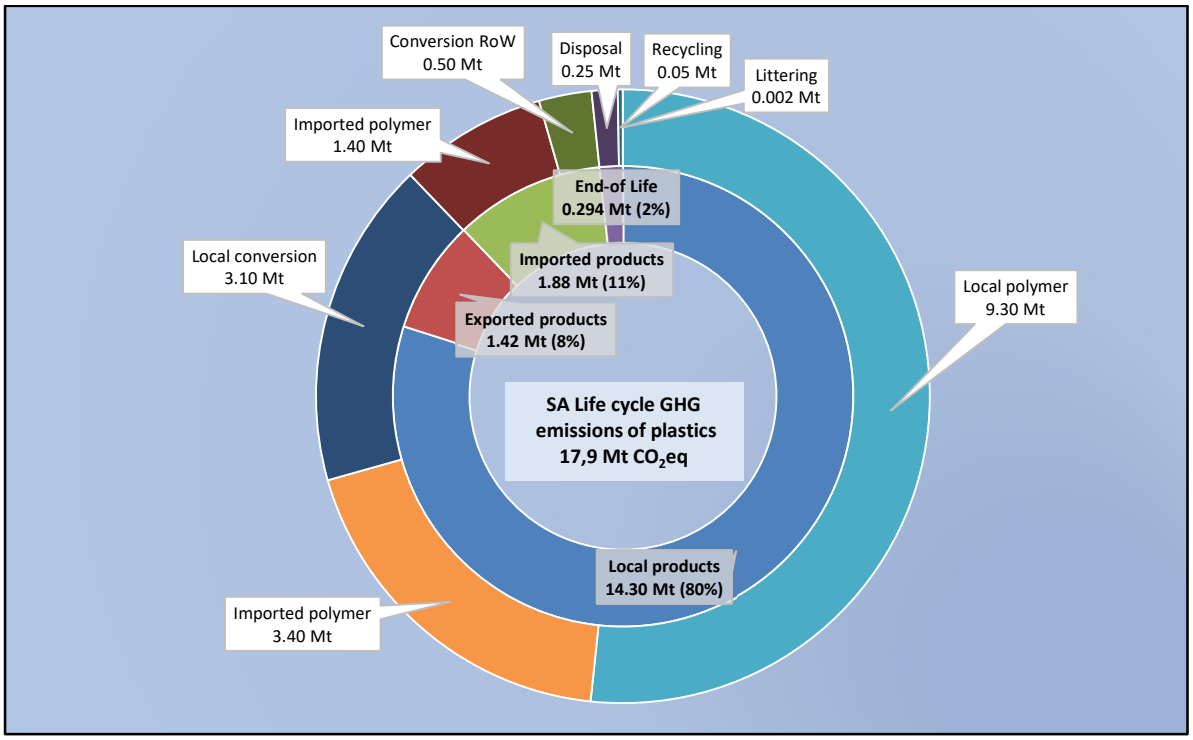

Figure 3: Provisional results for life cycle-based carbon footprint of plastics in South Africa for 2018

4.2 Model of future flows

Table Table 2 details the results of the baseline model, projected flows for 2025 (Business as usual models with 2% and 4% annual growth rate) as well as the potential impacts of an increased mechanical recycling rate as a mitigation strategy. The results show that increasing the recycling rate as in scenario 3 will increase the quantity of recyclate available by 241 kton which will subsequently decrease the need for virgin polymer. As anticipated, the quantity of plastics produced would increase from 1876 kton to 2155 and 2469 kton respectively under the two Business as usual (BAU) future models for 2025 with no intervention. This increase in production will lead to a projected increase in plastic consumption over the seven-year period to a maximum of 43 kg/capita.annum as per scenario 2. Consequently, the total waste generated would exceed 2000 kton if production increased at an annual growth rate of 4% per annum. In addition to an increased availability of recyclate, an increased recycling rate (scenario 3) will also decrease waste directed to landfill due to an improved collection rate for recycling purposes.

Table 2: Preliminary results for future model based on projected flows for 2025

Indicators	**Units**	**Baseline model 2018**	**Scenario 1 BAU (2%) 2025**	**Scenario 2 BAU (4%) 2025**	**Scenario 3 Increased recycling (2%) 2025**
Production					
Local polymer	kton	688	1078	994	1078
Imported polymer	kton	856	671	1010	431
Recyclate	kton	332	406	465	647
Total plastics produced	kton	1876	2155	2469	2155
Use					
Plastic consumption	kton	2108	2379	2726	2379
Plastic consumption	kg/capita.annum	36	38	43	38
Waste					
Waste generation	kton	1635	1846	2115	1846
Waste sent to landfill	kton	799	907	1039	658

5 CONCLUSIONS

To establish material flows and subsequent impacts arising from the plastic industry in South Africa, a combination of an MFA and an LCA was utilised. Results indicate that although recycling rates are higher than for other countries, a large quantity of waste is still disposed of via regulated and deficient landfills as well as self-help methods. The LCA reveals the total carbon footprint as 17.9 Mt CO_{2eq} with local monomer production and energy identified as the major contributing factors. A model of future

flows indicates that mitigation strategies such as increasing mechanical recycling rate has the capacity to reduce virgin polymer particularly imported polymer as well as waste directed to landfill. This is anticipated to have a positive impact on the total emissions generated by the local plastics value chain.

ACKNOWLEDGEMENTS

Technical assistance from Dr Valentina Russo (CSIR) is gratefully acknowledged as well as the financial support of the National Research Foundation.

REFERENCES

Babayemi, J. O. *et al.* (2019) 'Ensuring sustainability in plastics use in Africa: consumption, waste generation, and projections', *Environmental Sciences Europe*, 31(1). doi: 10.1186/s12302-019-0254-5.

Bogucka, R., Kosińska, I. and Brunner, P. H. (2008) 'Setting priorities in plastic waste management - lessons learned from material flow analysis in Austria and Poland', *Polimery/Polymers*, 53(1), pp. 55–59. doi: 10.14314/polimery.2008.055.

Brunner, P. H. and Rechberger, H. (2004) *Practical handbook of material flow analysis*. CRC press LLC.

Department of Environmental Affairs (2017) *Plastic Material Flow and End of Life Management: Final Report*. Pretoria.

Department of Trade and Industry (2020) *Plastics Industry 2020 - Master Plan for Growth*. Pretoria.

Ellen MacArthur Foundation (2013) *Towards the Circular Economy Vol. 1: Economic and business rationale for an accelerated transition*. Cowes.

Ellen MacArthur Foundation (2017) *The New Plastics Economy: Rethinking the future of plastics and catalysing action*. Cowes.

Van Eygen, E., Laner, D. and Fellner, J. (2018) 'Circular economy of plastic packaging: Current practice and perspectives in Austria', *Waste Management*, 72, pp. 55–64. doi: 10.1016/j.wasman.2017.11.040.

Friedrich, E. and Trois, C. (2011) 'Quantification of greenhouse gas emissions from waste management processes for municipalities - A comparative review focusing on Africa', *Waste Management*, 31(7), pp. 1585–1596. doi: 10.1016/j.wasman.2011.02.028.

Geyer, R., Jambeck, J. R. and Law, K. L. (2017) *Production, use, and fate of all plastics ever made*. Available at: http://advances.sciencemag.org/ (Accessed: 3 July 2020).

Global carbon project (2021) *CO2 Emissions | Global Carbon Atlas*. Available at: http://globalcarbonatlas.org/en/CO2-emissions (Accessed: 23 August 2021).

International Organisation for Standardisation (2006) *ISO 14040: Environmental Management - Life Cycle Assessment - Principles and Framework*. Geneva.

IUCN-EA-QUANTIS (2020) *National Guidance for plastic pollution hotspotting and shaping action,*

Country report South Africa.

Mutha, N. H., Patel, M. and Premnath, V. (2006) 'Plastics materials flow analysis for India', *Resources, Conservation and Recycling*, 47(3), pp. 222–244. doi: 10.1016/j.resconrec.2005.09.003.

Plastics SA (2018) *National plastics recycling survey 2017*. Johannesburg.

Plastics SA (2019) *National Plastics Recycling Survey 2018*. Johannesburg.

Rodseth, C., Notten, P. and von Blottnitz, H. (2020) 'A revised approach for estimating informally disposed domestic waste in rural versus urban South Africa and implications for waste management', *South African Journal of Science*, 116(1–2). doi: 10.17159/sajs.2020/5635.

Russo, V., Stafford, W. and Nahman, A. (2020) *Comparing Grocery Carrier Bags in South Africa from an Environmental and Socio-Economic Perspective:Evidence from a Life Cycle Sustainability Assessment*. Pretoria.

Sasol (2019) *Secunda Synfuels Operations, Secunda Chemicals Operations and Sasol Oil*.

Sevigné-Itoiz, E. *et al.* (2015) 'Contribution of plastic waste recovery to greenhouse gas (GHG) savings in Spain', *Waste Management*, 46, pp. 557–567. doi: 10.1016/j.wasman.2015.08.007.

Sevitz, J., Brent, A. C. and Fourie, A. B. (2003) 'An environmental comparison of plastic and paper consumer carrier bags in South Africa: implications for the local manufacturing industry', *South African Journal of Industrial Engineering*, 14(1), pp. 67–82.

The SA Plastic Pact (2021) *Roadmap to 2025*.

World Economic Forum (2016) *The New Plastics Economy- Rethinking the future of plastics*. Available at: http://www3.weforum.org/docs/WEF_The_New_Plastics_Economy.pdf (Accessed: 6 May 2020).

Zheng, J. and Suh, S. (2019) 'Strategies to reduce the global carbon footprint of plastics', *Nature Climate Change*, 9(5), pp. 374–378. doi: 10.1038/s41558-019-0459-z.

Flow sheet synthesis with heat engines for ITM air separation-based GTL Processes

P. Ziqubu and I. Greeff

University of the Witwatersrand, School of Chemical and Metallurgical Engineering, 1 Jorissen St, Johannesburg, 2000.

*Corresponding author e-mail: isabella.greeff@wits.ac.za

ABSTRACT

In large-scale production of liquids from natural gas, oxygen based autothermal reforming is typically used. This work focuses on substituting the traditional cryogenic air separation for oxygen production, with high temperature ion transport membrane (ITM) separation. ITM oxygen is one of the leading technologies promising to compete with the cryogenic process. The cryogenic air separation process requires significant amounts of power, which is provided by integration of heat engines to convert process heat to power. The main process heat source in the autothermal reformer is the high temperature synthesis gas, typically at temperatures above 900 °C. Steam is used as the working fluid in a Rankine cycle, however this approach suffers from large temperature differences between the process heat source and the working fluid, leading to inefficient conversion of process heat to power. The ITM process on the other hand requires significant amounts of heat. The ITM process integrates well with heat engines using a Brayton cycle wherein air is the working fluid. A new flow sheet for methanol production using autothermal reforming integrated with the ITM oxygen technology is developed and analysed, using energy analysis and comparing process and heat engine efficiencies. It was found that overall plant LHV efficiency was improved from 63.2 to 68.1%.

Keywords: Ion transport membrane; air separation; Rankine cycle; Brayton cycle; heat engine; autothermal reforming; methanol

1 INTRODUCTION

The vast demand and growing market of methanol has resulted in an increase in the installation capacity of a single methanol plant, with the largest capacity currently producing 5 225 ton/day in Turkmenistan, Asia, using autothermal reforming (ATR) licensed by Haldor-Topsoe (Brelsford, 2020). It is also generally known that ATR is the technology of choice in large scale gas-to-liquids (GTL) processes (Wilhelm, 2001).

In ATR oxygen is used for partial combustion of methane, which provides the heat required for the endothermic steam reforming reactions, all combined into one reactor vessel. The air separation unit (ASU) required for oxygen production is energy intensive and consumes large amounts of power, which is produced on site using recovered process heat and additional natural gas. Specific power consumption for this ASU typically varies between 0.464-0.639 kWh/nm^3 with a lower specific power consumption

for a large-scale ASU plant in China of 0.38 kWh/nm^3 (Tesch, 2020). Linde reported an even lower energy consumptions of 0.237 kWh/nm^3 for its advanced cryogenic ASU processes for oxygen purity of > 95% and 0.33 kWh/m^{3}n for > 99.5% purity (Beysel, 2021). It is important that power production to drive the ASU is done efficiently as this impacts the total plant efficiency, and on such a large scale even a small variation in this efficiency has a significant impact on plant economics.

Figure 1 shows a typical GTL plant block flow diagram. The amount of natural gas required for the utility systems depend on the following factors:

- amount of waste gases from process units available to use for heating or power generation
- how the process design has been integrated for heat recovery (typically using pinch analysis)
- type of power production cycle chosen for the design and its associated efficiencies, and
- how the process heat sources and sinks are integrated with the power and heat systems.

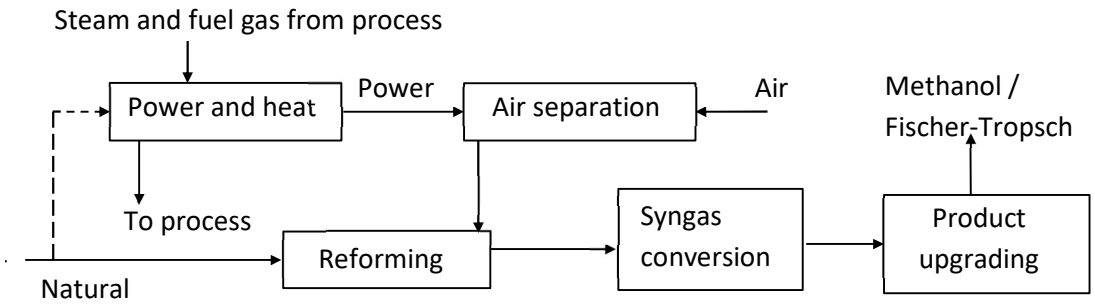

Figure 1: Schematic diagram of a typical GTL plant based on either Methanol or FT synthesis.

The high reaction temperature of the ATR leads to product streams at very high temperatures, typically above 900 °C, which needs to be cooled for condensate separation, before being sent to the liquid synthesis process. In conventional ATR the hot syngas is cooled in a waste heat boiler, generating steam, which is used to produce power. The challenge with using a steam cycle to convert the syngas heat to work is the limitation on the temperature due to the critical conditions of water at 374 °C and 210 bar, which means that the high temperature in the cycle is limited. This impacts the power cycle efficiency.

It is also reported by Iandoli at al. (2007), that this conventional method of syngas cooling by generating steam contributes 20% to the overall plant exergy losses, for a GTL plant based on low temperature Fischer-Tropsch synthesis and including the cryogenic ASU in the analysis. The combined ATR and ASU units were found to contribute a significant 69% to the total plant exergy loss.

The ion transport membrane (ITM) air separation is a fairly new technology which uses a ceramic membrane through which oxygen ions can permeate, to separate oxygen from air at high temperatures

of at least 900°C (Miller et al. 2014, Anderson, 2015). The high temperature nature of this technology requires effective energy recovery to ensure its competitiveness with the cryogenic ASU. This is achieved by integration into power cycles to efficiently convert the heat into work to drive a compressor and/or an electrical power generator (Anderson et al. 2011). In these schemes air is compressed, and fuel is used to heat the air to 800-900 °C, the hot air is sent to the ITM where it is separated into a reject and permeate stream, with the reject stream possibly subjected to further heating to much higher temperatures before being expanded. Note the turbine inlet temperature should be as high as possible, as this impacts cycle efficiency, and temperatures up to 1400 °C are used for combustion gas turbines.

Since the ITM air separation technology operates at high temperatures, around 900 °C, the integration of these technologies presents opportunities for alternative ways to cool the syngas in an ATR process and convert this heat to power, and possibly then improving overall plant efficiency.

In this work a flow sheet to produce methanol from natural gas, based on ATR reforming and the ITM ASU technology is developed, analysed and compared to a conventional case with cryogenic ASU. Compared to GTL processes based on Fischer-Tropsch (FT) liquids production, the methanol process additionally requires significant power for syngas compression up to the pressure requirement for the methanol synthesis, which is typically 40-110 bar combined with a temperature range of 250-300°C. The conversion of methanol has a direct dependence on pressure and inverse dependence on temperature (Balopi, 2019). The low conversion of methanol, typically 25% per pass (Lucking, 2017), also necessitates recycling of the unconverted feed gas. The methanol synthesis reactions are exothermic and require temperature control. This is similar to the FT synthesis. Two types of reactors are used for methanol production, namely isothermal and adiabatic. In this work the isothermal reactor is used as it is known to be more efficient due to energy recovery via generating medium pressure steam. Simulations for the cases were created in Aspen Plus™ V10. Process efficiency, overall efficiency and the efficiencies of the integrated heat engines are determined and compared. The new flow sheet was not further optimized.

2 FLOW SHEET DEVELOPMENT AND MODELLING

The basis of the model is a production capacity of 5 225 ton/day of methanol, as per the largest single capacity installed in Turkmenistan. The Soave-Redlich-Kwong (SRK) property method was used in Aspen Plus. The ATR unit and methanol synthesis unit were simulated as well as the associated power and heat systems. This comprises the HP and MP steam generation from ATR effluent and methanol reactor heat, and the fired heaters for superheating the steam and preheating feed streams to the ATR unit. This enabled calculation of the amount of natural gas used in the power and heat systems, in addition to the amount of natural gas fed to the ATR for syngas production. With this information it was possible to determine the process efficiency as well as the total plant efficiency. The cryogenic

ASU was not modelled in detail as the power requirement is known for the unit size required.

Table 1: Main process parameters and assumptions.

Natural gas composition (mol %) (Venter, 2002)								
CH_4	C_2H_6	C_3H_8	C_4H_{10}	C_5H_{12}	C_6H_{14}	N_2	CO_2	O_2
94.8	2.6	0.2	0.03	0.01	0.01	1.60	0.81	0.02

Process parameters					
	P (bar)	T (°C)		P (bar)	T (°C)
ATR gas inlet	24	602	Compressed air to ITM	6	254
ATR outlet	24	1 033	ITM exit streams	6	919
Methanol reactor	90	280	Reject (N_2) turbine exit	1	549
HP sat steam	40	250			
HP sup steam	40	411	LHV natural gas	47.1	kJ/kg
MP sat steam	10	180	LHV methanol	20.1	kJ/kg
MP sup steam	10	223			

Assumptions

- ATR is well insulated, adiabatic
- No long-chain heavy hydrocarbons in the natural gas requiring a pre-reformer
- No sulphur in natural gas
- Negligible heat losses from equipment
- Distillation and further processing of crude methanol have a negligible effect on the objectives and outcomes of this study and are not considered
- Isentropic efficiency of machines is 85%

Rankine cycle

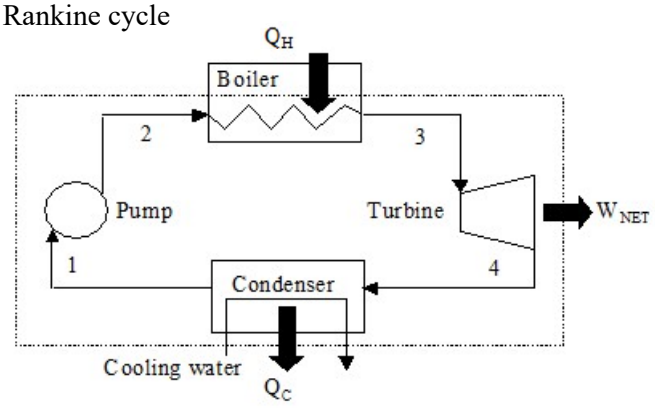

Table 1 presents the main process parameters and further assumptions. In the conventional flow sheet, Case A, shown in Figure 3, the heat engines used to provide power are the HP and MP steam cycles which are Rankine cycles. These are shown as blocks on Figure 3, however, the detail of the cycle configuration is shown in Figure 2, for the simple Rankine cycle. This is a vapour-liquid cycle with liquid being compressed, evaporated and vapour expanded in a turbine.

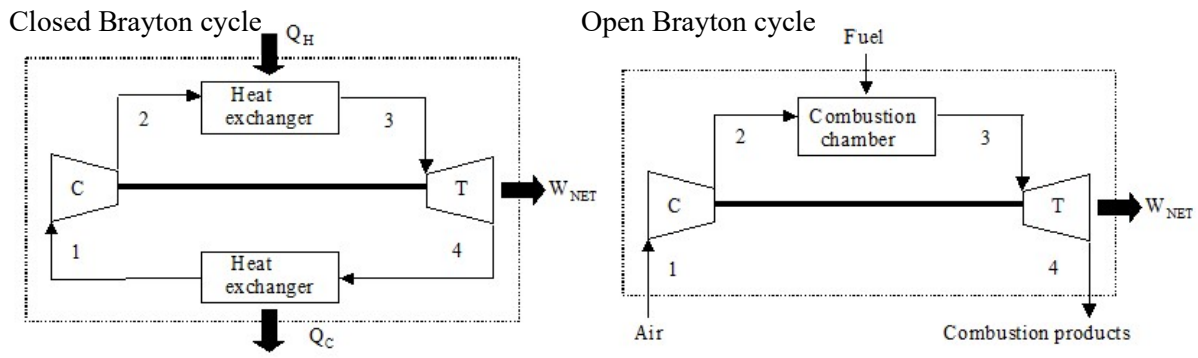

Figure 2: Rankine and Brayton cycles.

In Figure 3 the demarcated line is the system boundary for the HP steam system and cryogenic ASU. In Figure 4 this system is now replaced with the ITM and associated compressors, expander and heat exchangers, which is configured to represent a Brayton cycle. In order to comprehend this integration, the conventional open and closed Brayton cycles, as shown in Figure 2, should first be examined. In a combustion gas turbine, fuel is added to compressed air in the combustion chamber and the combustion products expanded, in a so-called open cycle configuration. However, a closed cycle is also possible, where combustion does not occur, but heat is transferred from an external source, e.g. a nuclear source or solar collector. The working fluid composition then does not change in such a cycle. The helium cycles used in pebble bed modular nuclear reactors is an example of such closed cycles.

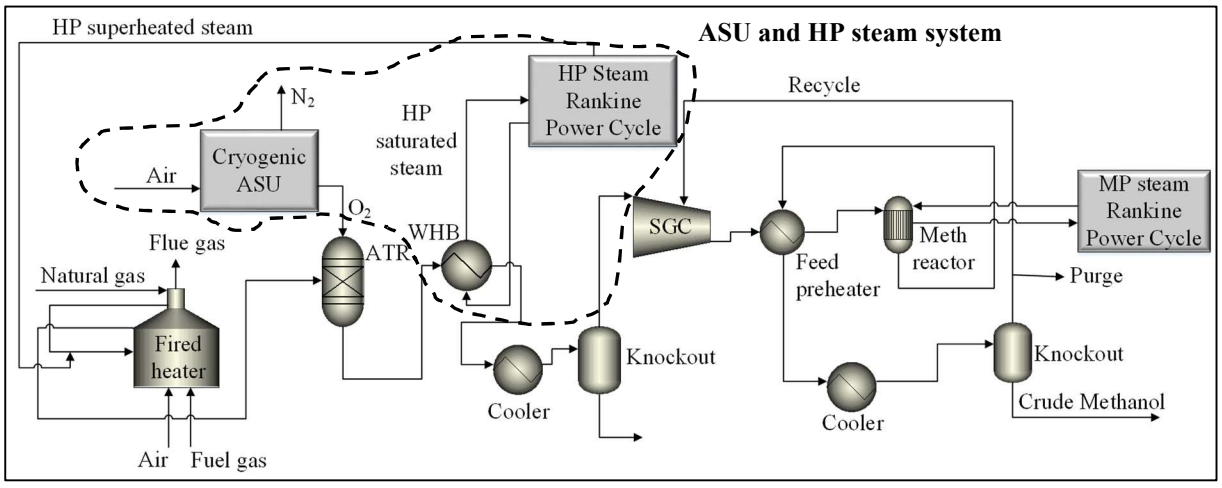

Figure 3: Conventional process flow diagram, Case A.

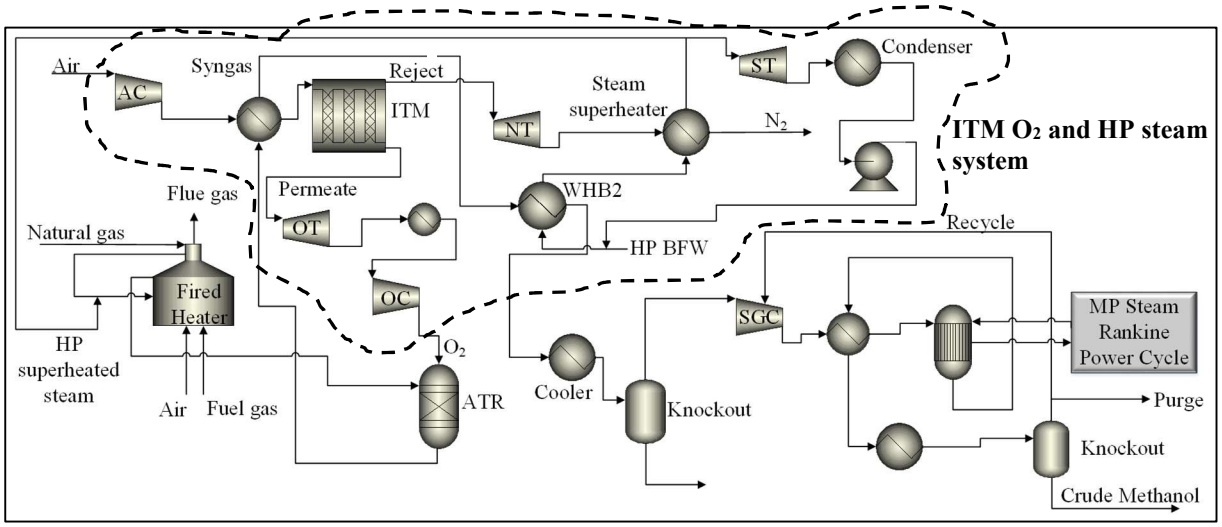

Figure 4: ITM O_2 integrated flow diagram, Case B.

The integrated ITM ASU system is shown in its heat engine configuration in Figure 5. The compression and expansion steps are grouped together here, with heat addition shown between compression and expansion. What is evident is that this system is a *combination* of an open and closed Brayton cycle. The reject stream, which is mostly nitrogen, is expanded and leaves the system. The permeate stream, which is mostly oxygen is expanded, cooled, and compressed again, and leaves the system at a much higher pressure, namely 24 bar, as this is required to enable feed to ATR, which operates at 24 bar.

Although there is no composition change of the working fluid due to a chemical reaction, the working fluid changes from the air which is compressed, to permeate and reject which are expanded in separate turbines. HP steam generation is still possible by using the remaining syngas heat, after cooling against the air to ITM, and the heat available from the ITM reject turbine outlet, which is still at very high temperatures of 626 °C and 540 °C, respectively. Note the HP steam cycle block which is still present for Case B in Figure 4, and the waste heat boiler WHB2 and superheater, which utilizes reject stream heat, are now used to generate HP steam. This cycle is however much reduced in size compared to Case A. This HP steam cycle is shown in Figure 6. A portion of the cycle is in reality part of a combined cycle, as it receives heat from another cycle, namely the ITM integrated Brayton cycle.

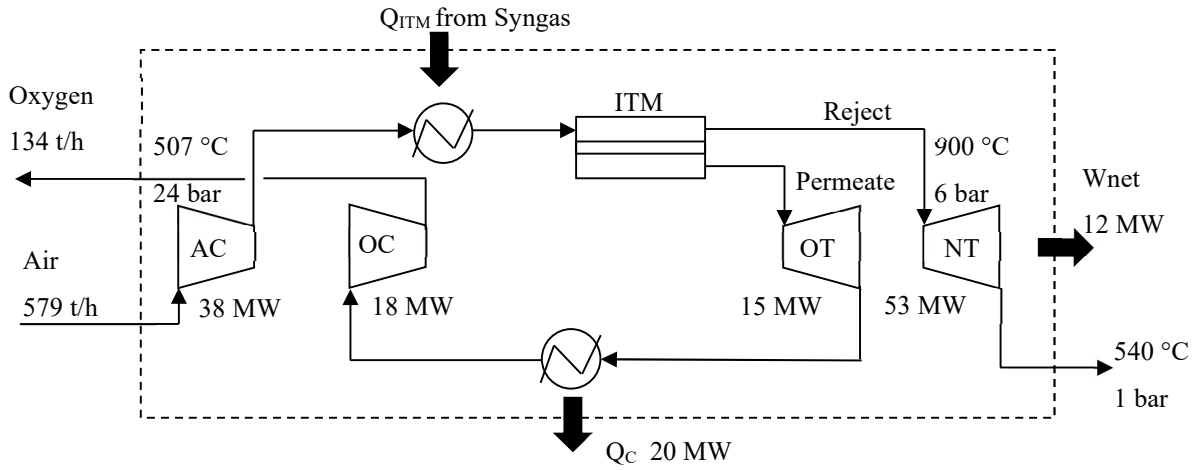

Figure 5: Integrated ITM process heat engine utilizing air/oxygen/nitrogen as working fluid.

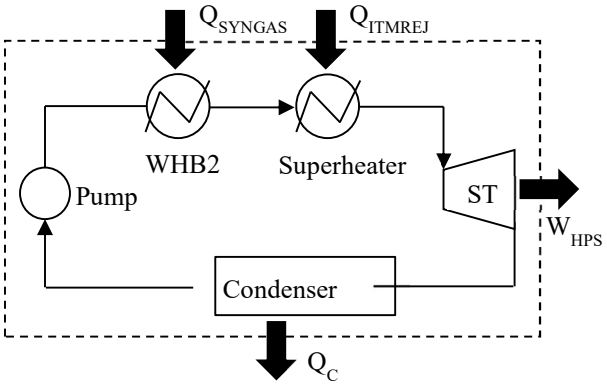

Figure 6: Cycle with heat from syngas and ITM reject stream.

3 RESULTS AND DISCUSSION

Results of the energy analysis are shown in Table 2. Note that the conventional Case A has a power excess of 17 MW. This can be used to supply other units on the plant, for example, the product upgrading, which was not modelled and considered in the analysis. Note that in Case B the excess power increased by 41%. This is an indication of overall efficiency improvement. Now looking at the LHV efficiency it is clear that there was a significant efficiency improvement in the utility systems, as the process efficiency remained the same, but the overall plant efficiency improved from 63.2 to 68.1%.

Steam cycle efficiencies are very low, as expected at these steam pressures of 40 bar and 10 bar. However, the integration of the ITM ASU gave the option to produce less power using these low efficiency cycles, and more power through the combination of the ITM air cycle and a combined smaller HP steam cycle, which receives heat from a combination of sources, directly from syngas at reduced temperature, and from the ITM air cycle reject turbine exhaust. The power production using the HP steam Rankine cycle reduced from 51 MW in Case A to only 14 MW in Case B. The ITM air cycle has

a low efficiency of only 10.1%, if one considers the system boundary as shown in Figure 5. However, the cycle was not specified to export power, but only needs to satisfy the demand of air and oxygen compressors included. There is a lot of scope for improvement by optimizing for pressure ratio and considering increasing the turbine inlet temperature by further combustion of fuel.

Table 2: Energy analysis results.

Heat and Work (MW)		
Case	A	B
Q_{MPS}	204	204
Q_{HPS}	235	61
Q_{ITM}		119
Compressors		
W_{ASU}	32	-
W_{AC}	0	38
W_{OC}	-	18
W_{SGC}	30	30
Expanders		
W_{OT}	-	-15
W_{NT}	-	-53
W_{HPST}	-51	-14
W_{MPST}	-28	-28
W_{TOTAL}	-17	-24

Case	A	B
Cycle efficiency (%)		
MP steam cycle	13.7	13.7
HP steam cycle	21.7	22.8
ITM air cycle	-	10.1
LHV efficiency (%)		
Process	73.4	73.4
Plant	63.2	68.1

The pressure ratio over the air compressor and expanders is 6, but over the oxygen compressor it is 24. The heat is supplied via heat exchange against hot synthesis gas. The heat engine efficiency is low due to the high pressure ratio required for the oxygen compression. In a conventional gas power cycle, the back work ratio (compressor work over turbine work) is typically 80%. However, in this ITM air cycle the back work ratio is only 53%.

4 CONCLUSIONS AND RECOMMENDATIONS

A flow sheet of a methanol production plant based on autothermal reforming and ITM oxygen technology was developed, analysed and compared to a conventional case, wherein cryogenic air separation is used. In the conventional case only Rankine steam cycles are used to convert process heat to power, mostly used to drive the air separation unit and syngas compressor.

The ITM with its associated compressors, heat exchangers and expanders was configured to operate as a heat engine, using the air, permeate and reject as working fluids. It was found that it is possible to use the high temperature heat from the syngas leaving the reformer to heat enough air to supply the

ITM oxygen system. Further, enough power can then be generated by expansion of the reject and permeate streams to drive the ITM air compressor and the oxygen compressor. The heat engines in the conventional and newly integrated flow sheet were identified and analysed. The efficiencies of the HP steam, MP steam and ITM air cycles were 13.8%, 22.1% and 10.1%, respectively. These low thermal efficiencies are expected for such simple steam cycles at the fairly low steam pressures, and for the ITM air cycle the parasitic oxygen compressor with its pressure ratio of 24, as opposed to the cycle pressure ratio of only 6, was contributing to low efficiency. But note this system was only expected to provide its own power requirement, and not optimized for excess power production. The total plant LHV efficiency improved from 63.2 to 68.1% while process LHV efficiency remained at 73.4 %.

Further improvement to the new flow sheets is certainly possible, e.g. by implementing Rankine and Brayton cycle modifications such as reheat, intercooling and regeneration, and integrating the MP steam with ITM air cycle exhaust for superheat, optimizing the cycles for pressure ratio and turbine and compressor inlet temperatures.

REFERENCES

Aasberg, K. 2001. Technologies for large-scale gas conversion. *Applied Catalysis: General 221*, 379-387.

Anderson, L.L., Armstrong, P.A., Broekhuis, R.R., Carolan, M.F., Chen, J., Hutcheon, M. D., Woods, C. M. 2015. *Advances in ion transport membrane technology for oxygen and syngas production.* Allentown: Elsevier.

Anderson, L.L., Armstrong, P.A., Repasky, J. M., & Stein, V. E. 2011. Enabling clean coal power generation: ITM oxygen technology. *International Pittsburgh Coal Conference.* Pittsburgh: Air Products and Chemicals, Inc.

Balopi, B., & Danha, P.A. 2019. Methanol synthesis chemistry and process engineering aspects - A review with consequences to Botswana chemical industries. *Procedia Manufacturing*, 367-376.

Beysel, G. 2021. *Enhanced cryogenic air separation. A proven process applied to oxyfuel.* Retrieved from The Linde Group: https://ieaghg.org/docs/oxyfuel/OCC1 /Plenary%201/Beysel_ASU_1stOxyfuel%20Cottbus.pdf

Brelsford, R. 2020. Turkmenistan commissions new methanol plant, *Oil and Gas Journal*, 14 January 2020.

Dong, L., Wei, S., Tan, S., & Zhang, H.(2008. GTL or LNG: Which is the best way to monetize "stranded" natural gas? *Petroleum Science*, 388-394.

Greeff, I.L. 2020. Integration of a turbine expander with syngas process - using gas as a working fluid. *Applied Thermal Engineering*, 165.

Greeff, I.L., Visser, J. A., Ptasinski, K. J., & Janssen, F. J. 2002. Utilization of reactor heat in methanol synthesis to reduce compressor duty - application of power cycle principles and simulation tools. *Applied Thermal Engineering*, 1549-1558.

Iandoli, C.L., & Kjelstrup, S. 2007. Exergy Analysis of a GTL Process Based on Low-Temperature Slurry F-T Reactor Technology with a Cobalt Catalyst. *Energy & Fuels*, 2317-2324.

Lucking, L. 2017. Methanol production from syngas, process modeling and design utilization biomass gasification and integration hydrogen supply. Master Thesis. Delft university of technology.

Miller, C.F., Chen, J., Carolan, M.F., & Foster, E.P. 2014. Advances in ion transport membrane technology for syngas production. *Catalysis Today*, 228.

Tesch, S., Morosuk, T., & Tsatsaronis, G. 2020. *Comparative evaluation of cryogenic air separation units from the exergetic and economic points of view*. Retrieved from Intechopen: https://www.intechopen.com/books/low-temperature-technologies/comparative-evaluation-of-cryogenic-air-separation-units-from-the-exergetic-and-economic-points-of-v

Venter, J. A. 2002. *Modelling and exergy analysis of the natural gas to hydrocarbon liquid (GTL) process.* Master Dissertation. Pretoria: University of Pretoria.

Wilhelm, D., Simbeck, D., & Karp, A. D. 2001. Syngas production for gas-to-liquids applications: technologies, issues and outlook. *Fuel processing technology*, 139-148.

Mesoporous Transition Metal Oxides as a Catalyst for Fischer-Tropsch Synthesis

L.U. Okonye[1*], D. Hildebrandt[1] and R. Meijboom[2]

[1] Institute for the Development of Energy for African Sustainability (IDEAS), University of South Africa (UNISA), Private Bag X6, Florida, 1710, South Africa.

[2] Department of Chemistry, University of the Johannesburg, PO Box 524, Auckland Park, Johannesburg, 2006, South Africa.

*Corresponding author: leonokonye@yahoo.com

ABSTRACT

The role of catalysts and catalysis in the development of clean chemical and petrochemical processes, and the drive towards sustainable energy production has been established as an indispensable factor. Gas-to-liquid (GTL) and biomass-to-liquid (BTL) technologies through the Fischer-Tropsch (FT) synthesis process can play an important role in the reduction of global carbon footprint. The efficiency of Fischer-Tropsch synthesis (FTS) can be enhanced by designing new catalysts, which can lead to improved catalytic properties. The arrival of novel meso-structured materials with porous interconnected networks can be taken advantage of, their unique properties favours wide-ranging applications. Mesoporous transition metal oxides have started receiving consideration in a number of reactions, because of their multiple oxidation states, and the effect of the ensuing metal-oxide interfaces on catalytic activity and selectivity. In this light, iron and cobalt mesoporous materials is anticipated to give better activity and hydrocarbon selectivity when compared to other catalytic systems previously used for FTS. This work describes the synthesis, characterization and catalytic evaluation of mesoporous cobalt oxide (Co_3O_4) for the Fischer-Tropsch synthesis reaction.

Keywords: Fischer Tropsch synthesis; catalytic activity; meso-Co_3O_4; Ru-Co_3O_4; reaction conditions

1 INTRODUCTION

This work describes the synthesis and catalytic evaluation of a mesoporous cobalt oxide (Co_3O_4), diluted with SiO_2 (<212 μm) in the ratio 25:75, represented as 25% (Ru [0.06%]-Co_3O_4)/SiO_2 for the Fischer-Tropsch synthesis reaction. The catalyst was characterized using XRD, BET, TPR, and TEM. The catalytic performance can be linked mainly to diffusion and mass transfer resistance effects, which reduced the conversion at low temperatures.

2 LITERATURE

Fischer–Tropsch synthesis (FTS) yields hydrocarbons (HCs) of varying chain lengths and functionalities, compared to normal refinery products. They are of high quality, and can, therefore, turn out to be a key alternative energy carrier, and contribute to the global final energy mix.[1-5] Historically, its acceptance was politically driven until recently where interest is motivated by economic practicality, energy security concerns and the aspiration of resource holders to monetize stranded gas reserves.[6-9]

The FTS reaction is heterogeneously catalysed by an active metal phase, dispersed on a support which might also contribute to the activity of the catalyst.[9-11] The conceptual use of pores was introduced to avoid the agglomeration of nanoparticles during a reaction, leading to the availability of a greater surface area, and higher selectivity in reactions. The porous structure plays a substantial role in both the physical and chemical properties of catalysts, and strongly influences the catalytic performance of many catalysts in several reactions.[12,13]

With the promise of better reactions and separations (of mesoporous materials), mesoporous transition metal oxides have started receiving consideration in some reactions, due to their multiple oxidation states, and the effect of the ensuing metal-oxide interfaces on catalytic activity and selectivity.[14] The view is that mesoporous iron and cobalt will give better catalytic performance for FTS reaction, when compared to other conventional supports such as TiO_2, SiO_2 and Al_2O_3.[15]

Ru content promotion (between 0.05–3 wt. %) of cobalt catalysts has been explored by several researchers over the years. This is to improve on Co reducibility, and boost hydrocarbon selectivity by enriching more Co-active sites. The Ru-Co synergy is often used to explain the increased catalytic performance of promoted catalyst.[16-20]

The objective of this study is to determine the catalytic performance of Ru nanoparticle application on mesoporous cobalt oxide, for FTS. The idea is that since the cobalt oxide already has a porous structure, which determines the ease with which reactants access the interior catalyst surface, the catalyst will tend to favour higher C_{5+} yields and lower methane selectivity.

3 EXPERIMENTAL PROCEDURE

3.1 Catalyst preparation/synthesis and characterization

The mesoporous metal oxide was synthesized from an adapted literature method, reported by Poyraz et al.,[21, 22] for the synthesis of mesoporous metal oxides, utilizing non-ionic triblock copolymer P123 in the soft templating approach, and the varied calcination steps.[21-24] The $Co(NO_3)_2 \cdot 6H_2O$ (10 g, 0.035 mol) was dissolved in a solution of P123 (5.0 g, 8.62 × 10-4 mol), HNO_3 (4.8 g, 0.076 mol) and 1-butanol (34 g, 0.66 mol). The resulting red solution was set in an oven at 50 °C, for 12 hrs to evaporate the 1-butanol solvent. The resulting gel was then heated in the oven for 6 hrs at 120 °C. The powder formed was allowed to cool and washed with ethanol, to remove the P123 surfactant template, and dried under vacuum. It was further calcined in air with heating cycles of 150 °C for 12 hrs and 250 °C for 4 hrs at a heating rate of 1 °C/min.

The Ru nanoparticles were synthesised by chemical reduction of $RuCl_3 \cdot 3H_2O$ precursor with $NaBH_4$, in the presence of an octylamine ligand to stabilize and protect the nanoparticles. This method was preferred due to the controllability of the size and shape of the nanoparticles.[25-27] The colloidal ruthenium solution was prepared by dissolving $RuCl_3 \cdot 3H_2O$ (40.5 mg, 0.2 mmol) in ethanol (15 cm^3),

octylamine (323.5 µL, 1.5 mmol) was added and left to stir continuously under an inert condition in a Schlenk tube for 24 hrs. A solution of $NaBH_4$ was prepared by dissolving 282 mg (7.5 mmol) in a mixture of methanol (5 cm^3) and ethanol (20 cm^3). The gradual addition of 5 cm^3 of the $NaBH_4$ solution 10 mins apart, to the mixture (five additions in total) produced Ru nanoparticle. The mixture was left under continuous stirring for 7 hrs after the last addition for effective reduction of the salt to the metal colloid. Pentane was added to provide an organic phase, then the solution was washed with water, before collecting the organic phase, and used for the catalyst synthesis. A measured amount (3.3313 g) of the synthesized mesoporous cobalt oxide (Co_3O_4) was added to the Ru nanoparticles solution and agitated to facilitate incorporation of the nanoparticle into the pores of the mesoporous Co_3O_4. The Ru promoted mesoporous cobalt oxide catalyst thus obtained is washed, allowed to settle, vacuum filtered, dried and characterized. The Ru composition of the catalyst was determined by elemental analysis using ICP–OES and ICP–MS methods to be 0.0564 (≈0.06) wt. %.

The X-ray diffraction (XRD) patterns for the synthesised 0.06% [Ru] promoted mesoporous Co3O4 catalyst were recorded using a Rigaku Miniflex 600 with a Cu Kα1 (λ = 0.1542 nm) as the radiation source, 40 kV/15 mA power, and a scanning rate of 0.2 °/min and 1.0 °/min for low and wide angles respectively. The surface area of the synthesized sample was determined by BET. The sample was degassed overnight at 90°C and measured at -195.8°C using a Micromeritics surface area and porosity (ASAP 2460, V2.01) analyser. Using the Barrett-Joyner-Halenda (BJH) model,[28] the pore size distribution was determined from the desorption stem of the isotherms. The TEM characterization of the catalyst was accomplished utilizing a JEOL-JEM 2100 electron microscope operating at 200 kV and a beam current of 101.6 µA. A drop of the sonicated suspension of the sample dispersed in ethanol was placed on a copper grid and allowed to dry before the analysis. The size distribution histograms for the catalyst were obtained by manually measuring the particles from the TEM images.

3.2 Fischer-Tropsch Synthesis Evaluation of the Catalyst

The synthesised catalyst, 0.06% [Ru] mesoporous Co_3O_4 was evaluated for Fischer-Tropsch activity on a conventional lab-scale fixed-bed reactor (16 mm i.d, with the thermocouple in direct contact with the catalyst). The catalyst was first diluted with SiO_2 (< 212 µm) in a ratio 25:75 (subsequently communicated as 25% (0.06%[Ru]-Co_3O_4)/SiO_2), to minimize hot spots and thermal runaway in the system. The synthesis was carried out at 20 bar and 160 – 260 °C for temperature study and the pressure was varied between atmospheric and 20 bars, to evaluate the effect of reaction pressure at 230 °C. A syngas (H_2/CO) feed ratio of 2 and flow rate of 7.665 NmL/min were used. The gas flow rates for reactant gases were controlled by Aalborg mass flow controllers (model GFC 17, with the flow range of 0 – 500 mL/min). Catalytic measurements for activity and selectivity of the Fischer-Tropsch synthesis reaction were carried out at least after 12 hrs to ensure stabilized steady-state condition, before a different mass balance period. Based on the TPR profile, 1 g of the catalyst sample was activated in

5% (v/v) H_2/Ar gas mixture with a flow rate of 30 mL/min at atmospheric pressure by increasing temperature from ambient to 350 °C, for 17 hrs, before the FTS reactions. After the reduction, the synthesis gas was fed to the reactor 20 bars and a space velocity of 0.46 $nl \cdot h^{-1} \cdot g^{-1}$cat at STP, before increasing the temperature to the desired reaction temperature

A Dani Master GC equipped with a thermal conductivity detector (TCD) and a flame ionization detector (FID), was used to analyse the reactant gases and products, while the chromatographs were processed using Clarity Software. The gases were analysed utilizing a Supel-Q Plot fused silica capillary column (30 m x 0.32 mm) and a 60/80 Carboxen 1000 column (15 ft x 1.8 in x 2.1 mm) connected to the detectors.

4 RESULTS AND DISCUSSION

4.1 Catalyst characterization

4.1.1 XRD

The wide-angle XRD peaks at 2θ between 10 and 90 (Figure 1a) show 6 peaks with Fd3m space group, cubic crystal structured phases 111, 220, 311, 400, 511, 440.

This is characteristic of Co3O4, usually observed around 19°, 32°, 37°, 45°, 60°, and 65° respectively (JCPDS card # 073-1701, 76-1802 and 43-1003), indicating that the cobalt species present is predominantly Co3O4. The peak at 43°, corresponds to the stable CoO specie (JCPDS card # 43-1004).22, 29, 30 On introducing the Ru (Figure 1b), the peak intensities are detected at roughly 38°, 41°, 45°, 60°, and 66°. This closely corresponds to the phases of rutile RuO2 and Ru, indicating well dispersed Ru species in the Ru-Co3O4 catalyst.31-33 The broad peak (19 – 20°) identified in Figure 1c) is associated with the non-crystalline nature of the SiO2 used as a diluent.34 Unreacted CoSiO2 due to strong metallic bond to SiO2 phase is also identified at 23° and 43° (JCPDS card # 72-1508).30 The mean diameter of cobalt oxide crystallites was 13.8 nm, estimated by applying the Debye-Scherrer equation to the most intense peak at 2θ = 37°.[35]

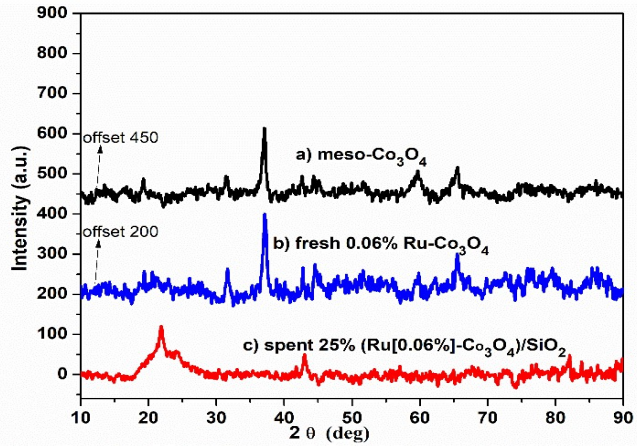

Figure 1: Wide angle XRD patterns: a) mesoporous Co_3O_4, b) fresh 0.06% Ru-Co_3O_4 catalyst and c) spent 25% (Ru [0.06%]-Co_3O_4)/SiO_2

4.1.2 XRD

Table 1 shows the BET surface areas, pore volumes as well as pore diameter.

Table 1: Table showing sorption properties of meso-Co_3O_4, 0.06% Ru/mesoCo_3O_4 and spent 25% (Ru[0.06]-Co_3O_4)/SiO_2 catalysts

Sample	Surface Area (m^2/g)	Pore Volume (cm^3/g)	Average Pore width (nm)
Meso-Co_3O_4	30	0.12	13.8
Fresh 0.06% Ru/Co_3O_4	6.5	0.05	24.5
Spent 25% (Ru [0.06%]-Co_3O_4)/SiO_2	67.7	0.68	40.2

The table shows that the introduction of ruthenium caused a decrease in the surface area and pore volume relative to the initial support materials after the impregnation of the catalyst due to partial blockage of the macrospores by the ruthenium species.[28,36] The average pore with of the material increased, which could be as a result of the varied Ru/Co interactions with the oxide specie during impregnation.

The BET isotherms, and pore size distribution based on the BJH models, for the mesoporous support, and catalysts are presented in Figure 2.

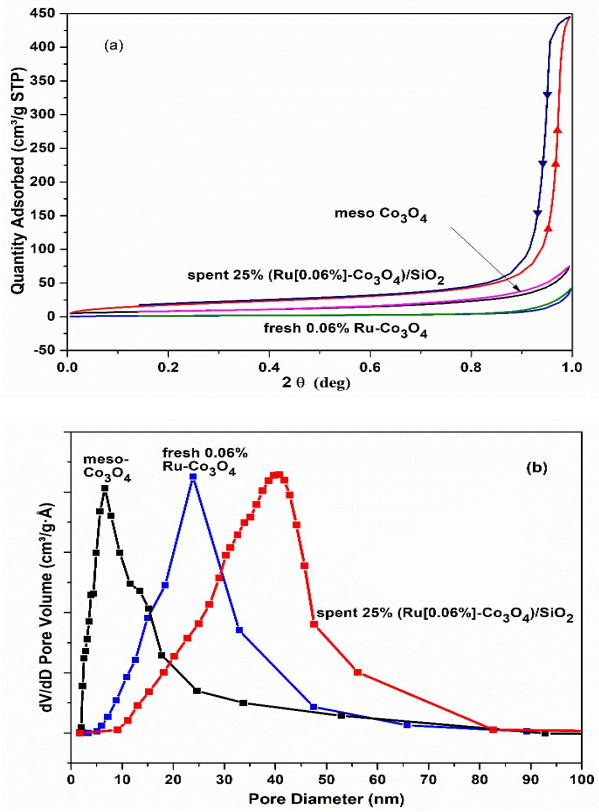

Figure 2: a) BET Isotherm plot, b) pore size distribution for meso-Co_3O_4, fresh 0.06% Ru-Co_3O_4 catalyst and

spent 25% (Ru [0.06%]-Co_3O_4)/SiO_2

The BET isotherms of the samples exhibited a type IV isotherm, with an H3 hysteresis loop. This indicates a random distribution of pores and an interconnecting pore system but does not indicate missing monolayer formation.[24] The diameter in the mesopore range is related to the P/P^0 positions of the inflexion points, with a sharp inflexion between P/P^0 range of 0.80 and 1, which demonstrates consistency in the mesopore size distribution.[36, 37]

4.1.3 TPR

The reducibility of the synthesised 0.06% Ru-mesoporous Co_3O_4 catalyst was evaluated by temperature programmed reduction of hydrogen (H_2-TPR), displayed in Figure 3. The reduction pattern shows one main reduction peak at a temperature range of 150 – 600 °C, suggesting a nearly uniform distribution of the cobalt oxide support. This is further deconvoluted to two overlapping peaks at temperature ranges of ca. 190 – 440 °C (broad peak with centre at roughly 300 °C), and 270 – 440 °C (with peak centre at roughly 356 °C), corresponding to a two-step reduction of the catalyst.

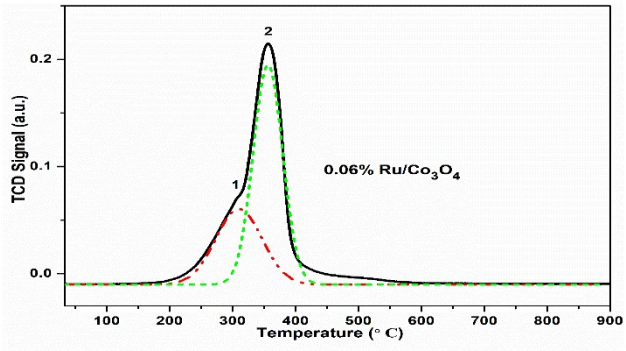

Figure 3: TPR pattern of 0.06% Ru-Co_3O_4 catalyst

The first peak corresponds to the initial reduction of the Co_3O_4 phase to CoO, which could be attributed to Ru promotional interaction with Co surface species and the subsequent reduction of CoO to Co^0. The percentage of the reduced Co is in correlation with the obtained reducibility for Co_3O_4 through standard reduction procedures.[11,13b,18b,38] As such, a temperature of 350 °C was selected as the reduction temperature for the catalyst before the Fischer-Tropsch reaction based on this data. The promotional effect of Ru on cobalt oxide is also identified on the TPR results, the small amounts of Ru improved, facilitated the reducibility of the catalyst, hence the peak centre at roughly ca. 300 °C.

4.1.4 TEM

The images and particle size histogram from the TEM analysis that was carried out to determine the morphology of the 0.06% Ru promoted Co_3O_4 catalyst, are shown in Figure 4.

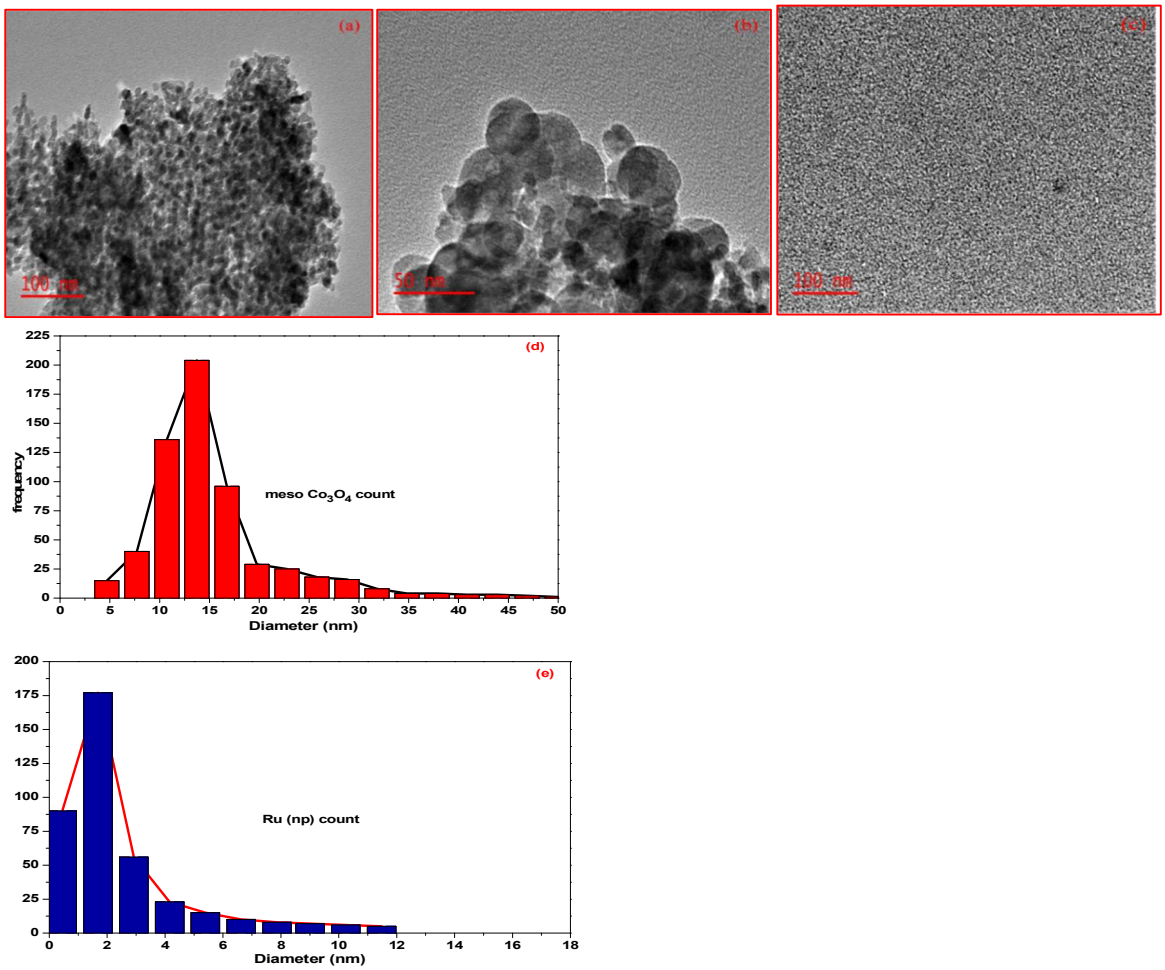

Figure 4: (a, b, and c) TEM micrographs, d) Co_3O4 particle count histogram, and e) Ru particle count histogram

The TEM images (Figures 4a and b) showed mostly spherical units and nearly spherical of various sizes, as well as some smaller hexagonal units which are not clearly shown in the images presented, which are all closely packed to form the mesoporous morphology. The estimated mean particle size of the mesoporous Ru-Co_3O_4 catalyst is 13.37 ± 5.70 nm (from 600 particles counted), and the mean particle size of the Ru nanoparticle is 1.52 ± 0.8 nm (from 397 particles counted). This value is in agreement with the 13.8 nm average cobalt oxide crystallites size from the XRD Scherrer equation.

4.2 Catalytic evaluation

The performance of the catalyst for the syngas conversion and product selectivity as evaluated on the prepared promoted mesoporous cobalt oxide catalyst, 25% (Ru[0.06%]-Co_3O_4)/SiO_2 for the effect of reaction temperature variation is shown in Figure 5a and pressure variation in 5b.

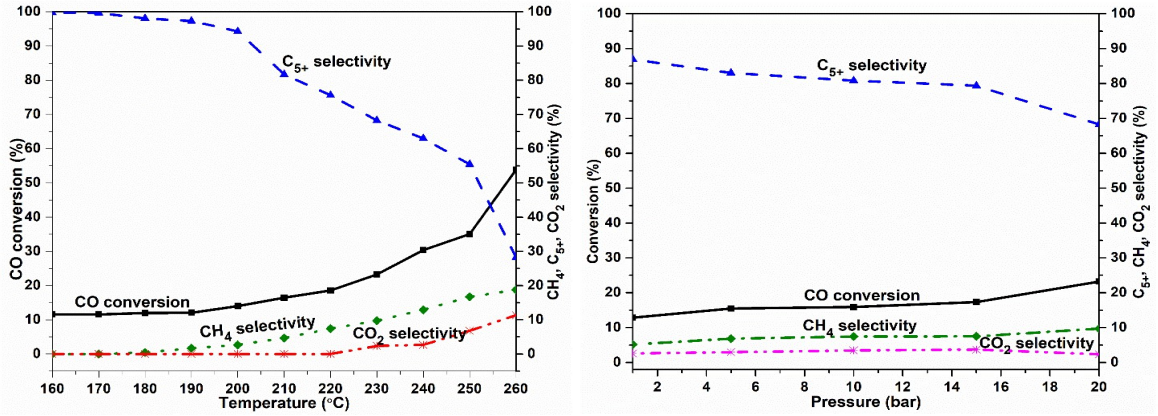

Figure 5: CO conversion, CH_4, CO_2 and C_{5+} product selectivity for 25% (Ru [0.06%]-Co_3O_4)/SiO_2: a) temperature variation (T = 160 – 260 °C, P = 20 bars); b) pressure variation (T = 230 °C, P = 1 – 20 bars)

As expected, increasing the reaction temperature leads to an increase in FTS catalytic activity and methane selectivity, but resulted in a decrease in selectivity towards C_{5+} hydrocarbon products.[37,39,40] From Figure 5a, upon increasing the temperature from 160 to 260 °C, the CO conversion increased from 11.57 – 53.83 %. Concurrently, selectivity towards the undesired methane and CO_2 increased from 0 – 18.76% and 0 – 11.32% respectively, while the production of CO_2 only started at 230 – 260 °C. The selectivity towards C_{5+} decreased from 99.80 – 28.26%. It is evident that while temperature increase increased CO conversion, it leads to a decrease in C_{5+} selectivity, an indication that an increase in syngas conversion, does not directly translate to an increase in the desired C_{5+} product.

At high synthesis gas pressures, the different components of the liquid phase in catalyst pores, will, therefore, affect the rate of fundamental steps in the process thereby inhibiting CO conversion.[43] An increase in pressure generally leads to condensation of hydrocarbons, those which at atmospheric pressure are usually in the gaseous state, thereby compelling catalyst pores saturation by liquid reaction products at high CO conversions.[41a,42] Figure 5b shows the pressure effect on the catalytic performance of the 25% (Ru[0.06%]-Co_3O_4)/SiO_2 catalyst in terms of CO conversion and products selectivity at 230°C. At atmospheric pressure, the CO conversion was about 12.85%, yielding mainly C_{5+} products (86.92%). Increasing the pressure to 20 bar, led to a CO conversion increase to 17.83%, while the selectivity to the C_{5+} product(s) reduced to 75.24%.

A deactivation study (shown in Figure 7), to evaluate the stability of the catalyst, with time on stream, was conducted for roughly 300 hrs at two different temperatures (190 and 230 °C). At 190 °C, the catalytic conversion was relatively stable compared to conversion at 230 °C, which reduced with time on stream, indicating some deactivation of the catalyst taking place at 230 °C and no deactivation at 190 °C. Extrapolating the data (assuming the sequence continues), will eventually lead to a situation where the % CO conversion at 190 °C, will be higher than the % conversion for 230 °C.

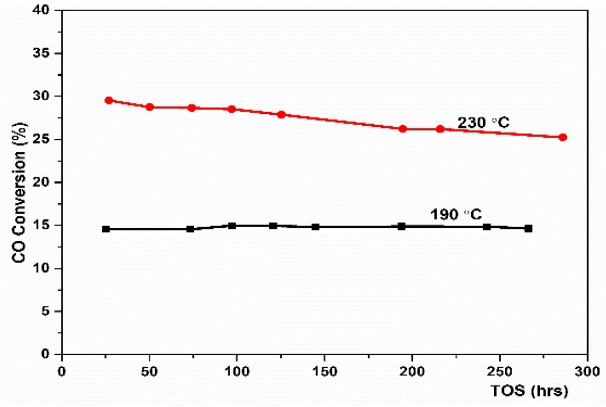

Figure 7: Catalyst deactivation with time on stream for 25% (Ru [0.06%]-Co_3O_4)/SiO_2; P = 20 bars, T = 190 and 230 °C

5 CONCLUSIONS

The synthesis of mesoporous cobalt oxide and the subsequent incorporation with Ru nanoparticle was successfully achieved. The CO conversion increased with temperature and pressure respectively, however, the selectivity towards C5+ decreased exponentially from 250 °C, but the selectivity to CH4 was gradual in respect to temperature and pressure increase. This can be linked to the re-oxidation of the catalyst at high temperatures, which also impacted the C5+ selectivity. The catalytic performance is ascribed mainly to diffusion and mass transfer resistance effects (causing the catalyst pore to be saturated), leading to an increased α-alkene re-adsorption on the growing chain, at low temperatures. The limited diffusion of the higher molecular weight hydrocarbons resulted in poor conversion due to blocking of the Co0 active site at low temperatures. This changed however, when the temperature was raised and there was enhanced diffusion of products from the catalyst pores.

It is important to note that the metal-support interaction and the associated O-vacancy defect laden surfaces, 43-45 in this case, played a great role in the activity of the catalyst. This is due to the unique charge transfer induced cooperative effects from the surface vacancy of the small nanoparticles and the support, which improved the number of cobalt active sites. Thus, the combination of electronic and geometrical effects resulted in a synergistic effect on the activity and selectivity pattern of the catalytic heterostructure.

REFERENCES

1. Velasco, J. A., Lopez, L., Velásquez, M., Boutonnet, M., Cabrera, S. and Järas, S. 2010. Gas to liquids: A technology for natural gas industrialization in Bolivia. *Journal of Natural Gas Science and Engineering*, 2010: vol. 2, pp. 222-228
2. Farias, F. E. M., Silva, F. R. C., Cartaxo, S. J. M., Fernandes, F. A. N. and Sales, F. G. 2007. Effect of Operating Conditions on Fischer-Tropsch Liquid Products. *Latin American Applied Research*, 2007: vol. 37, pp. 283-287

3. Zhang, C., Jun, K.-W., Ha, K.-S., Lee Y.-J. and Kang, S. C.2014. Efficient Utilization of Greenhouse Gases in a Gas-to-Liquids Process Combined with CO_2/Steam-Mixed Reforming and Fe-Based Fischer−Tropsch Synthesis. *Environmental Science Technology*, 2014: vol. 48, pp. 8251−8257
4. van Santen, R. A., Ciobîcă, I. M., van Steen, E. and Ghouri, M. M. 2011. Mechanistic Issues in Fischer–Tropsch Catalysis. *Advances in Catalysis*, 2011: vol. 54, pp. 127-187
5. (a) van Santen, R. A., Ghouri, M. M., Shetty, S. and Hensen, E. J. M. 2011. Structure sensitivity of the Fischer–Tropsch reaction; molecular kinetics simulations. *Catalysis Science Technology*, 2011: vol. 1, 891 –911; (b) van Santen R. A. and Markvoort, A. J. 2013. Catalyst nano-particle size dependence of the Fischer–Tropsch reaction. *Faraday Discussions*, 2013: vol. 162, pp. 267–279
6. James, O. O., Chowdhury, B., Mesubi, M. A., and Maity, S. 2012. Reflections on the chemistry of the Fischer–Tropsch synthesis. *RSC Advances*, 2012: vol. 2, pp. 7347–7366
7. Sun, B., Qiao, M., Fan, K., Ulrich, J. and Tao, F. F. 2011. Fischer–Tropsch Synthesis over Molecular Sieve Supported Catalysts. *ChemCatChem*, 2011: vol. 3, pp. 542 – 550
8. de Wit, M., Junginger, M., Lensink, S., Londo, M. and Faaij, A. 2010. Competition between biofuels: Modeling technological learning and cost reductions over time. *Biomass and Bioenergy*, 2010: vol. 34 (2), pp. 203–217
9. Beaumont, S. K. 2014. Recent developments in the application of nanomaterials to understanding molecular level processes in cobalt catalysed Fischer–Tropsch synthesis. *Physical Chemistry Chemical Physics*, 2014: vol. 16, pp. 5034-5043
10. Ali, S., Zabidi, N. A. M. and Subbarao, D. 2011. Correlation between Fischer-Tropsch catalytic activity and composition of catalysts. *Chemistry Central Journal*, 2011: vol 5, pp. 68 (8 pages).
11. Jacobs, G., Das, T. K., Zhang, Y., Li, J., Racoillet, G. and Davis, B. H. 2002. Fischer–Tropsch synthesis: support, loading, and promoter effects on the reducibility of cobalt catalysts. *Applied Catalysis A: General*, 2002: vol. 233, pp. 263–281
12. Iwasaki, T., Reinikainen, M., Onodera, Y., Hayashi, H., Ebina, T., Nagase, T., Torii, K., Kataja, K. and Chatterjee, A. 1998. Use of silicate crystallite mesoporous material as catalyst support for Fischer–Tropsch reaction. *Applied Surface Science*, 1998: vol. 130–132, pp. 845–850.
13. Panpranot, J., Goodwin, Jr., J. G. and Sayari, A. 2002. (a) CO Hydrogenation on Ru-Promoted Co/MCM-41 Catalysts. *Journal of Catalysis*, 2002: vol. 211, pp. 530-539; (b) Synthesis and characteristics of MCM-41 supported CoRu catalysts. *Catalysis Today*, 2002: vol. 77, pp. 269–284
14. Koh, T., Koo, H. M., Yu, T., Lim, B. and Bae, J. W. 2014. Roles of Ruthenium−Support

Interactions of Size-Controlled Ruthenium Nanoparticles for the Product Distribution of Fischer−Tropsch Synthesis. *ACS Catalysis*, 2014: vol. 4, pp. 1054−1060

15. Jahangiri, H., Bennett, J., Mahjoubi, P., Wilson, K. and Gua, S. 2014. A review of advanced catalyst development for Fischer–Tropsch synthesis of hydrocarbons from biomass derived syngas. *Catalysis Science & Technology*, 2014: vol. 4, pp. 2210–2229
16. Cai, Q. and Li, J. 2008. Catalytic properties of the Ru promoted Co/SBA-15 catalysts for Fischer–Tropsch synthesis. *Catalysis Communications*, 2008: vol. 9, pp. 2003–2006
17. (a) Iglesia, E., Soled, S. L. and Fiato, R. A. 1992. Fischer-Tropsch Synthesis on Cobalt and Ruthenium. Metal Dispersion and Support Effects on Reaction Rate and Selectivity. *Journal of Catalysis*, 1992: vol. 137, pp. 212-224; (b) Iglesia, E., Reyes, S. C., Madon, R. J. and Soled, S. L. 1993. Selectivity Control and Catalyst Design in the Fischer-Tropsch Synthesis: Sites, Pellets, and Reactors. *Advances in Catalysis*, 1993: vol. 39, pp. 221–302; (c) Iglesia, E., Soled, S. L., Fiato, R. A. and Via, G. H. 1994. Dispersion, support, and bimetallic effects in Fischer-Tropsch synthesis on cobalt catalysts. *Studies in Surface Science and Catalysis*, 1994: vol. 81, pp. 433-442
18. (a) Xiong, H., Zhang, Y., Liew, K. and Li, J. 2009. Ruthenium promotion of Co/SBA-15 catalysts with high cobalt loading for Fischer–Tropsch synthesis. *Fuel Processing Technology*, 2009: vol. 90, pp. 237 – 246; (b) Wang, S., Yin, Q., Guo, J., Ru, B. and Zhu, L. 2013. Improved Fischer–Tropsch synthesis for gasoline over Ru, Ni promoted Co/HZSM-5 catalysts. *Fuel*, 2013: vol. 108, pp. 597–603; (c) de Tymowski, B., Liu, Y., Meny, C., Lefèvre, C., Begin, D., Nguyen, P., Pham, C., Edouard, D., Luck, F. and Pham-Huu, C. 2012. Co–Ru/SiC impregnated with ethanol as an effective catalyst for the Fischer–Tropsch synthesis. *Applied Catalysis A: General*, 2012: vol. 419– 420, pp. 31– 40.
19. (a) Tavasoli, A., Mortazavi, Y., Khodadadi, A. and Sadagiani, K. 2005. Effects of Different Loadings of Ru and Re on Physico-Chemical Properties and Performance of 15% Co/Al_2O_3 FTS Catalysts. *Iranian Journal of Chemistry and Chemical Engineering*, 2005: vol. 35, pp. 9–15; (b) Tavasoli, A., Taghavi, S., Tabyar, S. and Karimi, S. Enhancement of ruthenium-promoted Co/CNTs nanocatalyst performance using microemulsion technique. *International Journal of Industrial Chemistry*, 2014: vol. 5, pp. 9 (11 pages).
20. Kungurova, O. A., Shtertser, N. V., Chermashentseva, G. K., Simentsova, I. I. and Khassin, A. A. 2017. Ruthenium Promoted Cobalt–Alumina Catalysts for the Synthesis of High-Molecular-Weight Solid Hydrocarbons from CO and Hydrogen. *Catalysis in Industry*, 2017: vol. 9, pp. 23–30
21. Poyraz, A. S., Kuo, C.-H., Biswas, S., King'ondu, C. K. and Suib, S. L. 2013. A general approach to crystalline and monomodal pore size mesoporous materials. *Nature*

Communications, 2013: vol. 4, pp. 2952

22. (a) Poyraz, A. S. Hines, W. A., Kuo, C.-H., Li, N., Perry, D. M. and Suib, S. L. Mesoporous Co_3O_4 nanostructured material synthesized by one-step soft-templating: A magnetic study. *Journal of Applied Physics*, 2014: vol. 115, pp. 114309 (11 pages); (b) Song, W., Poyraz, A. S., Meng, Y., Ren, Z., Chen, S.-Y. and Suib, S. L. 2014. Mesoporous Co_3O_4 with Controlled Porosity: Inverse Micelle Synthesis and High-Performance Catalytic CO Oxidation at −60 °C. *Chemistry of Materials*, 2014: vol. 26, pp. 4629–4639
23. Mogudi, B. M., Ncube, P. and Meijboom, R. 2016. Catalytic activity of mesoporous cobalt oxides with controlledporosity and crystallite sizes: Evaluation using the reduction of 4-nitrophenol. *Applied Catalysis B: Environmental*, 2016: vol. 198, pp. 74–82
24. (a) Polarz, S. and Antonietti, M. Porous materials via nanocasting procedures: innovative materials and learning about soft-matter organization. *Chemical Communications*, 2002: pp. 2593-2604; (b) Martín-Aranda, R. and Čejka, J. Recent Advances in Catalysis Over Mesoporous Molecular Sieves. *Topics in Catalysis*, 2009: vol. 53, pp. 141-153
25. Schon, G. and Simon, U. 1995. A fascinating new field in colloid science: small ligand-stabilized metal clusters and their possible application in microelectronics (a) Part I: State of the art. *Colloid and Polymer Science*, 1995: vol. 273 (2), 101-107; (b) Part I1: Future directions. *Colloid and Polymer Science*, 1995: vol. 273 (3), pp. 202-218
26. (a) Antonetti, C., Oubenali, M. and Galleti, A. M. R. 2012. Novel microwave synthesis of ruthenium nanoparticles supported on carbon nanotubes active in the selective hydrogenation of p-chloronitrobenzene to p-chloroaniline. *Applied Catalysis A: General*, 2012: vol. 421-422, pp. 99–107
27. (a) Soler-Illia, G. J. de A. A., Sanchez, C., Lebeau, B. and Patarin, J. 2002. Chemical Strategies To Design Textured Materials: from Microporous and Mesoporous Oxides to Nanonetworks and Hierarchical Structures. *Chemical Reviews*, 2002: vol. 102, pp. 4093-4138; (b) Soler-Illia, G. J. de A. A., Crepaldi, E. L., Grosso, D. and Sanchez, C. 2003. Block copolymer-templated mesoporous oxides. *Current Opinion in Colloid and Interface Science*, 2003: vol. 8, pp. 109–126
28. (a) Barret, E. P., Joyner, L. G. and Halenda, P. P. 1951. The Determination of Pore Volume and Area Distributions in Porous Substances. I. Computations from Nitrogen Isotherms. *Journal of American Chemical Society*, 1951: vol. 73(1), pp. 373-380; (b) Thommes, M., Kaneko, K., Niemark, A. V., Olivier, J. P., Rodriguez-Reinoso, F., Rouquérol, J. and Sing, K. S. W. 2015. Physisorption of gases, with special reference to the evaluation of surface area and pore size distribution (IUPAC Technical Report). *Pure and Applied Chemistry*, 2015: vol 87(9-10), pp. 1051–1069

29. G. Allaedini and A. Muhammad, 2013. Study of influential factors in synthesis and characterization of cobalt oxide nanoparticles. *Journal of Nanostructure in Chemistry*, 2013: vol. 3, pp. 77 (16 pages)

30. Fouad, O. A., Makhlouf, S. A., Ali, G. A. M. and El-Sayed, A. Y. 2011. Cobalt/silica nanocomposite via thermal calcination-reduction of gel precursors. *Materials Chemistry and Physics*, 2011: vol. 128, pp. 70–76

31. Paoli, E. A., Masini, F., Frydendal, F., Deiana, D., Schlaup, C., Malizia, M., Hansen, T. W., Horch, S., Stephens, I. E. L. and Chorkendorff, I. 2015. Oxygen evolution on well-characterized mass selected Ru and RuO_2 nanoparticles. *Chemical Science*, 2015: vol. 6, pp. 190-196

32. Wu, Z. and Jiang, H. 2015. Efficient palladium and ruthenium nanocatalysts stabilized by phosphine functionalized ionic liquid for selective hydrogenation. *RSC Advances*, 2015: vol. 5, pp. 34622–34629

33. (a) Biswa, A., Paul, S. and Banerjee, A. 2015. Carbon nanodots, Ru nanodots and hybrid nanodots: preparation and catalytic properties. *Journal of Materials Chemistry A*, 2015: vol. 3, pp. 15074–15081; (b) Rabe, S., Nachtegaal, M. and Vogel, F. 2007. Catalytic partial oxidation of methane to synthesis gas over a ruthenium catalyst: the role of the oxidation state. *Physical Chemistry Chemical Physics*, 2007: vol. 9, pp. 1461–1468

34. Yang, Z., Xia, Y. and Mokaya, R. 2006. Periodic mesoporous organosilica mesophases are versatile precursors for the direct preparation of mesoporous silica/carbon composites, carbon and silicon carbide materials. *Journal of Materials Chemistry*, 2006: vol. 16, pp. 3417–3425

35. Vosoughi, V., Dalai, A. K. and Abatzoglou, N. 2017. Performances of promoted cobalt catalysts supported on mesoporous alumina for Fischer-Tropsch synthesis. *Applied Catalysis A, General*, 2017: vol. 547, pp. 155-163

36. Khodakov, A. Y., Griboval-Constant, A., Bechara, R. and Zholobenko, V. L. 2002. Pore Size Effects in Fischer Tropsch Synthesis over Cobalt-Supported Mesoporous Silicas. *Journal of Catalysis*, 2002: vol. 206, pp. 230–241

37. Arsalanfar, M., Mirzaei, A. A., Bozorgzadeh, H. R. and Atashi, H. 2012. Effect of process conditions on the surface reaction rates and catalytic performance of MgO supported Fe–Co–Mn catalyst for CO hydrogenation. *Journal of Industrial and Engineering Chemistry*, 2012: vol. 18, pp. 2092–2102

38. (a) González, O., Pérez, H., Navarro, P., Almeida, L. C., Pacheco, J. G. and Montes, M. 2009. Use of different mesostructured materials based on silica as cobalt supports for the Fischer–Tropsch synthesis. *Catalysis Today*, 2009: vol. 148, pp. 140–147; (b) Kang, S.-H., Ryu, J.-H., Kim, J.-H., Prasad, P. S. S., Bae, J. W., Cheon, J.-Y. and Jun, K.-W. 2011. ZSM-5 Supported

Cobalt Catalyst for the Direct Production of Gasoline Range Hydrocarbons by Fischer–Tropsch Synthesis. *Catalysis Letters*, 2011: vol. 141, pp. 1464–1471

39. (a) de la Osa, A. R., de Lucas, A., Romero, A., Valverde, J. L. and Sánchez, P. 2011. Fischer–Tropsch diesel production over calcium-promoted Co/alumina catalyst: Effect of reaction conditions. *Fuel*, 2011: vol. 90, pp. 1935–1945; (b) Diaz, J. A., de la Osa, A. R., Sánchez, P., Romero, A. and Valverde, J. L. 2014. Influence of CO_2 co-feeding on Fischer–Tropsch fuels production over carbon nanofibers supported cobalt catalyst. *Catalysis Communications*, 2014: vol. 44, pp. 57–61
40. Bae, J. W., Park, S.-J., Lee, Y.-J., Park, H.-G., Kim, Y.-B., Lee, D. H., Kim, B.-W. and Park, M.-J. 2011. Effects of Reaction Variables on Fischer–Tropsch Synthesis with Co-Precipitated K/FeCuAlO_x Catalysts. *Catalysis Letters*, 2011: vol. 141, pp. 799−807
41. (a) van Santen, R. A., Markvoort, A. J., Filot, I. A. W., Ghouri, M. M. and Hensen, E. J. M. 2013. Mechanism and microkinetics of the Fischer–Tropsch Reaction. *Physical Chemistry Chemical Physics*, 2013: vol. 15, pp. 17038-17063; (b) van Santen, R. A., Neurock, M. and Shetty, S. 2010. Reactivity theory of transition-metal surfaces: a Brønsted-Evans-Polanyi linear activation energy-free-energy analysis. *Chemical Reviews*, 2010: vol. 110, pp. 2005–2048
42. Griboval-Constant, A., Khodakov, A. Y., Bechara, R. and Zholobenk, V. L. 2002. Support mesoporosity: a tool for better control of catalytic behavior of cobalt supported Fischer Tropsch catalysts. *Studies in Surface Science and Catalysis*, 2002: vol. 144, pp. 609–616
43. (a) Jia, J., Qian, C., Dong, Y., Li, Y. F., Wang, H., Ghoussoub, M., Butler, K. T., Walsh, A. and Ozin, G. A. 2017. Heterogeneous catalytic hydrogenation of CO_2 by metal oxides: defect engineering – perfecting imperfection. *Chemical Society Reviews*, 2017: vol. 46, pp. 4631—4644; (b) Strayer, M. E., Senftle, T. P., Winterstein, J. P., Vargas-Barbosa, N. M., Sharma, R., Rioux, R. M., Janik, M. J. and Mallouk, T. E. 2015. Charge Transfer Stabilization of Late Transition Metal Oxide Nanoparticles on a Layered Niobate Support. *Journal of the American Chemical Society*, 2015: vol. 137, pp. 16216–16224
44. de Lima, S. M., Silva, A. M., da Cruz, I. O., Jacobs, G., Davis, B. H., Mattos, L. V. and Noronha, F. B. 2008. H_2 production through steam reforming of ethanol over Pt/ZrO_2, Pt/CeO_2 and Pt/$CeZrO_2$ catalysts. *Catalysis Today*, 2008: vol. 138, pp. 162–168
45. (a) Nash, D. J., Restrepo, D. T., Parra, N. S., Giesler, K. E., Penabade, R. A., Aminpour, M., Le, D., Li, Z., Farha, O. K., Harper, J. K., Rahman, T. S. and Blair, R. G. 2016. Heterogeneous Metal-Free Hydrogenation over Defect-Laden Hexagonal Boron Nitride. *ACS Omega*, 2016: vol. 1, pp. 1343−1354; (b) Zhao, H., Zhu, Q., Gao, Y., Zhai, P. and Ma, D. 2013. Iron oxide nanoparticles supported on pyrolytic graphene oxide as model catalysts for Fischer Tropsch synthesis. *Applied Catalysis A: General*, 2013: vol. 456, pp. 233−239; (c) Wu, J., Wang, L.,

Yang, X., Lv, B. and Chen, J. 2018. Support Effect of the Fe/BN Catalyst on Fischer−Tropsch Performances: Role of the Surface B−O Defect. *Industrial & Engineering Chemistry Research*, 2018: vol. 57, pp. 2805−2810

A novel approach to produce a high purity cellulose product from sawdust waste material

S. Balkissoon[1,2*], J. Andrew[1*] and B. Sithole[1,2]

[1] College of agriculture, engineering and science, School of chemical engineering, Howard college, University of Kwa-Zulu-Natal, Durban, South Africa.

[2] Biorefinery Industry Development Facility (BIDF), Council for Scientific and Industrial Research, P.O. Box 59081 Umbilo 4075, Durban, South Africa.

*Corresponding authors: simikshab@gmail.com; jandrew@gmail.com

ABSTRACT

Approximately half of the wood processed in the Forestry, Timber, Pulp and Paper (FTPP) sector is accumulated as waste. The transition towards an almost paperless world driven by the rise of digital media has resulted in a decline in traditional paper markets, prompting the FTTP sector to reposition itself, and expand their product offerings by unlocking the potential of new value adding opportunities from remaining wood waste components to generate revenue. In this study, a novel approach to produce a dissolving wood pulp (DWP) grade from sawdust was developed. DWP is a high purity cellulose product used in several applications such as pharmaceutical, textile, food, paint and coatings industries. The proposed approach demonstrates the potential to eliminate several complex processing stages which are associated with traditional commercial processes to produce high purity cellulose products such as DWP, thereby making the process less chemical, energy and water intensive. Chemical characterisation of the cellulose product thus far has shown properties similar to commercially available products, making the proposed process a promising and viable option for the production of DWP from sawdust, a waste material from wood processing industries.

Keywords: Biomass, dissolving wood pulp, cellulose, chemical treatment

1 INTRODUCTION

The concept of a "green economy" encourages industries to employ revolutionary transformative technologies to eliminate waste generation by exploring the development of new value chains. According to Sithole (2017), the low timber utilization rate of around 47% is a broad challenge faced by the Forestry, Timber, Pulp and Paper (FTPP) sector since approximately 53% of the wood in the form of bark, chips and sawdust goes to waste.

The FTPP sector contributes to about 1% of South Africa's GDP (Tradingeconomics, 2020) and approximately 4.5% to its manufacturing GDP, making it a vital sector in the economy (Sea, 2020). The diminishing annual demand for forest products can assumingly be attributed to the decline in the demand for wood products such as paper which is no longer required as much today.

Although there are no recent figures available, in 2010 it was estimated that forestry and wood

processing in South Africa generates about 4-6 million tons of wood waste per annum, mainly as residues in the plantations and as sawdust and offcuts at the saw mills and pulp mills (Timberwatch, 2010). From all the sawmills in SA, 440 006 tons per annum of sawdust waste was generated from 218 saw mills (Stafford and Lange, 2018). More stringent government legislation will drive industry to consider processes that curtails waste accumulation and favors a more sustainable environment.

The abovementioned scenarios coupled together encourages the urgency for the industry to employ revolutionary change that that will prove to be environmentally superior to existing processes, enabling the industry to continue its legacy in the future.

Dissolving wood pulp (DWP) is a high purity cellulose product that is produced from wood chips (Potgieter, 2018). Such products are valuable for commercial applications for the production of end-user products such as pharmaceuticals, textiles like viscose, and microcrystalline cellulose (Sappi, 2019). Extensive research has been conducted over the years to produce DWP in alignment with pulping mills efforts for technological innovations to fractionate or convert lignocellulosic materials into a wide range of products and by-products for more effective utilisation of renewable feedstocks as opposed to accumulating waste (Lehto and Alen, 2014). Existing processes used to produce DWP from wood chips are time consuming, complex, and energy, water, and chemical intensive (Liu et al., 2016).

The study focused on developing a novel process to produce DWP from sawdust (a waste material) and with more favorable processing conditions which will address the drawbacks of the existing processes. It is anticipated that this will increase revenue by lowering the capital intensity (processing costs and time) whilst still rendering the support of global best practices to reduce waste to landfill and to rather turn waste into wealth, giving the South African producers of DWP a competitive edge.

2 LITERATURE

2.1 Dissolving wood pulp production

The DWP demand has shown a buoyant increase and is the basis of new forest products. The dissolving pulp industry exhibited prospective growth in developing countries in recent years. In 2018, the global revenue generated from DWP amounted to $9.3 Billion, this being a 6.5% increase from the previous year.

Dissolving pulps across the world are produced mainly by two conventional processes; acid sulphite (AS) process and the prehydrolysis kraft (PHK) process (Astuy, 2016, Strunk, 2012, Yang et al., 2018). Each of these chemical pulping processes follow different reaction mechanisms. However, they are analogous to selectively eliminate the lignin without extensive degradation of carbohydrates, and also remove extractives and other chromophoric structures in residual lignin.Both processes yield different qualities of dissolving wood pulp which then determines its applicability in other industries (Christoffersson, 2005, Jahan et al., 2008).

The chemical composition of the raw material is a predetermining factor and should be considered for production of dissolving pulp when selecting an appropriate pulping process (Chen et al., 2016, Shahzad, 2012, Jahan et al., 2008, Jardim et al., 2018, Li, 2016).According to Li (2016), wood still remains one of the widely used raw materials for dissolving pulp production . The principle of chemical pulp processing targets two main areas, namely removal of hemicelluloses and lignin. The former usually is carried out by some sort of pre-treatment process to target the lignin-hemicellulose matrix and improve the accessibility of cellulose, whilst the latter usually occurs during pulping/cooking (Othman, 2015). The primary aim of the pre-treatment stage is to disrupt the rigid crystalline structure of cellulose, and increase its structural accessibility and chemical reactivity (Ocwelwang, 2017). Lignin removal is important because it imparts a yellowish brown colour to the pulp which is undesirable property of the dissolving pulp since a high level of brightness and cellulose purity is important in the production of cellulose based products such as viscose and acetate fibres (Bodhlyera et al., 2015). The extracted waste liquor with higher concentration of impurities such as lignin and hemicelluloses and higher temperature is sent to the chemical recovery station for recovering the organic or inorganic matter in the waste liquid (acid and alkali recovery process).

Chemical treatments are applied to pulps to make it a suitable candidate for high purity cellulose derived end-user products. The resultant pulp emanating from either of the pulping processes requires further delignification to render it viable to produce a high purity dissolving wood pulp. Bodhlyera et al. (2015) mentions that the most common process employed by industry responsible for producing a dissolving wood pulp of such a standard, irrespective of the pulping process used, is the bleaching process (Bodhlyera et al., 2015). The bleaching process plays a vital role and assists in obtaining a quality pulp with certain whiteness, cleanliness, purity and excellent physical and chemical characteristics thus increasing its application potential.

The PHK process leads as the desired process, accounting for approximately 56% of the world DWP produced whilst the AS process accounts for 42% (Chen et al., 2016, Strunk, 2012, Bi et al., 2021, Rodrigues et al., 2018). The PHK process follows a combined process of pre-treatment (pre-hydrolysis) and alkali kraft cooking (Chen et al., 2016). The hemicelluloses are removed during the initial prehydrolysis stage which is followed by kraft cooking and a multi-stage bleaching process to achieve a high purity dissolving pulp. During prehydrolysis, a significant amount of the hemicelluloses and a small amount of the cellulose are hydrolysed into short chains.

2.2 Dissolving wood pulp (DWP) characterization and its end usage

Dissolving pulp is characterized by high cellulose content, high brightness and low macromolecular polydispersity (PDI) (Chen et al., 2019). DWP contains a high alpha cellulose content (> 90%), a low hemicellulose content (3-6%) and trace amounts of lignin and other impurities (<0.05%) (Dladla, 2018,

Chen et al., 2016). The viscosity of the pulp subsequent to the cooking process is often about or below 1100 ml/g, and between 400-600 ml/g post final bleaching (Wennerstrom and Bylund, 2017). According to Jesus et al. (2013), cellulosic pulps should satisfy the requisites of high α-cellulose content (≥ 91%), Kappa number less than 1, intrinsic viscosity (450-550 ml/g), a low amount of hemicelluloses and extractive compounds, and finally a high reactivity (> 60%), to be considered as dissolving pulps.

During dissolving pulp manufacturing, the controlled variable is the degree of polymerization (DP) of the cellulose because it gives an indication of the average length of the polymer chains (Shahzad, 2012). Dissolving pulp is the main feedstock for manufacturing regenerated cellulose such as viscose, lyocell and cellulose derivatives. DWP undergoes a variety of manufacturing processes that are used for the production of various cellulose based end-products (Ocwelwang, 2017, Schwaiger, 2019, Alam and Christopher, 2017). These manufacturing processes are classified according to the different alpha grades used to produce these cellulose derivatives. The versatility of dissolving pulp in a variety of economic and technical areas is due to its functionality, recyclability, and, most importantly, its biodegradability (Małachowska et al., 2020, Schwaiger, 2019) . The end user products of dissolving pulp are widely used in industrial products such as textiles, tyres, coatings, paints, tobacco products and food, as well as pharmaceutical products (Liu et al., 2016). Other applications include rheological modifiers in products such as lipstick, fillers in fat-free yoghurt, tablets and washing powders and micro crystalline cellulose (MCC) which is used as a binder in pharmaceuticals and as a thickener in food (Sappi, 2019).

Removing lignin and hemicellulose yields high purity DWP (91–98% cellulose) (Sappi, 2019). Lower grade dissolving pulps are believed to exhibit a cellulose content of approximately 90% whilst the medium grades possess a cellulose content of about 94%. The highest grade is said to have a cellulose content of approximately 96% or more (Liu et al., 2016). Chunilall (2009) suggests that 90%, 92 -94% and 96% α-cellulose are respectively utilised for the production of microcrystalline cellulose (MCC), viscose, and cellulose acetate.

3 EXPERIMENTAL PROCEDURE

3.1 Sawdust characterization

Two different species of wood was selected for evaluation; Pin chips (from the wood chip screening process) was obtained from a local pulp mill. The wood processed by the mill is a mixture of 53.02% Eucalyptus dunnii, 37.80% Eucalyptus grandis and 10.15% clone timber). The pin chips were milled into a finer sawdust particle using a hammer mill followed by a wiley mill. The second sample was a softwood (Pinus Patula) sawdust sample collected from a local saw mill. A shaker with several screens ranging in sizes from 0 to 1180 µm (0, 53, 150, 250, 425, 530, 710, 1180 µm) was used to determine the particle size distribution of the sawdust samples. 100 g aliquots of sawdust samples were screened

for 30 minutes in duplicate. The preparation process is shown in Figure 1. The sawdust remaining on each screen was weighed. The saw mill sawdust samples were screened to a particle size of below 1180 µm. The starting wood materials and pulps were chemically analysed using the Technical Association of the Pulp and Paper Industry (TAPPI) standard methods.

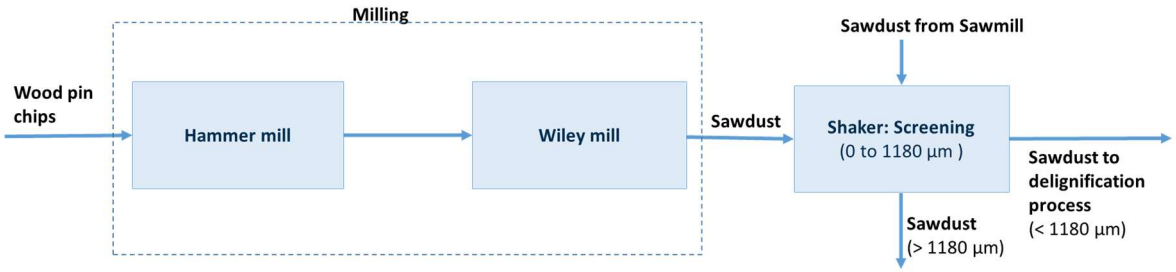

Figure 2: Process flow diagram of raw material preparation process

3.2 Dissolving pulp experiments

The screened sawdust samples were subjected to a two-stage non-disclosed process (Figure 2). The first stage involved delignifying the sawdust according to the conditions listed in Table 1. The sawdust samples were weighed according to the liquid to wood ratio (L: W) and the respective dosage of chemical was added in the form of a slurry to the sawdust. The mixture was then stirred for the desired time and temperature. Experiments were conducted in triplicate for each condition specified. The pulps from each step were washed under vacuum filtration following the experiment and left to air dry. Pulp yield was determined using the standard oven moisture technique (TAPPI test method T550-D) and the pulp was characterised in terms of intrinsic viscosity (SCAN method SCAN-CM 15), degree of polymerisation (SCAN method SCAN-CM 15), ISO brightness (ISO 2470) and hemicellulose content via high performance liquid chromatography (HPLC) (TAPPI test method no. T249 cm-85).

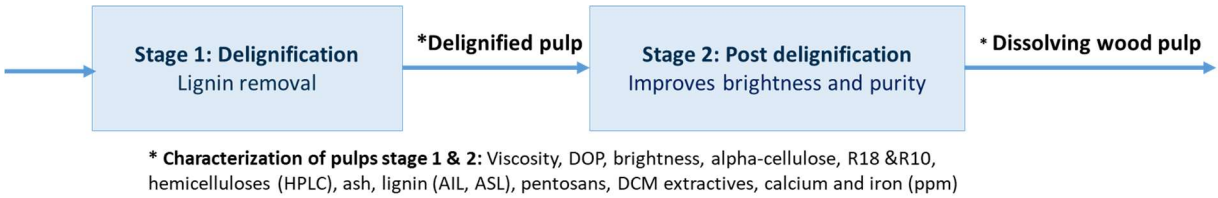

Figure 3: Two-stage process pathway for dissolving wood pulp production from sawdust.

Table 1: Summary of processing conditions optimised.

Process step	Parameter	Conditions
Delignification process	Temperature	60-90°C; Δ10°C
	Time	3-6 h
	Chemical concentration	1, 2 and 3M
	Liquid to wood ratio (L: W)	5:1, 7.5:1, 10:1

4 RESULTS AND DISCUSSION

4.1 Sawdust characterization

The particle size distribution of the two sawdust samples are shown in Figure 4.

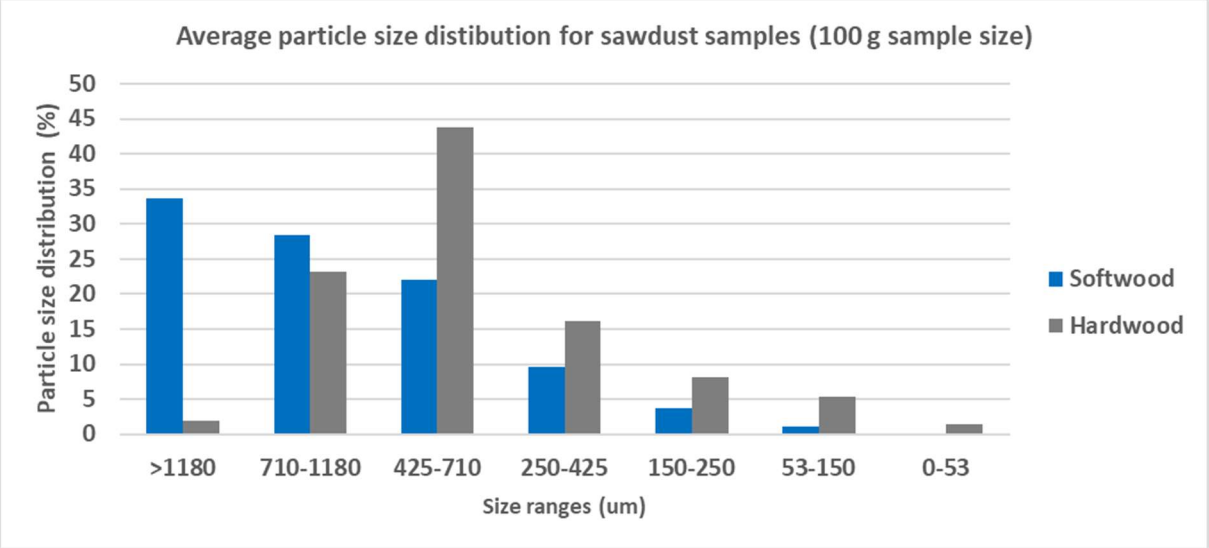

Figure 4: Particle size distribution (PSD) of sawdust species

The softwood sawdust sample showed a high composition of particles greater than 1180 µm. The fraction above 1180 µm was removed as it was not compatible with the delignification process due to its low surface area, which resulted in unreacted sawdust particles.

Each of the sawdust species was chemically characterized (Table 2) to identify the composition prior to treatment. The hardwood sample differed slightly from the softwood species for most of the components. The cellulose and lignin content from all species corresponds to the ranges specified in literature (Cellulose of 40-50% and lignin 15-35%) (Swst, 2017).

In terms of the monosaccharide compositions, higher compositions of xylose were present in the hardwood sample as compared to the softwood sample and higher compositions of mannose and galactose was observed in the softwood as compared to the hardwood sample which corresponds to literature (Gladyshko, 2011). The ash composition for the hardwood sawdust also was relatively higher compared to the softwood. According to literature hardwoods contain a high proportion of xylose units and by contrast, softwoods have a high proportion of mannose units and more galactose units (Gladyshko, 2011). This is evident in the results comparing the chemical compositions of the species. Furthermore, the hardwood sample shows a slightly higher cellulose composition in comparison to the softwood species.

Table 2: Chemical composition of different sawdust species used (Dry wood basis)

Analysis	Hardwood sawdust	Softwood sawdust
Solvent extractives (%)	0.40	0.29
Hot water extractives (%)	3.27	1.96
AIL (%)	31.74	30.83
ASL (%)	4.49	2.67
Siefert Cellulose (%)	44.08	41.59
Ash content (%)	0.70	0.17
Monosaccharides		
Arabinose (%)	0.66	0.95
Galactose (%)	0.86	1.94
Xylose (%)	13.07	6.05
Glucose (%)	39.88	42.94
Mannose (%)	0.95	3.09

4.2 Dissolving pulp experiments

The two-stage delignification and pulp purification processes showed that a temperature beyond 60 ℃ with chemical concentrations of 3 M caused effervescence of the product and thus delignification was not achieved. At lower treatment concentrations (1 and 2 M) for temperatures above 60 ℃, the conditions were still not effective enough to effect sufficient delignification, leaving a large proportion of unpulped sawdust even up to periods of 6 hours. Optimum conditions were found to be 3 M and 60 ℃ and L: W (10:1) for the softwood sample and 3 M, 70 ℃ and L:W (10:1) for the hardwood sample in about 6 hours, where a fully pulped product was achieved with minimal to no rejects.

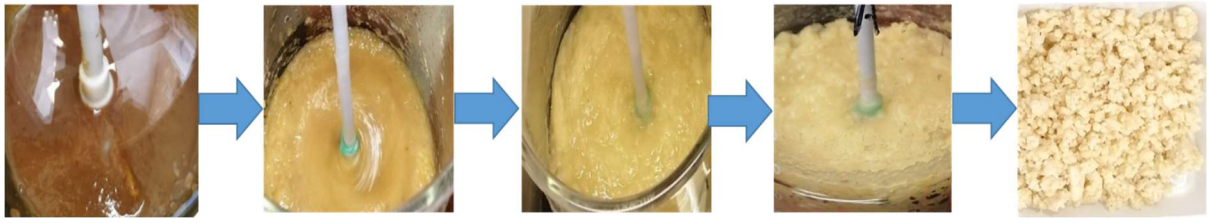

Figure 5: Transition of sawdust to pulp during delignification process.

A second set of tests was then done to optimize the reaction time for delignification of each species using the two abovementioned sets of conditions. For the hardwood sample at 70 ℃, delignification was achieved in 3 hours. Optimum conditions were established for each species in terms of concentration, temperature and time. A yield from 44-60% and 53% was achieved for sawdust species respectively. The yield obtained was similar to unbleached AS DWP (44.9-45.9%) and slightly higher

than unbleached PHK DWP (35-40%) (Dyunyasheva, 2017). PHK DWP is expected to show lower yields due to the prehydrolysis step. Figure 5 shows the transition of sawdust mixture to a pulp as time elapsed during the delignification process with the final stage showing a washed air-dried pulp.

The pulps were characterized and the results are summarized in Table 3.

Table 3: Results of chemical characterisation of pulps from each sawdust species using optimum conditions

Measurement	Hardwood sample	Softwood sample
Yield (%)	44-60	53
Intrinsic viscosity (ml/g)	110-180	304
Degree of polymerization (DOP)	283-505.35	934
ASL (%)	1.17-1.53	1.29
AIL (%)	4.27-4.89	5.13
ISO brightness (%)	65-66.69	66
Monosaccharides		
Glucose	74.59-80.37	90.14
Mannose	0.00	6.74
Arabinose	0.00	0.00
Xylose	2.63-5.15	1.04
Galactose	0.00	0.00

Both sawdust pulp samples derived from stage 1 showed a low intrinsic viscosity and corresponding degree of polymerization (DOP), between 110-304 mL/g and 283-934 respectively. The low viscosity and DOP were attributed to the possibility of cellulose degradation due to reduced polymer chains as mentioned in literature (Shahzad, 2012). The results suggest that the dissolving pulps achieved to date, without further chemical treatment, would be suitable to target an application that requires a low viscosity pulp such as MCC which requires a DOP < 400 corresponding to a viscosity of 148.03 mL/g. Brightness measurements ranged between 65-66.69% overall. Majority of literature reports on final bleached DWP brightness >85%. However, one source makes mention of unbleached PHK DWP 33.6-42,9%, highlighting that the proposed study pulps have advantage in this aspect and will require minimal improvement in brightness during the subsequent post delignification stage (Sixta, 2006). Lignin concentrations (AIL and ASL) showed significant decreases compared to the original sawdust

samples (70-80% reduction), indicating that the delignification process was efficiently removing lignin. Hemicellulose content overall following stage 1 was minimal which suggests that the hemicellulose was also degraded in the stage 1 delignification process. A low hemicellulose content is a key requirement for DWP grades. However, considering the initial raw material hemicellulose composition, separate studies will be undertaken to evaluate the pre-extraction of the hemicelluloses prior to stage 1 delignification for possible beneficiation of the hemicelluloses. Previous studies have shown that removal of hemicellulose prior to the process may aid in delignification, thus requiring milder delignification conditions (Miao et al., 2014, Christopher, 2017, Liu et al., 2013, Koradiyaa et al., 2016).

5 CONCLUSIONS

The proposed process has shown significant evidence in consistently producing a low viscosity and high brightness dissolving pulp grade cellulose product by the delignification of sawdust. Optimum conditions were established for pulps with little to no rejects for hardwood and softwood species. Concerns remain around cellulose degradation. However, the current product shows potential as feedstocks for end-user applications such as MCC which can service the pharmaceutical and possibly the food industry at large. Other end-user products such as viscose production is also been researched and considered in the pipeline.

In addition, efforts to extract more value from the sawdust material by applying pre-treatment methods such as prehydrolysis prior to delignification is underway. This will expand the value chain of the biomaterial. The process shows novelty and promising energy and water savings, and in turn, reduced processing costs by achieving a dissolving pulp grade cellulose product using moderate temperatures and reduced times in comparison to conventional processes. The next stages in the project entail developing a proof of concept of end-user products followed by a pilot scale up of the process as well as a techno-economic study.

REFERENCES

Alam, M. N. & Christopher, L. P. 2017. A novel, cost effective and eco-friendly method for preparation of textile fibers. *Carbohydrate polymers,* 173**,** 253-258.

Astuy, T. L. 2016. *Developments in a sulphite pulping process for the valorisation of its carbohydrate resources within the biorefinery concept.* PhD, University of Cantabria.

Bi, R., Khatri, V., Chandra, R., Takada, M., Figueroa, D. V., Zhou, H., Wu, J., Charron, D. & Jack Saddler 2021. Enhancing Kraft based dissolving pulp production by integrating green liquor neutralization,. *Carbohydrate Polymer Technologies and Applications***,** 9.

Bodhlyera, O., Zewotir, T., Ramroop, S. & Chunilall, V. 2015. Analysis Of The Changes In Chemical Properties Of Dissolving Pulp During The Bleaching Process Using Piecewise Linear Regression Models *Cellulose Chem. Techno,* 49**,** 317-332.

Chen, C., Duan, C., Li, J., Liu, Y., Ma, X., Zheng, L., Stavik, J. & Ni, Y. 2016. Cellulose (Dissolving wood pulp) manufacturing processes and properties: A mini review. *BioResources,* 11**,** 5553-5564.

Chen, Z., Zhang, H., He, Z. & Zhang, L. 2019. Current and future markets of dissolving pulp in China and other countries. *BioResources,* 14**,** 7627-7629.

Christoffersson, K. E. 2005. *Dissolving Pulp – Multivariate Characterisation and Analysis of Reactivity and Spectroscopic Properties* PhD, Umeå University.

Christopher, H. K. L. P. 2017. Recent trends and developments in dissolving pulp production and application. *Cellulose* 24**,** 2347–2365.

Dladla, V. P. 2018. *Pyrolysis-gas chromatography/mass spectrometry study of chromophores in dissolving wood pulp.* PhD, University of Kwa-Zulu-Natal, Howard college.

Dyunyasheva, V. 2017. *Dissolving pulp and its properties* Bachelor's Degree, Tampere University of Applied Sciences

Gladyshko, Y. 2011. *Extraction of Hemicelluloses by Acid Catalyst Hydrolysis.* Degree program in Paper Technology Bachelor's Thesis, Saimaa University of Applied Sciences.

Jahan, M. S., Ashan, L., Noori, A. & Quaiyyum, M. A. 2008. Process for the production of dissolving pulp from Trema Orientalis(Nalita)by Prehydrolysis Kraft and soda ethylenediamine (EDA) process. *Bioresouces,* 3**,** 816-828.

Jesus, L. L. D., Evtyugin, P. D. V. & Prates, E. a. F. D. S. Improving bleaching performance of sulphite dissolving pulps. XXII Tecnicelpa – International Forest, Pulp and Paper Conference, 2013 Tomar. CAIMA, 18.

Koradiyaa, M., Patelb, B., Davec, S. & Duggiralab, S. 2016. Physico-chemical and enzymatic treatment for saccharification of wood chips. *Sixth International Symposium on Energy from Biomass and Waste.* Great School of St. John the Evangelist, Venice, Italy: CISA Publisher.

Li, J. 2016. Cellulose(dissolving pulp) manufacturing processes and properties-A review. *Bioresouces,* 11**,** 5553-5564.

Liu, H., Hu, H., Nairy, A., Jahan, M. S., Yang, G. & Ni, Y. 2013. Viscosity of Prehydrolysis Liquor of a Hardwood Kraft-Based Dissolving Pulp Production Process. *Ind. Eng. Chem. Res,* 52**,** 3974−3979.

Liu, Y., Shi, L., Cheng, D. & He, Z. 2016. Dissolving pulp market and technologies: Chinese propective- a mini review. *BioResources,* 11**,** 7902-7916.

Małachowska, E., Dubowik, M., Lipkiewicz, A., Przybysz, K. & Przybysz, P. 2020. Analysis of Cellulose Pulp Characteristics and Processing Parameters for Efficient Paper Production. *Sustainability,* 12**,** 12.

Miao, Q., Chen, L., Huang, L., Tian, C., Zheng, L. & Ni, Y. 2014. A process for enhancing the

accessibility and reactivity of hardwood kraft-based dissolving pulp for viscose rayon production by cellulase treatment. *Bioresource Technology* 154**,** 109–113.

Ocwelwang, A. R. 2017. *Laser and ultrasound radiation pretreatment of cellulose in dissolving wood pulp.* PhD, University of KwaZulu-Natal.

Othman, R. M. T. a. M. Z. 2015. Alkali Pretreatment and Enzymatic Hydrolysis of Australian Timber Mill Sawdust for Biofuel Production. *Journal of Renewable Energy,* 2015**,** 1-9.

Potgieter, M. S. 2018. *Improving dwp quality using brown stock fractionation.* Master of Engineering, Durban University of Technology.

Rodrigues, P. F., Evtyugin, D. D., Evtuguin, D. V. & Prates, A. 2018. Extractive Profiles in the Production of Sulfite Dissolving Pulp from Eucalyptus Globulus Wood. *Journal of Wood Chemistry and Technology,* 38**,** 397-408.

Sappi. 2019. *Sappi sustainability FAQs-Dissolving pulp* [Online]. South Africa: SAPPI Limited. Available: https://cdn-s3.sappi.com/s3fs-public/Sappi-FAQs-Dissolving-pulp-8.pdf [Accessed 8 December 2020 Document SCA-27].

Schwaiger, N. 2019. Developing wood based biorefineries. Europe: Sappi.

Sea 2020. Masterplan for the Commercial Forestry Sector in South Africa:2020 – 2025. South Africa: Strategy Execution Advisers (Pty) Ltd.

Shahzad, M. A. 2012. *Effect of temperature and time on acid sulfite cooking for dissolving pulp.* Master of science in engineering, Karlstad University.

Sithole, B. 2017. Opportunities and challenges for the forest sector in contributing to the South African Bioeconomy. Durban: University of Kwa-Zulu Natal and CSIR.

Stafford, W. H. L. & Lange, W. J. D. 2018. Wood-based Bio-refineries: Value adding to sawmill waste from the Forestry industry. CSIR.

Strunk, P. 2012. *Characterisation of cellulose pulps and the influence of their properties on the process and production of viscose and cellulose ethers.* PhD, Umea university.

Swst 2017. Structure of Wood. *Teaching Unit Number 1-Slide Set 2.* Society of Wood Science and Technology

Tradingeconomics. 2020. *South Africa GDP From Manufacturing | 1993-2019 Data | 2020-2022 Forecast | Historical* [Online]. Available: https://tradingeconomics.com/south-africa/gdp-from-manufacturing [Accessed 3 July 2020].

Wennerstrom, M. & Bylund, S. 2017. *Method for controlling viscosity in dissolving pulps*.

Yang, B., Wang, B., Wang, G., He, Z. & Ni, Y. 2018. Integrated Forest Biorefinery:Value-added Utilization of Dissolved Organics in the Prehydrolysis Liquor of Prehydrolysis Kraft (PHK) Dissolving Pulp Production Process. *Integrated Forest Biorefinery,* 3**,** 47-58.

Cellulose films cast from a novel choline chloride and ionic liquid mixed solvent system: Characterisation and comparison

H. Oosthuizen[1], E. du Toit[1], M. Atanasova, J. Wesley-Smith[2], S. Crous[1], M. Weldhagen[1] and Walter W Focke[1*]

[1] Institute of Applied Materials, Department of Chemical Engineering, University of Pretoria Private Bag X20, Hatfield 0028 South Africa

[2] Sefako Makgatho Health Sciences University, South Africa.

*Corresponding author: walter.focke@up.ac.za

ABSTRACT

The affordability of preparing cellulose films with 1-ethyl-3-methylimidazolium acetate ([EMIm][OAc]) was improved by using a mixture of 50 wt-% choline chloride and 50 wt-% [EMIm][OAc] as solvent. Overall, cellulose dissolved to a greater extend in neat [EMIm][OAc], leading to transparent films with a smooth surface morphology. For films prepared with the mixed solvent, a fused fibre morphology was observed at higher temperatures compared to discrete fibre morphology at lower dissolution temperatures. These films were less transparent, but experienced less shrinkage and warpage. X-ray diffraction analysis together with Fourier-transform infrared spectroscopy (FTIR) showed that films of the fused fibre morphology can be classified as all-cellulose composites (ACCs). FTIR spectra further confirmed that the novel mixed solvent may be classed as a non-derivatising cellulose solvent. ACCs with tensile strengths of up to 23.5 MPa were prepared, which is comparable with those of commercially used polyolefin films. At some dissolution conditions, films prepared with the neat and mixed solvent had similar thermal and tensile properties. The results subsequently confirm the potential of the more cost-effective mixed solvent system to prepare competitive cellulose films.

Keywords: cellulose solvents; ionic liquid; 1-ethyl-3-methylimadazolium acetate; choline chloride; all-cellulose composite

1 INTRODUCTION

Despite its potential as commercial bio-polymer, cellulose remains underutilized as an alternative raw material. A class of novel cellulose solvents, the ionic liquids (ILs), hold promise to increase utilization of this resource (Rabideau *et al.*, 2014; Meenatchi *et al.*, 2017). ILs offer a number of distinct advantages over traditional solvents, including low volatility and outstanding cellulose solvation-ability (Rabideau *et al.*, 2014; Meenatchi *et al.*, 2017). However, most common cellulose-dissolving ionic liquids are still prohibitively expensive. According to a techno-economic analysis performed by Klein-Marcuschamer *et al.* (2011), advances are needed to reduce IL cost and/or IL load needed for processing and to recover IL by recycling. Therefore, the aim of this work was to investigate the use of a more cost-effective solvent system for cellulose dissolution. Specifically, a 1:1 mixture by weight of the ionic

liquid [EMIm][OAc] and choline chloride was considered. Choline chloride is a substituted quaternary ammonium salt (Abbott *et al.*, 2004) commonly used as an animal feed supplement. Unlike ILs, choline chloride is relatively inexpensive. In the past, choline chloride has been used in combination with several substances, like carboxylic acids (Florindo *et al.*, 2014), to produce deep eutectic solvents (DES). Choline chloride-based DES do dissolve small amounts of cellulose (Ren *et al.*, 2016; Lynam *et al.*, 2017). The hypothesis of this study is that mixtures of choline chloride with other ILs like [EMIm][OAc] may provide more cost-effective solvent systems - without sacrificing efficacy and recycle-ability. For this purpose, films were prepared after dissolving α-cellulose in either neat [EMIm][OAc] or the 1:1 [EMIm][OAc]/choline chloride mixed solvent. Visual inspection, tensile strength testing, XRD and FTIR spectroscopy, SEM imaging as well as TGA analysis were used to compare characteristics of the resultant films.

2 EXPERIMENTAL PROCEDURE

2.1 Materials

α-Cellulose pulp, supplied by Sappi, was used as raw material. [EMIm][OAc] (>98%) was purchased from Proionic. Choline chloride (98 %) was supplied by Shaanxi Yuan Tai Biological Technology Co., Ltd.

2.2 Methods

2.2.1 Film preparation

Discs of α-cellulose hand-sheets were prepared for cellulose dissolution. Each 90 mm diameter sheet contained about 2 g dry α-cellulose. The dissolution temperature, solvent to cellulose ratio, and dissolution time for film preparation were varied according to the conditions summarised in Table 4. Experimental conditions were selected based on results from a preliminary investigating (Thirion, 2015) where 1-butyl-3-methylimidazolium chloride were used as cellulose solvent. In total 15 different combinations of these parameters were used to prepare films using both the neat and mixed solvent. For each set of conditions, between 3 and 5 films were prepared.

Table 4: Different values of tested independent variables during α cellulose dissolution.

Solvent to cellulose ratio (g/g)	Dissolution temperature (°C)	Dissolution time (min)
9	80	30
14	90	75
19	105	120

Dried α-cellulose sheets were placed on top of the required amount of solvent – spread over the bottom of a petri dish and left in a temperature-controlled oven for the required dissolution time. After dissolution, the cellulose films were allowed to regenerate for 120 min in a closed chamber fitted with

an air humidifier. The regenerated films were rinsed with room temperature deionised water to remove the solvent from the films. After rinsing, the films were clamped over short pieces of a PVC pipe and left to dry for at least 24 h under ambient conditions.

2.3 Analysis of cellulose films

2.3.1 Tensile testing

All films that retained their structural integrity after drying were tested. For comparison purposes, the tensile strength of the undissolved α-cellulose sheets was also recorded. Rectangular pieces of film (40 mm x 7 mm) were conditioned at 27 ±3 °C and a relative humidity of 52 ± 1 % for 24 h prior to testing. Humidity control was achieved by using a saturated magnesium nitrate solution in a tightly sealed container. The stress-strain curves of the specimens were determined at 25 °C using a tensile tester (EZ-L from Shimadzu). A 200 N load cell, and an extension rate of 5 mm/min with a clamp distance of 20 mm.

2.3.2 X-ray diffraction (XRD)

XRD spectra of ball-milled α-cellulose, undissolved α-cellulose sheet as well as all the prepared cellulose films were recorded on a Bruker D2 PHASER XRD Instrument with Cu Kα radiation (λ=1.54060). The system was equipped with a LYNXEYE_XE-T detector with up to 4.99° PSD opening. Film fragments were scanned from 5º to 50° 2θ at a rate of 0.02° 2θ steps per second.

2.3.3 Fourier transform-infrared spectroscopy (FTIR)

FTIR spectra of undissolved α-cellulose sheets, as well as all the cellulose films prepared from the respective solvent systems were recorded using a PerkinElmer Spectrum 100 spectrophotometer. All the spectra were recorded in the ATR mode in the 4000 – 550 cm^{-1} region with 32 scans at a resolution of 4 cm^{-1}.

2.3.4 Scanning electron microscope imaging

All samples were sputter coated with chromium for 1 min and viewed using a Zeiss Supra 55VP. Most samples were viewed at an acceleration voltage of 2 kV, with the secondary detector. Very smooth samples were viewed at 0.5 kV with the in-lens detector in order to prevent degradation at high magnifications.

2.3.5 Thermogravimetric analysis

Thermogravimetric analyses (TGA) were performed using either a Hitachi STA7300 TGA-DTA or a TA Instruments SDT Q600. Approximately 18 mg of each sample was placed in an alumina pan and analysed in a N_2 atmosphere (flow rate of 100 ml·min^{-1}). Samples were heated from room temperature to 950 °C at a heating rate of 10 K·min^{-1}. The thermal degradation onset temperatures of the respective films were determined using the tangent line technique on the TG curve according to the standard ISO

11358-1 (International Organization for Standardization 2014).

3 RESULTS AND DISCUSSION

All films were ductile and could easily be bent without breaking. In general, films prepared with the neat IL solvent were more transparent as illustrated in Figure 1, where images of both film types prepared from similar dissolution conditions are shown.

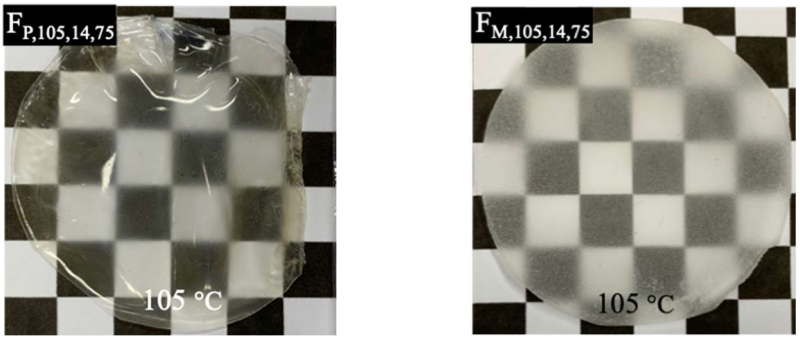

(a) (b)

Figure 6: Samples (a) FP,105,14,75 and (b) FM,105,14,75 showing the higher transparency of films prepared with the neat [EMIm][OAc]. Samples are named according to convention: FS,T,R,t were S is the solvent used, T the dissolution temperature, R the solvent to cellulose ratio and t the dissolution time.

SEM images of films prepared using the mixed solvent, indicated that a fused fibre and discrete fibre surface morphology were prevalent for these film types. At a dissolution temperature of 80 °C a discrete fibre surface morphology – characterised by individual fibres – was observed. An increase in the dissolution temperature to 90 °C and 105 °C led to the fused fibre morphology, where fibres are held together by a matrix, as illustrated in Figure 7. The presence of undissolved fibres in a matrix of dissolved and regenerate cellulose suggests that these films can be classified as all-cellulose composites (ACCs).

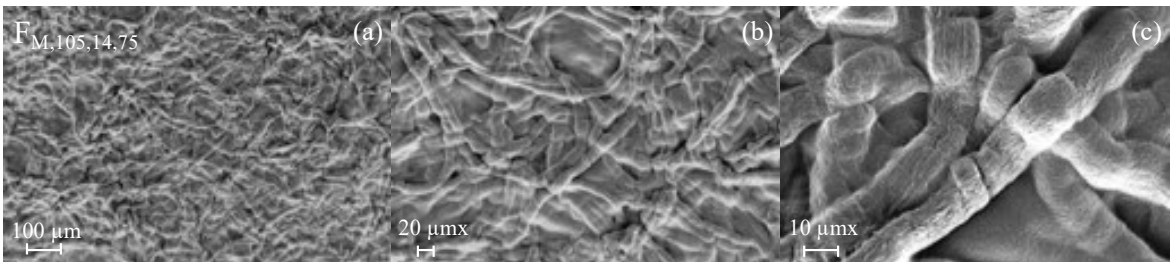

Figure 7: SEM images in order of increasing magnification from left to right of regenerated cellulose film FM,105,14,75 prepared using the mixed solvent system.

A smooth surface morphology – as shown in Figure 8 – was generally observed for films prepared from the neat IL solvent. The absence of fibrous structures suggests complete cellulose dissolution. The small globular structures visible at very high magnification in Figure 8 (c) resemble the morphology of

amorphous cellulose particles as observed by Ioelovich (2013).

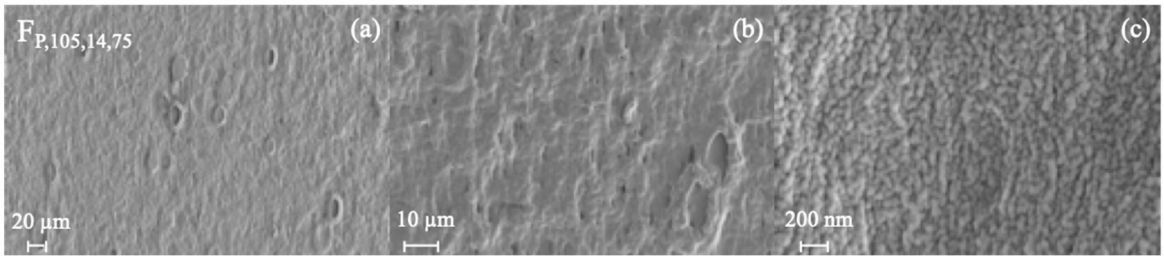

Figure 8: SEM images in order of increasing magnification from left to right of regenerated cellulose film $F_{P,105,14,75}$ prepared from neat [EMIm][OAc] solvent.

It was noticeable that films prepared from the mixed solvent experienced less warpage after drying when compared to those prepared using neat [EMIm][OAc]. These films also experienced less shrinkage during the regeneration and rinsing processes. The average diameter of film sheets prepared from the neat [EMIm][OAc] solvent was 7.2 cm compared to an average diameter of 8.8 cm calculated for the films prepared from the mixed solvent.

Results from XRD and FTIR spectra were used to confirm the conclusions drawn from the visual observations and SEM images. Figure 9 (a), (c) and (e) shows the XRD spectra of films prepared with neat [EMIm][OAc]. These films are highly amorphous. For most films, only a single broad reflection at 21.1° – 21.7° can be seen.

For films $F_{P,105,19,30}$; $F_{P,90,14,75}$; $F_{P,90,14,30}$; $F_{P,90,9,75}$; $F_{P,80,14,75}$; $F_{P,80,9,120}$; and $F_{P,80,9,30}$ this reflection was appeared broader and less intense – possibly due to convolution of the two primary cellulose II reflections and the amorphous reflection, which exist at almost the same position. The presence of cellulose II in these samples, is confirmed by its characteristic secondary reflection at 12.5° – 13.0°. With neat [EMIm][OAc], dissolved cellulose was therefore present as cellulose II and/or amorphous cellulose. For films $F_{P,80,14,75}$; $F_{P,80,9,120}$ and $F_{P,80,9,30}$ remnants of the cellulose I doublet were visible. As the primary reflection would be part of the broad reflection, this was taken as evidence that a small amount of cellulose I was still present in these films.

The crystallinity of the films prepared with the mixed solvent – spectra given in Figure 9 (b), (d) and (f) – was higher than those prepared with neat [EMIm][OAc]. In fact, their spectra still resemble that of cellulose I. The doublet at approximately 14.8° and 16.8° was still observable for these samples, however the two reflections were less distinct from each other and broader than in the case of undissolved α-cellulose sheets. The primary reflection of cellulose I, present at 22.6° in neat cellulose I and the α-cellulose sheets, shifted for the cellulose regenerated from the [EMIm][OAc]/choline chloride mixture to between 22.3° – 23.6°. At 105 °C the shift to the left is more pronounced, while the reflection at 2θ = 34.5° disappeared. This disappearance suggests longitudinal disorder (Duchemin *et*

al., 2007). The broad shape of the reflection, together with the shift and the disappearance of reflection (0 0 4) at 34.5° in films prepared at 105 °C could be explained by the presence of the paracrystalline form of cellulose as described by Duchemin *et al.* (2007). Films prepared at 80 °C and 90 °C are mainly composed of cellulose I with some amorphous cellulose also being present.

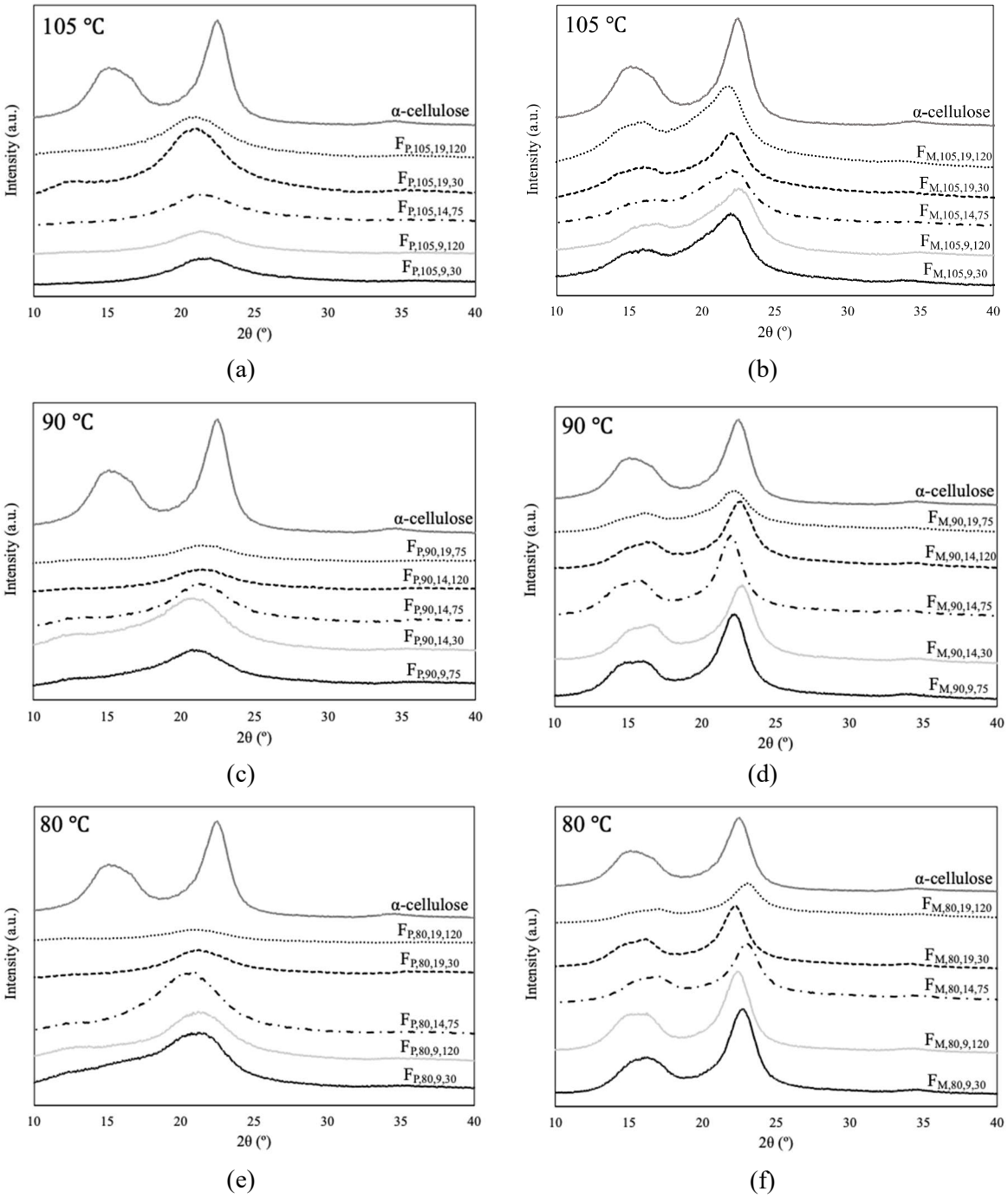

Figure 9: XRD spectra of regenerate cellulose films prepared at 105 °C with (a) neat [EMIm][OAc] and (b) a mixture of [EMIm][OAc] and choline chloride; films prepared at 90 °C with (c) neat [EMIm][OAc] and (d) the mixed solvent; and films prepared at 80 °C with (e) neat [EMIm][OAc] and (f) a mixture of [EMIm][OAc] and choline chloride.

Considering the high degree of residual, undissolved cellulose fibres in these films (resulting in the fused or discrete fibre morphology), this is an expected result. The presence of native cellulose in these films confirms that these samples can be classified as ACCs.

The FTIR spectra of the raw materials – undissolved α-cellulose, [EMIm][OAc] and choline chloride – and all the regenerated cellulose films prepared at a solvent ratio of 14 g/g are shown in Figure 10. Similar spectra were obtained for films prepared with solvent ratios of 9 g/g and 19 g/g

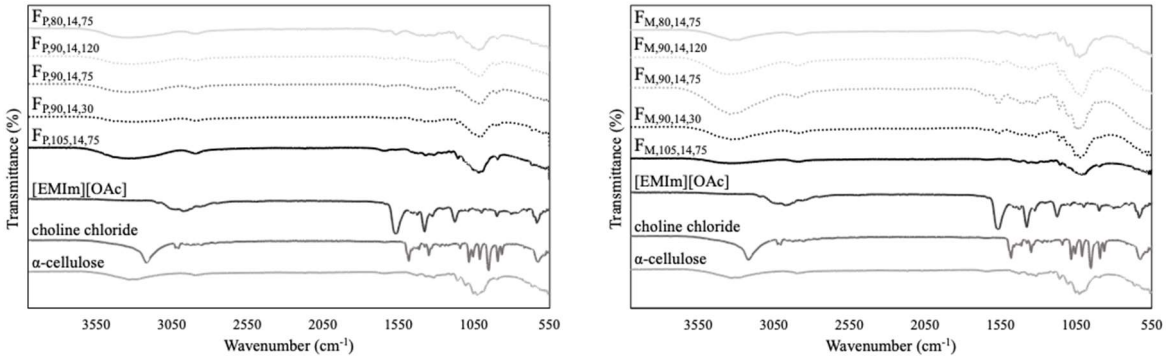

(a) (b)

Figure 10: FTIR transmittance spectra for samples prepared with 14 g solvent/g α-cellulose with (a) neat [EMIm][OAc] and (b) a mixture of [EMIm][OAc] and choline chloride.

All the major functional groups of cellulose can be observed in the spectra. The common bands at 3330 cm^{-1} (OH stretching vibration), 2880 cm^{-1} (CH_2 stretching vibration), as well as bands at 1420 cm^{-1}, 1369 cm^{-1}, 1317 $cm^{-1}$and 895 cm^{-1} were present (Pang *et al.*, 2014; Liu *et al.*, 2015; Reddy *et al.*, 2017). The 895 cm^{-1} band is associated with β-glucoside linkages between the sugar units and is more pronounced in amorphous cellulose and cellulose II (Pang *et al.*, 2014; Reddy *et al.*, 2017). In the case of the undissolved α-cellulose sheets, this band can therefore be attributed to a small fraction of amorphous material already present. The peak at ~1640 cm^{-1}, associated with absorbed water present in the amorphous phase (Pang *et al.*, 2014; Liu *et al.*, 2015), was also observed in all the samples. This peak increased in sharpness in the regenerated samples, especially those prepared with the mixed solvent. Another general observation was the broadening of the band located between 3000 cm^{-1} and 3600 cm^{-1} after dissolution and regeneration. This indicates the breaking of hydrogen bonds between hydroxyl groups upon dissolution (Raut *et al.*, 2015).

When considering the spectra of films prepared with neat [EMIm][OAc] as shown in Figure 10 (a), the sharpness of the 895 cm^{-1} band increased, while the band at 1430 cm^{-1} was weakened. As the band at 1430 cm^{-1} is usually more pronounced in cellulose I (Liu *et al.*, 2015; Reddy *et al.*, 2017), the reduced band intensity confirms cellulose dissolution. A new band appeared at 994 cm^{-1} and is assigned to C–O stretching vibrations in the amorphous region. It suggests crystal transformation of cellulose I to

cellulose II and amorphous cellulose had occurred. For films prepared with the mixed solvent (Figure 10 (b)) the band at 994 cm^{-1} was less intense when compared to films prepared with neat [EMIm][OAc], while the intensity of the band at 895 cm^{-1} was similar to that of the undissolved cellulose sheet. Furthermore, the band at 1430 cm^{-1} was still present. This suggests that these films were comprised of cellulose I with some amorphous cellulose, consistent with the conclusions drawn from the XRD data. Additional bands at 1562 cm^{-1} and 1350 cm^{-1} are associated with the presence of residual [EMIm][OAc] and choline chloride respectively, suggesting the need for an additional rinsing step. The general similarity between the spectra of the regenerated films and the α-cellulose sheets confirms that [EMIm][OAc] and choline chloride act as inert, non-derivatizing solvents for cellulose.

The presence of a small amount of residual solvent is supported by the recovery data of the solvents.

Regardless of cellulose dissolution conditions, an average of 90.6 wt-% ± 4.8 wt-% and 87.9 wt-% ± 3.5 wt-% of the [EMIm][OAc] and mixed solvent respectively could be recovered for potential re-use.

The mean thermal degradation onset temperature for the α-cellulose sheets was 335 °C. Lower onset temperatures were recorded for all the regenerated films. The average onset temperature for thermal degradation was 243 °C ± 5.6 °C and 210 °C ± 3.3 °C for the films prepared from the neat and mixed solvent respectively. Trends, due to variations in the dissolution temperature, solvent ratio or dissolution time, were not discernible. The lower onset temperature of thermal degradation of regenerated films was consistent with literature values (Liu *et al.*, D, 2012; Liu *et al.*, 2015; Lethesh *et al.*, 2016; Reddy *et al.*, 2017; Lethesh *et al.*, 2020). This confirms that the crystallinity of the regenerated films was reduced through dissolution and regeneration.

Stress strain curves illustrate the ductile nature of the films: Stress initially increases rapidly at small strains and then more slowly beyond a yield point. The average ultimate tensile strength of the α-cellulose hand sheets was 3.85 ± 0.5 MPa. The highest ultimate tensile strength values were 34 ± 12 MPa and 24 ± 6 MPa for films prepared from the neat and mixed solvent system respectively. The best preforming film was prepared with the mixed solvent system and it featured a fused fibre morphology. This compares with the best performing film prepared with neat [EMIm][OAc] which had a smooth morphology. These values are similar to those for films prepared by Duchemin, Newman, and Staiger (2009) from micro-crystalline cellulose (MCC) dissolved in Li/DMAc. The tensile strengths in the range of 20–40 MPa, are also comparable with commercially used polyolefin films, such as polyethylene (PE) and polypropylene (PP)(Pang *et al.*, 2014; Reddy *et al.*, 2017). These results show the potential of the proposed mixed solvent system for cost-effective preparation of environmentally friendly, biodegradable cellulose films that may find application in for packaging purposes.

4 CONCLUSIONS

Ductile cellulose films with plastic mechanical behaviour were successfully prepared following dissolution of α-cellulose hand sheets in either neat [EMIm][OAc] or a mixed solvent of 50 wt-% choline chloride and 50 wt-% [EMIm][OAc]. SEM images revealed three main film morphologies: smooth -, fused fibre - and discrete fibre morphology. Smooth film morphology was prevalent in films prepared from the neat solvent. With the mixed solvent, a fused fibre morphology was obtained at higher dissolution temperatures, while a discrete fibre morphology resulted at lower dissolution temperatures. The former film produced featured the highest average tensile strength (24 MPa). This value is comparable to that of films prepared from the neat solvent under the same process conditions. However, preparation conditions from the neat solvent still resulted in stronger films, with a maximum tensile strength value of 34 MPa recorded. Here a smooth film morphology was observed. FTIR spectra confirmed that both solvent types may be classed as non-derivatising cellulose solvents. Despite the lower tensile strength values of the films prepared from the mixed solvent, the results suggest that optimisation of dissolution conditions may produce films with comparable properties to traditional packaging material.

ACKNOWLEDGEMENTS

Financial support from PAMSA and the Department of Science and Innovation, under Grant DST/CON 0004/2019 is gratefully acknowledged. The authors also thank Sappi for the supplying of α-cellulose pulp samples as well as equipment to prepare hand sheets.

REFERENCES

Abbott, A. P. *et al.* (2004) 'Deep Eutectic Solvents Formed between Choline Chloride and Carboxylic Acids: Versatile Alternatives to Ionic Liquids', *Journal of the American Chemical Society*, 126(29), pp. 9142–9147. doi: 10.1021/ja048266j.

Duchemin, B. J.-C. Z., Newman, R. H. and Staiger, M. P. (2007) 'Phase transformations in microcrystalline cellulose due to partial dissolution', *Cellulose TA - TT* -, 14(4), pp. 311–320. doi: 10.1007/s10570-007-9121-4 LK - https://UnivofPretoria.on.worldcat.org/oclc/5659262984.

Duchemin, B. J. C., Newman, R. H. and Staiger, M. P. (2009) 'Structure–property relationship of all-cellulose composites', *Composites Science and Technology*, 69(7), pp. 1225–1230. doi: https://doi.org/10.1016/j.compscitech.2009.02.027.

Florindo, C. *et al.* (2014) 'Insights into the Synthesis and Properties of Deep Eutectic Solvents Based on Cholinium Chloride and Carboxylic Acids', *ACS Sustainable Chemistry & Engineering*, 2(10), pp. 2416–2425. doi: 10.1021/sc500439w.

Ioelovich, M. (2013) 'Nanoparticles of Amorphous Cellulose and Their Properties', *Journal of Nanoscience and Nanotechnology*, 1, pp. 41–45. doi: 10.11648/j.nano.20130101.18.

Klein-Marcuschamer, D., Simmons, B. A. and Blanch, H. W. (2011) 'Techno-economic analysis of a lignocellulosic ethanol biorefinery with ionic liquid pre-treatment', *Biofuels, Bioproducts and Biorefining*, 5(5), pp. 562–569. doi: 10.1002/bbb.303.

Lethesh, K. C. *et al.* (2016) 'Synthesis and Characterization of Nitrile-functionalized Azepanium Ionic Liquids for the Dissolution of Cellulose', *Procedia Engineering*, 148, pp. 385–391. doi: https://doi.org/10.1016/j.proeng.2016.06.494.

Lethesh, K. C. *et al.* (2020) 'Highly efficient cellulose dissolution by alkaline ionic liquids', *Carbohydrate Polymers*, 229, p. 115594. doi: https://doi.org/10.1016/j.carbpol.2019.115594.

Liu, D. *et al.* (2012) 'Investigations about dissolution of cellulose in the 1-allyl-3-alkylimidazolium chloride ionic liquids', *Carbohydrate Polymers*, 87(2), pp. 1058–1064. doi: https://doi.org/10.1016/j.carbpol.2011.08.026.

Liu, Z. *et al.* (2015) 'Preparation and characterization of regenerated cellulose from ionic liquid using different methods', *Carbohydrate Polymers*, 117, pp. 99–105. doi: https://doi.org/10.1016/j.carbpol.2014.09.053.

Lynam, J. G., Kumar, N. and Wong, M. J. (2017) 'Deep eutectic solvents' ability to solubilize lignin, cellulose, and hemicellulose; thermal stability; and density', *Bioresource Technology*, 238, pp. 684–689. doi: https://doi.org/10.1016/j.biortech.2017.04.079.

Meenatchi, B., Renuga, V. and Manikandan, A. (2017) 'Cellulose dissolution and regeneration using various imidazolium based protic ionic liquids', *Journal of Molecular Liquids*, 238, pp. 582–588. doi: https://doi.org/10.1016/j.molliq.2016.05.008.

Pang, J.-H. *et al.* (2014) 'Fabrication and Characterization of Regenerated Cellulose Films Using Different Ionic Liquids', *Journal of Spectroscopy*. doi: 10.1155/2014/214057 LK - https://UnivofPretoria.on.worldcat.org/oclc/8539311304.

Rabideau, B. D., Agarwal, A. and Ismail, A. E. (2014) 'The Role of the Cation in the Solvation of Cellulose by Imidazolium-Based Ionic Liquids', *The Journal of Physical Chemistry B*, 118(6), pp. 1621–1629. doi: 10.1021/jp4115755.

Raut, D. G. *et al.* (2015) 'A morpholinium ionic liquid for cellulose dissolution', *Carbohydrate Polymers*, 130, pp. 18–25. doi: https://doi.org/10.1016/j.carbpol.2015.04.032.

Reddy, K. O. *et al.* (2017) 'Preparation and characterization of regenerated cellulose films using borassus fruit fibers and an ionic liquid', *Carbohydrate Polymers*, 160, pp. 203–211. doi: https://doi.org/10.1016/j.carbpol.2016.12.051.

Ren, H. *et al.* (2016) 'The Properties of Choline Chloride-based Deep Eutectic Solvents and their Performance in the Dissolution of Cellulose', *BioResources; Vol 11, No 2 (2016)*. Available at: http://ojs.cnr.ncsu.edu/index.php/BioRes/article/view/BioRes_11_2_5435_Ren_Properties_Choline_Chloride_Eutectic_Solvents.

Thirion, C. (2015) *All-Cellulose Composites Production using Ionic Liquids: Dissolution of Wood Derived High Purity Cellulose with BMimCl.* University of Pretoria. Available at: https://repository.up.ac.za/handle/2263/56113.

COD and turbidity removal from restaurant wastewater using polyethersulfone ultrafiltration membrane containing sawdust-derived cellulose nanocrystals

A. Adeniyi[1*], G.O. Odo[1], D. Gonzalez-Ortiz[2], C. Pochat- Bohatier[2] and M. Onyango[1]

[1] Department of Chemical, Metallurgical and Materials Engineering, Tshwane University of Technology, Pretoria 0001, South Africa

[2] Institut Européen des membranes, IEM UMR-5635, Université de Montpellier, ENSCM, CNRS Place Eugène Bataillon 34095 Montpellier cedex 5, France

*Corresponding author email: adeniyia@tut.ac.za

ABSTRACT

An increase in the number of restaurants in major cities is putting more pressure on the municipality's supplies of water. Moreover, the wastewater generated can be treated at the source to protect the environment and for reuse purposes. In this work, an ultrafiltration (UF) membrane was fabricated for the treatment of restaurant wastewater. The membrane was fabricated using the phase inversion technique with polyethersulfone (PES) as the base polymer, 1-N-methyl-2 pyrrolidone (NMP) as the solvent, and cellulose nanocrystals (CNC) as additive. The membranes were characterized using SEM, EDX, FTIR, and contact angle measurement. The SEM images were analysed for surface characteristics using WSxM 5.0 Develop 9.1 software. The membrane performance was tested for water flux, turbidity, and Chemical Oxygen Demand (COD) removal in a test cell using both synthetic and raw restaurant water. Average water flux, turbidity, and COD removal were higher with a PES membrane containing 0.075% CNC. This was because of lower contact angle, lower pore size distribution but higher pore size. The formation of agglomerates was not observed in the membrane as seen in the PES membrane with CNC concentrations higher than 0.075%. The PES-CNC0.075 membrane shows a great prospect in the treatment of restaurant wastewater.

Keywords: Cellulose nanocrystals, ultrafiltration, restaurant wastewater, membrane, phase inversion

1 INTRODUCTION

Water usage is increasing worldwide because of the increase in population, industrial and agricultural activities (Borowski, 2020). One of the major contributors to the volume of water usage is the restaurants. Water usage in a medium-sized restaurant, with 25 employees, 60 seats, and 250 meals/day, is estimated at 95,000 L per day (Flusberg, 2016). In South Africa, Western Cape has the highest number of documented restaurants with 2656, while Limpopo has the lowest, with an average of 74 restaurants (dining-out, 2021). The number of restaurants is still growing. An increase in the number of restaurants in major cities is putting more pressure on the municipality's supplies of water. The wastewater generated is sent into the centralized wastewater treatment plant (Peter-Varbanets et al., 2009). However, a decentralized system, whereby the wastewater is treated at the source may be an option to

recover the water for immediate reuse.

Restaurant wastewater is contaminated loaded with food, soup particles, and other organic matter like oil and grease (Yau et al., 2018, Yao, 2020). Some of these contaminants are measured by the turbidity and COD of the wastewater. COD is a good indicator of organic contaminants in wastewater (Yang et al., 2016). Various technology options exist for the removal of turbidity and COD, but the membrane process offers a more compact, small footprint technique that can be applied at the restaurant (Bhojwani et al., 2019). Specifically, ultrafiltration (UF) offers a suitable treatment at low pressures (Abdessemed et al., 1999). The performance of the UF membrane can also be improved by adding suitable nanomaterials (Nasrollahi et al., 2019, Garcia-Ivars et al., 2014). One of the nanomaterials of current interest is the cellulose nanocrystals (CNC) (Reid et al., 2017, Tang et al., 2017). This is because of its properties, but more importantly, it can be obtained from sawdust, a wood waste that is in abundance (Thompson et al., 2019). The purpose of this work is to fabricate ultrafiltration (UF) membrane with CNC as an additive for the removal of turbidity and COD from restaurant wastewater in order to establish the potential of a low-pressure membrane system for immediate treatment of the water for reuse.

2 LITERATURE

Some work has been published that involved treatment of restaurant and other related wastewater. Khan et al. (2011) investigated the treatment of kitchen wastewater using aerobic treatment. They reported 87% removal of COD and a 73% reduction in turbidity after 45 days of treatment. The limitation of this method is the number of days required to achieve a suitable treatment level. Zulaikha et al. (2014) investigated the treatment of raw restaurant wastewater using commercial UF and nanofiltration (NF) membranes. They reported 97.8% and 99.9% removal of COD and turbidity respectively, irrespective of the membrane. This was significantly higher than the quality achieved by aerobic treatment after 45 days. However, the water flux was only 38% for the UF membrane. In India, restaurant wastewater is treated using chemical dosage, settling tanks, followed by a multimedia filter, and activated carbon filter before final discharge into the environment (Singh et al., 2014). This is a more complex setup than a membrane system, generates sludge, and requires the use of chemicals. Marchese et al. (2000) reported 90.1% removal of COD with a permeate flux of 20 $L.h^{-1}.m^{-2}$ at 400 kPa and 35 °C when Emulsified Oil Wastewater was treated with ultrafiltration membrane in a cross filtration set up. The membrane process with ultrafiltration shows great potential for effective removal of COD and turbidity from restaurant wastewater, however, it is important to have high contaminants removal with high flux in order to facilitate reuse after treatment. Lessan et al. (2020) investigated the effect of cellulose nanocrystals (CNC) as a hydrophilic nanoparticle on the characteristics of polyethersulfone (PES) based membranes. They reported 1.5 wt% of CNC concentration increased the water permeability of the membrane while retaining the same dye rejection and fouling resistance as

the membrane without CNC. This study shows the potential of UF membrane with CNC to remove contaminants while improving water flux. However, the application of UF membrane with CNC for the treatment of restaurant wastewaters has not been reported.

3 EXPERIMENTAL PROCEDURE

Polyethersulfone (PES) was obtained from Solvay while the non-woven support was obtained from Kavon Filters. 1-N-methyl-2 pyrrolidone (NMP) (>99%) was obtained from Sigma Aldrich. Commercial Cellulose Nanocrystals (CNC) powder was obtained from CelluForce, Canada. Restaurant wastewater was obtained from a city restaurant in South Africa. Synthetic turbid water was prepared with deionized water and zeolite.

The membrane was fabricated using the phase inversion technique. The separation of an initially homogeneous mixture into two separate phases, each containing a polymer, a solvent, and additional additives, is known as phase inversion (Lalia et al., 2013). The solid phase which is the polymer-rich phase, will give rise to the membrane matrix, where the solvent rich liquid phase also known as polymer-lean phase, will originate from the membrane pores. There are four techniques distinguished based on the mechanism exploited to induce such separation, often called defining or precipitation. These four techniques are evaporation-indiced PS (EIPS), vapor-indiced PS (VIPS), temperature indiced PS (TIPS), and nonsolvent-induced (or diffusion-induced) PS (NIPS or DIPS). In DIPS, precipitation of the casting solution is obtained by immersion into a non-solvent bath. DIPS is the technique used in this work. A polymer solution was prepared with polyethersulfone (PES) (18 wt %) in 1-N-methyl-2 pyrrolidone (NMP) as solvent. The PES was dried in an oven for 24 hours before use in order to eliminate any water that may be present. The solution was stirred using a magnetic stirrer for 24 hours before use. The polymer solution was then used to cast the membrane on non-woven support using an automatic casting machine. The non-woven was fixed on a glass plate using cello tape. The thickness was set at 250µm using the micrometer gauge on the casing knife. The polymer was then immersed into a bowl of water at room temperature. The procedure was repeated for polymer solutions containing cellulose nanocrystals (CNC) as an additive at 0.05%, 0.075%, 0.1%, and 0.15%.

The membranes were characterized using a contact angle analyser, Scanning electron microscopy (SEM), Fourier transform infrared (FTIR), and Energy dispersive X-Ray spectroscopy (EDX). The procedure is well documented in the literature (Adeniyi et al., 2020). The SEM images were analysed for roughness, pore size distribution, and morphology using WSxM 5.0 Develop 9.1 Software (Horcas et al., 2007).

Separation performance was conducted in a dead-end filtration cell. The active membrane area in the cell was 14.6 cm^2. The membranes were tested for pure water flux and for turbidity removal with synthetic turbid water. The pressure was varied from 0.2 bar to 1.0 bar while the initial turbidity was

varied from 80NTU to 140NTU. The membranes were also used for the treatment of raw restaurant waster. COD was analysed using a spectrophotometer while turbidity was analysed with a turbidity meter. The test and analysis were done in triplicates.

The water flux was calculated using equation 1, while the removal of Turbidity and COD were calculated using equation 2.

$$J_w = \frac{V}{At} \qquad \textbf{Equation 1}$$

Where J_w (L/m^2/h) and V (L) are the water flux and the permeate volume respectively. The active membrane area A is measured in m^2 while the filtration time t is in h.

$$R = \frac{(C_f - C_p)}{C_f} * 100 \qquad \textbf{Equation 2}$$

where R is the rejection in %, C_f is the initial turbidity or COD in the feed and C_p is the final turbidity or COD in the permeate.

4 RESULTS AND DISCUSSION

4.1 Effects of CNC on PES-UF membrane characteristics

Five membranes were prepared and compared in terms of their characteristics in order to determine the effect of CNC concentration on the membrane properties and performances. Figure 1 shows the FTIR spectra of the five membranes tested, where the membrane with pure PES without CNC is labelled PES, the other membranes with PES and CNC are labelled CNC with the percentage of CNC as the differentiating factor. For example, CNC0.05 means that 0.05wt% of CNC was added to the polymer solution. The normal peaks for membranes fabricated from polymer solutions containing PES were observed in all the membranes. This means that the membranes were properly formed. The peak for C-O bond stretching was observed at 1109 cm^{-1}, the peak for aromatic ether stretching was observed at 1242 cm^{-1}, the peak for C-C bond stretching was observed at 1487 cm^{-1} while the 1581 cm^{-1} peak indicates the presence of benzene ring stretching. Figure 2 shows typical FTIR spectra for CNC (Aguayo et al., 2018). However, none of the membranes with CNC showed any peak which could be attributed to the presence of CNC. This may be due to the low concentration of the CNC in the membranes indicating that the functional groups were not changed at low CNC concentration. All the membranes show a strong presence of sulfones and secondary amine as indicated by the peaks ranging from 1120 cm^{-1} to 1600cm^{-1}.

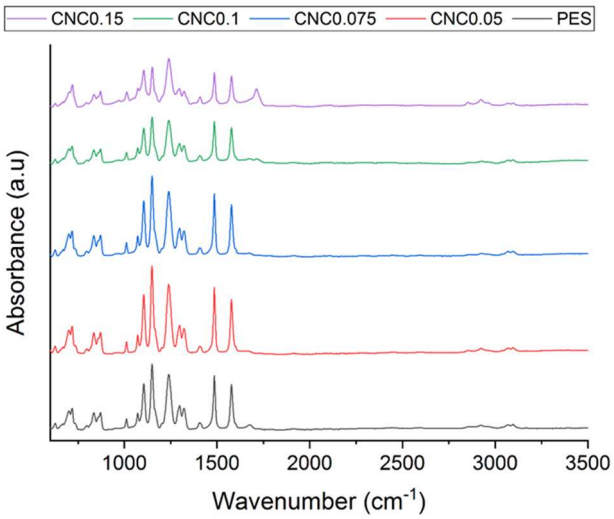

Figure 1: FTIR spectra of the five membranes

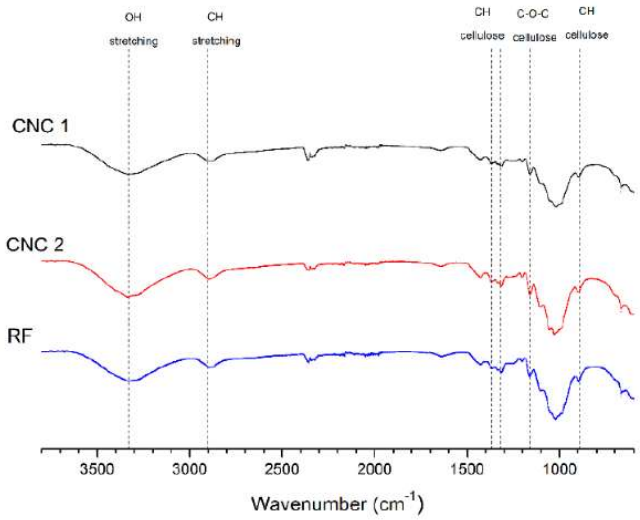

Figure 2: A typical FTIR spectra for cellulose nanocrystals (Aguayo et al., 2018)

The EDS results did indicate the presence of CNC in the membrane material. The results showed a gradual increase in the mass concentration of the oxygen as the percentage of CNC increased: PES (20.13% Oxygen), CNC0.05 (20.42% Oxygen), CNC0.075 (20.92% Oxygen), CNC0.1 (23.36% Oxygen), and CNC0.15 (26.95% Oxygen). This is evidence of the CNC in the membranes. For atomic composition, PES (17.15% Oxygen), CNC0.05 (17.35% Oxygen), CNC0.075 (17.78% Oxygen), CNC0.1 (20.18% Oxygen), and CNC0.15 (22.30% Oxygen). These values were obtained using EDX analysis. The values are important to determine whether there is a change in the elemental and atomic compositions of the membrane because of the addition of CNC. The increase in oxygen content may be from the OH group bonded to the CNC (Adeniyi et al., 2020). This was expected to have a direct impact on the contact angle of the membranes that was measured with Goniometer (Digidrop-GBX) using pendant drop method; however, a deviation was observed as shown in Figure 3 where CNC0.075

had the lowest contact angle (69º), and was the only CNC membrane with a lower contact angle than the PES membrane (71.4º). The lower the contact angle, the higher the hydrophilicity of the membrane (Hebbar et al., 2017). This is means that the CNC0.075 is more hydrophilic than the other membranes.

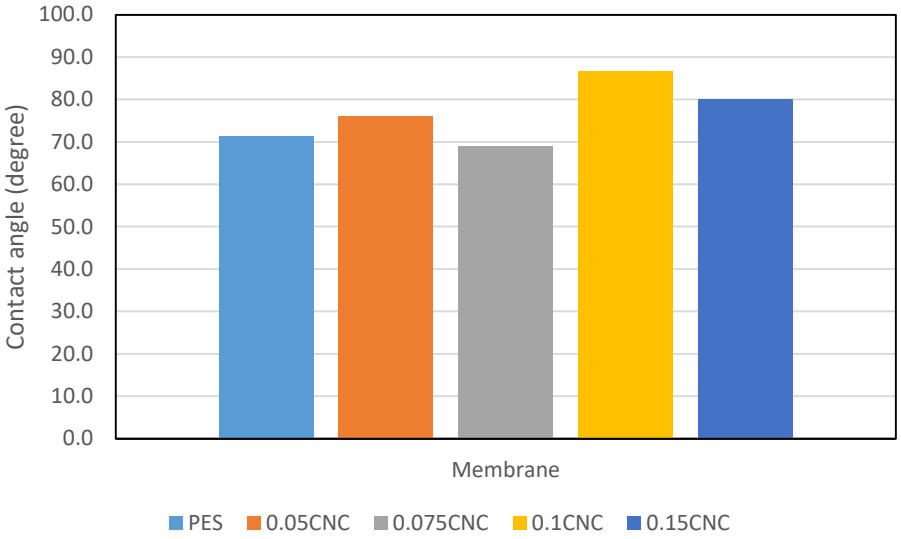

Figure 3: Contact angles of the membranes

SEM images of the membranes are shown in Figure 4 revealing the effect of CNC on the morphology of the PES UF membrane. The observed surface may explain why the CNC0.075 has the highest hydrophilicity. It seems that the polymer forms a perfect blend at a concentration of 0.075% CNC leading to a uniform dispersion of CNC in the polymer. While 0.05% CNC was too low to have a significant effect on the PES-UF membrane, concentrations higher than 0.075% were not homogenous, leading to the formation of agglomerates.

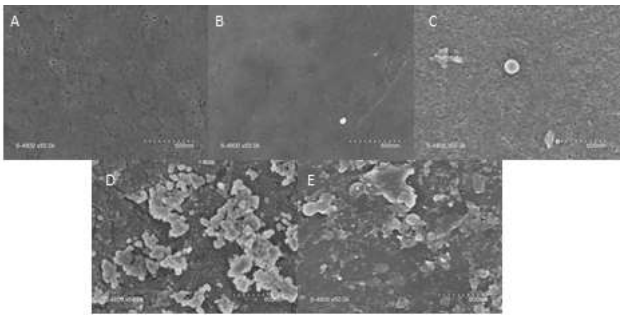

Figure 4: SEM images at 600nm of PES (A), CNC0.05 (B), CNC0.075 (C), CNC0.1 (D) and CNC0.15 (E)

The SEM images were analysed using WSxM 5.0 Develop 9.1 software for pore size distribution, roughness, and pore structure. The mechanism for separation in ultrafiltration is primarily steric exclusion. This means that the pore structure, surface morphology, and roughness will have a large impact on the membrane performance. The 3D images are shown in Figure 5 showing the effect of the addition of CNC into the polymer solution on the membrane morphology. There was no significant

change when 0.05% CNC was added. However, the addition of 0.075% CNC brought a change to the morphology of the membrane. The formation of agglomerates is clearly shown in the membrane with 0.1% and 0.15% CNC. The effect on the surface roughness and pore size distribution are shown in Figures 6 and 7 respectively. Root mean square roughness (RMS) for PES was 0.53nm, and 0.52nm, 0.82nm, 1.60nm, 1.32nm for CNC0.05, CNC0.075, CNC0.1, and CNC0.15 respectively. The surface roughness increased with the addition of CNC. The degree of formation of agglomerates was higher for CNC0.1 and this is clearly reflected in the roughness of the membrane as the membrane with the highest roughness.

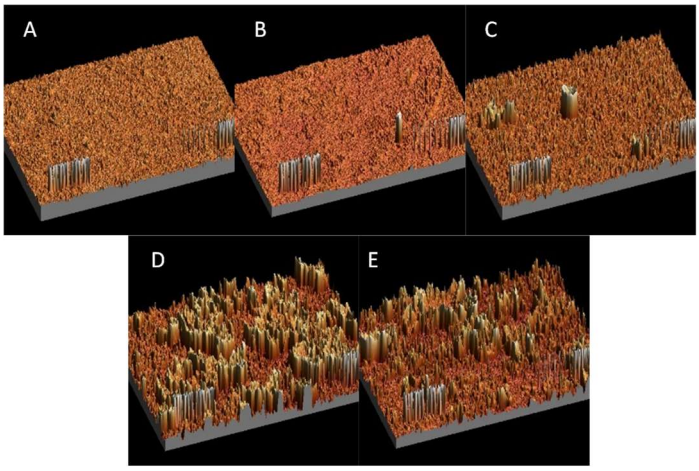

Figure 5: 3D pictures of the SEM images at 600nm of PES (A), CNC0.05 (B), CNC0.075 (C), CNC0.1 (D) and CNC0.15 (E)

The pore size distribution of the membranes for a scan area of 1µm by 1µm is shown in Figure 7. The figure shows that the pore size distribution is higher for PES than for other membranes, which means it has more pores of different sizes. The pore size distribution was greatly reduced by the presence of CNC in CNC0.05, however, this did not result in improvement of the hydrophilicity. CNC0.075 has the lowest size distribution and hence the lowest number of pores, however, the addition of CNC resulted in an increase in hydrophilicity. Also, most of the pores of CNC0.075 are over 4nm in diameter. Both CNC0.1 and CNC0.15 have a pore size distribution between that of PES and CNC0.05. The pores of CNC0.1 and CNC0.15 might have been affected by the agglomeration of CNC on the surfaces. This may mean that the optimum concentration of CNC in the dope solution is 0.075%. The membrane has the highest hydrophilicity, lowest pore size distribution, and increased roughness.

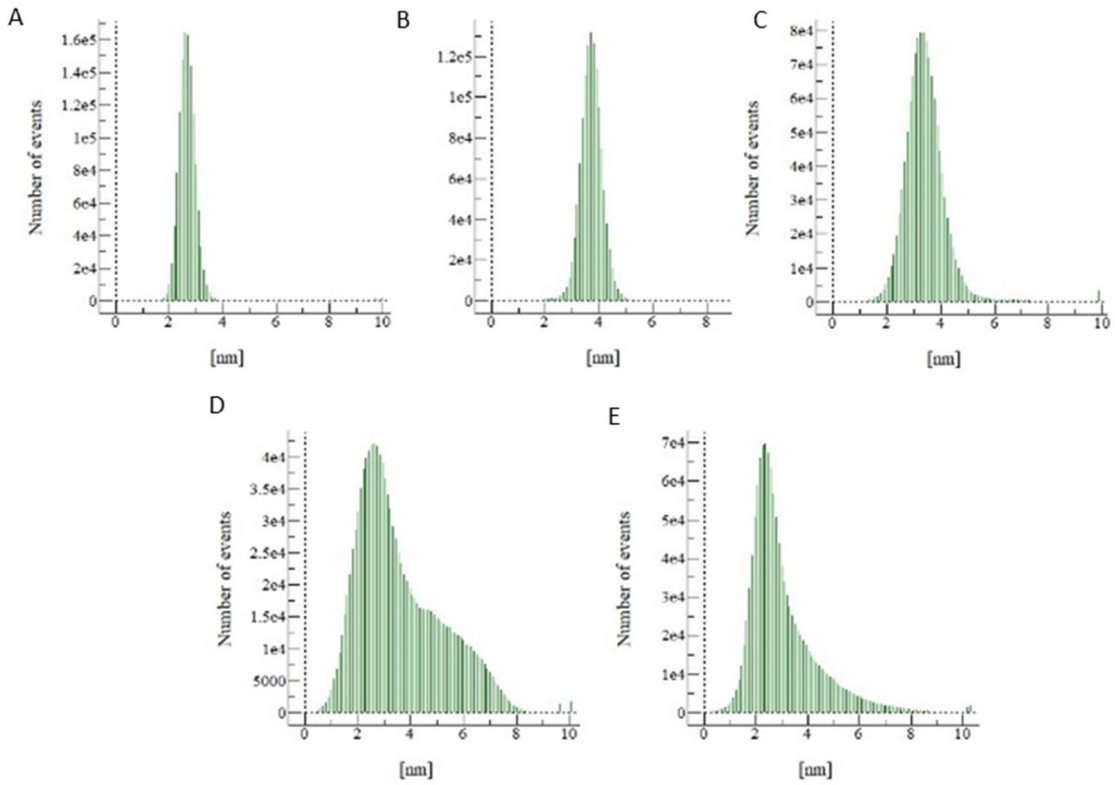

Figure 6: Surface roughness of PES (A), CNC0.05 (B), CNC0.075 (C), CNC0.1 (D) and CNC0.15 (E)

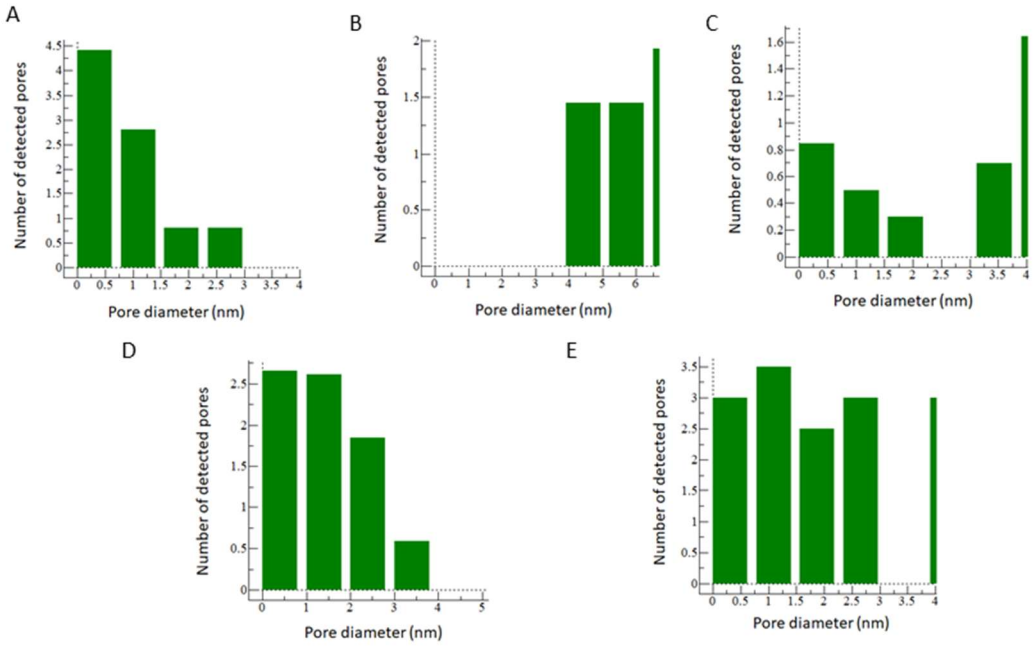

Figure 7: Pore size distribution of PES (A), CNC0.05 (B), CNC0.075 (C), CNC0.1 (D) and CNC0.15 (E)

4.2 Performance comparison

The performance of the membranes was evaluated and compared in terms of pure water flux, turbidity removal in synthetic water, water flux, and COD removal in real restaurant water. The results are shown

in Figures 8 and 9. Water flux was highest with CNC0.075 for both the pure water and the real restaurant water. This may be because of improved hydrophilicity and surface roughness as a result of adding 0.075% CNC. The agglomeration of CNC on the surface of the membrane may be the reason for the reduction of water flux for membranes with CNC greater than 0.075%. This might have resulted in the blockage of the pores of the membrane. It was observed that the average water flux reduced with the real restaurant water. This may be due to the presence of other contaminants such as oil in the water. Water flux increased with an increase in pressure as expected. Turbidity removal was more than 98% for all the membranes as is expected normally for ultrafiltration membranes. Average COD removal was 57% for the PES membrane, and 54%, 76%, 56%, and 59% for the CNC0.05, CNC0.075, CNC0.1 and CNC0.15 membranes respectively. The reason for this observation is not clear as it was expected that either CNC0.1 or CNC0.15 would have the highest rejection of COD because some of the pores were blocked by agglomeration effects. However, the preference of water molecules on the surface of the CNC0.075 membrane due to its higher hydrophilicity might have increased the COD rejection. This is because higher membrane surface hydrophilicity increases the absorption of water molecules towards the membrane resulting in higher water permeability than hydrophobic contaminants (Abdel-Aty et al., 2020). The PES membrane with 0.075% CNC shows a good prospect for removal of turbidity and COD from restaurant wastewater and also for improved water flux.

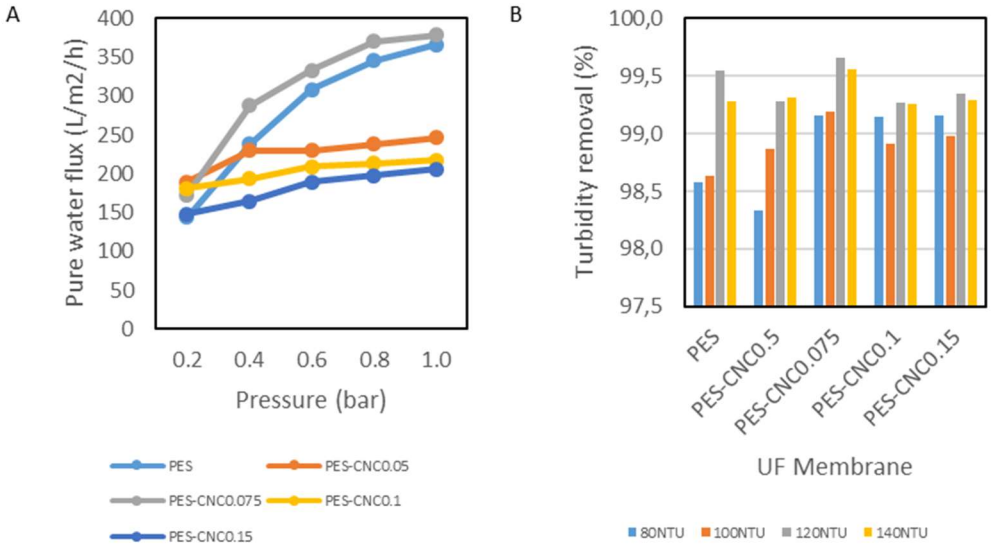

Figure 8: Pure water flux (A) and turbidity removal for the membranes for synthetic water

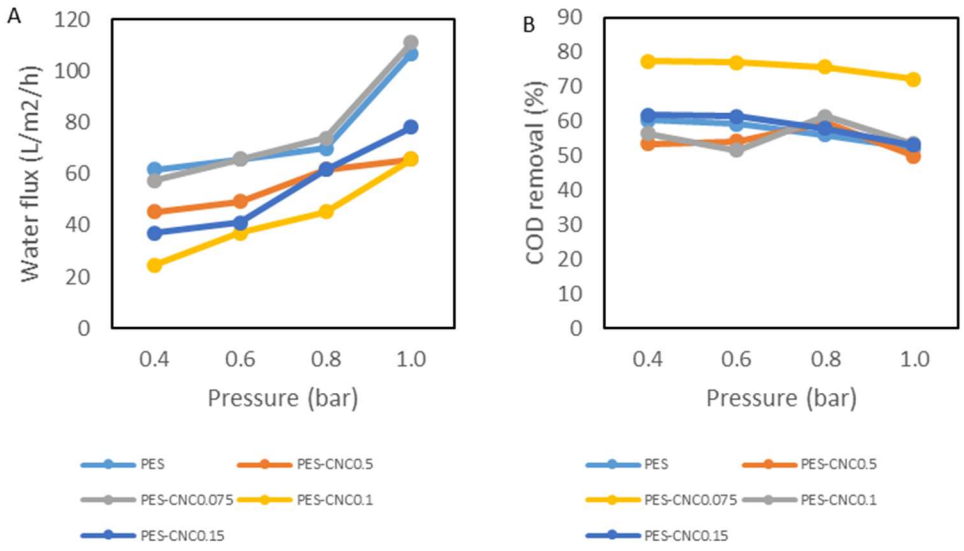

Figure 9 Water flux (A) and COD removal for the membranes for raw restaurant water

5 CONCLUSIONS

In this work, an ultrafiltration (UF) membrane containing cellulose nanocrystal as an additive was fabricated for the treatment of restaurant wastewater. The FTIR spectra showed characteristic normal peaks for PES membranes in all the membranes which indicates that the membranes were properly formed. However, none of the membranes containing CNC showed any peak which could be attributed to the presence of CNC. This may be due to the low concentration of the CNC in the membranes indicating that functional groups were not changed at low CNC concentration. The EDS results showed the presence of CNC with an increase in oxygen content as the percentage of CNC increased. CNC0.075 has the lowest contact angle (69º) and was the only CNC membrane with a lower contact angle than the PES membrane (71.4º). The lower the contact angle, the higher the hydrophilicity of the membrane. This is means that the CNC0.075 is more hydrophilic than the other membranes. It seems that the polymer forms a perfect blend at a concentration of 0.075% CNC leading to a uniform dispersion of CNC in the polymer. While 0.05% of CNC was too low for a significant effect on the PES-UF membrane, a concentration higher than 0.075% was not homogenous resulting in the formation of agglomerates. The 3D images from the SEM analysis revealed the effect of the addition of CNC on the morphology of the membranes. There was no significant change when 0.05% CNC was added. However, the addition of 0.075% CNC brought a change to the morphology of the membrane. The formation of agglomerates was clearly seen in the membrane with 0.1% and 0.15% CNC respectively. The surface roughness increased with the increase in CNC concentration. The degree of formation of agglomerates was higher for CNC0.1 and this was clearly reflected in the roughness of the membrane leading to the membrane with the highest roughness. The pore size distribution is higher for PES than for other membranes, which means it has the highest number of pores. The pore size distribution was

greatly reduced in CNC0.05 by the presence of CNC, however, this did not result in improvement of the hydrophilicity. CNC0.075 has the lowest size distribution and hence the lowest numbers of pores, however, the addition of CNC resulted in an increase in hydrophilicity. Also, most of the pores were over 4nm in diameter. Both CNC0.1 and CNC0.15 have a pore size distribution between that of PES and CNC0.05. The pores of the two membranes pores might have been affected by the agglomeration of CNC on the surfaces. This may mean that the optimum concentration of CNC in the polymer solution is 0.075%. The membrane has the highest hydrophilicity, lowest pore size distribution, and increased roughness. Average water flux, turbidity, and COD removal were highest with a PES membrane containing 0.075% CNC. PES-CNC0.075 membrane shows a great prospect in the treatment of restaurant wastewater.

ACKNOWLEDGEMENT

Tshwane University of Technology is acknowledged for providing facilities for the synthesis of the membranes. European Institute of Membrane, University of Montpellier, is acknowledged for providing the facilities for characterization of the membranes. This research has been sponsored by funding from the Science and Technology Department (DST), South Africa. The financial support is highly appreciated.

REFERENCES

Abdessemed, D., Nezzal, G. & Aim, R. B. 1999. Treatment of wastewater by ultrafiltration. Desalination, 126, 1-5.

Abdel-Aty, A. A., Aziz, Y. S. A., Ahmed, R. M., Elsherbiny, I. M., Panglisch, S., Ulbricht, M. & Khalil, A. S. 2020. High performance isotropic polyethersulfone membranes for heavy oil-in-water emulsion separation. Separation and Purification Technology, 253, 117467.

Adeniyi, A., Gonzalez-Ortiz, D., Pochat-Bohatier, C., Oyewo, O., Sithole, B. & Onyango, M. 2020. Incorporation of Cellulose Nanocrystals (CNC) derived from sawdust into polyamide thin-film composite membranes for enhanced water recovery. Alexandria Engineering Journal, 59, 4201-4210.

Aguayo, M. G., Fernández Pérez, A., Reyes, G., Oviedo, C., Gacitúa, W., Gonzalez, R. & Uyarte, O. 2018. Isolation and characterization of cellulose nanocrystals from rejected fibers originated in the kraft pulping process. Polymers, 10, 1145.

Bhojwani, S., Topolski, K., Mukherjee, R., Sengupta, D. & El-Halwagi, M. M. 2019. Technology review and data analysis for cost assessment of water treatment systems. Science of the Total Environment, 651, 2749-2761.

Borowski, P. F. 2020. Nexus between water, energy, food and climate change as challenges facing the modern global, European and Polish economy. AIMS Geosci, 6, 397-421.

Flusberg, M. 2016. Water, Water Everywhere… and 10 Ways for Restaurants to Stem the Flow.

Powerhouse Dynamics.

Garcia-Ivars, J., Alcaina-Miranda, M.-I., Iborra-Clar, M.-I., Mendoza-Roca, J.-A. & Pastor-Alcañiz, L. 2014. Enhancement in hydrophilicity of different polymer phase-inversion ultrafiltration membranes by introducing PEG/Al2O3 nanoparticles. Separation and Purification Technology, 128, 45-57.

Hebbar, R., Isloor, A. & Ismail, A. 2017. Contact angle measurements. Membrane characterization. Elsevier.

https://www.dining-out.co.za/restaurants/South-Africa/10. Accessed 16-08-2021

Horcas, I., Fernández, R., Gomez-Rodriguez, J., Colchero, J., Gómez-Herrero, J. & Baro, A. 2007. WSXM: a software for scanning probe microscopy and a tool for nanotechnology. Review of scientific instruments, 78, 013705.

Khan, T. M., Khalid, A., Habib, U., Ramay, M. I., Ali, U. & Samad, N. 2011. Aerobic treatment for recycling kitchen wastewater. International Journal of Agriculture Applied Science, 3.

Lessan, F., Karimi, M., Bañuelos, J. L. & Foudazi, R. 2020. Phase separation and performance of polyethersulfone/cellulose nanocrystals membranes. Polymer, 186, 121969.

Marchese, J., Ochoa, N. A., Pagliero, C. & Almandoz, C. 2000. Pilot-scale ultrafiltration of an emulsified oil wastewater. Environmental science & technology, 34, 2990-2996.

Nasrollahi, N., Aber, S., Vatanpour, V. & Mahmoodi, N. M. 2019. Development of hydrophilic microporous PES ultrafiltration membrane containing CuO nanoparticles with improved antifouling and separation performance. Materials Chemistry and Physics, 222, 338-350.

Peter-Varbanets, M., Zurbrügg, C., Swartz, C. & Pronk, W. 2009. Decentralized systems for potable water and the potential of membrane technology. Water research, 43, 245-265.

Reid, M. S., Villalobos, M. & Cranston, E. D. 2017. Benchmarking cellulose nanocrystals: from the laboratory to industrial production. Langmuir, 33, 1583-1598.

Singh, S., Kaushik, V., Soni, S. & Lamba, N. 2014. Waste management in restaurants: A review. International Journal of Emerging Engineering Research and Technology, 2, 14-24.

Tang, J., Sisler, J., Grishkewich, N. & Tam, K. C. 2017. Functionalization of cellulose nanocrystals for advanced applications. Journal of colloid and interface science, 494, 397-409.

Thompson, L., Azadmanjiri, J., Nikzad, M., Sbarski, I., Wang, J. & Yu, A. 2019. Cellulose nanocrystals: Production, functionalization and advanced applications. Reviews on Advanced Materials Science, 58, 1-16.

Yang, S., Hai, F. I., Price, W. E., Mcdonald, J., Khan, S. J. & Nghiem, L. D. 2016. Occurrence of trace organic contaminants in wastewater sludge and their removals by anaerobic digestion. Bioresource technology, 210, 153-159.

Yao, X. 2020. Handling of restaurant waste in China.

Yau, Y.H., Rudolph, V., Lo, C. C.M. & Wu, K.C. 2018. Restaurant oil and grease management in Hong Kong. Environmental Science and Pollution Research, 1-11.

Zulaikha, S., Lau, W., Ismail, A. & Jaafar, J. 2014. Treatment of restaurant wastewater using ultrafiltration and nanofiltration membranes. Journal of Water Process Engineering, 2, 58-62.

Synthesis and Characterization of Carbon Nanotube-Gold/iron oxide Nanocomposite (MWCNT-Au/Fe_3O_4) from Green Tea Leaves Extract

B.Z. Kunene[1], O.O. Sadare[1*], G.N. Hlongwane[1], G.S. Simate[2] and K. Moothi [2*]

[1] Department of Chemical Engineering, Faculty of Engineering and the Built Environment, Doornfontein Campus, University of Johannesburg, P.O. Box 17011, Johannesburg, 2028, South Africa, balamlile.kunene@gmail.com (B.K); gloriahlongwane@gmail.com (G.N.H)

[2] School of Chemical and Metallurgical Engineering, Faculty of Engineering and the Built Environment, University of the Witwatersrand, Johannesburg, Wits 2050, South Africa, geoffrey.simate@wits.ac.za (G.S)

*Corresponding authors: kmoothi@uj.ac.za; wumisadare@gmail.com

ABSTRACT

In this study, we reported a simple, cost effective and environmental friendly technique for the synthesis of gold/iron oxide nanoparticles using green tea leaves extract and attached on the walls of functionalized multi-walled carbon nanotubes to form a nanocomposite. The gold/iron oxide nanoparticles were synthesized by reacting green tea leaves extract with iron chloride ($FeCl_2$) and gold (III) chloride ($HAuCl4.3H_2O$) precursors while multi-walled carbon nanotubes (CNTs) were commercially obtained and functionalized with a mixture of H_2SO_4/HNO_3 acids. The composite was then cross-linked using N, N-Dimethylformadide (DMF). The surface morphology, functional groups, composition and properties were checked using Scanning electron microscope (SEM), Fourier transform infrared spectrometer FTIR, transmission electron microscope (TEM) and Energy-dispersive X-ray spectroscopy (EDS), respectively. SEM revealed that gold/iron oxide nanoparticles were spherical in shape. FTIR spectroscopy confirmed the involvement of functional groups that were responsible for the reduction of Au/Fe_3O_4. TEM analysis confirmed the attachment of synthesized nanocomposite on the walls of carbon nanotubes. Also, EDS confirmed the presence of all the elements in the synthesized MWCNT-Au/Fe_3O_4 nanocomposite. Results obtained in this study showed that MWCNT-Au/Fe_3O_4 was successfully synthesized from green tea leaves extract for possible application in water treatment.

Keywords: Carbon nanotube, Green leave extract, Gold/Iron oxide nanocomposite, Wastewater treatment.

1 INTRODUCTION

Nanotechnology is a reliable and environmental friendly process for the synthesis of nanoscale particles (Niraimathee et al., 2016). In the past decade, the study of nanoparticles has received great interest from many researchers due to their exceptional properties such as large surface area, reusability, and supermagnetic properties, low cost and ease of synthesis (Xu et al., 2012). Nanoparticles refers to the materials ranging in size from 1-100nm with unique properties. Physical and

chemical methods are conventionally used for synthesis of nanoparticles (Letchumanan et al., 2021). Physical methods include plasma, laser ablation, gamma radiation and mechanical milling (Cele, 2020; Kumar et al., 2014; Khan et al., 2019). On the other hand, chemical methods include precipitation, sonochemical route, sol-gel, hydrothermal approach, chemical bath deposition, chemical reduction and chemical vapour deposition (Herlekar et al., 2014). These methods have been widely used, however due to their limitations such as high energy demand, toxicity and dangerous by-products production, their use in the synthesis of nanomaterial has been limited (Gottimukkala et al., 2017). The focus of research has recently shifted to developing simple and eco-friendly protocols for synthesis of nanoparticles. Green synthesis methods uses biological materials such as various plant extract, algae, fungi, yeast and bacteria. Some of the advantages that green synthesis approaches have over the conventionally used physical and chemical methods are; the clean and eco-friendly method, as toxic chemicals are not used, small particles can be produced even during large scale production, and experimental conditions such as high energy and high pressures are not required and a large amount of energy is saved during the synthesis process.

2 LITERATURE

Over the past decades, there has been an increased emphasis on the topic of green chemistry. Green nanotechnology is a better solution to enhance the production and application of nanomaterials. The use of environmental benign solvents, non-hazardous chemicals, and renewable materials has given green synthesis approaches more attention in the research community (Niraimathee et al., 2016). The application of adsorbent during the adsorption process has been explored by many researchers owing to its applicability, large surface area, and low cost on large scale; and high adsorption capacity (Sadare and Daramola, 2019a; Sadare et al., 2020). The use of natural plant extracts to synthesize nanoparticles can eliminate the chemical residues they produce (Kharissova et al., 2013). The green synthesis of gold and iron oxide nanoparticles is more advantageous than chemical and physical synthesis because it is non-toxic, clean, cost-effective, and environmentally friendly method (Shafey, 2020). The synthesis of iron oxide nanoparticles using green tea leaves (Camellia sinensis) extract as a reducing agent has been reported by Gottimukkala et al. (2017). This was done by adding equal amounts of 0.01M ferric chloride and green tea leaves extract. Awwad and Salem (2012) synthesised iron oxide nanoparticles using carob leaf extract. Niraimathee et al. (2016) reported a successful synthesis of supermagnetic iron oxide nanoparticles using root extract of Mimosa pudica. The use of green synthesized nanoparticles have been extensively employed in many applications. However, incorporation of the gold/ iron oxide nanoparticles onto the surface of carbon nanotubes (CNTs) has not been widely studied and therefore there is limited literature available.

Carbon nanotubes (CNTs) have gained widespread attention as effective adsorbents for the removal

of various contaminant in wastewater treatment due to their large surface area which allows a great capacity for a wide range contaminants adsorption, light mass density, high porous, hallow structure and that they possess strong interaction between pollutants (Burakov et al., 2018). The CNTs sensitivity is enhanced by their functionalization in order to introduce functional groups that will enhance pollutants removal from aqueous solutions. This is mainly due to its porous structure and a wide variety of surface functional groups. The CNTs are mostly attractive because they have large surface area (Modekwe et al., 2020) and can be functionalized with various chemical groups to increase their affinity for target compounds (Sadare and Daramola, 2019b). Iron oxide-based materials have received a great attention in wastewater for the past years, due to their large surface area, reusability, supermagnetic properties, low cost and ease of synthesis. Iron oxides are unstable due to their ability to undergo oxidation easily. To overcome this issue, a combination with a noble metal such as gold (Au) reported by Fodjo et al., 2017. Gold nanoparticles (Au-Nps) are well known for contaminant detection and removal due to their unique properties such as high surface area per volume, ease surface modification and high stability. Against this background, this study focusses on the synthesis of iron oxide/gold nanocomposite from green tea leaves extract, and incorporated onto the external surface of MWCNT. In addition, it seeks to develop a proof of concept that the nano-adsorbent could be successfully synthesized for possible application in the removal of heavy metals from wastewater.

3 EXPERIMENTAL PROCEDURE

3.1 Chemical reagents and materials

Green tea leaves were purchased from a local tea merchant in Johannesburg, South Africa. Raw multi-walled carbon nanotubes (MWCNTs, >95% purity) with an average size ranging from 10-20nm and gold (III) chloride 99.995 % were purchased from Sigma Aldrich Pty (Ltd), Johannesburg, South Africa.

Nitric acid (HNO_3) 65 % purity, sulphuric acid (H_2SO_4) 98 % purity and dimethyl formamide (DMF) were all purchased from Associated Chemical Enterprise (ACE), Johannesburg, South Africa. Potassium Bromide extrapure, 99.5% and iron (II) chloride ($FeCl_2$) were purchased from Protea Laboratory Solutions (Pty) Ltd. All chemicals used in this study were of analytical or reagent grade unless stated otherwise and were used as obtained from the suppliers.

3.2 Preparation of green tea leaf extract

Green tea acts as a reducing agent for the synthesis of nanoparticles because it contains high amounts of polyphenols which are very important in the reducing salt precursors to nanoparticles. An amount of 5 grams of green tea leaves was mixed in 150 mL of distilled water, and then heated at 80 ºC in a hot water bath for 1 hour in order to obtain the tea extract. The residue was obtained by filtrated through 0.45 µm filter paper, and then centrifuged at 20,000 rpm for 10 minutes to remove any particles that may be suspended. The pH of the tea extract was determined at almost neutral ~6.5 (Fayemiwo et al.,

2018).

3.3 Synthesis of gold (Au) coated iron oxide (Fe3O4) nanoparticles

Gold-iron oxide nanoparticles were prepared by mixing 0.0162g of $FeCl_2$ in 10 mL to obtain a stock solution of 0.001 M. Approximately 1 mL of the prepared stock solution was added to 7.5 mL of pure water and stirred for 5 min. An addition of 1.5mL of tea extract was then added to the solution which resulted in the change of colour of the solution from yellow to dark green to black colour immediately confirming the synthesis of iron oxide nanoparticles at room temperature. Finally, 10 mL of 0.01 M $HAuCl_4$ was also added to the solution containing the tea to get it reduced and coated on iron oxide nanoparticles. The synthesized particles were centrifuged at 20,000 rpm for 15 minutes, washed with distilled water and ethanol to remove excess precursors and polyphenols that may be present. The nanoparticles were then dried at 100 ºC for 3h before being characterised (Gottimukkala et al., 2017; Sharma et al., 2012).

3.4 Functionalization of MWCNTs to prepare MWCNT-COOH

The purification of carbon nanotubes using acids was done to remove impurities that are found from the catalyst used during the synthesis process, also the functionalization by oxidation treatments introduces oxygen containing functional groups to their walls. The oxidation of MWCNTs was carried out as reported by Haider et al. (2015). Approximately 0.1g of raw-CNTs were dispersed in a flask containing a mixture of concentrated sulphuric acid 95% H_2SO_4 and nitric acid 65% HNO_3 (3:1). The mixture was sonicated for 3 h to remove residual metal impurities from the tubes and produce oxidized carbon nanotubes (CNT-COOH). The resulting solution was filtered, and the solids were continuously washed with deionised water until neutral pH was obtained. The sample was then dried at 70 °C for 24 h and taken for characterization.

3.5 Preparation of MWCNT-Au/Fe_3O_4 nanocomposite

MWCNT-Au/Fe_3O_4 was prepared by mixing 0.1 g of MWCNT-COOH with 10 mL N, N-Dimethylformadide (DMF) as a binder, with a constant stirring. While stirring, a 0.3 g of Au-Fe_3O_4 nanoparticles were added to MWNCNT solution. Then, a composite was ultrasonicated for 1 hour to allow the mixture to dissolve which resulted in Au / Fe_3O_4 nanoparticles being well coated on the surface of the oxidized CNTs. About 3 mL of the dough-like form of the CNT-Au/Fe_3O_4 nanocomposite was dried at 25 °C for overnight for the solvent to evaporate. The dried MWCNT-Au/Fe_3O_4 nanocomposite was stored in a clean, closed container for physicochemical analysis.

3.6 Characterization techniques

The surface morphology of the synthesized nanocomposites were performed using scanning electron microscope operated at 20kv (SEM JOEL JSM-5600) after coating the sample with carbon for better images. Transmission electron microscope analysis was carried out by TEM JEM2100 JEOL operating

at 200 kv, in which samples were prepared by diluting a few milligrams of a sample with ethanol, dropped on a copper grid coated with carbon and dried at room temperature (25°C). The Oxford INCA EDS detector system coupled with TEM was used to obtain elemental compositions. Functional groups on the surface of nanocomposite were detected using Fourier transform infrared spectrometer (FTIR) Perkin-Elmer Spectrum: Model 1000 series using KBr powder over the range of 400-4000 cm^{-1}.

4 RESULTS AND DISCUSSION

4.1 Physico-chemical characterization of Au/Fe3O4 nanoparticles and MWCNT-Au/Fe3O4 nanocomposite adsorbent

4.1.1 Characterization of the Au/Fe_3O_4 nanoparticles using scanning electron microscopy

Figure 1 depicts the surface morphology of the Au/Fe_3O_4 nanoparticles at different magnifications. Consistent with previous studies (Ruíz Baltazar,2021; Hao et al., 2021), SEM images of the Au/Fe_3O_4 nanocomposite at different magnifications shows highly agglomerated and polydisperse particles in the aqueous medium due to the phytochemicals present in the tea extract as shown in Figure 1.

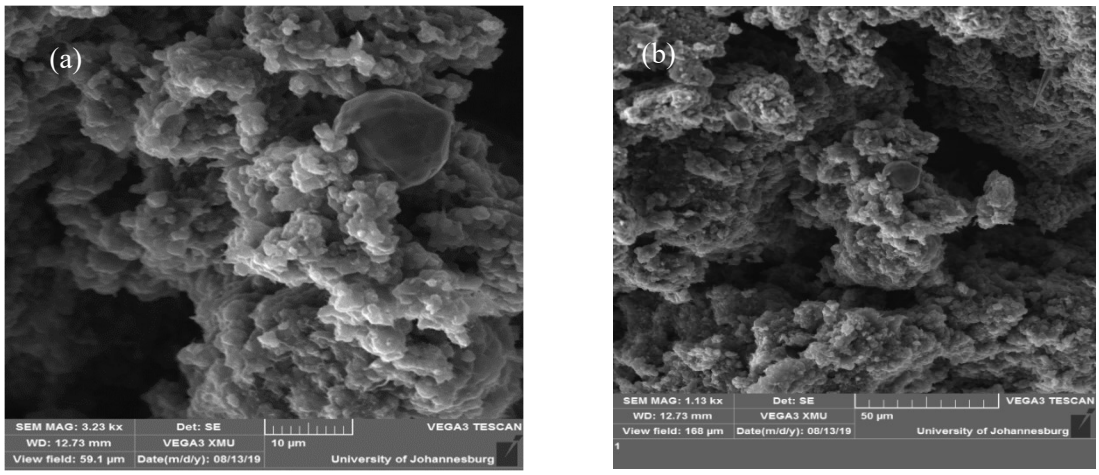

Figure 1: (a-b) SEM image of Au/Fe_3O_4 at 10 µm and 50 µm magnifications respectively

4.1.2 Morphology of as-received, functionalized CNTs and synthesized nanocomposites adsorbent

The chemical composition of the synthesized nanoparticles was analysed by EDS, as depicted in Figure 2. The EDS spectrum presents all the elements found in the MWCNT-Au/Fe_3O_4 and their corresponding atomic weight percentages (C: 62.3 %; Fe: 23.6 %; O: 8.0 %; Au: 4.3 %and Cu: 1.8 %). The presence of carbon in the EDS analysis is in line with compounds identified in the green tea extract by Fameyiwo et al. (2018) on GC-MS spectrum of green tea extract which are rich in carbon and oxygen. Also, the peak was obtained from carbon nanotubes. The peak obtained from copper (Cu) was caused by the copper grid that was used to fasten nanoparticles.

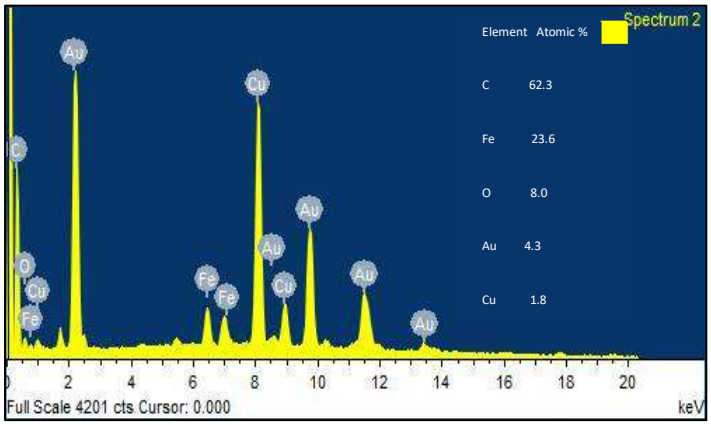

Figure 2: EDS spectrum and elemental composition of MWCNT-Au/Fe_3O_4

TEM analysis was conducted to investigate the morphology and internal structure of the adsorbents, Figure 3 shows the TEM images of (a) Au/Fe_3O_4 nanocomposite (b) Raw-MWCNT (c) MWCNT-COOH and (d) MWCNT-Au/Fe_3O_4 nanocomposite, at different magnifications.

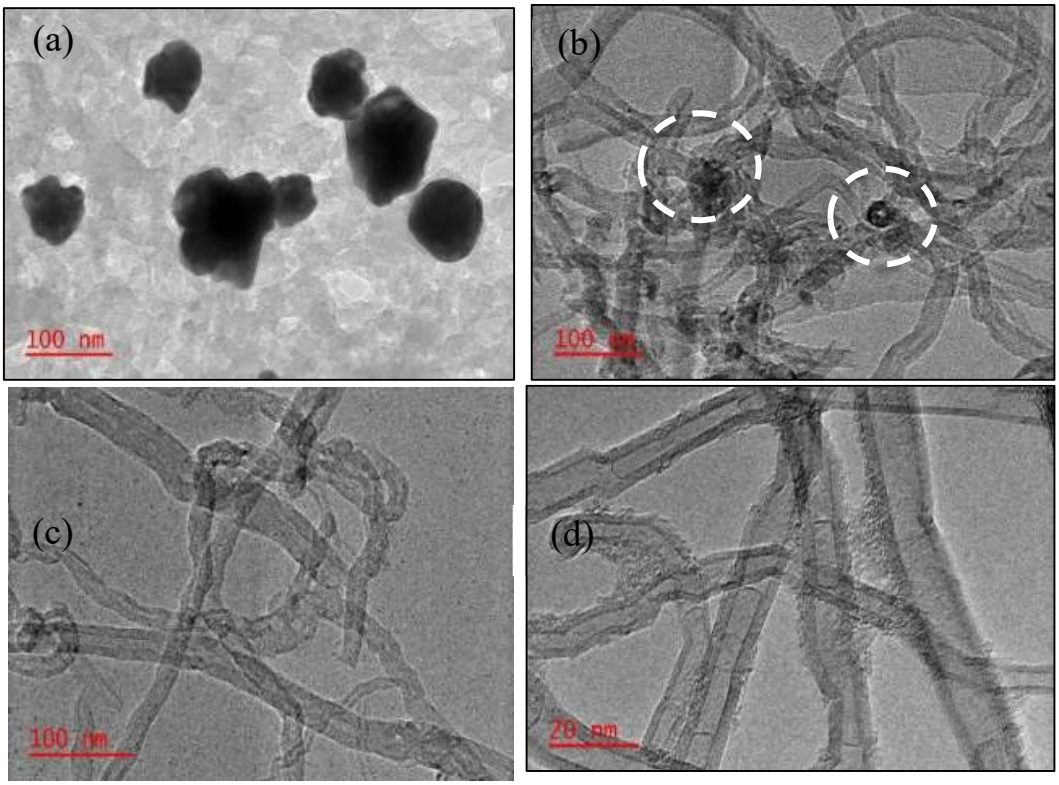

Figure 3: Morphological structure of (a) Au/Fe_3O_4 nanocomposite (b) Raw-MWCNT, (c) MWCNT-COOH and (d) MWCNT-Au/Fe_3O_4

Figure 3(a) displayed agglomerated spherical nanocomposite ranging from 20 to 30nm in size. Also, impurities were observed on the surface of the as-received MWCNTs (Figure 3 b, with broken white circle). However, Figure 3(c) revealed that functionalized MWCNTs appeared more spaced and less packed and clear of impurities such as metal nanoparticles (Modekwe et al., 2021; Ngoma et al., 2021).

The uniform pattern of Au/Fe_3O_4 nanoparticles can be observed and their attachment on the walls of CNTs. Figure 3(d), depicts an entangled network of MWCNT with clusters of Au/Fe_3O_4 attached to their walls. There is a homogenous distribution of Fe_3O_4/Au on the external surface of MWCNT (f-MWCNT) indicate the formation of MWCNT-Au/Fe_3O_4. Similar images of raw and functionalized carbon nanotubes were obtained by Aslam et al. (2021).

4.1.3 Surface functionalities of f-MCNTs and nanocomposites adsorbent.

Figure 4 shows the FTIR spectra of the MWCNT-COOH (f-MWCNT) and MWCNT-Au/Fe_3O_4 nanocomposite. This was carried out to check for the possible functional groups present on the surface of f-MWCNT and the MWCNT-Au/Fe_3O_4 nanocomposite. The absorption band at 1717 cm^{-1} corresponds to the C=O stretching of COOH. The broad peak at 1717 cm^{-1} is a stretch mode of carboxylic groups indicative of its attachment due to the oxidation of the MWCNT with the mixture of H_2SO_4 and HNO_3. The absorption bands at 3484cm^{-1} is related to the bending of O-H and this can be attributed to the oscillation of carboxylic groups, while the adsorption at 1011 cm^{-1} corresponds to the C-O stretching. The FTIR spectrum of f-CNT has similar observations to previously reported study by Aslam et al., (2021) and Sadare and Daramola (2019b).

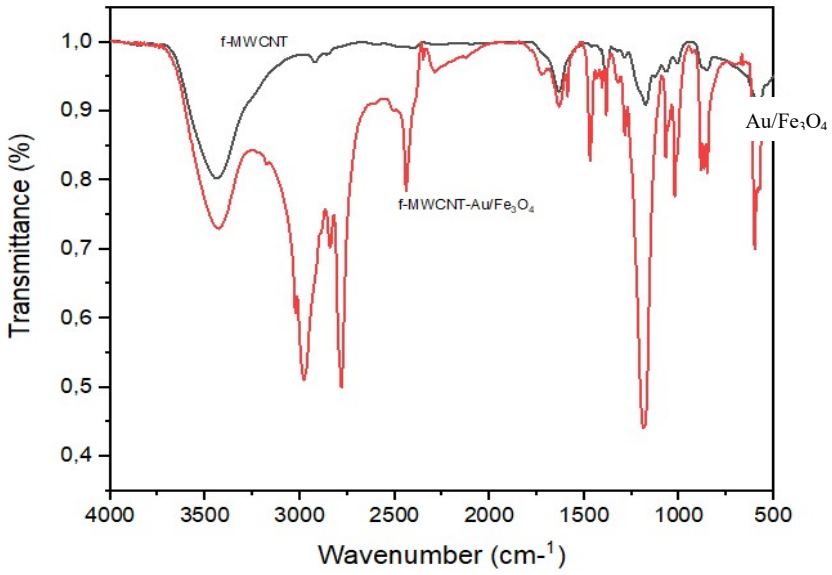

Figure 4: FTIR spectra of f-MWCNT and MWCNT-Au/Fe_3O_4 nanocomposite

4.2 Textural properties of Raw-MWCNT, MWCNT-COOH and MWCNT-Au/Fe3O4

The textural properties (surface area, pore volume and pore size) of the adsorbent analyzed by BET are presented in Table 1**.** The increase in surface area and pore volume of MWCNT-Au/Fe_3O_4 was due to increase in the degree of functionalization of MWCNT-COOH.

Table 1: The textural properties of the adsorbents from BET analysis

Adsorbent	Single point surface area (m^2/g)	Pore volume (cm^3/g)	Pore size (nm)
Raw-MWCNT	44.996	0.358	0.718
MWCNT-COOH	96.705	0.388	0.716
MWCNT-Au/Fe_3O_4	105.027	0.389	0.748

These results confirms that textural properties of nanomaterials can be increased based on functionalization of MWCNT-COOH and MWCNT-Au/Fe_3O_4 which have a large surface area and increased pore volume which is capable of increasing adsorption capacity for Pb^{2+} removal from aqueous solutions. Similarly to the results obtained in this study, Rodriguez et al., 2020 showed that the BET surface area of MWCNTs treated with HNO_3 increased from 157.34 to 179.53 m^2/g.

5 CONCLUSIONS

In this present investigation, gold/iron oxide nanoparticles were successfully synthesized in an easy and eco-friendly way in the presence of green tea leaves extract. The green tea leaves extract acted as a reducing agent during the synthesis period of iron oxide/gold nanoparticles. This was confirmed by using techniques such as FTIR, TEM, SEM and EDS. TEM was used to observe the surface coating and dispersion of nanoparticles and the analysis shows the spherical shape of Au/Fe_3O_4 and uniform distribution of Au/Fe_3O_4 on the external walls of MWCNTs. The results obtained using SEM analysis show that Au/Fe_3O_4 particles are agglomerated and uniform. FTIR analysis confirmed the presence of functional groups formed from functionalising MWCNT and the attachment of Au/Fe_3O_4 prepared in the presence of green tea leaves extract. The transformation in colour was observed from orange to dark green and immediately to black confirming the synthesis of nanoparticles. This study has successfully developed a proof of concept to synthesize an eco-friendly nanocomposite for possible removal of heavy metals from industrial.

REFERENCES

Aslam, M.M.A., Kuo, H.W., Den, W., Usman, M., Sultan, M. and Ashraf, H., 2021. Functionalized Carbon Nanotubes (CNTs) for Water and Wastewater Treatment: Preparation to Application. *Sustainability*, *13*(10), p.5717.

Awwad, A.M. and Salem, N.M. (2012). A green and facile approach for synthesis of magnetite nanoparticles. *Nanoscience and Nanotechnology*, 2(6), pp. 208-213.

Cele, T. Preparation of Nanoparticles. In Engineered Nanomaterials-Health and Safety; IntechOpen: London, UK, 2020

de Jesús Ruíz-Baltazar, Á. 2021. Sonochemical activation-assisted biosynthesis of Au/Fe3O4 nanoparticles and sonocatalytic degradation of methyl orange. *Ultrasonics Sonochemistry*, *73*,

p.105521.

Dehaghi, M., 2014. Removal of lead ions from aqueous solution using multi-walled carbon nanotubes: The effect of functionalization. *J. Appl. Environ. Biol. Sci*, *4*(2), pp.316-326.

El Shafey, A.M., 2020. Green synthesis of metal and metal oxide nanoparticles from plant leaf extracts and their applications: A review. *Green Processing and Synthesis*, *9*(1), pp.304-339.

Fayemiwo, O.M., Daramola, M.O. and Moothi, K., 2018. Tannin-based adsorbents from green tea for removal of monoaromatic hydrocarbons in water: Preliminary investigations. *Chemical Engineering Communications*, *205*(4), pp.549-556.

Fodjo, E.K., Gabriel, K.M., Serge, B.Y., Li, D., Kong, C. and Trokourey, A., 2017. Selective synthesis of Fe_3O_4 Au x Ag y nanomaterials and their potential applications in catalysis and nanomedicine. *Chemistry Central Journal*, *11*(1), pp.1-9.

Gholami-Shabani, M., Gholami-Shabani, Z., Shams-Ghahfarokhi, M., Jamzivar, F. and Razzaghi-Abyaneh, M., 2017. Green nanotechnology: biomimetic synthesis of metal nanoparticles using plants and their application in agriculture and forestry. In *Nanotechnology* (pp. 133-175). Springer, Singapore.

Gottimukkala, K.S.V., Harika, R.P. and Zamare, D., 2017. Green synthesis of iron nanoparticles using green tea leaves extract. *J. Nanomed. Biother. Discovery*, *7*(151.10), p.4172.

Haider, A.J., Mohammed, M.R. and Ahmed, D.S., 2014. Preparation and characterization of multi walled carbon nanotubes/Ag nanoparticles hybrid materials. *International Journal of Scientific & Engineering Research*, *5*(3), pp. 255-261.

Hao, R., Li, D., Zhang, J., and Jiao,T., 2021. Green Synthesis of Iron Nanoparticles Using Green Tea and its Removal of Hexavalent Chromium. *Nanomaterials*, 11(3), p.650.

Herlekar, M., Barve, S. and Kumar, R., 2014. Plant-mediated green synthesis of iron nanoparticles. *Journal of Nanoparticles*, *pp. 1-9.*

Kharissova, O.V., Dias, H.R., Kharisov, B.I., Pérez, B.O. and Pérez, V.M.J., 2013. The greener synthesis of nanoparticles. *Trends in biotechnology*, *31*(4), pp.240-248.

Khan, I., Saeed, K. and Khan, I., 2019. Nanoparticles: Properties, applications and toxicities. *Arabian journal of chemistry*, *12*(7), pp.908-931.

Kumar, P.V., Pammi, S.V.N., Kollu, P., Satyanarayana, K.V.V. and Shameem, U., 2014. Green synthesis and characterization of silver nanoparticles using Boerhaavia diffusa plant extract and their anti bacterial activity. *Industrial Crops and Products*, *52*, pp.562-566.

Letchumanan, D., Sok, S.P., Ibrahim, S., Nagoor, N.H. and Arshad, N.M., 2021. Plant-Based Biosynthesis of Copper/Copper Oxide Nanoparticles: An Update on Their Applications in Biomedicine, Mechanisms, and Toxicity. *Biomolecules*, *11*(4), p.564.

Modekwe, H.U., Mamo, M.A., Daramola, M.O., Moothi,K., 2020. Catalytic Performance of Calcium

Titanate for Catalytic Decomposition of Waste Polypropylene to Carbon Nanotubes in a single-Stage CVD Reactor. *Catalysts*, 10(9), p1030.

Niraimathee, V.A., Subha, V., Ravindran, R.E. and Renganathan, S., 2016. Green synthesis of iron oxide

nanoparticles from Mimosa pudica root extract. *International Journal of Environment and Sustainable Development*, *15*(3), pp.227-240.

Sadare, O.O. and Daramola, M.O., 2019. Adsorptive desulfurization of dibenzothiophene (DBT) in model petroleum distillate using functionalized carbon nanotubes. Environmental Science and Pollution Research, 26(32), pp. 32746-32758.

Sadare, O.O. and Daramola, M.O., 2019. Adsorptive removal of dibenzothiophene from petroleum distillates using pomegranate leaf (Punica granatum) powder as a greener adsorbent. *Chemical Engineering Communications*, *206*(3), pp.333-345.

Shamaila, S., Sajjad, A.K.L., Farooqi, S.A., Jabeen, N., Majeed, S. and Farooq, I., 2016. Advancements in nanoparticle fabrication by hazard free eco-friendly green routes. *Applied Materials Today,* pp.150-199.

Sharma, R.K., Gulati, S. and Mehta, S., 2012. Preparation of gold nanoparticles using tea: a green chemistry experiment. *Journal of Chemical Education*, *89*(10), pp.1316-1318.

Vukovic, G.D., Marinkovic, A.D., Skapin, S.D., Ristic, M.D., Aleksic, R., Peric-Grujie, A.A and Uskokovic, P.S., 2011. Removal of lead from water by amino modified multi-walled carbon nanotubes. *Chemical Engineering Journal*, 173 pp. 822-86.

Xu, P., Zeng, G.M., Huang, D.L., Feng, C.L., Hu, S., Zhao, M.H., Lai, C., Wei, Z., Huang, C., Xie, G.X. and Liu, Z.F., 2012. Use of iron oxide nanomaterials in wastewater treatment: a review. *Science of the Total Environment*, *424*, pp.1-10.

An attainable region analysis on the effect of multiple feeds on comminution

D.K. Zimucha[1*], D. Ming[1], N. Chimwani[2] and D. Hildebrandt[2]

[1] School of Chemical and Metallurgical Engineering University of the Witwatersrand Private Bag X3 P O Wits Johannesburg South Africa 2050

[2] Institute for the Development of Energy for African Sustainability (IDEAS), University of South Africa (UNISA), 28 Pioneer Road, Florida Park, Roodepoort, 1709, South Africa

*Corresponding author: deanzimucha@gmail.com

ABSTRACT

Comminution is the process of reducing the size of large particles into finer particles, through milling. Conventionally, milling occurs in tumbling mills in either wet or dry conditions under batch or continuous operating modes, where particle sizes progressively reduce through impact, attrition and abrasion by the motion of the mill charge. The attainable region (AR) approach uses a graphical interpretation of fundamental processes (for example: mixing, reaction, breakage) to determine the set of all achievable states; the AR can be searched to find the optimal performance of the system and the path to achieve this can be interpreted in terms of physical equipment required. Much of the existing literature on the AR has focused on constructing the AR from a single feed. We consider the effect of multiple feeds (i.e. several feeds with different particle size distributions (PSDs)) on the comminution process. We consider various performance targets, for example achieving a specified output PSD in order to determine how the optimal operation of the mill as well as the structure of the milling circuit changes as the number of feeds are added and changed.

Keywords: comminution; population balance model; attainable regions; multiple feeds; mixing; feed size distribution

1 INTRODUCTION

Comminution is the process of reducing the size of large particles, through milling, into finer particles – liberating valuable material held within the particle. Raw material of a certain size class is sequentially broken, increasing surface area for downstream processes. This process occurs under tumbling mills in wet or dry conditions in batch or continuous operating modes, where impact, attrition and abrasion dictate the breakage of the mill charge. It is commonly used in the mineral processing, pharmaceuticals and manufacturing industries.

AR theory is a performance targeting technique used to draw insight on the set of all practically achievable states as well as the physical equipment required to attain those states – state refers to the physical condition of a batch or continuous stream with respect to its attributes i.e. mass fraction, residence time, energy input. The AR approach couples fundamental chemical engineering concepts such as breakage, mixing and classification with geometry to find the optimal path of achieving a

specific target (Glasser et al., 1987). The AR method has been successfully applied to understand the effect of mill operating parameters such as load filling, ball size distribution, feed size distribution (FSD), energy requirement, classification and the design of more efficient comminution circuits (Khumalo et al., 2007, 2008; Chimwani et al., 2015; Hlabangana et al., 2018; Khumalo et al., 2019). AR theory has also been used to determine the optimal operating conditions for optimization of downstream processes such as leaching and froth flotation (Hlabangana et al., 2017; Sibanda et al., 2019).

This work presents an analysis on the effect of multiple feeds on the mill structure required to produce the desired product – a mill structure is a combination of mills arranged in a specific pattern to produce a desired PSD. Typically, mills are operated from a single feed wherein all the available feed material enters the system via a single batch or continuous stream. Recent work confirmed that the FSD influences the breakage rate in the mill, product quality and milling time. Tailoring the FSD affects the breakage rate within the mill up to a certain point (Chimwani et al., 2019). Therefore, there can be significant time savings and reduction in operating costs with careful consideration of the feed.

2 LITERATURE

2.1 Population balance model (PBM)

The PBM is used in design, optimization and control of grinding milling circuits to predict product PSDs. Although it is computationally intensive and requires many parameters, it effectively simulates industrial comminution machines and therefore it is frequently used to understand the effect of operating variables on mill circulating load and classification. The PBM describes the process of comminution through the specific rate of breakage and breakage distribution functions.

The breakage distribution function represents the breakage event while the selection function represents the rate of breakage. The selection function or specific rate of breakage (S_i) is the probability of a particle of size i being broken. It defines the fraction of particles selected for breakage and is a function of the representative size of the class, composition of the parent particle. It is empirically determined by the following expression (King, 2012):

$$S_i = a \cdot x_i^{\alpha} \left[\frac{1}{1 + \left({}^{x_i}/_{\mu} \right)^{\varphi}} \right] \qquad \textbf{Equation 1}$$

where x_i is the upper size of the particle size interval i under consideration, a and μ are parameters which are mainly a function of milling conditions, α and φ are parameters which are a function of the material. The breakage distribution function (B_{ij}) describes the fraction of the breakage product which falls into size i from size interval j. It defines the distribution of particle sizes of the progeny upon the breakage event. Material breaking out of the size distributes itself over other size classes according to

the breakage function which is specific to the material being broken. The representative form of B_{ij} is taken from the literature (King, 2012):

$$B_{ij} = \emptyset\left(\frac{x_{i-1}}{x_j}\right)^{\mu} + (1-\emptyset)\left(\frac{x_{i-1}}{x_j}\right)^{v} \quad \textbf{Equation 2}$$

where μ is a material-dependent parameter with values generally ranging between 0.5 and 1.5, v is a material dependent parameter with values generally ranging between 2.5 and 5, ∅ is the fraction of fines that are produced in a single fracture event. Once the S_i and B_{ij} is known, the PBM is used to predict the product PSD. The rate of breakage for material of a particular size is a strong function of the amount of material of that size present in the mill:

$$\frac{dw_i(t)}{dt} = -S_i w_i(t) + \sum_{j=1}^{i-1} B_{ij} S_j w_j(t) \quad \textbf{Equation 3}$$

where B_{ij} is the breakage distribution function, S_i is the selection function (specific rate of breakage) parameter of size class i and w_i is the mass fraction of particles of size class i.

2.2 Attainable region theory

2.2.1 Mixing

Mixing is the process of combining two or more batch or continuous streams to form a single stream in which the total mass flowrate is the summation of all incoming stream mass flowrates. A mass balance over size class i gives:

$$m_{tot,i} = m_{1,i} + m_{2,i} \quad \textbf{Equation 4}$$

where $m_{1,i}$ and $m_{2,i}$ are mass fractions of size class i from stream 1 and 2 respectively. Expressing the equation in terms of mass fractions gives:

$$w_i^* m_{tot} = w_{1,i} m_{1,tot} + w_{2,i} m_{2,tot} \quad \textbf{Equation 5}$$

Dividing by the total mass m_{tot} and substituting $\lambda = {}^{m_{1,tot}}/_{m_{tot}}$, we obtain:

$$w_i^* = \lambda w_{1,i} + (1-\lambda) w_{2,i} \quad \textbf{Equation 6}$$

where w_i^* represents the mass fraction of size class i in the mixture and total mass is conserved. Mixing is linear and we express the final product mixture as a linear combination of the incoming streams. For n size classes, these expressions are compactly written in the vector equation:

$$\mathbf{w}^* = \lambda \mathbf{w}_1 + (1-\lambda)\mathbf{w}_2 \quad \textbf{Equation 7}$$

where $\mathbf{w}^*$ is a linear combination of $\mathbf{w}_1$ and $\mathbf{w}_2$ (Fig. 1). Geometrically, $\mathbf{w}^*$ lies on the straight line joining $\mathbf{w}_1$ and $\mathbf{w}_2$ (Ming, et al., 2016).

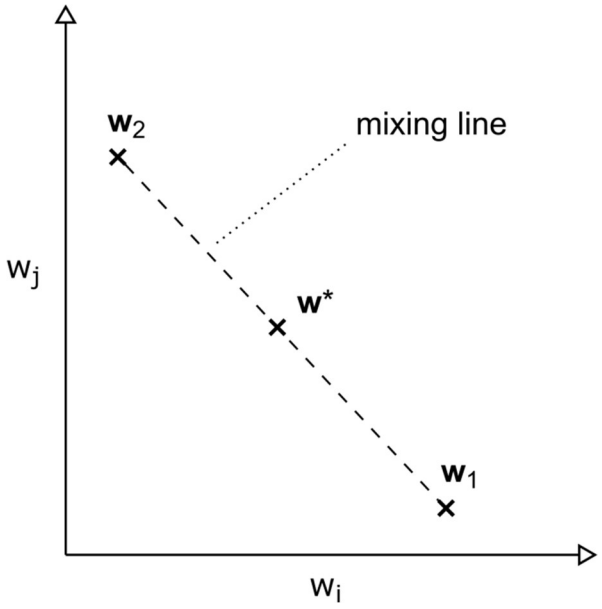

Figure 1: Geometric representation of mixing where w^* is a mixture of w_1 and w_2.

3 RESULTS AND DISCUSSION

Batch milling experiments were performed on Silica in a laboratory ball mill under constant ball filling conditions and mill rotational speed while increasing grinding times in a previous study by Khumalo, et al., (2007). The mill used in this experiment was made of steel with an inside diameter of 180 mm and 255 mm in length. 45 mm diameter steel balls were used. The ground material was classified by sieving using a vibratory sieve shaker and the mass of material in each size class determined by weighing on a laboratory scale. The ratio of aperture size of adjacent screens used was 2.

Table 1: Parameters for the determination of breakage kinetics.

Ball filling (%)	Mill speed (rpm)	a	b	S_1^{∞}	S_2
20	37	0.4141	0.1605	0.1114	0.1758

The ball mill was operated at 20% ball filling and 37 rpm (Table 1). These parameters were used in the PBM to predict how the product PSD changes with time. Size classes were grouped into three size classes; particle sizes greater than 4000 µm (x_1), between 4000 - 2000 µm (x_2) and less than 2000 µm (x_3).

Three feeds ($\mathbf{w}_{f,1}$, $\mathbf{w}_{f,2}$ and $\mathbf{w}_{f,3}$) are considered in this case study. $\mathbf{w}_{f,1}$ is pure silica of coarse material (x_1), whereas $\mathbf{w}_{f,2}$ and $\mathbf{w}_{f,3}$ are binary feeds consisting of coarse (x_1) and intermediate size class particles (x_2).

$$\mathbf{w}_{f,1} = \begin{bmatrix} 1 \\ 0 \\ 0 \end{bmatrix} \qquad \mathbf{w}_{f,2} = \begin{bmatrix} 0.5 \\ 0.5 \\ 0 \end{bmatrix} \qquad \mathbf{w}_{f,3} = \begin{bmatrix} 0.25 \\ 0.75 \\ 0 \end{bmatrix}$$

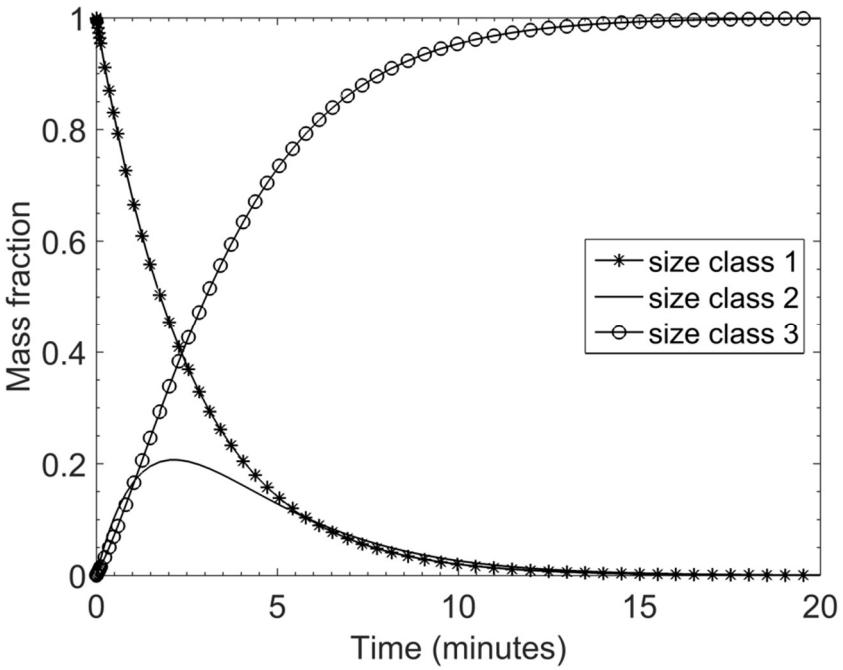

Figure 2a: Predicted mass fraction profiles of three size classes from the feed $w_{f,1}$ using PBM.

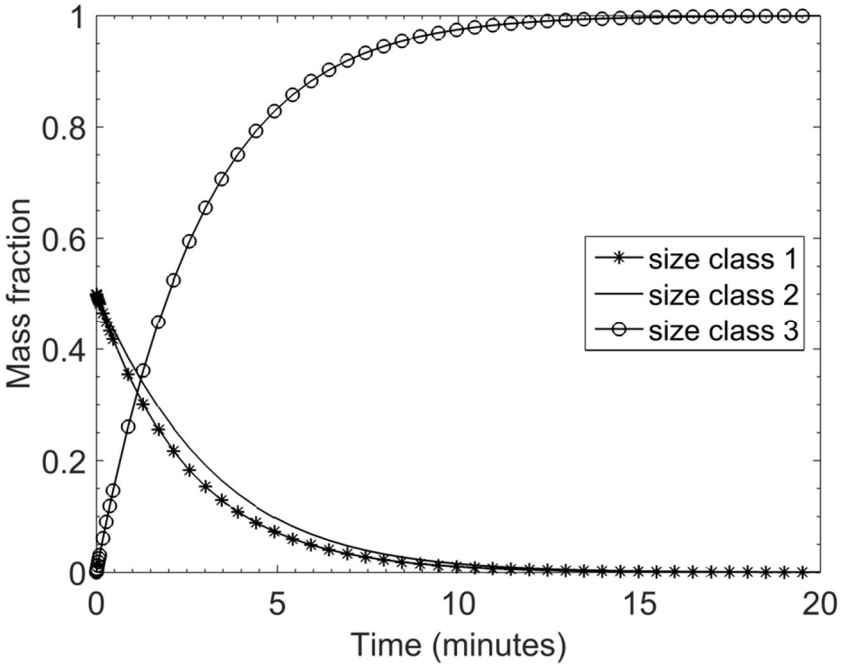

Figure 2b: Predicted mass fraction profiles of three size classes from the feed $w_{f,2}$ using PBM.

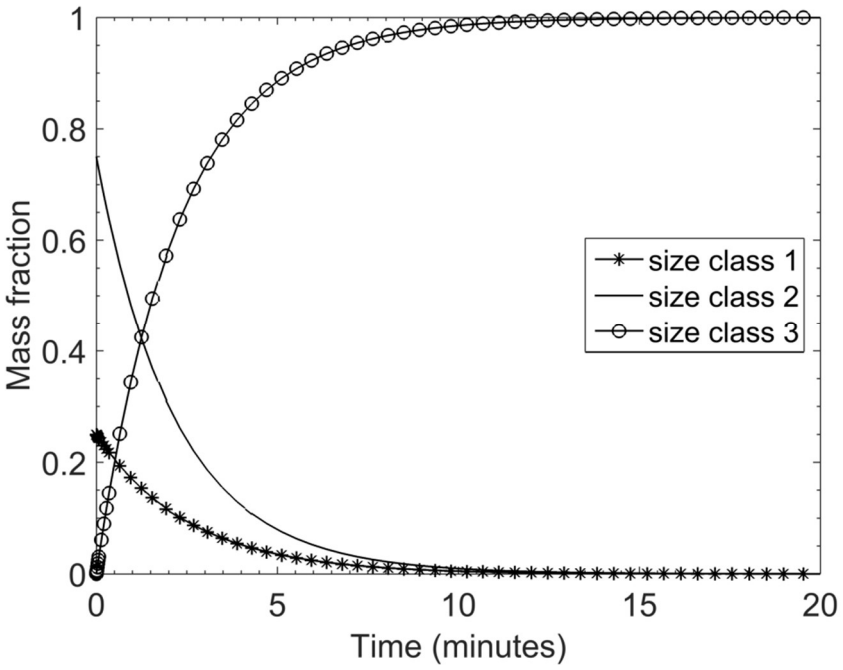

Figure 2c: Predicted mass fraction profiles of three size classes from the feed $\mathbf{w}_{f,3}$ using PBM.

Fig. 2a, b, c show the mass fraction profiles of feeds $\mathbf{w}_{f,1}$, $\mathbf{w}_{f,2}$ and $\mathbf{w}_{f,3}$ respectively. In Fig. 2a, the mass fraction of the largest size class (x_1) continually decreases as breakage in the ball mill occurs, whereas that of the fines (x_3) increases with time through breakage of x_1 and x_2. Intermediates (x_2) initially increase as coarse particles are broken and then decreases after reaching a maximum value near 2.5 minutes. Coarse and intermediate particles are completely broken into fines after approximately 17 minutes. Fig. 2b and 2c show similar profiles although the starting feed points in each plot are different. $\mathbf{w}_{f,2}$ and $\mathbf{w}_{f,3}$ are binary feeds with different proportions of x_1 and x_2 particles. They are broken down and milled until equilibrium at approximately 15 and 13 minutes respectively. From the milling data in Fig. 2a, b, c, we plot the points in mass fraction space, using two variables of interest, by removing the element of time. Although time is not visible in Fig. 3 - 6, it is embedded into the plot; time increases as you move away from the feed point until reaching equilibrium. Furthermore, we annotate these plots (Fig. 3 - 6) with the physical comminution circuit required to achieve that target in mass fraction space.

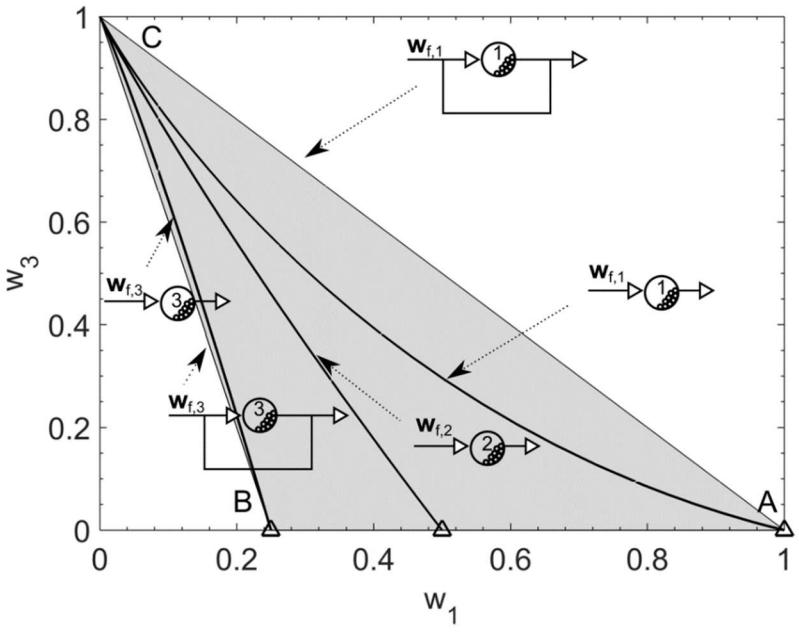

Figure 3: Two-dimensional multiple-feed AR from three feeds in $w_1 - w_3$ mass fraction space.

The number of feeds and their composition of particle size classes inherently influences the physical equipment required to achieve a point in the AR. In Fig. 3 it is shown that $\mathbf{w}_{f,1}$ is fed into Mill 1 whereas $\mathbf{w}_{f,2}$ and $\mathbf{w}_{f,3}$ are fed into Mill 2 and 3 respectively. All three mills have the same dimensions and operate under the same conditions, however they mill different feeds. Through mixing, we construct the AR by finding the convex hull. Mixing operations between the individual mill products are represented by the shaded region. The boundary of the AR is composed of straight and curved lines. Straight lines represent mixing, curved lines represent milling and the shaded interior of the AR is only achievable by mixing between unique points on the boundary of the AR. A combination of the three mills from each feed is required to produce any point within the region. Different portions of the AR are achievable by different milling structure in the system. To produce a mass fraction along the straight line AC, Mill 1 starting from $\mathbf{w}_{f,1}$ with a bypass is required. Any mass fraction along the straight line BC is produced by Mill 3 from the feed $\mathbf{w}_{f,3}$ with a bypass. In this instance, all mass fractions produced from milling $\mathbf{w}_{f,2}$ can be produced by mixing between Mill 1 and 3 from $\mathbf{w}_{f,1}$ and $\mathbf{w}_{f,3}$ as can be seen in Fig. 4.

Eq. 8 expresses how the feed $\mathbf{w}_{f,2}$ is produced by mixing between the two other feeds $\mathbf{w}_{f,1}$ and $\mathbf{w}_{f,3}$,

$$\mathbf{w}_{f,2} = \mathbf{w}_{f,3} + \lambda\left(\mathbf{w}_{f,1} - \mathbf{w}_{f,3}\right) \qquad \textbf{Equation 8}$$

where $\lambda = {}^{1}/_{3}$. Therefore, $\mathbf{w}_{f,2}$ is not required in producing a unique product PSD in this instance. Therefore, Mill 2 is not necessary in the final comminution circuit for the multiple-feed system. If characteristics of the mill are changed the resulting rate of breakage and residence time will change.

However, the required comminution circuit remains the same.

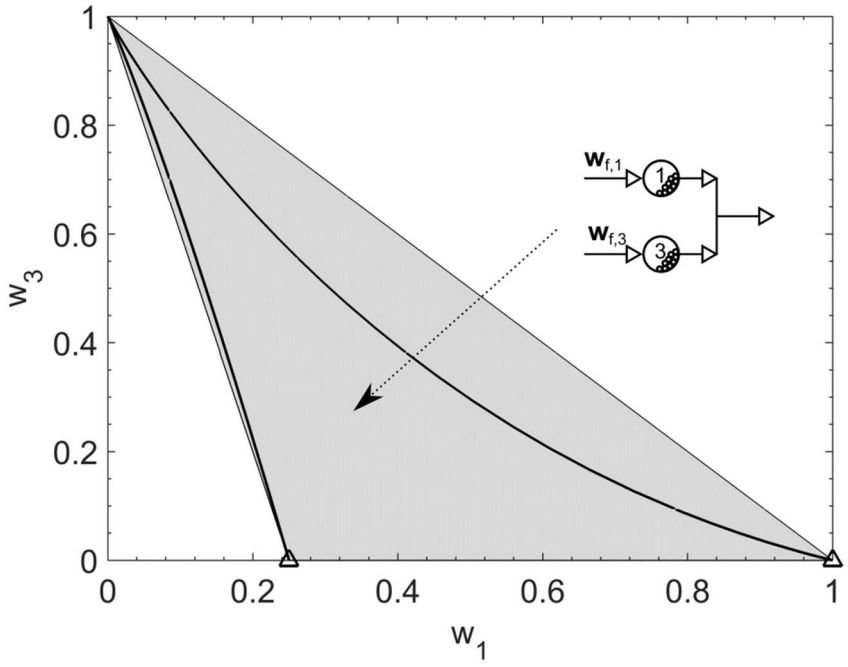

Figure 4: Two-dimensional multiple-feed AR from two feeds in $w_1 - w_3$ mass fraction space.

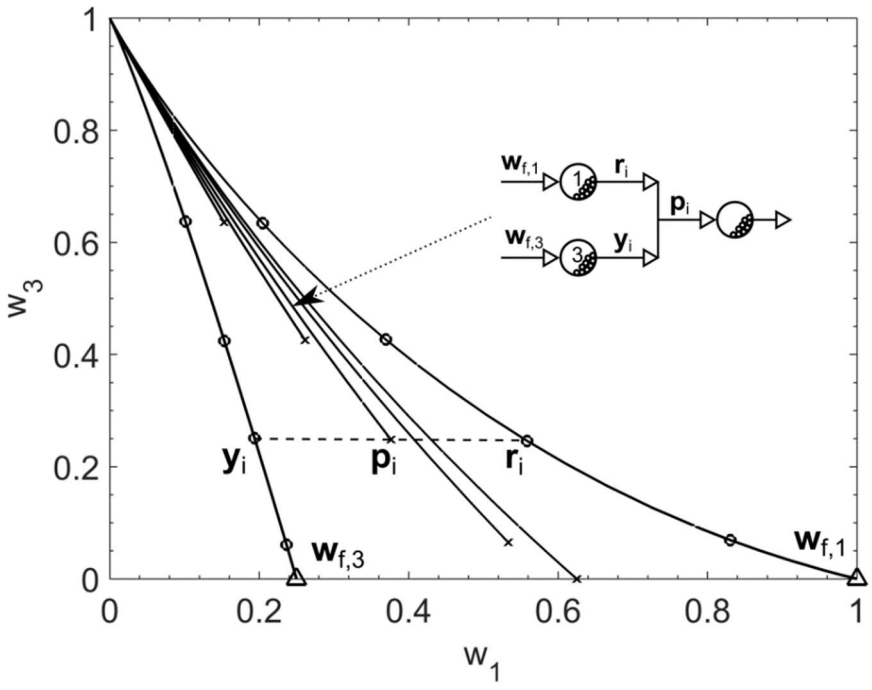

Figure 5: Possible mixtures produced from two mills and the comminution circuit corresponding to the final product.

Once we know which feeds are unique and which ones are not, we can form more mixtures by mixing between the two mils, Mill 1 and 3. Fig. 5 shows a set of mixtures ($\mathbf{p}_i$) produced through mixing

between attainable mill products such that,

$$\mathbf{p}_i = \mathbf{y}_i + \lambda(\mathbf{r}_i - \mathbf{y}_i) \qquad \textbf{Equation 9}$$

Hence, if we change the target product in the AR, we can also formulate the corresponding comminution circuit required to achieve that product as shown in Fig. 6.

This case study shows how multiple feeds influence the product PSD and comminution circuit required to achieve that product PSD. When a single feed is considered the resulting comminution circuit consists of a single mill. However, when multiple feeds are involved, the comminution circuit is made up of multiple mills all operating under the same conditions.

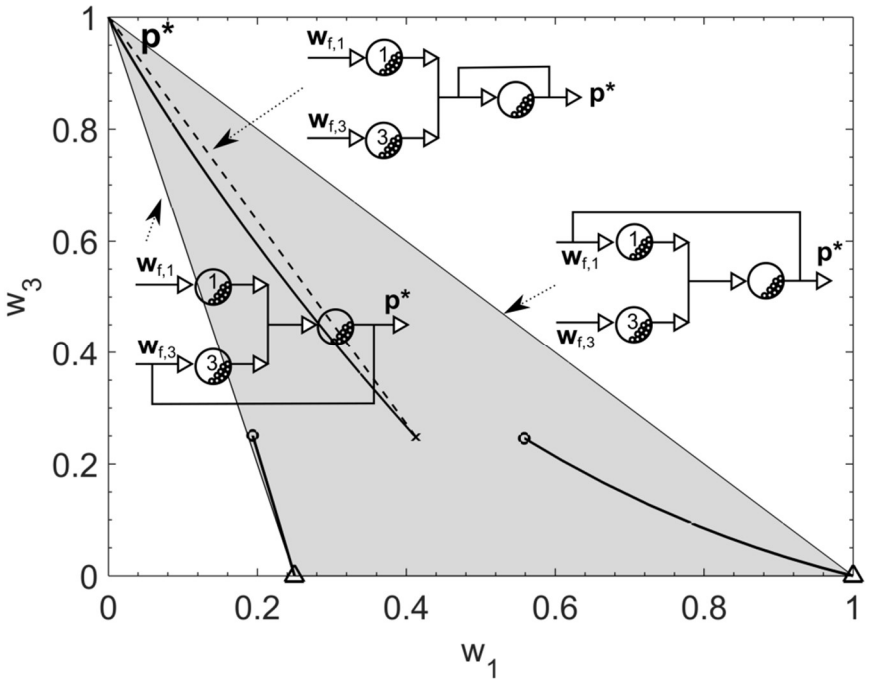

Figure 6: Physical mill structures for achieving different points in the AR.

Mixing coarse and intermediate particles to form a binary feed has been shown to influence breakage rate in the mill and final product quality. When there are intermediates present in the feed, the production of fines is less than that of a pure feed.

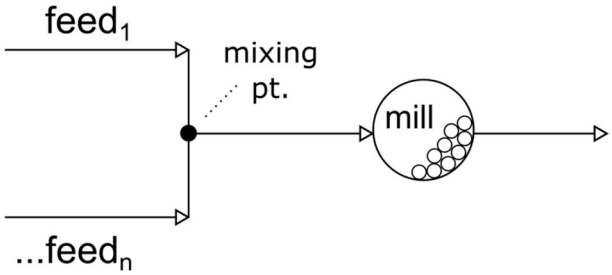

Figure 7a: Physical mill structure for feed mixing in comminution.

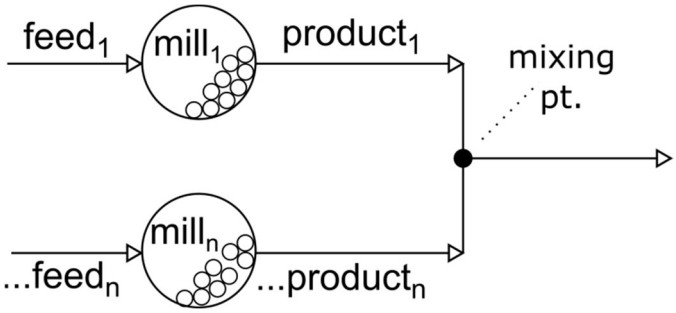

Figure 7b: Physical mill structure for product mixing from multiple feeds in comminution.

Tailoring the feed size distribution by mixing multiple feeds, as shown in Fig. 7a, influences the breakage rate within the mill up to a certain point. Hence, there can be significant time savings thereby reducing operating costs with careful consideration of the number of feeds and their respective feed size distributions. Therefore, the FSD must also be taken into account. As the FSD varies, the breakage rate also varies. When mill products are mixed, unique product size distributions are produced that could not be achieved from a single feed alone (as shown in Fig. 7b). When a single feed is considered the resulting comminution circuit consists of a single mill. However, when all independent feeds were considered, the comminution circuit is made up of multiple mills operating under the same conditions milling a feed with a unique feed size distribution. These mills operate in parallel with a mixing point to combine their respective products. However, if a feed can be produced via mixing other feeds in the system then it is redundant. Hence it is not required to produce the same PSD.

4 CONCLUSIONS

We have seen that when a single feed is considered the resulting comminution circuit consists of a single mill. However, when multiple feeds are involved, the comminution circuit is made up of multiple mills all operating under the same conditions. Mixing coarse and intermediate particles to form a binary feed has been shown to influence breakage rate in the mill and final product quality. When there are intermediates present in the feed, the production of fines is less than that of a pure feed.

As the FSD varies, the breakage rate also varies. When we mix mill products, unique product size distributions is produced that could not be achieved from a single feed alone. When a single feed is considered the resulting comminution circuit consists of a single mill. However, when all independent feeds were considered, the comminution circuit is made up of multiple mills operating under the same conditions milling a feed with a unique feed size distribution. These mills operate in parallel with a mixing point to combine their respective products. However, if a feed can be produced via mixing other feeds in the system then it is redundant. Hence it is not required to produce the same PSD. Therefore, the feed size distribution must also be taken into account.

Multiple feed and product mixing is utilised to reveal a set of mass fraction points that are not

achievable from a single feed alone. Mixing involving multiple mill products uncovers unique product PSDs that could not be achieved from a single feed alone. Each mill in the system operates in parallel with a mixing point to combine their respective products. Hence, the final PSD is a combination of multiple PSDs. Depending on the proportion of each product in the final mixture, an entirely different PSD is produced. Mixing multiple PSDs from different mills vastly increases the set of possible PSDs that can be achieved without changing the physical characteristics of each mill.

REFERENCES

Chimwani, N., Mohale, T., Bwalya, M. M. 2019. Tailoring ball mill feed size distribution for the production of a size-graded product. *Minerals Engineering*, 141.

Chimwani, N., Mulenga, F. K., Hildebrandt, D. 2015. Ball size distribution for the maximum product of a narrowly-sized mill product. *Powder Technology*, 285, pp. 12 - 18.

Glasser, D., Hildebrandt, D., Crowe, C. 1987. A geometric approach to steady flow reactors: The attainable region and optimization in concentration space. *Industrial and Engineering Chemistry Research*, 26, pp. 1803 - 1810.

Hlabangana, N., Danha, G., Bwalya, M. M., Hildebrandt, D., Glasser, D. 2017. Application of the attainable region to determine optimal conditions for milling and leaching. *Powder Technology*, 317, pp. 400 - 407.

Hlabangana, N., Danha, G., Mguni, N. G., Madiba, M. S., Bhondayi, C. 2018. Determining an optimal interstitial filling condition: An attainable region approach. *Powder Technology*, 327, pp. 9 - 16.

Khumalo, N., Glasser, D., Hildebrandt, D., Glasser, D., Hausberger, B. 2007. An experimental validation of a specific energy-based approach for comminution. *Chemical Engineering Science*, 62, pp. 2765 - 2776.

Khumalo, N., Glasser, D., Hildebrandt, D., Glasser, D., Hausberger, B. 2008. Improving comminution efficiency using classification: An attainable region approach. *Powder Technology*, 187, pp. 252 - 259.

Khumalo, S., Hlabangana, N., Danha, G., Muzenda, E. 2019. Effect of media shape on particle breakage in a batch ball mill: Lessons learnt from population balance model and attainable region technique. *Procedia Manufacturing*, 35, 75 - 79.

King, R. P. 2012. Modelling and Simulation of Mineral Processing Systems, Second ed., *Elsevier*, Englewood, CO, USA.

Ming, D., Glasser, D., Hildebrandt, D., Glasser, B., Metzger, M. 2016. Attainable region theory – An introduction to choosing an optimal reactor, First ed., *Wiley*.

Sibanda, V., Khan, R., Danha, G. 2019. The effect of chemical reagents on flotation performance of a pentlandite ore: An attainable region approach. *Powder Technology*, 352, pp. 462 - 469.

Model Predictive Control - Mineral Processing Adopts from Petrochem

K.S. Brooks*

School of Chemical and Metallurgical Engineering, University of the Witwatersrand, Johannesburg, South Africa

*Corresponding author: kevin.brooks@wits.ac.za

ABSTRACT

Model predictive control (MPC) has been a well-established technology in the petrochemical and oil refining industries since the mid-1980s. A survey in 2003 (the latest data publicly available) estimates some 4500 applications, with only 37 being in the mining, minerals and metals (MMM) industry. MMM has been slow to adopt this model-based real-time control and optimisation. Other advanced process control (APC) methods such as rule-based schemes and fuzzy logic were more popular.

This paper provides some hypotheses as to why this was the case, as well as describing the change that has occurred in the industry since the late 2000s. A brief introduction to MPC is given, and a literature review of MPC applications in the industry is provided, together with a summary of the benefits claimed from these applications. An examination of both the industrial and academic literature provides some guidance for future applications, technologies and areas for research.

Keywords: mineral processing; advanced process control; model predictive control; grinding; flotation

1 INTRODUCTION

After something of a slump, the mineral processing industry is set to take off. The World Bank (2017) states that "metals which could see a growing market include aluminium (including its key constituent, bauxite), cobalt, copper, iron ore, lead, lithium, nickel, manganese, the platinum group of metals, rare earth metals including cadmium, molybdenum, neodymium, and indium—silver, steel, titanium and zinc". This is an extensive list (with gold a notable exception). An implication is that current producers of these metals will want to increase production and operate more efficiently. It is in this field that optimising control systems play an important role.

Model predictive control (MPC) is a very well-established technology in the petrochemical and refinery sectors. Benefits of between 2 to 5% of margin are often used as rules of thumb. This translates to between $3.5M to $8.75M per annum for a 100,000 barrel per day refinery. These benefits arise from a combination of improved throughput, yield and energy savings. The latest review of industrial applications available (Qin and Badgwell, 2003) lists some 2500 applications in these sectors, but only 37 in the mining and metallurgical field.

In the minerals area, MPC has been a rich field of research in academia. As an example, an excellent review by Quintanilla et al (2020) of froth flotation control has 123 references; on an admittedly rough

count, only 16 of these have some industrial element. The authors state that "The analysis of the literature on the topic has shown that little evidence on successful MPC implementation in flotation at industrial scale is available. There remains a need for further research to enhance modelling for flotation control purposes". The first statement is demonstrably true, but this paper will attempt to demonstrate that the latter statement is not. The reason lies in the difference between the academic approach to MPC, and the industrial one. The academic approach is to derive first principles-based models because the researchers do not have access to a plant and so need a model to prove their particular control approach. The industrially proven approach is to generate an accurate empirical model for a particular plant. These "curve fit" models (as one of the author's ex-student now in academia once derogatorily referred to them as) are used in MPC to generate fast returns on investment for the company.

The remainder of this paper is arranged as follows. Section 2 gives an introduction to MPC and the use of empirical linear dynamic models. Section 3 lists successful industrial applications in the minerals industry and discusses why uptake has been slow. Section 4 provides some conclusions.

2 INTRODUCTION TO MPC

2.1 MPC Overview

As its name implies, MPC uses models of a plant to achieve multi-input multi-output (MIMO) control. The design process consists of identifying the outputs that need to be controlled in a range or at setpoints; these are known as the *controlled variables* (CVs). The inputs that can be changed to affect the CVs are the *manipulated variables* (MVs). The MVs are in general the setpoints the operators already use to control the plant. In addition, there may be variables that affect the CVs but cannot be manipulated; these are known as *disturbance variables* (DVs) or *feedforwards* (FFs).

The models used in the majority of industrial MPC implementations are linear dynamic models. These are obtained experimentally, by performing step-tests on the plant to allow for accurate system identification. A pre-step of approximately one week is performed to generate a seed model. This model is then used to perform automated stepping (Kalafatis et al, 2006). The step test period depends on the number of MVs and the settling time of the process but is typically in the region of one to two weeks.

Step testing is a tedious phase of the application design because it has to be performed in a manner that does not cause large negative impacts on the stability and performance of the plant but does yield the data required for the detection of appropriate responses. There will be disturbances to the circuit, but this is necessary to develop an accurate model.

The step test data is used in a custom program that generates different linear dynamic formulations, depending on the vendor. Typical examples are finite impulse response (FIR), sub-space (SS), prediction error models (PEM) auto-regressive with exogenous input (ARX) models, although others

are used (Shardt, 2015). The most appropriate models are used to generate a final model matrix, an example of which is shown in Figure 1.

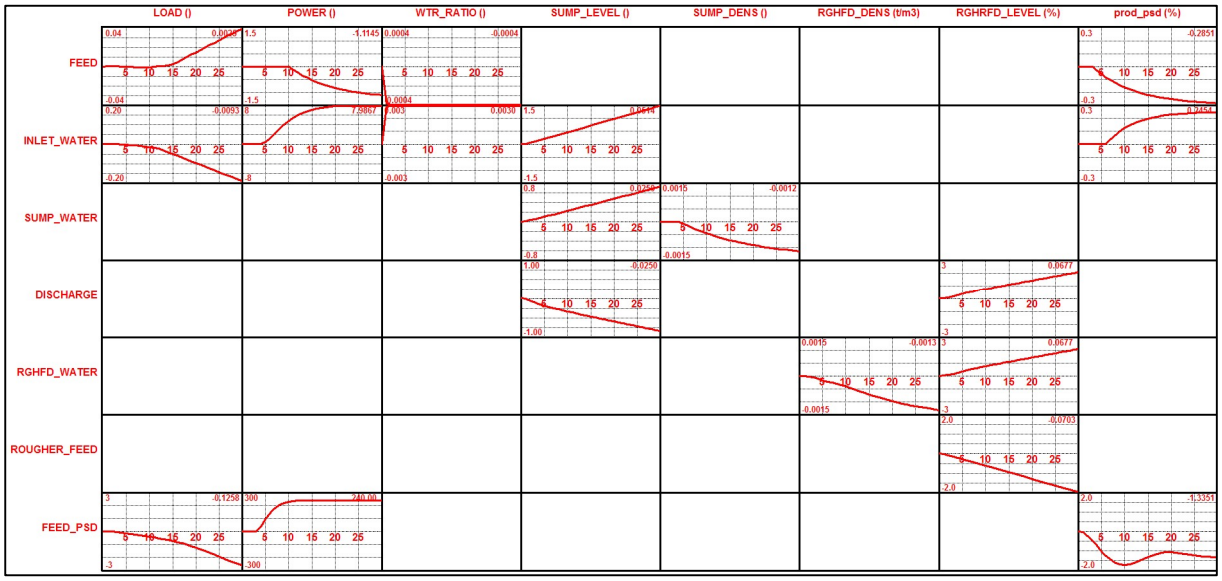

Figure 1: Unit Step Response Models for a Mill (time scale in minutes)

The curves shown in each cell of this matrix are known as *unit step responses*; they are the dynamic response of a CV to a unit change in an MV or FF. Whatever the particular modelling technique the results can be represented in this form. The time axis extends to the measured time to steady-state (TTSS) of the system. The matrix has the MVs and FFs as rows, with the CVs as columns.

Armed with these models, together with some tuning parameters, the MPC application can calculate the:

- Optimum steady-state operating point for the system
- The optimum dynamic path of the CVs
- The MV moves are needed to achieve these changes?

The MPC performs these calculations every minute (or faster if necessary). The calculation is performed for the control horizon of the controller, but only the first move is implemented.

2.2 Model and Control Formulation

While there are several formulations used for MPC, the dynamic matrix control (DMC) algorithm remains the most popular and will be described here. The models are assumed to be linear and the prediction of an output is given by (Garcia et al., 1989):

$$y(k) = \sum_{i=1}^{n-1} H_i \Delta u(k-i) + H_n u(k-n) \qquad \textbf{Equation 1}$$

where:

$y(k)$ is an output at time k

n is the number of coefficients

$u(k)$ is an input at time k

$\Delta u(k) = u(k) - u(k-1)$

H_i are the step response coefficients

Equation 1 is written for a single input but is easily generalised to multiple inputs, recalling that the models are linear and therefore the outputs may be superimposed. To calculate the control moves the algorithm minimises the following quadratic function by choice of the moves $\Delta u(k) \ldots \Delta u(k+m-1)$ (Garcia et al., 1989):

$$\sum_{l=1}^{p} \|\hat{y}(k+1|k) - r(k+l)\|_{\Gamma_l}^{\ 2} + \|\Delta u(k+l-1)\|_{B_l}^{\ 2} \qquad \textbf{Equation 2}$$

$$\hat{y}(k+l|k) = \sum_{i=1}^{l} H_i \Delta u(k+l-i) + \sum_{i=l+1}^{n-1} H_i \Delta u(k+l-i)$$

$$+ H_n \Delta u(k+l-n) + \hat{d}(k+1|k) \qquad \textbf{Equation 3}$$

$$\hat{d}(k+1|k) = y_m(k) - \sum_{i=1}^{n-1} H_i \Delta u(k-i) + H_n \Delta u(k+l-n) \qquad \textbf{Equation 4}$$

$$\sum_{i=1}^{p} C_{yl}^{j} \hat{y}(k+l|k) + C_{ul}^{j} u(k+l-1) + c^{j} \leq 0;\ j = 1, n_c \qquad \textbf{Equation 5}$$

where

$\hat{y}(k+l|k)$is the predicted value of y at time $k+l$ based on information at time k

$\hat{d}(k+l|k)$ is the predicted value of additive disturbances at time $k+l$ based on information at time k

$y_m(k)$ is the measurement of y at time k

$\Delta u(k+l) = u(k+l) - u(k+l-1)$

Hi, $i=1,n$ are the model step response matrix coefficient

n is the truncation order

n_c is the number of constraints

p is the horizon length

m is the number of manipulated variable moves in the future

$$\|x\|_Q^{\ 2} = x^T Q x$$

Γ_l and B_l are weighting matrices and C_{yl}^j, C_{ul}^j, c^j are constant matrices

Equations 2 to 5 define a quadratic program. This is solved online at every time step. Before solving the dynamic problem, the algorithm checks for steady-state feasibility by solving the problem:

$$\min \phi = \sum_{i=1}^{n_c} \epsilon_i^2 W_i \qquad \textbf{Equation 6}$$

subject to

$$\hat{y}_{i,ss} \leq y_{i,max} + \varepsilon_i \qquad \textbf{Equation 7}$$

$$\hat{y}_{i,ss} \geq y_{i,min} - \varepsilon_i \qquad \textbf{Equation 8}$$

where

ϕ is the objective function value, ϵ_i is a slack variable and W_i is a weight,

$\hat{y}_{i,ss}$ is the steady-state value of CV i and $y_{i,max}$ and $y_{i,min}$ are the high and low limits on CV i.

The objective function in equation 6 is minimised subject to the current constraints on the MVs and CVs. If there are slack variables that are non-zero, this implies the steady-state solution is not feasible. In this case, the CV limits are relaxed until the solution is feasible.

Should the minimisation of equation 6 prove that all the slack variable values are zero, then there exist one or more feasible steady-state solutions. In this case, the following economic optimisation is solved:

$$\min J = \sum_{i=1}^{N_i} c_i \, \Delta u_{i,ss} + \sum_{j=1}^{N_j} c_j \, |\Delta u_{j,ss}| \qquad \textbf{Equation 9}$$

where

J is the objective function value,

N_i is the number of MVs that have economic directions,

N_j is the number of MVs whose movement is to be minimised,

c_i and c_j are cost factors.

The $\Delta u_{i,ss}$ and $\Delta u_{j,ss}$ are the change in values of the MVs from the present time to the values at a

steady state. These are the variables chosen to minimise equation 9 subject to the MV and CV constraints. The steady-state values of the MVs are imposed on the solution as further constraints to equation 2.

2.3 Practical Implementation

The mathematics presented above are important in understanding how the solution is obtained, but not required by the practitioner of MPC technology. Having purchased a brand of MPC, the MPC engineer's job consists of:

1. Understanding the control and optimisation problem posed by a particular unit, and estimating the benefits from improving operation
2. Designing the MPC, by defining the inputs and outputs, control and optimisation objectives
3. Performing the necessary step testing to obtain the linear models.
4. Testing the MPC offline in simulation
5. Commissioning the MPC online, including training operations personnel.
6. Auditing the benefits obtained

The implementation details will not be discussed here; suffice it to say that generally the MPC process runs on a separate computer on the plant process control network, and communicates with the plant control system (PCS) via a standard client-server communication protocol called OPC.

Depending on the size of the unit in question, this process may take from 2 to 4 months. The amount of work scales with the number of inputs, although the time to steady-state of the system also plays a role.

3 MPC IN THE MINERALS INDUSTRY

Despite the demonstrated benefits, the technology is not yet embedded in the mining, minerals and metallurgy (MMM) field. Rogers et. al (2019) provide references to some 30 papers on MPC, but many of them are academic studies using simulated processes. The papers referenced in Rogers et. al. (2019) are summarised in Table 1.

Table 1: Analysis of references from Rogers et. al (2019)

Process Area	No of references	Industrial Applications
Grinding and Milling	15	4
Flotation	7	1
Thickeners	3	0
Other	4	1

Caution must be applied in analysing the results from one paper, but it is certainly true that there is

much more academic work on MPC reported than industrial applications. As mentioned, Quintanilla et al (2021) have a reference list in froth flotation of 120 odd papers; not all of these are MPC related.

The data backs up the comment by Bergh and Yianatos (2011) in a review of the progress in flotation control: "after more than one hundred years of history, there are few reports on applications of novel techniques in monitoring and control of flotation units, circuits and global plants".

The author and co-workers began implementing MPC together with Anglo Platinum in the late 2000s, with great success. Published papers from this work include Singh et.al (2010), Muller et. al (2010), Steyn et.al (2010), Steyn and Sandrock (2013) and Steyn and Brooks (2017)., Subsequently, work has been performed on the flotation of copper (Brooks & Munalula, 2017), lead and zinc flotation (Brooks & Koorts 2017, Price et. al, 2018), and on the base metal refinery of a platinum operation (Brooks, Burchell & Pieterse, 2017). Excellent results for the control of autoclaves in a nickel operation have also been reported (Brooks et. al, 2019).

Bouffard (2015) lists seven applications in grinding, with throughput gains ranging from 2% to 10%.

3.1 Published industrial benefits

In the literature on MPC in the oil refining and petrochemical industries, there is a reasonable amount of data on the financial benefits of implementing the systems. Robinson and Cima (2006) give a table of benefits for the application of MPC to seven different typical refinery operations. Annual benefits range from 0.02 to 0.10 $US/bbl for a hydrotreater to 0.15 to 0.30 for a fluidised catalytic cracking (FCC) unit. For a mid-size 100,000 barrel per day refinery, this translates to $0.7M to $3.5M for the hydrotreater, and $5.25M to $10.5M for the FCC. In the author's experience, the latter figures may be on the high side; nevertheless, a typical MPC project has a payback of less than six months.

In mineral processing published benefits are harder to find. Bouffard (2015) reports published benefits from twenty milling applications, (some of which employ technologies other than MPC). Throughput benefits for the four MPC applications reported range from 2 to 10%, with variability improvements of 46 to 66%. These benefits are reported to be in the same range as other technologies such as expert systems and fuzzy logic. Steyn and Sandrock (2013) discuss an MPC application on an autogenous mill with a variable speed drive; A 2.2% increase in product passing 75 µm is reported, with an indicated recovery increase of 0.32% through the whole circuit. The possible inaccuracies in this calculation are emphasised.

In the flotation area, Brooks and Koorts (2017) and Price et. al (2018) report an MPC application on a zinc flotation bank. Reductions of 21% in the use of the copper sulphate activator and 38% in the sodium ethyl xanthate collector were reported, with a small increase in recovery. These regent reductions represent very significant monetary savings. Brooks and Munalula (2017) discuss an MPC

cascade strategy for flotation of copper ore; a 4.5% increase in the recovery of total copper is reported.

Gouveia et. al (2009) describe an MPC scheme on a nickel reduction roaster. A 30% reduction in variability in the roaster together with a 2% increase in energy efficiency and 1.2% increase in nickel recovery is reported. Steyn and Brooks (2017) describe an MPC application designed to de-bottleneck a converter process and associated acid plant; a 27% increase in throughput was obtained. Brooks et. al (2017) applied MPC on an autoclave treating matte containing copper minerals and platinum group metals. Tight temperature control is necessary since a decrease in leaching temperature will prevent the leaching of ruthenium, rhodium and iridium (OPMs) without limiting copper leaching. An increase of 9% in plant throughput and a reduction of 50% in OPM leaching was observed.

In the alumina field, Jonas (2004) reports a conservative benefit for a 1,000,000 tonne per annum plant of $2.17M per annum. Nearly half of these benefits accrue from the milling and calcination areas of the plant. These calculations were based on an alumina price of $170/tonne, while current prices are in the region of $300/tonne.

3.2 Why the slow uptake?

Given the demonstrated benefits of MPC technology on a variety of mineral processing operations, why is the uptake of the technology still limited? Some of the reasons and discussed below, in no particular order, with the author's responses.

3.2.1 Mining companies in general being slow adopters of technology, Resistance to the use of modelling as a tool in mining

In this time of 4IR, AI, ML, digitalisation this is less of an issue than it was. Nevertheless, the practically oriented mindset of many operations people in the mining industry can present a barrier to adoption. More case studies of the kind mentioned in this paper can assist.

3.2.2 A belief that these complicated solutions get switched off very quickly

This may not be limited to MPC solutions, but digital solutions in general. While extremely important, An in-depth discussion of the embedding, management of change, change management, training, maintenance and ongoing care for MPC solutions is beyond the scope of this paper. Suffice it to say that all these areas need to be considered and planned at the outset of an MPC program. We should certainly be training our engineering students to be able to present to and train people in other disciplines.

3.2.3 Other advanced control technologies are preferred (fuzzy logic, expert system or advanced regulatory control)

These methods were employed before MPC and remain popular, with software and services supplied by well-respected companies. It is not the aim of this paper to give an in-depth comparison of different APC techniques. The chief advantage of MPC is that is it is inherently optimising, whereas including

optimisation in the fuzzy or rule-based systems can lead to rule explosion, in turn leading to complex maintenance. The advanced regulatory control methods have the advantage of not requiring additional software to that in the PCS; the chief disadvantage is that these schemes quickly become very complex, and can only be maintained by the engineer who developed them.

3.2.4 High initial cost, even acknowledging good returns on investment

This is a matter of the operation's appetite for risk. The publication of more case studies where MPC has proven its value will assist in making it easier for companies to adopt the technology.

3.2.5 Doubts about the use of linear models

Chemical and metallurgical engineers are taught first principles-based steady-state modelling; these models are by their very nature non-linear. When the empirical linear dynamic models used in industrial MPC are presented for the first time there can be resistance to the useability and accuracy of such models. The response to this is that the step tests are conducted at a typical operating point, and the models obtained can thus be thought of as a first-order Taylor series expansion of the true non-linear behaviour. In addition, the algorithm incorporates feedback, which can compensate for a certain amount of plant model mismatch. If the non-linearities are mild they can be handled using a technique known as gain scheduling (Brooks et al, 2014). If the non-linearities are severe it is possible to implement a non-linear MPC, although published industrial applications are rare.

4 CONCLUSIONS

The industrial application of MPC in the minerals industry has been described, with reference to the limited literature. The academic literature is replete with process models, mostly based on first principles type models. By contrast, the mathematical basis of the DMC algorithm has been presented, illustrating how a linear empirical model-based formulation leads to a quadratic program based solution, the solution of which is available in several commercial packages. The considerable financial benefits of MPC have been documented, and some reasons for the slow uptake of the technology in the minerals industry are discussed, together with a plea for more industrial case studies.

REFERENCES

Agostino, D. ', & Gl, G. 2012. Dynamic Real-Time Optimiser for Precipitation Solids Control, pp. 250–252.

Brooks, K. S., Carr, A., Dreyer, R. P., & Maksa, M. 2014. Energy and emissions optimisation at Chevron Cape Town. In *IFAC Proceedings Volumes (IFAC-PapersOnline)* (Vol. 19, pp. 1278–1283.

Brooks, K.S. and Koorts, R., (2017. Model predictive control of a zinc flotation bank using online X-ray fluorescence analysers. *IFAC-PapersOnLine*, *50(1),* pp.10214-10219.

Brooks, K. and Munalula, W., 2017. Flotation Velocity and Grade Control Using Cascaded Model

Predictive Controllers. *IFAC-PapersOnLine, 50(2),* pp.25-30.

Gouveia, R., Lewis, D.G., Restrepo, A., Rodrigues, L.A. and Gedraite, R., 2009. Application of model-predictive control to multi-hearth nickel reduction roasters. *IFAC Proceedings* Volumes, 42(23), pp. 292-296.

Jonas, R. K. 2004. Application and benefits of advanced control to alumina refining. In *TMS Light Metals* , pp. 43–49.

Kalafatis, A., Patel, K., Harmse, M., Zheng, Q., & Craik, M. 2006. Multivariable step testing for MPC projects reduces crude unit testing time: Clean fuels. *Hydrocarbon processing (International ed.)*, 85(2), pp. 93-100.

Muller, D., De Villiers, P. G. R., & Humphries, G. 2010. A holistic approach to flotation mass pull and grade control. *IFAC Proceedings Volumes, 43(9),* pp. 133-136.

Oliveira, A., Batista, J., Santos, J., Ribero, M., Charr, J., & Lopes, R. 2009. Advanced process control in alumina digestion unit. *Light Metals*.

Price, A, Okle, D and Brooks, K, 2018. Glencore Mount Isa lead zinc flotation circuit – experiences from the implementation of model predictive control, in P*roceedings 14th AusIMM Mill Operators' Conference 2018*, pp 101–110 (The Australasian Institute of Mining and Metallurgy: Melbourne).

Quintanilla, P., Neethling, S. J., & Brito-Parada, P. R. 2020. Modelling for froth flotation control: A review. *Minerals Engineering*, 106718.

Robinson, P.R. and Cima, D., 2006. Advanced Process Control. *In Practical Advances in Petroleum Processing* (pp. 695-703). Springer, New York, NY.

Rogers, W.P., Kahraman, M.M., Drews, F.A., Powell, K., Haight, J.M., Wang, Y., Baxla, K. and Sobalkar, M., 2019. Automation in the Mining Industry: Review of Technology, Systems, Human Factors, and Political Risk. *Mining, Metallurgy & Exploration*, pp.1-25.

Singh, A., De Villiers, P. G. R., Rambalee, P., Gous, G., De Klerk, J., & Humphries, G. 2010. A holistic approach to the application of model predictive control to batch reactors. *IFAC Proceedings Volumes,* 43(9), pp. 127-132.

Shardt, Y. A. 2015. *Statistics for chemical and process engineers*. Springer International Publishing: Berlin, Germany.

Steyn, C. W., Brooks, K. S., De Villiers, P. G. R., Muller, D., & Humphries, G. 2010. A Holistic Approach to Control and Optimization of an Industrial R Ball Milling Circuit. *IFAC Proceedings Volumes, 43(9)*, pp. 137-141.

Steyn, C.W. and Brooks, K.S., 2017. De-bottlenecking of the Anglo Platinum Converting Process Utilising Advanced Process Control. *IFAC-PapersOnLine, 50(2),* pp.1-6.

Steyn, C.W. and Sandrock, C., 2013. Benefits of optimisation and model predictive control on a fully

autogenous mill with variable speed. *Minerals Engineering*, 53, pp.113-123.

World Bank Group. 2017. *The growing role of minerals and metals for a low carbon future*. World Bank. Bouffard, S.C., 2015. Benefits of process control systems in mineral processing grinding circuits. *Minerals Engineering*, 79, pp.139-142.

Phase equilibria study of the Cu-K_2O-SiO_2-O system in air

W.D. Malan[1*], P. Taskinen[2], C. Dorfling[1], S. Bradshaw[1] and G. Akdogan[1]

[1] Department of Process Engineering, Stellenbosch University, Banghoek Rd, 7599, South Africa

[2] Metallurgical Thermodynamics and Modelling, School of Chemical Engineering, Aalto University, Finland

*Corresponding author: wmalan@sun.ac.za

ABSTRACT

In this study, the liquidus of the copper-potassium oxide-silica-oxygen (Cu-K_2O-SiO_2-O) system at silica saturation in equilibrium with air was studied experimentally between 1273 and 1773 K. Equilibration was carried out in vertical tube furnace, followed by rapid quenching and measurement of phase structures and assemblages using SEM-EDS and electron probe microanalysis technique. The results are in relatively good agreement with calculated liquidus contours from the MTOX database in MTDATA. Therefore, the results from this study may now be used for future thermodynamic assessments.

Keywords: Cu smelting, slag, thermodynamics, liquidus, phase diagram

1 INTRODUCTION

In this study, phase equilibria of the Cu-K_2O-SiO_2-O system in equilibrium with air have been investigated using the equilibration/quench/analysis technique up to 1773 K. The technique has been used extensively to obtain high temperature information for metallurgy, in particular for systems containing silica [18]. The silica-containing liquid converts rapidly to glass when quenched, thereby preserving phase assemblages at high temperatures. Compositions of equilibrated phases were measured with EPMA and SEM-EDS, respectively. The liquidus results from these experiments may subsequently be used to determine a set of self-consistent model parameters, which will allow us to extract property data from molten silicate melts containing Cu_2O and K_2O.

2 LITERATURE

In an earlier study, [1] the K-O-Si system in equilibrium with air was investigated and its industrial importance was articulated. This system was studied experimentally by means of the equilibration/quench/analysis technique at temperatures ranging between 770 °C and 1500 °C. Equilibrium at temperatures below 1000 °C was confirmed by long equilibration times, variation of initial composition, different preheating temperatures, sample homogeneity and sizes of less than 0.2 g. Phase compositions, structures and assemblages were measured with SEM-EDS (scanning electron microscope with energy dispersive spectrometry) and electron probe X-ray microanalysis technique. The results from both analytical techniques were in good agreement with the earlier work of Kracek et

al. [2], but the data showed lower solubility of SiO_2 in the liquid phase below 1100 °C. Similarly, the liquidus compositions of the SiO_2 primary phase field in the binary K_2O-SiO_2 system obtained by Santoso et al. [3] are in a good agreement with liquidus at and above 1100 °C. In addition, the data by Akdogan et al. [1] might suggest that $K_2Si_4O_9$ melts incongruently, as proposed by Zaitsev et al. [4], and not congruently as conceived by the thermodynamic assessment studies [5, 6, 7, 8, 9, 10]. The only major difference in these assessment studies is the model used to describe the liquid phase. Moreover, in all these studies, phase equilibria can only be estimated accurately in the SiO_2 rich region, because of the shortage of experimental data on the K_2O rich region.

In the more recent experimental investigation and thermodynamic assessment, Kim et al. [10] used a thermal analysis technique with sealed Pt crucibles to measure the eutectic transition temperature between K_4SiO_4 and K_2SiO_3. The focus of the experiment work was on the K_2O rich region of the K_2O-SiO_2 system in order to expand the reliability of the assessment beyond 50 % K_2O. The authors proceeded to thermodynamically evaluate the system by considering their experimental data points. Liquidus data of the $K_2Si_4O_9$-SiO_2 region from Kracek et al. [2] were included in the optimisation, but the data by Akdogan et al. [1] were omitted due to open crucibles used in their study. This supposedly caused deviations in sample composition during equilibration because of the hygroscopic and volatile nature of K_2O. However, no references were provided as to why open crucibles cannot be used to determine equilibrium in the K_2O-SiO_2 system. Furthermore, no such observations were made by Akdogan et al. [1] or Meshalkin and Kaplun [11]. This might be the case for samples containing less than 50 % SiO_2 and exposed to a humid atmosphere as was observed by Kracek et al. [2]. Akdogan et al. [1] only made mention to the sensitivity of polished sections to moisture in ambient atmosphere. No inhomogeneities were found in the liquid phase.

According to authors no mass gain or loss occurred amid equilibration and quenching [1] (private discussions 2018). Regarding the volatility of K_2O; there are good correlation between the results from Akdogan et al. [1], Kracek et al. [2] and Santoso et al. [3] at and above 1100 °C, signifying that K_2O in samples did not volatilize amid equilibration in an open crucible. Given the evidence, it is our collective consensus that the data from Akdogan et al. [1] and Meshalkin and Kaplun [11] are tangible and should not have been omitted from the optimisation of thermodynamic properties by Kim et al. [10].

Besides sub-solidus data from studied binary systems, no study has attempted previously to estimate the liquidus in the Cu-K_2O-SiO_2-O system experimentally or theoretically. It is possible to estimate the liquidus using optimised parameters from binary sub-systems, but there are no thermodynamic or phase diagram data of the Cu_2O−K_2O system available in the literature [12]. As a result, Samoilova

et al. [12] derived the Cu_2O-K_2O phase diagram and other system properties by extrapolation from the Cu_2O-Na_2O-K_2O system. From the general description of the FToxid database documentation in FactSage 7.3, it was noted that systems containing Cu_2O have been optimized with major oxide components limited to Al_2O_3, CaO, FeO, Fe_2O_3, MgO and SiO_2. Moreover, this was done only over limited composition ranges, generally for SiO_2-rich slags and in the composition region of fayalite slags [13].

Although the Cu-O-SiO_2 system has attracted more interest such as the recent assessment by Hidayat and Jak [14] at Cu saturation and the equilibrium study by Xia et al. [15] at various oxygen partial pressures, it has not been fully optimised in the FToxid database. Therefore, any equilibrium calculation of the Cu-K_2O-SiO_2-O system using the FToxid database may result in significant error and will be amplified by the positive deviation from ideal behaviour caused by SiO_2. When the modified quasichemical model is used to describe the slag phase, as in the case of the FToxid database, ternary and multicomponent systems containing SiO_2 often require an asymmetric ternary interpolation model and ternary parameters to reproduce phase diagram data within acceptable error limits [16, 17]. This stresses the need for experimental studies on the Cu-K_2O-SiO_2-O system.

3 EXPERIMENTAL PROCEDURE

3.1 Sample Preparation

The starting materials used for the experiments were Cu_2O(s), SiO_2(s) and K_2CO_3(s). The material, source and purity are given in Table1. Mixtures of selected bulk compositions were prepared by weighing the oxide powders, followed by mixing them thoroughly using an agate mortar and pestle. The mass of all samples were below 0.2 g. The advantage of a small pellet is the sample is brought to equilibrium at a faster rate during quenching, thereby contributing to a homogeneous phase assemblage.

Table 1 : Purity of initial materials and sources from which they were acquired.

Material	Source	Purity
Cuprous oxide powder	Umicore, Belgium	99.5%
Silica Powder	Umicore, Belgium	>99.99 %
Potassium carbonate Powder	SIGMA ALDRICH, RSA	99.5%

The bulk compositions were estimated with the assistance of the lever rule to assure we have a sufficient amount of slag and solid phases for SEM-EDS analysis and EPMA. Given the shortage of data, and shortcomings in the FToxid database on this system, FactSage could not be used to estimate initial compositions. Therefore, the initial compositions were selected from phase diagrams calculated by MTDATA software and its Mtox 8.2 database, since preliminary test results revealed better

agreement with phase diagrams from MTDATA compared to those from FactSage [19]. We assumed that superior agreement with phase diagrams from MTDATA is attributed by the complete assessment of the Cu-SiO_2-O system and the description of the liquid phase with the modified associate species model, which in this case may require no or less ternary parameters to reproduce liquidus more accurately compared to the modified quasichemical model (MQM). The latter model is used to describe slag phases in FactSage.

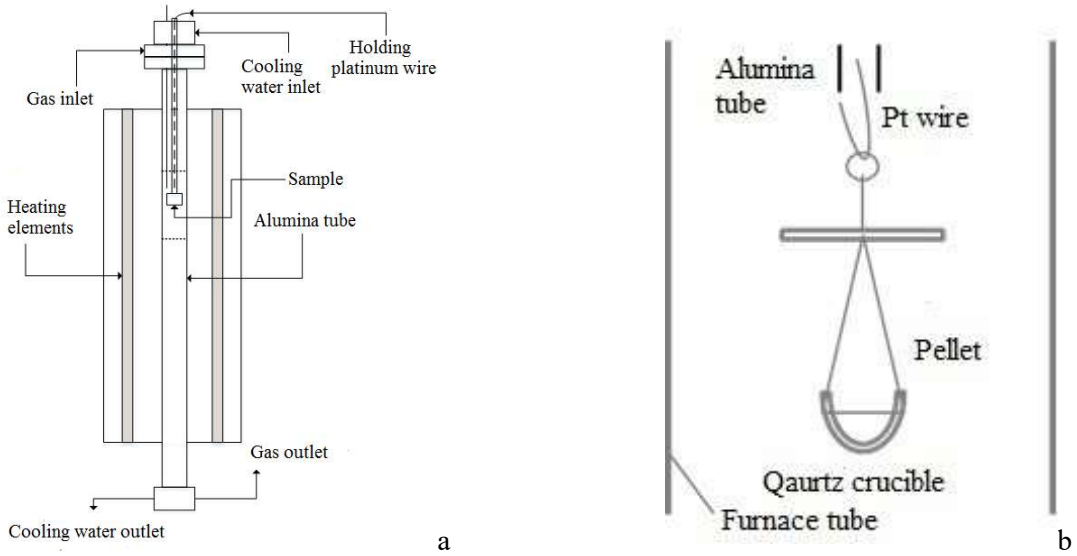

(a) a Schematic of the vertical front view section of the furnace and auxiliaries.

(b) Suspension of the pellet and crucible in the hot zone of the alumina furnace work tube.

Figure 1: Furnace and suspension design

An example where ternary interaction parameters was required to reproduce experimental observations, was in the assessment of the Cu_2O-SiO_2-CaO system [14]. Hidayat and Jak [14] used the MQM to describe the liquid phase. Moreover, an asymmetric Kohler/Toop interpolation method with SiO_2 as asymmetric component was used to carry out calculations [14]. Supported by the inclusion of ternary interaction parameters by Hidayat and Jak [14], the utilisation of an asymmetric ternary interpolation method and shortage of data in the Ftoxid database on the Cu- SiO_2-O system, we substantiated our assumption that FactSage produces large systematic errors for the investigated system. Liquidus results from this study are compared to liquid contours calculated with FactSage in section 3.

A quartz crucible with an inner diameter of 8 mm and depth of 5 mm, made by fusing high-purity silica rod, was used to contain samples.

3.2 Experimental Procedure

All equilibration experiments were carried out in a vertical electrical resistance tube furnace (Lenton, UK) with a 38 mm inner diameter alumina work tube (Friatec AG, Germany; impervious recrystallised

alumina) (Figure 1a). The maximum operating temperature of the furnace is 1600 °C.

Before experiments were carried out, a thermal profile of the furnace worktube was determined in order to identify the hot "spot/zone". The S-type thermocouples were calibrated against the melting point of copper and ice water, respectively. A calibrated S-type thermocouple connected to a Keithley 2010 DMM multimeter (Cleveland, OH, USA) and a cold junction compensation was connected to a Keithley 2000 multi-meter (Cleveland, OH, USA) to measure the ambient temperature with a PT100 sensor (Platinum Resistance thermometer, SKS Group, Finland). The temperature was captured and logged every 2 seconds with a NI labVIEW temperature logging program. A small hot zone of 4 - 5 cm in length was determined. The criterion of temperature deviation in the hot zone was less than 2 °C. The hot zone is depicted in Figure 1a as a region between the two dashed lines.

Experiments in air were undertaken with the bottom of the tube furnace open and exposed to the atmosphere. The sample was introduced into the furnace from the bottom by slowly pulling on the wire from the top of the furnace. Phase equilibrium was confirmed by comparing samples with identical initial composition at fixed time intervals to each other at constant temperature and measuring compositional homogeneity of the phases with SEM-EDS. Time- interval tests were conducted for 2, 4, 8, 24, 72 and 108 hours, respectively. Equilibrium was achieved after 72 and 24 hours of equilibration at 1273 K and 1473 K, respectively. Knowing equilibrium at 1473 K is guaranteed after 24 hours, all other experiments at and above 1473 K were equilibrated for 24 hours. All samples were released and quenched in a beaker containing ice-water. The samples were quickly removed from the water and dried with compressed air.

3.3 Application of the Phase Rule

The "phase rule" is a combination of phases and components, and is given, $f = c - p + 2$. Where c is the number of components and p is the number of phases. In this case, c = 5 (Cu, K_2O, SiO_2, O_2 and N_2), p = 3 (Slag, solid (SiO_2) and gas) and according to phase rule, f = 4. The pressure is fixed at 1 atm, the oxygen partial pressure is fixed at 0.21 atm, and the temperature is fixed at the set point, thereby reducing f to 2. With one last variable our discretion, the composition, another intensive property, of one species in the slag is fixed. However, fixing the composition of the slag was not possible, given that the objective was to determine the composition of the slag experimentally. Knowing that the initial composition is at our discretion, it was possible to directly choose a set of initial compositions that was confined to a region where the slag was in equilibrium with silica. This allowed one to fix the composition of one specie in the slag indirectly, thereby fully defining the system [20].

3.4 Analysis

After quenching and drying, small pieces of the quenched sample were mounted in epoxy resin. A

cross-section of the sample was prepared using conventional dry metallographic grinding and polishing techniques. A dry technique was employed because K_2O reacts vigorously with water forming KOH [21]. Moreover, K_2O it is a deliquescent and absorbs water from the atmosphere, initiating this vigorous reaction [21]. For these reasons, propylene glycol (Sigma Aldrich, Germany) and DP Lubricant Brown (Struers, Denmark) were used. The samples were stored in a desiccator to avoid/minimise moisture absorption from the atmosphere.

The polished samples were carbon-coated with a Leica EM SCD050 Coater (supplied by Leica Mikrosysteme GmbH, Vienna), before SEM-EDS analysis and EPMA. EPMA is a combined qualitative and quantitative analytical tool used for phase characterisation and composition estimation. The EPMA at the Geological Survey of Finland (GTK) is a CAMECA SX100 (Cameca SAS, France) and is equipped with five wavelength dispersive spectrometers. The samples for EPMA were analysed at 15 kV accelerating voltage and 10 nA beam current. Knowing that potassium may deplete under the EPMA electron beam [1], the EPMA exposure time under all samples was minimized. The electron beam was defocused to 10 μm to avoid sample damage and intensity loss of alkalis. The matrix correction in the probe software was based on the PAP matrix correction procedure [22]. The following standards and X-ray lines were used; Cu was calibrated on pure Cu metal (Cu Kα), Al_2O_3 as Al and oxygen standard (Kα lines for both elements), quartz (SiO_2) and sanidine (high temperature potassium feldspar, $(K)(AlSi)_4O_8$) was used for Si and K, respectively. All standards were from Astimex Scientific ltd., Canada.

4 RESULTS AND DISCUSSION

The samples were analysed with SEM-EDS and EPMA; however only results from EPMA are given. The agreement between these two analytical methods is within 1 wt. % for all measured elements. The EPMA measurement results of the phase equilibria experiments of the Cu-K_2O-SiO_2-O system in equilibrium with air in the SiO_2 primary phase field at temperatures ranging between 1273 K and 1773 K are reported in Table II. Moreover, the listed results were recalculated based on the measured elements (Cu, K, Si, O). Cu is the only transition metal, and transforms systematically from Cu^+ to Cu^{2+} under increased oxidising conditions [23], signifying that the slag from this study contains a mixture of Cu^+ and Cu^{2+} cations. However, the oxidation states of Cu were not analysed directly, because EPMA and SEM-EDS provide only the total element content. Consequently, all Cu was assumed to be in the Cu^+ oxidation state and recalculated subsequently as Cu_2O.

Sample homogeneity was confirmed by analysing at least six points near the silica crucible wall, a measured distance (100-500 μm) from the wall, and near the centre of the sample in order to calculate a

set of standard deviations for each element. The latter is given as part of Table 2 and were in most cases below 1 %. Furthermore, each experiment was repeated at least once to assert confidence in experimental procedure. It was established that the repeatability of experiments was satisfactory, because measured elements did not differ by more than 1 wt. % for all experiments.

Table 2: Summary of liquidus data from the Cu-K2O-SiO2-O system in equilibrium with air and solid silica analysed using EPMA.

Experiment	Initial composition in wt. %			Temperature K	Final Slag Composition in wt. %					
	Cu_2O	SiO_2	K_2O		Cu_2O	STD	SiO_2	STD	K_2O	STD
1	60.00	20.00	20.00	1273	19.89	0.63	54.99	0.39	25.13	0.42
2	0.35	76.00	23.65	1273	0.45	0.15	74.52	1.32	25.04	1.03
3	20.00	60.00	20.00	1373	10.43	0.53	71.23	1.12	18.34	0.41
4	60.00	20.00	20.00	1373	26.03	0.34	57.19	0.51	16.78	0.23
5	0.35	78.00	21.65	1373	1.20	0.24	79.63	0.62	19.17	0.32
6	4.10	73.00	22.90	1373	1.80	0.24	78.48	0.71	19.73	0.53
7	1.60	76.00	22.40	1373	1.78	0.19	76.38	1.11	21.84	0.51
8	60.00	20.00	20.00	1473	24.08	0.89	60.93	0.46	15.00	0.21
9	1.90	78.00	20.10	1473	0.91	0.27	79.29	0.77	29.70	0.36
10	5.70	76.00	18.30	1473	3.82	0.56	77.65	0.53	18.54	0.56
11	5.40	73.00	21.60	1473	4.07	0.46	77.60	0.35	18.34	0.26
12	19.00	76.00	5.00	1573	8.93	0.70	77.26	0.87	13.82	0.22
13	5.60	76.00	18.40	1573	4.86	0.81	77.97	1.16	17.17	0.72
14	5.40	73.00	21.60	1573	4.37	0.63	79.56	0.74	16.07	0.78
15	20.00	60.00	20.00	1673	10.08	0.85	75.57	1.46	14.36	1.03
16	30.00	60.00	10.00	1673	18.97	1.40	70.88	0.86	10.16	0.54
17	5.60	76.00	18.40	1673	3.74	0.28	83.04	0.61	13.23	0.26
18	11.00	73.00	16.00	1673	5.01	0.42	81.94	0.78	13.06	0.45
19	5.12	82.00	12.88	1673	5.02	0.43	82.49	0.74	12.49	0.19
20	7.20	76.00	16.80	1673	6.44	0.45	81.60	0.84	11.95	0.17
21	15.00	70.00	15.00	1773	4.61	0.36	85.67	0.79	9.72	0.34
22	20.00	60.00	20.00	1773	5.52	0.65	83.77	0.74	10.71	0.66
23	30.00	60.00	10.00	1773	13.26	0.87	78.84	0.61	7.9	0.41
24	1.20	90.10	8.70	1773	2.33	0.20	88.73	0.46	8.94	0.08
25	6.40	88.00	5.60	1773	5.46	0.38	85.96	0.77	8.58	0.11
26	6.00	89.40	4.60	1773	6.20	0.17	85.65	0.34	8.15	0.10
27	15.00	76.00	9.00	1773	6.48	0.39	84.85	0.48	8.675	0.33
28	13.70	82.00	4.30	1773	7.83	0.37	85.49	0.54	6.69	0.28
29	14.00	78.00	8.00	1773	8.74	0.46	82.83	0.32	8.44	0.34
30	19.00	73.00	8.00	1773	10.76	0.65	81.47	0.57	7.76	0.19

STD = Standard deviation

Micrographs captured from the SEM back-scattered detector of samples quenched at 1373 and 1773 K are shown in Figure 2. The samples shown in Figure 2a and Figure 2b were saturated with silica, therefore the liquid phase was always in equilibrium with tridymite or cristobalite, depending on the temperature. The crystal structure of silica converts from tridymite into cristobalite at 1738.48 K, which affects the crystal shape of silica [24, 13]. However, it is not known if the conversion materialised, given that the crystal structure of silica was not analysed.

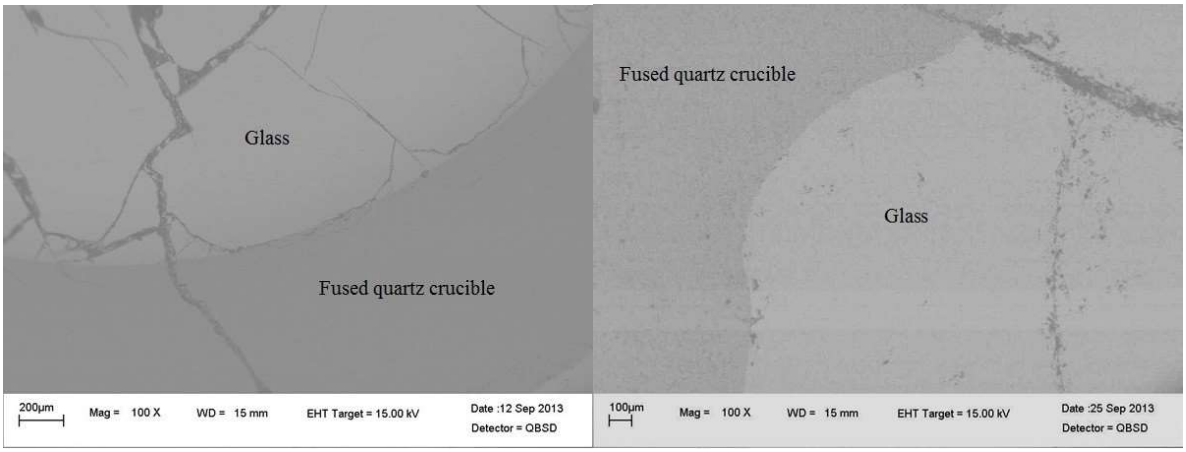

(a) 1373 K (b) 1773 K

Figure 2: BSE micro-images of quenched samples saturated with silica (quartz crucible).

The liquidus contours in Figure 3a and Figure 3b are based on the MTOX and FToxid databases by MTDATA 8.2 and FactSage 7.3. The results from this study are superimposed onto both phase diagrams. It can be observed that the calculated liquidus contours from the FToxid database agrees poorly with the results from this study. The calculated liquidus contours from the Ftoxid database show considerably greater silica solubility in the liquid phase. The liquidus contours from the Mtox database agree somewhat better with the results from this study but are not within experimental error limits. The poor agreement between experimental data and calculated liquidus contours is because of the shortage of experimental phase diagram and other thermodynamic data. As a result, no thermodynamic assessment was performed, signifying that the liquidus contours shown in Figure 3a and Figure 3b were derived using model parameters from binary sub-systems. As discussed in section 1, systems containing silica require additional ternary parameters and an asymmetric ternary interpolation technique to reproduce experimental data. We therefore recommend that the system be assessed using the data from this study and the other relevant studies published recently.

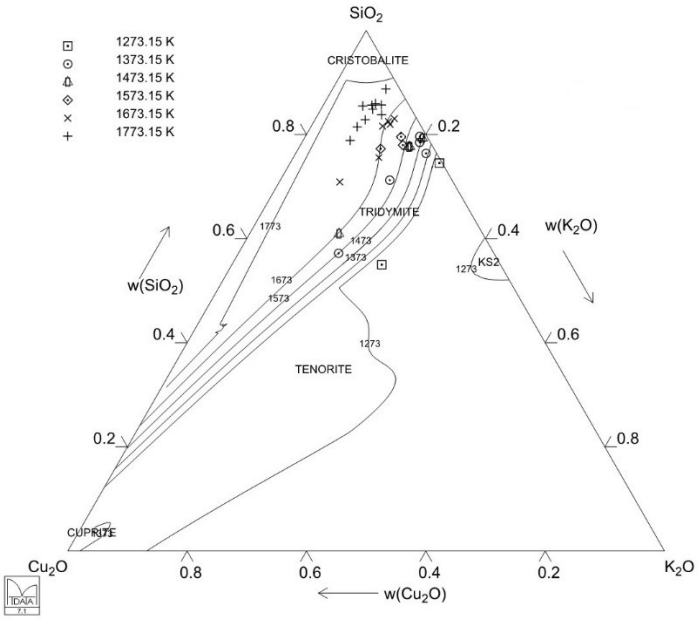

(a) Calculated with MtOX database using MTDATA[23].

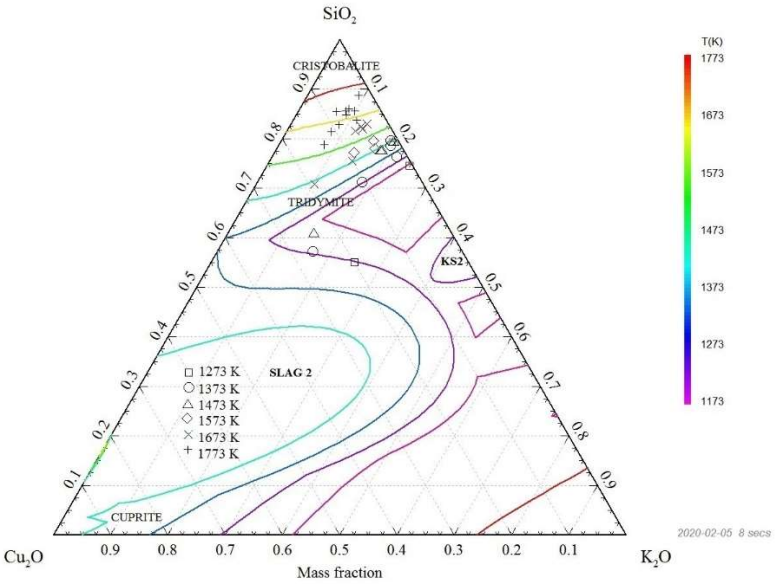

(b) Calculated with Ftoxid database using FactSage[13].

Figure 3: Liquidus isotherm plots of the Cu-K2O-SiO2-O in equilibrium with air; experimental data have been superimposed on the liquidus contours.

5 CONCLUSIONS

During sulphide smelting silica sand is added as flux, which contains impurity components such as K and Na. These impurities are known to affect the viscosity and liquidus temperature. Therefore, it becomes vital that viscosity and liquidus deviations in sulphide smelting slags caused by flux impurities

be known prior to a smelting operation to guarantee the effective separation of the slag from the alloy. Thermodynamic modelling software such as FactSage and MTDATA are typically used to estimate and model such deviations for multicomponent systems, provided that lower-order system properties have been assessed using reliable experimental data. However, there are a shortage of experimental data on binary and ternary systems pertaining to the Cu-K_2O-Na_2O-SiO_2-O system. As a result, accurate equilibrium estimations cannot be made for this system using FactSage or MTDATA.

To improve our understanding of chemical reactions taking place during copper smelting, the liquidus of the Cu-K_2O-SiO_2-O system in equilibrium with air was investigated in this study. Liquidus compositions at silica saturation were determined successfully at 1273, 1373, 1473, 1573, 1673 and 1773 K with the equilibration/quench/analysis technique. Starting experimental compositions were estimated initially using MTDATA but were adjusted systematically in order to have sufficient quantity of liquid in equilibrium with tridymite or cristobalite. Polished and coated samples were analysed with electron probe microanalysis technique (EPMA) and scanning electron microscope with energy dispersive X-ray spectroscopy (SEM-EDS); however only EPMA results were provided. The measured liquidus compositions were in poor agreement with the calculated liquidus contours from the Ftoxid database in FactSage but agreed relatively well with calculated liquidus contours from the MTOX database in MTDATA. Therefore, results from this study may now be used for future thermodynamic assessments.

ACKNOWLEDGEMENTS

We would like to express gratitude to Aalto University, School of Chemical Engineering for lending their facilities to carry out experimental work. Furthermore, the authors are indebted to Outotec for the provision of the EPMA analysis and funding the experimental work. Financial support by Tekes-ChemEnergy-ISS (ELEMET programme of Fimecc OY) and Lonmin is also kindly acknowledged.

REFERENCES

[1] G. Akdogan, H. Johto, P. Taskinen, Phase equilibria study of K-O-Si system in equilibrium with air, Journal of the European Ceramic Society 34 (2014) 4053–4058, URL http://dx.doi.org/10.1016/j.jeurceramsoc.2014.05.007.

[2] F. Kracek, N. Bowen, G. Morey, Equilibrium relations and factors influencing their determination in the system K_2SiO_3-SiO_2, Journal of physical chemistry 41 (9) (1937) 1183–1193.

[3] I. Santoso, P. Taskinen, A. Jokilaakso, M. Paek, D. Lindberg, Phase equilibria and liquid phase behavior of the K2O-CaO-SiO2 system for entrained flow biomass gasification, Fuel 265 (2020) 1–14, URL https://doi.org/10.1016/j.fuel.2019.116894.

[4] A. Zaitsev, N. Shelkova, N. Lyakishev, B. Mogutnov, Z. Khim, Modelling of the thermodynamic

properties of silicate melts and calculation of phase equilibria in the K_2O-SiO_2 system, Russian journal of Physical Chemistry 74 (7) (2000) 1033–1038.

[5] P. Wu, G. Eriksson, A. Pelton, Optimisation of the thermodynamic properties and phase diagrams of the Na_2O-SiO_2 and K_2O-SiO_2 systems, Journal of the American Ceramic Society, 76 (8) (1993) 2059–2064, URL https://doi.org/10.1111/j.1151-2916.1993.tb08333.x.

[6] S. Forsberg, Optimisation of thermodynamic properties of the K_2O-SiO_2 system at high temperatures, Journal of Phase Equilibria and Diffusion, 23 (3) (2002) 211–217, URL http://dx.doi.org/10.1361/105497102770331695.

[7] T. Besman, K. Spear, Thermodynamic modelling of oxide glasses, J. Am. Ceram. Soc. 85 (12) (2002) 2887–2994, URL https://doi. org/10.1111/j.1151-2916.2002.tb00552.x.

[8] A. Romero-Serrano, C. Gomez-Yanez, M. Hallen-Lopez, J. Araujo-Osorio, Thermodynamic modelling of alkali metal oxide-silica binary melts, Journal of the American Ceramic Society 88 (1) (2005) 141–145, URL http://dx.doi.org/10.1361/105497102770331695.

[9] L. Zhang, C. Schmetterer, P. Masset, Thermodynamic description of the /ceM2O-SiO_2 (M = K, Na) systems, Computational Materials Science 66 (1) (2013) 20–27, URL https://doi.org/10.1016/j.commatsci.2012.04.040.

[10] D. Kim, M. V. Ende, P. Hudon, I. Jung, Coupled experimental study and thermodynamic optimisation of the K_2O-SiO_2 system, Journal of non-crystalline solids 471 (2017) 51–64, URL https://doi.org/10.1016/j.jnoncrysol.2017.04.029.

[11] A. Meshalkin, A. Kaplun, The complex investigation of the phase equilibria and melt characteristics in borate and silicate systems, Journal of Crystal Growth 275 (e) (2005) 115–119, URL https://10.1016/j.jcrysgro.2004.10.136.

[12] O. Samoilova, L. Makrovets, E. Trofimov, Thermodynamic simulation of the phase diagram of the Cu_2O-Na_2O-K_2O System, Moscow University Chemistry Bulletin 73 (3) (2018) 105–110, URL https://doi.org/10.3103/S0027131418030057.

[13] C. Bale, E.Belisle, P. Chartand, S. Decterov, G. Eriksson, K. Hack, I. Jung, Y. Kang, J. Melancon, A. Pelton, C. Robelin, S. Petersen, FactSage thermochemical software and databases, 2010-2016, CALPHAD: Computer Coupling of Phase Diagrams and Thermochemistry 54 (2016) 35–53, URL https://doi.org/10.1016/j.calphad.2016.05.002.

[14] T. Hidayat, E. Jak, Thermodynamic modelling of the Cu_2O-SiO_2, Cu_2O-CaO, and Cu_2O-CaO-SiO_2 systems in equilibrium with metallic copper, International Journal of Materials Research 105 (3) (2014) 249–257, URL https://doi.org/10.3139/146.111023.

[15] L. Xia, Z. Liu, P. Taskinen, Equilibrium study of the Cu-O-SiO_2 system at various oxygen partial pressures, Journal of Chemical Thermodynamics 98 (2016) 126–134, URL http://dx.doi.org/10.1016/j.jct.2016.03.023.

[16] V. Prostakova, J.Cheng, E.Jak, S. Decterov, Experimental investigation and thermodynamic modeling of the NiO−CaO−SiO_2, NiO-CaO-$SiO_2$and NiO-CaO-MgO-SiO_2 systems, Journal of chemical thermodynamics 86 (2015) 130–142, URL http://dx.doi.org/10. 1016/j.jct.2015.01.017.

[17] A. Pelton, Phase diagrams and thermodynamic modelling of solutions, 2019 Elsevier Inc., Radarweg 29, P.O. Box 211, 1000 AE Amsterdam, Netherlands, URL https://doi.org/10.1016/C2013-0-19504-9, 2019.

[18] E. Jak, P. Hayes, Phase Equilibria determination in complex slag systems, Mineral Processing and Extractive metallurgy: Transactions of the institutions of Mining and Metallurgy 117 (1) (2008) 1–17, URL http://dx.doi.org/10.1179/174328508X272344.

[19] J. Gibsy, P. Taskinen, J. Pihlasalo, Z. Li, M. Tyrer, J. Pearce, K. Avarmaa, P. Bjorklund, H. Davies, M. Korpi, S. Martin, L. Pesonen, J. Robinson, MTDATA and the Prediction of Phase Equilibria in Oxide Systems: 30 Years of Industrial Collabo- ration, Metallurgical and Materials Transactions B 48 (B) (2017) 91–98, URL http://dx.doi.org/10.1007/ s11663-016-0811-x.

[20] W. Malan, G. Akdogan, P. Taskinen, J. Zietsman, Phase equilibria and thermodynamic evaluation of the Fe-Ti-V-O system in air, CALPHAD: Computer Coupling of Phase Diagrams and Thermochemistry 65 (2019) 141–154, URL https://doi.org/10.1016/j.calphad. 2019.02.014.

[21] H. Holleman, E. Wiberg, Inorganic Chemistry, Academic Press: San Diego., 525 B Street, Suite 1900, San Diego, California, USA, URL ISBN0-12-352651-59, 2019

[22] J. Pouchou, F. Pichoir, Un nouvea modele de calcul pour le microanalyse quantitative par spectrometrie de rayons X. Partie 1: Application a l'analyse d'enchantillions homogenes, La Recherche Aerospatiale 3 (1984) 167–192.

[23] D. Shishin, S. Decterov, Critical assessment and thermodynamic modelling of the Cu-O and Cu-O-S systems systems, CALPHAD: Computer Coupling of Phase Diagrams and Thermochemistry 38 (2012) 59–70, URL http://dx.doi.org/10.1016/j.calphad.2012.04. 002.

[24] H. Wriedt, The O-Si (Oxygen-Silicon) system, Bulletin of Alloy Phase Diagrams 11 (1) (1990) 43–61.

[25] R. Davies, A. Dinsdale, J. Gisby, J. Robinson, S. Martin, MTDATA - thermodynamic and phase equilibrium software from the national physical laboratory, CALPHAD: Computer Coupling of Phase Diagrams and Thermochemistry 26 (2002) 229–271, URL doi:10.1016/ S0364-5916(02)00036-6.

Performance Evaluation of Freeze Crystallization for recovery of Water, Sodium Sulphate and Sodium Chloride from brine.

PM Ramothole[1,3*], A Adeniyi[1], J P Maree[2,3] and M S Onyango[1]

[1] Department of Chemical, Metallurgical and Materials Engineering, Faculty of Engineering and the Built Environment, Tshwane University of Technology, Private Bag X680, Pretoria, 0001, South Africa

[2] Department of Water and Sanitation, University of Limpopo, University Street, Polokwane, Limpopo, South Africa

[3] ROC Water Technologies, P O Box 70075, Die Wilgers, Pretoria, South Africa

*Corresponding author:

ABSTRACT

Freeze crystallization is used for the treatment of highly saline effluents. Currently scraping ice from cold surfaces is a challenge that needs to be overcome. This investigation focused on a heat exchanger where no ice scraping is needed. The objectives of this investigation were to identify optimum conditions to achieve the following: Pre-cooling of brine from 60°C to ambient temperature; predict the behavior of Na_2SO_4 and NaCl during freeze crystallization, and calibration of the model through the recovery of water through ice formation. The following conclusions were made: Feedwater with temperatures of 60°C can be pre-cooled through ambient cooling in shallow pans to 10°C above room temperature within a contact time of 30 min; 100 g/L Na_2SO_4 can be removed through further cooling to its solubility of 45 g/L. The energy consumption for the recovery of 1 500 kg Na_2SO_4 per day amounts to 18.87 kW; 100 g/L NaCl can be treated through freeze desalination for recovery of salt due to its high solubility of 290 g/L. The energy consumption for the recovery of 1 500 kg NaCl per day amounted to 132.21 kW in the case of 90% ice recovery. Ice, could be recovered from a 34 g/L salt at -2°C. The ice purity improved over time, due to the improved ice brine separation method.

Keywords: Freeze crystallization; sodium sulphate; sodium chloride; ambient cooling; ice recovery

1 INTRODUCTION

Mine water and other industrial waters are rich in sodium salts linked to sulphate and/or chloride anions, with some streams being stored at temperatures as high as 60°C. Recently, strict legislation requires water of drinking quality to be discharged into public streams and approaching the ideal of zero waste disposal (Randall, Nathoo, & Lewis, 2011). Landfill disposal costs of liquid waste streams in Gauteng, South Africa, can vary up to R1 000/t and transportation costs up to R1 500/t, totaling R2 500/t. In Port Elizabeth, South Africa, the disposal costs (private facilities), were estimated to range from R3 670 to R9 500 per tonne (Gibb, 2017). These waste disposal costs may prove excessively expensive for some industries. Processes such as Nano Filtration (NF) and Reverse Osmosis (RO), are some of the remedial technologies that have been used. However, they become unattractive owing to

their generation of sludge which still requires disposal. RO is widely used for the treatment of industrial effluents and can recover as much as 90% of potable water. RO is also used for seawater desalination where water recovery typically amounts to 50%. Challenges experienced with RO include membrane fouling (Reddy, Lewis, Witkamp, Kramer, & & van Spronsen, 2010). Another technology, that has been utilized for highly saline water is Freeze Desalination (FD) (Melak, Ambelu, Astatkie, Du Laing, & Alemayehu, 2019). This technology forms part of the Reverse Osmosis/Cooling (ROC) process that has been developed for the treatment of highly saline water (Mtombeni T. , Maree, Zvinowanda, Asante, & Louw, 2014).

The ROC process makes provision for the treatment of industrial effluents intending to minimize waste streams through the recovery of saleable products. In the pre-treatment stage, metals e.g. Fe^{3+}, Al^{3+}, Fe^{2+}, Mn^{2+} are replaced with Na^{+} by dosing Na_2CO_3. In the reverse osmosis stage, the Na_2SO_4/NaCl-rich solution is desalinated to produce clean water and brine with a TDS of 80 g/L. This is possible due to the absence of scaling compounds such as $CaSO_4$. The brine is treated with freeze crystallization for removal of clean water, Na_2SO_4, and NaCl (Adeniyi., Mbaya., Onyango., Popoola., & Maree., 2016). Na_2SO_4 has the characteristic that it can be partially removed to 45 g/L only through cooling. This is due to its high solubility at room temperature (350 g/L) compared to only 45 g/L at 0°C (Mtombeni, Maree, & Zikalala, Desalination with combined membrane filtration/freeze desalination process, 2016). NaCl, unlike Na_2SO_4, has a high solubility of 350 g/L over the total temperature range from 0º to 100°C. This allows Na_2SO_4, to be recovered first, through cooling and water removal through ice formation, followed by NaCl removal after its solubility of 350 g/L has been exceeded. In a final thermal stage, Na_2SO_4 is processed to the raw material, Na_2CO_3, as investigated by Mokgohloa (Mokgohloa, Maree, van Vuuren, Modibane, & Mujuru, 2021). The purpose of this study was to identify and demonstrate a cost-effective solution for a generic brine stream with an initial temperature of 60°C, containing 50 g/L Na_2SO_4 and 50 g/L NaCl. Ice scraping is normally used for the removal of ice from the cold surface of the heat exchanger (Adeniyi, Mbaya, Popoola, Maree, & & Zvinowanda, 2014; Adeniyi., Mbaya., Onyango., Popoola., & Maree., 2016). Ice scale layers result in reduced energy transfer and resultant blockages. In this investigation, no ice scraper was employed for ice removal from cold surfaces.

The objectives of this investigation were to identify optimum conditions to achieve the following:

- Pre-cooling of brine from 60°C to ambient temperature;
- Predict the behavior of Na_2SO_4 and NaCl during freeze crystallization, and
- Calibration of the model through the recovery of water through ice formation

2 LITERATURE

2.1 Available freeze technologies

2.1.1 Available freeze technologies

The principle of salt rejection as water undergoes a phase change to become solid gave birth to freeze desalination, an alternative technology for salt and water recovery. The rejection of salt from water is a result of the formation of small dimension ice crystal lattice structures which rejects salt ions during phase change as opposed to being incorporated into the lattice (Melak, Ambelu, Astatkie, Du Laing, & Alemayehu, 2019). There are various ways of cooling and/or freezing saline water. One way involves precooling the feed, cooling, and ice formation through freezing in a heat exchanger followed by separation of ice from brine. The other critical component to the freezing and separation process is the size of crystals; the bigger the crystals the easier it is to separate them from brine (Lu & Xu, 2010).

2.1.2 Eutectic freeze crystallization

Researchers have carried out a good deal of work over the years on the concept of freezing water from solutes. Eutectic Freeze Crystallization (EFC) focuses on operating at a point where both ice and salt exist, which is the eutectic point. Depending on the salt concentration, different solutions have different eutectic compositions and temperatures. The point where a solution has the lowest crystallization temperature, compared to any other concentration of the solution, is the eutectic point. It is also the point where both solute and solvent exist in solid form and have crystallized out of solution (Chivavava, et al., 2018).

2.2 Salt behaviour

2.2.1 Solubility of Na2SO4

Solubility of Na_2SO_4 increases with temperature and this takes place in some industrial brines from plants that operate at a very high temperature. Different hydrated forms of sodium sulphate exist, namely, anhydrous Na_2SO_4, heptahydrate, $Na_2SO_4 \cdot 7H_2O$ and decahydrate, $Na_2SO_4 \cdot 10H_2O$ (South Africa Patent No. 2014/04734, 2014). Their solubility in water decreases with decreasing temperature, with decahydrate beginning to form crystals as soon as temperatures reach <30°C. In instances where the concentration is around 100 g/L only cooling is needed to crystallize the Na_2SO_4, with no need for freezing (Zikalala, Maree, Zvinowanda, & Akinwekomi, 2017).

2.2.2 Solubility of NaCl

A phase diagram of a binary solution representing a liquid and solid phase of material in equilibrium demonstrates the principle of freeze crystallization through which desalination takes place. Figure 1 shows the phase change diagram of salt water ($NaCl$-H_2O) (El Khadi & Janajreh, 2017). Line 1 (black) illustrates how the temperature of the water drops at different NaCl concentrations while Line 2 (green) is the NaCl solubility curve in water. Ice will crystallize first at sub-zero temperatures and the eutectic

point is at -21.2˚C, where ice and NaCl exist in solid form. The brine that remains in solution is completely saturated and a further drop in temperature results in NaCl crystallization and no brine remaining (El Khadi & Janajreh, 2017).

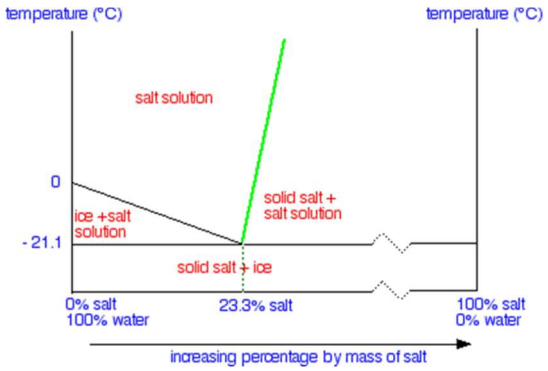

Figure 1: Phase diagram of NaCl in water solution (El Khadi & Janajreh, 2017). The graph illustrates that the freezing point drops as the concentration of NaCl increases.

2.3 Energy transfer

In instances where there are no work interactions e.g. electrical resistance heating, the energy conservation equation when a fluid is flowing steadily through a tube is expressed as follows:

$$\dot{Q} = \dot{m}C_p(T_e - T_i) \qquad \textbf{Equation 1}$$

T_i is the inlet temperature entering the tube and T_e is the exit temperature exiting the tube. $\dot{Q}$ is the rate of heat transfer to or from the fluid. The temperature of the fluid flowing through the tube remains constant when there are no energy interactions through the tube wall (Cengel & Ghajar, 2015). To approximate the surface's thermal conditions, it is assumed that either surface temperature, T_s, is constant, or the heat flux, q, is constant. The constant surface temperature condition is achieved when a phase change like boiling or condensation occurs on the outer surface of the tube. Surface heat flux is expressed as:

$$\dot{q} = h_x(T_s - T_m) \qquad \textbf{Equation 2}$$

Where h_x is the heat transfer coefficient and T_s and T_m are surface and mean temperatures, respectively (Cengel & Ghajar, 2015).

3 EXPERIMENTAL PROCEDURE

3.1 Model

The model was developed to predict the respective amounts of Na_2SO_4 and NaCl as functions of the following parameters: (i) Percentage ice recovery; (ii) Ice purity; (iii) Freezing point (calculated from NaCl in solution), and (iv) Na_2SO_4 and NaCl concentrations in the brine as functions of ice recovery.

From the above the following parameters were calculated: (i) Energy consumption due to Cooling and Freezing, (ii) Mass of Na_2SO_4 and NaCl production as a function of feed water composition, feed flow-rate, and percentage ice recovery, and (iii) Energy cost.

3.2 Feedstock

Industrial brine was used as feed, rich in Na_2SO_4 and NaCl.

3.3 Equipment

Figure 2 (schematic) shows the freeze crystallization unit used. It consists of the following items: 15 kW Chiller with primary refrigerant; pipe Heat Exchanger where the primary refrigerant is used to cool secondary refrigerant (30% MeOH, in water) and a Clarifier for salt/liquid/ice separation and a Filter for liquid/ice separation.

3.3.1 Ambient cooling

Feed, at a temperature of 60°C was cooled down in various containers to determine the effect of water depth on the rate of cooling.

3.3.2 Ice recovery

Semi-batch runs, were carried out. Brine was recycled through a heat exchanger (120 L), brine/ice filter, and a sump (30 L). Product ice, was removed and replaced with Feedwater. This was repeated until four times the system volume had been treated. Feed, ice, and brine samples were analyzed for chloride, sodium, TDS, ice, pH and conductivity.

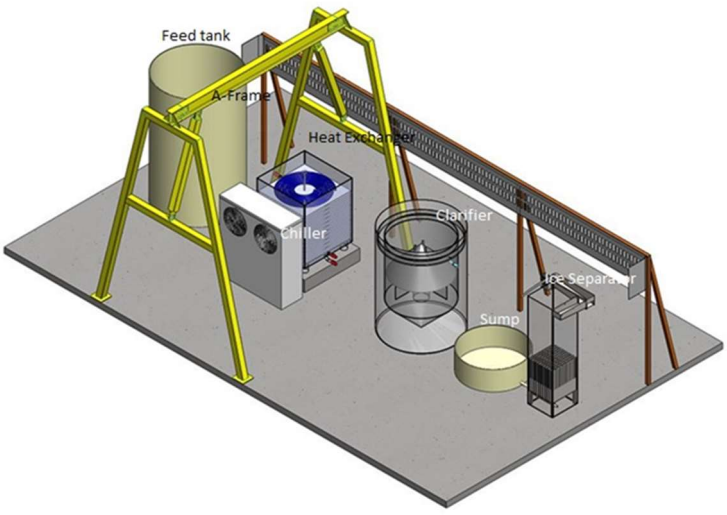

Figure 2: Schematic diagram of the Freeze Crystallization unit (15 kW Chiller, Heat exchanger for TDS cooling and ice separation and Clarifier for salt/liquid/ice separation

3.4 Experimental

The following features were investigated: (i) Effect of water depth on ambient cooling in a pan., (ii) Energy usage and energy cost for salt recovery using freeze crystallization (Na_2SO_4, NaCl), (iii) Ice purity and (iv) Salt recovery.

3.5 Analytical

The following analyses and measurements were performed: pH, Conductivity, Chloride by AgCl titration, Alkalinity, SO_4 by turbidity, metals by ICP spectroscopy.

Samples were collected at various stages in the treatment process, filtered (Whatman No.1), and analysed for pH, conductivity, chloride, sulphate, and TDS (Total dissolved solids) using standard procedures (American Public Health Association, 2012). A calibrated Knick Stratos Eco 2505 meter was used to measure electrical conductivity. Ice content was determined by mixing 250 mL ice slurry (mass m_1; temperature T_1) with 200 mL (m_2) warm water (T_2). The mass of ice (m_i) was determined from m_1, T_1, m_2, T_2, and the temperature (T_3) measured after the ice had melted. Microsoft Excel *Goal Seek* was used to calculate m_i using the following equation:

$$4.18(m_1 - m_i)(T_1 - T_3) + 330m_i + 4.18m_2(T_2 - T_3) = 0 \qquad \textbf{Equation 3}$$

4 RESULTS AND DISCUSSION

4.1 Ambient cooling

Figure 3 and Table 1 show the effect of depth on the cooling-rate at ambient temperatures. It was found that the lower the depth, the faster was the cooling rate. Feed-water with a high temperature of 60°C was cooled through ambient cooling in shallow pans down to 10°C above room temperature, within a contact time of 30 min.

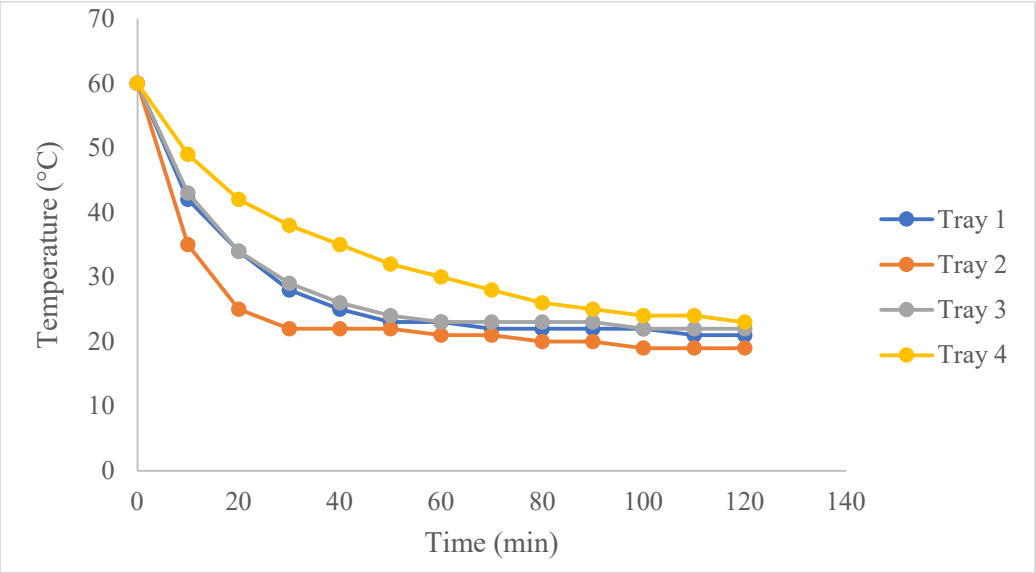

Figure 3: ambient cooling of brine in various containers

Table 1: Ambient cooling of water

Parameter	Unit	Container				
		1	2	3	4	Jojo Tank
Material		Steel	Steel	Steel	Steel	PVC
Depth	cm	2	1	3	6	196.5
Width	cm	36	10.5	10.5	10.5	
Length	cm	36	20.5	20.5	20.5	
Diameter	cm					180.0
Area	m^2	0.1296	0.0215	0.0215	0.0215	13.7
Volume	m^3	0.00259	0.00022	0.00065	0.00129	5.0
Mass	g	627.82	76.19	130.87	88.58	
Salt removed (wet)	g/L	242.21	353.96	02.66	68.59	
Cooling Time	min	26	15			5 760.0
Flow-rate	L/min	0.0997	0.0144			0.8681
Flux	L/(min.dm^2)	0.0077	0.0067			0.00064

4.2 Na_2SO_4 and NaCl: Behaviour during desalination through ice formation

Typical desalination operations involve solutions rich in Na_2SO_4 and NaCl. Due to the high disposal cost of untreated waste streams, such water requires desalination to minimize the volume of the final brine stream, or ideally, to eliminate it. To achieve steady-state conditions, an equal mass of salt as was introduced into the system needs to be removed.

The model employed the following numerical parameters: (i) The volume of water in the system = 150 m^3, (ii) Daily salt increase = 10 g/(L.day), which is equal to a salt intake of 1 500 kg/day, and (iii) Na_2SO_4/NaCl m/m ratio = 0.3.

An Excel spreadsheet-based model was developed to predict the water quality of water rich in Na_2SO_4 and NaCl after freeze crystallization (Table 2).

Table 2: Water volume and chemical composition

Parameter	Unit	Value
Water in system	m^3	150
Daily salt intake	kg/day	1500
Na_2SO_4/NaCl m/m ratio		0.3
Na_2SO_4	kg/day	450
NaCl	kg/day	1050

The energy needed for cooling and freezing was calculated from the first principles (Eq 1 for cooling

and E=mH for Freezing). The volume of the final brine stream that needs to be treated is a function of the operating salt concentration in the water network (Table 3).

Table 3: Relationship between operating salt concentration and desalination flow-rate.

Salt	Na_2SO_4	NaCl	Volume to be desalinated		Salt removed
g/L	g/L	g/L	m^3/d	m^3/h	kg/d
50	15	35	30.0	1.25	1 500
100	30	70	15.0	0.63	1 500
150	45	105	10.0	0.42	1 500
200	60	140	7.5	0.31	1 500

Table 4 shows the water quality of ice and brine produced during cooling and/or freezing of waters that contained (A) 70 g/L Na2SO4 and 30 g/L NaCl (B) 100 g/L Na2SO4 and (C) 100 g/L NaCl. The volume of water that needs to be treated and energy consumption were calculated for when 1500 kg/d Na2SO4 needed to be recovered from Water B and 1 500 kg/d NaCl from Water C. In the case of water C, the calculation was repeated for when the water recovery was taken at 90%, 97%, and 98%.

The following observations were made: (i) When 300 L/h of Water A was cooled to -2°C, 180 kg/d Na_2SO_4 was produced while 5.71 kW was needed. (ii) When Water B (100 g/L Na_2SO_4) was cooled from 25 to -2.17°C, a flow-rate of 1.14 m^3/h needed to be treated to produce 1 500 kg/d Na_2SO_4. The energy usage amounted to 18.87 kW. (iii) When Water C (100 g/L NaCl) was cooled from 25 to -21°C, for 90% ice recovery, a flow-rate of 0.88 m^3/h was required to be treated to produce 1 500 kg/d NaCl. The energy usage amounted to 132.21 kW. (iv) When Water C (100 g/L NaCl) was treated with the aim of increasing the ice recovery from 90%, as in (c), to 97 and 98%, the required flow-rate for the recovery of 1 500 kg/d NaCl amounted to 0.68 and 0.66 m^3/h, respectively. The corresponding energy usages amounted to 108.64 kW and 106.11 kW, respectively. (v) The final brine, can either be disposed of at a toxic waste disposal site, or it can be evaporated in an outside pond. The cost of evaporation of the final brine amounts to 35% of the cost when disposed of at a toxic waste disposal site. This excludes the disposal cost of the salt or its potential value. (vi)The evaporation cost of the flow equal to ice recovery amounted to 4.2 times the cost of cooling/freezing.

Table 4: Na_2SO_4 and NaCl recovery through cooling and/or freeze crystallization.

Parameter	Unit	Scenario				
		1	2	3	4	5
		Na_2SO_4/ NaCl	Na_2SO4	NaCl	NaCl	NaCl
		Water A	Water B	Water C	Water C	Water C
Salt rejection	%	0.00	0.00	100.00	100.00	100.00
Ice recovery	%	0.00	0.00	90.00	97.00	98.00
Feed						
Flow	m^3/h	0.30	1.14	0.88	0.68	0.66
FLow	kg/s	0.08	0.32	0.24	0.19	0.18
Feed Na_2SO_4	g/L	70.00	100.00	0.00	0.00	0.00
Feed NaCl	g/L	30.00	0.00	100.00	100.00	100.00
Feed TDS	g/L	100.00	100.00	100.00	100.00	100.00
Feed Temp	°C	**25.00**	**25.00**	**5.00**	**5.00**	**5.00**
Brine after Cooling/Freezing						
Brine Flow	m^3/h	0.300	1.136	0.088	0.021	0.013
Brine Flow	kg/s	0.08	0.32	0.02	0.01	0.00
Ice Flow	t/h	0.00	0.00	0.79	0.66	0.65
Ice Flow	kg/s	0.00	0.00	0.22	0.18	0.18
Brine Na_2SO_4 (aq+s)	g/L	70.00	100.00	0.00	0.00	0.00
Brine NaCl (aq+s)	g/L	30.00	0.00	1000.00	3333.33	5000.00
Brine Na_2SO_4 (aq)		45.00	45.00	0.00	0.00	0.00
Brine NaCl (aq)		30.00	0.00	290.00	290.00	290.00
Na_2SO_4 sol. (aq)	g/L	45.00	45.00	45.00	45.00	45.00
NaCl sol. (aq)	g/L	290.00	290.00	290.00	290.00	290.00
Brine TDS	g/L	100.00	100.00	1 000.00	3 333.33	5 000.00
Brine temp	°C	**-2.17**	**0.00**	**-21.00**	**-21.00**	**-21.00**
Freeze set point	°C	-5.17	-3.00	-24.00	-24.00	-24.00
Ice						
Ice Na_2SO_4	g/L	70.00	100.00	0.00	0.00	0.00
Ice NaCl	g/L	30.00	0.00	0.00	0.00	0.00
Ice TDS	g/L	100.00	100.00	0.00	0.00	0.00
Solids						
Salt Na_2SO_4 (s)	g/L	25.00	55.00	0.00	0.00	0.00
Salt NaCl (s)	g/L	0.00	0.00	710.00	3 043.33	4 710.00
Salt Total	g/L	25.00	55.00	710.00	3 043.33	4 710.00
Na_2SO_4	kg/day	180.00	1 500.00	0.00	0.00	0.00
NaCl	kg/day	0.00	0.00	1 500.00	1 500.00	1 500.00
Na_2SO_4 + NaCl	kg/day	**180.00**	**1 500.00**	**1 500.00**	**1 500.00**	**1 500.00**
Na_2SO_4 sol.	g/L	45.00	45.00	45.00	45.00	45.00
NaCl sol.	g/L	290.00	290.00	290.00	290.00	290.00
Energy						
dT	°C	3.00	3.00	3.00	3.00	3.00
NaCl Freeze point	°C	-2.17	0.00	-21.00	-21.00	-21.00
Chiller Set-Point		-5.17	-3.00	-24.00	-24.00	-24.00
E (m.Cp.dT)	kW	9.55	33.59	26.95	20.95	20.31
E (m.H)	kW	0.00	0.00	72.62	60.87	59.60
COP		1.67	1.78	0.75	0.75	0.75
T Total	**kW**	**5.71**	**18.87**	**132.21**	**108.64**	**106.11**
E	**kWh/t ice**	**#DIV/0!**	**#DIV/0!**	**166.87**	**163.61**	**163.19**
	kWh/t Feed	**19.03**	**16.60**	**150.19**	**158.71**	**159.92**
Cp		3.80	3.80	3.80	3.80	3.80
Electricity	R/kWh	1.00	1.00	1.00	1.00	1.00
	R/month	4 110	13 585	95 188	78 223	76 396
Brine disposal						
Disposal cost	R/t			2000.00	2000.00	2000.00
Final brine	m3/h			0.088	0.021	0.013
Disposal cost	R/month			126 761	29 573	19 108
Evaporation cost of final brine						
Enegy usage	kJ/kg			2 500	2 500	2 500
Brine Flow	t/h			0.088	0.021	0.013
Power	kW			61	14	9
Evaporation cost	R/month			44 014	10 268	6 635
Evaporation / Disposal cost	%			35	35	35
Evaporation of total stream						
Energy usage	kJ/kg			2 500	2 500	2 500
Flowequal to ice recovery	t/h			0.792	0.664	0.650
Power	kW			550	461	452
Evaporation cost	R/month			396 127	332 010	325 106
Evaporation / Freeze cost	Ratio			4.16	4.24	4.26

Note Disposal and transportation cost of final brine at disposal site = R2 000/t

4.3 Water recovery through ice formation

Water that contained 34 g/L salts (20% Na2SO4 and 80% NaCl) was treated by freeze crystallization for ice recovery and to produce concentrated brine. Table 5 showed that ice purity increased over time from 18 620 mg/L TDS after 3 h of operation to 7 450 mg/L TDS after 25 h. The improvement in ice purity was ascribed to improved brine separation and ice crystallization resulting from of the recirculation of ice seed-crystals. The ice recovery was 106 kg out of a total Feed of 253 kg, which represented 42% ice recovery. The theoretical energy usage from first principles amounts to 92.5 kWh/t ice (Energy usage*2). This was compared with the actual energy usage (Energy usage *1) of 392.1 kWh/t. This difference in energy values can be reduced through the following improvements: (i) Improve the efficiency of the heat exchanger by (a) using pipes with a smaller diameter, (b) using pipes with a thinner wall thickness, and (ii) minimize heat losses.

Table 5: Ice recovery by freezing.

Time	Temp	Ice	Acc Ice	Feed	Ice	Energy reading	Energy usage*1	Energy usage *2	TDS concentration			TDS mass*3		
									Feed	Ice	Brine	Feed	Ice	Brine
h	°C	kg/Intv	kg	kg	t/h	kWh	kWh/t ice	kWh/t ice	mg/L	mg/L	mg/L	kg	kg	kg
0.0	8.8	0.00	0.00	147.00	0.0000	0.0			34 590					
0.5	0.3	0.00	0.00	147.00	0.0000	1.7			34 590					
1.0	-1.4	0.00	0.00	147.00	0.0000	2.6			34 590					
1.5	-1.6	0.00	0.00	147.00	0.0000	3.6			34 590					
2.0	-1.7	3.98	3.98	150.98	0.0080	4.5			34 590					
2.5	-1.5	3.98	7.96	154.96	0.0080	5.3			34 590					
3.0	-1.5	3.98	11.95	158.95	0.0080	6.5			34 590	18 620	35 888	5.50	0.22	5.28
3.5	-1.6	3.98	15.93	162.93	0.0080	7.1			34 590					
4.0	-1.4	3.98	19.91	166.91	0.0080	7.7	170.7		34 590					
4.5	-1.4	5.53	25.44	172.44	0.0111	8.3	95.8	92.5	34 590					
5.0	-1.4	5.53	30.98	177.98	0.0111	8.8	88.6	92.5	34 590					
5.5	-1.4	5.53	36.51	183.51	0.0111	10.3	272.9	92.5	34 590					
6.0	-1.3	5.53	42.04	189.04	0.0111	11.3	191.6	92.4	34 590					
6.5	-1.2	2.14	44.18	191.18	0.0043	12.1	364.5	92.4	34 590					
7.0	2.5	2.14	46.32	193.32	0.0043	12.9	359.8	88.5	34 590					
7.5	-1.4	2.14	48.46	195.46	0.0043	13.8	453.3	96.7	34 590					
8.0	-1.2	2.14	50.60	197.60	0.0043	14.3	205.6	92.3	34 590					
8.5	-1.3	2.14	52.74	199.74	0.0043	14.8	229.0	92.6	34 590					
9.0	-0.2	2.14	54.88	201.88	0.0043	15.8	453.3	91.3	34 590	17 690	40 824	6.98	0.98	6.00
15.5	-0.8	1.25	74.72	221.72	0.0025	25.4			34 590	13 260	43 703	7.67	1.25	6.42
25.5	-0.9	1.94	105.95	252.95	0.0039	39.0			34 590	7 450	49 469	8.75	1.48	7.27
Average							392.1	92.5						

Feed (kg) = Innitial volume (147 L) + Volume of ice removed

Energy usage*1 = kWh reading / Ice production in t/h

Energy usage*2 = (m.Cp.dT + m.H) / ice production in t/h

TDS_{mass}*3 = Mass (kg) x Conc (mg/kg) /1000

5 CONCLUSIONS

From the investigation, the following conclusions were drawn:

- Feed-water, with a high temperature of 60°C can be pre-cooled to 10°C above room temperature, through ambient cooling in shallow pans, within a contact time of 30 min.

- 100 g/L Na_2SO_4, can be removed only through cooling to its solubility of 45 g/L. The energy consumption for the recovery of 1 500 kg Na_2SO_4 per day will amount to 18.87 kW.
- 100 g/L NaCl, can be treated only through freezing for recovery of salt due to its high solubility of 290 g/L. The energy consumption for the recovery of 1 500 kg NaCl per day will amount to 132.21 kW in the case of 90% ice recovery.
- Ice, can be recovered from a 34 g/L salt solution at -2°C. The ice purity improves over time, due to the improved ice and brine separation method.

REFERENCES

Adeniyi, A., Mbaya, R., Popoola, A., Maree, J., & & Zvinowanda, C. (2014). Performance comparison of hydraulic and gravitation HybridICE filters in freeze desalination of mine waters. Mbombela: Water Institute of Southern Africa (WISA) Biennial Conference.

Adeniyi., A., Mbaya., R. K., Onyango., M. S., Popoola., A. P., & Maree., J. P. (2016). Efficient suspension freeze desalination of mine wastewaters to separate clean water and salts. *Environmental Chemistry Letters*.

American Public Health Association, A. (2012). *Standard methods for the examination of water and wastewater* (22nd ed.). Washington: American Water Works Association, Water Environment Federation,.

Cengel, Y., & Ghajar, A. (2015). *Heat and Mass Transfer: Fundamentals and Applications* (5th ed.). New York: McGrow-Hill Education.

Chivavava, J., Aspeling, B., Jooste, D., Peters, E., Ndoro, D., Heydenrych, H., . . . Lewis, A. (2018). *Continuous eutectic freeze crystallisation.* Cape Town: University of Cape Town.

El Khadi, K., & Janajreh, I. (2017). Desalination by Freeze Crystallization: An Overview. *Int. J. of Thermal & Environmental Engineering, 15*(2), 103-110.

Gibb. (2017). *Feasibility Plan for a Hazardous Waste Treatment* . Port Elizaberth: Eastern Cape Development Corporation.

Lu, Z., & Xu, L. (2010). *Freezing Desalination Process Thermal Desalination Process– Vol. II. Encyclopedia of Desalination and* . Retrieved August 17, 2021, from http://www.desware.net/

Melak, F., Ambelu, A., Astatkie, H., Du Laing, G., & Alemayehu, E. (2019). Freeze desalination as point-of-use water defluoridation technique. *Applied water science, 9*, 34.

Mokgohloa, C. P., Maree, J. P., van Vuuren, D. S., Modibane, K. D., & Mujuru, M. M. (2021). Recovery of Na2CO3 and nano CaCO3 from Na2SO4 and CaSO4 wastes. In E. E. Fosso-Kankeu, *Nano Technology* (pp. 1-2). New York: Wiley Scrivener.

Mtombeni, T., & Maree, J. (2014). *South Africa Patent No. 2014/04734.*

Mtombeni, T., Maree, J. P., & Zikalala, N. (2016). Desalination with combined membrane

filtration/freeze desalination process. Durban: WISA Biennial Conference.

Mtombeni, T., Maree, J. P., Zvinowanda, C. M., Asante, O., & Louw, W. (2014). Improved freeze desalination process for recovery of water and salts from brines. Mbombela: WISA Biennial Conference.

Randall, D. G., Nathoo, J., & Lewis, A. E. (2011). A case study for treating a reverse osmosis brine using Eutectic Freeze Crystallization-Approaching a zero waste process. *Desalination, 266*, 256-262.

Reddy, S. T., Lewis, A. E., Witkamp, G. J., Kramer, H. J., & & van Spronsen, J. (2010). Recovery of Na2SO4-10H2O from reverse osmosis retentate by euctetic freeze crystallization technology. *Chemical Engineering Research and Design, 88*, 1153-1157.

Zikalala, N., Maree, J., Zvinowanda, C., & Akinwekomi, V. (2017). Treatment of sulphate wastewater by freeze desalination. *Desalination and water treatment, 79*, 93-102.

The effect of temperature and asphaltene content on the lubricating properties of fuel oils.

T. Thobejane[1*] and P.L. de Vaal [2]

[1] Department of Chemical Engineering, University of Pretoria, Pretoria, South Africa

[2] Department of Chemical Engineering, University of Pretoria, Pretoria, South Africa

[*]Corresponding author: u13121261@tuks.co.za

ABSTRACT

Asphaltenes are components of heavy fuel oils with complex aromatic structures containing heteroatoms (N, O, S) and metals (V, Fe, Ni) and contributes to the high viscosity of heavy fuel oils. Fuel oils are passed through pumps, filters, nozzles and other equipment before such fuel oils reach the burner section and therefore require good lubricating properties. In the recent past, several users of fuel oils have been experiencing problems such as blockages in the fuel oil filters and injector nozzles, increased wear and failures of pumps and, in some cases, decreased calorific efficiency. The HFRR lubricity tester (method ISO 12156-1) was used to perform lubricity tests on fuel oil samples at different temperatures to obtain a better understanding of the friction and wear behaviour of fuel oils. Three fuel oil samples with different asphaltene concentrations were selected for this purpose. Results indicate that the presence of asphaltenes changes the viscosity behaviour of fuel oils, which, in turn affects the lubricity behaviour. Key performance indicators like the wear scar diameter on the ball as well as the wear track on the test disk, showed unexpected results.

Keywords: asphaltenes, precipitation, lubricity, friction, wear.

1 INTRODUCTION

Severely-loaded systems such as injector or pressure pumps need fuels with high lubricity capacity to avoid any wear problems (Lapuerta *et al*, 2016). Poor lubricants have a potential for causing premature wear which leads to high repair costs and failure of pumps (Nickels, 2011). Fuel oils comprise of a range of liquid combustibles, mainly hydrocarbons, which are obtained either as distillates in the working up of petroleum or as residues after the lighter fractions have been removed (Harker & Allen, 1972: 120). Properties of heavy (residual) fuel oils show that the polar fraction, including asphaltenes, are likely to be irreversibly adsorbed onto a metal surface and are less resistant to oxidation as compared to paraffins because of their polarity (Ghanavati *et al*, 2013; Garaniya *et al,* 2018; Stachowiak & Batchelor, 2014: 38). Experimental results from a study, where asphaltenes were removed from heavy fuel oils and then added back to the maltenes (saturates, aromatics and resins), indicate that viscosity of the reconstituted heavy fuel oil samples increases exponentially as the asphaltene content increases at constant temperature. Distillate fuel oils can be used as a blending component in heavy fuel oil for viscosity adjustments in order to reduce the final viscosity of heavy fuel oil (Cao *et al,* 2021).

This investigation is focused on fuel oil used in industrial burners in order to obtain a fuel oil benchmark to quantify lubricity of fuel oils in a similar way to other oils, for which standardised lubricity specifications exist. The aim of this investigation was thus to determine the lubricating properties of selected fuel oils used in power generation by focusing on their friction and wear capabilities, whilst also taking into consideration the effect of the presence of asphaltenes in fuel oils at various temperatures. Friction and wear tests were performed for both filtered and unfiltered fuel oils, containing different asphaltene content, at different temperatures using a HFRR lubricity tester according to the ISO 12156-1 standard. Three fuel oil samples with unique characteristics were used, namely a light cycle oil (LFO), a medium wax-blend oil (MFO) and a crude-derived heavy fuel oil (HFO).

2 EXPERIMENTAL PROCEDURE

2.1 Precipitation of asphaltenes

Asphaltene fractions and solid particles were removed by precipitation from the three fuel oil samples by treatment with a non-polar hydrocarbon solvent. A sample of 10 mL of fuel oil was mixed with 400 mL of 99% purity n-heptane. The mixture was stirred for 24 h at 25 °C with a stirrer speed of 250 rpm and then allowed to settle for 3 h at 25 °C (Ancheyta et al, 2009: 2). Although LFO does not contain asphaltenes because LFO is a distillate fuel oil, the solid particles in LFO were removed. The precipitated asphaltenes and solid particles were separated by vacuum filtration through two 0.2 micron nylon filter papers for 24 h for LFO and HFO and 36 h for MFO (MFO had a waxy precipitant which took longer to separate from the asphaltenes). Some waxes were left behind when transferring to storage containers. The filtration setup is shown in Figure 1. The filtrate was then left in the desiccator for 24 h to evaporate the n-heptane. After filtration, the filter papers were dried and weighed. The concentration of asphaltenes and solid particles for LFO, MFO and HFO were 5.67, 23.5 and 48.7 g L-1 respectively.

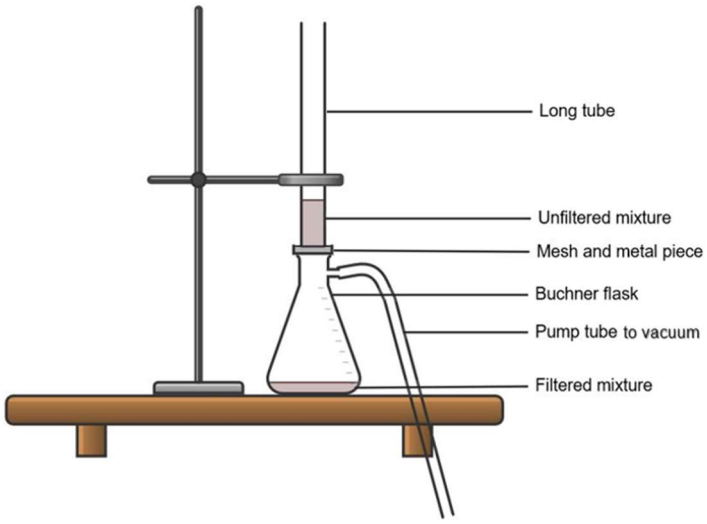

Figure 1: Diagram of the asphaltene vacuum filtration setup.

2.2 Lubricity tests

Lubricity tests were performed according to ISO 12156-1 on the HFRR for filtered and unfiltered fuel oil samples at different temperatures. The summary of the test conditions are shown in Table 1.

Table 1: HFRR test conditions.

Parameter	Value
Stroke length, mm	1 ± 0.02
Frequency, Hz	50 ± 1
Humidity, % (RH)	50 ± 5
Fluid temperature, ºC	115 ± 2, 100 ± 2, 60 ± 2, 25 ± 2
Load, g	200 ± 1
Test duration, min	75 ± 0.1
Fluid volume, ml	2 ± 0.2
Reservoir surface area, mm^2	600 ± 100

A humidifier was used to control the relative humidity of the HFRR chamber to 50% RH under atmospheric air. The humidity was monitored throughout the HFRR test using a Sensirion humidity sensor.

3 RESULTS AND DISCUSSION

3.1 Viscometer measurements

The Anton Paar SVM 3000 Stabinger viscometer was used to measure the dynamic viscosity of the fuel oils at different temperatures. The results are shown in Figure 2.

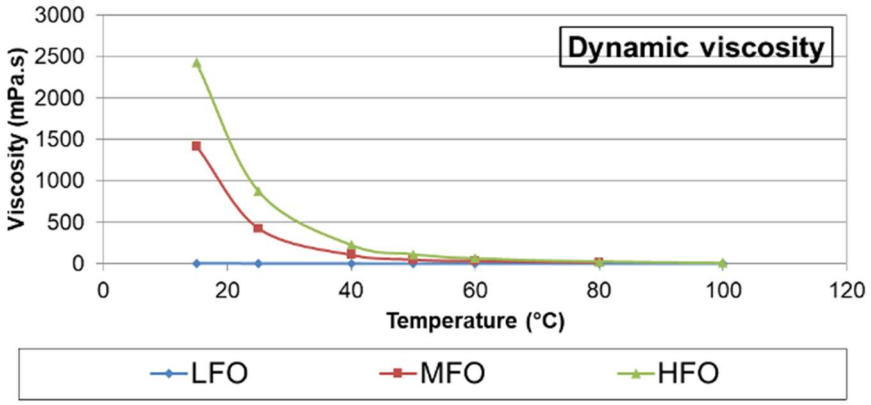

Figure 2: Dynamic viscosity of fuel oils at different temperatures.

The results show that the viscosity of the fuel oils tested decreases exponentially with increasing temperature. The absence of asphaltenes in LFO results in lower viscosity measurements and a gentle gradient for viscosity versus temperature graph as compared to MFO and HFO.

3.2 Elemental analysis

Elemental analysis of the fuel oils was performed using the Spectro Arcos inductively coupled plasma (ICP) machine from Ametek Materials Analysis Division which uses the technique known as ICP-OES (Inductively coupled plasma-optical emission spectrometry). The preparation method used for the ICP-OES was the wet washing procedure. HFO has the highest concentration of asphaltenes and solid particles compared to MFO and LFO shown in Table 2. The asphaltene concentration in HFO and MFO is shown by the concentration of vanadium, nickel and iron since LFO does not contain asphaltenes.

Table 2: ICP results for fuel oils.

Sample	HFO (mg/kg)	MFO (mg/kg)	LFO (mg/kg)
V	14.7	4.94	2.15
Ni	10.5	2.37	1.61
Na	80.8	1.78	6.80
Fe	28.6	6.71	18.1
Mn	1.69	1.18	1.07
Mg	9.21	2.96	4.65
K	11.1	2.76	4.11
S	883	118	159
Cr	4.32	1.58	3.76
Ca	124	60.6	85.2
Al	216	2.37	1.79
P	18.6	-	-
Zn	9.77	2.57	3.04
Si	5.26	8.69	11.3

3.3 Coefficient of friction

At 25 °C, the COF drastically increases for filtered LFO when compared to unfiltered LFO. The low temperature limits chemical wear from taking place because there is minimal frictional heat present (Garaniya et al, 2018; Bhushan, 2013: 359). Between 60 °C and 115 °C, the COF is similar for filtered and unfiltered LFO, although the roughness of the COF for unfiltered LFO is much more severe compared to filtered LFO. This is due to the solid particles in unfiltered LFO which interact with the surface resulting in concentration of heat at the contacts which results in a rougher COF profile (Stachowiak & Batchelor, 2014: 11).

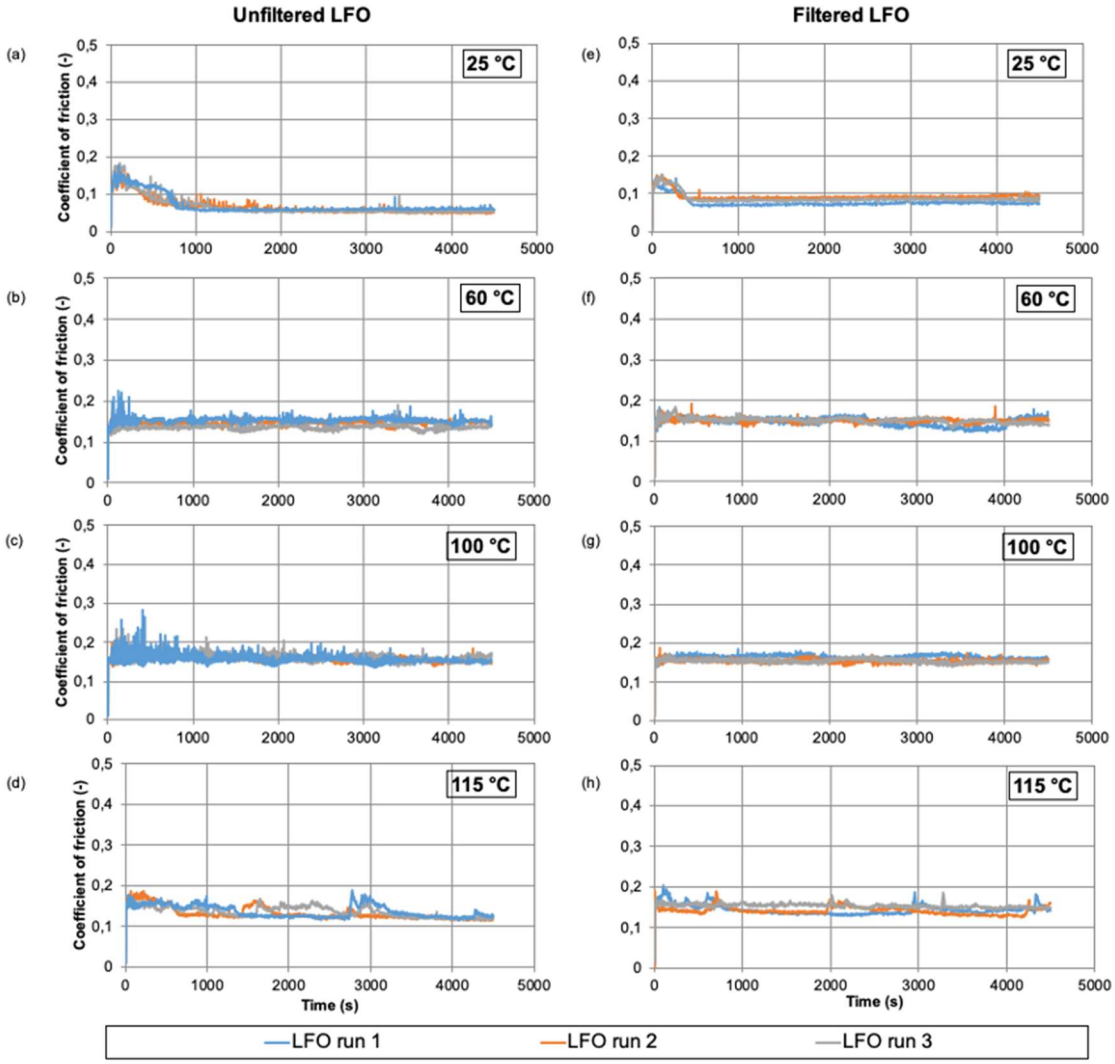

Figure 3: Coefficient of friction versus time graphs of unfiltered and filtered LFO for three runs at 50% RH.

The increase in temperature for unfiltered MFO and filtered MFO results in an increased stability of the COF, although there is a decrease between 100 to 115 °C shown in Figure 4. At 25 °C, the low temperature limits chemical wear taking place because there is minimal frictional heat present but as temperature increases the protective layer is more likely to be rubbed away due to increased frictional heat resulting in the instability of COF (Garaniya et al, 2018; Bhushan, 2013: 359).

There is minimal change in COF for filtered MFO and unfiltered MFO at different temperatures. Asphaltenes and some waxes were removed during the filtration process for MFO. Waxes have good lubricating properties and removal of some waxes and asphaltenes resulted in no apparent effect in COF when compared to unfiltered MFO. The asphaltenes in unfiltered MFO are very polar compounds which adsorb on the metal surface resulting in the formation of a protective layer. This results in similar COF values for unfiltered MFO and filtered MFO with smoother profile for filtered MFO due to removal of asphaltenes and solid particles.

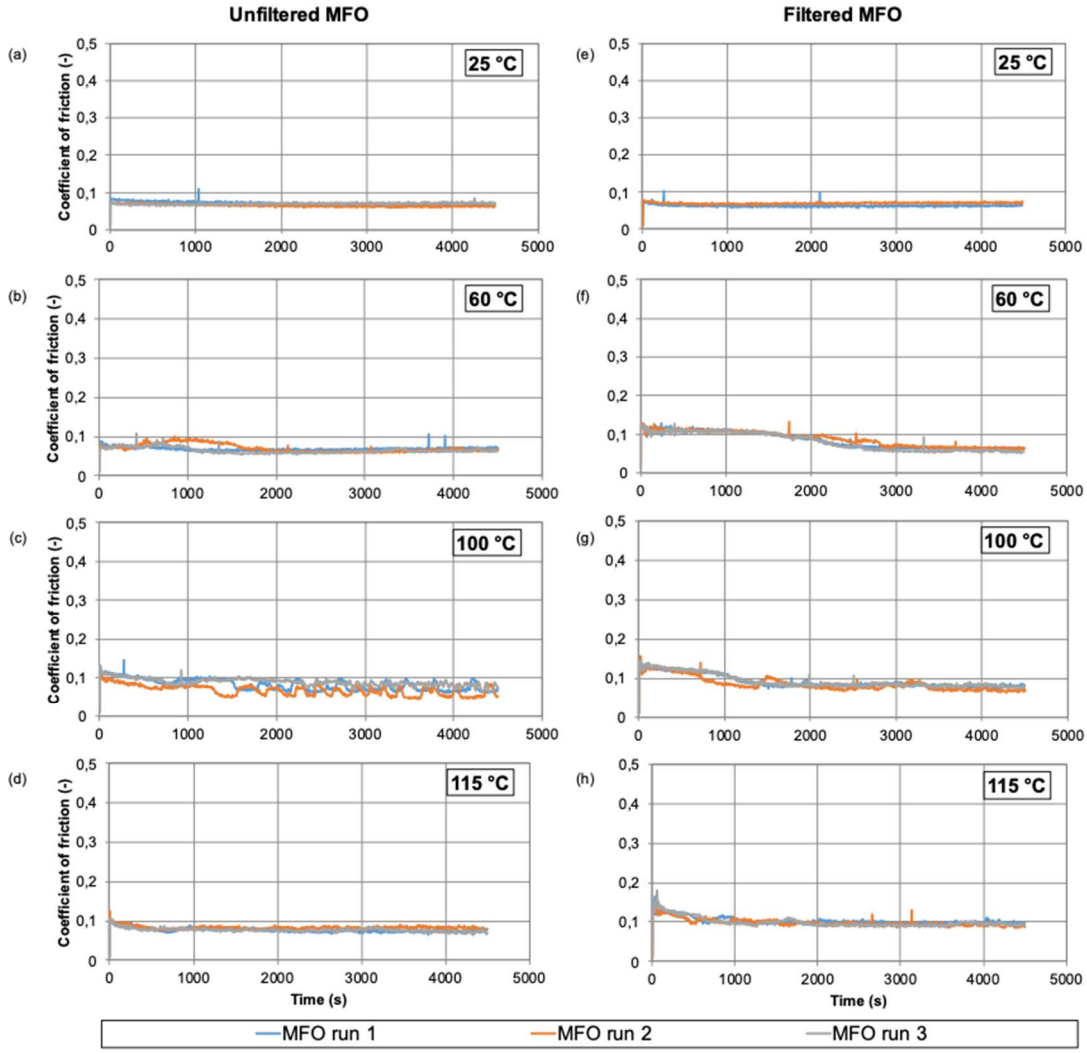

Figure 4: Coefficient of friction versus time graphs of unfiltered and filtered MFO for three runs at 50% RH.

The COF for filtered HFO and unfiltered HFO shown in Figure 5 decreases between 25 and 60 °C. The lower COF at 25 °C is due to the high viscosity at low temperatures resulting in more power for HFO to be sheared. The power losses are higher and more heat is generated resulting in increased heat of the contacting surfaces which leads to a higher COF at 25 °C compared to 60 °C (Stachowiak & Batchelor, 2014: 11). At 100 and 115 °C, the COF values for unfiltered HFO fluctuate throughout the test with high COF peaks. The high and rough COF at 100 and 115 °C could be due to breakthrough of the fuel oil; this will be confirmed by the wear results. Breakthrough of the fuel oil is determined by high COF and complete metal-to-metal contact. At high temperatures, the effects of the asphaltenes and solid particles for unfiltered HFO are most prominent due to the drastic decrease in viscosity and therefore the reduction in film thickness, resulting in more interactions between the asphaltenes and solids particles in unfiltered HFO and the surfaces. The interactions lead to the concentration of heat which increases the COF and results in a rougher COF profile (Stachowiak & Batchelor, 2014: 11). For

filtered HFO, the COF values are low (0.1) at 100 and 115 °C. The removal of asphaltenes and solid particles during filtration shows significant decrease of the COF.

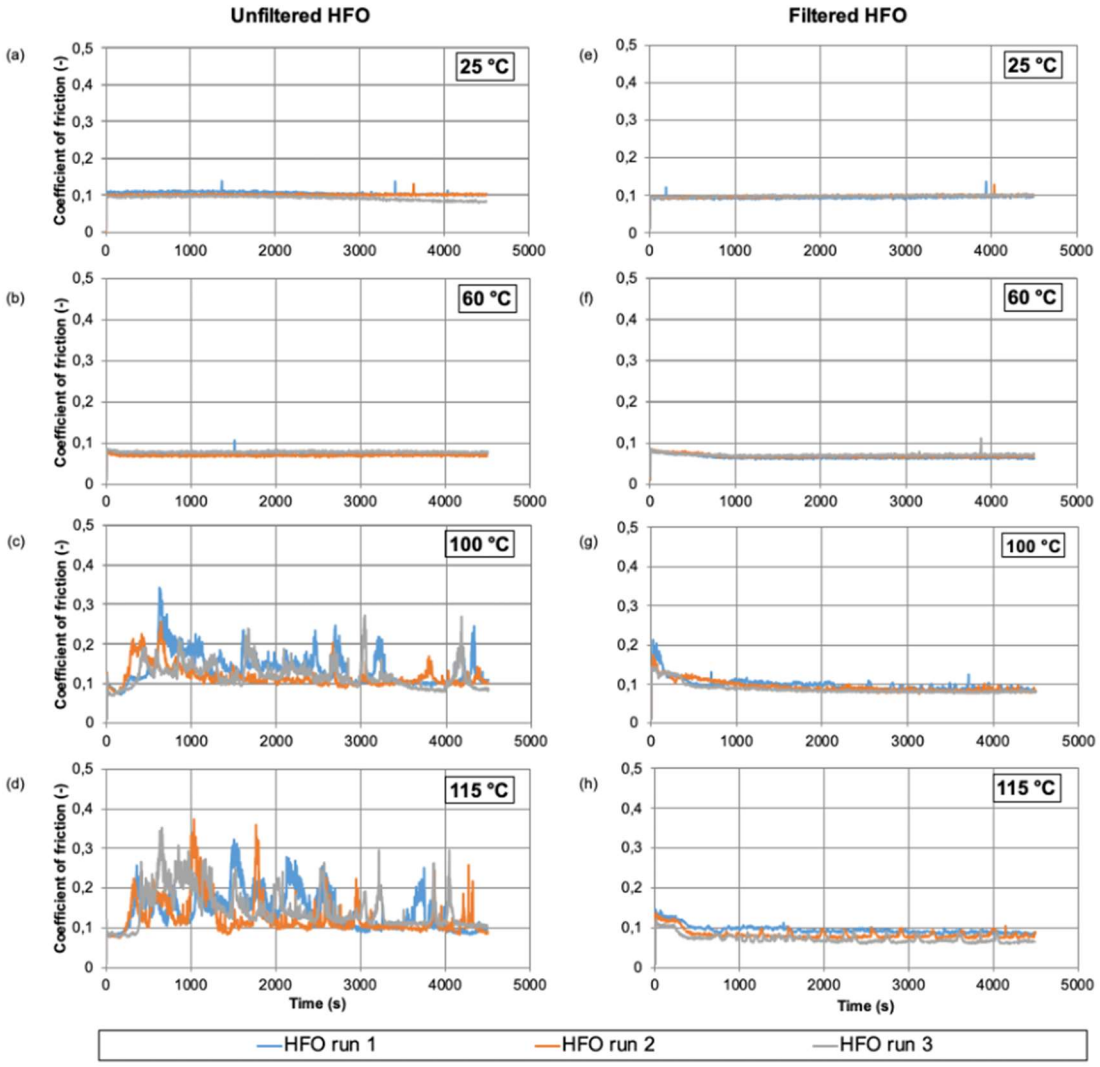

Figure 5: Coefficient of friction versus time graphs of unfiltered and filtered HFO for three runs at 50% RH.

3.4 Wear

The wear scar micrographs produced from the friction and wear tests are shown below with their respective complementary ratings (CR) and average corrected wear scar diameters (WS 1.4). The CR helps to identify different wear mechanisms which lead to different visual appearances on the ball. The CR is based on a 6-graded visual rating scale method with 1 being excellent lubrication and 6 being no lubrication with distinct wear marks inside the contact (Oláh *et al*, 2005).

Table 3: Wear scars for filtered and unfiltered LFO at different temperatures at 50% RH.

Temperature	25 °C	60 °C	100 °C	115 °C
Unfiltered LFO	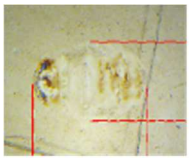	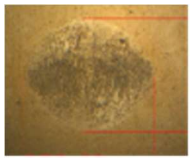	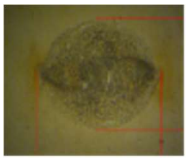	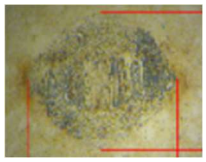
CR	3	2	3	4
WS 1.4 (µm)	191	360	364	295
Filtered LFO		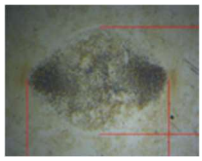	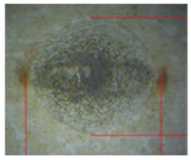	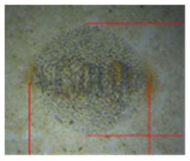
CR	3	2	2	2
WS 1.4 (µm)	145	348	375	307

For unfiltered LFO, the CR decreases from 25 to 60 °C and increases from 60 to 115 °C. At high temperatures slight abrasion occurs due to decrease in the viscosity which results in reduction of the film thickness and therefore less separation between the solid particles for unfiltered LFO and metal surfaces (Stachowiak & Batchelor, 2014: 11). As the temperature increases for unfiltered LFO, the degree of oxidation increases. This is seen by the darkening of the wear scar due to increased oxidation which causes oxide formation on the contact surface (Oláh et al, 2005). Oxidative wear is the lowest at 25 °C for filtered and unfiltered LFO because of the low temperature. Oxidative wear occurs at high temperatures (Bhushan, 2013: 359).

For filtered LFO, the CR is the highest at 25 °C and stays constant between 60 and 115 °C at a CR of 2. There is no abrasion for filtered LFO. The wear scars for filtered LFO and unfiltered LFO look similar with filtered LFO having less abrasive wear due to the removal of solid particles.

Table 4: Wear scars for filtered and unfiltered MFO at different temperatures at 50% RH.

Temperature	25 °C	60 °C	100 °C	115 °C
Unfiltered MFO	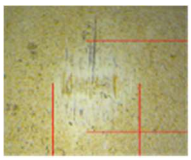	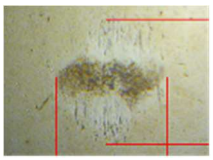	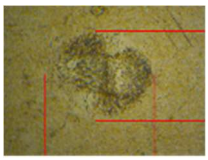	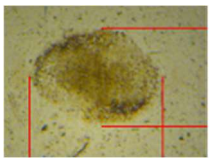
CR	3	3	2	2
WS 1.4 (µm)	177	191	185	184
Filtered MFO	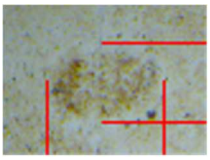	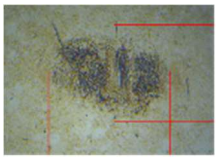	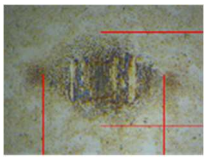	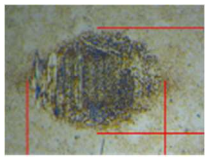
CR	3	2	4	4
WS 1.4 (µm)	85	206	188	175

For unfiltered MFO, the minimal change in the CR correlates with the minimal change in the COF with increasing temperature. As the temperature increases, the degree of oxidation on the wear scar increases resulting in the formation of a protective layer (ferrous oxide) and therefore a decrease in abrasive wear (Hudedagaddi *et al,* 2017). This is seen by the darkening of the wear scar and less visible scratch lines with increasing temperature (Oláh *et al*, 2005). There is more oxidative wear present in filtered MFO compared to unfiltered MFO with increasing temperature.

Filtered MFO shows abrasive wear at high temperatures (100 and 115 °C). The removal of some waxes during the filtration of asphaltenes resulted in more wear at high temperatures. The heavy fractions of MFO, waxes and asphaltenes, play an important role in the rheological behaviour (Alcazar-Vara & Buenrostro-Gonzalez, 2011). The presence of waxes can modify asphaltene behaviour, accelerate the dissolution of asphaltenes and modify their stability (Rogel *et al*, 2016). This means the transition of asphaltenes to liquid form is accelerated resulting in much higher viscosity of unfiltered MFO compared to filtered MFO. This results in better separation between the metal surfaces at 100 and 115 °C and therefore less wear for unfiltered MFO compared to filtered MFO.

Table 5: Wear scars for filtered and unfiltered HFO at different temperatures at 50% RH.

Temperature	25 °C	60 °C	100 °C	115 °C
Unfiltered HFO	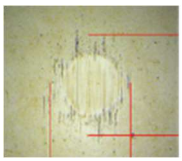		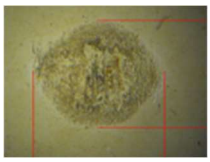	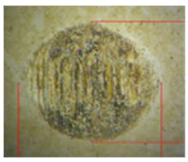
CR	6	3	4	5
WS 1.4 (µm)	217	222	343	431
Filtered HFO		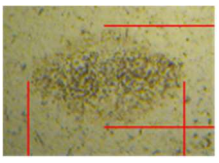	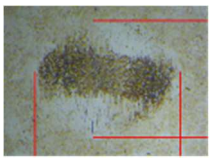	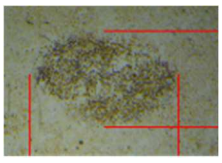
CR	-	3	3	3
WS 1.4 (µm)	**No wear scar**	137	201	168

The CR and abrasive wear for unfiltered HFO decreases from 25 to 60 °C, although the CR and abrasive wear increases between 60 to 115 °C. The high abrasive wear at 25 °C is due to the high viscosity at low temperatures resulting in more power for unfiltered HFO to be sheared. The power losses are higher and more heat is generated resulting in increased heat of the contacting surfaces which leads to more wear (Stachowiak & Batchelor, 2014: 11). As the temperature increases between 60 and 115 °C, the abrasive wear increases due to decrease in viscosity resulting in a thinner film thickness which leads to abrasive particles of asphaltenes and solid particles interacting with the metal surfaces. The high concentration of asphaltenes in unfiltered HFO results in asphaltene adsorption at the surface of the metal because of the very polar compounds in asphaltenes. The lower temperature (60 °C) limits chemical wear taking place because there is minimal frictional heat present but as temperature increases the protective layer is more likely to be rubbed away due to increased frictional heat resulting in increased wear (Garaniya *et al,* 2018; Bhushan, 2013: 359). For unfiltered HFO at 100 and 115 °C, although severe abrasive wear is present, the CR is not a 6 which is defined as no lubrication; therefore we can conclude that unfiltered HFO at 100 and 115 °C does not result in breakthrough but instead results in severe wear.

Filtered HFO has no wear scar at 25 °C, the high viscosity results in a thick film capable of separating the two contacting surfaces completely. As the temperature increases between 60 and 115 °C for filtered HFO, the CR stays the same. The absence of asphaltenes and solid particles in filtered HFO results in no abrasive wear present and oxidative wear becomes the dominant wear process which increases with increasing temperature.

4 CONCLUSIONS

The effect of temperature and asphaltene content were investigated in this work. Lubricity tests were performed on three filtered and unfiltered fuel oils. The following conclusions may be drawn:

- LFO with no asphaltenes (solid particles only) has little impact on the COF and wear from 60 to 115 °C. The trend for COF and wear is similar for both filtered and unfiltered LFO. The solid particles affect the roughness of the COF, minimal change in the WS 1.4 and slight abrasive wear due to the presence of metals in the solid particles. The removal of solid particles results in minimal change in COF except at 25 °C where the unfiltered LFO has a drastic reduction in COF compared to filtered LFO.
- MFO containing high molecular paraffin (wax) and asphaltenes results in a more stable fuel oil. The MFO performs better with asphaltenes because the wax stabilizes the asphaltenes resulting in the dissolution of asphaltenes at an accelerated rate. This results in good high temperature performance (less friction and wear at high temperatures). For MFO, the removal of asphaltenes results in minimal change in COF and minimal change in WS 1.4 from 60 to 115 °C. Due to the presence of waxes in MFO, the wear results for MFO do not follow the typical trend where the increase in temperature usually results in an increase in wear. For MFO, the removal of asphaltenes and solid particles resulted in a decrease in wear at low temperatures and an increase in wear at high temperatures.
- HFO containing high concentration of asphaltenes and solid particles results in very high COF and severe abrasive wear at high temperatures. At low and moderate temperatures, the HFO performs comparable to filtered HFO, while at high temperatures the COF, abrasive wear and WS 1.4 drastically increases compared to filtered HFO. Overall HFO performs better in the absence of asphaltenes and solid particles due to their abrasive nature particularly at high concentrations.

REFERENCES

Alcazar-Vara, LA, Buenrostro-Gonzalez, E (2011) “Characterization of the wax precipitation in Mexican crude oils”, *Fuel Processing Technology*, 92, 2366-2377.

Ancheyta, J, Trejo, F, Rana, MS (2009) *Asphaltenes Chemical Transformation during Hydroprocessing of Heavy Fuel Oils,* CRC Press, Boca Raton.

Bhushan, B (2013) *Introduction to Tribology*, 2nd edition, Wiley, West Sussex.

Cao, Z, Zhang, X, Xu, C, Huang, X, Wu, Z, Peng, C, Duan, A (2021) “Selective Hydrocracking of light cycle oil into high-octane gasoline over bi-functional catalysts”, *Journal of Energy Chemistry*, 52, 41-50.

Garaniya, V, McWilliam, D, Goldsworthy, L, Ghiji, M (2018) “Extensive chemical characterization of a heavy fuel oil”, *Fuel*, 227, 67-78.

Ghanavati, M, Shojaei, M, Ramazani, A (2013) “Effects of asphaltenes content and temperature on viscosity of Iranian heavy crude oil: Experimental and modelling study”, *Energy Fuels*, 27, 7217-7232.

Harker, JH, Allen, DA (1972) *Fuel Science,* Oliver & Boyde, Edinburgh.

Hudedagaddi, CB, Raghav, AG, Tortora, AM, Veeregowda, DH (2017) “Water molecules influence in the lubricity of greases and fuel”, *Wear*, 376-377, 831-835.

Lapuerta, M, Sánchez-Valdepeñas, J, Bolonio, D, Sukjit, E (2016) “Effect of fatty acid composition of methyl and ethyl esters on the lubricity at different humidities”, *Fuel*, 184, 202-210.

Nickels, L (2011) “Low fuel lubricity in thin distillates”, *World Pumps,* 2, 10.

Oláh, ZS, Szirmai, G, Resofszki, G (2005) “Micro and Macro analyses of wear scar surfaces- A complementary rating method to the evaluation of HFRR test results; International colloquium”, TAE, Ostfildern.

Stachowiak, GW, Batchelor, AW (2014) *Engineering Tribology*, 4th edition, Butterworth-heinemann, Oxford.

Effect of the new Major Hazard Installation Regulations on the South African Chemical Industry

M. G. Mabaso[1], R. Aphane[2], M. Atterbury[3], D. Rademeyer[4], B. Leshiba[5] and L. Grundlingh[6]

[1] MMRisk (Pty) Ltd, 1234 Sand Hills Close, Copperleaf, Centurion 0149

[2] Department of Employment and Labour, 215 Francis Baard St, Pretoria Central, Pretoria, 0001

[3] Eskom Holdings SOC Limited, Maxwell Dr, Sunninghill, Sandton, 2157

[4] Ishecon CC, Building H6 Pinelands Office Park, Maxwell Dr, Modderfontein, Lethabong, 1645

[5] Afrox South Africa, 23 Webber St, Selby, Johannesburg, 2001

[6] South African National Accreditation System (SANAS), Libertas Office Park, Corner Libertas and Highway Streets, Equestria, Pretoria, 0184

*Corresponding author: motlatsi@mmrisk.co.za

ABSTRACT

The Major Hazard Installation (MHI) Regulations of South Africa (2001), promulgated under the Occupational Health and Safety Act no. 85 of 1993 (the Act), regulate the handling by industrial facilities of chemical substances with potential to cause major chemical accidents adversely impacting employees and members of the public. The current set of regulations has become outdated when applied to modern chemical industries and therefore the need arose to revise the regulations in line with international trends, offer increased protection to safety of employees and the public and advise on land-use around industrial facilities. A technical committee assembled by the Department of Employment and Labour effected changes to the regulations, extensive public comment and industry consultation were conducted. This presentation will summarise the amendment process and highlight the main changes between the existing and proposed sets of regulations. Delegates likely work in industries where MHIs are present and may be exposed to potential chemical accidents which put them at risk of injury and death. This paper seeks to describe the regulatory basis in South Africa (SA) for managing risk (prevention and mitigation) of major chemical accidents.

Keywords: Major Hazard Installation Regulations; MHI; Occupational Health and Safety Act; South Africa; major chemical accidents; process safety; Department of Employment and Labour

1 INTRODUCTION

The Department of Employment and Labour (the Department) regulates installations which store, manufacture, handle and process chemicals at quantities and forms that have potential to pose a risk to employees and the public and which can cause a major incident. This is achieved through the Major Hazard Installation Regulations, GNR 692 of 30 July 2001 (the 2001 regulations), promulgated under the Occupational Health and Safety Act no. 85 of 1993 (the Act). Implementation of the 2001 regulations do not solely depend on the Department, but, the coregulators: Local Governments (LGs)

are also given duties to strategically place MHI facilities in a 'safe' area, to test Emergency Plans (EPs) and respond to emergency occurrences and major incidents. Currently, MHI facilities of varying magnitude are required to implement the same requirements under the 2001 regulations, placing a burden on smaller MHIs. To provide clear strategies, the 2001 regulations were studied and a need for improvement was identified. As such, different regimes internationally were considered with a view to align to global best practice. A revision of the 2001 regulations was initiated in 2013 and proposed draft MHI Regulations were published in November 2019. The final draft of the proposed MHI Regulations has been edited by State Law Advisers (SLA) and is due for submission to the Minister of Employment and Labour's Advisory Council on Occupational Health and Safety (ACOHS). This paper describes comparative regulations around the world, the methodology followed in updating the 2001 regulations, the structure of the proposed regulations which would replace the 2001 regulations and conclusions drawn from the exercise.

2 LITERATURE

Several countries globally regulate the management of process safety at industrial facilities; existing regulations were reviewed to align the South African legislation internationally. Countries whose legislation was included in this survey were Malaysia, Singapore, Australia, the European Union (SEVESO III Directive) with the United Kingdom (UK) Control of Major Accident Hazards (COMAH) Regulations of 2015, with the latter an example of an EU member state's implementation of the SEVESO III Directive.

In general, the objectives of each country or territory's risk regulations are the same, which is the prevention of major accidents due to dangerous chemical substances handled at industrial facilities. All of them require the registration or licensing of establishments handling dangerous chemicals and all of them refer to a threshold quantity of substance. There are differences between whether a single quantity qualifies an installation or establishment for registration or whether several quantities qualify them. All the regulations studied require the compilation of documents (risk assessments or safety assessments) to assess the risk associated with the facilities; the Australian and Singapore regulations require the preparation of a 'Safety Case' for all qualifying establishments, while the UK applies a staggered approach with only Upper Tier establishments requiring a Safety Report (equivalent to a Safety Case). The duration of registration ranges between three and five years after which renewal can be sought.

3 PROCEDURE FOR REVIEWING THE REGULATIONS

3.1 Gaps identified in the 2001 regulations

The Department is in the business of regulating the Act and its regulations and they do this by monitoring compliance through inspections, advocacy, and enforcement. In these processes the Department gathers information such as compliance levels, number of reported incidents, relevance and

practicality, improvement in technology, amongst others. Identification of gaps may culminate in the need for revision of regulations. The 2001 regulations had some gaps identified by the Department, the chemical industry, as well as the coregulator. Some of these gaps included:

- Inconsistency in conducting Risk Assessments required by the 2001 regulations;
- A high level of non-compliance with respect to implementation of organisational measures;
- Notifications not attended to or at times not received;
- No alignment with transporters of chemicals; and
- EPs not in place and not proportional or aligned to the operations onsite.

3.2 Revision of the 2001 regulations

Based on the gaps identified, the Department conducted a desktop study to establish if there was enough reason for the 2001 regulations to be revised. A study of various regulatory regimes internationally was conducted, the regulations were studied and compared (refer to Section 2) and lessons were drawn. A needs analysis was conducted to check if identified regulations would be easily implementable and sustainable without placing additional burden on the chemical industry. From this exercise the UK COMAH Regulations 2015 were chosen to be modelled and were considered a sustainable option for SA. The consideration to revise the 2001 regulations was tabulated to and approved by, the ACOHS.

3.3 Work of the MHI Technical Committee

Via the ACOHS, a MHI Technical Committee (MHI TC) comprising members from different stakeholders including Business, Organised Labour and subject-matter-experts was proposed. A nominations process was followed, and members were appointed in writing to serve in the MHI TC. The MHI TC commenced with meetings and a framework on revising the regulations was developed. The Department hosted annual workshops to gather more information and to solicit the opinions of the chemical industry and interested and affected parties. Furthermore, consultations were held with the UK Health and Safety Executive (HSE) to get buy-in to utilising the UK COMAH 2015 Regulations as the basis for revision of the 2001 regulations.

A need was identified for alignment with Department of Transport, the Civil Aviation Authority and therefore a dangerous substances concept was adopted.

3.4 Drafting of the proposed regulations

A first draft of the proposed regulations was concluded and submitted for approval to the SLA to align the draft with the Constitution and to check the legality of the proposed regulations. The draft was reworked following comments from the SLA until the first approved draft was published for public

comment in November 2019. Further, various members of industry and the public at large were consulted in March 2021 and all the received comments were attended to. At the time of writing the final draft of the proposed regulations was being discussed for finalisation.

4 KEY OUTCOMES AND DISCUSSION

This section summarises the outcomes of the process of updating of the regulations, presenting all the clauses contained in the proposed regulations in comparison to the clauses contained in the 2001 regulations. The main points relating to each regulation (by the number given to the proposed regulation) are presented in tabular form under each sub-section here.

4.1 Scope

Table 1: Discussion of Regulations 1 and 2

Regulation	Topic	Topic present in 2001 regulations?	Discussion
1	Definitions	Yes	Several definitions have been added to the regulations to give further nuance to the proposed regulations. The most notable additions include: • A definition for "Change". • "CLP Regulations Nations' Globally Harmonised System (GHS)". • "Establishment": categorization of major hazard installations as low, medium, or high. • "Licence to operate". • "Prescribed quantity": provides a definition for the quantities presented in the Annexures. • "Process safety management system". • "Responsible person". • "Safety report". • "SANS 1461" and "SANS 1514": Makes these newly published standards legal requirements for Risk Assessments and Emergency Plans, respectively.
2	Scope of application	Yes	Sets out which regulations apply to which establishments defined as either low, medium, or high hazard establishments. The exclusion of nuclear installations is confirmed.

4.2 Administrative Requirements

Table 2: Discussion of Regulations 3 – 8,16, 17, 21,22,23,24,25 and Annexure B

Regulation	Topic	Topic present in 2001 regulations?	Discussion
3	Management of MHI	New Concept	This regulation introduces a legal appointee called 'responsible person', who ensure compliance to these Regulations

Regulation	Topic	Topic present in 2001 regulations?	Discussion
4	Notification of establishment	Yes	• The information accompanying notification has been amended to contain more information for the Chief Inspector, provincial director, and local government (LG). • Advertisements in a local newspaper must now be completed in English and another dominant language of the area. • There is a requirement for the risk assessment report to be explained to interested parties.
5	Registration of MHI	New concept	• The MHI will be formally registered by issuing of a certificate and a national register of all MHI will be kept. • The Department has also been empowered to refuse registration with valid reasons.
6	Duration of registration and renewal	New requirement	• Registration is valid for a period of 5 years. • The chief inspector may renew the registration upon the updating of a risk assessment report and on payment of the appropriate renewal fee specified.
7	Alteration to particulars of registered establishment	New requirement	The duty holder must, where there is an alteration to any of the particulars, furnish the alterations to the chief inspector.
8	Revocation or suspension of registration	New requirement	• The Department has a direct prerogative to instruct the establishment to comply if the facility is unfit for occupation providing reasons. • The establishment is also given an opportunity to appeal the decision in terms of section 35 of the Act.
16	Reporting of risk and emergency occurrences	Yes	The requirements of this Clause are largely like the 2001 regulation.
17	Information and Training	New requirement	Training of Employees is required on the following: • The scope of these Regulations; • The nature of the establishment; • Potential major hazards and associated major incidents; • Potential risks to health and safety caused by the identified major hazards; • The practices and control procedures for a major incident; and Safety protocols and measures to be followed in case of an emergency.
21	Payable fees	New requirement	A fee will be charged for registration and renewals Fee structure is Annexure B.
Annexure B	Fees for the registration	New requirement	Provides a fee structure for registration and renewals.
22	Closure	Yes	The time frame for notification of closure has been increased from the original 30 days and now its 60 days.
23	Offenses and	New	Offences and penalties are now pronounced, fines are prescribed, and stringent punishments are introduced. Fines

Regulation	Topic	Topic present in 2001 regulations?	Discussion
	Penalties	requirement	are prescribed in Annexure E.
24	Repeal of Regulations	Yes	Repeals 2001 regulations.
25	Short title and commencement	New addition	Describes the name of regulations: Major Hazard Installation Regulations followed by the year of the regulations coming into force.

4.3 Consultation

Table 3: Discussion of Regulation 9

Regulation	Topic	Topic present in 2001 regulations?	Discussion
9	Sharing of information	Not explicitly dealt with	To make several installations in close proximately aware of each other's dangers, the Chief Inspector may issue a directive for each installation in the group to share information to facilitate coordinated emergency response.

4.4 Technical Requirements

Table 4: Discussion of Regulations 10 – 12, Annexures C and D, Regulations 13 and 15

Regulation	Topic	Topic present in 2001 regulations?	Discussion
10	Risk Assessment	Yes	• A risk assessment must be conducted by an approved inspection authority according to SANS 1461 for each establishment. • The establishment's Health and Safety Committee must be consulted when conducting a risk assessment.
11	Major incident prevention policy (MIPP)	New requirement	• Medium and High establishments are required to compile a policy on how they will prevent the occurrence of a major incident at an establishment within 36 months after promulgation of the regulations. • Review of the policy must be done every 5 years.
Annexure C	Principles to be taken into account when preparing major incident prevention policy (MIPP) document	New addition	Provides guidance on the compilation of a MIPP which will ensure consistency across all establishments in the principles to follow and uniformity of the management of risk of major incidents.
12	Safety report	New requirement	• Introduction of the requirement for a Safety Report aligns with other risk legislation around the world. • A High Hazard establishment must prepare a

Regulation	Topic	Topic present in 2001 regulations?	Discussion
			detailed safety report during the design phase, updated as the design progresses up to the start of operations. • Contents of this report are described in this regulation as well as in Annexure D.
Annexure D	Purpose and contents of safety reports	New requirement	• Describes the content of a Safety Report.
13	Licence to operate	New requirement	A duty holder who operates a high hazard establishment must apply for a licence to operate such an establishment.
15	Emergency plan	Yes	• Standardises the contents of EPs through the requirement to comply with SANS 1514 and includes additional requirements for the management of EPs.

4.5 Approval of MHI facility

Table 5: Discussion of Regulation 14

Regulation	Topic	Topic present in 2001 regulations?	Discussion
14	General duties of local government (LG)	Yes	The proposed regulations require that: • The LG "must not permit the erection of a new establishment or the expansion of an establishment at a separation distance that poses an unacceptable risk". • LG must follow SANS 1514 for the development of the off-site emergency plan. • There is a strong indication that all the requirements placed on LG are driven by a risk-based approach and by the information contained in the MHI Risk Assessment.

4.6 Supplier Requirements

Table 6: Discussion of Regulation 18

Regulation	Topic	Topic present in 2001 regulations?	Discussion
18	General duties of suppliers	Yes	The requirements of this Clause are largely like the 2001 regulation.

4.7 Obligations of Approved Inspections Authorities

Table 7: Discussion of Regulations 19 and 20

Regulation	Topic	Topic present in 2001 regulations?	Discussion
19	Approved inspection authorities	New addition	• This regulation details the process to be followed by accredited inspection bodies that wish to be approved by the Chief Inspector. • It also gives guidance on the actions to be taken when disputes occur between duty holders and approved inspection authorities.
20	Duties of approved inspection authority	New requirement	Duties of approved inspection authorities (AIAs) are defined: • Ensuring that risk assessments, reports and attachments are carried out in accordance with SANS 1461. • Providing results on the MHI establishment classification, acceptability of risk, and make recommendations. • Risk assessment reports shall be made available to the chief inspector and local government. • Reporting all MHIs assessed, to the Chief Inspector. • May be requested by the Chief Inspector to participate in investigations, inquiries, emergency occurrences and major incidents.

4.8 Annexure A Chapters 1 – 3

Table 8: Discussion of Annexure A Chapters 1 – 3

Regulation	Topic	Topic present in 2001 regulations?	Discussion
Annexure A Chapters 1 and 2	Dangerous Substances to which the regulations apply	New addition	• The provision of three columns (Columns 1, 2 and 3) provides a tailored approach to managing major accident risk for various sizes of establishments and companies, avoiding a one-size-fits-all approach. • The dangerous substances have been defined in line with the GHS system.
Annexure A, Chapter 3	Classification of pipelines as Major Hazard Establishments	Yes	Describes that a cross country pipeline handling fluids which complies with the conditions provided in the annexure will be classified as a Major Hazard establishment. This differs from the 2001 regulations where the criteria for pipelines being included were not specified.

4.9 Form A, Form B and Annexure E

Table 9: Discussion of Form A, Form B and Annexure E

Regulation	Topic	Topic present in 2001 regulations?	Discussion
Form A	Notification Form	New addition	• A notification template has been designed to direct the MHI facility to provide required information. • The filling of the form also requires that the MHI facility get an acknowledgement from the relevant Local Government to ensure appropriate communication between the establishment and the local government.
Form B	Application for registration as approved installation inspection authority	New addition	Provides an application form for companies wishing to register as AIAs.
Annexure E	Monthly AIA Reports	New requirement	• Annexure E contains a table that must be populated monthly by AIAs in terms on their reporting to the chief inspector. • Items that need to be reported on are described therein. • AIAs required to give monthly returns of accessed facilities to promote cooperative governance, track the MHI facilities, ensure that all MHI facilities are accounted for.

5 CONCLUSIONS

The proposed regulations introduce threshold chemical quantities which weren't present in the 2001 regulations which places the proposed regulations on par with global peers and align with the definition of MHI provided in the Act. Furthermore, the introduction of three columns of threshold quantities (with differing requirements per quantity of substance handled) allows a differentiated approach based on types and relative sizes of MHIs and companies – avoiding a one-size fits all approach. The introduction of standards SANS 1461 and 1514 standardise the approach to compiling MHI Risk Assessments and EPs. The principles regarding the roles and responsibilities of local government in the 2001 regulations have been retained, enhanced, and clarified based on lessons learnt through years of applying the existing regulations. On-site and off-site emergency plans are still key to well-planned response when all the preventative measures may have failed.

REFERENCES

Business.gov.au. 2021. *Work health and safety | business.gov.au*. [online] Available at: <https://business.gov.au/risk-management/health-and-safety/work-health-and-safety> [Accessed 20 August 2021]

DIRECTIVE 2012/18/EU OF THE EUROPEAN PARLIAMENT AND OF THE COUNCIL of 4 July 2012 on the control of major-accident hazards involving dangerous substances, amending and subsequently repealing Council Directive 96/82/EC (European Union)

Occupational Safety And Health (Control Of Industrial Major Accident Hazards) Regulations 1996 (Malaysia)

The Control of Major Accident Hazards Regulations 2015 (United Kingdom)

Workplace Safety And Health (Major Hazard Installations) Regulations 2017 (Singapore)

Work Health and Safety Regulation 2011 (Queensland, Australia)

An approach for evaluation of friction, viscosity and wear behaviour of polymer base stocks under low humidity Hertzian sliding conditions

S.R. Masilela[1*] and P.L. de Vaal[2]

[1]Department of Chemical Engineering, University of Pretoria, Hatfield 0083, South Africa

[2]Department of Chemical Engineering, University of Pretoria, Hatfield 0083, South Africa

*Corresponding author: u28411341@tuks.co.za

ABSTRACT

Polyalphaolefin (PAO) base stocks have historically proven to possess superior lubricating properties. However, their high production costs place them at a disadvantage. On the other hand, more affordable conventional mineral base stocks pose limited lubricating performance and environmental concerns for modern equipment designs. The development of hydrocracked base stocks with a "plus" (+) has shown great potential to achieve a balance between cost, environmental friendliness and lubrication performance. In this study, friction, viscosity and wear behaviour of a hydrocracked base stock is presented in comparison with solvent refined, hydro-processed and PAO base stocks over a range of selected temperatures. Results demonstrate that the shift towards the use of base stocks with a "plus" will be beneficial in the automotive industry. The hydrocracked base stock demonstrated friction and wear reduction performance similar to that of the PAO, indicating that hydrocracked base stocks can be used in place of PAO base stocks. This behaviour is attributed to free volume which is induced mid-chain branched alkyl chains of the Group 3+ base stock. Results also show that two base stocks in the same group, but produced from different sources of crude, can result in different friction and wear behaviour under certain temperature conditions.

Keywords: base stock, friction, pressure-viscosity coefficient, viscosity, wear

1 INTRODUCTION

Over the past 15 years, there has been growing awareness in the consequences of climate change. There has also been a continuing recommendation of the use of low viscosity lubricating oils by original equipment manufacturers (OEM) in the automotive industry (Dickmann et al., 2018; Gaal, 2021; Hoste, 2021). This has resulted in stringent environmental laws and demanding operating conditions brought by new automotive designs, and also exposed the need for continuous development of environmentally friendly, low cost, low viscosity and high performing lubricating oils (Devlin, 2018; Gaal, 2021; Hoste, 2021; Luzuriaga, 2019). Base stocks are the initial single polymer oils obtained after refining crude oil. Base stocks are key building blocks of lubricating oils and greases, and usually makes up 75 to 99 % of all lubricating oil compositions on a volume basis (Hope, 2018; Lee et al., 2017; Luzuriaga, 2019; Wang et al., 2019). A mixture of one or more base stocks in a fully formulated lubricating oil is usually referred to as a base oil. The two terms are usually used interchangeably, however, base oil is used in the context

of a fully formulated, ready to use, lubricant whereby blending with additives such as anti-oxidants and anti-foaming agents is complete (Hope, 2018; Lee et al., 2017). Base stocks are classified into five groups, shown in by the American Petroleum Institute (API) based on sulfur content, amount of saturated compounds and viscosity index as shown in Table 1 below (Adebogun et al., 2020).

Table 1: API base stock classification.

API Group	Sulfur (% w/w)		Saturates (% w/w)	Viscosity Index
1	> 0,03	and/or	< 90	80 - 120
2	≤ 0,03	and	≥ 90	80 - 120
3	≤ 0,03	and	≥ 90	> 120
4	All polyalphaolefins (PAO)		≥ 90	> 135
5	All base stocks not included in Groups I-IV			

Polyalphaolefin (PAO) base stocks, usually produced by oligomerization processes and classified as Group 4 base stocks, have demonstrated superior lubricating properties in automobile applications. However, their high production costs place them at a disadvantage (Adebogun et al., 2020; Biresaw, 2018; Gaal, 2021; Hope, 2018; Hoste, 2021). The development of severely hydrocracked Group 3+ (group three plus) base stocks has shown great potential to achieve a balance between the base stock cost and high lubricity (Brown, 2015; Gaal, 2021; Hoste, 2021). The “plus” in the base stock group indicates a highly refined base stock with an increased ability to hold its usable viscosity over a wider temperature range than other base stocks in the same API group. This is the property known as viscosity index (VI). The “plus” is not unique to the Group 3 base stocks. In the past decade, Group 2+ base oils started emerging and have gained attention in the base stocks market. This seems to be accelerated by the closure of Group 1 production facilities amid the start of the Covid19 pandemic due to lack of demand and environmental concerns which had been looming for decades due to the high content of sulfur compounds in the Group 1 base stocks (Gaal, 2021; Hoste, 2021). A performance baseline has to be established which will show clearly where the modern base stocks lie in comparison to the conventional Group 1 base stocks which are currently being phased out. This forms a basis for the current study. In this study, an approach is taken to determine and compare the friction, wear and viscosity characteristics of selected base stocks under specified range of temperature conditions. The approach takes into account the 15 °C density, VI as well as viscosity behaviour between 40 and 100 °C. These are some of the important physical properties considered when selecting base stocks in industry.

2 EXPERIMENTAL DETAILS

Viscosities and densities were determined using a Stabinger SVM 3001 rheometer. This was followed by friction and wear experiments which were conducted using the SRV4® tribometer with an oscillatory

sliding ball-on-disc configuration under four temperature conditions i.e., 40, 60, 80 and 100 ºC, and relative humidity (RH) of 20 %. To minimise the influence of moisture on lubricity, the lower humidity was chosen. Polar constituents of base stocks are capable of absorbing moisture from atmosphere into the oil matrix, especially at temperatures above 60 ºC, Water is capable of diffusing through the oil onto the contact surface where it will lubricity behaviour by adsorbing onto polar sites of the metal surfaces (Alazizi et al., 2015; Luo et al., 1998; Myshkin and Kovalev, 2019). Analysis and profiling of the ball and disc surfaces after each experiment was done using a Nanovea PS50 profilometer.

2.1 Selection of base stocks

A set of five commercial base stocks with a 100 ºC kinematic viscosity of 4 cSt were selected from different API groups. Though the 100 ºC viscosity is similar, it was expected to vary at lower temperatures due to differences in composition. The base stocks comprise a solvent refined mineral base stock (G1), two hydro-processed with hydrocracking base stocks from two different suppliers (G3 S1 & G3 S2), a hydro-processed with severe hydrocracked base stock (G3+) and an oligomerized polyaphaolefin base stock (PAO).

2.2 Rheological properties of base stocks

2.2.1 Viscosity and VI: Effect of temperature

Viscosity of base stocks is a very important property in lubrication. It is a measure of both shear strength and load carrying capacity of the base stock (Gold et al., 2001; Lu et al., 2019; Sander et al., 2015; Vengudusamy et al., 2014). By definition, dynamic viscosity is the resistance of a fluid to flow or shear under an applied shear stress at a specified temperature and pressure, and is given by the ratio of rate of shear stress to shear strain as shown in Equation 1 below (Lu et al., 2019).

$$\mu_o = \frac{\tau_s}{\gamma} \qquad \textbf{Equation 1}$$

Where μ_o is the dynamic viscosity at atmospheric pressure, τ_s is the shear stress required to flow or shear the fluid tested and γ the shear strain of the fluid. Kinematic viscosity is the resistance to shear caused by gravity, given by the ratio of dynamic viscosity and density:

$$\mu_k = \frac{\mu_o}{\rho} \qquad \textbf{Equation 2}$$

Where μ_k is the kinematic viscosity at atmospheric pressure, ρ is the density at atmospheric pressure. Measurements were done at temperatures i.e., 40, 60, 80 and 100 ºC, and at atmospheric pressure, using a Stabinger Viscometer (SVM 3001, Anton Paar GmbH, Austria) as per the standard method (ASTM D445-21, 2021). Viscosity index (VI) was also determined as per the standard (ASTM D2270-10, 2016).

2.2.2 Viscosity: Effect of pressure

Generally, viscosity of oils increases under compression. This effect reverses when the pressure of compression is removed (Dickmann et al., 2018; Zhang and Spikes, 2020). In high pressure rheology, this viscosity behaviour is known as the piezoviscous effect and it is represented by a coefficient defined as the pressure-viscosity coefficient (α) (Fernández et al., 2014). The value of the pressure-viscosity coefficient indicates the dependence between load (pressure) placed on a film of oil and its viscosity at that particular load, when all other factors (material, temperature, geometry and speed) are constant (Adebogun et al., 2020; Cai et al., 2015; Zhang and Spikes, 2020). Therefore, a large value of α indicates larger dependency of viscosity on pressure/load. In this investigation, the pressure-viscosity coefficients were estimated using Gold's equation (Equation 3) due to the unavailability of a high-pressure viscometer (Christiansen et al., 2018; Fernández et al., 2014).

$$\alpha = s\mu_k^{\,t} \qquad \textbf{Equation 3}$$

Where μ_k is the kinematic viscosity at standard pressure and test temperature, s and t are Gold's dimensionless constants. For paraffinic mineral and polyalphaolefin base stocks at high pressures, these are shown in Table 2 (Gold et al., 2001; Sander et al., 2015; Stachowiak and Batchelor, 2014; Vengudusamy et al., 2014). The pressure-viscosity coefficients were calculated for all experimental temperatures.

Table 2: Parameters for Gold's equation.

Base stock type	s	t
Paraffinic mineral	0.99	0.14
Polyalphaolefin	0.73	0.13

2.3 Friction and wear experiments

Experiments were carried out using the SRV4® tribometer with a steel ball-on-disc configuration, at 40, 60, 80 and 100 °C, and 20 % relative humidity (RH). The duration of each complete experiment was 120 minutes. The material grade of the 10 mm diameter ball and a 24 mm diameter disc specimen is DIN AISI 52100 (100Cr6) bearing steel with composition specified by the American Iron and Steel Institute (AISI). Three experiments were done with each base stock under similar conditions and average results are determined and reported. For each experiment, 2 mL of base stock was used on a batch basis. The lubricant was injected onto the clean unused disc surface, before the clean unused ball surface was allowed to make contact. At the start of each experiment, the normal load was held at 30 N for 30 s. This first stage is the "run-in" stage and was followed by a 30 s gradual load increase (at 8 $N.s^{-1}$) to a final load of 150 N. From this point the load was kept constant at 150 N for the remainder of the

test duration. The oscillating velocity of the ball (u_b) was 0.2 m.s^{-1} throughout and measurements of the coefficient of friction (COF) were done. Since the disc was held stationery (u_d = 0 m.s^{-1}), the average velocity (u_{avg}) was 0.2 m.s^{-1}.

3 RESULTS AND DISCUSSION

3.1 Density and viscosity

Figure 1 compares VI and 15 °C density of the base oils under investigation.

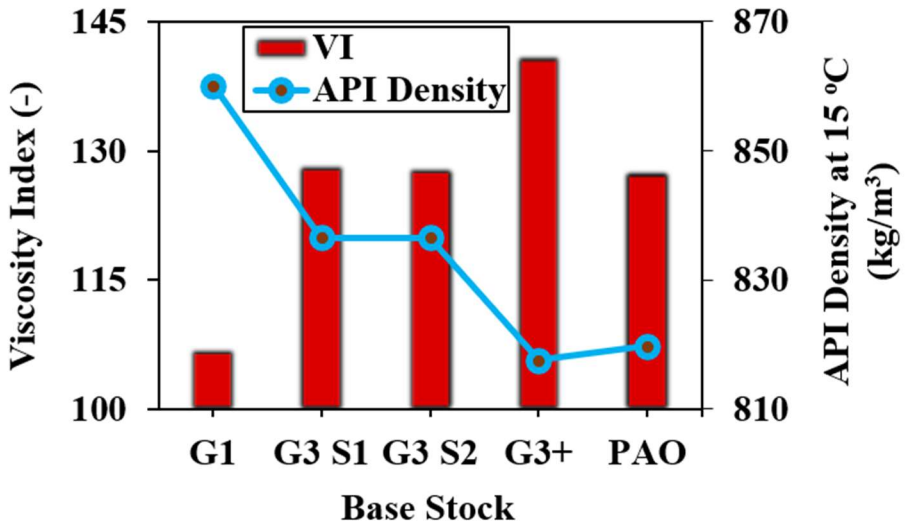

Figure 1: 4 cSt base stocks: Effect of base stock type on Viscosity Index.

G3+ base stock was found to have the highest VI and the smallest 15 °C density. Hydro-processing includes iso-isomerization. Combined with severe hydrocracking produces high quantities molecules with mid-chain branched alkyl chains (Sarpal et al., 2012; Sarpal et al., 2013). The branching increases intermolecular free volume in the oil matrix due to stearic effects, and lowers the number of molecules which can fit freely into a given volume, hence the low molecular weight. The base stock with the lowest VI and highest 15 °C density was the G1 base stock. This is attributed to longer molecular chains, with lower branching and saturation level. This lowers free volume, and renders the molecules more compact in the fluid, hence the larger molecular weight (Christiansen et al., 2018; Dickmann et al., 2018; Lugt and Morales-Espejel, 2011). The low VI behaviour suggests that solvent refined mineral oil's rheology is the most affected by changes in temperature and the G3+ is the least affected. It was surprising to observe that the hydro-processed G3 S2 and G3 S1 base stocks demonstrated higher and similar VI as that of the synthetic PAO base stock, respectively, even though they are heavier. Figure 2 and Figure 3Figure show the variation in kinematic viscosities (μ_k) and dynamic viscosity (μ_o) with temperature, respectively. The trends show a power relationship, with a decrease in dynamic and kinematic viscosity with increasing temperature. The G1 base stock shows the highest viscosities at all experimental temperatures, G3 S1 and G3 S2 base stocks show similar and intermediate viscosities, and

G3+ and PAO base stocks show similar and the lowest viscosities.

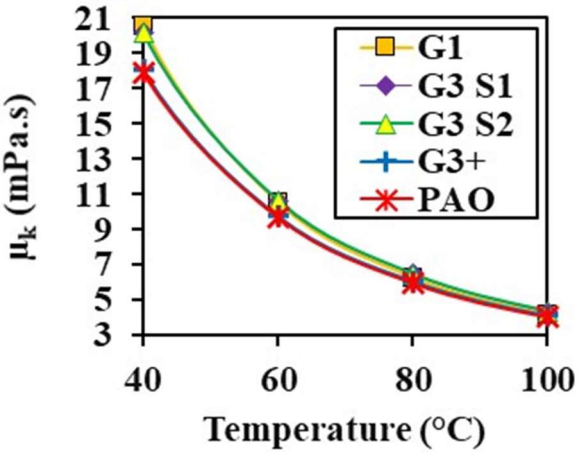

Figure 2: Kinematic viscosity variation with temperature based on base stock type.

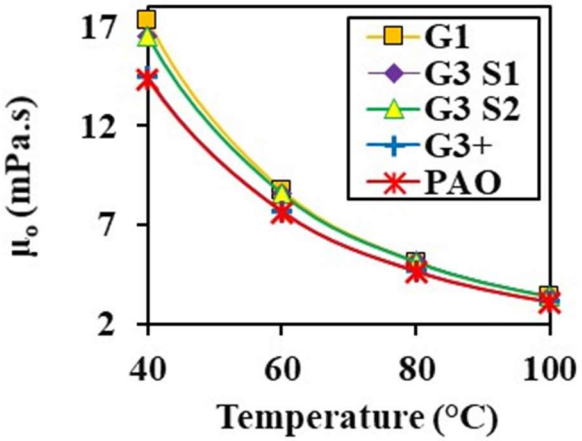

Figure 3: Dynamic viscosity variation with temperature based on base stock type.

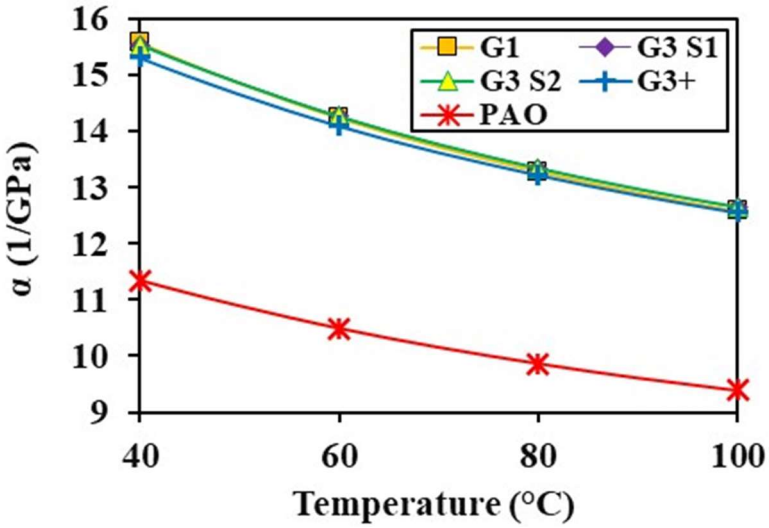

Figure 4: Viscosity-pressure coefficient variation with temperature based on base stock type.

Figure 4 shows the pressure-viscosity (α) relationship with temperature. The G1 base stock demonstrates the highest value of α at the four experimental temperatures, indicating a strong ability to resist molecular flow under pressure. This is attributed again to low branching, low free volume and low saturation, properties which induce stronger intermolecular cohesive forces under pressure (Kim and Spikes, 2020; Minami, 2017; Myshkin and Kovalev, 2019; Zhang et al., 2016). PAO base stock demonstrated the lowest values of α at all temperatures. This observation suggests that high saturation lowers the resistance to flow, since this is a fully saturated base stock. Overall, the pressure-viscosity coefficient shows strong dependency on the base stock composition and temperature.

3.2 Coefficient of Friction and wear quantities

In Figure 5, friction and wear results demonstrate that base stock composition is the main factor that influences of the friction and wear behaviour at the different temperatures.

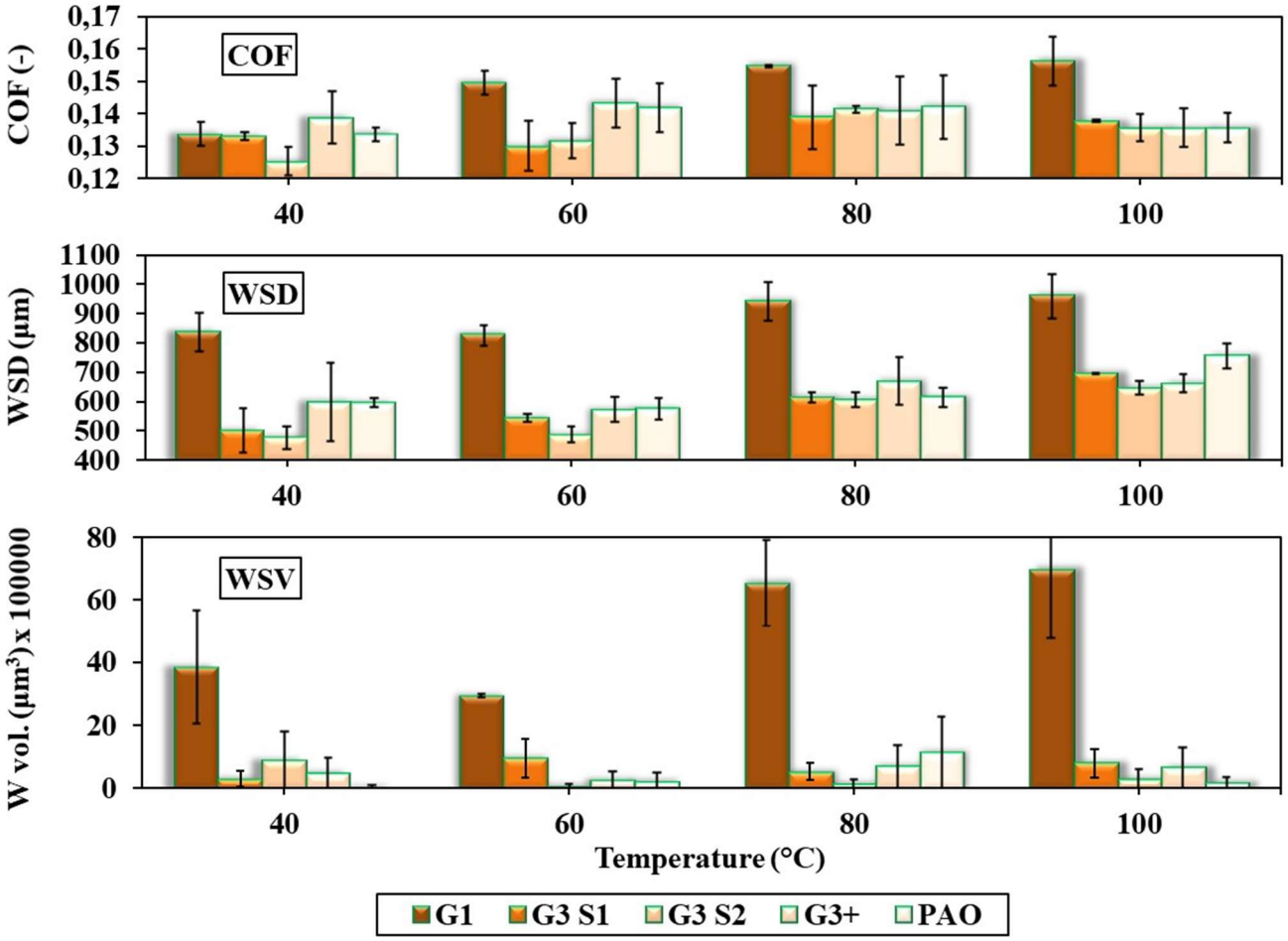

Figure 5: Dependence of COF, wear scar diameter (WSD) and wear volume (W vol.) on base stock type and test temperature.

The first graph in Figure 5 compares the average COF values taken between 2 and 120 minutes of the experiments. The G1 base stock resulted in the highest COF at all temperatures. G3 S1 and G3 S2

demonstrate lower COF between 40 and 80 ºC. G3+ and PAO, the lowest at 100 ºC. For low energy usage at a specific temperature and dry atmosphere, one can select a base stock based on the COF. In this study, wear volume refers to the amount of permanent deformation on the steel ball where it makes contact with the lubricant and disc during sliding. The deformation could be due to loading, or loss/removal of material due to sliding and/or poor lubrication, or a combination of both. In this study, we will only focus on the quantities measured. G1 base stock resulted in the largest wear diameters and volumes at all temperatures. The increase in viscosity due to compression due to loading and shear between the oscillating ball and stationery disc results in lower load carrying capacity by the oil film. This means there is more direct load transfer between the sliding steel ball and stationery disc. We could assume that the oil assumes a semi-solid like state when loaded due to the compact molecular structure and less intermolecular free volume (Kim and Spikes, 2020; Minami, 2017; Wang et al., 2019). This promotes severe deformation on the ball, hence the larger wear scar diameter and volume material loss. G3 S1 base stock resulted in a larger diameter and volume loss compared to G3 S2 between 60 and 100 ºC. At all temperatures, G3+ and PAO base stocks resulted in relatively larger wear scar and the wear volume loss is complex. These results demonstrate some level of correlation between the COF and the wear scar diameter between 60 and 100 ºC. However, there is no correlation between wear volume, diameter and COF, unless one focuses on one temperature condition. We also observe that G3 S1 base stock demonstrated more material loss compared to G3 S2, G3+ and PAO base stocks between 60 and 100 ºC. This result confirms that two base stocks in the same API groups but from different suppliers can result in different wear behaviour. G3+ base stock generated more wear volume than PAO base stock, except at 80 ºC, with relatively smaller wear diameters. PAO appears excellent in lowering wear. We had expected wear and wear volume to correlate well with the pressure-viscosity coefficient (α) behaviour. However, it is clear that there are other aspects of base stocks which play a role in wear behaviour in a lubricated contact area other than those investigated in this study.

4 CONCLUSIONS

G3+ base stock appears to be a strong competitor to the PAO base stock in reducing friction and wear. The G3 S1 base stock demonstrated more material loss compared to G3 S2, G3+ and PAO base stocks between 60 and 100 ºC. Results demonstrate that two base stocks in the same API groups but from different suppliers (difference source of crude) can result in different friction and wear behaviour. G3+ base stock generated slightly more wear volume than PAO base stock, except at 80 ºC, but with smaller wear diameters. The G3 S1 and G3 S1 base stocks demonstrated excellent friction and wear reduction, comparably better than the G3+ and PAO. However, the higher sulphur content and lower saturation levels renders them a concern in the environment compared to G3+ and PAO. In light of environmental compliance and production costs concerns, the market shift towards the use of base stocks with a “plus” will be beneficial in the automotive industry.

ACKNOWLEDGEMENTS

The authors would like to acknowledge Sasol for providing funding and supplying samples and the National Research Foundation (NRF) grant number: SFH170523232296 for financial support.

REFERENCES

Adebogun, A., Hudson, R., Matthews, A., Withers, P. J. (2020). Industrial Gear Oils: Influence of Bulk Oil Temperature and Contact Pressure on Tribological Performance and Subsurface Changes. Tribology Letters, *68*(1), 1-20. https://doi.org/https://doi.org/10.1016/j.triboint.2014.07.021

Alazizi, A., Barthel, A. J., Surdyka, N. D., Luo, J., Kim, S. H. (2015). Vapors in the ambient—A complication in tribological studies or an engineering solution of tribological problems? Friction, *3*(2), 85-114. https://doi.org/10.1007/s40544-015-0083-5

ASTM D445-21. (2021). Standard Test Method for Kinematic Viscosity of Transparent and Opaque Liquids (and Calculation of Dynamic Viscosity). In.

ASTM D2270-10. (2016). Standard Practice for Calculating Viscosity Index from Kinematic Viscosity at 40 °C and 100 °C. In.

Biresaw, G. (2018). Biobased Polyalphaolefin Base Oil: Chemical, Physical, and Tribological Properties. Tribology Letters, *66*(2), 1-16. https://doi.org/https://doi.org/10.1007/s11249-018-1027-9

Brown, S. F. (2015). Base oil groups: manufacture, properties and performance. Tribology & Lubrication Technology, *71*(4), 32. https://www.stle.org/images/pdf/STLE_ORG/BOK/OM_OA/Base%20Oils/Base%20Oil%20Groups_Manufacture_Prop_Perform_April15%20TLT.pdf

Cai, Z.-b., Zhou, Y., Qu, J. (2015). Effect of oil temperature on tribological behavior of a lubricated steel− steel contact. Wear, *332*, 1158-1163. https://doi.org/https://doi.org/10.1016/j.wear.2015.01.064

Christiansen, P., Hansen, N. S., Lund, M. T. O., Spangenberg, J., Bay, N. (2018). Determination of Viscosity Versus Pressure by Means of a Clearance Seal. Journal of Tribology, *140*(3), 034501. https://doi.org/https://doi.org/10.1115/1.4038579

Devlin, M. T. (2018). Common properties of lubricants that affect vehicle fuel efficiency: a north American historical perspective. Lubricants, *6*(3), 68. https://doi.org/https://doi.org/10.3390/lubricants6030068

Dickmann, J. S., Devlin, M. T., Hassler, J. C., Kiran, E. (2018). High Pressure Volumetric Properties and Viscosity of Base Oils Used in Automotive Lubricants and Their Modeling. Industrial & Engineering Chemistry Research, *57*(50), 17266-17275.

https://doi.org/10.1021/acs.iecr.8b03484

Fernández, J., Paredes, X., Gacino, F. M., Comuñas, M. J., Pensado, A. S. (2014). Pressure-viscosity behaviour and film thickness in elastohydrodynamic regime of lubrication of ionic liquids and other base oils. Lubrication Science, *26*(7-8), 449-462. https://doi.org/https://doi.org/10.1002/ls.1236

Gaal, D. (2021, February 2021). The "Plus" in Base stocks: Meaning & Lubricant Implications. Lube Magazine, February(161), 14 - 15. https://content.yudu.com/web/1vf9k/0A1vfnf/L161February2021/html/index.html?page=14&origin=reader

Gold, P., Schmidt, A., Dicke, H., Loos, J., Assmann, C. (2001). Viscosity–pressure–temperature behaviour of mineral and synthetic oils. Journal of Synthetic Lubrication, *18*(1), 51-79. https://doi.org/https://doi.org/10.1002/jsl.3000180105

Hope, K. (2018). PAO contributions to energy efficiency in 0W-20 passenger car engine oils. Lubricants, *6*(3), 73. https://doi.org/https://doi.org/10.3390/lubricants6030073

Hoste, K. (2021, February 2021). Europe Needs Group II/II+. Lube Magazine, (161), 10 - 12. https://content.yudu.com/web/1vf9k/0A1vfnf/L161February2021/html/index.html?page=10&origin=reader

Kim, H. M., Spikes, H. (2020). Correlation of Elastohydrodynamic Friction with Molecular Structure of Highly Refined Hydrocarbon Base Oils. Tribology Letters, *68*(1), 23. https://doi.org/10.1007/s11249-020-1265-5

Lee, S. K., Rosenbaum, J. M., Hao, Y., Lei, G.-D. (2017). Premium lubricant base stocks by hydroprocessing. In Springer Handbook of Petroleum Technology (pp. 1015-1042). Springer. https://doi.org/https://doi.org/10.1007/978-3-319-49347-3_34

Lu, J., Wang, Q. J., Ren, N., Lockwood, F. E. (2019). Correlation between pressure-viscosity coefficient and traction coefficient of the base stocks in traction lubricants: A molecular dynamic approach. Tribology International, *134*, 328-334. https://doi.org/https://doi.org/10.1016/j.triboint.2019.02.013

Lugt, P. M., Morales-Espejel, G. E. (2011). A review of elasto-hydrodynamic lubrication theory. Tribology Transactions, *54*(3), 470-496. https://doi.org/https://doi.org/10.1080/10402004.2010.551804

Luo, J., Wen, S., Sheng, X., Li, L. K. (1998). Substrate surface energy effects on a liquid lubricant film at nanometre scale. Lubrication Science, *11*(1), 35-36. https://doi.org/https://doi.org/10.1002/ls.3010110104

Luzuriaga, S. (2019). Supply exceeds demand in synthetic lubricants base stock market. Tribology &

Lubrication Technology, *75*(1), 18-20. https://www.proquest.com/scholarly-journals/supply-exceeds-demand-synthetic-lubricants-base/docview/2171603631/se-2?accountid=14717

http://UnivofPretoria.on.worldcat.org/atoztitles/link?sid=ProQ:&issn=1545858X&volume=75&issue=1&title=Tribology+%26+Lubrication+Technology&spage=18&date=2019-01-01&atitle=Supply+exceeds+demand+in+synthetic+lubricants+base+stock+market&au=Luzuriaga%2C+Sharbel&id=doi:

Minami, I. (2017). Molecular science of lubricant additives. Applied sciences, *7*(5), 445. https://doi.org/https://doi.org/10.3390/app7050445

Myshkin, N., Kovalev, A. (2019). Adhesion and surface forces in polymer tribology—A review. 摩擦学, *6*(02), 143-155. https://doi.org/https://doi.org/10.1007/s40544-018-0203-0

Sander, D. E., Allmaier, H., Priebsch, H.-H., Reich, F. M., Witt, M., Füllenbach, T., Skiadas, A., Brouwer, L., Schwarze, H. (2015). Impact of high pressure and shear thinning on journal bearing friction. Tribology international, *81*, 29-37. https://doi.org/https://doi.org/10.1016/j.triboint.2014.07.021

Sarpal, A. S., Sastry, M. I. S., Bansal, V., Singh, I., Mazumdar, S. K., Basu, B. (2012). Correlation of structure and properties of groups I to III base oils [https://doi.org/10.1002/ls.1172]. Lubrication Science, *24*(5), 199-215. https://doi.org/https://doi.org/10.1002/ls.1172

Sarpal, A. S., Sastry, M. I. S., Kumar, R., Bhadhavath, S., Rai, K., Bansal, V., Patel, M. B. (2013). Molecular Dynamics of Synthetic-Based Lubricant System by Spectroscopic Techniques—Part 1. Tribology Transactions, *56*(3), 442-452. https://doi.org/10.1080/10402004.2011.651772

Stachowiak, G., Batchelor, A. (2014). *Engineering Tribology (4th Edition)* (4 ed.). Elsevier. https://doi.org/https://doi.org/10.1016/C2011-0-07515-4

Vengudusamy, B., Grafl, A., Novotny-Farkas, F., Schöfmann, W. (2014). Influence of temperature on the friction performance of gear oils in rolling–sliding and pure sliding contacts. Lubrication Science, *26*(4), 229-249. https://doi.org/https://doi.org/10.1002/ls.1245

Wang, W., Li, P., Sheng, S., Tian, H., Zhang, H., Zhang, X. (2019). Influence of Hydrocarbon Base Oil Molecular Structure on Lubricating Properties in Nano-scale Thin Film. Tribology Letters, *67*(4), 111. https://doi.org/10.1007/s11249-019-1222-3

Zhang, J., Spikes, H. (2020). Measurement of EHD friction at very high contact pressures. Tribology Letters, *68*(1), 1-12. https://doi.org/https://doi.org/10.1007/s11249-020-1281-5

Zhang, J., Tan, A., Spikes, H. (2016). Effect of Base Oil Structure on Elastohydrodynamic Friction.

Tribology Letters, *65*(1), 13. https://doi.org/10.1007/s11249-016-0791-7

Leaving the 20th century behind: Exploring how a community-focused design project responds to the call for decolonising an engineering curriculum

A. Agrawal[1*], H. Heydenrych[2], J. M. Case[3,2], F. A. Guni[2] and S. Brown[2]

[1]National Institute of Technical Teachers Training and Research, Chennai, India

[2]University of Cape Town, South Africa

[3]Virginia Tech, USA

*Corresponding author: ashish@nitttrc.edu.in; ashishag@vt.edu

ABSTRACT

Student protests starting in 2015 under the umbrellas of #RhodesMustFall and #FeesMustFall further strengthened calls for curricula relevant to the diverse groups of students in the South African university classroom. To this end, the Chemical Engineering Department at a research-focused historically English-language university swopped out a semester-long conventional chemical industry project in the core second-year course for one investigating the treatment and usage of biogas products from anaerobic digestion in an urban informal community. This paper critically analyses the changes that were made in the project to explore the ways in which it meets the aims of decolonising the engineering curriculum. To this end, data in the form of course documents and staff interviews were collected and analysed. Findings suggest that the new project addressed the decolonisation goals by incorporating three elements: valuing students' voices; connecting learning to the local context; and engagement with the community. A key challenge that was revealed through the findings is that the standard engineering techniques are not always applicable to small-scale community-based projects. Hence, the findings indicate the need for a broadening of engineering knowledge and skills so that they can be applied to local community, as well as industrial and corporate, contexts.

Keywords: chemical engineering, community-based project, decolonisation, engineering curricula

1 INTRODUCTION

The student protests that started in South Africa in 2015 under the umbrellas of #RhodesMustFall and #FeesMustFall developed into one of the most important student protests in post-apartheid South African history, attracting the attention of the country's universities and national and provincial governments (Koopman, 2019). The #RhodesMustFall movement that led to a successful campaign to remove the statue of Cecil Rhodes overlooking the rugby field at the University of Cape Town led into the nationwide #FeesMustFall protests. While the naming of the latter protests made for an easy association with the reduction in the cost of university education in the country, these protests also pointed to multiple forms of exclusion in South African higher education (Postma, 2016) and hence the urgency to address racial and gender inequities at the universities and decolonise curricula (Jansen,

2017).

In light of these protests, several universities took initiatives to work on the transformation and decolonisation of their curricula (Koopman, 2019). One such effort at the research site for this study, a research-focused historically English-language university, was to revamp the existing second-year project in the chemical engineering undergraduate program. This paper critically assesses the new project from a decolonisation standpoint through an analysis of the course documents and interviews from a course lecturer and a tutor. Specifically, the paper addresses the following question: How does the new second-year project at the university meet the aims of decolonising the engineering curricula?

The scope of this paper includes analysis of only course documents and lecturer and tutor interviews. Although student interviews were also carried out as part of this project (and those data are in the process of being analysed), those are not in the scope of this paper and will be discussed in follow-up work (see section 6).

2 LITERATURE

Scholars across the world have worked on the decolonisation project for several decades (Nkoane, 2006). This section first discusses how different scholars have talked about the meaning of decolonisation of university and the curricula, and then discusses two examples of decolonising in detail. The first example is from Latin America that brings together different epistemological traditions in the classroom and the curriculum. The second example is from South Africa that proposes a decolonised engineering curriculum in consultation with various stakeholders.

2.1 Meaning of decolonisation

In the African context, Nkoane (2006) argues that decolonisation of universities and institutions is to make them more relevant to the African context. He further argues that:

> the African university needs to represent the African experience, ideas and finds its resources from within African culture, it also has to play a pivotal humanising role both locally and internationally. It needs to help liberate African people as well as the international community, from inhuman and dehumanising ideas and practices. This should be one of the primary objectives of the Africanising university across the sciences, and needs to include mental decolonization from stereotypes and strictures from the past, and mental emancipation for socially and communally engaged scientific projects. (p. 54)

Nkoane notes that mental decolonisation can be achieved by the African people by carrying out an analysis of who they are as people and how their minds and thoughts are controlled by Eurocentric discourses that are not always relevant to their contexts.

Thus, Nkoane's notion of decolonisation of the mind resembles the idea of critical consciousness

advanced by Freire (1970), who argued that education should empower students to critically think about their lives and situations. Drawing on Freire's work, Swartz, Nyamnjoh, and Mahali (2020) also note that a problem-posing education that helps students reflect on the causes and circumstances of their lived experiences and learn how to transform their lives is at the heart of decolonising pedagogy.

Mbembe (2016) notes two aspects of decolonisation of the university. The first is to critique the production of knowledge and theories that are based on European or Western traditions. The second is to imagine and develop an alternate model of knowledge production. Referring to the decolonisation of the university curriculum as its Africanisation, Le Grange (2014) suggests four mutually non-exclusive possibilities to meet these aims. First, he argues for a rethinking of academic disciplines in a way that moves beyond mere observation and listening as the only legitimate ways of knowing and also recognises knowing "through the tastes, pain, and hunger of their bodies and through expressions of anger, passion and desire" (p. 1289). Second, he calls for incorporating transdisciplinary knowledge into the curriculum. However, he cautions that this transdisciplinary knowledge should not only be produced by the university but also include ordinary citizens from the indigenous communities as agents of knowledge production. He further adds that it is through valuing other ways of knowing, as discussed in the first suggestion, that we can incorporate indigenous knowledge in the curriculum. Third, he suggests that locally-relevant curricula should be designed that move away from the domination of Western epistemologies and challenge the power relation between local and Western knowledge systems. A fourth approach is for students to learn about the achievements of African people so that they can free themselves from the dehumanisation imposed by the Western world.

Along similar lines, Ndlovu-Gatsheni (2016) identifies four steps to decolonising the university. These include: shifting the locus of understanding the world to Africa, i.e., experiencing the world as reflected in the historical experiences of the African people; moving away from the bounds of Eurocentrism; thinking about and accepting the limits of current knowledge systems; and unlearning the colonial and Eurocentric knowledge systems to re-learn from the knowledge accumulated in the community and society.

Mbembe (2016) extends the scope to decolonisation beyond the curriculum by arguing for what he calls "decoloni[sation of] the systems of access management" of universities. He notes:

> We need to decolonize the systems of access and management insofar as they have turned higher education into a marketable product, rated, bought and sold by standard units, measured, counted and reduced to staple equivalence by impersonal, mechanical tests and therefore readily subject to statistical consistency, with numerical standards and units. (p. 30)

Finally, Mbembe calls for a system of university education that breaks the cycle of turning students into consumers and customers. He argues that the universities that run according to business principles

produce students who are less interested in learning and knowledge for their intrinsic value; and that these students become more concerned with the material benefits that education provides, such as a well-paying job or the value of the degree in the job market. In such a system, students become the customers for commodities such as credits, courses, and degrees; and the goal of the universities becomes to keep them happy and satisfied. Mbembe notes that a decolonised university breaks this cycle by treating students as learners and helping them engage with the knowledge for its own sake.

One point that needs to be highlighted here is that these scholars do not advocate for a complete removal of the Western and the European canons of knowledge from the curricula. Rather, they call for an infusion of the Western knowledge systems with the indigenous ones such that "one knowledge system is not viewed as superior (Western) and other as inferior (indigenous)" (Le Grange, 2014, p. 1292). Similarly, for Mbembe, a decolonised university accepts and embraces "*a horizontal strategy of openness to dialogue among different epistemic traditions* (Mbembe, 2016, p. 37, italics in original)". Thus, decolonisation is not at all about closing doors to the Western traditions of knowledge production but shifting the focus from the Western traditions to the African ones.

2.2 Examples of decolonisation of curriculum

One of the prominent examples of decolonisation of curriculum is the "Meeting of Knowledges" project implemented at universities in Brazil and Colombia (DeCarvalho and Flórez-Flórez, 2014). As part of this project, masters of traditional knowledges, such as artisans, healers, shamans, traditional architects, and performers were invited to the universities as visiting professors to teach courses in architecture, music, theater, health, and environment. Prior to beginning their teaching, these masters did an internship in which they listened to the regular classes to learn about the pedagogical practices in the university. Thus, this effort infused the teaching of traditional knowledge with the pedagogical practices at the university.

Another example is the approach taken by the Intercultural University of the Indigenous Nations and Peoples, Amawtay Wasi, in Ecuador. In this approach, the pathway to learning at the university follows three stages: the cycle in the formation of ancestral sciences; the cycle of western sciences; and the cycle of interculturality. One of the objectives of this pathway is to help students gain an intercultural education that accepts the diversity of knowledges of the indigenous nations (for a detailed discussion, see DeCarvalho and Flórez-Flórez, 2014).

In the context of South Africa, Winberg and Winberg (2017) outline three scenarios for a decolonised engineering curriculum:

- Scenario 1: A specialized curriculum specifically designed to cater to the needs of Africa;
- Scenario 2: A curriculum with a strong focus on the historical, social, and cultural studies of engineering to help students understand the roots of engineering knowledge; and

- Scenario 3: A curriculum that includes elements from scenarios 1 and 2 while retaining significant elements of the traditional engineering curriculum.

Based on the feedback from faculty, industry partners, and fresh engineering graduates about these three scenarios, they propose a curriculum based on Scenario 3 to decolonise engineering curriculum. This curriculum, in addition to an internationally recognised qualification and attainment of graduate attributes, also includes understanding ethical and environmental considerations, valuing diversity, and a focus on the African continent. At the same time, the curriculum proposes the need for taking inputs from the broader communities that would be affected by engineering work and fostering partnerships with the local industries.

2.3 METHODS

To explore how the new second-year chemical engineering project at the research site meets the university's goal of decolonising the curricula, data were collected in the form of course documents and interviews. The course documents involved the project briefs used to provide instructions to students to complete the project. The information from these project briefs were supplemented with interviews with a course lecturer, who was deeply involved in designing the new project, and a course tutor who assisted the students with the project during part of the course. The interviews elicited their experiences of teaching the project and their understanding of how the project met the decolonisation goals. Additionally, the interview with the course lecturer focused on exploring in-depth the reasons for – and the processes involved in – incorporating the new project.

The course documents and the interviews were then analysed to understand the context and the background of the new project and how the project aligns with the different aspects of decolonisation as discussed above. Quotes have been provided from the lecturer and the tutor interviews to support the argument.

It should be noted that the course lecturer who was interviewed for this article reviewed a draft of the article. Additionally, another course lecturer who was involved in teaching the course was also asked to check for the accuracy of project details presented in the paper. The involvement of these two lecturers with the article helped to avoid misrepresentations of the details of the project and misinterpretation of the interview quotes.

3 FINDINGS

3.1 Context and background of the new project

Since its rollout in 2014, the chemical engineering curriculum at the university requires students to do semester-long design projects in each semester of their second and third years. From 2015 to 2018, the project in the first semester of second year dealt with the design of a large petrochemical plant, using refinery products to produce a precursor for the production of polymers. This meant that, except for

evaluating the potential impact of a catastrophic event on the nearby town, there was no direct reference to the local community. The project involved both technical and costing work, and the targets were framed by commercial concerns, i.e., capital and operating costs and revenues, feeding into the overall profitability of the process.

The new project in 2019 involved the analysis of several aspects of the treatment and use of biogas produced by an anaerobic digester to be installed in an urban informal setting, i.e., a food market near a transport hub and urban farming centre, in the outskirts of the city where the university is located. Feed materials to be considered were human excreta, slaughter wastes and garden wastes. A community-based organisation (CBO), whose members were role-played by the course instructors and tutors, was seen as the driver of the project. The teams of student-engineers acted only as consultants on particular aspects of the project. In addition, students were challenged to adopt an asset- rather than needs-based mindset as suggested by Mathews (2013). In this paradigm, students identified (with the help of the CBO) the human and material assets of the community and considered how these could be put to use in the process, rather than focusing on the perceived needs (or shortcomings) of the community and doing technical analysis on an imposed solution. Finally, while the project still addressed commercial concerns, this was balanced with the broader contributions by – and benefits to – the community.

3.2 Perceptions of the instructional team on the decolonisation role of the new project

The analysis of the lecturer and tutor interviews provides evidence suggesting that the new second-year chemical engineering project meets the goals of decolonisation in three areas: valuing students' voices; connecting learning to the local context; and engagement with the community. These aspects are discussed below in detail.

3.2.1 Valuing students' voices

One major impetus for the new project was the critique from the student body that, after an introduction to the social impact of engineering activities in first year, there was an almost complete absence of this social impact strand until fourth year. As the course lecturer noted in his interview:

> *In this course in particular, we had gotten quite a bit of critique from the student body in the years of the challenges on what the university is and how it operates, that the first year had set up an expectation of chemical engineering employed for environmental and social good. The first-year projects all are forward looking and [involve] an environmental impact, typically: biofuels, hydrogen, water projects... And then second year, they go in and it's like 20th century industrial chemistry... And there's nothing left of this intent.*

The new project addressed these student critiques by situating it in the context of a local community setting. This project setting also aimed to improve student engagement in the project, and several

students noted in their course feedback that working on this project was specifically meaningful to them. As the course instructor reflected during the interview:

> *To what extent that is a portion of the class that comes from socially disadvantaged backgrounds, from the types of backgrounds we want to benefit from this, it seemed to me there were people in group that had that relation, emotional or direct through family where they had personal experiences to that.*

3.2.2 Connecting learning to the local context

Connecting the course context to students' lived experiences and using engineering methods relevant to the context were also highlighted by both the lecturer and the tutor as a key aspect of decolonisation of engineering curricula. As the quotes below suggest:

> *Let's stick with a more practical view here of how do we do a project in a second year that brings the South African context into the project. That's the main bit. And thereby possibly challenge the engineering methods our students learn [and] whether [these] can work in such context. (Lecturer)*

> *The [project] scope remained the same in the case of the key result areas with the experience students do get, but I think the concept changed. [Thus, the new project addressed] that issue of decolonising science and trying to introduce concepts to students which were Africa-based or community-based. (Course tutor)*

It should be noted that modifying the project to address the needs of a local community also highlighted the gaps in the existing engineering knowledge. As the process plant being designed was at a much smaller scale than earlier, it was realised that the existing engineering methods were not adequate to meet the needs of this new project. As the lecturer reflected:

> *Because the plant was so much smaller than if it had been an industrial plant, all of the wonderful heuristics that are used were out of range... And so indeed there's a vacuum of engineering methods at community scale work. And that's an important finding actually of this piece of work.*

The lecturer further added that another important aspect of decolonising the engineering education is to develop engineering methods that are suitable for the context in which engineering work happens – in this case a peri-urban informal community.

4.2.3 Engagement with the community

Finally, the project had an active (though simulated) engagement with the community. As noted earlier, a role-played CBO was the driver of the project with students acting as consultants. Students

were provided with an opportunity to engage with a role-played CBO representative to identify community assets and better understand each other's roles. Also, feedback on their submissions was always framed from the perspective of the CBO partner. Thus, this project expanded the possibility of reconceptualizing engineering work to be more closely connected to the community that would be impacted by it, through a dialogical relationship with the student engineers. The lecturer had noted in his interview that decolonising engineering is also about "who gets to play in the engineering space."

It should be noted here that the instructors and the tutors for the course role-played as the members of the CBO. While not all of the instructors and tutors during a particular year necessarily had the experience of living in the community where the project was set up, it was assumed that their combined lived, academic, and industrial experiences provided a reasonably holistic understanding of the issues in the community. The course lecturer in his interview also noted that several students in their feedback appreciated the value they derived from interacting with the role-played CBO as the client for the project:

> *And the students commented, I saw that a lot in the feedback, that the client-specialist relation was something that was illuminating to them. Even with a community, one can phrase it in that form and define for the specialist a role of providing specialist advice, but not making decisions on behalf of the client.*

As is also evident in the quote, the interaction between the community as the client and the students as specialists also taught students an important lesson in how to conduct engineering work based first and foremost on the needs of and inputs from the client.

4 DISCUSSION

Much of the impetus for arguments to decolonise the curriculum has come from humanities disciplines and there has been limited debate within science and engineering disciplines. An important exception is the article by Winberg and Winberg (2017), who consider the practical options for decolonising the engineering curriculum. With regard to their three scenarios, this project focuses on the first scenario, in terms of considering problems in the local context. However, what the findings also show is that this curricular reform involved listening to engineering students' voices. In this regard, the project had a broader engagement with this challenge than might have been initially assumed.

An interesting further finding was that the standard chemical engineering techniques were not fully applicable to the small-scale community-based project. This finding opens up questions in relation to what the domain of engineering is. This is not necessarily an either/or debate since large-scale energy and/or water supply will be a need of large settlements, whether in the developed or developing worlds. However, but at the same time it is acknowledged that chemical engineering does incorporate knowledge related to smaller-scale processes in the context of local communities. It is not

clear though that these knowledge shifts really represent a shift away from Western knowledge. Rather they indicate a need for broadening the engineering knowledge and skills so that they can be applied to both the local contexts and the industrial and corporate sector. This shift towards the local context has been advocated by several decolonisation scholars (e.g., Le Grange, 2014; Mbembe, 2016).

While the curriculum under consideration had recently undergone reform (which allowed the flexibility for a rapid change in the project offering), student activist calls for decolonisation provided the impetus to take the local context more explicitly into the second-year curriculum. What this paper shows is how both the lecturer and tutor embraced the discourse related to decolonisation in their accounts of this new project. In relation to community engagement, it is key to note that this was role-played by the instructional team, rather than being engagement with a real community. This was prompted by practical concerns, but also allowed the team to manage closely the learning outcomes for the project.

5 CONCLUSION AND RECOMMENDATIONS

In this paper, the new second-year chemical engineering project at a historically English-language university in South Africa, aimed at decolonising the project context, was critically analysed. In conclusion, there are several challenges to decolonising an engineering curriculum, including designing the course material in a way that is relevant to the local context, re-thinking the scope of the projects that students work on, and providing students with an authentic experience of community engagement. This work provides one example of how some of these issues can be addressed and it is hoped that this will provide a starting point for other engineering educators who wish to decolonise their courses.

As part of this research, interview data from students were also collected to explore their experiences of the new project and their perceptions on how much the project meets the aims of decolonisation. The next step of this project involves analysis of student interviews so that a holistic view of the perception of the project from both the lecturer's and the students' perspectives can be obtained. It is hoped that this work will help universities, especially the engineering programs, move a step closer to engaging productively with the challenges posed by the notion of decolonisation.

ACKNOWLEDGEMENTS

The authors would like to thank Prof Harro von Blottnitz from the University of Cape Town (UCT) for his support in conducting this research; and the Department of Chemical Engineering at UCT for providing the funding for data transcription.

REFERENCES

DeCarvalho, J. J. and Flórez-Flórez, J. (2014) 'The meeting of knowledges: A project for the decolonisation of the university in Latin America', *Postcolonial Studies*, 17(2), pp. 122–139.

Freire, P. (1970) *Pedagogy of the oppressed*. Bloomsbury Publishing.

Jansen, J. D. (2017) *As by fire: The end of the South African university*. Cape Town, South Africa: Tafelberg.

Koopman, O. (2019) 'Is the decolonisation of the South African university curriculum possible in a neoliberal culture?', *Alternation*, 24, pp. 48–69.

Le Grange, L. (2014) 'Currere's active force and the Africanisation of the university curriculum', *South African Journal of Higher Education*, 28(4), pp. 1283–1294.

Mathews, S. (2013) 'Asset-based, community-driven development (ABCD) in South Africa: Rebuilding communities from the inside out', in. *4th Annual Soweto Conference*, Centre for Small Business Development Conference, University of Johannesburg.

Mbembe, A. J. (2016) 'Decolonizing the university: New directions', *Arts and Humanities in Higher Education*, 15(1), pp. 29–45.

Ndlovu-Gatsheni, S. J. (2016) 'Decolonizing the university and the problematic grammars of change in South Africa', in *Keynote address delivered at the 5th Annual Students Conference on Decolonizing the Humanities and Social Sciences in South Africa/Africa. University of KwaZulu-Natal*, pp. 6–7.

Nkoane, M. M. (2006) 'The Africanisation of the university in Africa', *Alternation*, 13(1), pp. 49–69.

Postma, D. (2016) 'The ethics of becoming in a pedagogy for social justice. A posthumanist perspective', *South African Journal of Higher Education*, 30(3), pp. 310–328.

Swartz, S., Nyamnjoh, A. and Mahali, A. (2020) 'Decolonising the social sciences curriculum in the university classroom: a pragmatic-realism approach' *Alternation Special Edition*, 36, pp. 165–187.

Winberg, S. and Winberg, C. (2017) 'Using a social justice approach to decolonize an engineering curriculum', in *2017 IEEE Global Engineering Education Conference (EDUCON)*. IEEE, pp. 248–254.

Case study - a critical analysis of the undergraduate Chemical Engineering Programme Qualification mix using Luckett's Model for an epistemically diverse curriculum

W. Mohamed* and B. Patel

School of Civil and Chemical Engineering, University of South Africa, Florida, South Africa

*Corresponding author: waseela.mohamed@gmail.com

ABSTRACT

The School of Engineering at UNISA, a comprehensive university, offers National Diploma and Degree courses through open distance e-learning (ODeL) to students who are interested in becoming professional technicians and technologists in a number of engineering disciplines. A substantial challenge exists for Universities of Technology and Comprehensive Universities in unpacking curriculum for Vocational Qualifications resulting from the measures that have been put in place by the Department of Higher Education and Training. This article evaluates curriculum in an ODeL environment following the review cycle, in order to appraise the epistemic diversity of the new curriculum introduced using Luckett's (2001) model as an analytical lens for an epistemically diverse curriculum. The undergraduate chemical engineering curriculum is conceptualised by categorising learning outcomes for courses across the programme into the different ways of knowing as described by Luckett. The author argues that a critical analysis of the programme helps to make explicit the organising principles of curriculum to the curriculum developers and academics that are then able to use the insights to strengthen the design, pedagogy and assessment of the courses in the programme.

Keywords: Open distance e-learning (ODeL), epistemic diversity, curriculum development, programme qualification mix

1 INTRODUCTION

The School of Engineering at UNISA is an open distance e-learning institute (ODeL), offering National Diploma and Degree courses to students who are interested in becoming professional technicians and technologists in various engineering disciplines. According to McGrath and Nickola (2009) a substantial challenge exists for Universities of Technology and Comprehensive Universities in South Africa, in unpacking curriculum for Vocational Qualifications resulting from the measures that have been put in place by the Department of Education. These measures include a change to the maximum and minimum number of credits in a qualification where 50% is required to be transferable to another qualification. Nel (2014) has further identified that the introduction of the updated Higher Education Qualifications Sub-Framework (HEQSF) introduced by the Department of Higher Education and Training (DHET), has caused many Universities and Vocational institutes to rethink their Program Qualification Mix (PQM). Further factors around curriculum reform include meeting standards set by

Engineering Council of South Africa (ECSA) and the need to prepare students for various categories of professional registration with ECSA.

Taking into account the reforms proposed by DHET, Luckett (2001) has proposed a model of curriculum design in response to DHET's call for 'over-all curriculum reform' to cater for the diverse knowledge needs of South Africa. The model is proposed as a conceptual tool placing emphasis of the four ways of knowing and how each of these ways of knowing could be addressed when considering curricula. This paper aims to evaluate curricula in an ODeL environment following the review cycle, in order to appraise the epistemic diversity of the proposed PQM introduced using Luckett's (2001) model for an epistemically diverse curriculum. The purpose of the analysis is to elucidate the principles of the curricula to the institute and academics involved in developing the curriculum.

2 LITERATURE

2.1 The Open Distance Learning (ODL) institute

The University of South Africa (UNISA) aims to provide higher education opportunities through open distance learning and e-learning both nationally and internationally. The concept of distance learning is defined by the institute to be a "set of methods or processes for teaching a diverse range of students located at different places and physically separated from the learning institution, their tutors/teachers as well as other students" (UNISA ODL policy, 2008).

The strategic plan finalised by UNISA in 2005 and titled "An Agenda for transformation" focusses on transformation as the centre of its identity and in 2016, an updated vision statement reads: "The African University shaping futures in the service of humanity." The 2030 mission statement identifies "lifelong higher education and knowledge creation that is nationally responsive and globally relevant" as well as a need for the institute to be "a leading student-centred ODeL comprehensive university producing quality graduates" and to make provision to implement "cutting-egde ICT applications and platforms". The relevance of the Programme Qualification Mix (PQM) was thus questionable in line with its strategic vision to create an African University and the 2030 mission statements.

2.2 Higher education qualification sub framework (HEQSF)

The Higher education qualification framework (HEQF) was gazetted by the Department of Education (DoE) in 2007 and has since been updated in January 2013 to the Higher education qualification sub framework (HEQSF). Detailed background to the development of the HEQSF is discussed by McGrath and Nickola (2009) and Nel (2014) as well as provided in the Government Gazette (2014). The complexities around the different bodies contributing to the framework will not be discussed in this paper. The focus will be on the impact that the new framework has on the ODeL institute and in particular what this means for the Chemical Engineering Programme Qualification Mix.

2.3 SAQA learning outcomes and the different ways of knowing

According to the HEQSF, undergraduate certificates and diplomas are now categorised within the vocational route (theoretical knowledge), while the professional Bachelor, Master's, and Doctorate degrees are characteristic of the professional route (research at a higher level). The qualifications and standards are based on learning outcomes as opposed to content based as was previously required. These learning outcomes have been set by the South African Qualifications Authority (SAQA) and are deemed to be critical for the development of the capacity of life-long learning regardless of the specific area or discipline and are considered to be 'general transferable skills'. The learning outcomes as identified in the NQF and Curriculum development framework (2000) include identifying and solving problems using critical and creative thinking, critically evaluate information, effective team work and communication skills and is socially cognisant. These training and education reforms are intended to give due regard to the needs of society as well as the individual, rather than the occupation alone. Similarly, the professional body ECSA, has identified outcomes such as problem solving, application of scientific and engineering knowledge, independent learning ability, sustainability and impact of engineering activity, professional and technical information, amongst others.

Luckett (2001) attempts to address the pedagogic challenge of teaching and learning of 'general transferable skills' embedded in the SAQA learning outcomes in her article *A proposal for an epistemically diverse curriculum for South African higher education in the 21st Century*. She argues that whilst SAQA has prescribed the learning outcomes, these reforms are limited to structural change in curriculum design and do not engage directly with teaching and learning challenges. Furthermore a quality higher education curriculum should enable students to integrate theory and practice into the discourse. Based on the challenges proposed by SAQA's curriculum reform and learning outcomes, Luckett (2001) has proposed a conceptual model in order to inform the "multiple, differentiated and diverse curricula that the South African higher education system requires". The conceptual model aims to address four ways of knowing which Luckett proposes should be present in a higher education curriculum (see Figure 1):

- Quadrant one: the kind of learning taking place in the first quadrant is termed propositional knowledge which is considered to be foundational competence. Gibbons et al. (1994) has labelled this type of knowledge Mode 1 knowledge. Primary cognitive knowledge of the discipline is taught to the student and in such a manner, a disciplinary conceptual framework is constructed.
- Quadrant two: Practical knowledge addressing application of disciplinary knowledge from quadrant 1 is introduced to the student. Students can begin applying their knowledge in a controlled environment. Whilst this is still considered to be Mode 1 knowledge, a shift into quadrant two occurs by introducing application of disciplinary knowledge.

- Quadrant three: In this quadrant the student gains reflexive competence by developing meta-cognition, thinking epistemically and contextually. The ways of knowing are developed; the student engages in tasks developing personal competence, learning about themselves and their thinking process. A shift to Mode 2 knowledge encompassing a broader transdisciplinary social and economic context develops.
- Quadrant four: Students are encouraged to develop higher levels of cognition by drawing on experiential knowledge, engaging personally and thinking reflexively. Much of SAQA's learning outcomes are achieved by the shift into quadrant four.

Following the curriculum review cycle, we attempt to appraise the epistemic diversity of the new PQM in order to expound the structural principles of the chemical engineering curricula to both curriculum developers as well as academics involved in teaching the curricula. A critical analysis would strengthen the design, pedagogy and assessment of the courses in the programme.

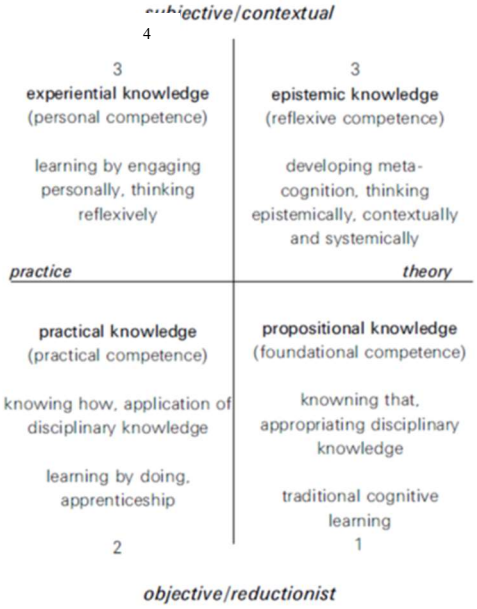

Figure 1: Model of an epistemically diverse curriculum (Luckett, 2001)

3 EVALUATING THE EPISTEMIC DIVERSITY OF THE UNDERGRADUATE CHEMICAL ENGINEERING PROGRAMME

The undergraduate chemical engineering programme at UNISA offers courses in core chemical engineering principles together with mathematical and science courses forming a strong background to the core courses. Other crucial courses in environmental and economic studies, computing, health, safety and communication are offered, forming co-requisites to the core courses. A detailed analysis of the core chemical engineering programme is provided in Appendix A. Table 1 lists a set of engineering courses extracted from Appendix A to order to provide a practical example for evaluating the epistemic diversity.

The set of courses are listed in a scheme where courses are pre requisites to each other. In this manner we can easily see the change in cognitive complexity as the level of study increases as well as the coherence and progression of the curriculum through the different levels of the undergraduate degree.

Table 1: Evaluating the epistemic diversity for a set of courses

Knowledge dimension	**CHF1501 (1st yr level - Diploma)**	**REE2601 (2nd yr level - Diploma)**	**REE3701 (3rd yr level- Advanced Diploma)**	**CED4801 (4th yr level – BEng Tech Hons)**
Factual knowledge	Define the basic and fundamental units and dimensions in engineering analysis and calculate their value.			
Conceptual knowledge	Measure and/or calculate the conditions of process streams and process units.	Perform unsteady state material balances, stoichiometric and reaction equilibrium calculations.	Apply the energy balance to isothermal and non-isothermal reactors.	
Procedural knowledge	Apply material balances in simple batch and continuous systems.	Perform chemical reaction kinetics calculations.	Model the kinetics and design chemical reactors for heterogeneous systems.	Perform complete mass and energy balance on a process flowsheet.
Meta-cognitive knowledge	Formulate and solve material balances to reactive systems and multi-stage systems.	Model ideal reactors under isothermal conditions.	Design complex and non-traditional reactor systems.	Research, conceptualise, and formulate a process flowsheet. Perform design and sizing calculations on certain unit processes such a reactor, heat exchanger and separation unit. Identify and quantify hazards and emissions and suggest methods of remediation.
	Quadrant 1: Propositional knowledge	**Quadrant 2: Propositional + Practical knowledge**	**Quadrant 3: Epistemic knowledge**	**Quadrant 4: Experiential knowledge**

In order to unpack the structural principles of the programme, it is important to analyse the nature of knowledge in curricula. Categorising the ways of knowing across the programme is achieved by analysing the nature of the knowledge present in engineering courses and how it might enable learning and knowledge building. An analytical tool for achieving this is Bloom's taxonomy (Hoffmann, 2008) which is used as a system for conceptualising courses and the learning outcomes associated with the

course, into the different knowledge domains. Evaluating the courses using Blooms taxonomy, we find that the course outcomes in the knowledge domain begin by introducing factual knowledge particularly for the lower levels of study, and have outcomes for each cognitive domain with an increase in cognitive complexity (1st and 2nd year levels of study). As we move horizontally across the table into the higher levels of study, outcomes primarily fall into the procedural and meta-cognitive dimension (3rd and 4th year level of study). Looking at the knowledge dimensions across the 4 years of study, we find that there is a cyclic process of apply, analyse and evaluate. Kolb (1984) has suggested a learning cycle which begins with experience and progresses to reflection on that experience. Carlile and Jordan (2005) describe Kolb's (1984) cycle as "A synthesis of experience, reflection and theory leads to a modification of the learning cycle. The iteration of the learning cycle leads to a growth in knowledge, depth of understanding and improved practice". The elements of the cycle consist of concrete experience, observation, the formation of abstract concepts and testing in new situations. The experiential learning cycle stresses a role of experiential and active learning. This is evident from the learning outcomes analysed at 4th year level. If we look at the verbs describing the learning outcomes, the student is required to understand, apply, analyse and evaluate (Table A.1). Whilst Kolb's model presents an ideal scenario on experiential learning, there is an attempt to create a continuous learning cycle allowing for cumulative knowledge building as we progress through a course vertically.

Luckett's model for appraising epistemic diversity applied to the undergraduate chemical engineering programme is used as a "thinking tool" to provide an analysis of the programme. The model does not propose that thinking in each quadrant has to be linear. In the section below, an attempt to analyse how each quadrant applies to the Chemical Engineering programme across the different NQF levels.

- *Quadrant one:* the kind of learning taking place in the first quadrant is considered propositional knowledge which is about students gaining foundational competence. Courses taught at 1st and 2nd year levels provide the fundamental disciplinary knowledge. Emphasis in this quadrant is placed on factual knowledge, conceptual knowledge and introduction to procedural knowledge. Luckett (2001) has suggested that learning in this quadrant "needs to be challenged and complemented by other ways of knowing". Biggs (1999) has described learning as a way of interacting with the world: "Acquisition of information does not bring about a change, rather the way we structure and what we do with the information does". In order to create epistemic scaffolding between the different ways of knowing, students are encouraged to develop conceptual frameworks, understanding and to evaluate and analyse knowledge. In terms of the learning outcomes, meta-cognitive knowledge is introduced as a scaffold for developing practical knowledge in quadrant two.
- *Quadrant two*: Practical knowledge addressing application of disciplinary knowledge from

quadrant 1 is introduced to the student. Students can begin applying their knowledge in a controlled environment. Practical competence is developed in this quadrant. Emphasis is placed on developing procedural knowledge. We find that this is likely to develop in Engineering design courses where there is application of disciplinary knowledge and theory. Luckett (2001) cautions against the application of practical knowledge to "well-structured problems" but rather students should be encouraged to solve problems in unfamiliar situations.

- *Quadrant three*: In this quadrant the student gains reflexive competence by developing meta-cognition, thinking epistemically and contextually. The ways of knowing are developed; the student engages in tasks developing personal competence, learning about themselves and their thinking process. The student is required to 'understand', 'apply' and 'analyse'. Development of epistemic knowledge happens at 3rd and 4th year level where the epistemic shift in quadrant 4 starts to develop. These are developed through skills orientated courses such as practical laboratory projects and engineering design projects. The practical and design projects at these levels are designed to allow the student to gain experiential knowledge in a controlled setting by reflecting on knowledge gained in the first two quadrants.
- *Quadrant four*: Students are encouraged to develop higher levels of cognition by drawing on experiential knowledge, engaging personally and thinking reflexively. To be categorised in this quadrant, a high level of meta-cognitive awareness is developed, thinking epistemically and systematically. In the Chemical Engineering Programme, courses typically placed in this quadrant are higher level courses, typically 3rd and 4th year courses. In courses such as Chemical Engineering research project and Chemical Engineering Design project, the student is required to 'research', critically evaluate' , 'design' and 'conceptualise' as part of the learning outcomes(Table A.2). This requires a high level of reflexivity and where knowledge changes into knowing. The epistemic shift from quadrants 1 and 2 into quadrants 3 and 4 could be described by Barnett (2009) as a distinction between knowing and coming to know (being). Such a process is edifying where through the challenges of engaging over time with the discipline and their standards, worthwhile virtues and dispositions may develop. In this manner, the pedagogic challenge of teaching and learning of 'general transferable skills' embedded in the SAQA learning outcomes could thus be achieved.

4 DISCUSSION

Integration of the four quadrants at the end of Chemical Engineering Programme is essential in achieving coherence and progression in the curriculum. Luckett's model is used to provide a critical analysis of the programme in terms of epistemic diversity. In the engineering discipline, the building blocks of knowledge start from a disciplinary context with increasing levels of complexity through the programme. The process of knowledge building is seen as progressive providing a space for

interpretation, construction and contextualization. As we move through the different knowledge domains we see a process of re-iteration, coherence and progression. At the lower levels of study, development of the student is primarily in the first two quadrants of Luckett's model. Knowledge in these quadrants has been shown not to be linear but rather progressive in cognitive complexity. Increase in cognitive complexity within a quadrant allows for epistemic shifts into the different quadrants of Luckett's model. In the higher levels of study, the courses have been designed to allow for reflection of the propositional knowledge and how it might relate to the discipline as well as for their future roles as engineers. The programme has been designed so that on completion of the programme, the student uses and practices all four kinds of knowledge in Luckett's model.

Much of the analysis using Luckett's model as an analytical lens is based on the intended learning outcomes associated with a course and the design of the programme. The nature of constructive alignment has been discussed by Biggs (2014) where learning outcomes that students are intended to achieve, are defined before teaching takes place. These learning outcomes are designed to communicate to students what they intend to learn as well as how they should express themselves. In other words it identifies both the kind of behaviour to be developed and the context in which the student will operate. Biggs (2014) articulates that the "teaching is then designed to engage students in learning activities that optimise their chances of achieving those outcomes, and assessment tasks are designed to enable clear judgements as to how well those outcomes have been attained". As academics the teaching and learning experience requires us to develop teaching and learning activities that would engage the student in each learning outcome as well as using assessment techniques and tasks that would appropriately judge how well the student meets the learning outcome criteria. These require that all course modules, including those courses offered by service departments, would need to be constructively aligned in order to achieve coherence and progression across the programme.

Curriculum is defined by the author as a set of purposeful, intended experiences which is much like the definition proposed by Lovat and Smith (1995) where curriculum is defined as 'the educational experience, the educational journey'. The concept that curriculum is more than just acquisition of knowledge and experiences have been categorized into four parts: content, organization, learning and teaching methods and assessment. The forms that Knight (2001) proposes these experiences may take are: the planned curriculum, the created curriculum and the understood curriculum. He further proposes that 'an aspect of coherence is what is planned should be created and that what has been created should be understood'. In order to achieve this, progression is required where first encounters are at an appropriate level to novices and as the study levels increase, experts in making are developed. In turn the programme is seen as an educational device for developing epistemic virtues in an effective and efficient way. Barnett (2009) has described this as being where an individual's personal hold on the world is developed as opposed to mere acquisition of knowledge.

As academics teaching in an ODeL environment, there is very little room for deviating from the intended curriculum due to the lack of face to face contact with the student. It is thus important for us to ensure that the intended curriculum becomes the created and understood curriculum. Full implementation of the PQM is expected to be in 2020. It is recommended that constructive alignment is evaluated for all courses across the programme in order to evaluate the extent of cognitive complexity across the programme. Teaching experiences within a quadrant should be non-linear where students are expected to extend their knowledge and go beyond their existing skills and capabilities. Progression into the higher cognitive levels in the knowledge dimension is essential in creating dispositions needed for the critical epistemic shift into Luckett's quadrants 3 and 4. Further principles underlying the chemical engineering programme could be achieved through a critical evaluation of constructive alignment across the programme once full implementation of the new PQM is in effect.

5 CONCLUSIONS

In this paper, the Programme Qualification Mix of the undergraduate Chemical Engineering Programme at UNISA has been critically evaluated. The design structure of the curriculum, through the use of learning outcomes, attempted to make explicit the underlying principles governing the design of the programme. The shift in epistemic knowledge is evaluated using Luckett's model as an analytical lens. Primarily focus was on the pedagogy of the programme with the different knowledge dimensions evaluated alongside Luckett's model. This has allowed me to demonstrate how the course was designed to meet its outcomes and evaluate the extent of epistemic diversity.

A profound challenge exists in the implementation of the curriculum where knowledge and skills are augmented with qualities and dispositions. Much of this depends how the conceptualised curriculum is put into practice and the learning experience is de-linearized to promote the epistemic shift from knowing into being. Further understanding and evaluation of constructive alignment in the programme would critically enhance the evaluation of the epistemic diversity of the PQM for the chemical engineering programme.

REFERENCES

Barnett, R. 2009. Knowing and becoming in the higher education curriculum, Studies in Higher Education, 34(4), pp. 429–440

Biggs, J. (1999) What the Student Does: teaching for enhanced learning, *Higher Education Research & Development*, 18(1), pp. 57-75

Biggs, J. (2014). Constructive alignment in university teaching, *HERDSA Review of Higher Education*, Vol. 1

Carlile, O. and A. Jordan (2005), It works in practice but will it work in theory? The theoretical underpinnings of pedagogy, In S. Moore, G. O'Neill, and B. McMullin (Eds.), *Emerging Issues*

in the Practice of University Learning and Teaching, Dublin: AISHE.

Gibbons, M.; Limoges, C.; Nowotny, H.; Schwartzman, S.; Scott, P. and Trow, M. (1994) The new production of knowledge: the dynamics of science and research in contemporary societies, California: Sage

Government Gazette (2014), Higher Education Qualifications Sub-Framework (HEQSF), Vol. 592, No. 38116

Hoffmann, M.H.W. (2008) Using Bloom's Taxonomy of Learning to Make Engineering Courses Comparable, 19th EAEEIE Annual Conference, pp 205-209; Retrieved July 18, 2018 from https://www.researchgate.net/publication/4369327

Knight, P. T. (2001) Complexity and curriculum: a process approach to curriculum-making, *Teaching in higher education*, 6(3), pp. 369-381

Kolb, D. A. (1984), Experiential learning: Experience as the source of learning and development, New Jersey: Prentice-Hall

Lovat, T. and Smith, D. (1995) Curriculum Action and reflection revisited, 3rd ed., Wentworthfalls, NSW. Social Science Press, pp. 8-21

Luckett, K. (2001) A proposal for an epistemically diverse curriculum for South African higher education in the 21st century, *South African Journal of Higher Education* 15(2), 49-61

McGrath, P and Nickola, L. (2009) A new education framework and the impact on vocational qualifications offered by South African comprehensive universities and universities of technology, Retrieved July 18, 2018 from http://uir.unisa.ac.za/bitstream/handle/10500/2930/nikola.pdf

Nel, W.P. (2014) Universities and decision-making: programme and qualification mix - four learning pathways. Journal of the Southern African Institute of Mining and Metallurgy, 114(5), 01. Retrieved July 18, 2018 from http://www.scielo.org.za/scielo.php?script=sci_arttext&pid=S2225-62532014000500010

NQF and Curriculum development framework (2000), Retrieved October 14, 2018 from http://www.saqa.org.za/docs/pol/2000/curriculum_dev.pdf

UNISA open distance learning policy (2008), Retrieved October 11, 2018 from https://www.unisa.ac.za/static/corporate_web/Content/Colleges/CGS/schools,%20institutes%20&%20research%20chairs/institutes/documents/odl-policy_version5_16Sept08.pdf

UNISA annual report (2016), Retrieved October 11, 2018 from https://www.unisa.ac.za/static/corporate_web/Content/News%20&%20Media/Publications/docs/10085798_UNISA_Annual_Report_2016.pdf

Table A1: Conceptualising theoretical course learning outcomes across the undergraduate programme – cognitive domain

The knowledge dimension	1st year of study	2nd year of study	3rd year of study	4th year of study	The cognitive process dimension
	Chemical Engineering Fundamentals 1 CHF1501	**Chemical Engineering Fundamentals 2 CHF2601**	**Chemical Engineering Design CED3601**	**Chemical Process Design Principles PDP3701**	
Factual knowledge	Define the basic and fundamental units and dimensions in engineering analysis and calculate their value.	Determine the physical properties of compounds and mixtures, and derive relations between these properties and process variables.			Remember Understand Apply
Conceptual knowledge	Measure and/or calculate the conditions of process streams and process units.	Provide an outline of the different forms of energy and the principle of conservation of energy.	Assemble a logical sequence of interconnected unit operations for a chemical engineering process. Determine sizes and select materials of construction of equipment commonly used in the chemical processing industries.		Understand Apply
Procedural knowledge	Apply material balances in simple batch and continuous systems.	Explain and apply fundamentals of energy balances in a non-reactive steady state system.	Perform an economic evaluation of the process. Incorporate environmental and safety concerns into the process design.	Perform procedural detailed design of process equipment. Apply various techniques to mitigate safety, controllability and environmental issues.	Apply Analyse
Meta-cognitive knowledge	Formulate and solve material balances to reactive systems and multi-stage systems.	Apply fundamentals of energy and mass balances to multi-stage and reactive systems.	Present the design in an organised manner.	Evaluate and screen process sheet alternatives. Apply the approaches of mass and energy integration for synthesis and optimisation of	Apply Analyse Evaluate

				flow sheets.	
The knowledge dimension	**1st year of study**	**2nd year of study**	**3rd year of study**	**4th year of study**	**The cognitive process dimension**
		Reaction Engineering REE2601	**Advanced Reaction Engineering REE3701**		
Factual knowledge					Remember Understand Apply
Conceptual knowledge		Perform unsteady state material balances, stoichiometric and reaction equilibrium calculations.	Apply the energy balance to isothermal and non-isothermal reactors.		Understand Apply
Procedural knowledge		Perform chemical reaction kinetics calculations.	Model the kinetics and design chemical reactors for heterogeneous systems.		Apply Analyse
Meta-cognitive knowledge		Model ideal reactors under isothermal conditions.	Design complex and non-traditional reactor systems.		Apply Analyse Evaluate
	Quadrant 1: Propositional knowledge		**Quadrant 2: practical knowledge**	**Quadrant 3: Epistemic knowledge**	

Table A2: Conceptualising practical course learning outcomes across the undergraduate programme – skills domain

The knowledge dimension	1st year of study	2nd year of study	3rd year of study	4th year of study	The cognitive process dimension
	Chemical Engineering Practicals 1 CEP2601	**Chemical Engineering Practicals 2 CEP3601**	**Chemical Engineering Practicals 3 CEP3701**	**Chemical Engineering Research project HRCEN83**	
Factual knowledge					Remember
Conceptual knowledge	Operate laboratory equipment and pilot plants in various chemical engineering fields.	Conduct laboratory and pilot plant experiments in various chemical engineering fields.	Conduct laboratory and pilot plant experiments in various chemical engineering fields.		Understand Apply
Procedural knowledge	Presents data in an appropriate manner. Develops effective team work.	Presents data in an appropriate manner. Develops effective team work.	Presents data in an appropriate manner. Develops effective team work.	Collect, analyse and interpret experimental data.	Apply Analyse
Meta-cognitive knowledge	Collect, analyse and interpret experimental data.	Collect, analyse and interpret experimental data.	Collect, analyse and interpret experimental data.	Research, conceptualise, and formulate an experimental investigation on an ill-defined topic which is complex. Critical evaluation of conclusions drawn from the data and determine the applicability of conclusions to other situations or contexts.	Analyse Apply Evaluate
			Process Design Project **PDP3702**	**Chemical Engineering design project** **CED4801**	
Factual knowledge					Remember Understand
Conceptual knowledge			Performs complete mass and energy		Understand Apply

			balance on an existing flowsheet.		
Procedural knowledge			Identify and quantify the environmental and safety aspects of a process.	Perform complete mass and energy balance on a process flowsheet.	Apply Analyse
Meta-cognitive knowledge			Perform sizing and costing calculations on typical process equipment. Plan, layout and write a technical design report	Research, conceptualise, and formulate a process flowsheet. Perform design and sizing calculations on certain unit processes such a reactor, heat exchanger and separation unit. Identify and quantify hazards and emissions and suggest methods of remediation.	Apply Analyse Evaluate
Quadrant 3: Epistemic knowledge + experiential knowledge			**Quadrant 4: Experiential knowledge**		

Degree Accreditation Report Auto-generation by Logic Encoding and Processing

M. Chetty[1*] and R. Rawatlal[2]

[1] Department of Chemical Engineering, Durban University of Technology

[2] Department of Chemical Engineering, University of Kwa-Zulu Natal

*Corresponding author: chettym@dut.ac.za; ORCID: 0000-0003-4035-739X

ABSTRACT

Maintaining the accreditation profile of an academic programme is a key activity in so-called professional degrees such engineering, commerce and law. The complexity of the accrediting criteria tends to rise over time as accrediting bodies require quantitative evidence of competence of increasingly specific graduate attributes. Evaluation of graduate attributes may therefore require complex logic processing which challenges the human capacity. This has the negative side effect of discouraging curriculum revision not for pedagogic reasons but simply due to the complexity of evaluating complex logic patterns against a data set whose structure is shifting. These challenges can be overcome through the application of logic encoding and processing. A computing system is better suited to such processing tasks since logic processing is fundamental and well-established to such systems. On the other hand, the efficient representation of a complex accreditation logic rule base then becomes the challenge. This paper describes the representation of the accreditation logic of eight engineering academic programmes at the Durban University of Technology through the AutoScholar Advisor System in preparation for evaluation by the Engineering Council of South Africa. It is shown that the system generates accurate reports even with deeply nested logic structures and with changes in curriculum over time.

Keywords: engineering education, accreditation

1 INTRODUCTION

Accreditation maintains the quality of a degree and sets a minimum guaranteed standard which facilitates the employment of students across geo-locations. The modern trend is for such criteria to become increasingly quantitative and specific. An accrediting body outlines a set of graduate attributes. Higher education, in general, is responsible for formally preparing the next generation of leaders, technical professionals, government officials and educators. Engineering education, in particular, plays a central role in our increasingly technology-based societies. The education of engineers must prepare them for the multi-disciplinary nature of the problems they will face developing a new set of skills and competencies. On an international level, the recruitment, management and retention of students have become as high-level priorities for decision makers in HEIs. Especially improving the student retention starts and the under-standing of the reason behind and/or prediction of the attrition has come in the focus of attention due to the financial losses, lower graduation rates, and inferior school reputation in

the eyes of all stakeholders. In recent years the engineering profession and the accreditation bodies have called for change in the curriculum to address the graduate attributes which are related to the learning outcomes. This has sparked a call for the revision of national accreditation criteria for engineering programs in the United States, the United Kingdom and Australia. Engineering programs are now required to demonstrate a set of outcomes and show industry relevance. The Engineering Council of South Africa (ECSA) has revised its accreditation criteria to include a set of graduate attributes. Traditional and technology universities are now required to indicate the exit level outcomes of the programs they offer at the various levels. ECSA have stated generic exit level outcomes for different qualifications where individual institutions have to design curricula to meet these standards. The Higher Education Qualification Sub-Framework (HEQSF) policy revision provides the backdrop to curriculum renewal at all higher education institutions (HEIs). Maintaining the accreditation profile of an academic programme is a key activity in so-called professional degrees such engineering, commerce and law. The complexity of accreditation implementations tends to rise over time as accrediting bodies require quantitative evidence of competence of increasingly specific graduate attributes. Evaluation of graduate attributes may therefore require complex logic processing which challenges the human capacity. These days, higher education institutions (HEIs) are collecting more and more data than ever before, to maximize strategic outcomes. Universities have to deal with the rapidly changing technologies that have arisen with the entry of the digital age. In the course of this, institutions collected enormous amounts of relevant data as a by-product. A computing system is better suited to such processing tasks since logic processing is fundamental and well-established to such systems. On the other hand, the efficient representation of the accreditation logic rule base then becomes the challenge. Accreditation maintains the quality of a degree and sets a minimum guaranteed standard which facilitates the employment of students across geo-locations.

2 LITERATURE

Virtually all fields of human endeavour are now accelerated by the application of computing systems. Statistics, gamification and artificial intelligence offer new insights and facilitate automation of even those processes traditionally considered to be the exclusive domain of human operation. As the field academia evolved and new processes developed to aid the process of teaching and learning, the complexity grew. Decision-making in an academic programme now requires the navigation of a labyrinth of “hard” and “soft” rules. The latter refers to discretionary cases that once required the application of human minds to gauge the likelihood of a break in the published rules, and which is now being replaced by machine learning models. With the increasing popularity and importance of higher education, degree cohorts are becoming larger and it is becoming increasingly difficult for lecturers and advisors of studies to engage with students personally. As a result, students who are struggling with course material are receiving feedback and advice too late or are being missed out altogether which

increases the number of students failing or dropping out of higher education. The increase in research into machine learning and advances in technology have made complex and computationally expensive machine learning algorithms a viable solution to this problem (Bruce, 2019). The low academic performance of students affects students, tutors, institutions and the society in varieties of ways. To deal with this problem, researchers have applied several methods and most recently, researchers have employed data mining methods (Ekubo, 2020). In Australia, the possibility of predicting final exam performance in terms of high performance or low performance was investigated using 220 first year university student records in a computer programming unit. The study used attributes such as: scores in assignments, degree type, local or a foreign; and some demographic attributes. Experiments were conducted with both standard decision tree (DT) and association rules (AR) classifiers and the discrimination aware (DA) versions of the two. Results indicate that the standard classifier attained the highest accuracy of 83.46% even though all the other three classifiers attained accuracies that were nearly similar to the best classifier. In a different approach, study habits in programming were used as indicators to predict whether college students will pass or fail a mathematics course (Vihavainen *et al*., 2013). A total of 52 students participated. Modelling was carried out using Bayesian networks. Accuracy, recall, precision and F-Measure metrics were calculated. The study was able to record an accuracy of 84.6 % likelihood of a student failing their mathematics course only after five weeks of programming lessons, giving time for possible intervention.

Engineering qualifications are primarily industry oriented where the knowledge emphasises general principles and application or technology transfer. The qualification provides students with a sound knowledge base in a particular field or discipline and the ability to apply their knowledge and skills to particular career or professional contexts, while equipping them to undertake more specialised and intensive learning. Programmes leading to this qualification tend to have a strong professional or career focus and holders of this qualification are normally prepared to enter a specific niche in the labour market. The purpose of educational programmes designed to meet this qualification are to build the necessary knowledge, understanding, abilities and skills required for further learning towards becoming a competent practicing engineer. They offer preparation for careers in engineering and areas that potentially benefit from engineering skills, for achieving technological proficiency and to make a contribution to the economy and national development. Engineering students completing this qualification will demonstrate competence in all the Exit Level Outcomes (ELOs) contained in the standard as prescribed by ECSA (ECSA, 2012). A key step in this process is the definition of the engineering graduate profile, the skills and competencies s/he must possess to be successful as an engineer. Engineers face problems as a way of life. Engineers must not only be knowledgeable about science and technology but also have the skills, competencies and values to address problems and opportunities in effective and creative ways (Morell, 2010). This international mobility of engineering

graduates has compelled educational institutions to enhance the quality and standard by introducing various quality assurance and professional accreditation processes. The educational institutions, employers, and professional organizations have a keen interest in the quality of education received by engineering graduates who aspire to be internationally mobile especially in today's globalised economy. This quality assurance and professional accreditation are more important for countries which rely on human resources export and import. Quality assurance mechanisms for engineering education vary considerably from country to country ranging from strong peer-run accreditation programs to large government bureaucracies. The accreditation methods used by the Washington Accord signatory countries (details are given later) are considered to be the best developed and most well-respected systems for the accreditation of engineering education in the world (Chowdhury et al, 2013). ECSA has been part of the international drive to globalise the curriculum and all new engineering curricula in South Africa confirm to the prescribed standards.

Traikova (2019) developed a tool to supported performance management of engineering education. This prototype was called the Graduate Attribute Information Analysis (GAIA) in collaboration with the School of Electrical Engineering and Computer Science at the University of Ottawa, to support a systematic approach for accreditation of three engineering programs. A systematic approach was followed to develop tool that supports it, a set of related data transformations, and a tool-assessment checklist. This approach addressed the system architecture, a common continuous improvement process, a common set of key performance indicators, and identified the performance management forms and reports needed to analyse graduate attribute data.

3 METHODOLOGY

3.1 Implementation of an accreditation system

A regulating body such as ECSA generally avoids the prescription of the method of accreditation implementation, and instead defines the principles or attributes that the graduates of such a programme should possess. It is then the responsibility by the programme management at the institution to propose methods for evaluating whether a graduate exhibits such attributes. In modern academic programmes, such evaluations must be quantitative and evidence based. The clearest method for accomplishing this is through the assessments attached to the coursework delivered in that programme. A set of criteria must therefore be defined which comprehensively tests the student knowledge. At the same time, these criteria must be carefully balanced against the level of difficulty required to graduate from that programme. If the criteria are too rigorous, the additional requirement may negatively influence the graduation rate; if the criteria have too low a standard, the accreditation status may be negatively influenced. This careful balancing act therefore requires criterion sets that draw on the results of assessments across potentially multiple combinations of coursework. This results in deeply nested logic criteria which are relatively complicated and onerous to administer. Accreditation therefore typically

requires dedicated teams of academics spending many man-hours in debating accreditation criteria and many more man-hours of administration to evaluate. Clearly, computing methods may be applied to offer relief, but the complexity then shifts to the problem of accurately representing the criterion sets.

3.2 Representing accreditation logic

For automated advising of an academic programme, the accreditation rules and criteria must be specified and encoded.

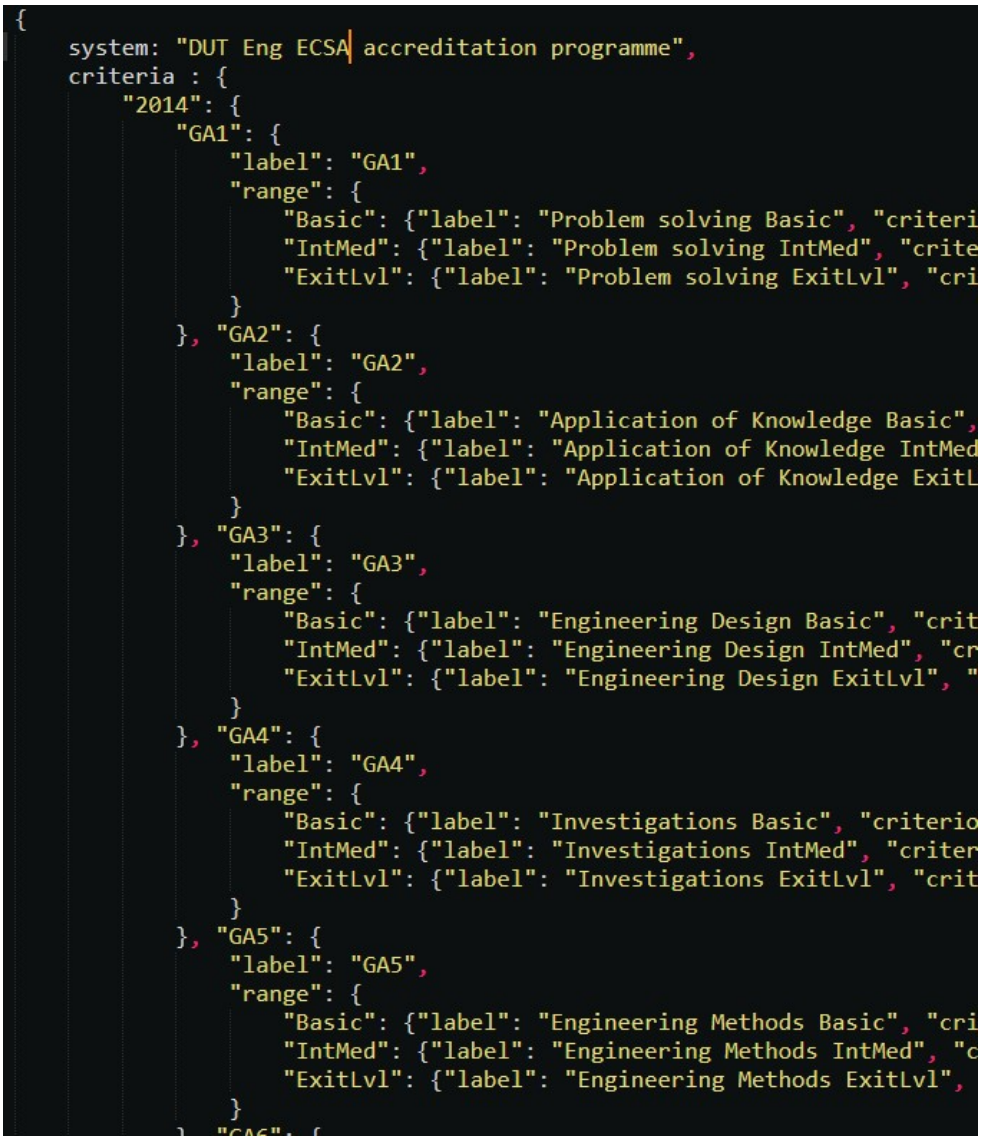

Figure 1: Framework of accreditation attributes

The criterion editor in the AutoScholar Advisor system makes it possible for staff to edit and maintain the accreditation rules. The system borrows certain concepts from the field of Graph Theory and uses an open-ended logic processor based on infinitely recursive tree structures. By accepting the result of an assessment as the basic unit of operation, the criterion set may be assembled through the construction

of a logic graph. This may be considered as a tree of potentially deeply nested AND and OR logic operations. Before describing the logic encoding, we note that the accreditation attribute set must first be embedded in a framework such as the one represented in the Figure 1. All graduate attributes are recorded at the three stages of basic, intermediate and exit level. The criterion for each such range statement is itself is represented by a JavaScript Object Notation (JSON) object. According to this logic pattern, the criterion is for the student to pass [either TCHL101 OR TCLT101], together with [CSTN101 AND CEFA101 AND CEDS101]. It can be seen that the user may specify an arbitrarily deeply nested logic pattern through this representation. More specific criteria can be imposed by specifying minimum marks rather than requiring just a pass, or by setting criteria according to specific assessments.

3.3 Policy for evaluation with changing curriculum

Changes to accreditation structures due to changes in criteria or curriculum revision are not only unavoidable but a sign of a healthy evolving academic programme. However, as the curriculum or the accreditation criteria change with time, the evaluation of the accreditation must remain fair to all students who are, in effect, trying to hit a moving target. This is complicated by the potentially significant number of students undertaking various elements of the academic programme out of synch with the cohort completing in minimum time. The algorithm, provides a suitable procedure for maintaining the fairness and the accuracy of the process. Let's assume that an accreditation criterion system is defined at implementation of an accreditation system at an institution in year y_0.

1. A new instance of the criterion set is defined in each year according to
    a. For criteria unchanged by accreditation system changes or curriculum changes, that criterion is simply inherited in the new instance of the accreditation object.
    b. In the case of a change, the criterion is updated in the new instance only.
2. When a student's profile is evaluated, the criterion instance for each year of the academic record is evaluated against the criteria specified for that year. If the student satisfies any criterion, the criterion is checked off and removed from further evaluation for that student.
3. In order to avoid a limitation of the rate of progression by students, there should be more than one opportunity to pass a criterion in the programme. In other words, if a criterion is not passed in one semester, there should be at least a second opportunity in a later semester. If the student does not pass the criterion on the first opportunity, s/he cannot be made to re-take the course; however, for the last opportunity, the criterion functions as a sub-minimum for progression through the course.

This procedure has been found to accurately and fairly assess the accreditation position of students in an academic programme. It has been used in real accreditation processes at three (3) South African institutions.

3.4 Previous experiences

The AutoScholar Accreditation sub-systems has been successfully applied in practice. The Figure 2 illustrates the accurate advice generated to a student which reports on accreditation compliance even in the face of significant changes to both accreditation structure and curriculum during the lifetime of the student at the institution.

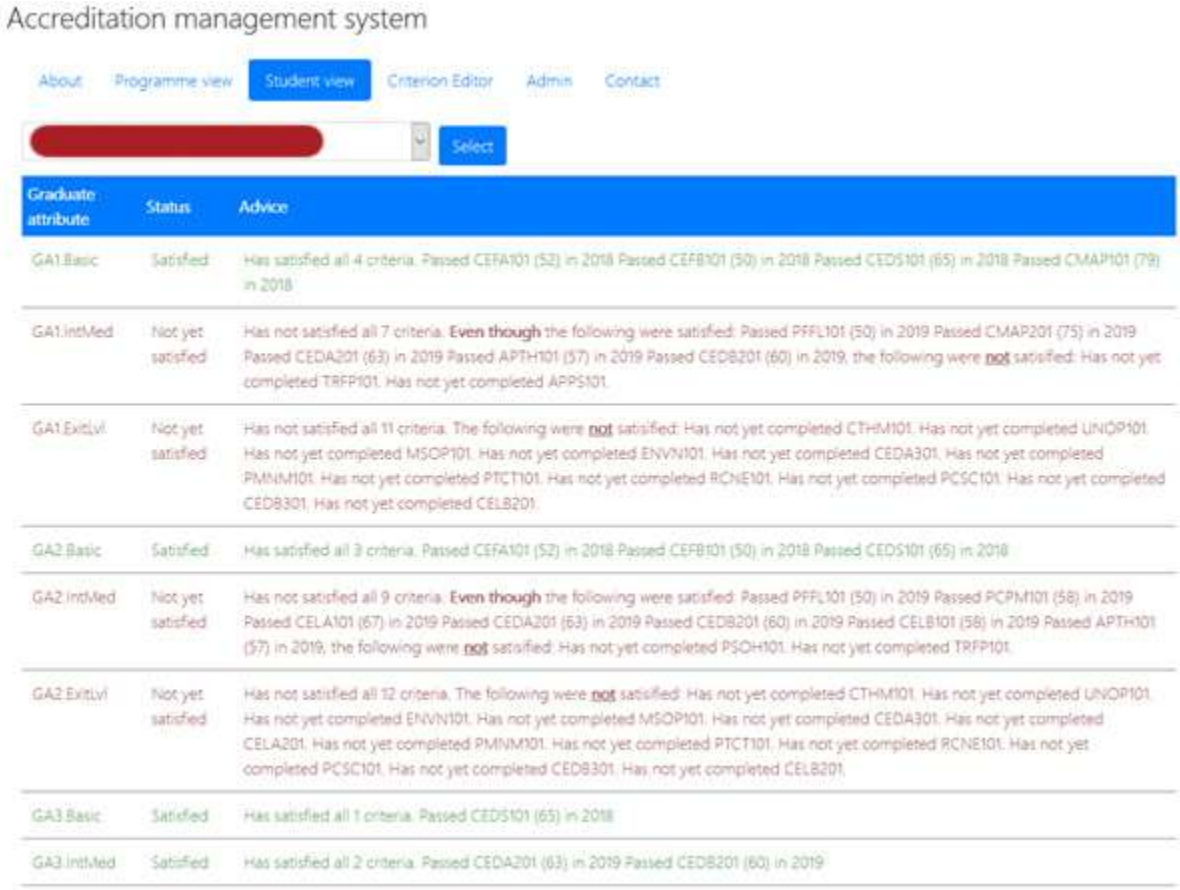

Figure 2: Student advice on accreditation compliance

This report illustrates the accreditation profile of an individual student. For reporting across an entire academic programme, this process can simply be repeated for all students registered. The following Figure 3 illustrates such a programme-level report. There are not any automated systems reported in the literature on GAs for engineering students. Traikova (2019) implemented a system which and created a database of statistics which included reports and forms filled in by the academics. The results showed a statistical analysis of how the GAs were achieved at a given point in time for a course or program. In contrast the Autoscholar program is able to trace an individual student's progress together with course and program information. The ECSA accreditation of all programs now requires proof that each student has met the GA requirements for the whole program.

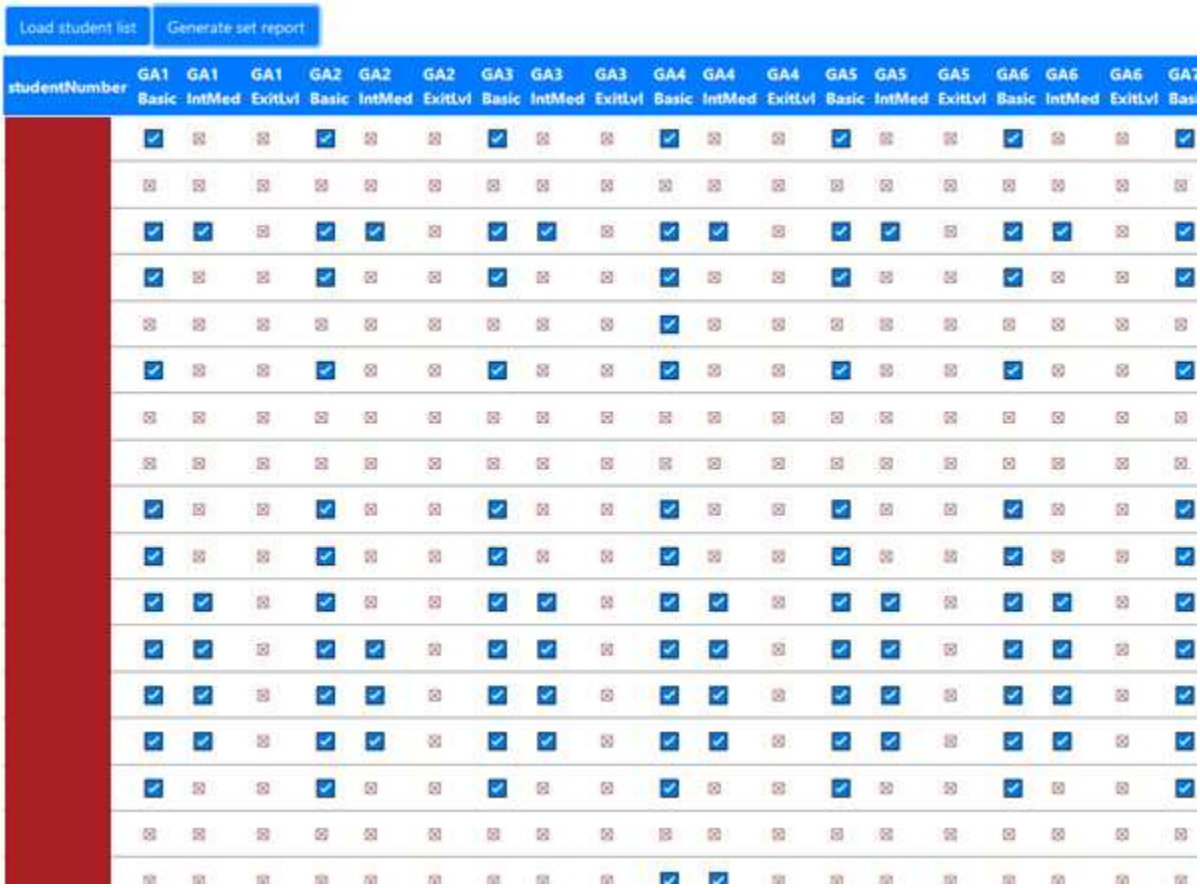

Figure 3: Program level report

Among the observations made during the implementation of the system has been the unintended gamification. When granting students access to the system, it was observed that the awareness of the accreditation structure and the accreditation criteria was raised significantly. Even though student awareness of the accreditation structure is an important principle to accrediting bodies, this is rarely achieved or demonstrated by students. In practice, institutions will often groom students who are due to be interviewed by accreditation panels, which defeat the purpose of the accrediting body. The observed increase in awareness by students is thought to be due to be highly specific reporting which shows the accreditation with reference to the progress by the student. Especially when highlight with green and red colours, which have been associated with “good” and “bad” behaviour, there are powerful motivators for the student to become implicitly engaged with the institutions implementation of the accreditation system.

4 CONCLUSIONS

In the engineering profession the additional challenge is the accreditation process which requires HEIs to track and provide evidence for the assessment of the GAs. A robust and reliable management system

is vital to keep students, academics, administrators and the accreditation bodies with "live" data of every registration. The system described here can represent arbitrarily complex and/or deeply nested logic patterns as part of the criterion rule definitions. A method for managing the change in accreditation rules was developed and found to be effective in the application of the implementation at the Durban University of Technology (DUT). The system was used to generate the accreditation report at the programme level as well as to generate detailed reports on the logic pattern down to the level of individual students. The unintended positive outcome observed from previous releases of the system for access by students was that a high level of awareness of the accreditation rules was developed. We therefore consider the application of computing methods such as those facilitated by the AutoScholar Advisor System to be effective means of operating a rigorous implementation of an accreditation system.

ACKNOWLEDGEMENTS:

Durban University of Technology. This project has received ethical clearance from the university to use student data.

REFERENCES

Bruce, A. (2019). The Prediction of Student Performance Through the Use of Machine Learning. *MSc Software Development, University of Strathclyde.*

Chowdhury, H. Alam, F. Biswas, S. K. Islam, M.T. and Islam, A.K.M. (2013). *Quality assurance and accreditation of engineering education in Bangladesh*. Procedia Engineering. 56: 864:869.

ECSA. (2012.) *Qualification Standard for Bachelor of Engineering Technology: NQF Level 7***.** Document E02-PT. www.ecsa.org.za.

Ekubo, E.A. (2020). Predictive system for characterizing low performance of Undergraduate students using machine learning techniques. *DPhil.* North West University.

Morell, L. (2010). Engineering Education in the 21st Century: Roles, Opportunities and Challenges. *International Journal of Technology and Engineering Education*. 7: 2.

Nair, C. S.., Patil, A. and Mertova, P. (2011) Enhancing the quality of engineering education by utilising student Feedback. *European Journal of Engineering Education*. 36:1:312.

Traikova, A. (2019). A systematic approach for tool supported performance management system of engineering education. University of Ottawa, Canada**.** *PhD thesis.*

Vihavainen, A., Luukkainen, M., and Kurhila, J. (2013). Using students' programming behaviour to predict success in an introductory mathematics course. *Educational Data Mining.*

Transforming the Chemical Engineering Curriculum to Gear towards the Fourth Industrial Revolution

T. Gore[1], L. Murugan[2], A. Singh[1], A. Philipp[2] and A Stark[1*]

[1] University of KwaZulu-Natal, School of Engineering, Discipline of Chemical Engineering, Durban, 4041, South Africa

[2] University of KwaZulu-Natal, School of Education, Discipline of Teacher Development Studies, Durban, 4041, South Africa

*Corresponding author: starka@ukzn.ac.za; +27 (0) 31 260 3383.

ABSTRACT

The world is at the advent of the Fourth Industrial Revolution (4IR). Several entities in South Africa and abroad have recognized the need for curriculum content and delivery transformation to the requirements of 4IR. Hence, a project was initiated by the Schools of Engineering and Education at the University of KwaZulu-Natal, which aims at a fundamental curriculum transformation in engineering, addressing sustainable development challenges. Transforming the engineering curriculum content, structure, and delivery in preparation for 4IR is essential if Higher Education Institutions (HEIs) want to continue providing quality education relevant to locally and internationally required engineering practices. The project focuses on relevant 4IR skills of a future workforce and how these can be fostered through teaching at HEIs. An integral part of engineering education is laboratory work. In this paper, we discuss online experimentation as a possible alternative to physical laboratories, present selected online laboratory platforms and focus on how online experimentation may foster the development of 4IR skills. A SWOT analysis of online laboratories shows that these allow for more flexibility to conduct an experiment or work remotely, provide opportunities for HEIs to target other student groups and generate additional revenue. However, a move to online laboratories may also come with challenges related to the development of both novel pedagogies and student self-regulated learning, as well as to threats concomitant with the necessary accreditation processes. Yet, if HEIs in South Africa and their STEM graduates want to remain competitive, they need to embrace novel technologies such as online experimentation to advance in the 4IR and remain relevant in a changing world.

Keywords: Fourth Industrial Revolution, 4IR, Chemical Engineering, Curriculum Transformation, Virtual and Remote Laboratories

1 INTRODUCTION

The Fourth Industrial Revolution is defined as combining physical, digital, and biological spheres through technology at a very fast pace and with a large scope (Schwab, 2016). It refers to the dismantling of boundaries between these sectors as digitalization and automation increase within daily life. Different terms for the revolution itself include: '4IR', 'FIR' 'Industry 4.0', 'Industrie 4.0', 'I4.0', 'I4' and, according to a book of the same name, the 'Second Machine Age' or '2MA' (The Second Machine

Age, 2021), herein summarily referred to as 4IR. As with any revolution, it is a step-change of development, and it is instructive to analyze in which countries, disciplines, and years academic scholars respond to the 4IR in their publications.

2 LITERATURE

Web of Science was utilized to search for such publications on this topic. The terms '4th Industrial Revolution, '4IR', 'Industry 4.0', 'Industrie 4.0', 'I4.0' or '2nd Machine Age' were used in the search.

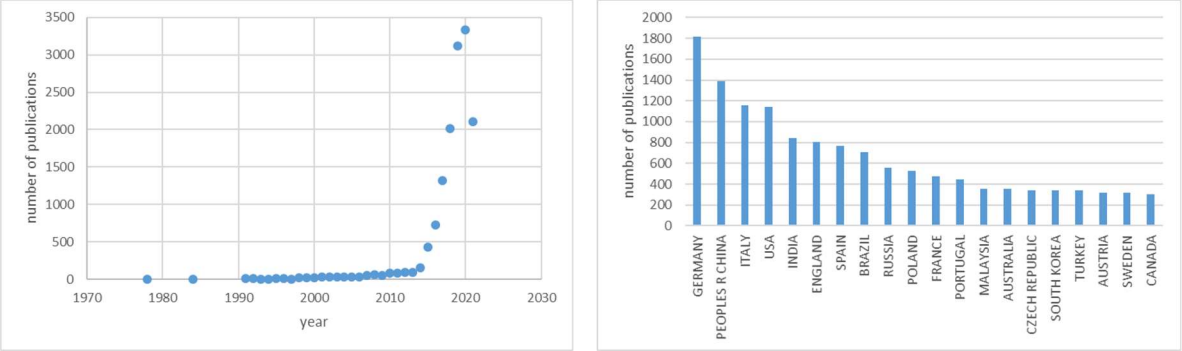

Figure 1: Number of publications mentioning one of the terms related to 4IR (left) and top-20 publishing countries (right); Web of Science, topics: '4th Industrial Revolution', '4IR', 'Industry 4.0', 'Industrie 4.0', 'I4.0' or '2nd Machine Age', as of 20. August 2021.

Figure 1 (left) shows that overall, over 14,000 publications exist worldwide using the terms indicated, starting with the first publication in 1978. While a relatively low number of publications had one of the keywords until 2014 (below 100 per year), an exponential increase is witnessed since then.

Figure 1 (right) shows the top-20 publishing countries in the arena, most of them considered to be developed countries. It is noteworthy that not one country is from Africa. However, taking the disparities in size, the total number of researchers and research expenditure of individual countries into account, this finding does not mean that the topic receives no attention in Africa. A closer look at the data reveals that African countries with at least ten publications in this area are South Africa (239), Morocco (46), Egypt (29), Tunisia (24), Nigeria (17) and Algeria (11). It can hence be concluded that compared to the research efforts conducted worldwide, African contributions are few. This highlights the risk of developing countries not keeping up with technological advancements and not benefitting from the advantages of a 4IR-transformed industrial activity, such as safer industrial working conditions, higher processing efficiencies and lower environmental impact, to name but a few.

The Research Areas that featured most often were Engineering (29% of overall publications), Computer Science (17 %) and Business Economics (7 %), highlighting the industrial relevance and interdisciplinarity of the topic. Statistically, the publications were almost entirely written in English.

Judging from the literature analysis, it is evident that developing countries such as South Africa are yet to harness the 4IR and implement it in production processes. Many developing countries experience challenges that render their citizens unable to enjoy even the benefits of the previous industrial revolutions. For example, South Africa does not have a constant electricity supply, frequently experiencing power outages, and many people do not have easy access to clean water and sanitation. Regaining on the provision of services providing for basic needs requires capital, which is scarce. Hence, it is difficult to simultaneously advance in high-tech areas at the same pace as developed countries.

Furthermore, there is a severe lack of knowledge workers in 4IR-relevant subject areas. This has been recognized by various South African universities and other organizations. Already in 1998, the University of Pretoria formed a Computational (Artificial) Intelligence Research Group (Gleason, 2018). In more recent times, the University of Johannesburg has been adapting its curriculum to incorporate 4IR relevant content by extending engineering education to encompass aspects of humanities and social sciences, offering programs that involve specific 4IR topics such as Big Data Analytics and considering bringing virtual reality into undergraduate programs. Specifically, they offer the courses 4IR for Professionals in Business, Blockchain Technology for Professionals in Business and Artificial Intelligence Perspectives for Professionals in Business (University of Johannesburg, 2021). A recent initiative, "Bringing Life to our Engineering Curricula" (2021), is an exciting collaboration between several universities in South Africa and the United Kingdom in collaboration with the South African Society for Engineering Education, showcasing curriculum strategies at South African Higher Education Institutions. Also, certain local industries are currently moving towards 4IR, such as the sugar industry, which has embarked on a private sector / DSI-funded programme (Sugar Factory 4.0) to drive the competiveness of their business (Hancock, 2019).

At the University of KwaZulu-Natal (UKZN), an interdisciplinary team has embarked on a project seeking to analyze the existing curriculum in chemical engineering and determine how to revise the curriculum and foster relevant 4IR skills in future graduates to be able to meet the needs of the industries when moving towards the 4IR. The project's overall aim is to lay the foundation for a knowledge-based curriculum transformation, to equip today's students with knowledge, skills, and competencies for tomorrow's engineering workspace. This will allow them to fully exploit their innovative and intellectual capacity, technical skills and contextual understanding, and also impact the economic advancement of South Africa. The outcome of this project can serve as a blueprint for other STEM disciplines UKZN and other HEIs. This paper focusses specifically on laboratory experience gained in STEM subjects, analysing skills and competencies gained in labs, and key findings presented in form of a SWOT analysis.

3 METHODOLOGY

As a first step of the overall project, the pre-COVID, ECSA-accredited curriculum for chemical engineers is analysed to display which skills are trained, at what level of study, to what extent and by which pedagogy to establish a baseline of analysis. A stakeholder workshop, including a consortium of academic, industrial and governmental representatives, is planned to determine skill profiles of the prospective workforce in chemical engineering in South Africa. This will then culminate in an analysis of the current curriculum (remote teaching and learning under COVID-19 conditions) and determine which further steps need to be made to prepare future graduates for the 4IR in South Africa.

The project is conducted by an interdisciplinary group from Engineering and Education and is applying a mixed-method design (questionnaires to be distributed to stakeholders to determine and rank relevant 4IR skills, focus group discussions with stakeholders on finalizing the identification of relevant 4IR skills of chemical engineers). The resulting 4IR-transformed chemical engineer skillset is compared to pre-pandemic skills and competencies. As part of this analysis, pathways to use other forms of teaching relevant skills are explored.

For this paper, the literature was analysed regarding skills and competencies gained in physical versus online labs. Additionally, a large number of existing online labs were assessed regarding their scope, user friendliness and adaptability to supplement or replace current physical lab offerings. A SWOT analysis approach is applied to highlight key strengths, weaknesses, opportunities, and threats of implementing online laboratories into the curriculum.

4 RESULTS AND DISCUSSION

There is a need for HEIs in South Africa to offer 4IR-transformed education and reimagine spaces. Of particular importance for STEM subjects is experiences gained through physical laboratory experimentation. This space can profit from 4IR-derived technologies, and exposure to these is essential for the preparation of future graduates. A move away from physical laboratory work towards virtual and remote laboratories seems pertinent. In this paper, we explore the advantages and disadvantages of virtual and remote laboratories and their possible use in the teaching of chemical engineering students.

4.1 Skills Gained in a Physical vs Online Laboratories

A comparison is presented between skills gained in physical laboratories in relation to alternative forms of teaching laboratories. In modern times, three different types of laboratories can be distinguished. A *physical laboratory* involves the user's physical presence in the space. It is the traditional type of lab, while a *remote lab* is a physical lab operated by a user via a digital interface. A *virtual lab* is a simulation existing only in cyberspace that does not physically exist, operated via digital technology. Due to differences in operation, different skills may be gained from the different labs, although overlap does exist.

First, we focus on *communication, problem-solving* and *team-working* skills. Physical lab work very often involves working in groups, where the skills of communication, solving conflict and teamwork should be developed (Mackay and Fisher, 2014). These skills are often relatively easy to train in a physical lab space due to sharing space and being exposed to interpreting social cues and reading facial expressions. In many existing virtual or remote lab platforms, however, the possibilities to develop such skills are limited due to video and audio restrictions. However, those that offer access of multiple user teams can allow students from different countries and higher education organizations to work together (Mackay and Fisher, 2014), which broadens student horizons and can help develop cultural awareness and sensitivity in addition to communication, problem solving and team working skills.

Next, we focus on *time management and the ability to work under stress*. These skills can potentially be gained from all lab types, although to varying extents. Whereas physical labs tend to be bound to strict timelines, remote and virtual labs are more flexible, providing opportunities to adapt timelines, pause or redo experiments. Another set of relevant engineering skills are *making predictions*, *performing calculations*, *interpreting and expressing results*. Again, these skills are developed equally in all labs. However, some *technical skills* are only gained through physical labs. The ability to set up, handle and operate equipment can only be fully acquired in a physical lab. Despite some shortcomings, a massive benefit of remote labs is that students gain *remote working skills*, which become increasingly relevant. Mackay and Fisher (2014) also state that virtual and remote labs improve *IT skills*, crucial for the 4IR.

Finally, certain *skills link specifically to the 4IR*. According to the literature, relevant 4IR skills include (among others) creativity, originality and initiative, people management, emotional intelligence, cognitive flexibility, analytical thinking and innovation (Gray, 2016 and Wessels, 2020). Including these into laboratory teaching will be challenging, even in physical lab spaces. Many of these skills relate to human interaction and creativity, which will be more difficult to replicate by machines in online laboratories. In the next section, we focus on how existing platforms that can contribute to developing such skills.

4.2 Lab Training in 4IR Transformed Curricula

The potential of virtual and remote labs is now examined in more detail. Various offerings are available on the market, some may be used online, and others require software to be downloaded. Some are free to use, but others require a license or subscriptions. Virtual labs can be divided into two broad categories: those which seek to mimic physical labs and labs focusing on illustrating concepts. The first category aims at providing a realistic set-up (glassware to be cleaned before the experiment, balances to be tared, and titrations to be repeated multiple times). In these labs, visuals provided resemble the physical experiment set-up. Labs focusing on illustrating concepts, on the other hand, eliminate some

procedures, and visuals tend to be more simplistic, focusing on what result or process is being observed.

Several online labs are now compared, starting with virtual labs, followed by remote and virtual reality labs. *Labster* offers virtual labs in the fields of Biology, Chemistry, Physics and Medicine. Beyond common lab experiments, Labster also offers an engineering section that includes wastewater treatment, silo design and concrete materials testing. These more specialized simulations could be of use to various engineering students. A futuristic lab is presented with a lab assistant that offers instructions and advice, making the software the most user-friendly of those sampled. The simulation was found to be very thorough, and it covers various general safety aspects. Theory and lab quiz questions are presented as the user proceeds, keeping one engaged and testing knowledge. Students can immediately determine whether they understand the work. The software is enjoyable to use, interesting, and interactive, which encourages students to engage with it actively. The flexibility of the simulation is impressive, and a student can make mistakes and even cause accidents, rather than being confined to a set of forced actions which many other simulations offer. This is extremely important for a student's learning. They should be free to explore the consequences of their actions and improve their competence to the point where they make safe decisions without being heavily guided. Such a procedure can help foster complex problem-solving and analytical skills, which are relevant in the 4IR.

Labster is geared towards university students, offering an intellectually challenging and stimulating environment, engaging students in lab work and contributing to creative thinking and innovation (possible link to 4IR skills). This platform also offers benefits for HEIs using Learning Management Systems (LMS). Labster can integrate with LMSs, facilitating its incorporation into a module. Labster currently operates on computers, although they are exploring the use of tablets and smartphones. Once developed, students at HEIs in South Africa who sometimes only have smartphones available can actively participate in this lab.

PraxiLabs is another program that mimics a physical lab and offers simulations for Biology, Chemistry and Physics. The simulation itself is quite thorough but does not offer the opportunity to learn from mistakes, as only the actions aligning with exact experimental steps are permitted. These labs can be run on various devices, but they are less user-friendly than *Labster*.

Other virtual lab offerings include those of the *Royal Society of Chemistry*, *hhmi BioInteractive* and *LabXchange*. For the Royal Society of Chemistry, only two labs were available on titrations and aspirin synthesis (Royal Society of Chemistry, 2021). Although limited in number, the labs have thorough procedures, are engaging and easy to use. A benefit of this software is that it forces the user to consider economic, environmental and safety factors. Thus, not only is the user required to relate the experiments to real-life situations but also to consider environmental factors, which is increasingly relevant in the 4IR. *hhmi BioInteractive* is a website offering activities and videos that focus on biology (hhmi

BioInteractive, n.d.). The immunology lab was sampled and proved to be very user-friendly, with clear instructions, theory and explanations provided as the user progressed through the lab. The steps were also very thorough with the necessary repeats of tests and safety practices. *LabXchange* provides its content as well as displaying content from various other sources and programs. The content types are extensive, with various other offerings besides simulations, covering Physics, Chemistry, Biological Sciences, Economics, and Science and Society (The President and Fellows of Harvard College, 2021). This profile also offers the opportunity to establish skills in relevant 4IR domains, for example, by focusing on the interface of Science and Society. The gel electrophoresis simulation was sampled and found to be very extensive and easy to operate, mimicking a physical lab well.

Next, the focus is on remote labs. *LabsLand* responds in real-time to user instructions, whilst their ultra-concurrent labs are real labs that have been recorded previously and display the appropriate results based on what the user selects. The categories offered are Biology, Chemistry, Electronics, Physics, Robotics and Technology. The titration lab was sampled, and a video explaining the lab was provided beforehand. An advantage here is that real equipment is shown, which can assist students in correctly identifying things in a physical setting. However, interactions are more limited than in the previous programs mentioned. These labs are accessible via all devices.

A slightly different type of virtual lab involves *Virtual Reality* (VR) or *Augmented Reality (*AR), a fully simulated environment presented as if it were real. A user may interact within, or virtual elements are juxtaposed over the physical world, respectively. Recent advancements in VR and AR allow students to experience physical sensations of touch through handheld devices, which simulate touching and holding objects. An offering in this category is *VRLab Academy*. Both desktop and VR versions of VRLab Academy's labs are available. Broad topics include Optics and Waves, Mechanics, Popular Science, Chemistry and Biology (VRLab Academy, 2021). Over 100 experiments are available, with more being added monthly; additionally, VRLab can create specific experiments for institutions. This allows for a more personalized experience and can ensure that the specific needs of students at an HEI are met. LMSs can also be linked to the lab software. A disadvantage, however, compared to the alternative labs presented above, is that computers with specific requirements are needed, along with VR headsets, the costs of which may be prohibitive in the South African HEI context.

4.3 SWOT Analysis of Online Labs

In a SWOT analysis, we summarize *S*trengths, *W*eaknesses, *O*pportunities, and *T*hreats offered by online labs, which were evaluated with a specific focus on the South African context. One of the major *strengths* of online labs is their time availability which benefits students because they are not bound to opening hours and time slots available in physical labs. With a virtual lab, access may be available any day of the week and at any hour since no physical equipment, set-up or monitoring is required. Remote

labs may still have limited hours and days, but flexibility is still offered to students compared to physical labs. This allows students to choose a time slot that suits them and perhaps work with their natural biorhythms or work around other obligations. Another strength is geographical availability. These labs can be completed in a student's own home, work, or any location provided they have internet access. It should be noted that certain labs may also be downloaded, which would then not require constant internet access to use.

Remote labs help prepare students for remote work. The ability to work remotely is a valuable skill for the working world as it is becoming a more popular form of working with many companies using it. Using both virtual and remote labs can also improve students' IT and computer skills (Mackay and Fisher, 2014). Such skills are very important in a 4IR-transformed world and an asset to students and future employers alike.

One of the main *weaknesses* of online labs is that students could suffer academically. They have to rely on their self-discipline and time management much more when partaking in online labs. There may be no set timetable and no lecturer monitoring students. Instead, each student is responsible for completing the labs allocated to them within a given timeframe, which can be challenging for students who need more structure. However, since a future 4IR-transformed workforce needs to be more flexible and adaptive, such skills can be trained through this option – provided scaffolding is offered to develop students as self-regulated learners. Online labs do not foster a student's necessary sensory lab skills and techniques due to interaction via a screen. However, as VR and AR technologies are refined and advanced, such labs will increasingly benefit the training of techniques and physical lab skills through virtual means, overcoming this weakness. Many virtual and remote labs do not allow students to make mistakes, which impacts their learning (Mackay and Fisher, 2014). Thus, troubleshooting and problem-solving skills may remain underdeveloped. The virtual and remote environments can also make teamwork difficult (as not all software support this). Students can find it difficult to communicate, work together and solve conflict when they are unable to read body language and see each other's facial expressions.

Another threat is presented in the lack of adoption of new pedagogies fostering 4IR relevant aptitudes, and educators must be institutionally empowered to do: Conventionally, physical labs are rather restrictive in that they instruct to replicate data, minimise experimental errors, and reproduce methods, leaving little room for creativity, originality, initiative and innovation.

A clear *opportunity* is presented to HEIs utilizing online labs, in that these may serve to attract new types of students, increasing both, revenue and diversity of their student body. This may lead to the development of new programmes and degrees. Students who find it difficult to study (care-takers, full time employed, students with disabilities, pregnant students) could be able to complete STEM degrees,

positively affecting student throughput and increasing the body of the workforce in scarce skill areas. Overall, online platforms allow for an expansion of what is possible in physical labs. Experiments deemed too dangerous, too expensive or difficult to visualise (e.g. microscopic processes and observations) may be completed in virtual and remote settings. Such opportunities can extend skills, as students can engage with more complex matter and understand theoretical concepts better than in conventional settings.

Another opportunity of online labs lies in the fact that crises do not affect laboratory operability: Protests, strikes and extreme weather conditions, which are adversely affecting the academic calendar of some HEIs, would not prevent students to partake in the labs.

A significant *threat* is that many students, educators, and accreditation boards are resistant to making the change to virtual and remote labs. Many view these as not being able to teach students the same skills as physical labs. Mackay and Fisher (2014) specifically mention that numerous institutions do currently not accept courses containing virtual labs.

5 CONCLUSIONS

In conclusion, a major transformation of STEM curricula must take place when moving towards the 4IR. Both developed and developing countries are preparing for this. However, the analysis of the literature has shown that the engagement with the topic predominantly stems from developed countries, which drive the debate on the 4IR. It is clear that the country-specific context, in particular that of developing countries, needs to be taken into account, both in terms of technologies and pedagogies used.

In order to keep up with technological and educational developments in the transformation to the 4IR, graduates at HEIs in South Africa need to be supported in developing relevant skills. A specific focus must be on engineering and other STEM subject students, due to their relevance for the various producing industries in the future. While some initiatives already exist, more innovation in offering 4IR transformed curricula to engineering students is needed. One avenue for HEIs to develop relevant skills of future engineers is through online experimentation.

Different platforms offering virtual, remote and virtual reality labs exist, and this field is still expanding and changing. They offer major strengths such as allowing for flexibility to experiment or work remotely, making them independent of travel or other constraints at South African HEIs. They provide opportunities for HEIs to increase revenues, and target additional student groups by offering an adaptive environment. This could contribute to equity in education and an increase of the much needed highly skilled STEM workforce. However, students must be supported to succeed in self-regulated learning (scaffolding). Threats lie in the accreditation of programs featuring online labs. HEIs need to embrace novel technologies to advance in the 4IR and provide education that is relevant in a changing

world. The question arises whether the skills trained in physical labs are actually those that engineering graduates of HEIs require in the future, and which will become obsolete? It is evident that keeping up with the developments of the 4IR requires a step change in mind-set of educators and students alike, and an adaption to new pedagogies and ways of learning.

ACKNOWLEDGEMENTS

The authors would like to thank the JW Nelson foundation for funding of the project. This work is based on research supported in part by the National Research Foundation of South Africa (grant number: 115465). We are indebted to Profs. Bright, Tapamo and Lokhat (School of Engineering) for institutional support.

REFERENCES

Bringing Life to our Engineering Curricula (2021). Retrieved August 2021, from https://iecurricula.co.za

Gleason, N. W. (2018). *Higher Education in the Era of the Fourth Industrial Revolution.* Palgrave Macmillan.

Gray, A. (2016). *The 10 skills you need to thrive in the Fourth Industrial Revolution*. Retrieved May 3, 2021, from https://www.weforum.org/agenda/2016/01/the-10-skills-you-need-to-thrive-in-the-fourth-industrial-revolution/

Hancock, T. (2019). *Industry 4.0 advancing in local sugar milling*. Retrieved August 20, 2021, from https://www.engineeringnews.co.za/article/industry-40-advancing-in-local-sugar-milling-2019-12-06

hhmi BioInteractive (n.d.). *Classroom Resources*. Retrieved April 30, 2021, from https://www.biointeractive.org

LabsLand (2021). *Pricing*. Retrieved April 14, 2021, from https://labsland.com/en/pricing

Labster (2021). *Pricing*. Retrieved April 7, 2021, from https://www.labster.com/pricing/

Mackay, S. and Fisher, D. (2014). *Practical Online Learning and Laboratories, for Engineering, Science and Technology.* West Perth: IDC Technologies Pty Ltd.

Praxilabs (2019). *Pricing*. Retrieved April 12, 2021, from https://praxilabs.com/en/pricing

Royal Society of Chemistry (2021). *Screen experiments*. Retrieved April 16, 2021, from https://virtual.edu.rsc.org/

Schwab, K. (2016). *The Fourth Industrial Revolution: what it means, how to respond*. Retrieved March 8, 2021, from https://www.weforum.org/agenda/2016/01/the-fourth-industrial-revolution-what-it-means-and-how-to-respond/

Steipe, L. (1978) *Micro-electronics today – 3rd of 4th industrial revolution*, Nachrichtentechnische Zeitschrift, 31,11, 767-768.

The President and Fellows of Harvard College (2021). Retrieved April 29, 2021, from

https://www.labxchange.org/library

The Second Machine Age. (2021). *About 2MA*. Retrieved August 20, 2021, from The Second Machine Age: http://secondmachineage.com/about-2ma/

University of Johannesburg (2021). *UJ 4IR Courses*. Retrieved July 28, 2021, from https://universityofjohannesburg.us/4ir/uj-4ir-courses/

VRLab Academy (2021). Retrieved July 8, 2021, from https://www.vrlabacademy.com/

Wessels, L. (2020). How South African universities can contribute to preparing the future workforce for the fourth Industrial Revolution. *Thesis (MPhil),* Stellenbosch University.

Optimum flowsheet synthesis for the integrated gasification combined cycle using mathematical modelling

J. Bonsu and T. Majozi*

NRF/DST Chair in Sustainable Process Engineering, School of Chemical and Metallurgical Engineering University of the Witwatersrand, Johannesburg, South Africa

*Corresponding author: Thokozani.Majozi@wits.ac.za

ABSTRACT

This study proposes a novel approach for the synthesis of an optimal flowsheet for the Integrated Gasification Combined Cycle (IGCC). The approach entails developing a superstructure that provides options for the optimal gasifier design, and the degree of integration between the air separation unit and gas turbine. The mathematical model based on the superstructure is used in the synthesis of an IGCC plant while exploring three scenarios. Scenario 1 is the simulation of a standard IGCC plant. Scenario 2 is the synthesis and design of an optimal gasifier with a background IGCC process. The decision variables in scenario 2 were the gasifier volume, reactor configuration, steam to coal ratio, and the oxygen to coal ratio. The third scenario is the determination of the optimal flowsheet path for the IGCC process. In addition to the decision variables in scenario 2, scenario 3 also determined the optimal integration between the air separation unit and the gas turbine. The objective function for the example is the maximization of the thermal efficiency of the plant. The results show that improvement of 6.79% and 10.96% in the objective function relative to scenario 1 is achieved for scenario 2 and scenario 3 respectively.

Keywords: IGCC, optimization, flowsheet synthesis

1 INTRODUCTION

Access to modern energy has a close relationship with human development due to its effect on national productivities, quality healthcare, quality education, production of safe drinking water, agriculture, and modern communication services (Gaye, 2008). Electricity is the most useful form of energy in the modern world. Thus, the efficient conversion of primary energy sources to electricity is critical for human civilization (Majoumerd et al., 2012). Coal is one of the most widely used fossil fuel for electricity generation. It is used to generate approximately 40% of the world's electricity (IEA, 2019). However, the environmental impact of coal combustion for electrical power generation is significant. The combustion process produces a range of pollutants such as nitrous oxides, Sulphur oxides, fly ash, and heavy metals. In addition to the pollutants above, coal combustion is also a significant contributor to climate change. Hence, there is a need for research into cleaner and more efficient ways of generating electricity from coal. The Integrated Gasification Combined Cycle (IGCC) plant is an alternative way of generating electricity from coal. The technology combines two

technologies, viz. gasification and the combined cycle. IGCC power plants have several advantages over conventional coal-fired power plants. The major advantages of the IGCC over competing technologies include higher thermal efficiency, low pollutant emission, less water consumption, and less solid-waste generation (Ratafia-Brown, 2002). The IGCC technology is still undergoing full commercialization, and a further improvement of its efficiency will expedite the commercialization process. The IGCC process comprises two main parts namely the gas-side and steam-side subsystems. The gas-side of the IGCC plays a significant role in the efficiency of the process. This is because the gas turbine generates 60% of the gross power produced, while the air separation unit is the highest consumer of power in the IGCC plant. The gasifier is also responsible for the generation of the fuel-gas, which is the main source of energy for the combined cycle. Hence, optimizing the gas side of the IGCC will have a significant impact on the efficiency of the entire plant. A common approach in optimizing the gas-side of the IGCC is the feeding of part of the nitrogen product from the air separation unit (ASU) to the gas turbine, and the extraction of air from the gas turbine into the ASU. Several studies have explored the interconnectivity between these units using sensitivity analysis (Frey and Zhu, 2006; Lee et al., 2007) and nonlinear programming (Wang et al., 2016). What these studies have excluded is the effect of gasifier optimization on the flowsheet of the gas-side of the IGCC. Hence, this study focuses on exploring the effect of optimizing the gasifier on the flowsheet of the gas side of the IGCC plant and its impact on the overall efficiency of the plant.

Although there are different gasification technologies, the entrained flow gasifier (EFG) has several advantages over other gasifiers. Approximately 75% of existing and planned IGCC plants worldwide use EFG technology (Minchener, 2005). Consequently, this study focuses on the synthesis and design of an EFG with a background IGCC process. The decision variables of interest in this study include the feed conditions of the gasifier, the configuration of the gasifier, and the degree of integration between the gas turbine and the ASU. This leads to the synthesis of the optimal flowsheet for the gas side of the IGCC process.

The problem statement for the synthesis of an optimal IGCC flowsheet is as follows.

Given coal of known composition and flowrate, a set of reactions occurring in a gasifier and their kinetic data, the enthalpy and density of reacting species, different process units and their interconnections in the IGCC process, the operating temperature and pressure for the different process units, the efficiency of the compressors and turbines and the source and target temperatures for various process streams, we are to determine the optimal reactor network, the volume of reactor units, the optimal steam to coal ratio, the optimal coal to oxygen ratio, the feeding strategy, optimal nitrogen flowrate into the gas turbine and the optimal air extraction from the gas turbine.

2 MODEL DEVELOPMENT AND OPTIMIZATION

The stages in the model development include developing a superstructure, formulating mathematical equations from the described superstructure, and the choice of the objective function for the optimization problem.

2.1 Superstructure development

Figure 1 shows the superstructure representation on which the proposed model is developed.

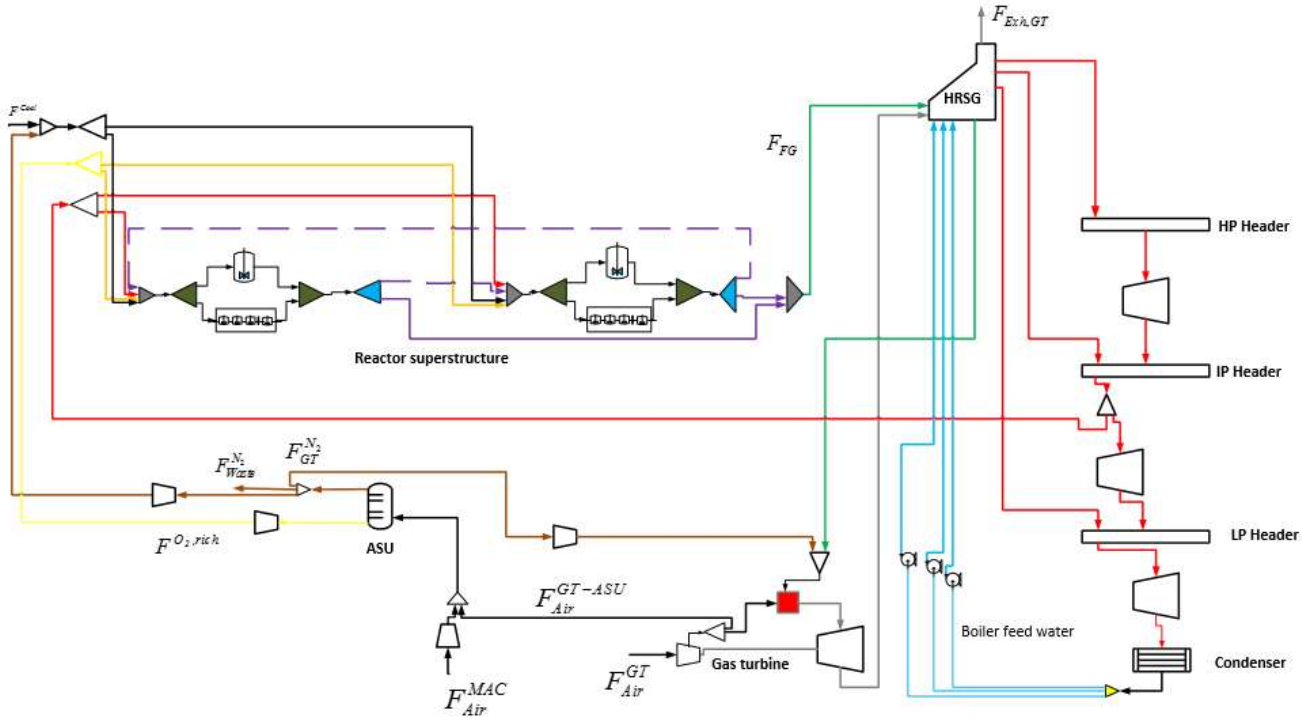

Figure 1: A superstructure for the optimal synthesis of an optimal IGCC plant

The superstructure was developed via the introduction of design options into a baseline IGCC plant. The main difference between the superstructure and the baseline IGCC plant includes replacing the gasifier in the plant with a reactor superstructure. Another modification includes the introduction of integration options between the ASU and the gas turbine. The decision variables in the reactor superstructure include the type and volume of the reactors, the amount of oxygen and steam fed to the gasifier, and the feed points into the reactor. These determine the composition, flowrate, and temperature of the fuel-gas product. These outputs determine the power generated in the combined cycle.

Other optimization options provided by the superstructure include the amount of nitrogen injected into the gas turbine as part of its feed. This has the potential of increasing the power output of the gas turbine. Another decision variable in the superstructure is the degree of air extraction from the gas turbine to the ASU. The main air compressor (MAC) of the ASU has a lower efficiency than the

compressor of the gas turbine. Hence, the extraction of air from the compressor of the gas turbine to the ASU reduces the net power consumption but can also lead to a decrease in the gas turbine power output (Frey and Zhu, 2006). Hence, there is the need to find the optimal extraction of air from the gas turbine into the ASU. The approach is taken in this work, therefore, contributes to the field by determining the optimal flowsheet for the gas-side of the IGCC process.

2.2 Mathematical formulation

This section explains the mathematical equations, describing the superstructure. The units include a reactor superstructure, an ASU, the gas turbine, and the heat recovery steam generator (HRSG).

2.2.1 Reactor superstructure

The reactor superstructure consists of repeated units of reactor compartments connected with a comprehensive feed distribution and product withdrawal network (Figure 1). From Figure 2, it is observed that a reactor compartments consist of a Continuous Stirred Tank Reactor (CSTR) and a Plug Flow Reactor (PFR). The equations used in describing the superstructure include reactor design equations, equations for mixers and splitters.

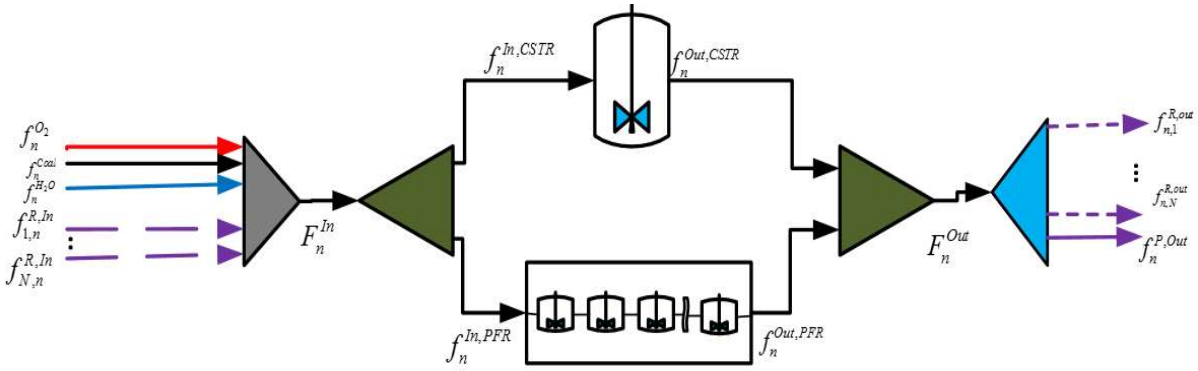

Figure 211: A reactor compartment

Equations (1) and (2) are design equations for the CSTR. Equation (1) states that the mass flowrate of a component out of a CSTR, $f_{i,CSTR}^{Out}$, equals the algebraic sum of the mass flowrate into the CSTR, $f_{i,CSTR}^{In}$, and the net consumption or generation rate of the component. Equation (2) states that the net enthalpy change across the CSTR equals the net heat generated by the reactions when corrected for heat losses. Equations (3) and (4) are the mass and energy balance of the PFR, which is the differential form of Equations (1) and (2) due to dependence the mass flow, $f_{i,PFR}$, enthalpy, H, and the reaction rate, r_j , on the normalized volume, ξ. The reactions in the reactors include pyrolysis and other chemical reactions. The pyrolysis of coal is assumed to be an instantaneous process. This study uses a

modified Merrick model to estimate the products of the pyrolysis process using the proximate and ultimate data of coal (Merrick, 1983). The reactions used in the model were taken from literature (Jones and Lindstedt, 1988; Westbrook and Dryer, 1981; Lee et al., 2014)

$$f_{i,CSTR}^{Out} = f_{i,CSTR}^{In} + Mw_i \times V_{CSTR} \sum_{j=1}^{|J|} \left(v_{ij} \times r_j\right), \forall i \in I. j \in J \tag{1}$$

$$H^{Out} - H^{In} + Q_{Loss} = V_{CSTR} \sum_{j=1}^{|J|} \left(-\Delta h^{rxn} \times r_j\right), \forall j \in J \tag{2}$$

$$\frac{df_{i,PFR}}{d\xi} = Mw_i \times V_{CSTR} \sum_{j=1}^{|J|} \left(v_{ij} \times r_j\right), \forall i \in I. j \in J \tag{3}$$

$$\frac{dH}{d\xi} + Q_{Loss} = V_{CSTR} \sum_{j=1}^{|J|} \left(-\Delta h^{rxn} \times r_j(\xi)\right), j \in J \tag{4}$$

Equation (5) states that the mass flowrate of the feed into a reactor compartment, F_n^{In}, is the sum of the mass flowrates of the fresh feed, i.e. f_n^{Coal}, $f_n^{O_2}$ and $f_n^{H_2O}$, and the reuse streams, $f_{n',n}^{R,in}$, from the other reactor compartments. Equation (6) states that the mass flowrate out of a reactor compartment, F_n^{out}, equals the sum of the mass flow of the fuel-gas product, $f_n^{P,out}$, and the mass flowrate to the other reactor compartments, $f_{n,n'}^{R,out}$.

$$F_n^{in} = f_n^{Coal} + f_n^{O_2} + f_n^{H_2O} + \sum_{n'=1}^{|N|} f_{n',n}^{R,in}, \forall n' \in N, n \in N, n' \neq n \tag{5}$$

$$F_n^{out} = f_n^{P,out} + \sum_{n'=1}^{|N|} fn_{n,n'}^{R,out}, \forall n' \in N, n \in N, n' \neq n \tag{6}$$

Equation (7) states that the mass flowrate of the product fuel-gas, F^P, equals the sum of the mass flowrate from the reactor compartments that contributed to the formation of the fuel-gas, $f_n^{P,out}$.

$$F^{\mathrm{P}} = \sum_{n=1}^{|N|} f_n^{P,out}, \forall n \in N \tag{7}$$

Other equations describing the reactor superstructure includes logical equations that ensure that a reactor only receives feed when it exists, distribution equations for the CSTR and PFR a reactor compartment.

2.2.2 Air Separation Unit

This study employs a lumped model in the modelling of the ASU unit. This model was used in the study of Jillson et al. (2009). The ASU model assumes a one-stage flash that produces an oxygen-rich stream and a nitrogen-rich stream. The air entering the ASU unit is assumed to contain only nitrogen and oxygen. Based on the composition of the oxygen-rich stream ($Y_{N_2}^{O_2 rich}$), equation (8) is used to predict the composition of the nitrogen-rich stream ($Y_{N_2}^{N_2 rich}$). Equation (9) states that the total airflow into the ASU, F_{Air}^{ASU}, is equal to the sum of the air from the MAC, F_{Air}^{MAC} and the air from the gas turbine, F_{Air}^{GT-ASU}.

$$Y_{N_2}^{N_2,rich} = \frac{\alpha Y_{N_2}^{O_2,rich}}{\alpha Y_{N_2}^{O_2,rich} + Y_{N_2}^{O_2,rich}} \tag{8}$$

$$F_{Air}^{ASU} = F_{Air}^{MAC} + F_{Air}^{GT-ASU} \tag{9}$$

Equation (10) states that the flowrate of the nitrogen-rich stream, $F^{N_2 rich}$, equals the nitrogen used to transport coal into the gasifier, $F_{Gasifier}^{N_2}$, injected into the gas turbine, $F_{GT}^{N_2}$, and/or disposed of as waste, $F_{Waste}^{N_2}$. For slurry-fed gasifiers, $F_{Gasifier}^{N_2}$, is set to zero.

$$F^{N_2 rich} = F_{Gasifier}^{N_2} + F_{GT}^{N_2} + F_{Waste}^{N_2} \tag{10}$$

2.2.3 Compressors and turbines

The power produced or consumed by all turbines and compressors is calculated based on isentropic expansion or compression. Using the isentropic efficiencies, actual powers are calculated.

2.2.4 Gas turbine

Equation (11) states that the total airflow into the compressor of the gas turbine, F_{Air}^{GT}, equals the sum of the flowrate of the air into the combustion chamber, F_{Air}^{CC}, and the flow of the air extracted, F_{Air}^{GT-ASU}. Equation (12) computes the temperature of the combustion chamber. Each of the reactions occurring in the combustion chamber has an extent of reaction, $\in_m$, and a heat of reaction, $\Delta h_{Comb,m}$.

$$F_{Air}^{GT} = F_{Air}^{CC} + F_{Air}^{GT-ASU} \tag{11}$$

$$F_{Air}^{CC} h_{air} + F_{FG} h_{FG} + F_{GT}^{N_2} h_{N_2} = \sum_{m=1}^{M} \in_m \left(-\Delta h_{Comb,m}\right) = F_{CE} Cp_{CE} \left(T_{Comb} - T_{\mathrm{Re}f}\right) \tag{12}$$

2.2.5 Heat recovery steam generator (HRSG)

The configuration of the HRSG is taken from the work of Majoumerd et al. (2012). The HRSG is the heat exchanger network (HEN) used to recover heat in the steam side flowsheet. The HRSG has two heat sources namely, the raw fuel-gas and the gas turbine exhaust stream with flowrates and operates at a minimum temperature of 10 Kelvin.

2.3 Objective function

The optimization problem presented in this study is focused on maximising the overall efficiency of the IGCC process.

$$MaxZ = \frac{\dot{W}_{GT} + \sum_{j=1}^{|J|} \dot{W}_{Actual,ST,j} - \sum_{n=1}^{|N|} \dot{W}_{Comp,n} - \sum_{p=1}^{|P|} \dot{W}_{P}^{Pump}}{F^{Coal} HHV^{Coal}} \quad (13)$$

2.3 Optimization

This section describes the use of the developed model in the synthesis of an optimal IGCC power plant with a dry-fed gasifier. Three scenarios were explored. The base case or scenario 1 is the simulation of a standard IGCC plant. The second scenario is the synthesis and design of an optimal gasifier with a background IGCC process. The decision variables in scenario 2 were the gasifier volume, reactor configuration, steam to coal ratio, and the oxygen to coal ratio. The third scenario is the determination of the optimal flowsheet path for the IGCC process. In addition to the decision variables in scenario 2, scenario 3 also determined the optimal integration between the air separation unit and the gas turbine. In each of these examples, scenarios 2 and 3 were compared to the base case. The objective function of both examples was the thermal efficiency of the IGCC plant. Table 1 shows the optimization parameters considered. These include the flow interval of the steam and oxygen.

Table 1 also shows the optimization parameters for the gasifier and ASU-gas turbine. The maximum air extraction ratio is limited to 0.5. The percentage of ASU feed extracted from the compressor of the gas turbine is limited to 50% because a 100% supply of ASU air from the gas turbine will lead to start-up and operability issues. Table 1 also contains data on the HRSG. The data includes the pressure levels of the HRSG, the superheated temperatures, and the source and target temperatures of the heat sources. The properties of the coal were taken from literature (Campbell et al., 2000; Ju and Lee, 2017).

Table 1: Optimization parameters for the synthesis of an IGCC plant with a dry-fed gasifier

Gasifier parameters				**HRSG HEN data**		
$F_{Max}^{H_2O}$ (kg/s)	5.0	$F_{Min}^{H_2O}$ (kg/s)	0	Stream	T_S (°C)	T_T (°C)
$F_{Max}^{O_2}$ (kg/s)	30	$F_{Min}^{O_2}$ (kg/s)	15	Fuel-gas	900	35
T_{Max} (K)	2400	T_{Min} (K)	1511	GT exhaust	577	100
V_{Max} (m^3)	50	Pr (bar)	45	$P_{HP}/P_{IP}/P_{LP}$ (bar)	140/45/4	
ASU-gas turbine parameters				$T_{SH,HP}, T_{RH,1P}$ (°C)	500	
$\alpha_{N_2}^{Min}$	0	$\alpha_{N_2}^{Max}$	1			
$\alpha_{Air,ASU}^{Min}$	0	$\alpha_{Air,ASU}^{Max}$	0.5			

3 RESULTS AND DISCUSSION

Table 2 summarizes the result of the optimization processes. From Table 2, it is observed that both Scenarios 2 and 3 lead to an improvement of the IGCC performance.

Table 2: Summary of the optimization results for the synthesis of an optimal IGCC plant

	Base case	**Scenario 2**	**Scenario 3**
Net IGCC efficiency (% LHV)	45.6	48.7	50.6
% increase	-	6.79	10.96
Net power output (MW)	406.6	434.5	451.3
Gas turbine power (MW)	277	291.9	291.4
Steam turbine power (MW)	164.6	179.5	185
Gross power generated (MW)	441.6	471.4	476.3
ASU compression power demand (MW)	30.7	32.3	19.5
Gasification power demand (MW)	2.9	3	3
HRSG pumping power (MW)	1.4	1.6	1.6
Total auxiliary power demand	35	37	25

The main reason for the improvements observed is the properties of the fuel-gas produced. The fuel-gas properties directly affect the amount of gas turbine power output and indirectly affect the steam

turbines' power output. The increase in the heating value and flowrate of the fuel-gas leads to an increase in the gross power generated. Comparing Scenarios 2 and 3, it is observed that the integration of the ASU and gas turbine leads to a further improvement in the efficiency of the IGCC plant. The effect of ASU-gas turbine integration on the efficiency of the IGCC has been well documented in literature (Frey and Zhu, 2006; Maustard, 2005). However, in this study, it has been performed simultaneously with the optimization of the gasifier variables. From Table 2, it is observed that Scenarios 2 and 3 have similar gross power outputs but a higher variation in their net power outputs. This is due to the lower ASU compression power. From Table 3, it is observed that Scenarios 2 and 3 have similar oxygen flowrates. Hence, the reduced ASU compression power is due to 40% of the ASU air supply is taken from the compressor of the gas turbine. The extraction of air from the compressor leads to a marginal decrease in the gas turbine power generated; however, this is not observed in Scenario 3. This is because the nitrogen injected into the gas turbine replaces the loss in mass due to air extraction. From Table 3, it is observed that the oxygen to coal ratio for Scenarios 2 and 3 are higher than that of the base case. The high oxygen rate keeps the high temperature of the fuel-gas. From Table 3, it is observed that both Scenario 2 and 3 consume a higher amount of steam compared to the base case. The increase in oxygen and steam flowrates leads to an increase in the fuel-gas flowrate. Scenarios 2 and 3 have the same optimal gasifier design which is a CSTR followed by a PFR. However, they do have different volumes.

Table 3: Optimal gasifier and ASU-gas turbine parameters for an IGCC plant

	Base case	**Scenario 2**	**Scenario 3**
(a) Gasifier properties			
Oxygen: Coal ratio	0.80	0.84	0.85
Steam: Coal ratio	0.04	0.12	0.14
$V_{Gasifier}$ (m^3)	8.00	9.15	6.03
(b) ASU-gas turbine			
α_{N_2}	0	0	0.64
$\alpha_{Air,ASU}$	0	0	0.40

4 CONCLUSIONS

In conclusion, a novel optimization approach that leads to the synthesis of an optimal flowsheet of the IGCC process has been explored in this study. The approach entails examining the effect of the

gasifier design and the gas turbine-ASU integration on the efficiency of the IGCC plant. To achieve this, mathematical equations were formulated based on a developed superstructure. The developed model has been applied to an illustrative example. The results show that an improvement of 10.96% in the objective function relative to the base case was achieved.

REFERENCES

Campbell, P.E., McMullan, J.T., Williams B.C., 2000. Concept for a competitive coal-fired integrated gasification combined cycle power plant. *Fuel*, 79. pp. 1031–1040

Gaye, A., 2008. Access to Energy and Human Development. Human Development Report Office Occasional Paper. Available online at http://hdr.undp.org/en/content/access-energy-and-human-development [Accessed 20th May 2020]

Frey, H. C., Zhu, Y., 2006. Improved System Integration for Integrated Gasification Combined Cycle (IGCC) Systems. *Environmental Science and Technology*, February, 40(5), p. 1693–1699.

IEA. Electricity Information 2019. Available online at https://www.iea.org/subscribe-to-data-services/electricity-statistics [Accessed 3rd March 2020]

Jillson K.R., Chapalamadugu V, Ydstie B.E., 2009. Inventory and flow control of the IGCC process with CO2 recycles. *J. Proc. Cont.* 19(9):1470–1485.

Jones, W. P., Lindstedt, R. P., 1988. Global Reaction schemes for Hydrocarbon Combustion. Combustion and Flame, Volume 73, pp. 233-249

Ju, Y., Lee, C.H., 2017. Evaluation of the energy efficiency of the shell coal gasification process. Energy Conversion and Management, Volume 143, pp. 123–136.

Lee, C., Lee, S. J. and Yun, Y., 2007. Effect of air separation unit integration on integrated gasification combined cycle performance and NOx emission characteristics. *Korean Journal of Chemical Engineering,* March, 24(2), pp. 368-373.

Majoumerd, M.M., De S., Assadi M., Breuhaus P., 2012. An EU Initiative for Future Generation of IGCC Power Plants using Hydrogen-rich Syngas: Simulation Results for the Baseline Configuration. *Applied Energy*, Volume 99, pp. 280-290.

Maurstad, O. 2005. An Overview of Coal based Integrated Gasification Combined Cycle (IGCC) Technology; MIT LFEE 2005-002 WP; Massachusetts Institute of Technology: Cambridge, MA

Merrick, D., 1983. Mathematical models of the thermal decomposition of coal. *Fuel,* Volume 62, pp. 534-539.

Minchener, J., 2005. Coal gasification for advanced power generation. *Fuel*, *84*, pp. 2222–2235.

Lee, H.H., Lee, J.C., Joo, Y.J., Oh M., Lee C.H., 2014. Dynamic modeling of Shell entrained flow gasifier in an integrated gasification combined cycle process. Applied Energy 131. pp. 425–440

Ratafia-Brown, J.A., Manfredo, L.M., Hoffmann, J.W., Ramezan, M., Stiegel G.J., 2002. An

Environmental Assessment of IGCC Power Systems. Nineteenth Annual Pittsburgh Coal Conference, September 23 – 27, 2002

Wang, M., Liu, G., Hui, C. W., 2016. Simultaneous optimization and integration of gas turbine and air. *Energy,* Volume xxx, pp. 1-8.

Reaction Kinetics for the Production of Xylitol from Xylose Laden Waste Stream

V. Revelas[1], T. Majozi[1*] and B. Sithole[2]

[1] School of Chemical and Metallurgical Engineering, University of the Witwatersrand, 1 Jan Smuts Avenue, Braamfontein, Johannesburg, 2000, South Africa

[2] Biorefinery Industry Development Facility, Council for Scientific and Industrial Research (CSIR), South Africa: University of KwaZulu-Natal, Durban 4125, South Africa

Corresponding author: thokozani.majozi@wits.ac.za; bsithole@csir.co.za

ABSTRACT

A statistically designed study was conducted to ascertain kinetics of conversion of xylose to xylitol using borohydrogentaion. Batch kinetic experiments were performed for the reaction of xylose and sodium borohydride in the presence of sodium hydroxide solution. Analysis of xylose concentration-time data showed that the reaction order kinetics with respect to xylose follows a first-order rate law. This finding supports the mechanistic theory that the first hydride transfer is the rate-determining step. The study shows rate constants to be 0.03437 1/s and 0.00976 1/s at 25 ºC and 60 ºC. Additionally, the activation energy and frequency factor were 31.74442 kJ/mol and 19146.72164, respectively. Furthermore, a two-level factorial design was utilised to determine the influence of initial xylose concentration and temperature at certain reaction times. The analysis of these reaction factors indicated that the most significant factor was temperature. Furthermore, interactions between time and concentration and the three-way interaction were significant.

Keywords: reduction; HPAEC-PAD; xylose; aldehyde; sodium borohydride; factorial design; kinetics

1 INTRODUCTION

Xylitol is a platform molecule industrially obtained by the catalytic hydrogenation of xylose, a major hemicellulose component in lignocellulosic biomass. Xylitol has gained significant importance in the food and pharmaceutical industries owing to its low caloric content and anticarcinogenic properties (Hyvönen et al., 1982). Furthermore, xylitol can be converted into polyethylene glycol and ethylene glycol, making it a substitute fossil-based raw material. However, commercial processes involve the hydrogenation of xylose using catalysts which have shown to be environmentally and economically taxing. These methods lead to steep prices, and with smaller market volumes thus, a small portion of the population has access to xylitol. Therefore, the study assesses alternative chemical methods that reduce xylose with sodium borohydride (Equation 1) to shift away from commercial processes.

$$NaBH_4 + 4C_5H_{10}O_5 \rightarrow 4C_5H_{12}O_5 + H_3BO_3 + NaOH \quad (4)$$

Sodium borohydride ($NaBH_4$) is a commonly used reductant for organic synthesis on the industrial scale due to its high chemical yields, practicality in handling, and relative safety (Periasamy and Kumar,

2000). Xylose is reduced in sodium borohydride in the presence of sodium hydroxide to produce xylitol, boric acid, and sodium borohydride. A further benefit of this reaction is the formation of boric acid, which can synthesise various products (Briggs, 2001). Therefore, the rapid and selective reductions of aldehydes generated by NaBH4 makes it suitable for synthesising xylitol. However, only two studies have looked at reducing xylose using sodium borohydride. An early paper by Abdek-Akher, Hamilton and Smith in 1951 provides evidence of its application with a reported reaction time of 5 min and an acetylated product yield of 80 %. A patent by Nygren *et al.* in 1997 established several methods for producing xylitol utilising sodium borohydride. However, these studies have not adequately established the reaction kinetics, and this study provides a basis to determine the feasibility of this reaction for industrial application.

2 MECHANISM

Sodium borohydride has complex structural characteristics in that it is a Lewis acid and electrophilic at the metal centre.

(5)

(solvent)

$NaBH_4$ reduction of aldehydes and ketones consists of two mechanistic steps. The first consists of a nucleophilic attack by BH_4^- on the carbonyl group. The solvent protonates the resulting alkoxide anion from the solvent to give the final alcohol product (Carey and Sundberg, 2007). However, it is speculated that the alkoxyborohydrides produced can act as reducing agents by successive hydride transfers shown below.

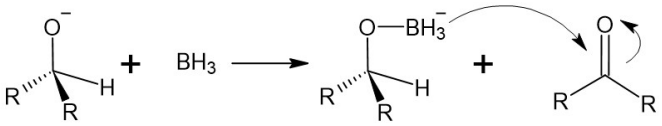

(6)

Thus, the analysis of rate data becomes complicated due to the different routes available. In any case, kinetic studies have all shown that the overall reaction rate is second-order, with the first hydride transfer being the rate-limiting step (Yamamoto, 2003).

Early studies by Brown, Mead and Subba Rao in 1955 investigated suitable solvents for sodium borohydride reductions. It was established that the reaction between aldehydes and ketones follow overall second-order kinetics. The mechanism was considered to proceed by a stepwise hydride ion transfer to the carbonyl carbon, which forms tetraalkoxyborate. This molecule contains the substrate, which is reduced, forming the alcohol product (Brown et al., 1955).

Consequently, they noticed the rate constant was altered in different solvents, demonstrating that solvents play a role in the reaction mechanism. These effects were later re-examined to understand the effects of solvents due to the discovery of iodometric determination of borohydrides (Brown and Ichikawa, 1961). Houk et al. devised a model in 1991 which utilised a transition state geometry model to describe the mechanism of sodium borohydride reductions. The study involved an investigation of cyclohexanones and the remote electrostatic effects. The results make a strong case that the preferential axial attack of hydride to cyclohexanone is caused by torsional strain in the transition state of equatorial attack, and electrostatic effects were also shown to play a role (Wu et al., 1991). Furthermore, a study investigated the concerted and stepwise pathways of the borohydride reduction of formaldehyde. However, these models do not account for solvent and counterion effects (Eisenstein et al., 1982).

Wigfield suggested an alternative model that considers the role of solvents, yet it does not establish the sodium ion (Na+) role. These studies assume the solvent alkoxy is contained in the alkoxyborate anion intermediate rather than the product (Wigfield, 1979). Furthermore, isotope studies refuted the initial concept that disproportionation of the intermediate reverts back into BH_4^- (Wigfield and Gowland, 1977). Several years later, Glass and coworkers demonstrated the critical role of Na^+ by an experimental study on the reduction of carboxylic acids in 2-propanol with $NaBH_4^-$ (Glass et al., 1980). The results showed that sodium ions are coordinated by oxygen atoms found in the alkoxy and carbonyl groups. However, reductions are still possible without Na^+ present. This notion was also substantiated by the work of Yadav, Jeyaraj and Balamurugan in 2000. The most recent study in 2018 was performed by Patel et al. The study established kinetic and mechanistic insights by detailed calculations of the electronic structure of the reduction of indophenol by sodium borohydride. Their work suggested that the reaction occurs in three steps. The first step involves a nucleophilic attack on the carbonyl group forming intermediates. This step is followed by intermediates undergoing proton abstraction assisted by the hydroxyl ion, and the molecule is protonated. Finally, the reduction process is completed by a hydrolysis reaction (Patel et al., 2018).

Despite the conflicting ideas on certain features of sodium borohydride reduction, all studies agree that the rate-limiting step is the initial hydride attack. This assumption is based on the fact that transfers of a hydride ion from relatively weak Lewis acids (alkoxyborines) must be easier than its transfer from stronger Lewis acid borine. This theory is also supported by the potential energy surface constructed by Patel et al., which describes the system's potential energy. The initial step of reduction is at the peak of (PES) diagram, thus indicating it is the rate-limiting step (Patel et al., 2018).

3 MATERIALS AND METHODOLOGY

A granular form of sodium borohydride (98%) obtained from Merck is used in all experiments. Xylose (≥ 99), sodium hydroxide (≥ 97) and hydrochloric acid (6N) were obtained from Sigma Aldrich. A

sodium borohydride stock solution was prepared by diluting sodium hydroxide pellets in distilled water until the solution reached a pH of 13. The solution must be alkaline to suppress the reaction between the solvent and sodium borohydride (Lo et al., 2007). Both solutions' volume was held constant at 10ml with initial concentrations of xylose and sodium borohydride were 0.4∓0.05 mol/L and 0.28∓ 0.03mol/L, respectively. The moles of sodium borohydride was measured to be roughly three times the amount of xylose to meet the assumption for the method of excess. The experimental set-up consisted of a 500 ml three-neck round bottom flask equipped with a reflux condenser, temperature probe and a 50 ml dropping funnel. The three-neck round bottom flask is placed within a glycerol bath to ensure even heating of the solution. Typical runs consisted of placing xylose solution into the flask and adding the alkaline solution of sodium borohydride through the dropping funnel. The entire set-up was placed on a hot plate combined with a magnetic stirrer providing heat and agitation to the reaction solution. After a certain period, the reaction solution was withdrawn at different times and placed in an ice bath while adding hydrochloric acid until the solution reached a pH of 2 to quench the reaction. The time required for quenching was 2.8±0.2 seconds, and the overall concentration of the solution was assumed to remain constant as a result of constant agitation. Analysis was conducted using High-Performance Anion-Exchange Chromatography with Pulsed Amperometric Detection (HPAEC-PAD) to determine the concentration of xylose and xylitol in the solution. This experiment was then repeated, and samples were withdrawn at different time intervals to improve the time resolution. The factorial design followed the same experimental procedure at different conditions. The independent variables selected were: initial xylose concentration, temperature, and reaction time. Table 1 below summarises the levels for each operating factor.

Table 5: The experimental ranges and levels of independent variables

Levels	[$C_5H_{10}O_5$] (mol/L)	T (ºC)	Time (s)
-1	0.4	25	50
+1	1	60	300
0	0.7	42.5	175

Time was selected as a factor in order to understand the optimal reaction time. The selected ranges are based on initial trials and work that similarly reduce xylose (Abdek-Akher et al., 1951)(Nygren et al., 1997). Both experiments were replicated three times to ensure accurate results were achieved.

4 RESULTS AND DISCUSSION

4.1 Kinetic Study

Measured concentrations as a function of time allow comparing their time dependence with the appropriate integrated rate laws. The isolation method is employed, which is a technique for simplifying the rate law to determine its dependence on a single reactant's concentration. The dependence of the reaction rate on the xylose concentration is isolated by having all other reactants present in excess so

that their concentration remains nearly constant throughout the reaction, as indicated in the following equation set. (Fogler, 2016)

The purpose of nonlinear regression is to seek values of a and k that minimise *S* according to the integral rate equation shown in equation 4. The sum of the squares of the deviations of the calculated xylose or xylose concentration values from the observed ones. Nonlinear regression is an iterative process; thus, suitable software such as Minitab® Statistical Software is used to conduct the regression analysis. The fitting method selected was the least-squares method. The initial values are selected for each parameter and then repeatedly changes those values to improve the 'goodness of fit'.

$$s^2 = \sum_{i=1}^{N} (t_{mi} - t_{ci})^2 = \sum_{i=1}^{N} \{t_{mi}{}^2 - ([C_{xyl_0}{}^{1-a} - C_{xyl}{}^{1-a}]/(1 - a)k'\}^2 \quad (7)$$

The parameter range is stipulated in table 2 and was selected as reaction order must range between 0-3. The reaction rate constant (k') value ranges between 0,0001 and 1 because a negative reaction rate would imply the reaction is reversed. Furthermore, rate data obtained from previous studies of aldehydes show the rate constant to lie within the range of 1.9×10^4 ($M^{-1}s^{-1}$) and 161×10^4 ($M^{-1}s^{-1}$) (Brown, et al., 1957) (Brown & Ichikawa, 1957). Regression terminates when varying parameter values results in negligible changes in the goodness of fit. If a solution provides convergence, it does not guarantee that the model fit is optimal or that the sum of squared errors (SSE) is minimised. Therefore, analysis of the residual plots is required to support the estimated result.

The experimental xylitol concentration data showed erratic behaviour and provided little information regarding the reaction kinetics. This behaviour can be attributed to the complexity of the mechanism outlined earlier. Therefore, the study focused on utilising the xylose concentration data shown below to determine the reaction kinetics.

Figure 1 shows a more gradual rate of xylose consumption in batch 1. Additionally, batch 2 reaches a conversion of 98.89% within 225 seconds, and the maximum conversion achieved in batch 1 is 81.47% in 223 seconds.

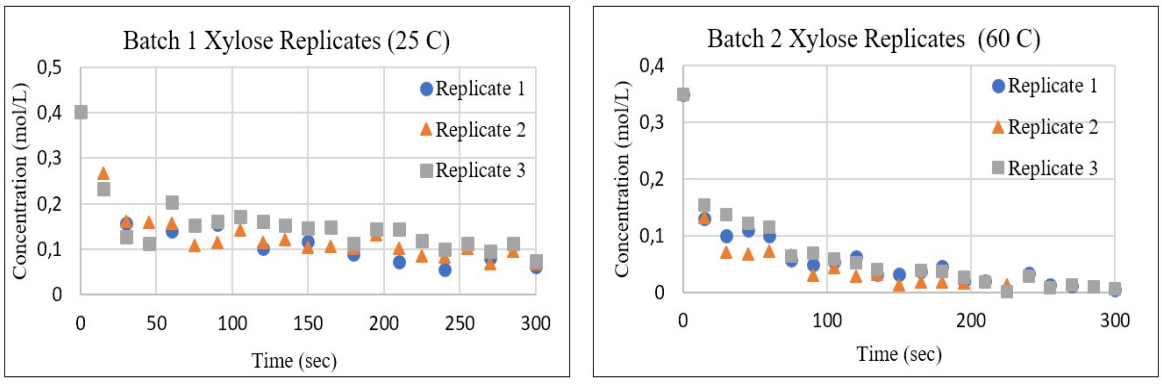

Figure 12: Replicate Xylose Concentration Data

Furthermore, the half-life is reached at 54 seconds at 25º C and 9 seconds at 60 ºC. These values are similar to previous studies that report a complete xylose conversion after 5 min (Abdek-Akher et al., 1951). In batch 1 the concentration of xylose varies slowly and becomes linear past 253 seconds; this is because the majority of xylose has reacted, and thus, the reaction rate has slowed significantly. Nonlinear regression techniques were used to solve for both the reaction order and rate constants. Minitab® Statistical Software was used to conduct the regression analysis. The fitted line plots (Figures 2) represent the replicate xylose concentrations at 15-second intervals. The regression line (bold red) follows the curvature in the points relatively closely. The points sufficiently cover the entire range of predictor values. The 95% confidence interval (CI) is stipulated in these tables, representing the likelihood (95% confidence) of the results lying within the interval. The CI can be seen graphically as the dotted green line in Figures 4-8 and 4-9. The prediction interval (PI) for the fit provides a range of probable values that will fall within the interval with 95% confidence indicated by the purple lines (Motulsky and Christopoulos, 2004).

Minitab's estimates show that the reaction order is 1.3702 and 1.251 for batch 1 and 2, respectively. The estimates for the reaction rate constants are 0.03437 1/s and 0.00976 1/s in batch 1 and 2, as shown in Table 2 below. Therefore, the following estimates for kinetic parameters are reasonable and indicate the rate law can be represented as follows:

$$dC_{xyl}/dt = -k'C_{xylose}^{\,1.3\pm 0.07} \quad k' \text{ (25 ºC)} = 0{,}03437 \text{ 1/s} \; ; \; k' \text{ (60 ºC)} = 0{,}00976 \text{ 1/s} \qquad (8)$$

The rate constants lie within the range of other aldehyde and ketone studied (Table 1). The rates measured are faster than ketones which supports the chemoselective nature of aldehydes relative to ketones.

Table 6: Summary of Key Results in NLR Analysis

Starting Values		Parameter Estimates		Summary	
Parameter	Values	Estimate	95% Cl	Iterations	S
Batch 1					
a	0-3	1.25198	(0.7401; 1.6843)	7	31.9947
k	0.0001-1	0.00976	(0.0040; 0.0217)		
Batch 2					
a	0-3	1.3702	(1.1888; 1.4196)	18	55.8971
k	0.0001-1	0.03437	(0.0247; 0.0481)		

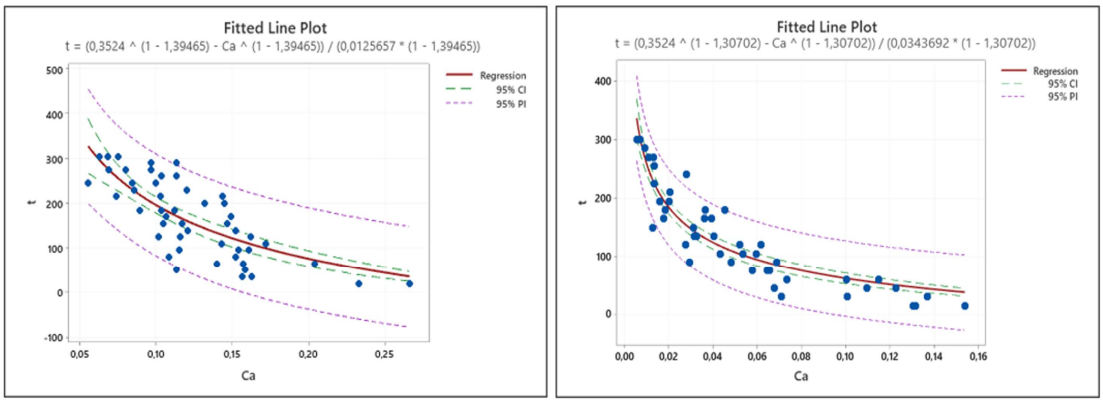

Figure 13: Fitted Line Plots for Batch 1 and 2

Comparisons between p values for the lack of fit test and a chosen significance level of 0.05 are required to ascertain whether the model that the model correctly specifies the relationship between the response and the predictors. The p values for batch 1 and 2, respectively, are 0.783 and 0.993, both greater than the significance level; hence the test does not detect a significant lack of fit. The standard error of the regression (S) represents how far the data values fall from the fitted values and are used to determine the model's efficiency in describing the response. The S values calculated are 31.994 and 55.897, which are relatively large. However, a low S value alone does not indicate that the model assumptions are met. Therefore, residual plots are used to assess the estimates. The residuals plots verify that the residuals are randomly distributed and have constant variance. Figures 3(a) and 4(a) represent the residuals versus fits plot; this is a scatter plot of residuals on the y-axis and fitted values (estimated responses) on the x-axis. The residuals are randomly scattered around the x-axis on both figures and form a rough horizontal band. This pattern supports the assumption that the relationship is linear and the variance of error terms are equal. Furthermore, no one residual deviates significantly from the residuals' basic pattern, which suggests no outliers.

Figures 3(b) and 4(b) display the residuals versus order plots for batches 1 and 2. The plot is used to support the claim that the residuals are independent of one another. Patterns such as a cycle or shift imply that residuals close to each other may be correlated and not independent.

Independent residuals show no trends or patterns when displayed in time order. Furthermore, residuals exhibit normal random noise around the x-axis, suggesting no serial correlation. The activation energy (E_a) and frequency factor (A) were 31.74293 kJ/mol and 19146.72141 1/s using the Arrhenius equation. The expected E_a of bimolecular reactions lies typically in the order of 300 kJ/mol; therefore, anything above this value would cause concern (Seoud et al., 2016).

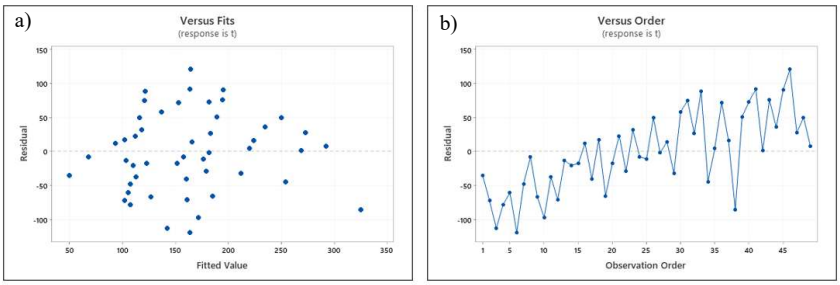

Figure 3: Residual Plots for Batch 1

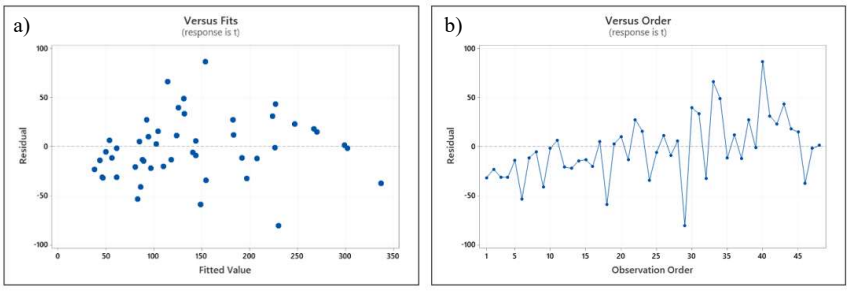

Figure 4: Residual Plots for Batch 2

This claim supports the assumption that the first mechanistic step is rate-controlling and controls the overall reaction rate. However, it cannot prove the assumption as this study only provides a pseudo-order rate law. Previous studies of the reduction of vanillin and cinnamyl all follow first-order rates with respect to the carbonyl compound with similar aldehyde conversions reported by Ward and Rhee (1989), Yadav and Lande (2006) and Lecher (2007) According to reaction classifications set out by Marin and Yablonsky (2011), the reaction speed can be categorised as moderate.

4.2 Factorial Design

The model coefficients were estimated using Stat-Ease Design-Expert software. This transformed empirical model is represented below:

$$(y)^3 = -0{,}195429 + 0{,}00247(x_1) + 0{,}237041(x_2) + 0{,}000829(x_3) + 0{,}001464(x_2)(x_3) - 0{,}000068(x_1)(x_2)(x_3) \quad (9)$$

The analysis of variance (ANOVA) results is tabulated in Table 3. The p-value for both the model and curvature is < 0.0001, verifying that the model is statistically significant and no curvature exists. The p-value for curvature in the ANOVA summary was given as 0,7628. The coefficient of determination (R-Squared) is 0.9252 and verifies that the model provides an acceptable fit for the data. Initially, the normal probability plot showed an S-shaped curve, and the plot displayed a megaphone pattern. These trends suggest a case of expanding variance, and a transform is required. Referring to the Box-Cox plot, the optimal lambda (λ) value for the transformation was 3. Updated residual plots show a random distribution of the residuals, indicating constant variance and no signs of lurking variables

that influenced the experiment's response.

Table 7: Summary of ANOVA Results

Source	Sum of Squares	df	Mean Square	F-value	p-value	Fit Results	
Model	1,08	7	0,1548	27,72	< 0.0001	R^2	0,9510
A-	0,2681	1	0,2681	47,99	< 0.0001	Adjusted R^2	0,9167
B-	0,2255	1	0,2255	40,36	< 0.0001	Predicted R^2	0,8343
C-Time	0,5023	1	0,5023	89,90	< 0.0001	Adequate	14,801
AB	0,0023	1	0,0023	0,4153	0,5338		
AC	0,0080	1	0,0080	1,44	0,2584		
BC	0,0458	1	0,0458	8,20	0,0169		
ABC	0,0319	1	0,0319	5,71	0,0380		
Curvature	0,0123	1	0,0123	2,21	0,1683		
Pure	0,0559	10	0,0056				
Cor Total	1,15	18					

The Pareto plot depicted in Figure 5(a) visualises all components' main and interaction effects. The chart shows the absolute values of the standardised effects from the highest effect to the smallest effect. Time is not considered as a factor in this case as time cannot be varied.

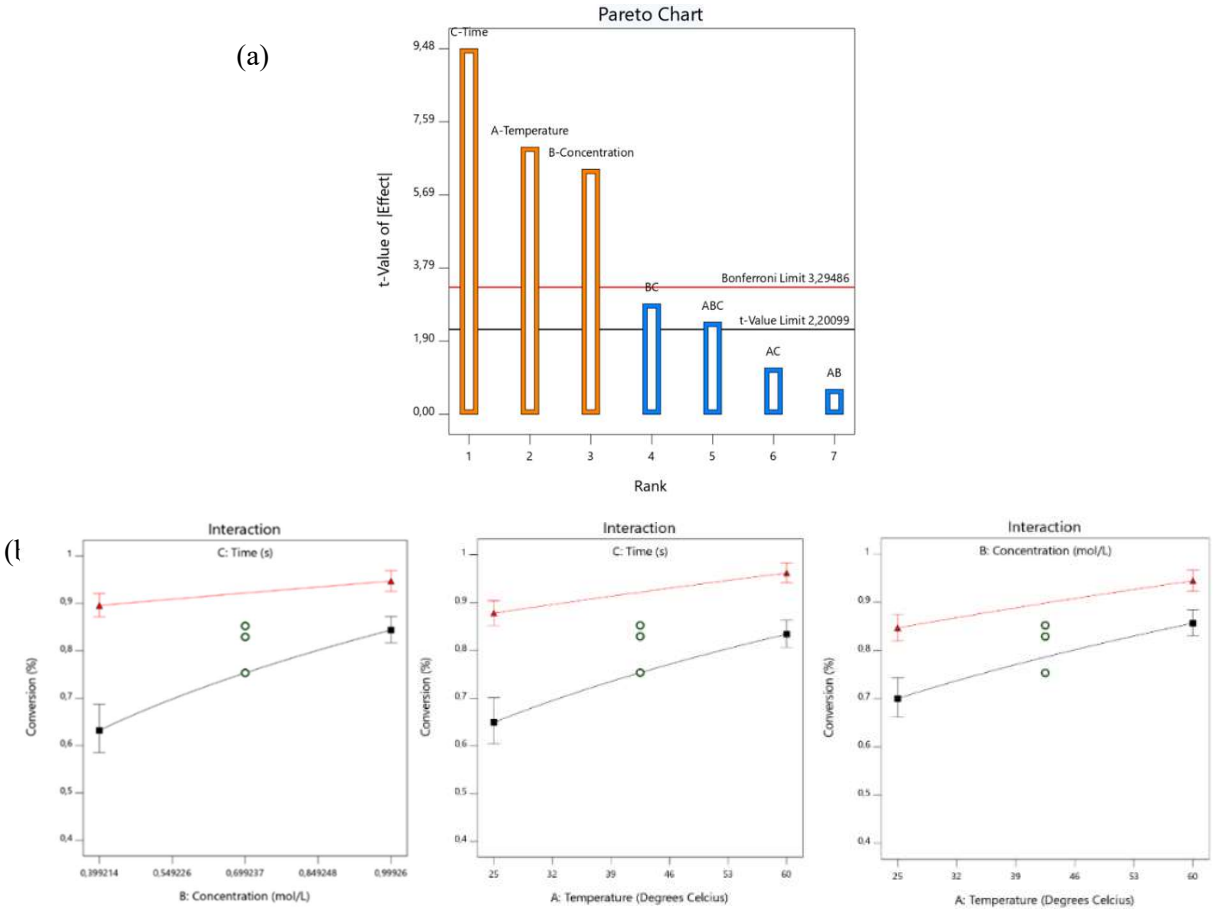

Figure 5: Factorial Plots (a) Pareto Plot (b) Interaction Plots

The Pareto plot indicates that the most influential factor is temperature then concentration. Furthermore, the interaction between time and concentration and the three-way interaction are significant, as shown in the analysis of variance. This observation is further supported by the interaction plots depicted in Figure 5(b). Nonparallel lines signify that the time and concentration factors are the most significant while the other interactions are negligible due to their parallel interaction plots. Comparison of the available literature shows that reported conversion performance is similar to those achieved by top-performing hydrogenation techniques (Table 4). However, sodium borohydride reduction can achieve this conversion at temperatures 60 ºC-90 ºC below current commercial techniques without a catalyst present. Additionally, this relatively simple technique produces similar conversions in a much shorter period.

Table 8: Summary of Top Performing Hydrogenation Techniques Reported

Catalyst	T (ºC)	P (H_2) (MPa)	Conversion (%)	Xylitol Yield
Ru/TiO2 [a]	120	2.0	100	98
Ru/C [b]	100-110	4.0-6.0	99.7	98.1
Raney Ni [c]	120	5.5	96.6	93.7
Ru/NiO-TiO [d]	120	5.5	99.9	99.7
Co/SiO_2 [e]	150	5	100	98

[a](Hernandez-Mejia et al., 2016) [b](Pham et al., 2016) [c](Mishra et al., 2013) [d] (Yadav et al., 2012) [e](Audemar et al., 2020)

The advantage of hydrogenation is that catalysts can last for many cycles showing little degradation, whereas large quantities of sodium borohydride are required to reduce xylose on a commercial scale. However, further analysis is required to determine whether the use of sodium borohydride would be more cost-effective despite lower operating conditions and no catalyst present. Other viable xylitol producing methods have been studied extensively, such as the biotechnological conversion of xylose to xylitol. These methods provide an environmentally friendly and low-cost route to produce xylitol from hemicellulosic hydrolysates. Yeasts and filamentous fungi reduce xylose in a single step by a xylose reductase (XR) enzyme to produce xylitol. They can be based on sugar mixtures such as lignocellulosic hydrolysates to save energy and substrate purification costs (Dasgupta et al., 2017). However, current literature shows that this technique is still not commercially competitive due to process bottlenecks; only a selected number of microorganisms can significantly reduce xylose, hindering optimisation space significantly (Zhao et al., 2020) (Buijs et al., 2013). Additionally, glucose present in many microorganisms represses xylose metabolism through carbon catabolite repression (Park et al., 2012). Consequently, this leads to poor xylose conversion efficiency coupled with high reaction times. Therefore, comparisons with other xylitol production techniques indicate that reducing xylose with a metal hydride offers a high xylose conversion with milder operating conditions, making it a promising technique in xylitol production.

5 CONCLUSION

This research initially aimed to determine reaction kinetics for conversion of xylose while simultaneously determining yield results of xylitol. Despite the limitations of the analysis, a pseudo-order rate law was deduced based on xylose concentration data. Through nonlinear regression techniques, the reaction is shown to be first order with regards to xylose. This observation correlates with literature regarding reducing carbonyl compounds with metal hydrides and supports the theory that the first hydride transfer is the rate-determining step. Furthermore, the factorial design provided an empirical model to assess xylose conversion over chosen reaction parameters. A maximum conversion of 98.8% was achieved at conditions significantly milder compared to hydrogenation techniques. Thus, the results obtained provide a basis for further study and indicate that the reduction of xylose with sodium borohydride shows the potential to compete with hydrogenation techniques.

REFERENCES

Abdek-Akher, M., Hamilton, J., Smith, F., 1951. The Reduction of Sugars with Sodium Borohydride1. https://doi.org/10.1021/JA01154A061

Audemar, M., Ramdani, W., Junhui, T., Ifrim, A.R., Ungureanu, A., Jérôme, F., Royer, S., Vigier, K. de O., 2020. Selective Hydrogenation of Xylose to Xylitol over Co/SiO2 Catalysts. ChemCatChem 12, 1973–1978. https://doi.org/10.1002/cctc.201901981

Brown, H.C., Ichikawa, K., 1961. The Influence of Solvent and Metal Ion on the Rate of Reaction of Alkali Metal Borohydrides with Acetone1. J. Am. Chem. Soc. 83, 4372–4374.

Brown, H.C., Mead, E.J., Subba Rao, B.C., 1955. A Study of Solvents for Sodium Borohydride and the Effect of Solvent and the Metal Ion on Borohydride Reductions1. J. Am. Chem. Soc. 77, 6209–6213. https://doi.org/10.1021/ja01628a044

Buijs, N.A., Siewers, V., Nielsen, J., 2013. Advanced biofuel production by the yeast Saccharomyces cerevisiae. Curr. Opin. Chem. Biol. 17, 480–488. https://doi.org/10.1016/j.cbpa.2013.03.036

Carey, F.A., Sundberg, R.J., 2007. Advanced Organic Chemistry: Part A: Structure and Mechanisms, 5th ed, Part A: Structure and Mechanisms. Springer US. https://doi.org/10.1007/978-0-387-44899-2

Dasgupta, D., Bandhu, S., Adhikari, D.K., Ghosh, D., 2017. Challenges and prospects of xylitol production with whole cell bio-catalysis: A review. Microbiol. Res. 197, 9–21. https://doi.org/10.1016/j.micres.2016.12.012

Eisenstein, O., Schlegel, H.B., Kayser, M.M., 1982. Theoretical study of borohydride addition to formaldehyde. A one-step, nonsynchronous transition state. J. Org. Chem. 47, 2886–2891. https://doi.org/10.1021/jo00136a015

Glass, R.S., Deardorff, D.R., Henegar, K., 1980. Highly stereoselective reductions of α-alkoxy-β-keto esters. Aspects of the mechanism of sodium borohydride reduction of ketones in 2-propanol.

Tetrahedron Lett. 21, 2467–2470. https://doi.org/10.1016/0040-4039(80)80101-8

Hernandez-Mejia, C., S. Gnanakumar, E., Olivos-Suarez, A., Gascon, J., F. Greer, H., Zhou, W., Rothenberg, G., Shiju, N.R., 2016. Ru/TiO 2 -catalysed hydrogenation of xylose: the role of the crystal structure of the support. Catal. Sci. Technol. 6, 577–582. https://doi.org/10.1039/C5CY01005E

Hyvönen, L., Koivistoinen, P., Voirol, F., 1982. Food Technological Evaluation of Xylitol, in: Chichester, C.O., Mrak, E.M., Stewart, G.F. (Eds.), Advances in Food Research. Academic Press, pp. 373–403. https://doi.org/10.1016/S0065-2628(08)60114-7

Lo, C.F., Karan, K., Davis, B.R., 2007. Kinetic Studies of Reaction between Sodium Borohydride and Methanol, Water, and Their Mixtures. Ind. Eng. Chem. Res. 46, 5478–5484. https://doi.org/10.1021/ie0608861

Mishra, D.K., Dabbawala, A.A., Hwang, J.-S., 2013. Ruthenium nanoparticles supported on zeolite Y as an efficient catalyst for selective hydrogenation of xylose to xylitol. J. Mol. Catal. Chem. 376, 63–70. https://doi.org/10.1016/j.molcata.2013.04.011

Motulsky, H., Christopoulos, A., 2004. Fitting Models to Biological Data using Linear and Nonlinear Regression. Oxford University Press, New York.

Nygren, J., Nikander, H., Puuppo, O., Tylli, M., Lindroos, M., Eroma, O.-P., Heikkila, H., 1997. Method for producing xylitol. CA2258866A1.

Park, J.M., Vinuselvi, P., Lee, S.K., 2012. The mechanism of sugar-mediated catabolite repression of the propionate catabolic genes in Escherichia coli. Gene 504, 116–121. https://doi.org/10.1016/j.gene.2012.04.074

Patel, P., Lingayat, S., Gulvi, N., Badani, P., 2018. Mechanistic and kinetic insights of reduction of indophenol by sodium borohydride: A theoretical study to explore the effect of solvent and counter ion. Chem. Phys. 504, 13–21. https://doi.org/10.1016/j.chemphys.2018.02.021

Periasamy, M., Kumar, M., 2000. Methods of Enhancement of Reactivity and Selectivity of Sodium Borohydride for Applications in Organic Synthesis. J. Organomet. Chem. 609, 137–151. https://doi.org/10.1016/S0022-328X(00)00210-2

Pham, T.N., Samikannu, A., Rautio, A.-R., Juhasz, K.L., Konya, Z., Wärnå, J., Kordas, K., Mikkola, J.-P., 2016. Catalytic Hydrogenation of d-Xylose Over Ru Decorated Carbon Foam Catalyst in a SpinChem® Rotating Bed Reactor. Top. Catal. 59, 1165–1177. https://doi.org/10.1007/s11244-016-0637-4

Seoud, O.A.E., Baader, W.J., Bastos, E.L., 2016. Practical Chemical Kinetics in Solution, in: Encyclopedia of Physical Organic Chemistry. American Cancer Society, pp. 1–68. https://doi.org/10.1002/9781118468586.epoc1012

Wigfield, D.C., 1979. Stereochemistry and mechanism of ketone reductions by hydride reagents.

Tetrahedron 35, 449–462. https://doi.org/10.1016/0040-4020(79)80140-4

Wigfield, D.C., Gowland, F.W., 1977. The kinetic role of hydroxylic solvent in the reduction of ketones by sodium borohydride. New proposals for mechanism, transition state geometry, and a comment on the origin of stereoselectivity. J. Org. Chem. 42, 1108–1109. https://doi.org/10.1021/jo00426a048

Wu, Y.D., Tucker, J.A., Houk, K.N., 1991. Stereoselectivities of nucleophilic additions to cyclohexanones substituted by polar groups. Experimental investigation of reductions of trans-decalones and theoretical studies of cyclohexanone reductions. The influence of remote electrostatic effects. J. Am. Chem. Soc. 113, 5018–5027. https://doi.org/10.1021/ja00013a042

Yadav, G.D., Lande, S.V., 2006. Novelties of kinetics of chemoselective reduction of citronellal to citronellol by sodium borohydride under liquid–liquid phase transfer catalysis. J. Mol. Catal. Chem. 247, 253–259. https://doi.org/10.1016/j.molcata.2005.11.015

Yadav, M., Mishra, D.K., Hwang, J.-S., 2012. Catalytic hydrogenation of xylose to xylitol using ruthenium catalyst on NiO modified TiO2 support. Appl. Catal. Gen. 425–426, 110–116. https://doi.org/10.1016/j.apcata.2012.03.007

Yadav, V.K., Jeyaraj, D.A., Balamurugan, R., 2000. The Cation Complexation Model Predicts the Experimental π-Facial Selectivity of 2-ax- and 2-eq-Substituted Cyclohexanones. A Detailed Ab Initio MO Investigation. Tetrahedron 56, 7581–7589. https://doi.org/10.1016/S0040-4020(00)00663-3

Yamamoto, J., 2003. Sodium Borohydride Digest.

Zhao, Z., Xian, M., Liu, M., Zhao, G., 2020. Biochemical routes for uptake and conversion of xylose by microorganisms. Biotechnol. Biofuels 13, 21. https://doi.org/10.1186/s13068-020-1662-x

Process intensification in octene hydrogenation: Application of nanocatalysts and ultrasonic irradiation in a slurry phase reactor.

O. Mupomoki* and D. Lokhat

Reactor Technology Research Group, School of Engineering, University of KwaZulu-Natal, Howard College Campus, King George V Avenue, Durban 4041, South Africa.

*Corresponding author: obertmupomoki@yahoo.com

ABSTRACT

Sonochemistry has been discovered to influence the rate of chemical reactions that experience a lot of mass transfer resistance in slurry phase reactions. Applications of sonochemistry have been developed in virtually all areas of chemistry and related chemical technologies and the hydrogenation of alkenes, which occur in the presences of a metal catalyst such as nickel, palladium, platinum or rhodium is one such reaction of vital industrial importance. In this study, the influence of ultrasonic irradiation on the reaction rate and catalyst deactivation for the hydrogenation of 1-octene using a commercial nanosized Pt/AI_2O_3 catalyst was investigated. A three phases slurry reactor was used to allow for adequate contact between the solid, liquid and gas phases. To enhance reactor performance and intensify the process, ultrasonic irradiation was used. It is believed that the technology improves contact between the solid, liquid and gas particles in aiding the transfer of materials across phase boundaries. This is done via the generation of cavitation microbubbles, where the growth and collapse of these bubbles generate localized regions of high temperature and pressure. The experimental design was divided into two parts in which the first part investigated both sonicated and unsonicated hydrogenation reactions at varying temperatures. The second part involved sonicated and unsonicated hydrogenation reactions at a fixed temperature for different reaction times whilst reusing the Pt/AI_2O_3 catalyst. The products of the reaction were analysed using a Shimadzu (2014) gas chromatography system to determine the conversion of 1-octene and the yield of hydrogenated products. Octene conversions of varying proportions were observed and conversions of approximately 97% were realised especially at higher temperatures.

Keywords: Process Intensification; octene hydrogenation, nanocatalysts; ultrasonic irradiation.

1 INTRODUCTION

Hydrogenation of alkenes is an important industrial reaction which optimally occurs in the presence of metal catalysts. The overall reaction is however often hindered due to significant mass transfer limitations between the three phases and catalyst poisoning during the reaction. A possible way of mitigating these hindrances can be through the application of ultrasonic irradiation, also known as sonochemistry. The ultrasound assists in improving the contact between the interacting phases and enhancing the transfer of material across the phase boundaries. Additionally, the ultrasonic waves can

aid in prolonging the catalyst lifetime by reducing the coke laydown on the catalyst surface resulting in the unwanted effects of catalyst deactivation. Ultrasonic irradiation uses acoustic cavitation which is the formation, growth and sudden collapse of bubbles in a liquid. Cavitation produces large amounts of energy which improves physical and chemical processes. This work focused on investigating the influence of ultrasonic irradiation on reaction rate enhancement and catalyst deactivation for the heterogenous hydrogenation reaction of 1-octene over a commercial supported platinum catalyst. The study was aimed at looking at the possibility of using process intensification in commercial octene hydrogenation reactions and many other applications. Process intensification provides a pathway that can replace large expensive energy intensive equipment or processes with ones that are smaller, less costly and more efficient. It usually brings about process miniaturization, reduction in capital costs, enhanced safety and energy efficiency and often improved product quality. It also encompasses improvement in process chemistry, process steps, and gives rise to multifunctional reactors, membrane reactors and the use of more intensified methods of processing such as the use of microwaves and magnetic fields in chemical processing.

2 LITERATURE

Multiphase reactions consist of gas, liquid and/or solid reacting simultaneously with one another and can be categorised according to the phases. These reactions are generally more difficult to perform than homogenous reactions, due to the low interaction efficiency and poor mass transfer rate between the reacting phases therefore resulting in reduced reaction rates. Commercially, these reactions usually conducted in huge slurry or trickle bed reactors. A trickle bed reactor is a continuous packed bed reactor where the liquid phase flows downwards through a packing medium, where gas is applied in either a co-current or counter-current direction (Wu and Tu, 2016).

Slurry reactors on the other hand consist of a solid catalyst suspended within the liquid through which a soluble gas phase is bubbled. A fine solid phase is usually dispersed in the bulk liquid phase to significantly enhance the gas-liquid mass transfer rate (Brilman et al., 2000). The three phases are brought into contact with each other with the aid of mechanical agitation such as stirring. Techniques such as stirring have been developed to accelerate the reaction rate of multiphase catalytic reactions but these are only limited to the macroscopic level. The vigorous stirring energizes the reacting phases causing the phases to interact more, thereby increasing the interfacial area for mass transfer, hence increasing the reaction rate (Kobayashi et al., 2004).

The reaction mechanism for multiphase catalytic reactions occur in various steps consisting of processes such as diffusion, adsorption and desorption. Heterogenous catalytic reaction occurs on the surface of the catalyst, however the reactants are present in the bulk fluid phase that surrounds the solid particles. The catalytic reaction begins by the gas phase reactant externally diffusing through the

boundary layer surrounding the solid in a process known as film diffusion. Once the reactant passes the boundary layer, it diffuses internally through the catalytic pores to reach the active site of the internal catalytic surface. Within the internal catalytic surface, the reactant is adsorbed onto the inner catalytic surface and reacts with the active sites of the solid. A certain contact time is required for this reaction to result in the formation of a product that is then desorbed from the inner surface of the solid. Diffusion takes place once again, through the catalyst pores and boundary layer to transfer the product to the bulk fluid (Klaewkla, Arend and Hölderich, 2011).

Hydrogenation reactions in organic processes which involve the addition of elemental hydrogen to the unsaturated bonds of an alkene or alkyne to produce a saturated product are examples of reactions that suffer considerable mass transfer limitations and as a result catalytic hydrogenation reactions typically occur in the presence of a finely divided metal catalyst such as nickel, palladium, platinum or rhodium. The reaction involves either connecting two atoms of a molecule by adding hydrogen or may result in the dissociation of the molecule, known as destructive hydrogenation. These hydrogenation methods are used in multiple industries such as the food industry for the production of edible fats from liquid oils, or in the petroleum industry to manufacture gasoline and petrochemical products. During the alkene hydrogenation reaction, two hydrogen atoms are added to the double bond which results in a saturated alkane. The hydrogenation of alkenes typically forms a more stable product and is therefore a thermodynamically favourable reaction. However, in order for the reaction to reach completion, the addition of a catalyst is needed for the reaction.

As stated above, catalysts that are commonly used for hydrogenation reactions comprise of nickel, palladium, platinum or rhodium. Platinum metal hydrogenation catalysts exists as two types, namely supported and unsupported catalysts. Suitable catalyst supports consist of silica or alumina, whereby the catalyst is attached to the support material pores thereby increasing the surface area of active catalyst (Rylander, 1979). The unsupported catalysts are less likely to be used in hydrogenation due to low efficiency and significant loss of recoverability. Supported platinum metal catalysts offer greater advantages as the support provides a higher efficiency of the metal by increasing the active metal surface area and facilitating metal recovery. Furthermore, supported catalysts have a higher resistance to poisoning which leads to catalyst deactivation (Rylander, 1967).

Catalyst deactivation is the decrease of catalytic activity or selectivity over time and this ultimately decreases the rate of the heterogenous catalytic reaction. Catalyst deactivation occurs due to multiple reasons such as newly formed products or by-products attaching to the active catalyst sites causing pore blockage or sometimes undesired materials such as coke is formed and deposited onto the catalytic surface resulting in lowering the catalyst activity. The catalyst deactivation mechanisms are categorised into groups and have significant effects on the rate of reactions.

The application of ultrasonic irradiation to reacting species which is also known as sonochemistry involves the use of powerful ultrasonic waves in a slurry medium that contains the reacting species. Ultrasound has been known to accelerate dissolution, improving the reaction rate as well as regenerating surfaces of solid reactants or catalysts. This is all achieved through acoustic cavitation (Qiao, Liu and Max Lu, 2017). Acoustic cavitation results in the formation and rapid growth and sudden collapse of bubbles in liquid mixtures which are under the influence of high-intensity ultrasonic irradiation. The collapse of the bubbles (vacuum bubbles) generates a large concentration of energy due to the conversion of kinetic energy from the motion of the liquid into heat and localised pressure. The collapse of the bubbles produces temporary regions of high pressure and high temperatures known as localized hot-spots. These hot-spots act as 'microreactors' that drive the chemical reactions (Suslick et al., 1999).

All chemical reactions require a significant amount of energy to occur and this energy can be made available in several forms. Ultrasonic irradiation provides an alternate source of energy for chemical reactions to occur, as compared to traditional methods such as the addition of heat. The concentrated localized pressures and temperatures coupled with the heat generated from cavitation provides suitable conditions for chemical reactions. In ultrasonic irradiation, the collapse of the bubbles provides a unique mechanism for the generation of high-energy chemistry (Suslick et al., 1999). However, the cavitation bubbles are largely dependent on the intensity of the ultrasonic waves which rely on various operating parameters such as wave frequency as well as the physicochemical properties and compressibility of the liquid.

Ultrasonic irradiation can be utilised to play various roles in chemical reactions. This may include prolonging the catalyst activity, the breakage of chemical bonds to form highly reactive species as well as providing the necessary activation energy required for reactions to occur. Once applied to a reacting mixture, the concentrated ultrasonic waves result in interesting physical and chemical effects such as emulsification, luminescence and chemical transformation. According to Shibata et al, the application of ultrasound has been widely used in the synthesis of organic reactions due to its improvement of the overall reaction rate and the ability to alter the catalyst selectivity (Shibata et al., 1990). Furthermore, ultrasonic irradiation is a popular technique used in chemical reactions as it is simple to control, reduces the reaction time, minimizes waste material and reduces the energy consumption required thereby enhancing the chemical reactivity (Schiel et al., 2015). Currently, ultrasound is applied in large scale industrial processes to increase selectivity and yield as well as to reduce impurities and side reactions.

3 EXPERIMENTAL PROCEDURE

The experimental procedure was divided into two parts. Part one included performing sonicated and unsonicated hydrogenation reactions at varying temperatures, whereas part two included performing sonicated and unsonicated hydrogenation reactions at a fixed temperature whilst reusing the Pt/Al_2O_3

catalyst. The purpose of part one of the study was to investigate the effect of ultrasonic irradiation on the conversion of 1-octene and yield of octane, at various reaction temperatures. It entailed performing sonicated and unsonicated hydrogenation reactions at varying temperatures of 40ºC, 50ºC and 60ºC. The hydrogenation reaction proceeded for 2 hours, thereafter the reactor was cooled to 25ºC. The hydrogenated product was then analysed utilizing a Shimadzu (2014) GC/FID to determine the conversion of 1-octene and yield of the hydrogenated product. Part two entailed performing sonicated and unsonicated hydrogenation reactions at a fixed temperature of 50ºC, whilst varying the reaction time from 0,5 hours, 1 hour and 1,5 hours; and reusing the spent catalyst in each run. The spent catalyst was collected from part one and analysed using SEM-EDX to determine the extent of in-situ catalysts regeneration using ultrasound. It was also used to ascertain the extent of catalysts coking.

Prior to performing the hydrogenation reaction, the commercial Pt/Al_2O_3 catalyst was ground using a pestle and mortar, and thereafter sieved into a fine powder. For the hydrogenation reactions to run smoothly, a 300ml Parr autoclave reactor fitted with an impeller was used. The reactor along with the temperature controller and ultrasonic probe were all submerged a water bath. The reactor was then heated to the desired reaction temperature with the aid of the water bath and temperature controller within the unit. The temperature of the reactor was monitored via a temperature probe, that was inserted into the reactor vessel.

A hydrogen gas line was connected directly to the reactor and the hydrogenation reaction occurred at a pressure of 20 bar. Once the reaction was completed, the cooling water unit was connected to the reactor jacket and utilized to quench the reactor with cold water to ensure the reactor rapidly cools to room temperature. Both the reactant and catalyst amount fed into the reactor, remained at fixed values throughout the experiment. For all the reactions, the reactor contained 30ml of 1-octene and 1g of ground commercial Pt/Al_2O_3 catalyst.

4 RESULTS AND DISCUSSION

Mass transfer limitations have a significant role on the performance of a chemical reaction, specifically the overall conversion of a reactant and product yield. The purpose of this study was to investigate the influence of ultrasound on reactant conversion, product yield and catalyst deactivation. Several parameters were varied throughout the experimentation such as reaction temperature, reaction time and catalyst usage.

4.1 Part One: Effect of ultrasonic irradiation on the conversion of 1-octene and yield of octane using a fresh catalyst.

In the first part of the study where 30ml of 1-octene and 1g of freshly ground Pt/Al_2O_3 catalyst was added into the reactor vessel, the reactor was allowed to heat to the desired temperatures of 40ºC, 50ºC and 60ºC for the different experimental runs and thereafter hydrogen fed into the reactor for

hydrogenation to occur and the ultrasonic probe was switched on for the sonicated reactions. Figure 1(a) and (b) below show the results that were obtained from these experiments.

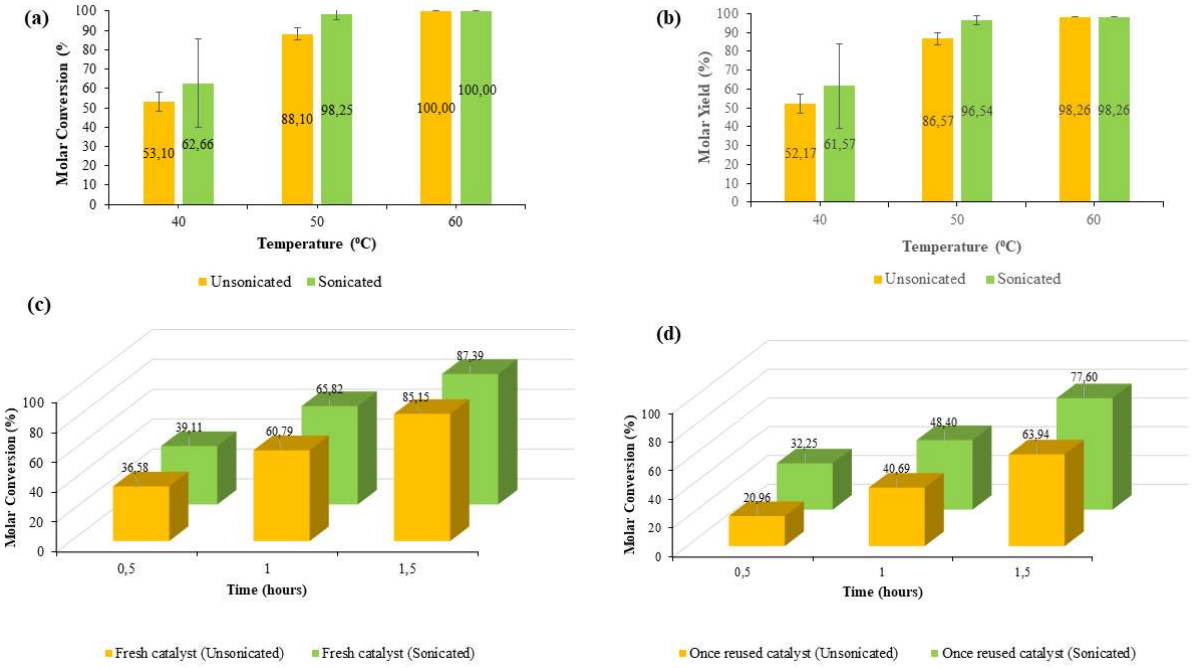

Figure 1: (a) – Conversion of 1-octene to octane at 40 °C, 50 °C and 60 °C; (b) – Yield of octane at 40 °C, 50 °C and 60 °C; (c) – Conversion of 1-octene using a fresh Pt/Al_2O_3 at 50 °C for 0.5 hour, 1hour and 1.5 hours; (d) – Conversions using a 1x Recycled Pt/Al_2O_3 catalyst at 50 °C for 0.5 hr, 1hr and 1.5 hrs.

From Figure 1(a), it can be observed that an increase in the reaction temperature resulted in an increase in the conversion for both sonicated and unsonicated reactions. This is expected as higher temperatures increase the reaction rate, resulting in better reaction performance. At 60ºC, a 100% conversion of 1-octene for both sonicated and unsonicated reactions was observed. This can be attributed to the fact that at the higher temperature, the Pt/Al_2O_3 catalyst reaches maximum catalytic activity in converting the 1-octene to octane. The substantially high conversion indicates the platinum catalyst to be highly active. Additionally, hydrogen is fed into the reactor at a relatively high pressure of 20bar. This high pressure causes the hydrogen gas to diffuse into the reacting liquid phase at a faster rate and collide with the reacting molecules, thereby increasing the hydrogenation reaction rate hence an increase in conversion. Similar reasons can be applied to the high conversions observed at 50ºC. At 50ºC, the conversion for the sonicated and unsonicated reactions were determined to be 98,25% and 88,10%, respectively. The data obtained for 50ºC and 60ºC were deemed statistically acceptable, as the associated error bars did not overlap. It was however noticed that as the reaction temperature decreases from 60ºC to 40ºC, the conversion of 1-octene decreased but the effect of ultrasound became more noticeable for the sonicated reactions. As the temperature decreases, the activity of the Pt/Al_2O_3 catalyst declines significantly

therefore the effect of ultrasound is more prominent. At the higher temperature of 60ºC and higher, the platinum catalyst is extremely active and drives the chemical reaction to completion with noticeably high conversions. Therefore, at 60ºC, there is no significant difference in effect of ultrasound observed in Figure 1(a). At 40ºC and 50ºC, the conversions of the sonicated reactions and unsonicated reactions are 62,66% and 53,10% as well as 98,25% and 88,10% respectively. There are large differences in conversions and this was attributed to the catalyst having lower activities at the lower temperatures of 40ºC and 50ºC. The ultrasonic irradiation compensated for the low catalyst activity by providing energy through cavitation. This energy is used to overcome mass transfer limitations existing between the three phases, thereby increasing the reaction rate. It was therefore observed that as the reaction temperature decreases, the ultrasonic effect increases resulting in a higher conversion for the sonicated reactions. This is advantageous to industries utilizing ultrasonic irradiation in chemical processes, as the ultrasonic device can be operated at lower temperatures thus reducing operating costs and increasing profitability. In any reaction, an optimal reaction temperature is required to obtain an appropriate selectivity but sometimes conversions may be low. It can therefore be noted that by applying ultrasonic irradiation at an optimal temperature, an appropriate selectivity as well as a high conversion can be achieved for most reactions.

The yield of the hydrogenated product was determined for both sonicated and unsonicated reactions as seen in Figure 1(b). As expected, the trend for the product yield correlated to the trend for the conversion of 1-octene. As the reaction temperature increased, the yield increased.

4.2 Part two: Effect of ultrasonic irradiation on reducing catalyst deactivation at 50 ºC.

From the second part of the study which consisted of performing sonicated and unsonicated reactions at similar conditions to part one with 30ml of 1-octene and 1g of freshly ground commercial Pt/Al_2O_3 catalyst added to the reactor or recycled catalysts. The reactor was heated to a fixed temperature of 50ºC whilst varying the reaction time between 0,5 hours, 1 hour and 1,5 hours. The purpose of part two was to investigate the effect of ultrasonic irradiation on the catalyst deactivation, essentially to study how the Pt/Al_2O_3 catalyst deactivates over time by reusing the spent catalyst and measuring conversion with time. Figures 1(c), 1(d) and Figure 2 below show the results that were observed from these experiments.

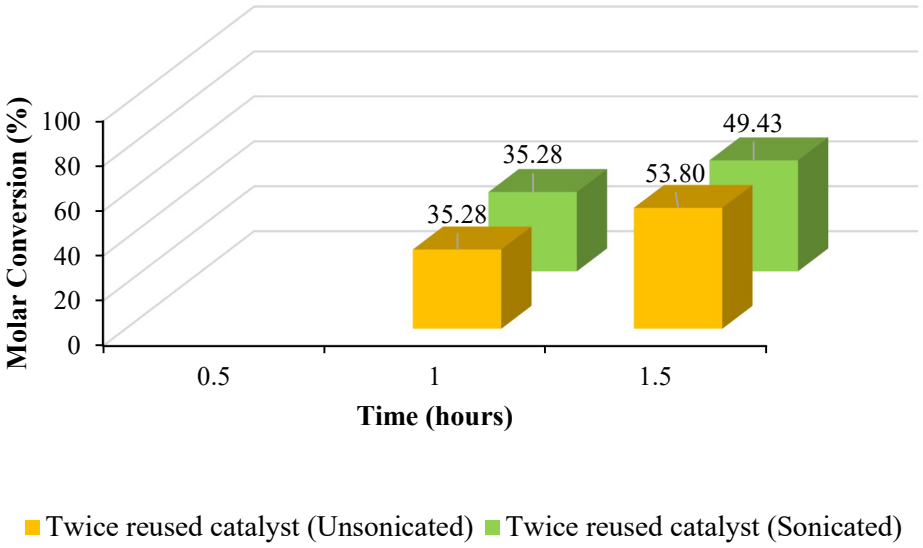

Figure 2: Conversions using a 2x Recycled Pt/Al_2O_3 catalyst at 50 °C for 0.5 hr, 1hr and 1.5 hrs

For both sonicated and unsonicated reactions, it can be seen that as the Pt/Al_2O_3 catalyst is being reused, the overall conversion of 1-octene decreases. This is evident for all three reaction times of 0,5 hours, 1 hour and 1,5 hours. This is a result of catalyst deactivation due to coking. Coking is a form of catalyst deactivation where compounds rich in carbon are deposited onto the catalytic pores therefore resulting in pore blockage and reducing the catalyst activity. Coking is common for reactions involving hydrocarbons. Therefore, as the platinum catalyst is being reused, the carbon content present on the catalyst increases. From Figures 1(c), it is noticed that the conversion for the sonicated reactions for all three catalyst types are higher than those for the unsonicated reactions. This is expected as the ultrasonic irradiation assists in prolonging the catalyst lifetime and reduces the effect of coking. The effect of the ultrasound is largely evident for the catalyst that was recycled once at a reaction time of 1,5 hours, the maximum conversion for the sonicated and unsonicated reactions are 77,60% and 63,94%, respectively. However, in Figure 2, the conversion for the sonicated and unsonicated reactions at 1 hour are equal. This is a result of the Pt/Al_2O_3 catalyst reaching complete deactivation as it was used in two reactions prior to this run. By taking a closer look at the 1,5-hour reaction, the unsonicated reaction produced a higher conversion than the sonicated reaction. This result is unpredicted and should be further investigated, as ultrasound should produce a better conversion. A possible reason for this result could be the frequency setting on the ultrasonic device which might have dropped to lower values and therefore having little impact on the conversion. A higher frequency will have a greater impact on the collapse of the cavitation bubbles, resulting in more energy provided to drive the chemical reaction. Hence, increasing the reaction rate and conversion.

From the above results, it can be observed that the ultrasonic irradiation had a significant effect on the catalyst deactivation, specifically through reducing coking on the catalyst. From the analysis of part one, it showed that at lower temperatures the conversion increased due to the effect of the ultrasound on the hydrogenation reaction but as evidenced by Energy Dispersive X-ray spectroscopy (SEM-EDX) that was utilised to analyse the coking on the spent catalyst obtained from run one of part one, at 40ºC, 50ºC and 60ºC, sonication was also found to have a profound effect on the insitu catalyst regeneration for those reactions that involved the use of ultrasound. This is depicted in Figure 3 below.

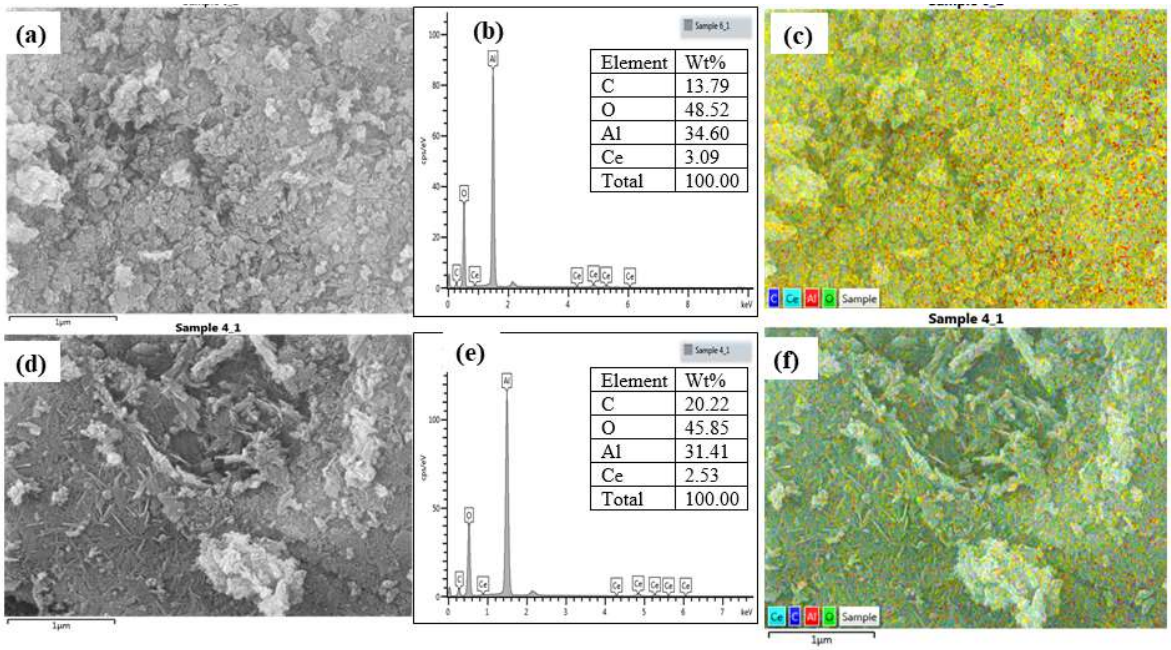

Figure 3: SEM micrographs and corresponding EDX mapping of spent Pt/Al_2O_3 catalysts after reaction for 2 hours. (a) – Pt/Al_2O_3 with sonication, (d) – Pt/Al_2O_3 without sonication.

From Figure 3 (b) and (e), it can be observed that the amount of catalyst coking was more significant on (c), the unsonicated reaction as the amount of elemental carbon that was present on the surface of the spent catalysts was more than that on the sonicated reaction. The elemental carbon on the sonicated spent catalyst was 13,79wt% while for the unsonicated reaction was 20.22wt% as shown on Figure 3. The same trend was also observed for the recycled catalysts but these had significantly more carbon deposition as analysed by EDX.

5 CONCLUSIONS

It was observed that it is possible for a reactor employing sonication to achieve greater conversions and yields whilst operating at lower temperatures, thus reducing operating costs. Catalysts deactivation had an impact on the reactor performance in part two of the study since the recycled catalysts showed a decrease in 1-octene conversion obtained for a specific run but when comparing the sonicated versus unsonicated reactions for a particular catalyst in this work, it was observed that the sonicated reactions

achieved higher conversions thus showing the impact of cavitation on the reaction rate. Therefore, cavitation can prevent excessive laydown of coke whilst also aiding its removal from the catalyst surface and in the process prolonging catalysts life. The achievement of even better conversions at lower temperatures implies that process intensification is possible in octene hydrogenation and even other heterogenous reaction when using ultrasonic irradiation and nanocatalysts at lower temperatures.

REFERENCES

Argyle, M. and Bartholomew, C. (2015). Heterogeneous Catalyst Deactivation and Regeneration: A Review. Catalysts, 5(1), pp.145-269.

Brilman, D., Goldschmidt, M., Versteeg, G. and van Swaaij, W. (2000). Heterogeneous mass transfer models for gas absorption in multiphase systems. Chemical Engineering Science, 55(15), pp.2793-2812.

Ebnesajjad, S. (2014). Surface and Material Characterization Techniques. Surface Treatment of Materials for Adhesive Bonding, pp.39-75.

French, L. (2004). Addition Reactions Synthesis - ppt video online download. [online] Slideplayer.com. Available at: https://slideplayer.com/slide/9318783/ [Accessed 5 May 2019].

Irvine, W. (2011). Eley–Rideal Mechanism. Encyclopedia of Astrobiology, pp.485-485.

Klaewkla, R., Arend, M. and Hölderich, W. (2011). A Review of Mass Transfer Controlling the Reaction Rate in Heterogeneous Catalytic Systems. Germany: ResearchGate.

Kobayashi, J., Mori, Y., Okamoto, K., Akiyama, R., Ueno, M., Kitamori, T. and Kobayashi, S. (2004). A Microfluidic Device for Conducting Gas-Liquid-Solid Hydrogenation Reactions. Science, 304(5675), pp.1305-1308.

Laidler, K. (1996). A glossary of terms used in chemical kinetics, including reaction dynamics (IUPAC Recommendations 1996). Pure and Applied Chemistry, 68(1), pp.149-192.

Pavia, L., Lampman, G., Kritz, G. and Engel, R. (2006). Introduction to Organic Laboratory Techniques, 4th ed. Thomson Brooks/Cole., pp.797-817.

Qiao, S., Liu, J. and Max Lu, G. (2017). Synthetic Chemistry of Nanomaterials. Modern Inorganic Synthetic Chemistry, pp.613-640.

Richards, W. and Loomis, A. (1927). The Chemical Effects of High Frequency Sound Waves I. A Preliminary Survey. Journal of the American Chemical Society, 49(12), pp.3086-3100.

Rylander, P. (1979). Hydrogenation Catalysts, Reactors, and Reaction Conditions. The Catalytic Hydrogenation in Organic Syntheses, pp.1-12.

Rylander, P. (1967). Platinum Metal Catalysts. Catalytic Hydrogenation Over Platinum Metals, pp.3-29.

Schiel, M., Chopa, A., Silbestri, G., Alvarez, M., Lista, A. and Domini, C. (2015). Use of Ultrasound in the Synthesis of Heterocycles of Medicinal Interest. Green Synthetic Approaches for

Biologically Relevant Heterocycles, pp.571-601.

Shibata, K., Katsuyama, I., Matsui, M. and Muramatsu, H. (1990). Synthesis of Ferrocenyl-Substituted 3-Cyano-2-methylpyridines. Bulletin of the Chemical Society of Japan, 63(12), pp.3710-3712.

Suslick, K., Didenko, Y., Fang, M., Hyeon, T., Kolbeck, K., McNamara, W., Mdleleni, M. and Wong, M. (1999). Acoustic cavitation and its chemical consequences. Philosophical Transactions of the Royal Society of London. Series A: Mathematical, Physical and Engineering Sciences, 357(1751), pp.335-353.

Wu, C. and Tu, X. (2016). Biological and fermentative conversion of syngas. Handbook of Biofuels Production, pp.335-357.

Investigation of a Heterogenous Bi-functional Catalyst in the (Trans)esterification of High FFA Feedstock

L.Maina and O.Oyekola*

Department of Chemical Engineering, Faculty of Engineering and The Built Environment, Cape Peninsula University of Technology, P.O Box 1906, Bellville 7535, South Africa;
lindamaina47@gmail.com (L.M)

*Corresponding authors: oyekolas@cput.ac.za

ABSTRACT

There has been growing concern about the depletion of the world's oil reserves as well as the negative environmental impacts fossil fuels pose. Biodiesel is a renewable substitute for petrodiesel used in compression ignition engines. This study investigated the simultaneous esterification and transesterification of various low-cost feedstocks using bifunctional catalysts. Four catalysts ($CaO:Al_2O_3$ ratios of 80:20, 70:30, 60:40, and 50:50) were synthesised via co-precipitation and calcined at 600 °C. Catalysts were characterised using BET. The synthesised catalysts exhibited adequate morphological and catalytic characteristics (pore sizes ≥209 Å; surface areas ≥11 m^2/g; pore volumes ≥0.072 cm^3/g). High free fatty acid feedstocks (waste palm oil and neem oil) contents were 2.47 to 3.25% respectively and a low FFA feedstock (virgin palm oil) content was 0.67%. Feedstocks underwent simultaneous esterification and transesterification under optimised reaction conditions of 65 °C, 1200 rpm, 2.5 wt% catalyst loading and a methanol to oil molar ratio of 12:1 at a reaction time of 4 hours under reflux conditions. Optimum biodiesel yields of 97.85, 99.51 and 97.63% were obtained from virgin palm, waste palm and neem oil using 80%CaO:20% Al_2O_3, 70%CaO:30%Al_2O_3 and 60%CaO:40%Al_2O_3 bi-functional catalysts respectively.

Keywords: Biodiesel; Bifunctional catalyst; Heterogenous catalyst; FAME; Esterification; Transesterification; Waste cooking oil; Non-edible oil; Free Fatty Acid; CaO/ Al_2O_3 Catalyst

1 INTRODUCTION

Energy is the most lucrative and precious resource since the dawn of humanity itself. There is increasing energy demand with an exponentially increasing population. Moreover, the depletion fossil fuels has contributed to the strain on energy production. Climate change has become a major factor in the sense that it has motivated and perpetuated the importance of environmentally friendly and renewable energy sources (Rehan and Arabia, 2017).

Biodiesel, also known as FAAE (Fatty acid alkyl esters) can be produced from virgin, waste and non-edible oils. Biodiesel produced from triglycerides containing feedstock, via the transesterification process, has attracted immense attention over the past decades as a biodegradable, renewable and sustainable fuel (Alaba *et al.* 2016). Currently, biodiesel production faces several limitations, and the

main production route is arguably expensive. For example, the most common production method is via base catalysis such as sodium or potassium hydroxide. One of the major advantages of using homogeneous base catalysts is that they are relatively easy and inexpensive to procure.

However, due to the inevitable saponification reaction associated with using an alkali the presence of a feedstock with high FFA, solid catalysis has become increasingly popular as it eliminates this side reaction. Therefore, special attention has been directed to applying heterogeneous catalysis for biodiesel production due to the green and recyclable catalytic properties of heterogeneous catalysts (Ramli et al., 2016). Heterogeneous catalysts have the ability to alleviate the above-mentioned challenges and, furthermore, reduce reactor corrosion, decrease FFA as well as simplify separation and purification downstream (Ramli et al. 2016).

The use of supported solid catalysts such as calcium oxide or magnesium oxide ensures the eradication of saponification reactions (Yadav, Singh & Sharma, 2017). The most prominent advantage is that the transesterification and esterification processes occur simultaneously. Other than that, such catalysts have proved to be reusable while still producing high yields of biodiesel (Frost and Sullivan, 2016). Bi-functional solid catalysis involves the use of catalyst possessing both acidic and basic active sites to mediate biodiesel production. Bi-functional catalysts are associated with efficient biodiesel production from a variety of feedstocks. Consequently, with the aid of these catalysts, simultaneous esterification of free fatty acids and transesterification of triglycerides take place. This results in higher yields and more economical processes for biodiesel production.

2 LITERATURE

2.1 Fatty Acid Methyl Esters

FAME (biodiesel from methanolysis) has a structure that contains a long carbon chain and an ester functional group. Diesel engines can burn biodiesel fuel with no modifications (except for some rubber tube replacement to combat oxidation and corrosion). This is possible because biodiesel is chemically very similar to conventional diesel from petroleum. The only difference in structure is the lack of an active ester group in perodiesel. Furthermore, the sizes of the molecules in biodiesel and petroleum diesel are about the same, but they differ in chemical structure (Devi *et al.,* 2017). Biodiesel molecules consist almost entirely of fatty acid alkyl esters, which contain unsaturated “olefin” components. Low-sulphur petroleum diesel, on the other hand, consists of 95% saturated hydrocarbons and 5% aromatic compounds (Devi *et al.,* 2017)

2.1.1 Advantages of FAME

- Less production costs compared to petroleum diesel.
- Less emissions such as CO_2, CO, SO_2, and particulate matter.
- Prolonged engine performance due to high lubricity and cetane number.

- No mining/ drilling needed, therefore there is a decrease in environmental pollutants.
- Less volatile compared to fossil diesel.
- Engine modification is not required for blends up to B20 (20% biodiesel: 80% fossil diesel).
- Its nontoxic and non-flammable nature reduces fumes, emissions and unpleasant odours.
- Higher combustion efficiency compared to petroleum diesel (Altaie, 2020; Hassan and Kalam, 2013).

2.1.2 Disadvantages of FAME

- A higher cloud point and pour point proves not to be ideal in cold weather which causes challenges in vehicle and ignition start-up.
- Biodiesel has a slightly higher level of NO_x emissions.
- Decreased oxidation stability causes degradation in storage over prolonged periods of time.
- Biodiesel has a viscosity up to 17 times greater than fossil diesel. This leads to difficulties and problems in injector systems, atomisation, pumping as well as combustion in the engine.
- Long-term high viscosity operation effects include the formation of injector deposits, rig sticking, filter plugging, gumming formation and incompatibility of standard conventional lubrication oils (Altaie, 2020; Hassan and Kalam, 2013).

2.2 FAME Production Technologies

There are numerous accepted procedures employed in the synthesis of biodiesel that have been well established over the years with the preference for vegetable oils and animal fats as the main source of feedstock. These feedstocks can be modified to rectify properties such as viscosity in order to produce biodiesel consisting of physical properties suitable for diesel engines (Abbaszaadeh *et al.*, 2019).

2.2.1 Transesterification of Triglycerides

Transesterification otherwise known as alcoholysis is the reaction between an alcohol and triglyceride (Meher *et al.* 2016). It has been widely used to decrease the viscosity of triglycerides. In biodiesel production, these triglycerides are reacted with a basic alcohol, usually methanol to produce FAME and glycerol as a by-product. Transesterification takes place in three successive and reversible intermediate reactions (figure 1) which are highly influenced by the amount of alcohol introduced to the reaction. Even though excess alcohol proves to drive the forward reaction, in some conditions where the operating temperature is higher than the alcohol's boiling point, a lower biodiesel yield is observed (Meher *et al.,* 2016).

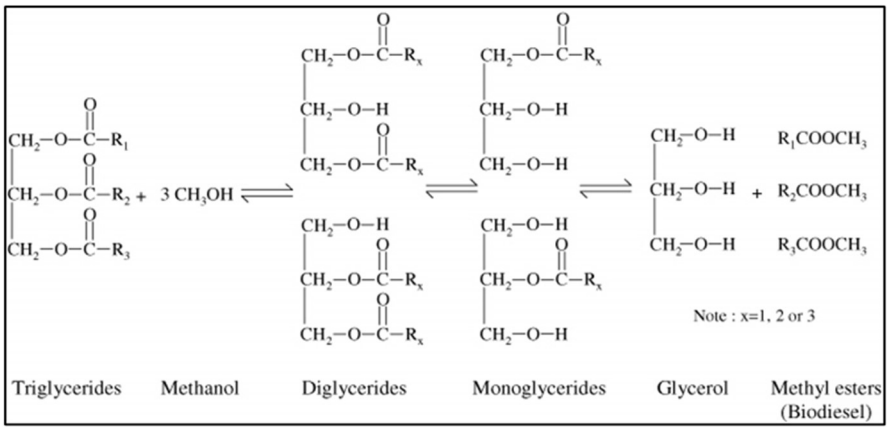

Figure 14: Intermediate reactions in the transesterification process adapted from Rehan et al., (2017)

2.2.2 Esterification of Free Fatty Acids (FFA)

Apart from the presence of triglycerides, many oils contain free fatty acids (FFA). FFA content varies depending on the source of oil as well as whether it has been used or not. Waste cooking oil (WCO) usually has a high FFA content due to their exposure to animal fats and high temperatures. Non-edible plant-based oils such as neem, castor, coconut, Karanja and jatropha also contain higher levels of free fatty acids (Banković *et al*., 2012). A high FFA content poses a great disadvantage to this process as they undergo a saponification reaction in the presence of a basic catalyst. This side reaction is highly undesirable as a lower yield of biodiesel is achieved (Ramadhas, *et al.*, 2015). The by-product (soap) also proves to be tedious and costly to separate from the biodiesel. However, the presence of an acid catalyst aids in the conversion of FFA into methyl esters in the presence of methanol. This process is known as an esterification process (Antolín *et al.*, 2015).

2.3 Catalysts

Catalysts can be mainly classified into two main groups namely homogenous and heterogeneous, where the heterogeneous catalyst can be either mono, bi-functional or bio catalysts. The choice of catalyst in FAME production depends on numerous parameters that include among others the type of oil as well as the alcohol to oil molar ratio used to synthesise biodiesel.

2.3.1 Homogenous Catalysts

Homogenous catalysts, which can be basic or acidic, are catalysts that exist in the same phase as the feedstock and reactants (Hanif *et al.,* 2017). Homogenous base catalysts are extensively used for biodiesel production because of their high rate of reaction as they favour the transesterification of triglycerides due to their reduced mass transfer effect which facilitates faster reaction efficiency (Mansir *et al.*, 2018). The most commonly used homogenous catalysts on an industrial scale are alkoxides and hydroxides of alkali metals such as sodium hydroxide (NaOH), potassium hydroxide (KOH) and sodium methoxide (CH_3ONa) (Mansir *et al.*, 2018). However, a problem arises when the feedstock has

a high FFA content (>1 wt%) (Chuah *et al.*, 2016). An elevated FFA content results in the formation of soap which is undesirable. The use of an acid catalyst hinders this saponification reaction as it favours the esterification of free fatty acids. Acid catalysts have a much slower rate of reaction compared to basic catalysts (Leung *et al.,* 2015). Moreover, the use of homogenous catalysts proves to be expensive as the separation process is very extensive and difficult. Although conventional homogeneous catalysts offer high yields, they are associated with several drawbacks such as an extra neutralisation step, tedious purification process and wastewater generation which result in increased production costs of biodiesel (Guldhe *et al.*, 2017).

2.3.2 Heterogenous Catalysts

Heterogenous catalysts are defined as catalysts that are in different phases from the reacting medium in a reaction process (Gaurav *et al.*, 2019). In the production of biodiesel, the feedstock and reaction medium are in liquid phase and the heterogenous catalyst for the reaction in solid phase (Gaurav *et al.*, 2019). These catalysts could be acidic or basic in nature and can be utilised in the alcoholysis process depending on the feedstock's FFA content (Mansir *et al.*, 2018). Heterogeneous catalysts are gaining interest for conversion of oils to biodiesel due to their advantage of easy separation from the reaction mixture and reuse (Ramli *et al.*, 2016). However, the use of heterogeneous catalysts comes with a fair share of disadvantages. One of the major hurdles associated with the use of solid heterogeneous catalysts for biodiesel production is their very high cost (Tabatabaei *et al.*, 2019). The cost of most solid heterogeneous catalysts is significantly higher than that of homogeneous catalysts. Therefore, the use of solid heterogeneous catalysts at an industrial scale is limited. Furthermore, heterogenous catalysts require some preparatory processes for their synthesis which can be time-consuming. In addition, atmospheric exposure for a prolonged period of time might deter the activity and stability of the catalyst (Mansir *et al.*, 2018).

2.3.3 Bi-functional Catalysts

Bi-functional catalysts exhibit both acidic and basic characters. Consequently, under such catalysis, simultaneous esterification of free fatty acids and transesterification of triglycerides take place (Sánchez-Bayo *et al.*, 2019). More importantly, a bi-functional catalyst can easily be modified and altered to introduce the desired properties and yield so that the presence of FFAs or water do not affect the reaction steps during the transesterification process (Rehan *et al.*, 2017). This flexibility proves to be advantageous as the catalyst can be tailor-made according to the FFA content of the raw material in order to achieve a high yield. For example, any oil with a high FFA (> 2 wt. %) content will require a larger acid to base ratio in order to favour the esterification reaction (Sánchez-Bayo *et al.*, 2019). Whereas for any oil with a relatively low FFA content (< 1 wt. %) a higher conversion to biodiesel will be achieved if a higher ratio of basic to acidic catalyst is used (Sánchez-Bayo *et al.*, 2019). Furthermore, heterogenous bi-functional catalysts can be reused, recycled and regenerated with minimal energy

consumption and inhibit soap formation during the synthesis of methyl esters (Elias *et al.*, 2020). This process requires simple purification and does not require catalyst recovery or aqueous treatment stages (Elias *et al.*, 2020). Solid bi-functional catalysts, due to their heterogenous nature, give better FAME yields as they are more tolerant to feedstocks containing high FFA and water content (Elias *et al.*, 2020). Moreover, they are not soluble in the feedstock which facilitates easy and cheap separation (Elias *et al.*, 2020).

3 EXPERIMENTAL PROCEDURE

3.1 Materials

The feedstock for FAME production included methanol, virgin palm oil (VPO), waste palm oil (WPO), and neem oil. The virgin and waste oils were procured from an oil manufacturing company SupaOil (Cape Town, South Africa). Methanol (>99.9% purity) was procured from Merk Millipore. Catalyst synthesis required the use of Calcium nitrate $Ca(NO_3)_2.4H_2O$ (98%, AceChem), aluminium nitrate, $Al(NO_3)_3.9H_2O$ (98%, AceChem) and sodium hydroxide (NaOH) pellets (Merck, 98%), as the initial reagents for co-precipitation. Calcium oxide (99%, Merk) and recalcined aluminium oxide (98%, Merk) were utilised in the impregnation method for catalyst preparation.

3.2 Catalyst Preparation and Analysis

The heterogeneous bi-functional catalyst of choice was a mixture of calcium oxide (CaO) and alumina (Al_2O_3) providing basic and acidic sites respectively. The basic to acidic ratios were 50:50, 60:40, 70:30 and 80:20. Respective to these ratios, on a weight basis, the corresponding amounts of calcium nitrate ($Ca(NO_3)_2.4H_2O$) and aluminium nitrate ($Al(NO_3)_3\ 9H_2O$) were, in a 2L flask, mixed well in enough deionised water to dissolve the salts. The solution was then heated with the use of a hot plate. Separately,4M NaOH solution was heated until slight bubbling was visible. The two solutions were mixed under a stirrer and instantaneous precipitation took place. The very viscous suspension/solution was then continuously stirred for 45 minutes at 1500 rpm and was kept at a temperature of 100 °C to promote the nucleation dissolution process. The milky solution was then taken off the hot plate and was allowed to cool down for 30 minutes. The precipitate was then filtered and oven dried overnight. Thereafter, the dried precipitate was ground up using a pestle and mortar and calcined (600 °C, 5 °C/ min, 13.3 h).

The samples were then characterised via BET where they were dried via nitrogen purging or vacuum applied at elevated temperatures. The volume of the gas absorbed to the surface of the particles was measured at the boiling point of nitrogen (-196 °C). Thereafter, the amount of absorbed gas was correlated to the pores and surface area of the sample. Nitrogen was used as the adsorbate gas which enabled the determination of volume and size distribution of the catalyst micropores between the measurements of 0.35 – 2.0 nm. The catalyst samples were degassed at a temperature of 200 °C and

p/p0 ranged between 0.05 and 0.3. This was done to determine catalyst pore size, pore volume and surface area.

3.3 FAME Production

The trans(esterification) reaction was carried out in a 200ml flask using a 12:1 methanol/oil ratio and catalyst loading of 2.5 wt%. the temperature was maintained at 65 °C under continuous mixing at an agitation rate of 1200 rpm (Zabeti et al., 2009). The reaction apparatus was then turned off and the flasks were allowed to cool down for 5 min. This was followed by the sieving out of the catalyst and the decanting of the now synthesised FAME and by-product mixture into a separating funnel. The top layer consisted of methyl esters whereas the bottom layer predominantly consisted of glycerol with visible traces of unreacted methanol and water. These by-products were drained out after 1 h. The biodiesel was then subjected to centrifugation (6000 rpm) for further separation of intermediates and glycerol present. Further purification was achieved by cleaning the biodiesel with hot distilled water. This was done to dissolve any remnants of glycerol or methanol in the crude biodiesel. This washing procedure was repeated until the water drained was colourless which indicated that the various impurities were completely removed. To ensure minimal water content, the biodiesel was subjected to a drying agent (Na_2SO_4, >90%, Sigma-Aldrich) and was heated up until no bubbling was present, indicating complete water absorption and evaporation. Thereafter, the biodiesel was allowed to cool for 15 minutes and yield was calculated using equation 1

$$\%\,\boldsymbol{Yield} = \frac{\boldsymbol{Mass_{Biodiesel}}}{\boldsymbol{Mass_{Feeddstock\ oil}}} \times \mathbf{100} \qquad \textbf{Equation 10}$$

4 RESULTS AND DISCUSSION

4.1 Catalyst Characterisation

The catalyst surface areas were in the range of 11 – 13.5 m2/g. An adequate surface area required for good catalytic activity on a heterogeneous catalyst in the transesterification of oils is >8 m2/g (Chingakham, Tiwary and Sajith, 2019). Hence the catalyst surface areas were adequate and effective. Pore diameters of >209.5 Å were measured. Similarly, a high pore volume is crucial in the activity of a catalyst as it assists in the efficient diffusion as well as an increased rate of absorption of reactants (Tshizanga, 2015). High pore volumes (0.72 to 0.91 cm3/g) were observed (Table 1). The catalysts are considered to be very porous as a high pore diameter and volume are reported to be above 100 Å and 0.07 cm3/g respectively (Chingakham, Tiwary and Sajith, 2019). High surface area, porosity and pore volumes are crucial as they enhance overall catalytic activity and catalyst performance. Good catalytic activity might reduce catalyst loading, improve biodiesel yield and ultimately, biodiesel production costs (Ngoie et al., 2019)

Table 1: Catalyst Pore Diameter, surface Area and Pore Volume

$CaO:Al_2O_3$ ratio	Surface Area (m^2/g)	Pore Diameter (Å)	Pore Volume (cm^3/g)
80:20	13.47	227.09	0.090
70:30	13.30	233.82	0.091
60:40	11.11	231.76	0.076
50:50	11.04	209.51	0.072

4.2 Overall Biodiesel Yields

Three feedstocks (virgin palm, waste palm and neem oil) with FFA contents of 0.67, 2.47 and 3.25 wt% respectively, underwent trans(esterification) catalysed by 80%CaO:20%Al_2O_3, 70%CaO:30%Al_2O_3, 60%CaO:40%Al_2O_3 and 50%CaO:50%Al_2O_3. Virgin palm oil (VPO) had the lowest FFA content amongst the three feedstocks and achieved its highest yield of 97.9% with the use of 80%CaO20%Al_2O_3. Due to its low FFA content, minimal esterification was required and consequently, less acidic sites (Al_2O_3) (Sánchez-Bayo *et al.*, 2019). Moreover, the basic catalysed transesterification reaction was dominant and therefore the catalyst with the highest ratio of basic sites (80%CaO) was most efficient. This is further elaborated by the steady decline in VPO FAME yield as CaO content in the catalysts decreased (Figure 2).

Waste palm oil had a high FFA content (>1wt%) (Mansir *et al.*, 2018). The lowest yield was produced with the use of 80%CaO:20%Al_2O_3. This is attributed to the lack of sufficient acidic sites to facilitate optimal FFA conversion. Moreover, the high amount of basicity in 80%CaO:20%Al_2O_3 produced glycerol in the presence of FFA which consequently lowers the yield (Bhoi, Singh and Mahajani, 2017). In contrast, 70%CaO:30% Al_2O_3 produced the highest yield at 99.51% (Figure 2). The presence of FFA in conjunction with an acid catalyst accelerates the formation of biodiesel (Bhoi, Singh and Mahajani, 2017), as an increase in acid ratio facilitated the esterification of FFA (Sánchez-Bayo *et al.*, 2019). Moreover, FFA enhances solubility in the oil phase under acid catalysed conditions (Bhoi, Singh and Mahajani, 2017). 60%CaO:40%Al_2O_3 and 50%CaO:50%Al_2O_3 produced yields of 94.08% and 89.88% respectively. This decline in yield is attributed to the amount of alumina beyond the 70:30 ratio, which hindered the main transesterification reaction as the number of basic sites were not sufficient for optimal triglyceride conversion.

Neem oil had the highest FFA content and therefore a catalyst with more acidic sites would be more favourable. This is evident as 60%CaO:40%Al_2O_3 produced the highest yield (97.63%). The poorest performing catalyst however was 50%CaO:50%Al_2O_3, which had the highest amount of alumina and therefore acidic sites. The initial calcium oxide to alumina ratio plays a major role in the microstructure as well as the physical properties of the catalyst where the more the calcium particles are dispersed in

the alumina matrix, the more porous the structure (Salomão *et al.*, 2017). A decrease in CaO content therefore results in a decrease of catalyst porosity and surface area. Due to this, there is inadequate mass transfer as the conversion of large triglyceride molecules are hindered (Ljupkovi *et al.*, 2014). This is seen in the decline of neem FAME yield beyond the 60:40 ratio (Figure 2).

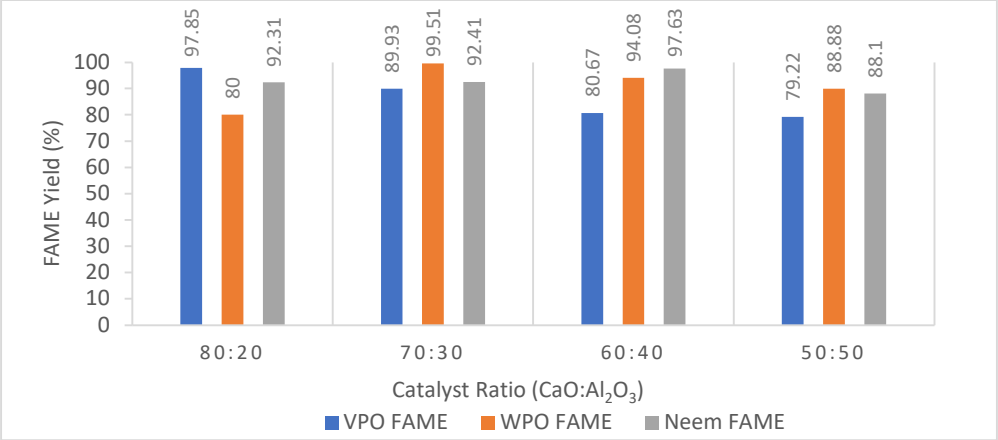

Figure 2: Overall Biodiesel Yields

5 CONCLUSIONS

This study showed that catalysts synthesised via co-precipitation proved to be highly effective in improving FAME yield (99.51%) through the simultaneous esterification and transesterification of low-grade high FFA feedstocks (2.47-3.25). Under optimum conditions, the FAME yield obtained using low-cost waste feedstocks was higher to what was obtained (97.85) using edible oil. The four catalysts were characterised with large pore sizes (>209 Å), high surface areas (>11 m^2/g) and pore volumes (>0.072 cm^3/g). The most basic catalyst (80%CaO:20%Al_2O_3) was most effective for the feedstock with least FFA content while the counterpart catalyst (60%CaO:40%Al_2O_3) which had a higher alumina loading and resultantly more acidic sites, achieved an optimal biodiesel yield in the feedstock with the highest FFA content. Hence, the higher the FFA content, the more amenable it is to a higher acidic content catalyst. This emphasises the need to synthesise tailor-made catalysts according to FFA content of raw material in order to achieve high yields.

REFERENCES

Abbaszaadeh, A., Ghibadian, B., Omidkah, M. R., Najafi, G. (2019) 'Current biodiesel production technologies: A comparative review', *Energy Conversion and Management*, 63, pp. 138–148.

Alaba, P., Sani, Y. and Ashri Wan Daud, W. (2016). Efficient biodiesel production via solid superacid catalysis: a critical review on recent breakthrough. *RSC Advances.*, 6(82), pp.78351-78368.

Antolín, G.Tinaut, F. V., Briceo, Y., Castao, V., Perez, C., Ramirez, A. I. (2015) 'Optimisation of biodiesel production by sunflower oil transesterification', *Bioresource Technology*, 83(2), pp. 111–114.

Banković-Ilić, I. B., Stamenković, O. S. and Veljković, V. B. (2012) 'Biodiesel production from non-edible plant oils', *Renewable and Sustainable Energy Reviews*, 16(6), pp. 3621–3647.

Bhoi, R., Singh, D. and Mahajani, S. (2017) 'Reaction Chemistry & Engineering simultaneous esterification and transesterification', Reaction Chemistry & Engineering. Royal Society of Chemistry, 2, pp. 740–753.

Chingakham, C., Tiwary, C. and Sajith, V. (2019) 'Waste Animal Bone as a Novel Layered Heterogeneous Catalyst for the Transesterification of Biodiesel', *Catalysis Letters*. Springer US, 149(4), pp. 1100–1110

Chuah, L. F., Yusup, S., Aziz. A. R. A., Klemes, J. J., Bokhari, A., Abdullah, M. Z. (2016) 'Influence of fatty acids content in non-edible oil for biodiesel properties', *Clean Technologies and Environmental Policy*, 18(2), pp. 473–482.

Devi, A., Das, V. K. and Deka, D. (2017) 'Ginger extract as a nature based robust additive and its influence on the oxidation stability of biodiesel synthesized from non-edible oil', *Fuel*. Elsevier Ltd, 187(September), pp. 306–314.

Elias, S. Rabiu, A., Okeleye, B. I., Okudoh, V., Oyekola, O. (2020) 'Bifunctional heterogeneous catalyst for biodiesel production from waste vegetable oil', *Applied Sciences (Switzerland)*, 10(9).

Frost, A. and Sullivan, G. (2016) *Innovation earns company biofuels award*.

Gaurav, A. Dumas, S., Mai, C. T. Q., Ng, F. T. T. (2019) 'A kinetic model for a single step biodiesel production from a high free fatty acid (FFA) biodiesel feedstock over a solid heteropolyacid catalyst', *Green Energy and Environment*, 4(3), pp. 328–341.

Guldhe, A. Singh, P., Ansari, F. A., Singh, B., Bux, F. (2017) 'Biodiesel synthesis from microalgal lipids using tungstated zirconia as a heterogeneous acid catalyst and its comparison with homogeneous acid and enzyme catalysts', *Fuel*. Elsevier Ltd, 187(January), pp. 180–188.

Hanif, M. A., Nisar, S. and Rashid, U. (2017) 'Supported solid and heteropoly acid catalysts for production of biodiesel', *Catalysis Reviews*, 59(2), pp. 165–188.

Leung, D. Y. C., Wu, X. and Leung, M. K. H. (2015) 'A review on biodiesel production using catalyzed transesterification', *Applied Energy*. Elsevier Ltd, 87(4), pp. 1083–1095.

Ljupkovi, R. B. Mi, R> D., Tomi, M. D., Radulovi, N. S., Aleksander, L. J., Zarubica, A. R. (2016) 'Significance of the structural properties of CaO catalyst in the production of biodiesel : An effect on the reduction of greenhouse gas emissions', *Hemijska Industrija,* pp. 399–412.

Mansir, N., Teo, S. H., Rashid, U., Saiman, M. I., Tan, Y. P., Alsultan, G. A., Taufiq-Yap, Y. H. (2018) 'Modified waste egg shell derived bifunctional catalyst for biodiesel production from high FFA waste cooking oil. A review', *Renewable and Sustainable Energy Reviews*, 82(October), pp. 3645–3655.

Meher, L., Vidyasagar, D. and Naik, S. (2016) 'Technical aspects of biodiesel production by transesterification—a review', *Renewable and Sustainable Energy Reviews*, 10(3), pp. 248–268.

Ngoie, W. I., Welz, P. J., Ikhu-Omoregbe, D., Oyekola, O. O. (2019) 'Heterogeneous nanomagnetic catalyst from cupriferous mineral processing gangue for the production of biodiesel', *Catalysts*, 9(12).

Ramadhas, A. S., Jayaraj, S. and Muraleedharan, C. (2015) 'Biodiesel production from high FFA rubber seed oil', *Fuel*, 84(4), pp. 335–340.

Ramli, A., Farooq, M., Naeem, A., Khan, S., Hummayun, M., Iqbal, A., AHmed, S., Shah, L. A. (2016) 'Bifunctional Heterogeneous Bifunctional Heterogeneous Catalysts Catalysts for for Biodiesel Biodiesel Production using Low Cost Feedstocks : A Future Production using Low Cost Fe'. *World ' s largest Science , Technology & Medicine Open Access book publisher*

Rehan, M. and Arabia, S. (2017) 'Influence of homogenous and heterogeneous catalysts on biodiesel production', *Renewable Energy Sources.*

Sánchez-Bayo, A. (2019) 'Biodiesel production (FAEEs) by heterogeneous combi-lipase biocatalysts using wet extracted lipids from microalgae', *Catalysts*, 9(3), pp. 1–15.

Sebastian, J., Muraleedharan, C. and Santhiagu, A. (2016) 'A comparative study between chemical and enzymatic transesterification of high free fatty acid contained rubber seed oil for biodiesel production', *Cogent Engineering*. Cogent, 3(1), pp. 1–12.

Tabatabaei, M., Aghbashlo, M., Dehhaghi, M., Panahi, H. K. S., Mollahosseini, M., Soufiyan, M. M. (2019) 'Reactor technologies for biodiesel production and processing: A review', *Progress in Energy and Combustion Science*, 74, pp. 239–303.

Tshizanga, N. (2015) 'A study of biodiesel production from waste vegetable oil using eggshell ash as a heterogeneous catalyst', *South African Journal of Chemical Engineering*

Yadav, M., Chavan, S. B., Singh, R., Bux, F., Sharma, Y. G. (2019) 'Experimental study on emissions of algal biodiesel and its blends on a diesel engine', *Journal of the Taiwan Institute of Chemical Engineers*. pp. 160–168.

Zabeti, M.; Daud, Wan, M.A.W.; Aroua, M.K. Activity of solid catalysts for biodiesel production: A review, *Fuel Process. Technol*ogy. 90(6), 770–777

Performance Evaluation of Activated Carbon Derived from Macadamia Nut Shells and Multiwalled Carbon Nanotubes for Effective Removal of BTEX Compounds from Industrial Wastewater using Adsorption Process: Comparative Study

K. Melaphi[1], O.O. Sadare[1*], K. Moothi[1] and G.S. Simate[2]

[1] Department of Chemical Engineering, Faculty of Engineering and the Built Environment, Doornfontein Campus, University of Johannesburg, P.O. Box 17011, Johannesburg, 2028, South Africa

[2] School of Chemical and Metallurgical Engineering, Faculty of Engineering and the Built Environment, University of the Witwatersrand, Johannesburg, Wits 2050, South Africa.

*Corresponding author: wumisadare@gmail.com

ABSTRACT

Benzene, Toluene, Ethylbenzene and Xylenes (BTEX) compounds are aromatic compounds present in common groundwater and potable water as pollutants. The negative health effects that result from exposure of these pollutants have necessitated research in this direction. This study investigated the adsorptive performance of multiwalled carbon nanotubes (MWCNTs) and macadamia nuts-derived activated carbon (MACs) for the removal of BTEX compounds from synthetic industrial wastewater. The adsorbents were characterised using Fourier Transform Infrared Spectra (FTIR) to check the surface functional groups of the adsorbents, the textural properties were obtained by Brunauer-Emmett-Teller (BET) and Scanning Electron Microscopy (SEM) was used to check the surface morphology of the adsorbents. Adsorption capacitiies for activated carbon were calculated to be 17.59 mg/g, 57.59 mg/g, 55.59 mg/g and 51.59 mg/g for benzene, toluene, ethylbenzene and xylene removal, respectively. The adsorption capacities of carbon nanotubes were at 17.46 mg/g, 41.63 mg/g 35.23 mg/g and 37.98 mg/g for benzene, toluene, ethylbenzene and xylene removal, respectively. The adsorption mechanisms of the adsorbents were comprehensively described using Langmuir and Freundlich isotherm isotherms. Experimental data showed that Langmuir isotherm model best described the adsorption mechanism of MWCNTs and MACs adsorbents. Pseudo first -order and Pseudo second –order kinetic models were used to describe the adsorption kinetic studies. MACs proved to be a better adsorbent precursor than MWCNTs based on high surface area and large pore volume.

Keywords: Adsorption; BTEX; multiwalled carbon nanotubes; macadamia nut activated carbon, wastewater.

1 INTRODUCTION

The scarcity of fresh water is continuously increasing due to the increase in water pollution. The release of untreated pollutants to surface water and ground water by industries is affecting the livelihood of aquatic animals and human health. BTEX compounds are common ground water and surface water

pollutants especially from petroleum industries (Hackbarth et al., 2014). These compounds have many applications such as manufacturing of thinners, adhesives, inks, and many pharmaceutical products (Almedia et al., 2012, Saha et al., 2011).They are often not treated or detected in municipal treatment systems. An example of this is seen in a study conducted by Makhathini et al., 2015, which stated that BTEX compounds limits were not reported in the effluent trade acceptance document at the EThekwini municipality, thus, the wastewater treatment plants are unable to adequately remove all BTEX pollutants from industrial wastewater. As a result of this, exposure of BTEX compounds has led to many health problems such as drowsiness, cancer, respiratory problems and sensory irritation. Due to the health problems caused, removal of BTEX is essential.

2 LITERATURE

BTEX compounds are introduced to the environment through leakages from underground storage tanks, pipelines, accidental spillages and improper waste disposal practices, causing contamination of surface soils, sea water and groundwater environment (Chriac et al., 2007). The United States Environmental Protection Agency (USEPA) categorized BTEX as pollutants that are highly toxic (Fadaei et al., 2017; Mohammadi et al., 2017). According to the World Health Organization, benzene is the most toxic among the BTEX, as it is a strong carcinogenic (Mathur, 2007, Njobuenwu et al., 2005). Various techniques have been applied to remove BTEX from aqueous solution such as bioremediation (Toth et al., 2015), phytoremediation (Dhankher et al., 2012), air stripping (El-Behlil et al., 2012) and adsorption (Makhathini et al., 2017; Hackbarth et al., 2014). However, these techniques have limitations such as, fouling, high operational costs, and they are time consuming (Toth et al., 2015, Godambe et al., 2017). Among these, adsorption techniques have been considered to be the most effective technique for removing BTEX compounds because, it can incur low cost while showing high efficiency and it is easy to operate (Fayemiwo et al 2017, Agarwal et al.,2017). Various adsorbents such as polysterine resin, tannin based-adsorbent, natural zeolites, carbon nanotubes and activated carbons, have been used to remove BTEX compounds from wastewater through adsorption processes. The Macadamia nut shells are agricultural waste materials which are abundant. In the world, South Africa is the third largest producer of macadamia nutshells (Edokpayi et al., 2020). Activated carbon derived from Macadamia nutshells are promising adsorbent precursors for the removal of various pollutants (Pakade et al., 2016, Wongcharee et al., 2017). Dao et al. (2020) reported the removal of Cu2+ and Zn2+ using activated carbon derived from macadamia nut shells. Pezoti et al. (2014) also reported the adsorptive capability of activated carbon derived from macadamia nutshells for the removal of methylene blue. Activated carbons from macadamia nutshells are known for their microporous and mesoporous structures with high surface area between 700-1100 m2/g (Rotocarb activated carbon, 2020). Therefore, they have reactive sites on their surface, which make them have high adsorption

capacity. However, as far as it can be ascertained, there are limited studies in literature on the treatment of BTEX contaminated water using activated carbon derived from macadamia nutshells

Carbon nanotubes (CNTs) have gained popularity as effective adsorbents because of their physical and chemical properties (Pillai et al., 2011). They are used in various industrial applications such as water treatment plants as membrane structures, energy storage as well as sensor applications. Simate et al., (2012) reported the removal of heavy metals and inorganic pollutants using CNTs. Carbon nanotubes have high adsorption characteristics for adsorption of BTEX (Fadaei et al., 2017; Bina et al., 2014). This is because they have surface functional groups, porous structure and have large surface area (Simate et al., 2011). These attributes are essential for adsorption process. For the first time, in this study, activated carbon obtained from Macadamia nut shells was used for effective removal of BTEX compounds from water, and compared to the adsorption performance of carbon nanotubes. Effect of operating variables such as contact time, adsorbent dosage and adsorbate concentration were also studied. In order to study and provide information about the nature of interactions between the adsorbent and adsorbate, the Langmuir and Freundlich isotherm models were used in this study. Furthermore, Pseudo first-order and Pseudo second-order kinetic models were used to give information about the adsorption rate, path way and mechanism of the adsorption process.

3 EXPERIMENTAL PROCEDURE

3.1 Materials and Methods

The macadamia nutshell activated carbons (MAC, 250 microns) used in this study were donated by Rotocarb Activated Carbons, Olifantsfontein, South Africa. As-received multi-walled carbon nanotubes (MWCNTs, 95 % purity), with pore size of 263.717 nm were purchased from Sigma Aldrich Pty (Ltd), Johannesburg. Benzene (purity: 99.7%), toluene (purity: 99.7%), ethylbenzene (purity: 99.7%), and Xylene (purity: 99.7%) were also purchased from Sigma Aldrich. The macadamia nut activated carbons, MWCNTs and chemicals were used as received without any further purification. The laboratory glassware used were washed with 5 % v/v nitric acid and rinsed thoroughly with distilled water. All experiments were carried out at room temperature.

3.2 Characterization of macadamia nut shell and multiwalled carbon nanotubes

The surface morphology of the adsorbents was checked using Scanning Electron Microscope (SEM), the samples were initially coated with carbon to obtain good images. Brunauer-Emmet-Teller (BET) was used to check textual properties such as specific surface area, pore volume, and pore size distribution. The samples were determined by physical adsorption of nitrogen at 77 K using a Nova 3200e instrument. The samples were degassed at 150 °C up to 4 hours before measurement. The surface functional groups of the nanomaterials were checked using Fourier-Transformed Infrared (FTIR) spectroscopy Perkin Elmer Two ATR-FTIR equipment A portion of KBr powder was combined with

MACs and MWCNTs. The combination was pulverized for 5 minutes in a mortar to fine powder. The pellets were placed on the FT-IR sample holder for analysis. The spectra for MAC and MWCNT were obtained in a frequency band range from 500 to 4000 cm^{-1}.

3.3 Removal of BTEX using MACs and MWCNTs

The adsorption of BTEX onto MACs and MWCNTs was conducted by using batch adsorption experiments. The synthetic wastewater was prepared by dissolving 100 mg/L of each of the compounds (Benzene, Toluene, Ethyl benzene and Xylene) in distilled water in a 250 mL volumetric flask to prepare the stock solution The adsorption experiments were performed by varying the adsorbent dosage (20 mg – 65.5 mg) and adding to 100 mL BTEX synthetic wastewater at different BTEX initial concentrations (50, 100, 150, 200, and 250 mg/L) at contact times between (2 – 60 min. The flasks were enclosed with a cap and placed in the orbital shaker incubator running at 180 rpm at room temperature for 60 minutes to allow dissolution of BTEX compounds (Fadaei et al., 2017). The samples solutions were filtered after specific time intervals (2-60 mins) of agitation using 0.45 microfiber filter. The concentration of the filtrate left was then determined and recorded using the UV- Vis between 215 nm and 261 nm. The percentage removal of the BTEX compounds was calculated using Equation 2. All experiments were done in duplicates, to ensure accuracy of the results and only the mean values were reported. Blank experiments, without the addition of adsorbents, were also conducted to ensure that the decrease in BTEX concentration was not due to adsorption on the wall of the glass bottle or volatilization.

$$\%Q = \left(\frac{(C_o - C_e)}{C_o}\right) \times 100 \qquad \textbf{Equation 1}$$

Where %Q is the BTEX removal with respect to initial concentration, C_o is the Initial concentration of BTEX in the flask in mg/L, C_e is the concentration at equilibrium in mg/L. To determine the percentage removal of BTEX, the expression in Equation 2 was used;

$$\text{Removal efficiency, } \% = \frac{C_o - C_e}{C_o} \text{ x } 100 \qquad \textbf{Equation 2}$$

Results from Equation 1 were used to determine the Langmuir (Equation 3) and Freundlich (Equation 4) isotherms. The adsorption kinetics were modelled using pseudo first order (Equation 5) and pseudo second order (Equation 6) equations.

$$\frac{1}{q_e} = \frac{1}{q_{max}} + \frac{1}{k_L q_{max}} x \frac{1}{c_e} \qquad \textbf{Equation 3}$$

$$\ln_{q_e} = \ln_{kf} + \frac{1}{n}\ln_{ce} \qquad \textbf{Equation 4}$$

$$(q_e - q_t) = \ln_{qe} - k_{1t} \qquad \textbf{Equation 5}$$

$$\frac{t}{q_t} = \frac{1}{k_2\, q^2} + \frac{t}{q_e}$$ **Equation 6**

4 RESULTS AND DISCUSSION

4.1 Characterization of MACs and MWCNTs

Table 1, presents the textural properties of the MACs and MWCNTs adsorbents. The Brunauer-Emmett-Teller (BET) technique was used to check the textural properties of MACs and MWCNTs. From Table 1, it is shown that MACs has higher specific surface area compared to MWCNTs. This might be due to its micro-pore size of 24.189 nm and the temperature employed during synthesis which determine the specific surface area (Kemp et al., 2015).

Table 1: Textural properties of the adsorbent from BET analysis

Adsorbent	Surface area (m^2/g)	Pore Volume (cm^3/g)	Pore Size (nm)
Activated Carbon	405.56	0.2051	24.19
Carbon nanotubes	56.86	0.0057	263.72

Figure 1, shows the SEM surface morphology of MACs and MWCNTs. The MACs shows a surface structure which has high porosity, with elongated pores this confirms that MAC has plant based lignocellulose structure which indicates that during activation process non carbon materials were removed (Phele et al., 2019). The presence of mesopores and macropores is observed which explains the high surface area from the BET results. The structure also appeared to be glossy and smooth. Similar results were obtained by Wongcharee et al. (2018). Moreover, multiwalled carbon nanotubes had large agglomerations which were packed tightly with a rough surface. This might be due to structural defects during their growth and interactions of van der Waals forces (Alig et al., 2012).

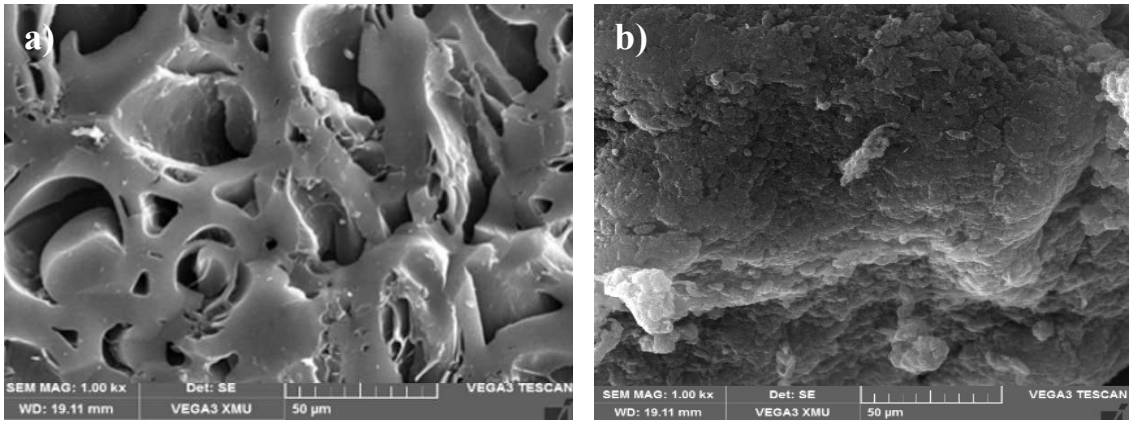

Figure 1: SEM image of (a) macadamia nut activated carbon, (b) multiwalled carbon nanotubes

Figure 2. Illustrates the surface functional groups on the surfaces of MACs and MWCNTs. The infrared spectrum of the MACs shows more intense bands than MWCNTs, although some bands are visible. The adsorption band at 3455 cm-1 represents the OH stretching vibration of hydroxyl functional groups for MAC. The decreasing intensity of OH for MWCNTs could be associated with the water used and the stretching of the carbon nanotubes (Azri et al., 2017). The bands at 1634 cm -1 to 1119 cm-1 are ascribed to C-O and C=O which attributes to the presence of carboxylic acids (Wongcharee et al., 2018; Sadare and Daramola, 2019). The presence of carboxylic groups can be attributed to partial oxidation during purification by the manufacturer (Azri et al., 2017). The adsorption band at 1351 cm-1 is ascribed to C=C stretching of the aromatic rings, which indicates the presence of carbon in the macadamia nut activated carbon and multiwalled carbon nanotubes (Mopoung et al., 2015). The results observed in this study are comparable to literature (Tsolele et al., 2019, Phele et al., 2019, Azri et al., 2017)

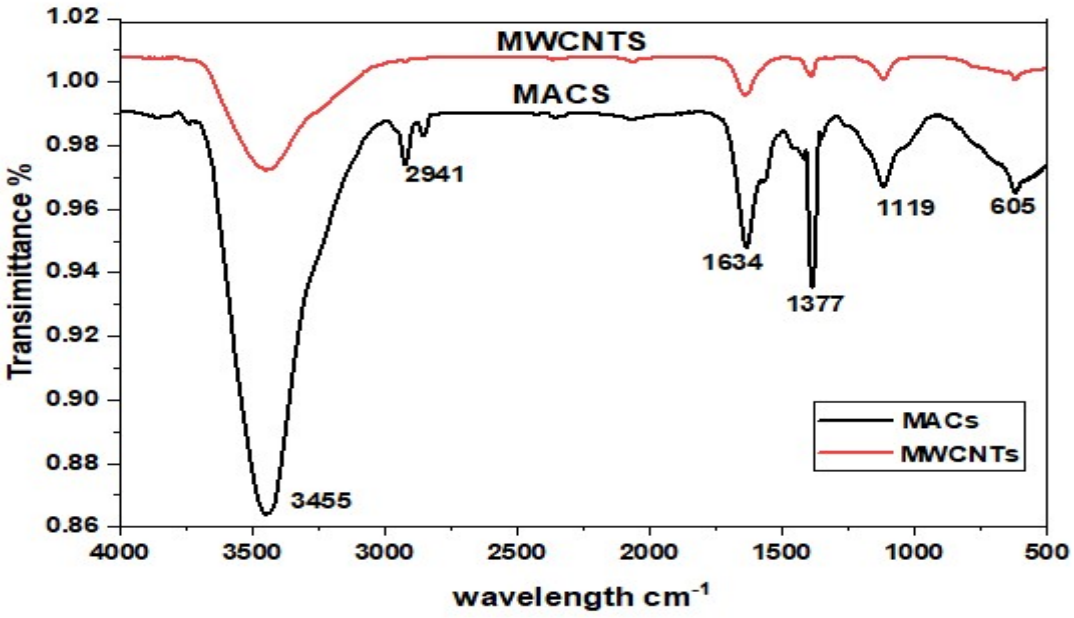

Figure 2: FTIR spectra of MWCNTs and MACs

4.2 Performance Evaluation of MAC and MWCNT for Adsorptive Removal of BTEX Compounds from a Synthetic BTEX Solution

4.2.1 Effect of contact time

The results for the effect of adsorbent contact time are shown in Figure 3. The contact time was varied from 2 to 60 minutes. The removal percentage of BTEX increased with increase in contact time. The gradual increase from 0 to 20 minutes for MACs might be due to the large adsorption sites that are

available at the beginning of the adsorption. However, they subsequently decreased with an increase in contact time as the adsorption sites become saturated (Sadare and Daramola 2019 b; Sadare et al., 2020). The equilibrium contact time was achieved after 20 minutes for MACs whereas for MWCNTs it was achieved after 40 minutes. This might be due to the increase in pore volume from BET results.

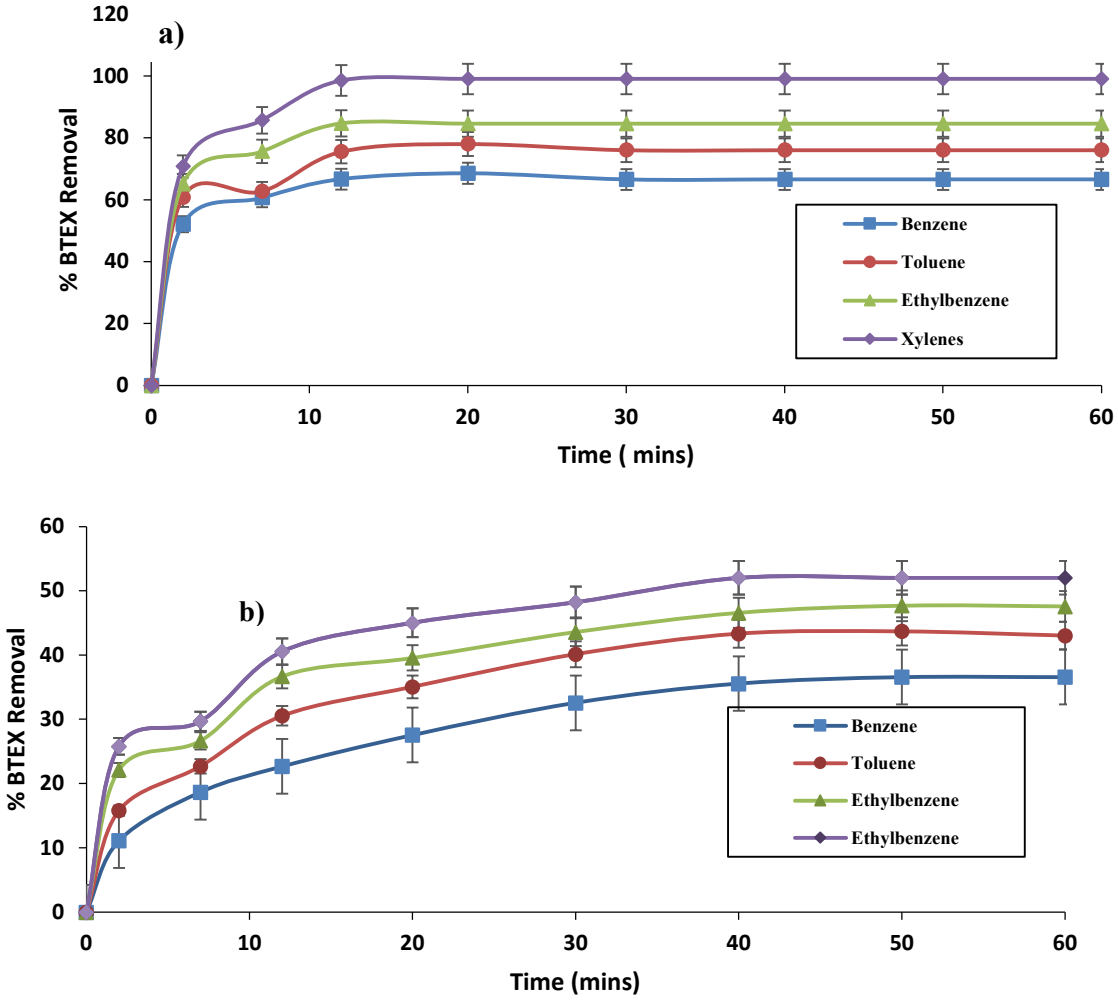

Figure 3: Effect of contact time on the adsorption of BTEX compounds from synthetic aqueous solution using (a) MACs, (b) MWCNT. (m= 0.025g, Co=100 mg/L, speed= 180 rpm, temp=25°C)

4.2.2 Effect of adsorbent dosage

Figure 4a and Figure 4b depict the effect of adsorbent dosage 0.02 g – 0.0655 g at 100mg/L MACs and MWCNTs, respectively. The percentage removal of BTEX compounds increased when the amount of dosage increased. This might be due to the increase in active adsorption sites (Godwa et al., 2012, Phele et al., 2019). It can be seen that increasing the adsorbent loading beyond 0.025g has little effect on the equilibrium loadings of the BTEX compounds of the adsorbents. This could be as a result of accumulation of BTEX compounds onto the surfaces of the MACs and MWCNTs (Rodrigues et al.,

2013).Therefore, 0.025g was used as the optimum dosage. As observed, removal percentage using MACs was higher than MWCNTs with approximately 30 %. The removal percentage of BTEX followed the order B<T<EB<X.

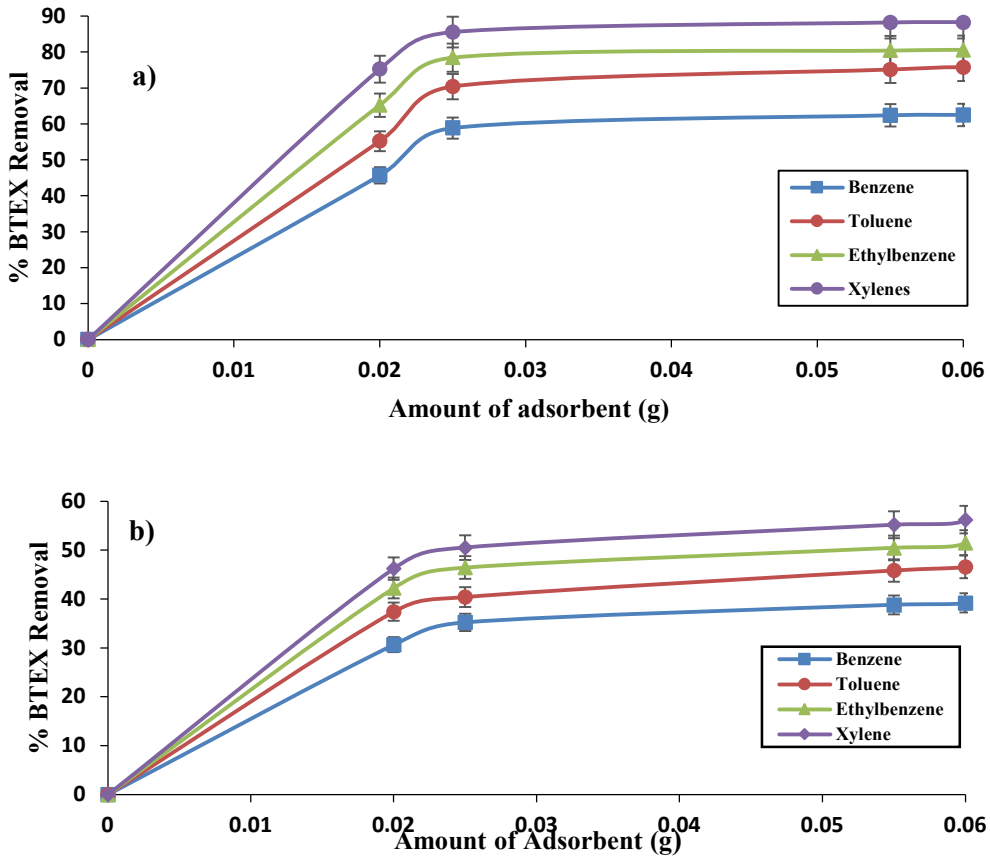

Figure 4: Effect of adsorbent dosage on the adsorption of BTEX compounds from synthetic aqueous solution using a) MACs, b) MWNTs (contact time= 60 minutes, Co= 100 mg/L, speed: 180 rpm, temp 25 °C)

4.2.3 Effect of initial concentration of BTEX compounds

The effect of initial adsorbate concentration on the removal of BTEX compounds by MAC and MWCNTs is shown in Figure 5a and Figure 5b, respectively. The initial concentration of BTEX was varied from 0 to 250 mg/L while all other adsorption parameters were kept constant. The adsorption removal of BTEX increased from 0 to 100 mg/L for MAC while for MWCNTS there was increase from 0 to 150 mg/L. The results indicate that at lower concentrations, there was reduction in adsorption rate while at higher concentrations there was depletion of active sites. However, decrease in percentage removal of BTEX was observed at increased initial concentration. Similar results were obtained by Tsolele et al. (2019) and Sadare and Daramola (2019a).

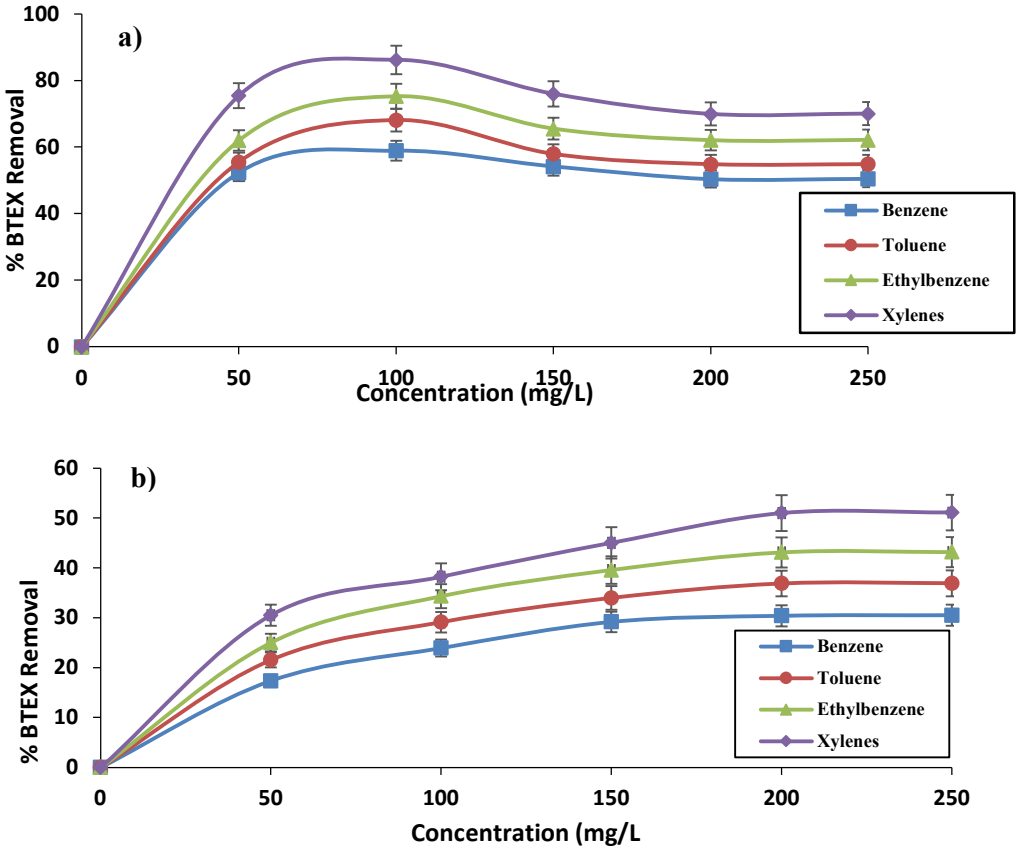

Figure 5: Effect of initial concentration on the adsorption of BTEX compounds from synthetic aqueous solution using a) MACs, b) MWCNTs. (Contact time = 60 minutes, Mass of adsorbents = 0.055 g, Stirring speed: 180 rpm, Temp = 25°C).

5 CONCLUSIONS

This study successfully evaluated the performance of macadamia nut activated carbon (MACs) and multiwalled carbon nanotubes (MWCNTs) for the removal of BTEX compounds from a synthetic BTEX-containing water. The following conclusions were drawn from the study;

According to the results MACs performed better than MWCNTs, this might be due to the larger surface area and larger pores (Table 1). Results obtained from this study indicate that MACs and MWCNTs are good alternative adsorbent materials for effective removal of BTEX compounds, from wastewater. They can be regenerated and have good adsorption capacities, making the adsorption process a cheaper technique compared to other conventional techniques of treating BTEX-contaminated water (Makhathini et al., 2017; Dehdashti et al., 2017).

REFERENCES

Alig, I., Pötschke, P., Lellinger, D., Skipa, T., Pegel, S., Kasaliwal, G.R. and Villmow, T., 2012. Establishment, morphology and properties of carbon nanotube networks in polymer melts. *Polymer*, *53*(1), pp.4-28.

Agarwal, M. and Singh, K (2017). Heavy metal removal from wastewater using various adsorbents: a review. *Journal of Water Reuse and Desalination*, *7*(4), pp.387-419.

Almeida, I.L.S., Filho, N.R.A., Alves, M.I.R., Carvalho, B.G. and Coelho, N.M.M., 2012. Removal of BTEX from aqueous solution using Moringa oleifera seed cake. *Environmental technology*, *33*(11), pp.1299-1305.

Azri, F.A., Sukor, R., Hajian, R., Yusof, N.A., Bakar, F.A. and Selamat, J., 2017. Modification strategy of screen-printed carbon electrode with functionalized multi-walled carbon nanotube and chitosan matrix for biosensor development. *Asian Journal of Chemistry*, *29*(1), p.31.

Bina, B, Amin, M.M, Rashidi, A. and PourzamanI, H (2014). Water and wastewater treatment from BTEX by carbon nanotubes and Nano-Fe. *Water resources*, *41*(6), pp.719-727.

Chiriac, R., Carre, J., Perrodin, Y., Fine, L. and Letoffe, J.M., 2007. Characterisation of VOCs emitted by open cells receiving municipal solid waste. *Journal of hazardous materials*, *149*(2), pp.249-263.

Dao, M.T, Nguyen, T.T, Nguyen, X.D, LA, D.D, Nguyen, D.D., Chang, S.W, Chung, W.J. and Nguyen, V.K. (2020). Toxic Metal Adsorption from Aqueous Solution by Activated Biochars Produced from Macadamia Nutshell Waste. *Sustainability*, *12*(19), p.7909.

Dhankher, O.P., Pilon-Smits, E.A., Meagher, R.B. and Doty, S., 2012. Biotechnological approaches for phytoremediation. In *Plant biotechnology and agriculture* (pp. 309-328). Academic Press.

Edokpayi, J.N., Alayande, S.O., Adetoro, A. and Odiyo, J.O., 2020. The Equilibrium, Kinetics, and Thermodynamics Studies of the Sorption of Methylene Blue from Aqueous Solution Using Pulverized Raw Macadamia Nut Shells. *Journal of analytical methods in chemistry*, *2020*.

El-Behlil, M.A., El-Gezawi Sead, M. and Sabri, A., 2012. Volatile Organic Chemicals Removal from Contaminated Water using Air Stripping Low Profile Sieve Tray Towers. In *Sixteenth International Water Technology Conference.*

Fadaei, S., Moghadam, F.N, Hashemi, M. and Pourzamani, H (2017). BTEX removal from aqueous solution by modified multi-walled carbon nanotubes with ozone. *Anuario do Instituto de Geociencias*, *40*(1), pp.235-242.

Fayemiwo, O.M., Daramola, M.O. and Moothi, K., 2017. BTEX compounds in water-future trends and directions for water treatment. *Water SA*, *43*(4), pp.602-613.

Gowda, R., Nataraj, A.G. and Rao, N.M., 2012. Coconut leaves as a low cost adsorbent for the removal of nickel from electroplating effluents. *Int J Sci Eng Res*, *2*(12), pp.1-5.

Godambe, T. and Fulekar, M., 2017. Journal of Environmental Science and Pollution Research. *J. Environ. Sci*, *3*(3), pp.189-199.

Hackbarth, F.V., Vilar, V.J., De Souza, G.B., De Souza, S.M.G.U. and De Souza, A.A.U., 2014. Benzene, toluene and o-xylene (BTX) removal from aqueous solutions through adsorptive processes. *Adsorption*, *20*(4), pp.577-590.

Kemp, K.C., Baek, S.B., Lee, W.G., Meyyappan, M. and Kim, K.S., 2015. Activated carbon derived from waste coffee grounds for stable methane storage. *Nanotechnology*, *26*(38), pp.1-8

Pakade, V. E., Ntuli, T. D. and Ofomaja, A. E (2016). 'Biosorption of hexavalent chromium 128 from aqueous solutions by macadamia nutshell powder', Applied water science. Springer Berlin Heidelberg, 6, pp. 1–16. doi: 10.1007/s13201-016-0412-5.

Phele, M.J., Ejidike, I.P. and Mtunzi, F.M., 2019. Adsorption efficiency of activated macadamia nutshell for the removal Organochlorine pesticides: Endrin and 4, 4-DDT from aqueous solution. *Journal of Pharmaceutical Sciences and Research*, *11*(1), pp.258-262.

Pillai, S.K., Ramontja, J. and Ray, S.S., 2011. Amine functionalization of carbon nanotubes for the preparation of CNT based polylactide composites-A comparative study. *Nanostructured Materials and Nanotechnology V*, *549*, p.43.

Jawad, A.H., Mamat, N.F.H., Abdullah, M.F. and Ismail, K., 2017. Adsorption of methylene blue onto acid-treated mango peels: kinetic, equilibrium and thermodynamic study. *Desal Wat Treat*, *59*, pp.210-219.

Makhathini, T.P, and Sudesh R, 2017. Investigation of BTEX compounds onto polystyrenic resin.South African Journal of Chemical Engineering 23 (2017):71-80.

Mathur, A. K., Majumder, C. B. & Chatterjee, S. 2007. Combined removal of BTEX in air stream by using mixture of sugar cane bagasse, compost and GAC biofilter media. *Hazardous Materials,* 148**,** 64-74.

Mohammadi, L., Bazrafshan, E., Noroozifar, M., Ansari-moghaddam, A., Barahuie, F. and Balarak, D (2017). Adsorptive removal of Benzene and Toluene from aqueous environments by cupric oxide nanoparticles: kinetics and isotherm studies. Journal of Chemistry, 2017.

Mopoung, S., Moonsri, P., Palas, W. and Khumpai, S., 2015. Characterization and properties of activated carbon prepared from tamarind seeds by KOH activation for Fe (III) adsorption from aqueous solution. *The scientific world journal*, *2015*.

Njobuenwu, D.O., Amadi, S.A. and Ukpaka, P.C., 2005. Dissolution rate of BTEX contaminants in water. *The Canadian Journal of Chemical Engineering*, *83*(6), pp.985-989.

Pakade, V. E., Ntuli, T. D. and Ofomaja, A. E (2016). 'Biosorption of hexavalent chromium 128 from aqueous solutions by Macadamia nutshell powder', Applied Water Science. Springer Berlin Heidelberg, 6, pp. 1–16. doi: 10.1007/s13201-016-0412-5.

Pezoti Jr, O., Cazetta, A.L., Souza, I.P., Bedin, K.C., Martins, A.C., Silva, T.L. and Almeida, V.C., 2014. Adsorption studies of methylene blue onto ZnCl2-activated carbon produced from buriti shells (Mauritia flexuosa L.). *Journal of industrial and engineering chemistry*, *20*(6), pp.4401-4407.

Phele, M.J., Ejidike, I.P. and Mtunzi, F.M (2019). Adsorption efficiency of activated macadamia nutshell for the removal Organochlorine pesticides: Endrin and 4, 4-DDT from aqueous solution. *Journal of Pharmaceutical Sciences and Research*, *11*(1), pp.258-262.

Rodrigues, L.A., de Sousa Ribeiro, L.A., Thim, G.P., Ferreira, R.R., Alvarez-Mendez, M.O. and dos Reis Coutinho, A., 2013. Activated carbon derived from macadamia nut shells: an effective adsorbent for phenol removal. *Journal of Porous Materials*, *20*(4), pp.619-627.

Rotorcarb Activated Carbon. Rotorcarbs products [online]. Available at https: http://www.rotocarb.co.za.. [Accessed 3 August 2020]

Tsolele, R., Mtunzi, F.M., Klink, M.J. and Pakade, V.E., 2019. An alternative low-cost adsorbent for gold recovery from cyanide-leached liquors: Adsorption isotherm and kinetic studies. *Adsorption Science & Technology*, *37*(1-2), pp.3-23.

Toth, A.J. and Mizsey, P., 2015. Comparison of air and steam stripping: removal of organic halogen compounds from process wastewaters. *International journal of environmental science and technology*, *12*(4), pp.1321-1330

Sadare, O.O. and Daramola, M.O., 2019 a. Adsorptive desulfurization of dibenzothiophene (DBT) in model petroleum distillate using functionalized carbon nanotubes. Environmental Science and Pollution Research, 1-18. https://doi.org/10.1007/s11356-019-05953-x

Sadare, O.O. and Daramola, M.O., 2019 b. Adsorptive removal of dibenzothiophene from petroleum distillates using pomegranate leaf (Punica granatum) powder as a greener adsorbent. *Chemical Engineering Communications*, *206*(3), pp.333-345.

Saha, B., 2011. *Removal of benzene from wastewater by enzyme-catalyzed oxidative polymerization combined with a modified Fenton reaction*. University of Windsor (Canada).

Simate, G.S., Iyuke, S.E., Ndlovu, S., Heydenrych, M. and Walubita, L.F., 2012. Human health effects of residual carbon nanotubes and traditional water treatment chemicals in drinking water. Environment international, 39(1), pp.38-49.

Wongcharee, S., Aravinthan, V., Erdei, L. and SanongraJ, W (2017). Use of macadamia nut shell residues as magnetic nanosorbents. *International Biodeterioration & Biodegradation*, *124*, pp.276-287.

Wongcharee, S., Aravinthan, V., Erdei, L. and Sanongraj, W., 2018. Mesoporous activated carbon prepared from macadamia nut shell waste by carbon dioxide activation: C omparative

characterisation and study of methylene blue removal from aqueous solution. *Asia-Pacific Journal of Chemical Engineering*, *13*(2), p.2179.

Yah, C.S., Simate, G.S., Moothi, K., Maphutha, K.S. and Iyuke, S.E., 2011. Synthesis of large carbon nanotubes from ferrocene: the chemical vapour deposition technique. *Trends in Applied Sciences Research*, *6*(11), p.1270.